AN ABSTRACT OF THE DISSERTATION OF

<u>Amit Bashyal</u> for the degree of <u>Doctor of Philosophy</u> in <u>Physics</u> presented on <u>February 9, 2021</u>

Title: <u>DUNE and MINERvA Flux Studies and a Measurement of the Charged-Current Quasielastic Antineutrino Scattering Cross Section with $< E_\nu > \sim 6$ GeV on a CH Target</u>

Abstract approved: _____

Heidi M. Schellman

One of the biggest open questions in physics is the prevalence of matter over anti-matter in the present universe. One of possible answers lies in the violation of charge and parity symmetry in the lepton sector that would favor matter over anti-matter so that the universe becomes dominated by matter over time. Recent results from neutrino experiments like T2K and NOvA have indicated that there is CP violation in the leptonic sector [1]. However, the precise measurement of CP violation will require an unprecedented level of accuracy in these oscillation experiments. One of the challenges lies with the systematic uncertainties that come with the measurements, which include uncertainties related to the neutrino flux mod-

eling, interaction modeling and detector related systematic uncertainties.

The first part of this thesis will go through the challenges related to flux uncertainties. It will discuss the flux uncertainties related to hadron production in the LBNF beamline for the DUNE experiment. Hadron production models used in flux simulations vary widely depending on the simulation and choice of physics models used to simulate the hadron production. This thesis will explain the method of using existing hadron production data to constrain these uncertainties, a method which has been used in MINERvA experiment.

The second part of the thesis goes through the effect of possible flux mismodeling and MINERvA's approach to address this effect. In doing so, we discovered that the suspected mismodeling could also result from incorrect estimation of the energy scale of the muons. This project not only demonstrated the challenges of flux modeling but also led to a novel approach of using neutrino energy spectra to understand the correlation between detector and neutrino beamline parameters.

A high statistics measurement of the anti-neutrino scattering cross section in the charged current quasielastic (CCQE) channel is the final part of the thesis. The 2-body interactions in this channel have the advantage of allowing reconstruction of the interaction kinematics from the outgoing muon trajectory which can be measured very well. Double differential cross sections as a function of muon kinematics, one of the deliverables of this analysis, will

help future oscillation experiments understand their data. The cross-section as a function of the four-momentum transferred from the leptonic system to the hadronic system (Q_{QE}^2) can be used to test models used in simulating antineutrino interactions and the nuclear effects that can modify the predicted cross sections. Nuclear effects arise from the complex nuclear environment and both modify the initial scattering and change the fate of the particles produced from in neutrino-nucleus interactions. Study of nuclear effects will help to understand the structure of the atomic nucleus and its impact on neutrino interactions.

DUNE and MINERvA Flux Studies and a Measurement of the
Charged-Current Quasielastic Antineutrino Scattering Cross Section with
$< E_\nu >\sim$ 6 GeV on a CH Target

by

Amit Bashyal

A DISSERTATION

submitted to

Oregon State University

in partial fulfillment of
the requirements for the
degree of

Doctor of Philosophy

Presented February 9, 2021
Commencement June 2021

Doctor of Philosophy dissertation of Amit Bashyal presented on February 9, 2021.

APPROVED:

_____

Major Professor, representing Physics

_____

Head of the Department of Physics

_____

Dean of the Graduate School

I understand that my dissertation will become part of the permanent collection of Oregon State University libraries. My signature below authorizes release of my dissertation to any reader upon request.

_____

Amit Bashyal, Author

ACKNOWLEDGEMENTS

TABLE OF CONTENTS

TABLE OF CONTENTS (Continued)

TABLE OF CONTENTS (Continued)

LIST OF FIGURES

LIST OF FIGURES (Continued)

LIST OF FIGURES (Continued)

LIST OF FIGURES (Continued)

LIST OF FIGURES (Continued)

LIST OF TABLES

LIST OF TABLES (Continued)

LIST OF APPENDIX FIGURES

LIST OF APPENDIX TABLES

1 Neutrinos

1.1 Introduction

Neutrinos are electrically neutral elementary particles with an extremely small interaction cross-section. Since neutrinos are electrically neutral, have extremely small mass and rarely interact with matter (due to small cross-section), they can help us to probe the structure of the atomic nucleus, convey information from the far edges of the universe and also help us to understand the origin of matter in the universe. Since they rarely interact with matter, for a neutrino experiment to gather enough interactions to make any measurements, experiments need to have either an intense source of neutrinos or large detectors. We cannot control natural sources of neutrinos like radio-active decay of elements, solar or super novae neutrinos. However, we can control the intensity, energy spectrum and the type of neutrino beams in particle accelerators, making them a better candidate for neutrino experiments that require large statistics and known neutrino energy spectrum to do their physics measurements. The high intensity neutrino beams, Neutrinos from the Main Injector (NuMI) in the US and Tokai to Kamioka (T2K) in Japan are currently in operation, and a new Long Baseline Neutrino Facility (LBNF) is being built in the US. Experiments like NOvA (NuMI Off-axis

Neutrino Experiment) using the neutrinos from these beamlines will help to search for the answers to questions like origin of matter in the universe and asymmetry between matter and anti-matter (via Charge Parity or CP violation). Experiments like the MINERvA (Main Injector ν-A experiment) use accelerator neutrinos to measure neutrino cross-sections, the structure of the nucleus and the how the nuclear environment effects the neutrino-nucleon interaction.

The precision of these measurements depend upon our ability to understand the neutrino flux produced by the accelerators. Estimation of the neutrino flux and the uncertainties related to the flux usually becomes a major part of collaboration effort for any neutrino experiment. For experiments like DUNE aiming to reach the 5 σ sensitivities in CP violation, understanding the neutrino flux and constraining the flux related uncertainties significantly is very important. Similarly, studies done by MINERvA experiment have shown that sometimes mismodeling of flux parameters can look very similar to the mismodeling of the energy calibration in the detector. In this section, I will discuss the basics of neutrino physics and oscillations, and work by MINERvA and DUNE (anti) neutrino flux, and how this work impacts the broader global neutrino program.

The second part of this chapter will discuss the theory of neutrino nucleus interactions and cross-section measurements. One of the deliverables of this thesis is to measure the

antineutrino-nucleus cross-sections with a final topology consistent with charged-current quasi-elastic (CCQE) scattering.

1.2 Neutrinos in the Standard Model

The content of this section is based on section 1.2 of [128], [93] and [119]. The Standard Model of particle physics predicts 3 flavors of massless neutrinos, namely electron neutrino (ν_e), muon neutrino (ν_μ) and tau neutrino (ν_τ), that interact through weak charge and neutral current exchange. The flavor names come from the fact that the neutrinos are produced along with their lepton partners, for example:

$$n \rightarrow p + e^- + \bar{\nu}_e$$

$$\pi^+ \rightarrow \mu^+ + \nu_\mu$$

(1.1)

In the first reaction, which is the beta decay of the neutron, the electron is always accompanied by the electron anti-neutrino. Similarly in the second equation, the decay of a pion to a muon is always accompanied by ν_μ. Conservation of lepton flavor requires the flavor of the neutrino to match that of its lepton partner. Similarly, conservation of lepton number dictates whether a neutrino or an anti-neutrino is produced in a given reaction. For example, in the first reaction above, since the lepton number of electron is 1, the accompa-

nying neutrino should have lepton number -1 (hence $\bar{\nu}_e$) to match the lepton number 0 in the left hand side of the reaction.

The Standard Model predicts that neutrinos are massless. It implies that in neutrino experiments, charged current interactions by a beam of muon neutrino will always produce muons and a beam of electron neutrino will always produce electrons. However, experiments have found that neutrinos starting as muon neutrino sometimes produce an electron and vice versa. In 1998, the Super Kamiokande experiment confirmed that neutrinos change their flavor from one type to another type as they travel [77]. In 2015, the Nobel prize was awarded to Takaaki Kajita and Art McDonald for the discover of neutrino flavor transformation which shows neutrinos have mass [145]. The rest of this section will explain the basics of the neutrino oscillations.

1.2.1   Flavor and Mass Eigenstates of Neutrinos

Let us consider a W boson decay:

$$W^- \rightarrow l^- + \bar{\nu}_l \tag{1.2}$$

where $l = e, \mu, \tau$. ν_e, ν_μ and ν_τ are the weak interaction eigenstates of the neutrino. They are coupled with their lepton partners (like ν_e with electron and ν_μ with muon) in weak interactions. For a freely propagating massive neutrinos, the flavor states can be written as a superposition of mass eigenstates.

$$\nu_l = \sum_m U_{lm} \nu_m \tag{1.3}$$

Here, l represents the flavor eigenstate and m represents the mass eigenstate of the neutrino. U is a unitary rotation matrix i.e.

$$UU^\dagger = U^\dagger U = I \tag{1.4}$$

where I is an identity matrix. Hence, each flavor state of the neutrino ν_l is a super-position of the mass eigenstate (and vice versa). In the neutrino experiments, charged leptons (l) produced alongside neutrinos (ν_l) help us to identify the flavor of the neutrinos. Neutrinos of some flavor α that travel certain distance L can be detected as another flavor β such that $\alpha \neq \beta$ or $\alpha = \beta$. This phenomenon is called neutrino oscillation. The next section discusses the probability of neutrino oscillating from flavor α to β ($P(\nu_\alpha \to \nu_\beta)$).

1.2.2   Neutrino Oscillation

Neutrino oscillation usually refers to the change in neutrino flavor as neutrinos travel through space and time. Charged leptons produced alongside the neutrinos via weak interactions help us to determine the flavor of the neutrinos. In this section, we want to calculate the probability, $(P(\nu_\alpha \rightarrow \nu_\beta))$ of a neutrino of flavor α changing into another flavor β when it travels a distance L. Here $\alpha, \beta = e, \mu, \tau; \alpha \neq \beta$.

Since the flavor eigenstate ν_α is the superposition of mass eigenstates ν_i:

$$\nu_\alpha = \sum_i U_{\alpha i} \nu_i \tag{1.5}$$

Although the neutrinos are detected in their flavor eigenstates, all the calculations relevant to their oscillation are done in mass eigenstates. When a neutrino oscillates from flavor α to β, the contribution of mass eigenstate ν_i in the oscillation probability $P(\nu_\alpha \rightarrow \nu_\beta)$ depends upon:

- Contribution of ν_i for a neutrino ν_α produced in the source and is given by $U_{\alpha i}$.

- Contribution of ν_i to ν_α/ν_β when a neutrino travels from source to detector.

- Contribution of ν_i to ν_β when a neutrino ν_β is detected in the detector and is given by $U_{\beta i}^*$

A more detailed info on the mixing matrix $U^\dagger$ is given in section 1.2.3. While the contribution (or amplitude) of ν_i for the first and third item is given by the unitary matrix U, we need to calculate the contribution (amplitude) of ν_i for the second item. In the rest frame of the neutrino (ν_i), let:

- $|\nu_i(0)\rangle$ be the initial state of the neutrino (i.e. at the source)

- $|\nu_i(\tau_i)\rangle$ be the final state of the neutrino (i.e. at the detector) after travelling some time τ_i.

- m_i be the rest mass of the neutrino.

The time evolution of the state vector $\nu_i(\tau_i)$ is given by the Schrodinger's equation:

$$i\hbar\frac{\partial}{\partial\tau}|\nu_i(\tau_i)\rangle = m_i|\nu_i(\tau_i)\rangle \tag{1.6}$$

Let's use the natural units $\hbar = c = 1$ such that the above equation becomes:

$$i\frac{\partial}{\partial\tau_i}|\nu_i(\tau_i)\rangle = m_i|\nu_i(\tau_i)\rangle \tag{1.7}$$

The solution of this equation is:

$$|\nu_i(\tau_i)\rangle = e^{-m_i\tau_i}|\nu_i(0)\rangle \tag{1.8}$$

So, we can calculate the amplitude (in the neutrino rest frame) of ν_i when neutrino travels from source to detector in a given time τ_i as:

$$\langle \nu_i(0)|\nu_i(\tau_i)\rangle = e^{-m_i\tau_i} \tag{1.9}$$

Note that this amplitude is calculated in the rest frame. We can do the Lorentz transformation to find this amplitude in the lab frame. Let $E' = m_i$ be the energy of neutrino in the neutrino rest frame and E and p be the energy and momentum in the lab frame. Also, let t be the time required by the neutrino to travel from the source to the detector in the lab frame. Then,

$$E' = \gamma E_i + \gamma \beta p_i$$
$$m_i = \gamma E_i + \gamma \beta p_i \tag{1.10}$$
$$m_i\tau_i = \gamma E\tau_i + \gamma \beta p\tau_i$$

Using $\gamma = \frac{t}{\tau}$ and $L = \gamma\beta\tau$ (c = 1), where L is the distance between the source and the detector, the above equation can be written as:

$$m_i\tau_i = E_i t - Lp_i \tag{1.11}$$

Hence, the propagator term $m_i \tau_i$ has a time dependent term $E_i t$. Note that t here is the time taken by neutrino from its source to the detector in the lab frame. In practice, this time is unknown and the neutrino events measured by the detector is the average over this time t. If the two states with energy E_1 and E_2 (in lab frame) are created in the source, by the time they reach the detector, they will pick up the phase factors $e^{-iE_1 t}$ and $e^{-iE_2 t}$. The detector measurement involves the phase difference $e^{-i(E_1 - E_2)t}$ which disappears for a measurement over average time t [93]. Only the states with $E_i = E_j = E$ $(i \neq j)$ are measured. Now, we can rewrite equation 1.2.2 as:

$$m_i \tau_i = L p_i \tag{1.12}$$

And using special relativity, we can rewrite p_i as:

$$
\begin{aligned}
p_i &= \sqrt{E^2 - m_i^2} \\
p_i &= E - \frac{m_i^2}{2E}
\end{aligned}
\tag{1.13}
$$

assuming $m_i^2 \ll E^2$ (Taylor expansion). Finally, we can rewrite equation 1.9 as:

$$\langle \nu_i(0) | \nu_i(\tau_i) \rangle = e^{-i \frac{m_i^2}{2E} L} \tag{1.14}$$

And the amplitude of neutrino oscillation from flavor α to β is given as:

$$A(\nu_\alpha \to \nu_\beta) = \sum_i U_{\alpha i} e^{-i\frac{m_i^2}{2E}L} U_{\beta i}^* \tag{1.15}$$

And the probability of ν_α to ν_β is given by:

$$\begin{aligned}
P(\nu_\alpha \to \nu_\beta) &= |A(\nu_\alpha \to \nu_\beta)|^2 \\
&= [\sum_i U_{\alpha i} e^{-i\frac{m_i^2}{2E}L} U_{\beta i}^*]^* [\sum_j U_{\alpha j} e^{-i\frac{m_j^2}{2E}L} U_{\beta j}^*] \\
&= \sum_i \sum_j U_{\alpha i}^* U_{\beta i} U_{\alpha j} U_{\beta j}^* e^{i\frac{L}{2E}(m_j^2 - m_i^2)} \\
&= \sum_i U_{\alpha i}^* U_{\beta i} U_{\alpha i} U_{\beta i}^* + \sum_{i \neq j} U_{\alpha i}^* U_{\beta i} U_{\alpha j} U_{\beta j}^* e^{i\frac{L}{2E}(\Delta m_{ji}^2)}
\end{aligned} \tag{1.16}$$

Here $\Delta m_{ji}^2 = m_j^2 - m_i^2$. The exponential term $e^{i\frac{L}{2E}(\Delta m_{ji}^2)}$ can be written as:

$$\begin{aligned}
e^{i\frac{L}{2E}(\Delta m_{ji}^2)} &= \cos[\frac{L}{2E}(\Delta m_{ji}^2)] + i\sin[\frac{L}{2E}(\Delta m_{ji}^2)] \\
&= 1 - 2\sin^2[\frac{\frac{L}{2E}(\Delta m_{ji}^2)}{2}] + i\sin[\frac{L}{2E}(\Delta m_{ji}^2)]
\end{aligned} \tag{1.17}$$

Rewriting the exponential term of equation 1.16 as shown in equation 1.17,

$$P(\nu_\alpha \to \nu_\beta) = \sum_i U^*_{\alpha i} U_{\beta i} U_{\alpha i} U^*_{\beta i} + \sum_{i \neq j} U^*_{\alpha i} U_{\beta i} U_{\alpha i} U^*_{\beta j}$$

$$- 2 \sum_{i \neq j} U^*_{\alpha i} U_{\beta i} U_{\alpha i} U^*_{\beta j} \sin^2[\frac{L}{4E} \Delta m^2_{ji}] + \qquad (1.18)$$

$$i \sum_{i \neq j} U^*_{\alpha i} U_{\beta i} U_{\alpha i} U^*_{\beta j} \sin \frac{L}{2E} (\Delta m^2_{ji})$$

Equation 1.18 can be simplified as [119]:

$$P(\nu_\alpha \to \nu_\beta) = \delta_{\alpha\beta} - 4 \sum_{i > j} \mathcal{R}(U^*_{\alpha i} U_{\beta i} U_{\alpha j} U^*_{\beta j}) \sin^2[\Delta m^2_{ij} \frac{L}{4E}]$$

$$+ 2 \sum_{i > j} \mathcal{I}(U^*_{\alpha i} U_{\beta i} U_{\alpha j} U^*_{\beta j}) \sin[\Delta m^2_{ij} \frac{L}{2E}] \qquad (1.19)$$

In equation 1.19 $\mathcal{R}$ and $\mathcal{I}$ represent the real and imaginary terms respectively.

Based on equation 1.19 we can make following observations [31]:

- Observation of neutrino oscillation is a natural consequence of neutrinos having non-0 mass. If the neutrinos were mass-less $\Delta m^2_{ij} = 0$ reducing equation 1.19 to $\delta_{\alpha\beta} = 0$ for $\alpha \neq \beta$ which means neutrino oscillation is not possible if neutrinos were massless.

- To calculate the oscillation probability of anti-neutrinos ($P(\bar{\nu}_\alpha \to \bar{\nu}_\beta)$), the imaginary term in equation 1.18 needs to reverse sign. As we will see in equation 1.21 in next
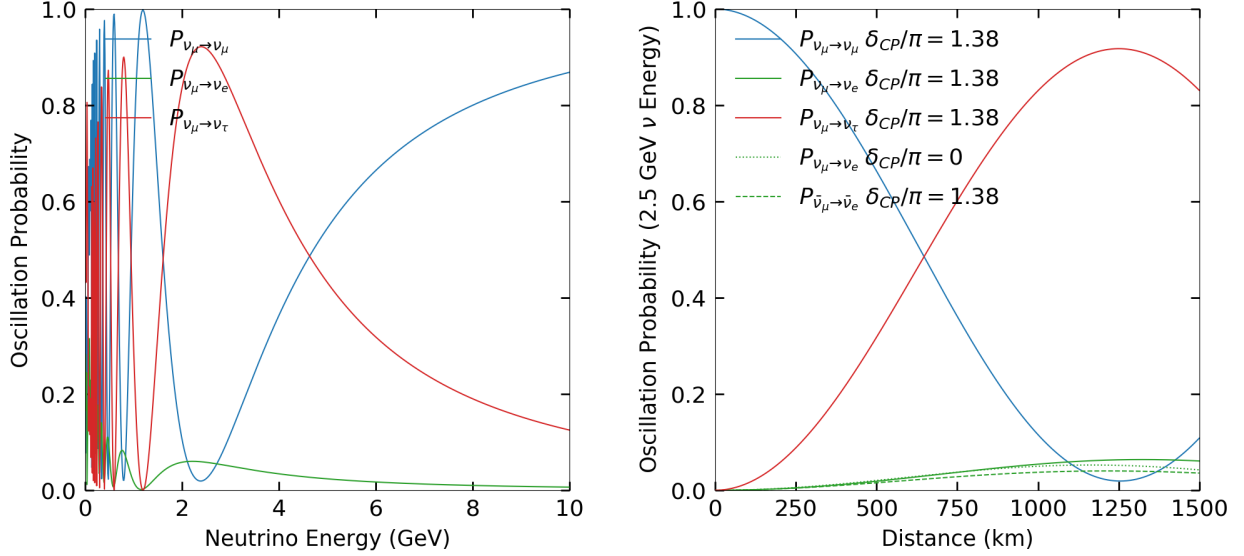
Figure 1.1: Left figure shows the probability of ν_μ oscillations as a function of ν energy at a distance of 1200 km (location of DUNE far detector). Right figure shows the probability of 2.5 GeV ν_μ oscillations as a function of distance for different values of δ_{CP} Note that the peak of oscillations is at around 1200 km which is the location of DUNE far detector. As we will see in later chapters, the DUNE neutrino flux is optimized to have the flux peak near 2.5 GeV.

section, the imaginary term of the mixing matrix is related to the CP violation. $P(\bar{\nu}_\alpha \to \bar{\nu}_\beta) = P(\nu_\alpha \to \nu_\beta)$ if there is no CP violation and vice versa.

- All the terms in equation 1.19 are constant except for $\frac{L}{E}$ which means the probability of neutrino oscillation depends upon the distance between source and detector and the energy of the neutrino.

- The neutrino oscillation equation has the term Δm_{ij}^2 which means oscillation alone can
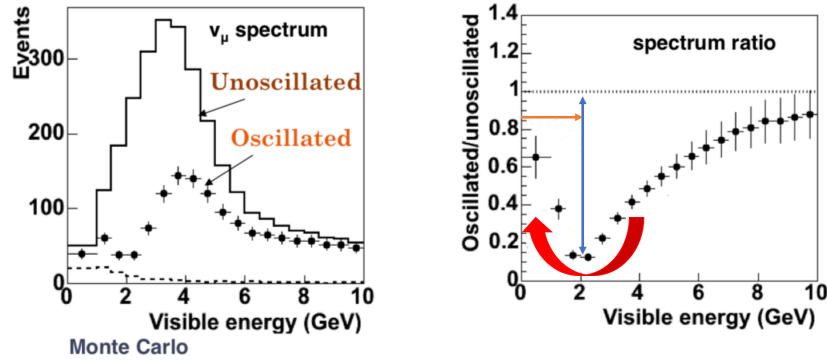
Figure 1.2: Left figure shows the ν_μ events with oscillation (black dots) and without oscillation (solid black lines) as they travel from Fermilab, IL to a MINOS experiment detector 734 km away in Minnesota [7]. Right figure shows the ratio of oscillated neutrino events to un-oscillated(ν_μ events that didn't oscillate by the time they reach the MINOS detector) events. In the right figure, most of the ν_μ events oscillate to ν_e events at 2 GeV neutrino energy. This is called "oscillation maxima". The location of oscillation maxima (orange line) can tell us about Δm^2, the size of oscillation maxima (blue line) can tell us about the mixing angle θ. The sinusoidal shape of the oscillation (curved red arrow) comes from the $\sin \frac{1}{E}$ (for a constant L) term of the oscillation equation. Figure taken from [152].

only tell us the difference in masses.

1.2.3   PMNS Matrix

For the 3 flavor standard scenario, the mixing matrix is known as PonteCorvo-Maki-Nakagawa-Sakata (PMNS) matrix and is given as[2]:

$$
\begin{bmatrix} |U_{e1}| & |U_{e2}| & |U_{e3}| \\ |U_{\mu1}| & |U_{\mu2}| & |U_{\mu3}| \\ |U_{\tau1}| & |U_{\tau2}| & |U_{\tau3}| \end{bmatrix} \approx \begin{bmatrix} 0.8 & 0.5 & 0.1 \\ 0.5 & 0.6 & 0.7 \\ 0.3 & 0.6 & 0.7 \end{bmatrix}
\tag{1.20}
$$

Note that these numbers are just the current measured values and with more data and new experiments, these numbers might change and the errors on these numbers will shrink. Since this matrix is unitary, it will preserve the length of any vector it acts upon and conserve total probability. This condition is only valid for 3 neutrino flavor/mass eigenstate paradigm. This matrix can be rewritten to decompose into 3 mixing angles and 3 CP violating phases.

$$
U_{PMNS} = U_{23}(\theta_{23}, 0)U_{13}(\theta_{13}, \delta)U_{12}(\theta_{12}, 0)
$$

$$
= \begin{bmatrix} 1 & 0 & 0 \\ 0 & c_{23} & s_{23} \\ 0 & -s_{23} & c_{23} \end{bmatrix} \begin{bmatrix} c_{13} & 0 & s_{13}e^{-i\delta} \\ 0 & 1 & 0 \\ -s_{13}e^{i\delta} & 0 & c_{13} \end{bmatrix} \begin{bmatrix} c_{12} & s_{12} & 0 \\ -s_{12} & c_{12} & 0 \\ 0 & 0 & 1 \end{bmatrix}
\tag{1.21}
$$
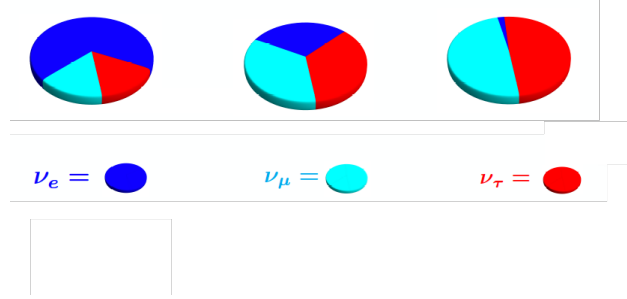
Figure 1.3: Mixing of the flavor eigenstates in each of the 3 mass eigenstates of the neutrinos

Here $c_{ij} = cos\theta_{ij}$ and $s_{ij} = sin\theta_{ij}$ and δ is the amount of CP violation in lepton sector. The neutrino flavor state can be written as:

$$\begin{bmatrix} \nu_e \\ \nu_\mu \\ \nu_\tau \end{bmatrix} = \begin{bmatrix} U_{e1} & U_{e2} & U_{e3} \\ U_{\mu1} & U_{\mu2} & U_{\mu3} \\ U_{\tau1} & U_{\tau2} & U_{\tau3} \end{bmatrix} \begin{bmatrix} \nu_1 \\ \nu_2 \\ \nu_3 \end{bmatrix}. \tag{1.22}$$

This mixing of flavor and mass eigenstate can be visualized as in figure 1.3. Equation 1.19 shows that the oscillation of neutrinos depends upon the squared difference of mass eigenstates (Δm_{ij}^2 where $i, j = 1, 2, 3$). The value of δ_{CP} (delta CP) determines how different neutrino and anti-neutrino oscillations are.

1.2.3.1   Neutrino Mass Ordering

Neutrino oscillation depends upon the squared difference of the mass eigenstates ($\Delta m_{ij}^2 = m_i^2 - m_j^2$) as discussed in section 1.2.2. We do not know the absolute masses of each of these eigenstates and since the mass difference is squared, the ordering of the mass states is also unknown (i.e we do not know heaviest to lightest neutrino masses). Results of all the current neutrino oscillation experiments can be fitted in terms of two squared mass differences i.e. $\Delta m_{31}^2 \approx 2.5 \times 10^{-3} eV^2$ and $\Delta m_{21}^2 \approx 7.6 \times 10^{-5} eV^2$ [54]. The mass splitting Δm_{21}^2 is also called solar mass splitting and measured via the solar neutrinos (electron neutrinos produced in the sun). Δm_{31}^2 also known as the atmospheric neutrino splitting and is measured via the neutrinos produced in the atmosphere of the earth. They are usually produced when cosmic ray particles (usually proton) hit a nucleus in the air around 15 km above us. The huge difference between the two splitting indicates that at least one of the mass eigenstate is very heavy (normal ordering) or very light (inverted ordering) compared to the other two mass states.

Available data on neutrino oscillation prefers the normal mass ordering at a nearly 3 σ level [54].

   With the available data on mass splitting, the lower and upper bound on two neutrino

mass eigenstate is:

$$[55] \quad \begin{aligned} \sqrt{\Delta m_{21}^2} &\approx 8meV \\ \sqrt{\Delta m_{31}^2} &\approx 50meV. \end{aligned} \tag{1.23}$$

The sum of three neutrino eigenstates $\sum m_\nu = m_1 + m_2 + m_3$ can be written in terms of the mass splitting as:

$$\sum m_\nu^{NO} = m_1 + \sqrt{m_1^2 + \Delta m_{21}^2} + \sqrt{m_1^2 + \Delta m_{31}^2} \tag{1.24}$$

$$\sum m_\nu^{IO} = m_3 + \sqrt{m_3^2 + \Delta m_{31}^2} + \sqrt{m_3^2 + \Delta m_{31}^2 + \Delta m_{21}^2}. \tag{1.25}$$

In the normal ordering (NO), the lightest mass is m_1 and in inverted ordering (IO), it is m_3. With the available current data, the lower bound on $\sum m_\nu^{IO}$ is 0.10 eV/c^2 and $\sum m_\nu^{NO}$ is 0.06 eV/c^2 [55]. Neutrinos produced in supernova explosion (by looking at the time of flight of neutrinos and photons from the super nova explosion events) [107] and neutrino-less tritium decay experiments like KATRIN (by looking at the spectrum of tritium decays) [125] are some of available best candidates to measure the absolute masses of neutrinos.
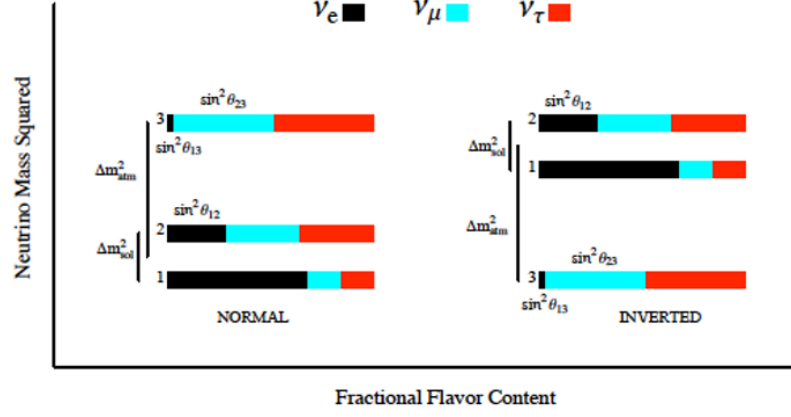
Figure 1.4: Ordering of mass states in two different scenarios. The figure also shows the experiment types from which the square difference of these mass states are extracted.

1.2.3.2 Mixing Angles and CP violation term

The mixing matrix can be parametrized by 3 mixing angles $(\theta_{12}, \theta_{23}, \theta_{13})$ and a CP violation term δ_{CP} as shown in equation 1.21. As of 2018, according to the particle data group (PDG) [160], current best estimates on the mixing angles and δ_{CP} are given in table 1.1. The values

Mixing Matrix Parameters	σ	Best fit values	Value range for Allowed σ
$\sin^2 \theta_{23}$ (Normal Ordering)	3	0.425	0.381-0.615
$\sin^2 \theta_{23}$ (Inverted Ordering)	3	0.58	0.384 - 0.636
$\sin^2 \theta_{13}$ (Normal Ordering)	3	0.0215	0.0190 - 0.0240
$\sin^2 \theta_{13}$ (Inverted Ordering)	3	0.0216	0.0190-0.0242
$\sin^2 \theta_{12}$	3	0.297	0.250-0.354
δ_{CP}/π (Normal Ordering)	2	1.38	1.0-1.9
δ_{CP}/π (Inverted Ordering)	2	1.31	0.92-1.88

Table 1.1: Current best estimates of mixing angles and δ_{CP} in the PMNS matrix. Numbers taken from [160].

of δ_{CP} and the mass ordering are not yet known. The latest measurements published by NOvA [5] and T2K [1] strongly disfavor the CP conserving values ($\delta_{CP} = 0, \pi$) and indicate maximal CP violation. NOvA shows some preference to normal ordering over inverted ordering of mass eigenstates.

Neutrino oscillation experiments can only measure the neutrino interactions in the detector. Neutrinos, being electrically neutral, will not leave the evidence of their presence except in the interactions via the electroweak force with the electrons or the nucleons. The energy of the neutrino can be estimated by measuring the energy and type of the particles produced by the interaction. However, the physics processes inside the nucleus modifies the energy seen by the detector and final particles that exit the nucleus. The physics inside the atomic nucleus is not well known and the theoretical models that we use to simulate and understand these nuclear effects are not accurate enough to describe these physics processes over a wide neutrino energy range. A more detailed discussion of nuclear models is given in section 1.7. By measuring the neutrino nucleus cross-section, these models can be tested and improved which in turn can help the oscillation experiments to reach their physics goal. A more detailed discussion on cross-section models that is relevant to the cross-section measurement part of this thesis is given in 1.4 and chapter 6 goes through the measurement of neutrino nucleus interaction in a particular channel (charged current quasi elastic) and how cross-

section measurements can test measured data against predictions made by nuclear models and help to improve them.

1.3   Neutrino Nucleus Interactions

Neutrino-nucleus interactions are characterized by the type of incoming neutrinos and outgoing leptons and hadrons. At different energy scales, the neutrino interacts with the nucleus in different ways. In fact, the goal of cross-section measurement experiments like MINERvA is to study these interactions that happen at different energy scales. This section will briefly go through the various types of neutrino-nucleon interactions that happen in energy scales in which experiments like MINERvA and DUNE are sensitive. Since the aim of this thesis is to do a cross-section measurement for a neutrino-nucleus scattering process, only the relevant scattering processes are explained. A comprehensive plot of neutrino cross-sections for the processes described below is shown in figure 1.5.

1.3.0.1   Neutrino Nucleon Scattering at Intermediate Energy

In the neutrino energy range of 0.1 to 20 GeV, various type of scattering processes come into play ranging from purely elastic to inelastic ones [76]. A brief description of neutrino scattering at very low and low energies are also given in [76].
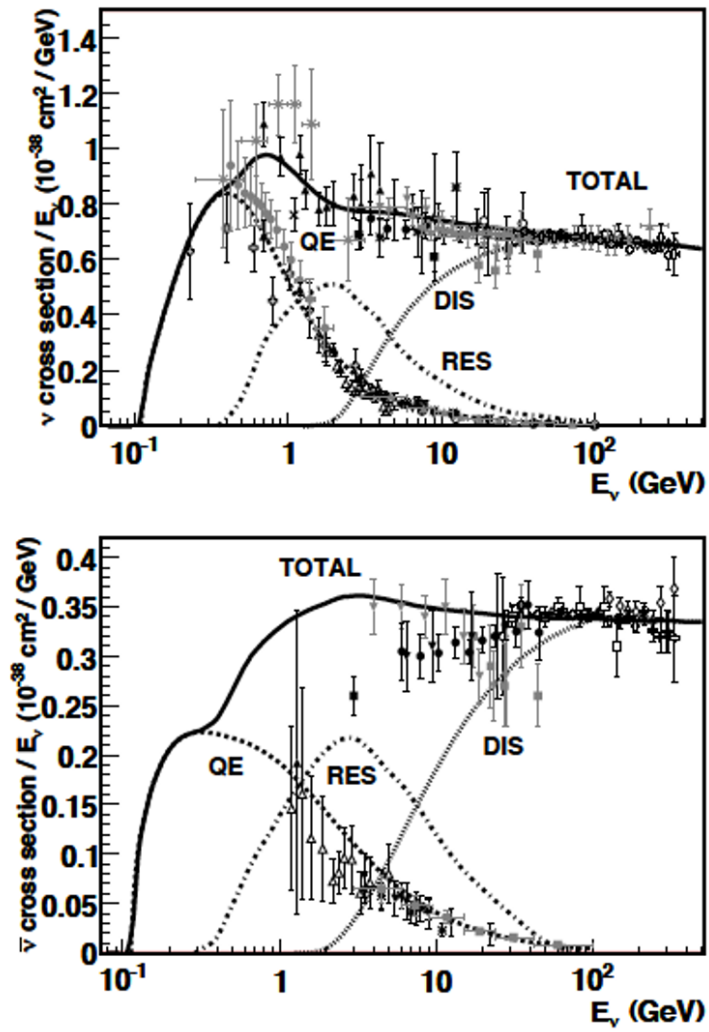
Figure 1.5: Total neutrino (top) and anti-neutrino(bottom) per nucleon cross-section for charged current processes. The X axis is the neutrino energy (in GeV) in log axis to show the cross-section over wide range of neutrino energies. Figure taken from [76].

1.3.0.2   Elastic Scattering

Elastic scattering off the nucleon occurs when a neutral Z^0 boson is exchanged.

$$\nu_l + N \rightarrow \nu_l + N \tag{1.26}$$

Here N is the nucleon (n,p). Note that this scattering is still off of the nucleon. The elastic processes dominate the neutrino-nucleon scattering cross-section from few hundred MeV to around 1 GeV.

1.3.0.3   Charge current Quasi-elastic (QE)

Quasi Elastic (QE) or Charged Current Quasi Elastic (CCQE) processes are similar to the elastic ones except they are mediated by the charged $W^\pm$ boson. An example of this reaction is:

$$\bar{\nu}_\mu + p \rightarrow \mu^+ + n$$

Assuming the target nucleus is rest, we can reconstruct the energy of the incoming neutrino for CCQE process as:

$$E_\nu^{QE} = \frac{m_n^2 - (m_p - E_b)^2 - m_\mu^2 + 2(m_p - E_b)E_\mu}{2(m_p - E_b - E_\mu + p_\mu \cos\theta_\mu)}$$
$$Q_{QE}^2 = 2E_\nu^{QE}(E_\mu - p_\mu \cos\theta_\mu) - m_\mu^2 \tag{1.27}$$

As we will see in section 6.5 of this thesis, the nucleon is not at rest and sometimes nuclear effects modify the final state particles making it look like a non CCQE process. Final state particles are the particles that exit the nucleus after neutrino-nucleon interaction (in the above example neutron).

1.3.0.4   Charge Current Resonances (RES)

Neutrinos in the energy range of few hundred MeV to few GeV can interact with the nucleons and excite them to resonance states like Δ which immediately decay to give mesons like pions and kaons along with nucleons. The resonance process dominates the neutrino energy range between 1 and 4 GeV. Delta particles with short life will quickly decay to give pions and nucleons. An example resonance interaction is:

$$\bar{\nu}_\mu + n \rightarrow \mu^+ + \Delta^-.$$

However the Δ particle is short-lived and quickly decays:

$$\Delta^- \to n + \pi^-.$$

Sometimes, the π^- might get absorbed in the nucleus leaving only neutron to exit the nucleus. Since the particles that actually exit the nucleus, in this case are μ^+ and n, it will look like a CCQE process. This is an example where a resonance process fakes to be a CCQE process. A more detailed discussion of processes like these that will complicate the true CCQE processes (as explained in section 1.3.0.3) is given in chapter 6.

1.3.0.5   Charge Current Deep Inelastic (DIS)

At high enough neutrino energy, the neutrino can probe inside the nucleons and scatter off of quarks. DIS or Deep Inelastic processes are characterized by the production of hadron showers resulting from the breaking of the nucleons. Beyond few GeV, all the neutrino-nucleus scatterings are dominated by DIS processes.

1.4   Theory of Neutrino Nucleus Cross-Sections

This section will go through the theory of neutrino cross-section but mainly focuses on the Charged Current Quasi-Elastic (CCQE) (see figure 1.13) channel cross-section. Neutrinos interact with the matter with the exchange of $W^{\pm}$ and Z bosons via the electroweak interaction. Because neutrinos interact with the nucleons, the cross-sections are modeled as a function of nucleon parameters. At very high energies where the neutrinos probe into the nucleons themselves, the cross-sections are parameterized as a function of partons or quarks. Hence neutrino cross-section measurements are not only important for oscillation experiments, but also for understanding the structure of the nucleus and nucleons themselves.

1.5   Importance of Neutrino Cross-section measurements

Recall that the probability of a ν_μ to oscillate to a ν_e is given by:

$$P_{\nu_\mu \to \nu_e} \approx \sin^2 2\theta \sin^2(\frac{\Delta m^2 L}{4E}). \tag{1.28}$$

To observe this oscillation, a near detector is placed near the source of the neutrino beam of energy E to characterize the intense muon neutrino beam and a far detector is placed at some distance L to measure the oscillated neutrinos. The quantity that is being measured

is:

$$P_{\nu_\mu \to \nu_e}(E, L) \propto \frac{\Phi_{\nu_e}(E, L)}{\Phi_{\nu_\mu}(E, 0)} \tag{1.29}$$

where Φ_{ν_μ} and Φ_{ν_e} are the muon neutrino flux(seen by the near detector) and oscillated electron neutrino flux (seen by the far detector) per steradian. However, the detectors measure the event rates and not the flux directly. The event rates seen by the detector then is given by:

$$N_e(E_{rec}, L) \propto \sum_i \Phi_e(E, L)\sigma_i(E)f_{\sigma i}(E, Erec)dEdM \tag{1.30}$$

where $\Phi_e(E, L)$ is the neutrino flux, $\sigma_i(E)$ is the cross-section of a neutrino nucleon interaction in some channel i (like CCQE,CCRES or DIS as described in 1.3.0.1),f_σ is the smearing matrix that maps the true neutrino energy (E) to the reconstructed neutrino energy E_{rec} and depends upon detector properties. To measure the neutrino oscillations, an estimation of the flux is made as described later in section 3.3 of the thesis. The second term $\sigma_e(E)$ is the cross-section of a neutrino nucleus interaction in some channel i (For example CCQE, RES or DIS as described in 1.3.0.1). The summation over i is to account for all possible neutrino nucleus interactions at that given energy E. The third term $f_{\sigma i}$ is the smearing matrix that maps the true neutrino energy (E) to the reconstructed neutrino energy E_{rec} and depends upon the the detector properties and M is the mass of the target nucleon. We observe neu-

trino events, and want to measure oscillation parameter that modifies the neutrino flux. In order to extract the parameters from the event rate, we need a model of all the terms in the above equation. While the $f_\sigma(E)$ depends upon our knowledge of the detector used for the measurement, $\sigma(E)$ depends upon the cross-section modeling and systematics uncertainties on those modelings. Experiments like DUNE and HK which aim to resolve the ambiguity regarding the neutrino mass ordering and CP violation will have larger uncertainties from cross-section modeling than statistics.

Figure 1.6 shows the sensitivity of the DUNE experiment to the neutrino mass hierarchy [3]. The 100% sensitivity means the experiment is going to be sensitive to the complete parameters phase space that goes into determining mass hierarchy. Similarly, figure 1.7 shows the effect of different systematic uncertainties scenarios on CP violation sensitivity. Recent T2K results on δ_{CP} violation had an overall systematic uncertainty from cross-section modeling of around 3% (4%) for ν_μ ($\bar{\nu}_\mu$) [1] and [62]. DUNE needs to constrain these systematics to 2% to achieve its physics goal. Current cross-section models, which are relatively accurate in simpler nuclei like hydrogen and deuterium, cannot model the nuclear effects which change the final state particles (particles that exit the target nucleus after interaction with the incoming neutrino probe). Cross-section measurements with heavier targets will help to reduce uncertainties and help current and future oscillation experiments.
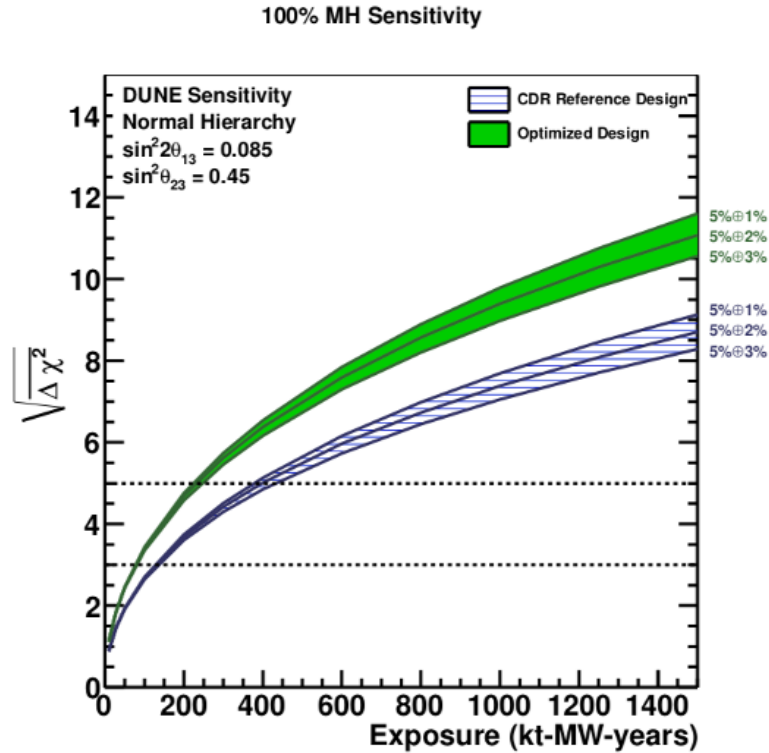
Figure 1.6: Sensitivity to the mass ordering as a function of beam exposure on the data. The exposure has the units for KT-MW-Years (kilo tonnes to account for the fiducial volume of the neutrino detector, MW to account for the intensity of the beam and years to account for the duration for which the detector gets the beam). The 2 bands shows the sensitivity for two different beam designs. The solid green is the beam design adopted by the LBNF. The numbers $5\% \bigoplus X\%$ where $X = 1, 2, 3$ are the normalization uncertainty on ν_μ (5%) with different assumed normalization uncertainties on ν_e which depend upon the cross-section modeling. Figure from [3].

CP Violation Sensitivity
50% δ_CP Coverage
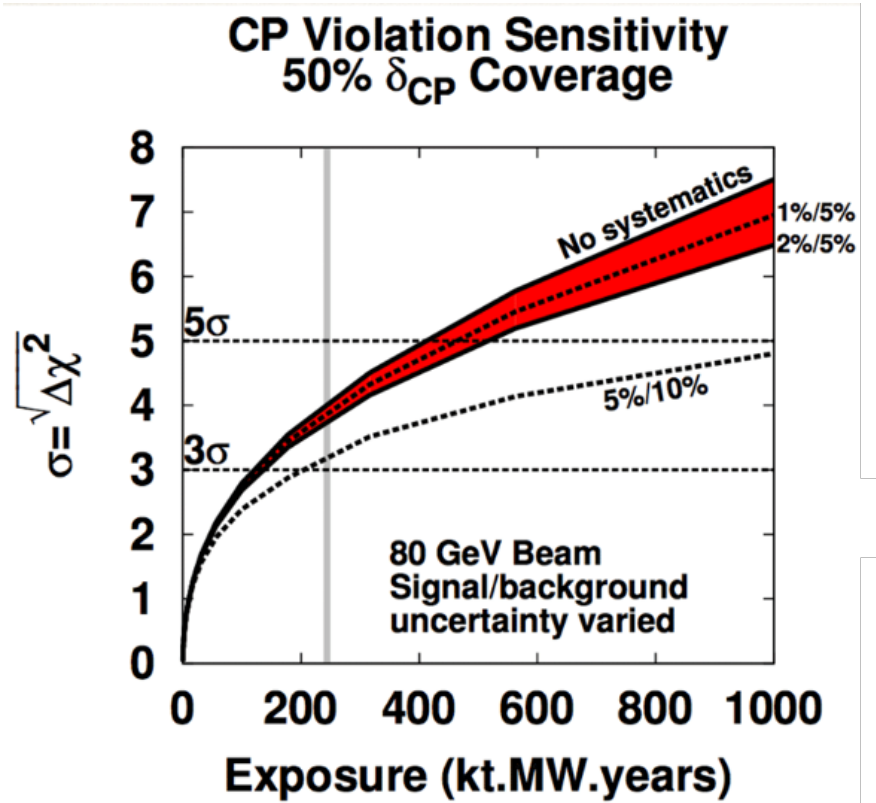
Figure 1.7: Sensitivity of the DUNE to 50% of the possible δ_{CP} values as a function of exposure. Without taking systematics into account, DUNE reaches sensitivity of over 5σ in just 400 kt.MW.years exposure. With 2% absolute uncertainty on ν_e event normalization and 5% on NuMI event rate normalization, it takes 500 kt.MW.years exposure. Figure taken from [33].

Neutrino experiments rely on neutrino MC generators like GENIE [25], NuWro [80], GIBUU [102] etc to model the neutrino-nucleus interactions. In experiments like MINERvA , DUNE, NOvA etc, the target nuclei are made of heavier materials like carbon, lead, iron (MINERvA), water (MINERvA and T2K), mineral oil (NOvA) and argon (DUNE,MicroBooNE, Mini-BooNE, ArgoNeut etc). MC generators need to account for the nuclear effects that take place in these complex nuclei as shown in figure 1.8. Not all models implemented in the generators might account for all nuclear effects. Similarly, some models are only valid up to certain kinematic regions or for certain neutrino flavors only. Cross-section models that are used in the generators are based on simple but well understood physics models. Experimental results are used to constrain and improve these models. This circular process of using models to do experimental measurements and using the experimental data to constrain the same model helps to expand the simple cross-section interaction models to heavier nuclei and cover larger phase space. Similarly, they will also help to understand the overall nuclear structure of the nucleons.
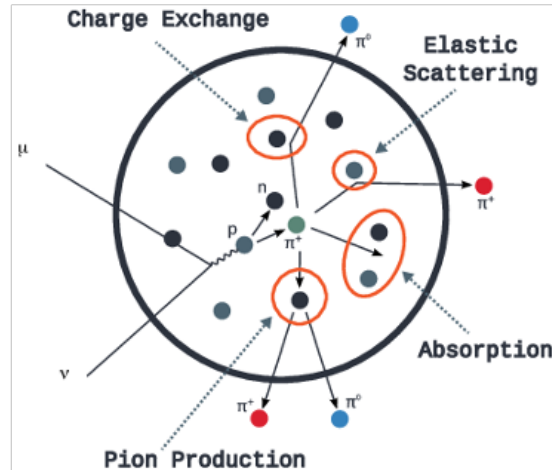
Figure 1.8: Schematic diagram showing various possible interactions that take place in the nuclei when a neutrino interacts with the proton. Although a cascade of interactions happen inside the nucleus producing various intermediary particles, only a muon, 2 neutral pions (π^0) and 2 charged pions (π^+) exit the nucleus and can be detected by the detector. These particles are called final state particles and we can only estimate the possible interactions of these final state particles before exiting the nucleus.

Figure 1.9: Experimental setup of a fixed target experiment with an incoming beam of N_i particles on a solid target of surface area S and length d.

1.6   Overview of CCQE Neutrino Nucleus Cross-section

1.6.1   Cross-section: A Basic Definition

For a fixed target experiments like neutrino experiments, the experimental setup can be roughly represented as shown in figure 1.9. In the figure:

- N_i is the number of incoming neutrinos through the detector.

- S is the surface area of the detector.

- d is the length of the detector.

Let ρ be the number density of the detector material. Then the number of target materials per unit area is ρd. If the rate of interaction between the incoming particle and the detector material is given by $\frac{dN_r}{dt}$, then this rate can be calculated as:

$$\frac{dN_r}{dt} = \sigma_r \frac{dN_i}{dt} \rho d \tag{1.31}$$

Here σ_r is the cross-section for the particular interaction and can be rewritten as:

$$\sigma_r = \frac{N_r}{N_i} \frac{1}{\rho d} \tag{1.32}$$

The term $\frac{N_r}{N_i}$ is the probability that an interaction happens and this term can be rewritten as:

$$\frac{N_r}{N_i} = \sigma_r \rho d$$

The second term in the RHS can be related to the total number of target nuclei and the area of the detector seen by the neutrinos as:

$$\frac{N_r}{N_i} = \sigma_r \frac{N}{S}$$

Note that N and S are not the total target nuclei and the surface area of the detector but the total target nuclei seen by the incoming beam and the surface area that is illuminated by the incoming beam. Hence, in a very rough sense, the cross-section can be defined as the effective area of the target seen by the incoming beam.

In the next few sections, we will go through the cross-section for scattering processes. To make the transition smooth, we will look at the lepton-lepton scattering in section 1.6.2, lepton-nucleon scattering in section 1.6.3 and finally neutrino-lepton scattering in section 1.6.4.

1.6.2   Scattering Cross-section: Lepton-lepton scattering

For a scattering process given by :

$$1 + 2 \rightarrow 3 + 4 + 5 + ... + n$$

the cross-section formula is given by [85]:

$$\sigma = \frac{S\hbar^2}{4\sqrt{(p_1.p_2^2 - (m_1 m_2 c^2)^3}} \int |\mathcal{M}^2|(2\pi^2)^4 \delta^4(p_1 + p_2 - p_3 - p_4 - p_5... - p_n) \times$$
$$\prod_{j=3}^{n} 2\pi\delta(p_j^2 - m_j^2 c^2)\theta(p_j^0)\frac{d^4 p_j}{(2\pi^4)} \tag{1.33}$$

Here, $\mathcal{M}$ is the amplitude of the reaction which contains the dynamics of the scattering process. S is the statistical factor which takes into account the double counting of scattered particles (for example, if the reaction is $A + B \rightarrow a + a + b + b + b$, then $S = \frac{1}{2!}\frac{1}{3!}$). The first delta function ensures that the momentum is conserved in the reaction and the second one ensures that the outgoing particles are on their mass shell. The simplest EM scattering process is given by Mott Scattering process: $\mu^- + e^- \rightarrow \mu^- + e^-$. This is the scattering of two point body objects by the exchange of a photon (γ). The differential cross-section for Mott scattering is given by:

$$\frac{d\sigma}{d\Omega} = (\frac{\hbar}{8\pi m_\mu c})^2 |\mathcal{M}|^2 \tag{1.34}$$
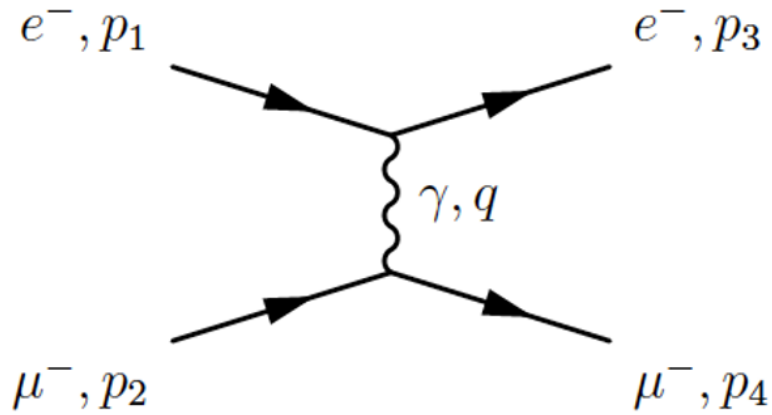
Figure 1.10: Feynman diagram of Mott Scattering showing electron to muon scattering via the exchange of photon. Figure taken from [128].

where the amplitude $\mathcal{M}$ contains the dynamics of the interaction and is given by:

$$\mathcal{M} = \frac{g_e^2}{(p_1 - p_3)^2)}$$

$$[\bar{u}^{s3}(p3)\gamma^\mu u^{s1}(p_1)]$$ (1.35)

$$[\bar{u}^{s4}(p_4)\gamma_\mu u^{s2}(p_2)]$$

Here, $u^{sn}(p_n)$ corresponds to the spin sn and momentum p_n of the nth lepton in the reaction

and each of the spin states are given by:

$u^1 =$

$$N \begin{pmatrix} 1 \\ 0 \\ \frac{(p_z)}{E+mc^2} \\ \frac{c(p_x+ip_y)}{E+mc^2} \end{pmatrix}$$

and $u^2 =$

$$N \begin{pmatrix} 0 \\ 1 \\ \frac{c(p_x-ip_y)}{E+mc^2} \\ \frac{(c-p_z)}{E+mc^2} \end{pmatrix}$$

Here, N is the Normalization factor. Going back to the the term $[\bar{u}^{s3}(p3)\gamma^\mu u^{s1}(p_1)]$, expanding it over all all dirac matrices becomes:

$$\prod_{\mu=0}^{3} \bar{u}^{s3}(p3)\gamma^\mu u^{s1}(p_1) \tag{1.36}$$

This amplitude $\mathcal{M}$ can be found using the method of trace as:

$$|\mathcal{M}|^2 = L^{\mu\nu}_{electron} L^{muon}_{\mu\nu} \tag{1.37}$$

as given in [85] where:

$$L^{\mu\nu}_{electron} = 2p_1^{\mu}p_3^{\nu} + p_1^{\nu}p_3^{\mu} + g^{\mu\nu}[(m_ec)^2 - (p_1.p_3)] \tag{1.38}$$

The term for muon will also be similar. Following the procedure from chapter 7 of [85], the differential cross-section for the Mott scattering is given by:

$$\frac{d\sigma}{d\Omega} = \left(\frac{\alpha\hbar}{2\mathbf{p}^2\sin^2(\theta/2)}\right)^2[(mc)^2 + \mathbf{p}^2\cos^2(\theta/2)] \tag{1.39}$$

Here, α is the fine structure constant and is given by $\approx 1/137$. Since the coupling constant $g_e = \sqrt{4\pi\alpha}$ is very small, higher order contributions have negligible contributions in the overall scattering. It is important to notice that this scattering process only includes the Dirac matrices and spin information of the particles to calculate the final cross-section. Compared to scattering with composite particles, Mott scattering process is relatively simple but the rules of cross-section calculations are similar for all scattering processes.

Since the cross-section calculation mostly revolves around solving the amplitude $\mathcal{M}$ which depends upon the kinematics around the vertex of the Feynman diagram of the interaction, we can try to understand the complexity of the scattering processes involving nucleons.

1.6.3   Scattering Cross-section:Lepton-nucleon scattering

Unlike the scattering off of point like objects, scattering off of a composite structure like a proton or a neutron needs to take into account that the electric and magnetic charge are distributed over some finite area. These distributions are accounted by the terms called form factors. Rewriting the amplitude for an electron proton reaction:

$$|\mathcal{M}|^2 = \frac{g_e^4}{q^4} L_{electron}^{\mu\nu} K_{\mu\nu \; proton}. \tag{1.40}$$

Here, $K_{\mu\nu}$ is a second rank tensor and depends upon the variables p_2, p_4 and q in figure 1.11. The term $K_{\mu\nu}$ describes the photon proton vertex (the shaded circle in figure 1.11) and is a second rank tensor which is constructed out of two 4 momenta vectors (incoming and outgoing proton momenta).

$$[85] K^{\mu\nu} = -K_1 g^{\mu\nu} + \frac{K_2}{(Mc)^2} p^\mu p^\nu + \frac{K_4}{(Mc)^2} q^\mu q^\nu + \frac{K_5}{(Mc)^2} (p^\mu q^\nu + p^\nu q^\mu) \tag{1.41}$$

Again using the results from [85],

$$K^{\mu\nu} = K_1 \left(-g_{\mu\nu} + \frac{q^\mu q^\nu}{q^2} \right) + \frac{K_2}{Mc^2} \left(p^\mu + \frac{1}{1} q^\mu \right) \left(p^\nu + \frac{1}{2} q^\nu \right) \tag{1.42}$$
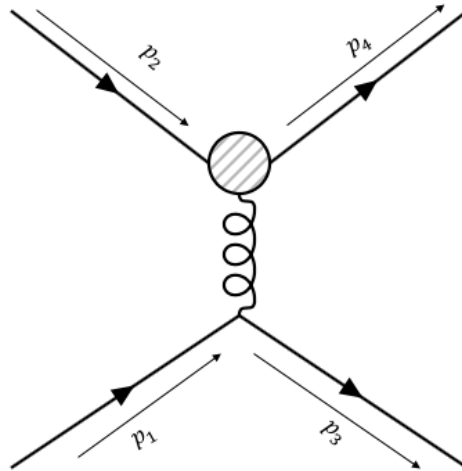
Figure 1.11: Feynman diagram for electron-proton scattering. The shaded circle represents the virtual photon interacting with the proton. It is shaded to highlight the fact that this interaction is unknown.

The terms trailing K_1 and K_2 are functions of q^2, and are usually condensed as:

$$K_1 = -q^2 G_M^2,$$

$$K_2 = (2Mc)^2 \frac{G_E^2 - [\frac{q^2}{(2Mc)^1}]G_M^2}{1 - [\frac{q^2}{(2Mc)^2}]}$$

(1.43)

G_E and G_M are related to the electric charge and magnetization of the proton which are usually represented by F_V^1 and F_V^2 (vector form factors) respectively.

$$F_V^1(q^2) = \frac{G_E(q^2) - \frac{q^2}{(4M^2)}G_M(Q^2)}{1 - \frac{q^2}{(4M^2)}}$$

(1.44)

$$F_V^2(q^2) = \frac{G_M(q^2) - G_E(q^2)}{1 - \frac{q^2}{4M^2}}$$

(1.45)

Accurate determination of $G_E(q^2)$ and $G_M(q^2)$ depends upon the theory models to describe everything happening inside the nucleus and available experimental data to compare with.

In summary, starting from the Mott scattering, we can rewrite the scattering cross-section for an electron-nucleon scattering $(l(k) + N(p) \rightarrow l(k') + N(p'))$ as:

- Mott Scattering off a 0 spin point particle:

$$\frac{d\sigma}{d\Omega} = \frac{\alpha^2}{4E^2 \sin^2 \frac{\theta}{2}} \frac{E_{k'}}{E_k} \cos^2 \frac{\theta}{2} \tag{1.46}$$

- Scattering off a spin 1/2 particle:

$$\frac{d\sigma}{d\Omega} = (\frac{d\sigma}{d\Omega})_{Mott}[1 - \frac{q^2}{2M^2} \tan^2 \frac{\theta}{2}] \tag{1.47}$$

- And scattering off a nucleon that has some internal structure is given by:

$$\frac{d\sigma}{d\Omega} = (\frac{d\sigma}{d\Omega})_{Mott}[\frac{G_E^2(q^2) - \frac{q^2}{4M^2}G^2(q^2)M}{1 - \frac{q^2}{4M^2}} - \frac{q^2}{2M^2}G(q^2)_M^2 \tan^2 \frac{\theta}{2}] \tag{1.48}$$

This summary on electron-nucleon scattering is mostly based on a talk from [134]. This electron-nucleon scattering cross-section as a function of $G_E(q^2)$ and G_M is also known as Rosenbluth formula [140]. The values of $G(q^2)_E$ and $G(q^2)_M$ as a function of four momentum transferred squared q^2 are usually measured using this formula.
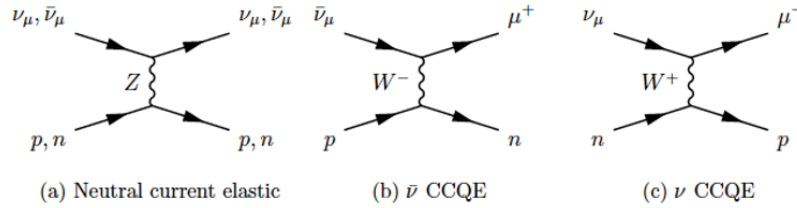
Figure 1.12: 3 different ways neutrinos interacts with the nucleons. Interactions involving electroweak neutral Z boson are called neutral current interactions. Charge current quasi elastic (CCQE) interactions occur by the exchange of W bosons.

1.6.4   Scattering Cross-section:Neutrino-nucleon Interactions

Unlike electrons, neutrinos interact only by the exchange of $W^{\pm}$ or Z^0 bosons which are described by the Electroweak theory. Unlike photons, the W and Z bosons are massive and the $\pm$ in $W^{\pm}$ means the electroweak charge (not to be confused with electric charge). Figure 1.12 shows various ways neutrino scatters from the nucleons. While neutral current scatterings can be truly elastic (i.e. initial and final state products are same), charged current scatterings can change the initial and final states without breaking the nucleus. Hence they are called quasi elastic interactions.

Since neutrinos are electrically neutral and only interact through the electroweak force, it is not possible to contain and control neutrinos (like electrons or protons in a synchroton for example) and study their properties directly. Accelerator neutrino experiments rely on the broad energy spectrum of neutrinos produced in the beamline to do oscillation and
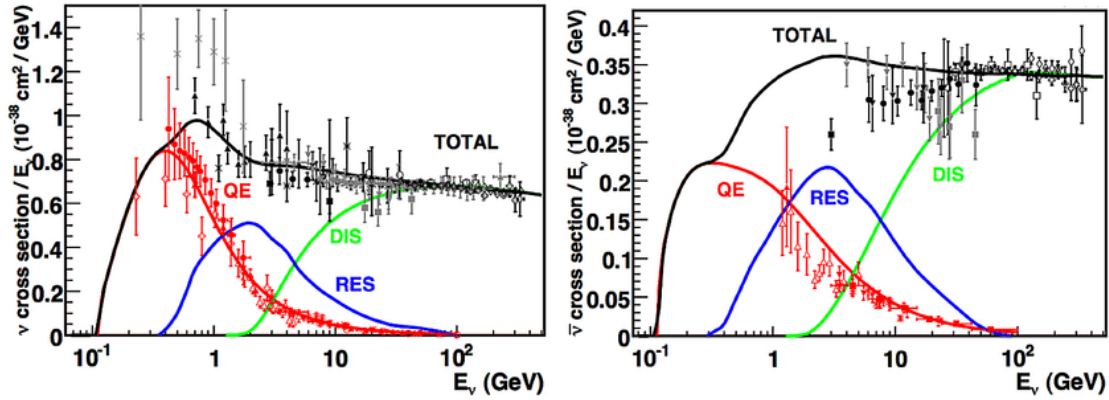
Figure 1.13: Neutrino nucleon interaction cross-sections for different channels plotted per nucleon and as a function of neutrino energy. The left plot is the cross-section for neutrinos whereas in the right is the cross-section as a function of anti-neutrinos. The points represents the data measured over years. The bars in the points represents the errors (statistical and systematic) on the measurements). The predictions (solid line) is made using the NUANCE neutrino generator and the figure is taken from [76].

cross-section measurements. Because of their small interaction cross-sections (in the order of $10^{-40} cm^2$), detectors with huge fiducial volumes are placed in front of the neutrino beam. Any interactions that happen inside the detectors are recorded and saved in terms of energy deposited, time of interactions etc. Figure 1.13 shows the neutrino cross-section over a 3 orders of magnitude (0.1 to 1000 GeV) and shows various types of interaction cross-section dominating at different energy levels. Quasi elastic and elastic (QE in figure 1.12) represent the elastic scattering of the neutrinos off an entire nucleon. The struck nucleon (or nucleons) will get enough kick from the incoming neutrino to overcome the binding energy and exits the target nucleus. If this scattering happens by the exchange of W bosons, it is called quasi

elastic interaction. If the scattering occurs by the exchange of neutral Z bosons, they are called neutral current scattering (and known as just elastic interactions). This thesis will mostly concentrate on the antineutrino quasi elastic interactions.

Neutrino-nucleon interactions at intermediate energies is described in 1.3.0.1. There is an intermediate energy region between resonance and DIS cross-section where the mesons are produced from resonant as well as non-resonant channels. This region of final state inter-mixing is usually called shallow inelastic region (SIS) and has recently gained attention in the neutrino experiment community [141].

Although figure 1.13 shows the cross-section as a function of neutrino energy, reconstructing neutrino energy is a huge challenge. The energy of the neutrinos can be reconstructed by two different ways.

- Kinematic Reconstruction

  In an interaction $\nu + N \to N' + \mu$ where the nucleon (N) is initially at rest, the energy of the incoming neutrino can be reconstructed by the kinematics of the outgoing lepton (here muon):

$$E_\nu = \frac{2 m_n E_\mu - m_\mu^2 - m_N^2 + m_{N'}^2}{2(m_N - E_\mu + p_\mu \cos\theta)} \tag{1.49}$$

This assumes that the target nucleon is a free nucleon which means it doesn't consider various effects due to the neighboring nucleons. If the final state produces additional hadrons besides N', the neutrino energy is not reconstructed properly. A more detailed explanation of this equation will be given in the next section since this is the primary way of reconstructing neutrino energy for the CCQE interactions.

- Calorimetric reconstruction

  As their name imply, calorimeters are the instruments that measure the energy. Calorimeters are used to measure the energy deposited by hadrons. Using this method, the neutrino energy can be reconstructed as:

$$E_\nu = E_\mu + E_{had} \tag{1.50}$$

However, reconstructing hadronic final states by the calorimetric method is not very accurate and relies on simulations. Undetected mesons and neutrons will result in underestimation of the neutrino energy (at least equivalent to the rest mass of hadrons). Often for the QE processes, kinematic reconstruction is used to reconstruct the neutrino energy. Although there are a few assumptions about the model of the nucleus, energy of final state lepton (specially muons) can be reconstructed very accurately. Even though measuring energy of the final state hadrons is a challenge, detecting them and distinguishing them from leptons

is fairly easy.

1.6.5 Neutrino Nucleon Scattering Cross-section

The differential cross-section for the CC and NC scattering processes are given as [134]:

$$\frac{d^2\sigma}{dE'd\Omega'} = \frac{1}{16\pi^2}\frac{G^2}{2}L_{\mu\nu}W^{\mu\nu} \tag{1.51}$$

Here, E' is the energy of the neutrino and Ω' is the scattering angle. For a NC process:

$$G = G_F \tag{1.52}$$

And for a CC process:

$$G = G_F \cos\theta_c \tag{1.53}$$

where $G_F = 1.1803 \times 10^{-5}\ GeV^{-2}$ and $\cos\theta_c = 0.97425$. $L_{\mu\nu}$ is the leptonic tensor and $W^{\mu\nu}$ is the hadronic tensor. For an interaction like figure 1.14, the leptonic tensor contains the information about the processes happening in the bottom right figure that involved only lepton. Similarly the hadronic tensor contains the information about the hadronic vertex as shown in bottom left of figure 1.14. The leptonic tensor is given as:
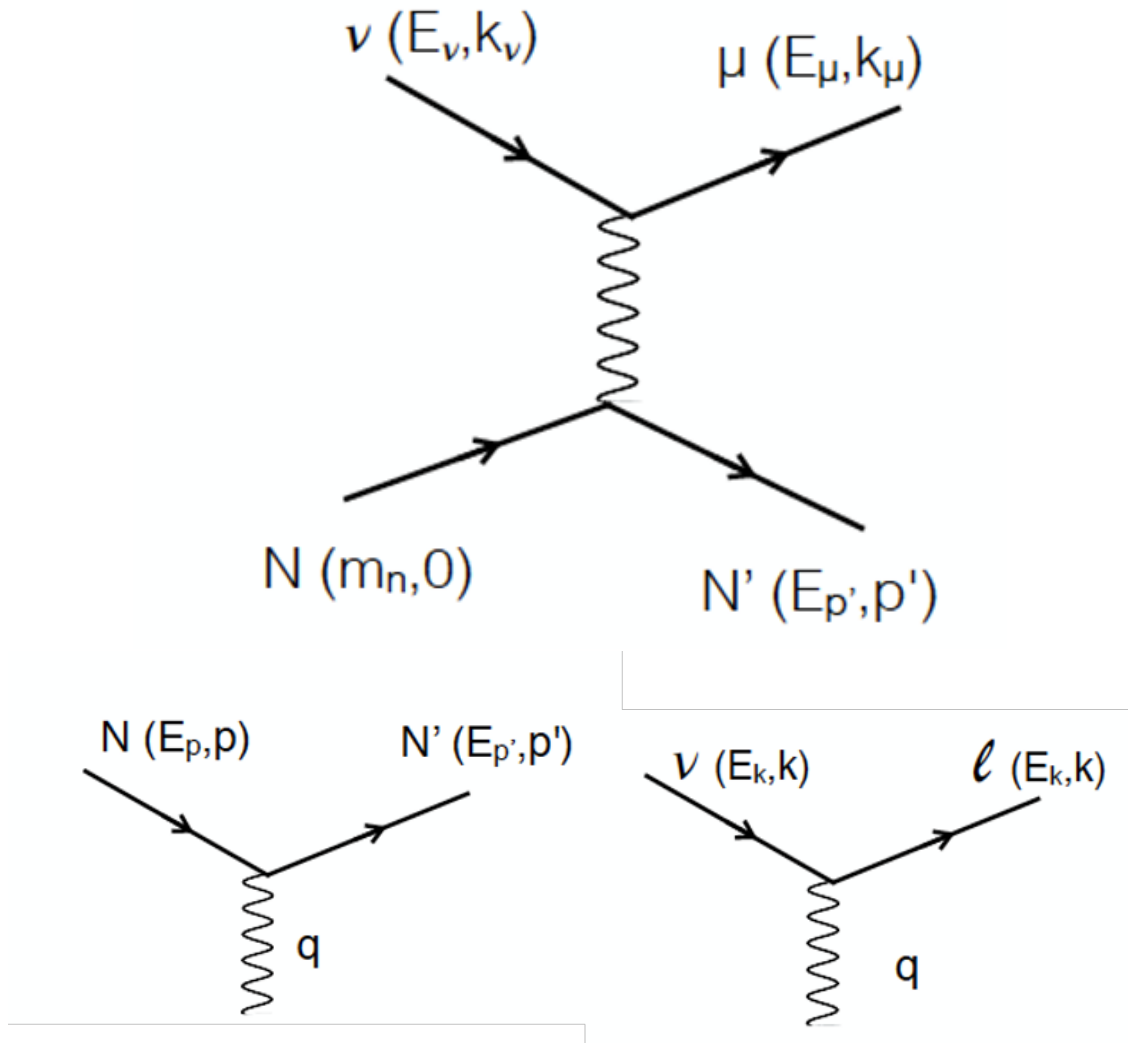
Figure 1.14: Hadronic (bottom left) and leptonic (bottom right) parts of the neutrino nucleon interaction (shown in top).

$$L_{\mu\nu} = [\bar{u}_\nu(k')(\gamma^\mu - \gamma^\mu\gamma^5)u_{\nu l}(k)][\bar{u}_\nu(k')(\gamma^\nu - \gamma^\nu\gamma^5)u_{\nu l}(k)]^* \quad (1.54)$$

And the hadronic tensor is given by:

$$W_{\mu\nu} = [N(p)J^\mu N'(p')][N'(p')J^\nu N(p)] \quad (1.55)$$

Equations 1.54 and 1.55 are taken from [155]. In the hadronic tensor, J^μ is the electro weak current operator and can be divided into the vector and axial part:

$$J^\mu = J^\mu_\mathcal{V} + J^\mu_\mathcal{A} \quad (1.56)$$

Again the vector contribution is given by[102]:

$$J^\mu_\mathcal{V} = \mathcal{F}_1\gamma^\mu + i\sigma^{\mu\nu}q_\nu\frac{\mathcal{F}_2}{2M} \quad (1.57)$$

and the axial contribution is given by[102]:

$$J^\mu_\mathcal{A} = -\gamma^\mu\gamma_5\mathcal{F}_A - q^\mu\gamma_5\frac{\mathcal{F}_P}{M} \quad (1.58)$$

Here, M is the mass of the target nucleon (p,n) and $\mathcal{F}_i$ (i=1,2) are the form factors for the CC (or NC if the reaction is mediated by Z boson) current. The form factors $\mathcal{F}_P$ and $\mathcal{F}_A$

(F_A is also called axial form factor) are related to one another as:

$$\mathcal{F}_P(Q^2) = \frac{2M^2}{Q^2 + m_\pi^2}\mathcal{F}_A(Q^2) \tag{1.59}$$

All the form factors are function of Q^2 which is the four momentum transferred squared $(-q^2)$ between the leptonic system and hadronic system. In the top figure of 1.14: $q = k' - k$, where k' and k are the four momentum of the outgoing and incoming leptons. In the case of neutral current cross-section, the term $\mathcal{F}_P$ can be neglected since this term only comes with the outgoing lepton mass. The axial form factor can be written in a standard dipole form as:

$$\mathcal{F}_A(Q^2) = g_A(1 + \frac{Q^2}{M_A^2})^{-2} \tag{1.60}$$

Here, g_A = -1.267 [160]. M_A is the axial mass and measured to be 0.999 $\pm$ 0.011 GeV [96].

1.6.6 Charged Current Quasi Elastic Neutrino Nucleon Scattering Cross-section

CCQE interactions generally given by:

$$
\begin{aligned}
\nu_l + n &\rightarrow l^- + p \\
\bar{\nu}_l + p &\rightarrow l^+ + n
\end{aligned}
\tag{1.61}
$$

are mediated by the $W^{\pm}$. Because these interactions are one of the significant contributions in neutrino events that are seen by current and future oscillation experiments, they are of particular interest. For example, DUNE will have peak neutrino energy at around 3 GeV. The NuMI low energy program had a peak energy at around 3 GeV and the medium energy at around 6 GeV with MINERvA seeing the peak at 6 GeV and NOvA seeing at around 2.5 GeV. The difference in observed neutrino energy peak is due to on-axis (in the case of the MINERvA experiment) and off-axis (in the case of the NOvA experiment) decay kinematics of pion. See appendix A.1 for relation between pion and neutrino energy for different decay kinematics. Furthermore, since the CCQE interactions are relatively cleaner in terms of the final state (because a CCQE interaction involves a lepton and a nucleon only), it is possible to calculate the four momentum transferred squared (Q^2) precisely and relatively easily. Since the nucleon form factors are a function of Q^2, measurements as a function of

this quantity helps to test our cross-section models. For a CCQE interaction with a muon anti-neutrino scattering off a proton:

$$E_\nu^{QE} = \frac{m_n^2 - (m_p - E_b)^2 - m_\mu^2 + 2(m_p - E_B)E_\mu}{2(m_p - E_b - E_\mu + p_\mu \cos\theta_\mu)}$$

$$Q_{QE}^2 = 2E_\nu^{QE}(E_\mu - p_\mu \cos\theta_\mu) - m_\mu^2$$

(1.62)

Here, E_ν^{QE} is the reconstructed energy of the incoming muon neutrino. The superscript QE means the reconstruction is based on CCQE hypothesis. m_p is the rest mass of the struck proton and m_μ is the rest mass of the outgoing muon. p_μ and θ_μ are the momentum and angle (with respect to the direction of the incoming neutrino) of the outgoing muon. E_b represents the binding energy of the proton in the nucleus. As we can see, all the kinematic information comes from the outgoing lepton and all the contributions from the hadronic terms are assumed to be constant. Since muons deposit energy as minimum ionization particles (MIP), which are well understood, the kinematic variables can be reconstructed with high precision.

1.6.7 Llewellyn Smith model for QE cross-section

In 1971, C.H. Llewellyn Smith published a summary of the then known theories and results from accelerator neutrino experiments. However, this paper is also commonly referenced for

the expression of the neutrino charged current cross-section [105].

$$\frac{d\sigma}{dQ^2}\begin{pmatrix} \nu n \to l^- p \\ \bar{\nu} p \to l^+ n \end{pmatrix} = \frac{M^2 G_F^2 \cos^2 \theta_c}{8\pi E_\nu^2}[A(Q^2) \mp B(Q^2)\frac{(s-u)}{M^2} + \frac{C(Q^2)(s-u)^2}{M^4}] \qquad (1.63)$$

This expression is the final form of the general differential cross-section in the lab frame assuming the target nucleus is at rest:

$$\frac{d\sigma}{dQ^2} = \frac{1}{64\pi E_\nu^2 M^2}\frac{G_F^2 \cos^2 \theta_c}{2}|\mathcal{M}| \qquad (1.64)$$

Here,

$$M = \frac{m_p + m_n}{2}$$

and the coefficients A,B and C are given as:

$$A(Q^2) = 4\frac{Q^2}{4M^2}[|F_A|^2(1 + \frac{Q^2}{4M^2}) - |F_V^1|^2(1 - \frac{Q^2}{4M^2}) +$$
$$|\xi F_V^2|^2\frac{Q^2}{4M^2}(1 - \frac{Q^2}{4M^2}) + 4F_V^1\xi F_V^2\frac{Q^2}{4M^2}] \qquad (1.65)$$

$$B(Q^2) = 4\frac{Q^2}{4M^2}[F_A(F_V^1 + \xi F_V^2)] \qquad (1.66)$$

and

$$C(Q^2) = \frac{1}{4}[|F_A|^2 + |F_V^1|^2 + \frac{Q^2}{4M^2}|\xi F_V^2|^2] \qquad (1.67)$$

Here, F_V^i (i=1,2) and F_A are the vector and axial form factors. s and u are the Mandelstam

variables with

$$s - u = 4ME_\nu - Q^2 - m_l^2$$

where E_ν is the energy of the incoming neutrino and m_l is the mass of the lepton.

This final form of this equation neglects the higher order term coming with $\frac{m^2}{m_l}$. This is

appropriate as long as the lepton is electron or muon. If the produced lepton is a tau

then this term should also be considered, introducing the pseudo-scalar form factor $F_P(Q^2)$.

Switching from neutrino to anti neutrino, the term $B(Q^2)$ switches its sign.

In the limit where $Q^2 \to 0$, the terms A and B go to 0 and

$$C(0) \to \frac{1}{4}(|F_A(0)|^2 + |F_V^1(0)|^2) \approx 0.63 \tag{1.68}$$

$$(s - u)^2 \approx (4ME_\nu)^2 \tag{1.69}$$

This reduces the quasi-elastic cross-section at low Q^2 to:

$$(\frac{d\sigma}{dQ^2})_{Q^2=0} = \frac{G_F^2 \cos^2 \theta_c}{2\pi}(|F_A(0)|^2 + |F_V^1(0)|^2) \tag{1.70}$$

which is independent of the energy of the incoming neutrino (E_ν).

Similarly, in the limit where the energy of the neutrino $E_\nu >> M$, the Mandelstam variable $s = (p_n + k_\nu)^2$ (where p_n and k_ν are the 4 momenta of target nucleon and incoming neutrino respectively) dominates, making the $C(Q^2)$ term dominant.

This discussion of properties of the Llewellyn Smith equation is based on [112].

1.6.7.1 Form Factors of Lleweyllyn Smith Equation

A very detailed discussion of the form factor terms is given in section 2.2.2 of [128]. This section will only go through the relevant form factors of this equations briefly.

In a neutrino nucleus interaction, the leptonic vertex is described by the tensor $L_{\mu\nu}$ which has the term $\gamma^\mu - \gamma^\mu \gamma^5 = \gamma^\mu(1 - \gamma^5)$. However, for the hadronic side, this term needs to take into account the modifications to the interactions due to internal strong force components inside the nucleus. A weak vector term (c_v) and an axial term c_A are added such that:

$$(1 - \gamma^5) \rightarrow (c_v - c_A \gamma^5) \tag{1.71}$$

In the next two subsections, we will go through the vector and axial form factors.

1.6.7.2   Vector Form Factors

According to the Conserved Vector Current Hypothesis (CVC) [79],[67], the vector compo-nent (c_v) for both the charged current interaction $(n\nu_l \to n'l)$ and electro magnetic inter-action is 1. This means the vector form factors of the CCQE interaction can be measured from charged lepton nucleus scattering. So, the vector form factors can be written in terms of electric and magnetic form factors as in equations 1.44 and 1.45. The terms G_E and G_M can be further written as:

$$G_E(Q^2) = G_E^p(Q^2) - G_E^n(Q^2)$$

$$G_M(Q^2) = G_M^p(Q^2) - G_M^n(Q^2)$$

(1.72)

where G_E^p, G_E^n and G_M^p, G_M^n are the electric and magnetic form factors of proton and neutron respectively that are extracted from electron nucleon scattering experiments. At $Q^2 = 0$,

$$G_E^p = 1$$

$$G_E^n = 0$$

$$G_M^p = \mu_p$$

$$G_M^n = \mu_n$$

(1.73)

where μ_p and μ_n are the nuclear magnetic moment of proton and neutron respectively and are given by:

$$\mu = g\frac{e}{2m_p}I \tag{1.74}$$

where m_p is the mass of proton. For proton $g = 5.5856947$ and for neutron $g = -3.82608$. In case where $Q^2 > 0.0$, the vector form factors are determined experimentally from electron scattering experiments. Rewriting the elastic electron nucleon cross-section as [44]:

$$\frac{d\sigma}{d\Omega} = \frac{\alpha^2 E'_e \cos(\frac{\theta_e}{2})}{4E_e^3 sin^4(\frac{\theta_e}{2})}[(G_E^N)^2 + \frac{\tau}{\epsilon}(G_M^N)^2](\frac{1}{1+\tau})b \tag{1.75}$$

Here, E is the energy of the incident electron and E' is the energy of the scattered electron with an scattering angle of lab θ_e,

$$E' = \frac{E - \frac{W^2 - M^2}{2M}}{1 + 2\frac{E}{M}\sin^2\frac{\theta}{2}} \tag{1.76}$$

where

$$W^2 = M^2 + 2M\nu - Q^2$$

$$\nu = E - E'$$

$$\tau = \frac{Q^2}{4M^2} \tag{1.77}$$

$$\epsilon = [1 + 2(1 + \tau)\tan^2\frac{\theta_e}{2}]^{-1}.$$

The ϵ is the polarization of the mediating photon during scattering and N is neutron or proton. Note that $\frac{\alpha^2 E'_e \cos(\frac{\theta_e}{2})}{4E_e^3 \sin^4(\frac{\theta_e}{2})}$ is the scattering cross-section of the point like particles (for example electron electron scattering). One of the earliest form of measurement techniques used the Rosenbluth separation method [140],[131],[24] where the reduced elastic cross-section is measured at various ϵ keeping Q^2 constant with θ_e as a fit parameter in a linear fit. The reduced cross-section is given by:

$$\sigma_R = \epsilon(G_E^p)^2 + \tau(G_M^p)^2 \tag{1.78}$$

These measurements seemed to perform well assuming the nucleon has a charge distribution given by $\rho(r) = \rho_o e^{-Mr}$ where r is the distance from the center of the nucleon and M is the mass of the nucleon. The Fourier transformation of these charge distribution gives the dipole form of the form factors:

$$G_d = \frac{1}{(1 + \frac{Q^2}{\Lambda^2})^2} \tag{1.79}$$
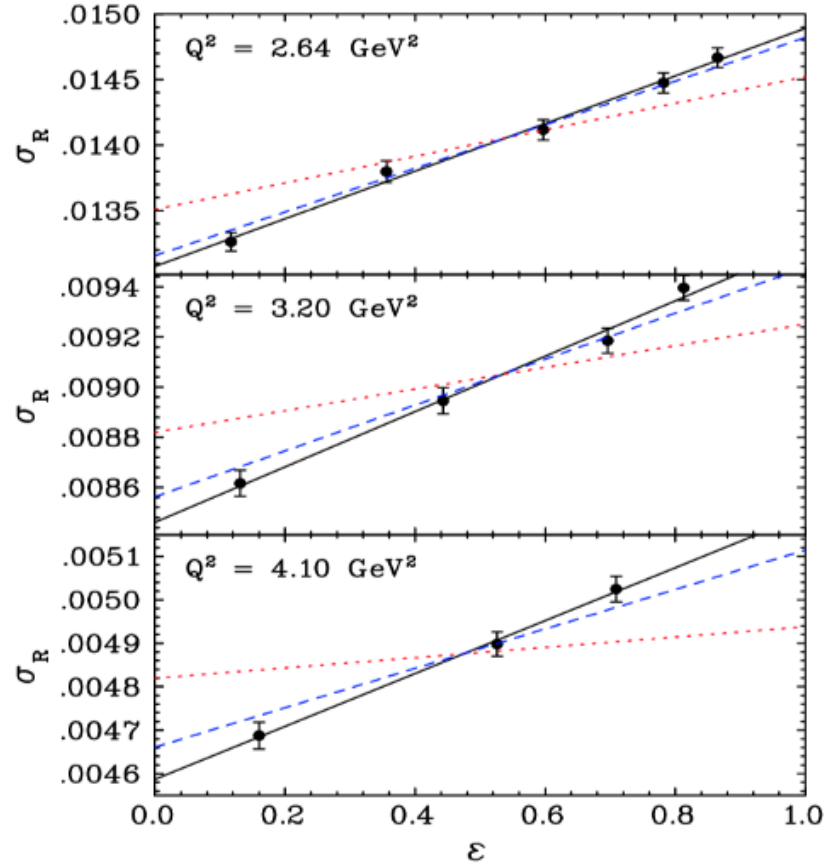
Figure 1.15: Reduced cross-section as a function of ϵ for different values of Q^2. Here, the black line is a linear fit which depends linearly on ϵ with slope $(G_E^p)^2$ and intercept $\tau(G_M^p)^2$. The blue dashed line is the slope predicted by the Rosenbluth separation method and the red dotted line is the slope predicted from polarization transfer experiments. Figure taken from [131].

where $\Lambda^2 = 0.71 GeV^2$ [44]. The electric and magnetic form factors are given by:

$$G_E^p(Q^2 = G_D(Q^2)$$

$$G_E^p(Q^2 = G_D(Q^2)$$

$$G_M^p(Q^2) = \mu_p G_D(Q^2) \tag{1.80}$$

$$G_E^n(Q^2) = 0$$

$$G_M^n(Q^2 = \mu_n G_D(Q^2)$$

This method gave values of form factors at $Q^2 < 1 GeV^2$ but at high Q^2, the electric form factor (G_E^N) is damped by a factor of $\frac{1}{\tau}$ making the magnetic form factor (G_M^N) dominant. Similarly, although the neutron itself is electrically neutral, it does have a charge distribution which means G_E^n is not 0. Since this method requires elastic cross-section measurements at various Q^2, the systematic errors gets propagated into the form factor values. Furthermore, this method doesn't account for higher order processes such as 2 virtual photon exchange processes, which turned out to be important. Based on the derivation from [14], polarization transfer method has also been used to measure the ratios of the form factors. This method employs simultaneous measurements of the two recoil polarization components from electron proton scattering data to extract the ratio as:

$$R_p = \mu_p \frac{G_E^p}{G_M^p} = \mu_p \sqrt{\frac{\tau(1+\epsilon)}{2\epsilon}} \frac{P_t'}{P_l'} \tag{1.81}$$
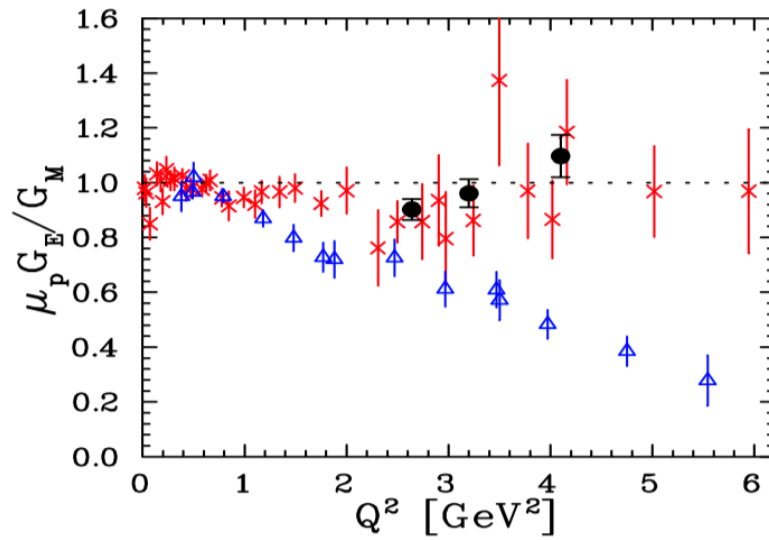
Figure 1.16: Extracted values of the form factor ratio using Rosenbluth method (red stars and black points) and polarization transfer methods. The 2 different methods giving different answers with huge discrepancies generated confusion and doubts regarding lepton scattering experiments and form factor extraction methods at that time. Figure taken from [14].

where:

$$P'_t = -P\sqrt{\frac{2\epsilon(1-\epsilon)}{\tau}}\frac{r}{1+\frac{\epsilon}{\tau}r^2}$$

$$P'_l = P\frac{\sqrt{1-\epsilon^2}}{1+\frac{\epsilon}{\tau}r^2}$$

(1.82)

Here, P' is the momentum of scattered electron whereas P is the momentum of incident electron and $r = \frac{G_E^p}{G_M^p}$ Since, the form factors are extracted from the momentum ratios, most of the uncertainties cancel. Scattering data from the GEp-I,GEp-II and GEp-III experiments in Jefferson Laboratory confirmed that the drop in $\frac{\mu_p G_E}{G_M}$ as a function of Q^2 is expected.

1.6.7.3 Axial Form Factors

While the electro-magnetic interactions have mainly a vector component, the electroweak interactions have both vector and axial components. Unlike the vector form factors which are extracted from electron scattering experiments, the axial components need to be extracted from neutrino scattering experiments. Just like the vector form factor, the simplest and most commonly used ansatz for the axial form factor is the dipole approximation given by
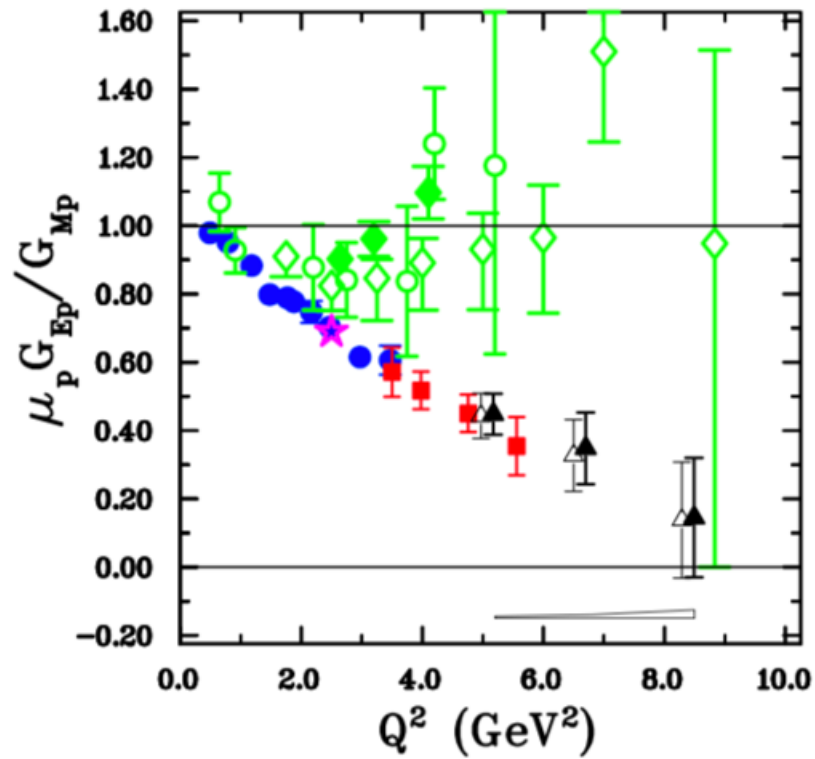
Figure 1.17: Data extracted from the Rosenbluth separation data are shown in filled and empty green diamonds. The GEp experiments data that are extracted using the polarization transfer method show a general downward trend in the ratio as a function of Q^2 (blue, red and black points). Figure is taken from [130].

[88]:

$$G_A(Q^2) = \frac{G_A(0)}{1 + \frac{Q^2}{M_A^2}}$$

$$<r_A^2> = \frac{12}{M_A^2} \tag{1.83}$$

$$G_A(0) = g_A$$

where g_A = -1.267 [39]. The value of G_A at Q^2= 0 is well known from neutron beta decay. The Q^2 dependence of $G_A(Q^2)$ can only be extracted from neutrino scattering experiments. Currently the most direct access to F_A over a large range of Q^2 is provided by bubble chamber experiments listed in [22]. While there are alternate parameterization to extract the value of M_A (like z expansion method [38] and BBBA parameterization [39].), GENIE, the default neutrino nucleus interaction generator of the MINERvA experiment, assumes a dipole form factor with a default value of $M_A = 0.99 GeV/c^2$ [25] as the default method. The M_A is kept as a free parameter of the model.

In general, the axial form factor of a proton is given by:

$$G_A^p(Q^2) = \frac{1}{2}[-G_A^u(Q^2) + G_A^d(Q^{2)} + G_A^s(Q^2)] \tag{1.84}$$

where G_A^x where $x = (u, d, s)$ are the up, down and strange contribution to the axial form factor. The contribution from up and down, $(-G_A^u + G_A^d)$ are measured in charge current scattering experiments like the K2K, T2K, MiniBooNE, SciBoone, and MINERvA [76]. The
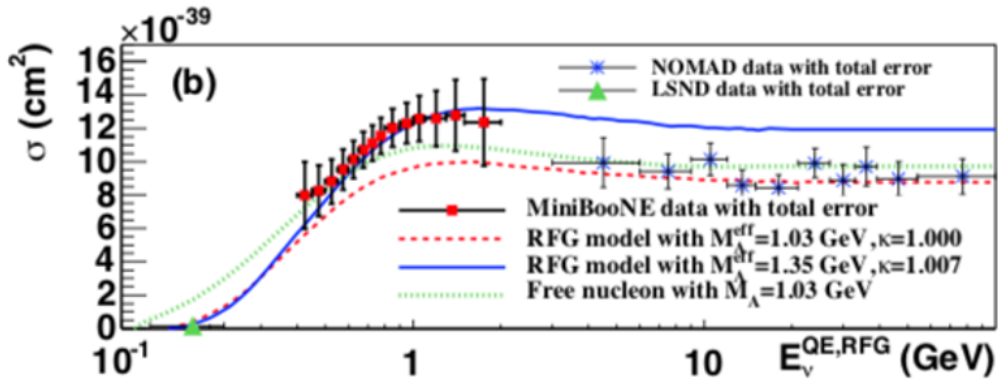
Figure 1.18: CCQE cross-section as a function of neutrino energy shown for MiniBooNE (red dots), LSND (green triangles) and NOMAD (blue stars). MiniBooNE data follows the cross-section prediction with axial mass of $M_A = 1.35 GeV/c^2$ whereas NOMAD and LSND agrees with the axial mass of $M_A = 1.03 GeV/c^2$. Figure is taken from [11].

strangeness contributions were measured in few experiments like BNL 734 [15],MiniBooNE [118], MicroBooNE [159] etc. The axial mass extracted by deuterium target experiments using the dipole form factor ansatz predicts an average axial mass of $M_A = 1.01 \pm 0.014 GeV/c^2$ [39]. This is incompatible with the measurements from MiniBoonE's $M_A = 1.35 \pm 0.17 GeV/c^2$. Other similar experiments done in heavy targets predicted higher than world average axial mass. The general consensus is that the axial mass seen by the MiniBoonE and other heavy target experiments is an effective axial mass that is caused by nuclear effects, such as Meson Exchange Current (MEC), giving a larger than world average mass value. MEC is the nuclear effect in which the two nucleons inside the atomic nucleus are correlated to one another by exchanging virtual mesons (like pions).

1.7 Nuclear Models in Neutrino Scattering Processes

1.7.1 Nuclear Models

Since MINERvA and many other current and future experiments will employ heavy targets for neutrino-nucleus interaction measurements, understanding of nucleons inside the nucleus is very important to model these scattering processes. In the context of neutrino scattering experiments, the nuclear models and effects that are being currently used are mostly taken from models developed to explain electron scattering processes. Since both electron and neutrino scattering processes are lepton scattering processes, the physics and assumptions used to explain these processes are similar (in some cases the same). The electron scattering experiments have an advantage of being able to measure both incident and scattered electron kinematics allowing robust test of these models and assumptions. In fact, some of the nuclear effects and related theoretical frameworks were developed decades ago in the light of electron scattering processes and have been recently applied and used to explain neutrino scattering processes [150]. In this section, various nuclear models and nuclear effects that explain the neutrino scattering processes are discussed. Because electron-scattering experiments were the pioneers in the development of models for scattering processes, most of these models are explained in the context of electron-scattering experiments and processes. Extension to neutrino-scattering processes is discussed wherever further modifications and extensions

were made.

1.7.2 Relativistic Fermi Gas Model

A Fermi Gas is a collection of non-interacting fermions inside a rectangular potential well obeying Fermi-Dirac statistics and Pauli's exclusion principle. The Fermi-Dirac statistics are given by:

$$n_i = \frac{1}{e^{\beta(E_i - \mu)} + 1}. \tag{1.85}$$

Here n_i is the number of nucleons (protons or neutrons) in a given energy level i. E_i is the energy of the level and μ is the chemical potential. $\beta = \frac{1}{kT}$ where k is the Boltzmann constant and T is the temperature in Kelvins. Since the neutrons and protons are different particles, their potential wells are also going to be different. They will follow the Pauli Exclusion principle and a given energy level is occupied by a maximum of two neutrons (or protons) in their respective potential well with opposite spin. Even at absolute 0 temperature, the particles will fill the energy levels below a maximum energy given by $E_F = \mu(T = 0)$. When the two particles of different energy levels interact with each other, they will simply exchange their energy levels leaving the overall configuration of the nucleus unchanged. According to this model, the lepton-nucleus quasi elastic scattering is assumed as lepton nucleon scattering. Since nucleons are independent in the Fermi gas, the elastic scattering cross-section of the
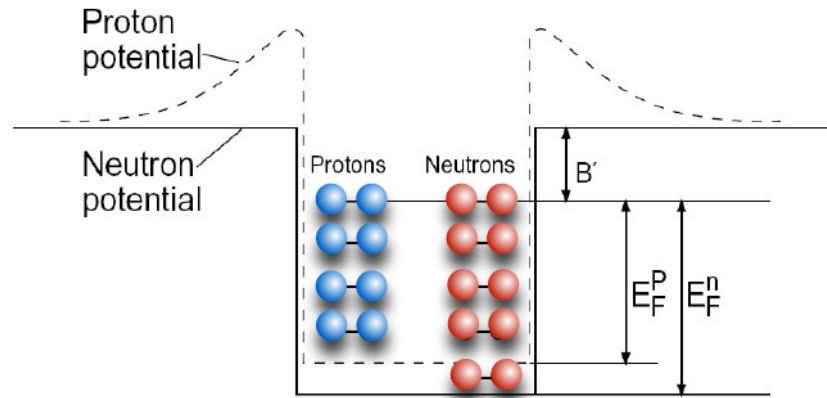
Figure 1.19: A nuclear potential well with distinct wells for protons and neutrons. Protons and neutrons fill energy levels upto below Fermi energy level (E_F) with an additional difference between E_F and top of the well called binding energy. Binding energy per nucleon is around 7 to 8 MeV. The proton has a exponential drop of potential outside well because of the additional coulomb potential unlike neutral neutron potential. Figure taken from [134].

lepton and nucleus is the incoherent sum of scattering between lepton and individual nucleon.

The energy transferred by the lepton to the nucleon will be gaussian with a mean of $Q^2/2M$

(where $Q^2 = -q^2$ is the negative square of four momentum transferred between lepton and

nucleus and M is the mass of the struck nucleon) and a width of $\vec{q}.\vec{p}/M$ where $\vec{p}$ is the

initial momentum of the nucleon level. Once the nucleon gets energy from the lepton, it is

only allowed to reach an energy level that is not occupied. This phenomena is called Pauli

blocking and gives an upper and lower bound on the energy of the target nucleon for which

an elastic scattering is allowed to occur. A more detailed discussion of Pauli blocking is

given in [104]. Although the RFG model is simple, it doesn't account all nuclear effects. For

example inside a nucleus, nucleons are not independent non-interacting particles. Several additional correlated effects should be accounted for.

1.7.3   Local Fermi Gas Model

In the case of RFG, the Fermi momentum of the nucleus is constant and is given by:

$$p_F^{RFG} = \frac{h}{R_o}(\frac{9\pi n}{4A})^{1/3}, \tag{1.86}$$

where $R = R_o A^{1/3}$ is the nuclear radius with an atomic mass A. n is the total number of neutrons (or protons) in the nucleus. In the case of Local Fermi Gas model, the Fermi momentum becomes:

$$p_F = h[3\pi^2\rho(r)\frac{n}{A}], \tag{1.87}$$

where $\rho(r)$ represents the charge distribution in the nucleus. The overall effect is that instead of having a constant Fermi momentum, the nucleons will have a position dependent Fermi momentum. As with the RFG, the nucleons are independent particles and move freely within the nuclear potential well.
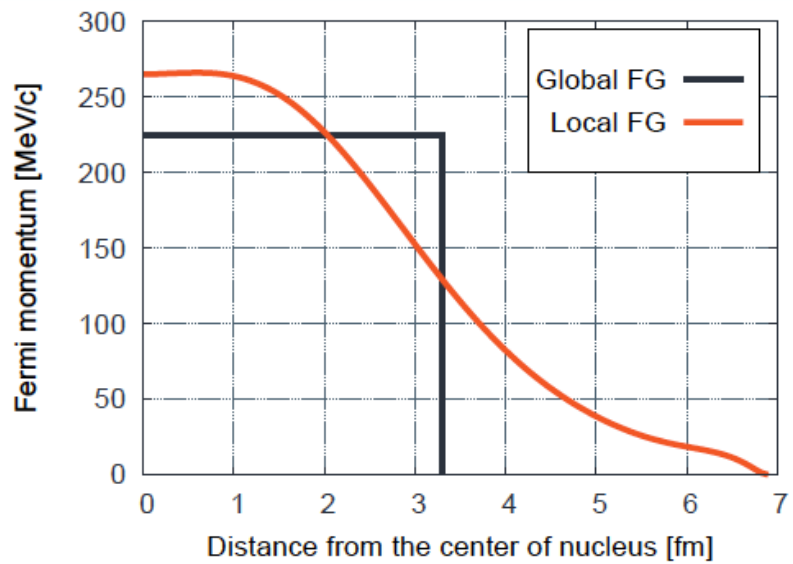
Figure 1.20: Fermi momentum of neutrons in Local (LFG) and relativistic (Global) Fermi gas models. Figure taken from [134].

1.7.4   Nuclear Shell Model

Just like the atomic shell model which explains the stability of various elements when the electron orbitals are filled, nuclear shell model explains the stability of certain nuclei. In the periodic tables, inert gases are more stable than their neighboring elements because of their complete (electron) shell configuration. In the case of the nucleus also, there are certain elements for which the nucleus is much more stable than the neighboring isotopes. These numbers of protons or neutrons are called magic numbers and they are 2,8,20,28,50,82 and 126. As long as the nuclei has the number of protons or neutrons or combination of protons and neutrons to be one of the magic numbers, these nuclei are stable and have a large number of stable isotopes and isotones and have a spherical charge distribution. As in the Fermi gas model, the nucleons move independent of one another inside the nucleus but they are subject to a central potential. In the nuclear shell model, a nucleon sees an effective potential due to rest of the nucleons. The shape of this effective nuclear potential is chosen to match experimental observations. It turns out that neither the square potential or the harmonic oscillator potential could predict the magic numbers. The solution is a potential which is an intermediate between a square and a harmonic oscillator potential known as the Woods and Saxon potential as shown in figure 1.21.
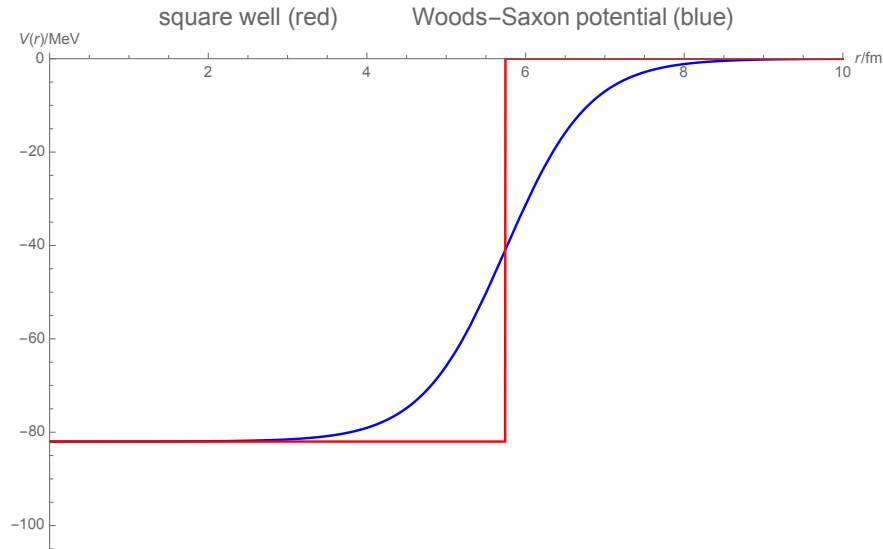
Figure 1.21: Illustration of Woods and Saxon potential (blue) shown along with a rectangular potential well for a nuclei of same atomic number, well depth and nuclear radius. Figure made using [6].

1.7.5 Nucleon-Nucleon Correlations

While the mean field technique was quite successful to explain the magic numbers and energy levels of the nucleons to some extent, electron-proton scattering experiments have shown that only 60% to 70% of the predicted protons were scattered off the valence shell [97]. It was already speculated that the discrepancy between model prediction and observation was coming from nucleon-nucleon correlations. Some of these correlations were found to be coming from long range correlations between the nucleons [59] at lower momentum transfers (momentum transfers between leptonic and hadronic system). This long range correlation is a screening effect and can be modeled by an RPA (Random Phase Approximation) [120]. According to
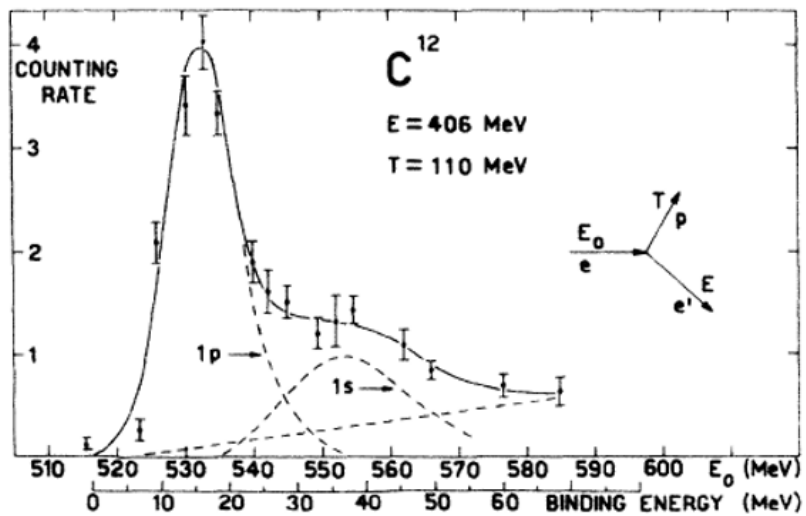
Figure 1.22: Figure shows the protons inside the Carbon 12 nucleus in various energy levels in terms of binding energies. With fixed energies of scattered electron (e') and proton (p), the missing energy from the incident electron energy is used to estimate the binding energy of the proton that was scattered off. Figure shows 4 protons in 1p shell. The 2 1s protons are not clearly resolved. This experiment didn't assume any final state interactions during the electron-proton scatterings. Figure taken from [38].

this approximation, the values of inter-nucleon electro-weak couplings will change from their free nucleon values due to strong force interactions between the nucleons. This phenomenon can be thought of as the modification of electric field inside a dielectric medium ($D = \epsilon E$) where the effect of ϵ is played by the strong force in the nucleons.

However, the long range correlations only predict half of the predicted correlated pairs and later experiments done in Hall A of Jefferson National Lab showed that the neutron-neutron correlation, neutron-proton correlation and proton-proton correlation at short range also emerge from the strong force field at higher momentum transfers [150]. The experimental data combined with measurements from other experiments show that 80% of carbon-nucleon scattering events have independent nucleon scatterings as predicted by the nuclear shell model. The remaining 20% of the nucleons are interactions on SRC (short range correlation) pairs. $90 \pm 10\%$ of the SRC pairs were neutron-proton pairs, $5 \pm 1.5\%$ were proton-proton pair and $5 \pm 1.5\%$ were neutron-neutron pair. In the SRC interaction, when a high momentum probe hits a nucleon (let's say a proton), which is part of a correlated nucleon pair, one of the correlated proton will carry a part of momentum and energy of the probe and the other correlated nucleon will carry the remaining momentum and energy of the probe. The remnant nucleus remains at rest.

One of the tests for validity of the short range correlation effect is the universality of short range correlations in different nuclei. If the high momentum tail is coming from the short range correlations between two nucleons, this should be observed in all nuclei regardless of number of nucleons (nuclei with at least 2 nucleons). Jefferson's E02-2019 measured the scattering cross-section (with electrons as a probe) for deuterons and other heavier materials as a function of Bjorken x (Bjorken x is a scaling variable that measures the inelasticity of an interaction. An elastic scattering occurs at $x = 1$ and inelastic interactions occur at $x < 1$. Correlated nucleons can have $x > 1$ due to their motion (See more info in A.3). These measurements found that at the very high x region, the cross-section ratio remains constant which means that SRC is a nucleon-nucleon effect and is independent of the size of nucleus. Figure 1.23 shows the universality of the SRC. Short and long range correlation effects in neutrino-nucleon interactions can arise from the exchange of mesons between nucleons inside the nucleus [124] (also known as meson exchange current or MEC). Using the same argument of 2 nucleons correlation, the 3 nucleon correlations can be observed at $2 < x \leq 3$ and for carbon, 0.5% of the nucleons are found to be involved in 3 nucleon correlations [64]. These short and long range nuclear effects are also observed in neutrino-nucleus scattering experiments [11]. The nominal neutrino-nucleus interaction generator that is used in this
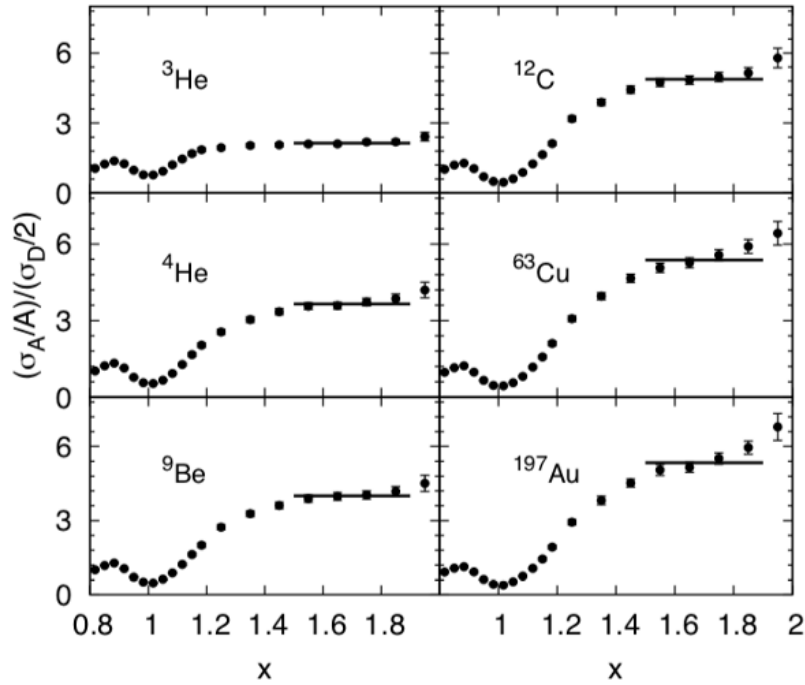
Figure 1.23: Cross-section ratios (various materials with respect to deuteron) as a function of Bjorken x. Short range correlation events occur at $x > 1$. However, from x=1 to $x \approx 1.5$, the remnant nuclei sometimes go through further excitations or breakup giving a rising slope. After x=1.5, there is a plateau in the cross-section ratio for all materials (illustrated by a solid black line). This observation of plateau meant that SRC is truly a nucleon nucleon effect independent of atomic number of the nucleus. The last data point at $x \approx 1.95$ is because x is approaching the kinematic threshold of $\frac{M_D}{M_p} \approx 2$. Figure taken from [75].

analysis is GENIE [25]. This generator uses Relativistic Fermi gas to model the nucleons inside the nucleus and adds a high energy tail using the prescription from [41].

1.7.6 Scaling in the Fermi Gas Model

In particle physics, scaling of certain phenomena is considered to occur when energy transfer (ν) and momentum transfer ($\mathbf{q}$) occurs in an individual nucleon instead of the whole nucleus. The result is that this phenomena will produce identical results independent of several nuclear models.

The parity conserving electron nucleon cross-section can be generally written in terms of transverse and longitudinal functions which represent the polarization of exchanged photon and are given as [32]:

$$\frac{d\sigma}{d\Omega d\nu} = \sigma_{Mott} \frac{E'}{E} [\frac{Q^4}{q^4} R_L(Q^2,\nu) + (\frac{Q^2}{2\vec{q}^2} + \tan^2\frac{\theta}{2}) R_T(Q^2,\nu)]. \tag{1.88}$$

Here R_L and R_T are nuclear response functions which are functions of momentum transfer q and energy transfer ν. Dividing them by an appropriate nucleon form factor, we can get a scaling function given as:

$$f_{L,T}(q,\nu) = p_F \frac{R_{L,T}}{G_{L,T}}. \tag{1.89}$$

Here G_L is related to G_E (electric form factor of the nucleon) and G_T is related to G_M (magnetic form factor of the nucleon). At large values of q, $f(q, \nu)$ instead of depending on two variables q and ν, has been observed to be described by a scaling function $\psi(q, \nu)$ i.e. $f(q, \nu) \rightarrow f(\psi)$. The scaling function ψ is given as [146]:

$$\psi = \frac{1}{\sqrt{\xi_F}} \frac{\lambda - \tau}{\sqrt{(1 + \lambda)\tau + \kappa\sqrt{\tau(1 + \tau)}}}, \tag{1.90}$$

where

$$\lambda = \frac{\nu}{2m},$$
$$\kappa = \frac{|\mathbf{q}|}{2m},$$
$$\tau = \kappa^2 - \lambda^2, \tag{1.91}$$
$$\xi_F = \frac{\sqrt{p_F^2 + m^2}}{m} - 1.$$

Scaling of the second kind is achieved when the scaling function is written in terms of ψ' which is approximately $\frac{y}{k_F}$ [47] where variable y is given as:

$$y(q, \nu) = \frac{(m_A + \nu)\sqrt{\Lambda^2 - m_{A-1}^2 W^2} - q\Lambda}{W^2}, \tag{1.92}$$
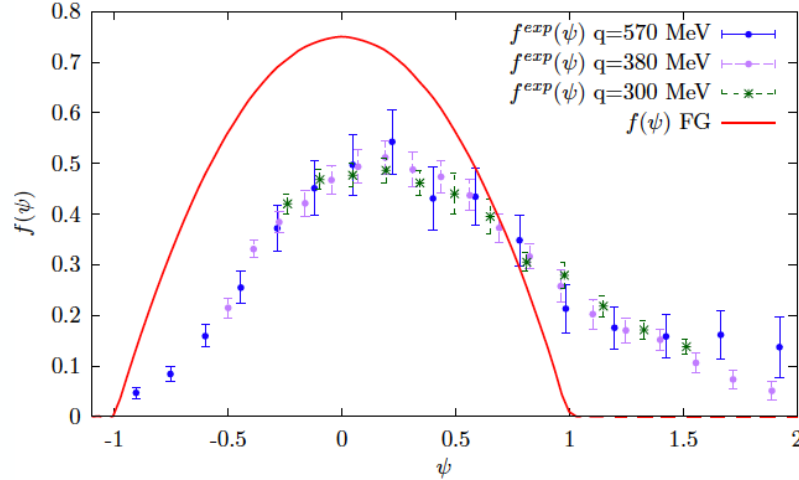
Figure 1.24: Longitudinal scaling function ($f_L(\psi)$) for different values of q obtained for C12. The $f^{exp}(\psi)q$ is obtained by using response functions extracted for Carbon [135]. This scaling is observed for both f_L and f_T. Solid red line shows the prediction from Fermi gas model. Figure taken from [134].

where

$$W = \sqrt{(m_A + \nu)^2 - q^2},$$

$$\Lambda = (m_{A-1}^2 - m_A + W^2)/2.$$

(1.93)

The response functions in terms of ψ' shows an independence from atomic number A. Here

m_A is the mass of the nucleus with atomic number A in an scattering experiment where an

incoming electron scatters off a nucleus of atomic number A such that a proton is ejected.
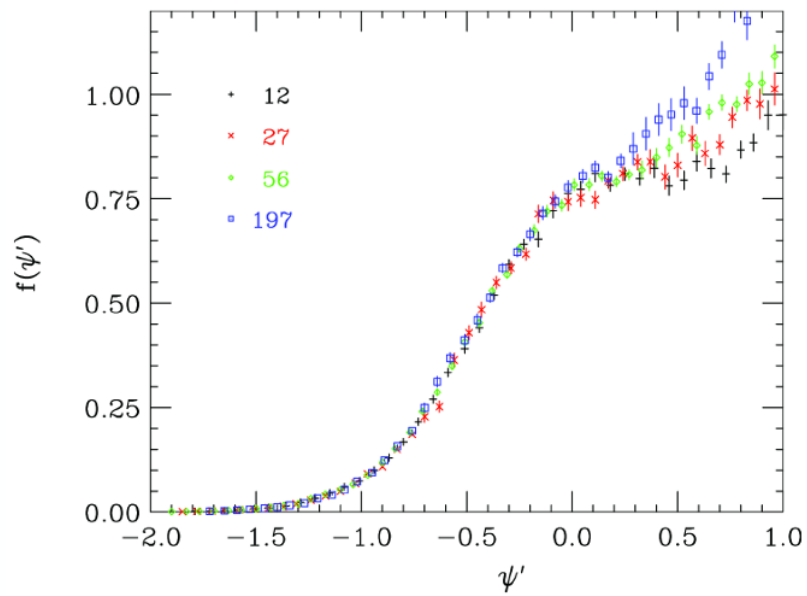
Figure 1.25: $f_L(\psi')$ as a function of ψ' for different atomic numbers. The scaling function is largely similar for all nuclei. Figure taken from [61].

1.7.7   Enhancement of Transverse Scaling function and Scaling Violation

When plotting the longitudinal and transverse scaling functions as a function of scaling function ψ' (both first and second kind of scaling), the transverse scaling function f_T seemed to be enhanced relative to the longitudinal scaling function f_L. As seen in figure 1.26, the f_T is enhanced compared to f_L with significant enhancement starting near the quasi elastic peak ($\psi' = 0$). Furthermore, there is a violation of scaling at $\psi' > 0$ (this is observed for both kinds of scalings). It is assumed that the f_L is mostly due to the single nucleon function while f_T are mostly affected by the multi nucleon effects [128]. Hence, the enhancement on f_T shows the relative strength of the multi nucleon effect. At $\psi' > 1$, we can see that the scaling is violated and this violation is mostly prominent for f_T. Both of these effects are assumed to be coming from multi nucleon exchange current and inelastic scatterings [22].

The enhancement in the transverse scaling function was quantified by Bodek, Budd and Christie [40]. Using various results at low Q^2 and high Q^2, a fit was constructed with 4 parameters: transverse and longitudinal quasi-elastic components, inelastic contributions and the transverse enhancement of the QE. A transverse enhancement ratio was extracted as:

$$\mathcal{R}_T = \frac{QE_{Transverse} + TE}{QE_{Transverse}}. \tag{1.94}$$
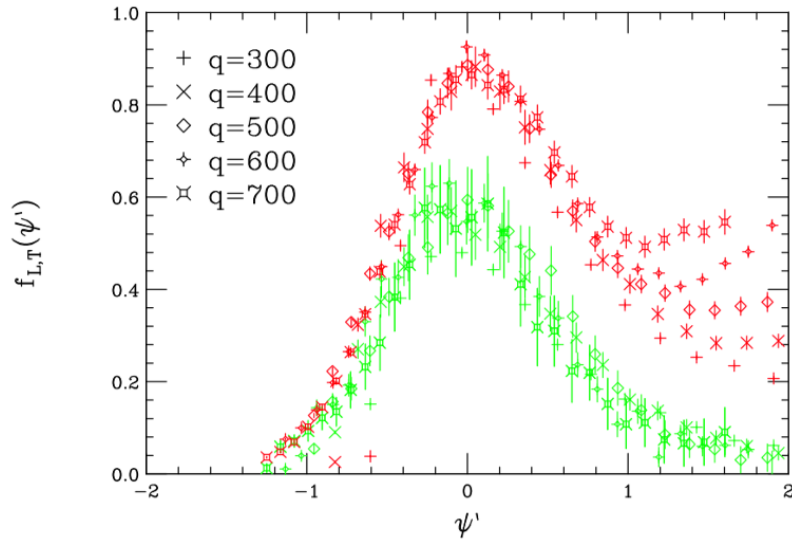
Figure 1.26: Scaling functions f_L (green) and f_T (red) as a function of ψ' The quasi-elastic peak is at $\psi' = 0$. Different shapes represent different momentum transfers. Figure taken from [47].

This $\mathcal{R}_T$ was used in neutrino-nucleus scattering by applying a multiplier corresponding to $\mathcal{R}_T$ to the magnetic form factors of the nucleons. When this correction was applied to the Relativistic Fermi Gas Model, the predictions were consistent with the low energy neutrino scattering results from MiniBooNE [10] and high energy results from NOMAD [26]. This scaling has been extended from the QE region to the resonance region [111] and inelastic regions [23] as well.

Besides the 2 scalings (first and second kind) mentioned above, the (e,e') experiments allow us to introduce two more types of scaling. In the case of EM scattering, the longitudinal and

lateral EM scaling functions are equal ($f_L^{EM} = f_T^{EM} = f^{EM}$). These are observed in inclusive (e,e') scattering experiments and are also known as the 0th kind of scaling. The fourth or the final type of scaling is known as the super scaling (SuSA). This occurs when both the first and the second kind of scaling occur simultaneously. This was first proposed in [16] and later tested and verified by [61] using the global (e,e') data. In fact, Donnelly *et al* showed that the violation in the second type of scaling is not coming from A dependence but due to overlap with non-QE processes like Δ and π production[61]. Similarly with increasing atomic number, the MEC (Meson Exchange Current) contributions also increase which are strongly nuclear density dependent [156]. MEC or meson exchange current events are the processes where the two nucleons are correlated to one another by exchanging virtual mesons (like pion) [156].

1.7.8   Impulse Approximation and Spectral Functions

The model of a bound system of independent nucleons (which are Fermions) breaks for nucleons which are in the orbits near the Fermi momentum. As mentioned earlier, only 80% of the nucleons act like independent nucleons while the rest 20% are correlated to one another. Somehow, one needs to address this behavior to model the lepton scattering off the nucleons.

When a lepton interacts with the nucleus, it will transfer momentum $\mathbf{q}$. This is equivalent to the lepton probing the nucleus of depth $\frac{1}{\mathbf{q}}$. When the momentum transfer $\mathbf{q}$ is small, the $\frac{1}{\mathbf{q}}$ is large which means the incoming electron sees more than one nucleon. Similarly at high $\mathbf{q}$, the lepton can see individual nucleon. Hence, at high momentum transfers, electron is assumed to scatter off a single nucleon. This approach of describing the electron-nucleon scattering where the electron scatters off a single nucleon given a high enough momentum transfer is called the Impulse Approximation (IA) [49]. Under this approximation, the lepton-nucleus scattering process is the sum of all possible scatterings between the incident particle and nucleons inside the nucleus. Mathematically, the nuclear cross-section for this scattering is given as:

$$d\sigma_A = \int dE d^3\mathbf{k} d\sigma_N P(\mathbf{k}, E). \tag{1.95}$$

Here σ_A is the cross-section for nuclear scattering. σ_N is the cross-section for scattering off an individual nucleon. Hence, the cross-section for scattering off a nucleus becomes an integral over all possible scatterings off individual nucleons (inside that nucleus) of given momentum and leaving the residual spectator system with excitation energy (E) [34]. The term $P(\mathbf{k}, E)$ is known as the spectral function which basically is the probability of removing a nucleon of momentum $\mathbf{k}$ from the nucleus leaving the spectator nucleon with excitation energy E. The formalism of spectral functions depends upon the models used for describing the scat-

tering process as well as the underlying nuclear effects. However, based on previous results from lepton scattering experiments, a realistic spectral function should have at least a 80% contribution from the shell model (individual nucleons) at low momentum and low residual energy E, and a 20% contribution from SRC. The spectral functions can be generalized to include various nuclear effects.

1.8 Neutrino-Nucleus Scatterings in QE Regime : A Summary

While both electron scattering (e,e') and neutrino scattering experiments $[(\nu, \nu')$ or $(\nu_l, l)]$ experiments are lepton scattering experiments, only electron scattering experiments can directly measure observables like momentum and energy transfer. Most of the nuclear models are based on these physical variables. Since neutrinos are electrically neutral and only interact through electroweak channels, it is very hard to measure the initial state energy, although we can often estimate the direction. Instead, most of the neutrino-nucleus interaction models are based on Q^2 which depends upon the kinematics of the outgoing lepton. However, neutrino-nucleus scattering is still a lepton scattering event. Hence, most of the nuclear models are based on the developments in electron scattering experiments (especially in the QE regime as discussed in section 1.3.0.1.). Particularly, separation of longitudinal and transverse components in the electron-nucleon scattering cross-sections helped to un-
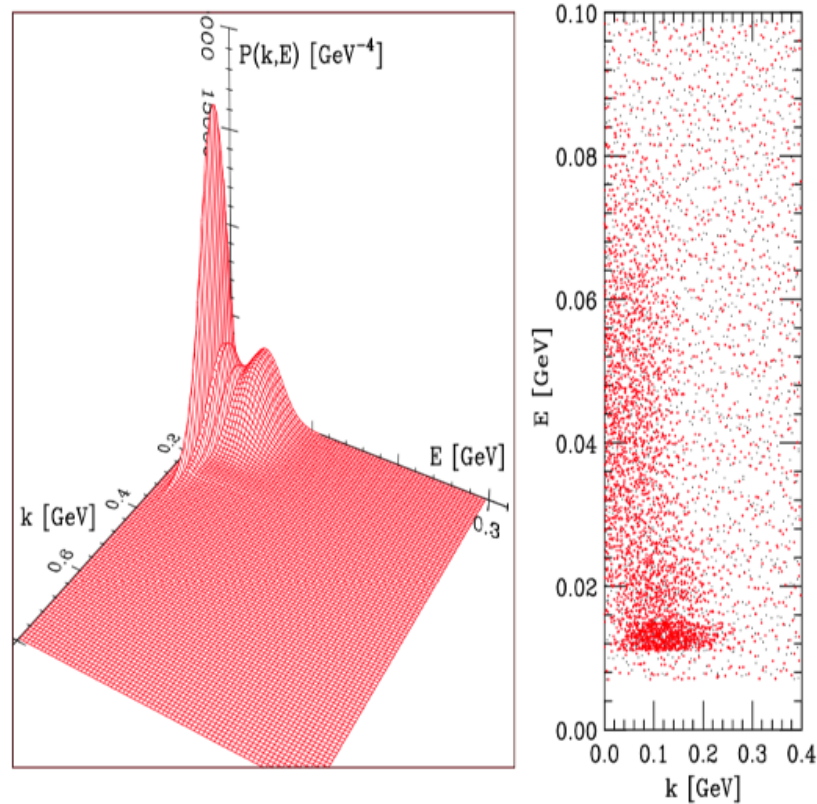
Figure 1.27: Spectral function for Oxygen obtained using the Local Density Approximation method in which the experimentally obtained measurements is combined with theoretical calculations of the spectral functions at different nuclear densities [35]. This method encapsulates contributions from both independent and correlated nucleons. On the left is the 3D distribution of the spectral function with the nucleon momentum (k), excitation energy (E) of the spectator nucleus (nucleus that remains after scattering) and the value P(k,E) which is related to the amplitude of the scattering process. Almost 80% of the contribution comes from shell model mean field theory whereas the remaining 20% at high momentum and high excitation energy comes from short range correlations [36].

derstand the electric form factor G_E, and magnetic form factor G_M. However, neutrino scattering processes need to take into account the additional contribution from axial currents. A formalism for weak current which includes the vector component (that arises from G_E and G_M) and axial component that arises from (axial form factor, G_A) was proposed by Llewellyn and Smith [105].

Multi-nucleon effects (see section 1.7.5)) that were measured and recently reported [150] are also seen in neutrino-nucleus scattering processes. For example, [113] treats the short range and long range correlations in neutrino-nucleus scatterings in the random phase approximation (RPA). Gran, Nieves *et al*[84] and the MiniBooNE results [11] showed that the contributions from 2p2h, an SRC effect (2 particles (nucleons) producing 2 holes), is significant in the QE rich region with additional enhancement from intermediate delta (Δ_{1232}) production and decay mode. One of the limitations of incorporating the SRC, especially the 2p2h, has been that these processes are treated non-relativistically. This means these processes are not extended to the high momentum/high energy transfer regions. The model implemented by MINERvA and discussed in [84] (also called the Valencia 2p2h Model) treats 2p2h effect non-relativistically and is truncated at momentum transfer (energy transfer) of 1.2 GeV/c (1.2 GeV) [122].

Recently there have been progress in expanding these effects into the domain where rel-

ativistic effects are significant. One of the approaches has been to utilize the super scaling phenomena that is observed in (e,e') cross-section when written as a function of momentum and energy transfer. Super Scaling, as explained earlier in 1.7.7, assumes that scaling properties of both (e,e') and (ν_l, l) use universal scaling function to extend the multi-nucleon effects into higher kinematic regime. Studies done by Donnelly et al [61] showed that the longitudinal scaling function of (e,e') agrees with $((\nu_l, l))$ processes but the agreement is poor for the transverse scaling function. Response functions for electron scattering have both iso-scalar and iso-vector contributions whereas neutrino scattering response functions are purely iso-vector. Furthermore, the addition of axial currents for neutrino scattering processes along with its interference with the vector current makes the two scattering processes different. An improved version known as SuSAv2 was proposed by Jimenez *et al*[81] where these differences were addressed while still utilizing the relativistic approach of SuSA.

Figure 1.28 shows that low energy MINERvA data agrees better with SuSAv2. Recently GENIE version 3 has implemented the SuSAv2 as one of the available models to simulate the multi-nucleon processes for neutrino-nucleus scatterings along with already existing Valencia 2p2h model [60].
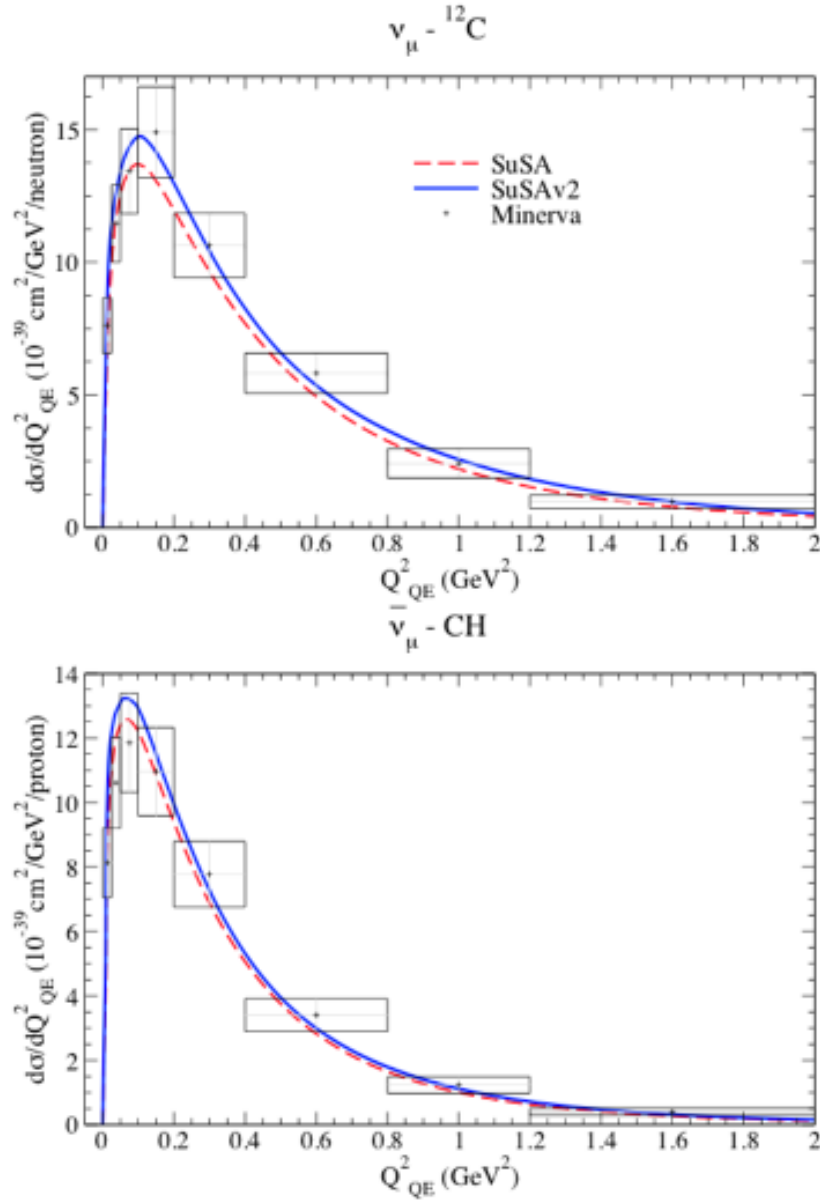
Figure 1.28: Neutrino (above) and anti-neutrino (below) cross-sections extracted using MINERvA data (black dots) is compared against SuSA (red dashed line) and SuSAv2 (solid blue line). The SuSAv2 seems to better agree with MINERvA data than SuSA. Figure taken from [81]. MINERvA data is taken from [69] and [72].

2 Neutrino Beamline and Neutrino Flux

2.1 The Neutrino Beamline

Construction of the Alternating Gradient Synchroton (AGS) [143] at Brookhaven National Lab opened the way for neutrino energy research at GeV energies with intense neutrino beams. The beamline consisted of a proton beam and a beryllium target which was struck by protons accelerated in the AGS to produce pions and hadrons. A 21 meter long decay pipe allowed the pions to decay to produce neutrinos. The detector was only sensitive to muon neutrinos.

Since then, with new developments, neutrino beamlines have evolved to produce more intense beams, broader energy spectra and less contamination of wrong signed neutrinos. Many beam line components come into play to produce an intense neutrino beam with the desired characteristics. At the same time, characteristics of these beamline components and their effect on the neutrino beam needs to be well understood to understand the neutrino flux. In the following section, I will discuss about the properties of neutrino beamline in the context of the NuMI Beamline.
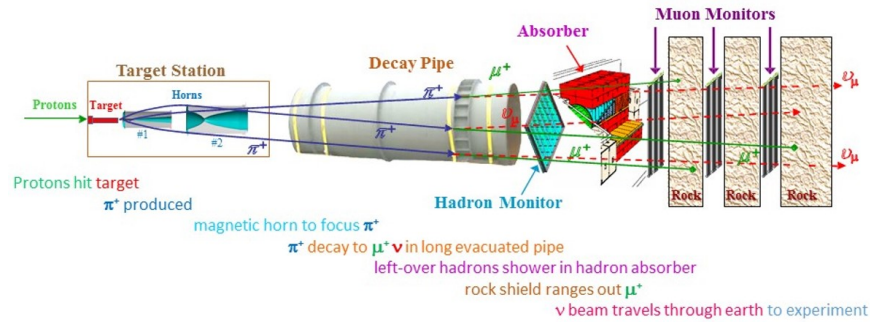
Figure 2.1: Schematic diagram of the NuMI beamline showing the various components. Figure taken from [17].

2.2 NuMI Beamline

NuMI or the Neutrinos at Main Injector is the intense neutrino beam produced at Fermilab and directed towards Minnesota for the MINOS, MINOS+ [53], and NOvA [27] experiments. The neutrinos are produced by hitting a fixed target with an energetic bunch of protons which then produce pions and kaons that further decay to give neutrinos and other hadrons. The incoming proton beam is produced in the main injector in the pulses of 10 μs seconds with each pulse containing between 1.5×10^{11} to 4.5×10^{13} protons per pulse. Each pulse is extracted every 1.33 seconds.

2.3   Production of 120 GeV Main Injector Proton

The main injector is the source of the 120 GeV energy proton beam. The production of this energetic beam starts from the acceleration of the hydrogen ions in the LINAC (Linear Accelerator). The LINAC accelerates hydrogen ions (H^-) from 750 KeV to almost 400 MeV with 1.5 billion ions per bunch. The proton bunch coming out of the LINAC has a long pulse length of almost 80 μs seconds.

The hydrogen ion beam produced at the LINAC is then stripped of electrons and injected into the booster which accelerates the protons to 8 GeV. The booster is a circular accelerator which contains an array of dipole magnets and RF (Radio Frequency) cavities to accelerate the beam into higher momentum. Before entering the booster, the beam goes through the debuncher where the high momentum ions of the beam are slowed down whereas the low momentum ions get the kick. This decouples the momentum and longitudinal position of the ions in the bunch and prevents the spreading of the beam.

Unlike the linear accelerators, the circular track keeps the protons in uniform circular motion by bending the particles with the dipole magnets and accelerating them each time they pass through the RF. We can actually calculate the magnetic force required by the dipole magnets to confine the beam in a circular track of radius r. The force due to the magnetic

field is given by:

$$F = q\mathbf{v} \times \mathbf{B} \tag{2.1}$$

where:

- F is the force experienced by the protons as they travel through the magnetic field.

- q is the charge of the proton

- **v** is the velocity of the proton

- **B** is the magnetic field of the dipole magnet.

This force balances the centripetal force that tries to kick the particles out the circular motion. In classical limit:

$$q(E + v \times B) = \frac{mv^2}{r} \tag{2.2}$$

Since the electric field is 0 inside the circular ring (except where the RF is installed), in the relativistic limit, it becomes:

$$q(c\beta \times B) = \gamma \frac{m_o c^2 \beta^2}{r} \tag{2.3}$$

The curvature of the particle in circular motion is usually given by the inverse of the
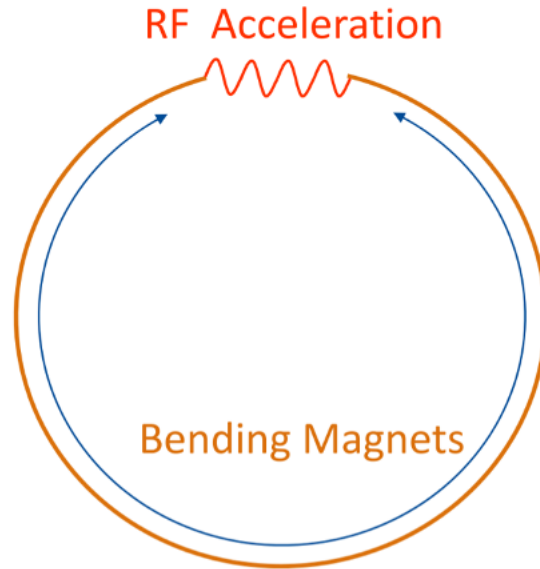
Figure 2.2: Schematic diagram of a typical synchrotron. The bending dipole magnets steer the particles along the circular trajectory whereas the RF cavities accelerates them.

radius of the circular motion:

$$\frac{1}{r} = \frac{\gamma\beta E}{ec} \tag{2.4}$$

The booster has the radius of around 75 meters with the ability to bunch 4-5 trillion protons per batch [28].

The dipole magnetic field allows the protons to be in the circular motion. However since protons are positively charged, they tend to repel from one another. So, to focus the beam, sets of focusing and defocusing quadruple magnets are arranged alternately. Series of focusing and defocusing quadruples correct for the divergence of the beam as it drifts
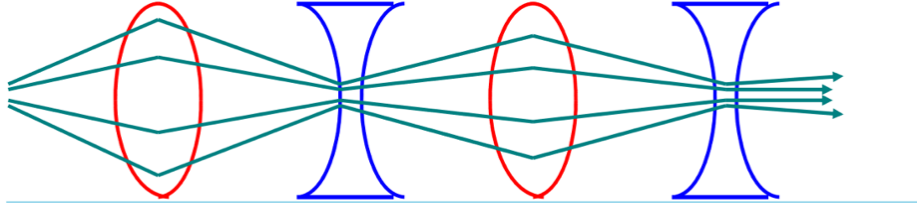
Figure 2.3: Schematic diagram of the arrangements of dipoles and quadrupoles to show the focusing-defocusing-drifting of the proton beam.

through the accelerator.

The 8 GeV proton beam is then injected into the main injector which accelerates the beam to 120 GeV in less than 2 seconds. By utilizing slip-stacking, which allows multiple batches from the booster to be combined, the main injector manages to achieve a proton beam intensity of over 700 kW. To slip-stack multiple pulses of the beam, first of all the beams from the booster are passed through a fast kicker magnet such that two pulses are adjacent to each other in the main ring. This way the overall current density in the ring increases (because more and more pulses of beam are forced to be adjacent to one another). This procedure is called box-stacking. In this case, the number of protons in each batch remains the same but time difference between two consecutive batch decreases. Slip stacking is the process where the two consecutive boxcar batches are forced to coincide with each other by slowing down the front batch and accelerating the front batch [161]. This way, within each RF bucket of the main injector, the number of protons increases and hence the intensity of

Proton Beam Parameters	Values
Beam Energy per proton	120 GeV
POT per spill	4.9×10^{13}
Spill time	10 μ seconds
Repetition Time	1.33 seconds
Proton Beam Power	700 kW (upwards)
Maximum Energy Deposition per spill	310 J/g
Maximum power Deposition per spill	235 W/g
Instantaneous power during spill	30 MW/g

Table 2.1: Characteristics of the MI proton beam [161].

the proton beam. Currently the main injector slip-stacks up to 12 batches of protons in the main injector at 120 GeV.

As far as the neutrino physicists are concerned, relevant physics starts once the 120 GeV proton beam hits the fixed target.

2.4   Proton Beam

In accelerator neutrino physics, the term proton beam basically refers to the beam that hits the target of the beamline producing mesons (parent neutrinos). In the case of NuMI experiments, the proton beam of interest is the beam extracted from the MI accelerator and has the energy of 120 GeV. Table 2.1 shows the characteristics of the proton beam that is extracted from the main injector. The size of the medium energy era (where the neutrino flux peaks at 6 GeV compared to low energy era where the peak was 3 GeV) proton beam

is larger than that during the low energy run era because of the requirement to place more protons in the same spill (to increase the intensity). The transverse size of the proton beam in the medium energy run (the configuration in which this analysis was done) is 1.7 mm along X and Y where Z is the direction of the motion of the beam. We can assume the proton beam to be a 2 dimensional gaussian structure (where both dimensions are perpendicular to the direction of the motion of the beam) and the numbers are the 1 σ spread of the beam from its central value (x=0, y=0, z = direction of the motion of the beam).

2.5 Target

For any accelerator neutrino experiment, the target is one of the most important components. The size and dimensions of the target determine the characteristics and the uncertainties of the neutrino flux.

$$p + N \rightarrow H + X$$

Here p is the incoming proton beam, N is the number of protons or neutrons of the target at rest, H are the hadrons coming out that can range from re-interacting protons and neutrons to pions, kaons etc.
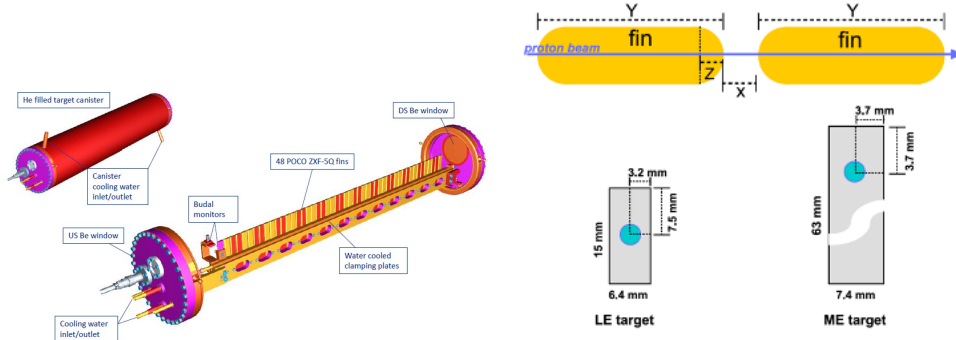
Figure 2.4: NuMI Medium Energy Target system showing the rectangular fins, cooling system, Budal Monitor and beryllium windows through which the beam enters and exits. The proton beam enters from the left Be window and exits through the downstream beryllium window. Schematic diagram of the NuMI target fins are shown on the right along with the LE target fin for comparison. Figure is taken from [56].

The medium energy NuMI target is made from graphite with density $1.78g/cm^3$. There are 50 fins in total with a transverse area of $24 \times 7.4mm^2$. The first 2 fins are called Budal Monitors (BM) that are used to measure the vertical and horizontal position of the proton beam on the target. The BM that measures the vertical position of the target is located 28.5 mm upstream of the rest of the target fins. The BM that measures the horizontal position of the target is located 57.5 mm upstream of the rest of the target fins. The separation between remaining 48 target fins is 0.5 mm. The overall length of the target is 1200 mm (2.5 interaction lengths). Since the proton beam coming out of the main injector is high energetic and intense, small deviations of the beam from its nominal trajectory could cause damage to the target instruments, its cooling and support structures and even the focusing horns. To prevent such beam related incidents and protect the beamline materials, a 1.5

meter long baffle is placed upstream of the target. The baffle has a graphite core and beryl-lium windows to protect the core. It has a hole of 13 mm in the center through which the proton beam passes. The baffle can withstand mis-steering of the beam for a few pulses. An interlock system with thermocouples is installed in the beryllium window which can detect if the beam goes off its nominal trajectory and turn off the beam pulsing.

The design of the target and choice of material are driven by safety factors, pion yield and endurance of the structure under the intense beam. Compared to the low energy era, the proton beam spot size is larger (1.1 versus 1.3 mm $\sigma_{x,y}$). So the fins are designed to be wide enough to contain most of the proton beams and the thermal energy generated by the inter-action of protons on target. At the same time, they should be small enough to minimize the re-absorption of outgoing pions and kaons. The length of the target has to be long enough so that most of the proton beam can interact with the target materials and produce secondary particles. Figure 2.4 shows the medium energy NuMI target.

Figure 2.5 shows that for a 120 GeV proton, the optimal pion production occurs at 160 cm with the density of $1.2 g/cm^3$. Since graphite density is around 1.7 g/cm^3, the individual fins separated by air are used to decrease the effective density of the target.

Every time a proton spill hits the target, a large amount of heat is produced. The tem-
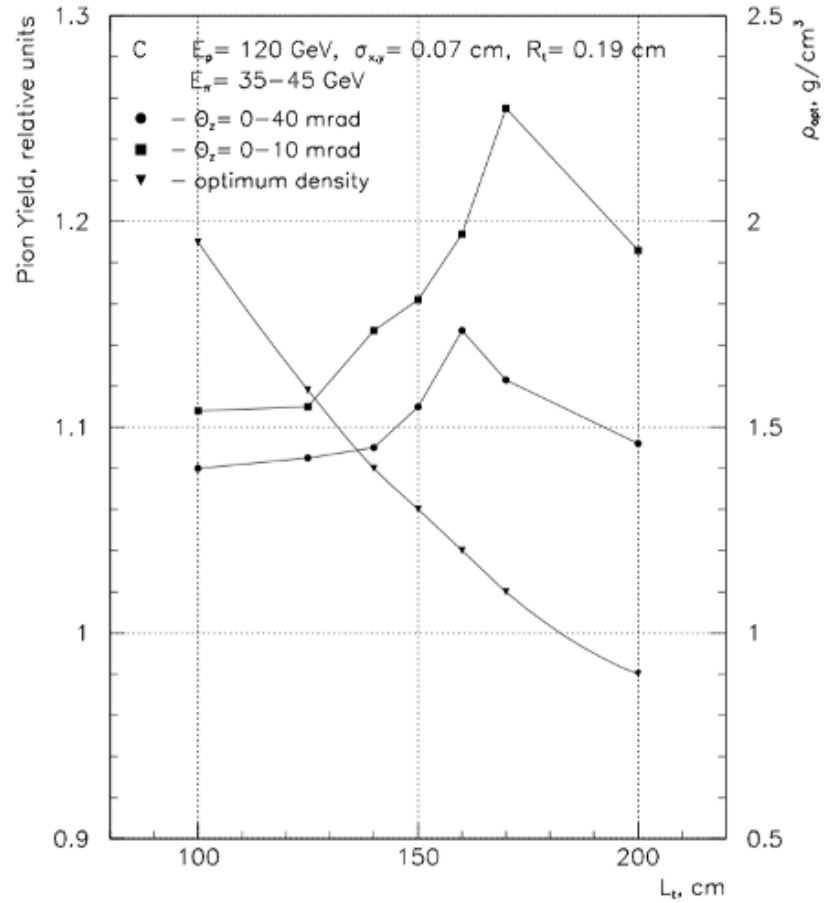
Figure 2.5: Pion Yields from 120 GeV protons with spot size 0.7 mm and target radius of 1.9 mm. Plotted are the yields of pions of energy 35 to 40 GeV. Yields are shown for two different production angles (with respect to the beam) and the optimal target density for each of those yields for different lengths of target (X axis of the plot) is shown by triangles.[92].
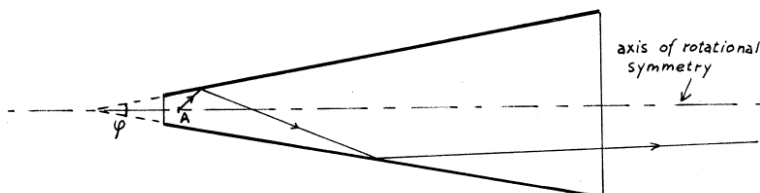
Figure 2.6: Schematic diagram of a horn that shows the opening angle of the horn. A charged particle **A** is produced at some transverse angle with respect to the horn axis. At each point of interaction with the horn, the particle changes the sign of transverse momentum but loses the overall absolute transverse momentum making the particle go more forward.[116]

perature distribution is more stable in a round target. The NuMI target is rectangular with

smooth edges to create a uniform thermal distribution. The target containment vessel is

Helium filled with a water cooling system running on the outer can of the target structure

as shown in figure 2.4.

2.6   Focusing Horns

The initial design of the focusing horns was first proposed by Simon Van de Meer in his 1962

paper **A Directive Device for the Charged Particle and Its Use In an Enhanced**

Neutrino Beam [116]. Figure 2.6 shows the working principle of an ideal focusing horn. The
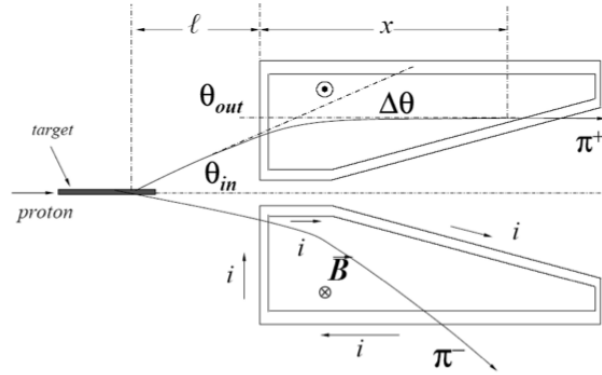
Figure 2.7: Focusing (defocusing) of an incoming π^+ (π^-) by a conical horn

focusing horn is conical in shape with an opening angle ψ. The horn is azimuthally symmetric and as the particle interacts with the horn, the angle between the particle trajectory and horn axis goes down by $\delta\theta$ [116]. In an actual experiment, the particles passing through the horns are charged particles and the toroidal magnetic field gives the kick required to reduce their transverse momentum (relative to the horn axis). The horn axis is parallel to beam axis.

Figure 2.7 horn shows how focusing or defocusing of the particle works in a simple conical horn. A π^+ is produced at an angle θ_{in} which is given by:

$$\theta_{in} = \frac{r}{l}. \tag{2.5}$$

For the pions to be perfectly focused, its outgoing angle should be 0 i.e. $\theta_{out} = 0$. That

means:

$$\delta\theta = \theta_{out} - \theta_{in}$$

$$\delta\theta = \theta_{in}. \tag{2.6}$$

The angle θ_{in} can also be (small angle) approximated by the momentum of the pion and is given by:

$$\delta\theta \approx \frac{<p_T>}{p}. \tag{2.7}$$

The change in outgoing angle depends on the magnetic field B and the magnetic path-length x seen by the pion.

$$\delta\theta = \frac{Bx}{p}. \tag{2.8}$$

where p is the momentum of the hadron. The term on the right hand side is the transverse momentum kick experienced by the pion as it travels through the horn. This term is obtained by doing the path length integral of B :

$$\delta p = \int_x B dx. \tag{2.9}$$

Now substituting the values of $\delta\theta$ and $\bar{\theta}_{in}$,

$$\frac{Bx}{p} = \frac{<p_T>}{p}. \tag{2.10}$$

The magnetic field in the toroid follows the Ampere's law and is given by:

$$B = \frac{\mu_o I}{2\pi r}.$$
(2.11)

So the magnetic path-length that the pion needs to see before being completely focused is given by :

$$x = <p_T> \frac{2\pi r}{\mu_o I} r.$$
(2.12)

This means a pion that is produced more upstream of the target (larger r) will need to see longer path-length (larger x). Since the $<p_T>$ of the pion is constant, we end up with a conical shape horn. Note that there are few approximations done to get the above equation.

- The entering angle θ_{in} has to be small.

- The focusing horn is ideal with no deformities introducing perturbation in the current.

- The pions exiting the target do not have constant $<p_T>$. This means the angle θ_{in} is not constant itself.

The main limitation of the conical horn is that it will only work for pions that have the constant momentum p_T which is not true in the real experiments. We want the focusing system to be able to focus pions for any angle. Earlier, we saw that the change in p_T
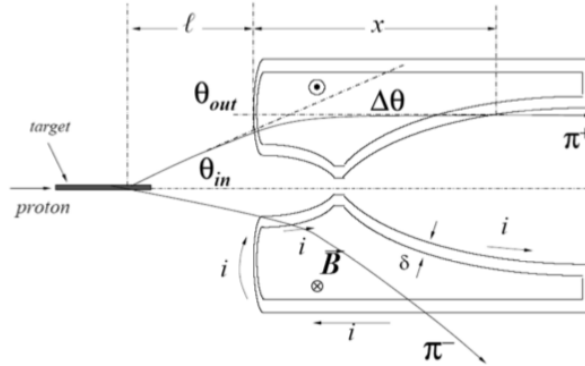
Figure 2.8: Figure showing the focusing by a parabolic horn. Here the point from which the pions originate is the focal point of the parabola. l is the focal length of the parabola and x is the magnetic path length seen by the pion as it goes through the horn. Figure is taken from [161].

experienced by the pions due to magnetic kick is given by:

$$\delta\theta = \frac{Bx}{p} = \frac{\mu_o I x}{2\pi r p}. \tag{2.13}$$

If we start out with a parabola given by $z = ar^2$ such that a is the parabolic parameter (unit cm^{-1}), the focal point of the parameter can be considered to be the point in target from where the pions are exiting.

As shown in figure 2.8, a parabolic shape can focus any particles produced at any angle. If the shape of the inner conductor is given by a parabolic equation $z = ar^2$, then the path length of the pion is $x = 2ar^2$. The term is twice the parabolic equation of the horn IC

because of the second parabola of the bi-conical horn. Substituting this in the $\delta\theta$:

$$\delta\theta = \frac{Bx}{p} = \frac{\mu_o I x}{2\pi r p}. \tag{2.14}$$

Again in the case of focused pion $\delta\theta = \theta_{out} - \theta_{int} = -\theta_{in}$, the equation becomes:

$$\frac{\mu_o I x}{2\pi r p} = \frac{r}{l} \tag{2.15}$$

where l is the focal length of the parabola in this case. So, the parabolic horn focuses all pions (or any right signed charged particles) regardless of their entrance angle. Similarly, the focal length of the parabola depends on the momentum of the hadron.

Still there are small angle approximations and neglecting corrections due to horn deformity, temperature, non-uniform current pulsing etc., but the above equation shows the reason behind the shape of NuMI horns. In case of ideal parabolic horns, the region inside the inner conductor and the region outside the outer conductor is generally field free. However, deformities on the horn shape could create some non-zero magnetic field in these regions.

The thickness of the horn inner conductor (IC) is driven by two requirements:

- Horn IC should be thin enough to minimize the meson absorption that pass through it.

Figure 2.9: Simulated Image of the Inner conductor of the two NuMI focusing horns. The focusing horns are bi-conical in structure. Both horns are 3 meters long. The neck (the smallest aperture of the horn) is 9 mm radius in the case of first focusing horn and 3.9 cm in the second focusing horn. The first focusing horn (left) is closer to the target than the second focusing horn.

- Horn IC should be thick enough to withstand the mechanical stress and fatigues due to the proton beam.

In order to minimize the thermal stress in the horns, the inner conductor is continuously sprayed by water at a rate of 30 gal/min [56]. Figures 2.9 and 2.10 shows the structure of the NuMI horns. The horns are made of aluminum and the wire strip conducts electricity from the outer conductor to the inner conductor forming a loop such that a toroidal magnetic field is formed. The shape of inner conductor and the choice of number of focusing horns are driven by the optimization of the neutrino beam. Not all pions and kaons are perfectly focused by the horns. Some of the particles get over-focused or under-focused.

Figure 2.11 shows the different ways the particles are focused by the two horns. As we can see, the kick given by the magnetic field of the focusing horn is not always equal to the required p_T by the particles to get focused perfectly. By placing a second focusing horn, those imperfections can be corrected resulting in a less divergent beam of neutrino parents (mostly pions). As much as a 20% increase in the neutrino flux can be obtained by placing a
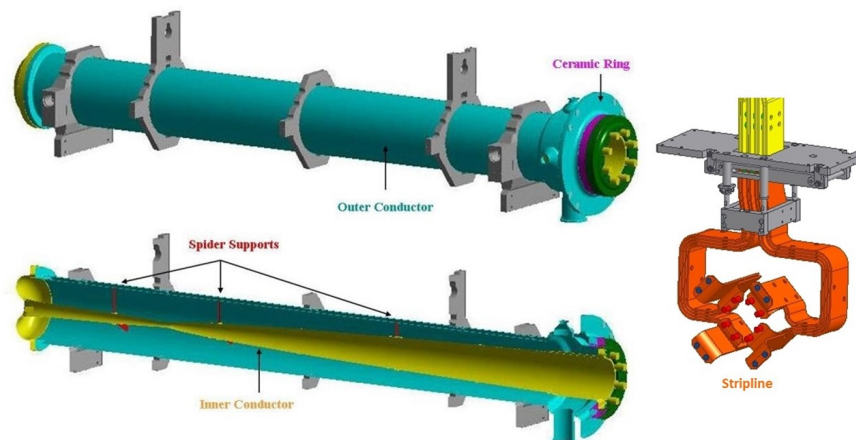
Figure 2.10: Outer conductor of the first focusing horn (top) and the arrangement of inner and outer conductors (bottom). On the right is the diagram of the strip line mounted on the rear end of the focusing horn.The strip line carries the current across the outer/inner conductor of the focusing horn. Figure is taken from [56].
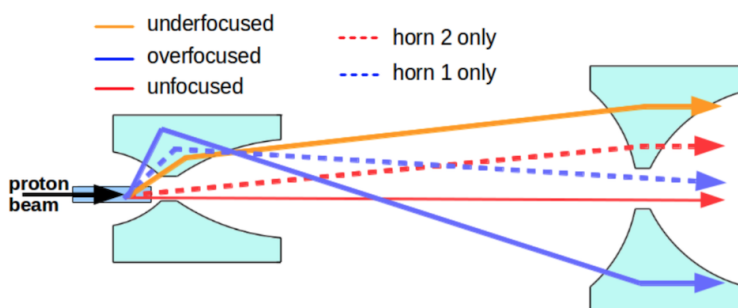
Figure 2.11: Various ways pions are focused from the NuMI horns. [18].
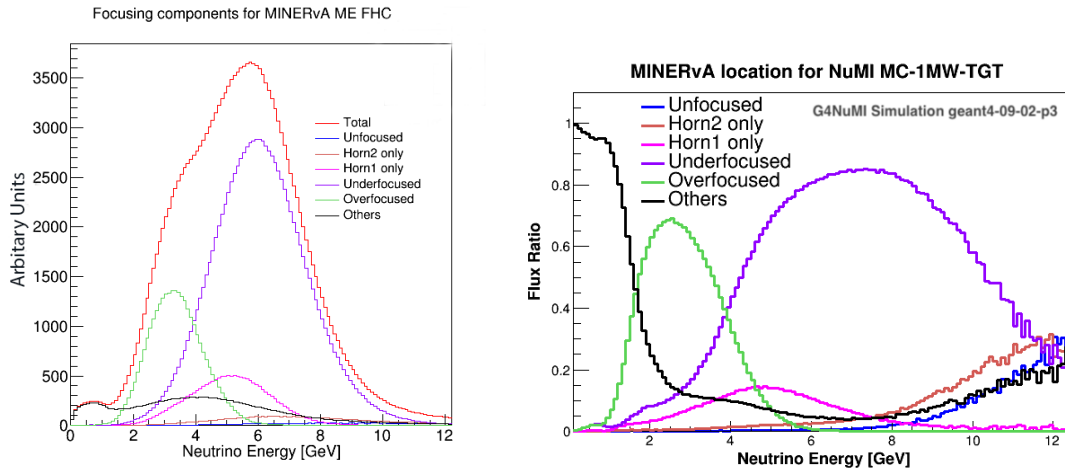
Figure 2.12: Left plot shows the contribution of various kinds of neutrino parents focusing on the neutrino flux as seen by the MINERvA detector. On the right is the ratio of flux from various focusing contributions to the total flux. Figure taken from [43].

second focusing horn [161]. Similarly, a third focusing horn could correct for the additional divergence of the beam. In the case of NuMI , two focusing horns with the later having larger focal length are placed consecutively.

Figure 2.12 shows the contribution of various kinds of focusing on the MINERvA neutrino flux. Note that horn 1 focuses less than 10% of neutrino parents perfectly (i.e. not requiring horn2 for further correction). The bump of flux at less than 1 GeV comes from scraping of various beamline materials (mainly baffle). The rising part of the flux is mostly coming from the parent pions which are over-focused by horn 1 but corrected by horn 2. Similarly, the falling part of the flux is mostly coming from the under-focused parent pions. Both under-focused and over-focused parent neutrinos have significant contributions in the overall

neutrino flux which is only possible due to the correction from the second focusing horn. Because of their position relative to the target, horn1 focuses mainly low momenta parent neutrinos resulting in low energy neutrinos compared to horn 2 (compare horn1 and horn2 only categories). Adding the second focusing horn increases the focusing by almost 50%. In the ME configuration, 200 kA current is pulsed into the horns.

2.7 Decay Pipe

Charged pions and kaons, that are produced by the proton beam interacting in the target are focused by a set of magnetic horns. The focused pions and kaons then continue on until they decay to give neutrinos and leptons. The decay pipe gives the required length for the pions and kaons to decay. The NuMI decay pipe is a 675 meters long and hollow cylindrical structure with a diameter of 2 meters. It provides a low density environment for the particles to decay without going through significant multiple interactions with air. The decay pipe is made of steel pipes with each unit of length 12 meters reinforced against each other. Since the interaction of particles through the decay pipe might cause the decay pipe to heat, a copper cooling line is installed outside the steel decay pipe. The outer layer is then re-enforced with concrete to prevent radiation contamination to the ground water and surrounding area.

The required energy profile of the neutrinos drives the length of the decay pipe. The decay

length of the pion and kaons going through the decay pipe is given by:

$$L = \gamma\beta c\tau \tag{2.16}$$

where $\gamma = \frac{E}{m}$ is the Lorentz factor,

$\beta \approx \frac{E}{p}$ and

$\tau = \frac{1}{\lambda}$ is the mean life time of the particle which is inverse of the decay rate. The mean

life time of the particle relates is the time required for the population of the particle to be

reduced to e^{-1} of the initial value. This value comes from the equation:

$$N = N_o e^{-\frac{t}{\tau}} \tag{2.17}$$

The peak of the NuMI medium energy neutrino flux is around 6 GeV. Assuming this comes

from a focused beam of roughly 10 GeV pions, we can see that the decay length required for

the pions to go from initial value of $1/e$ of the initial value is:

$$L(meters) = 86 \times 1 \times 3 \times 10^8 \times 2.6 \times 10^{-8}$$

which is around 670 meters. So by the time 6 GeV pions travel 670 meters, 63% of them would decay to give muons and neutrinos. Energy of the neutrino coming from a pion decay is related to that of neutrino as $E_\nu = 0.43 E_\pi$. A more detailed explanation on pion decay kinematics is given in appendix A.1.

Similarly, the radius of the decay pipe affects the neutrino flux at the low energy spectrum. The low energy pions which decay to give low energy neutrinos has relatively larger transverse momentum. As seen in figure 2.12, the low energy pions are over-focused pions that are later corrected by horn 2. Not all pions get corrected perfectly by horn 2 leaving them with some residual transverse momentum. Some of these pions can get absorbed in the decay pipe before they decay.

The length of the decay pipe is a delicate balance between the desired neutrino flux and the cost. The cost of excavation and the concrete required to construct the decay pipe and the desired neutrino flux drives the length and the radius of the decay pipe. For neutrino near detectors like MINERvA (and near detectors of other oscillation experiments), the location at which pions decay will determine the neutrino energy spectrum. This is covered in more detail in section 3.4 of this thesis.
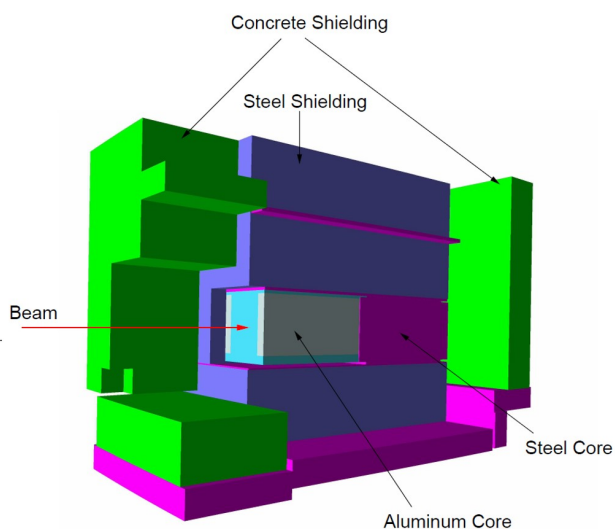
Figure 2.13: NuMI hadron absorber showing the steel and aluminum core with steel shielding. The steel shielding is further reinforced by concrete shielding. Figure is taken from [56].

2.8 Hadron Absorber

Out of 1 MW beam power, 85% contributes to the secondary particle production. The remaining 15% of the beam power has to be deposited somewhere safely. The hadron absorber is a solid structure made of aluminum and steel shields at the end of the decay pipe. The remaining primary protons, and hadrons that didn't decay in the decay pipe are absorbed by the hadron absorber. The hadron absorber is 5.5 m wide x 5.6 m tall x 8.5 m long. The hadron absorber is designed to withstand the power deposited by the residual primary proton beam. It can also withstand the power deposited by a few spills of 1 MW beam under beam failure conditions.
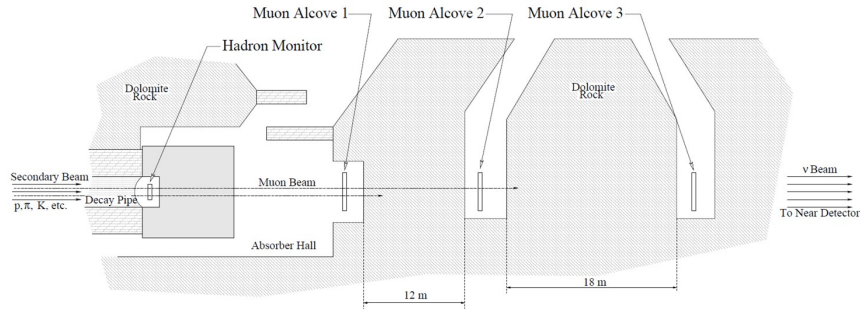
Figure 2.14: Schematic diagram showing the beam monitoring system in the NuMI beamline. The hadron monitor is upstream of the absorber whereas the 3 muon monitors are downstream of the absorber separated by some materials to let the muons of different energies range out.

2.9   Beam Monitoring System

The beam monitoring system includes 4 monitors: 1 hadron monitor and 3 muon monitors.

The hadron monitor is installed before the hadron absorber. It is an array of radiation

hardened 7×7 ceramic pixels that measure the profile of the proton beam and undecayed

secondary hadrons. The profile of the proton beam gives information about the possible

failures in target, scrapping in beam line materials etc.

Because muons have a life time of around 2 μs and can travel through hadron absorber with

minimum ionization, they can be used to understand and characterize the neutrino beam

along with possible beam related incidents. As seen in figure 2.15, the energy of the muons

(which is almost 63% of the pion energy) is in the order of few GeVs to few tens of GeVs.

The muons go through the energy loss described by the Bethe equation [86]:
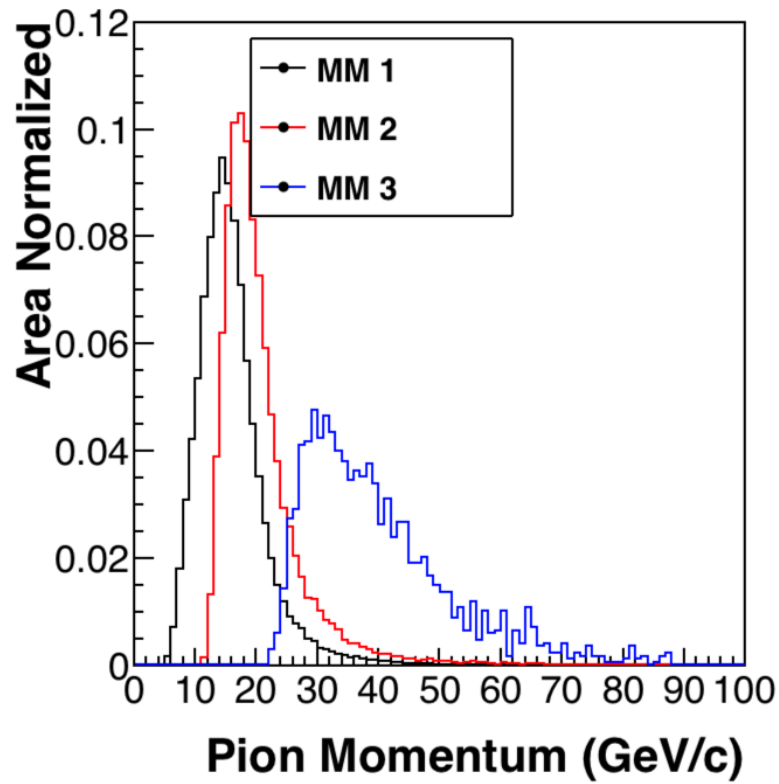
Figure 2.15: Required momentum of the pions that decay to give muons making it to the 3 muon monitors. Because of the earth materials in between each muon monitor, the low energy muons ranges from a few GeV to a few tens of GeV before reaching the third muon monitor (MM 3). Muons coming from less than 10 GeV pions range out inside the hadron absorber.
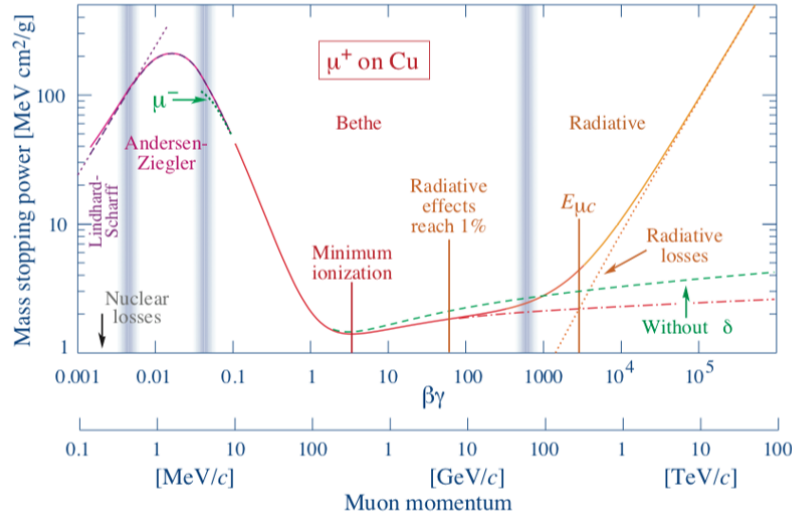
Figure 2.16: Energy loss for the muons in copper from MeV to TeV range. The muons seen by muon monitors are in the few GeV range and fall in the minimum ionization region of the curve which is around 2 MeV cm^2/g. The curve is relevant as long as the bremsstrahlung isn't significant. For electrons, the bremsstrahlung kicks in at above 240 MeV whereas for muons it is above 2300 GeV. Figure taken from [160].

$$\frac{1}{\rho} < -\frac{dE}{dx} >= Kz^2\frac{Z}{A}\frac{1}{\beta^2}[\frac{1}{2}ln\frac{2m_ec^2\beta^2\gamma^2W_{max}}{I^2} - \beta^2 - \frac{\delta(\beta\gamma)}{2}]. \tag{2.18}$$

The above equation is given for copper but is also relevant for earth materials of similar Z. The $\frac{dE}{dx}$ is in the units of MeV/cm. The muons seen by the muon monitors lose energy by minimum ionization which is around 2 MeV per cm for the density of materials we are interested in.

The Muon monitors are 3 9×9 ionization chambers with a total coverage of $2 \times 2m^2$. Since the muon beam is very divergent by the time it reaches these monitor, their resolution
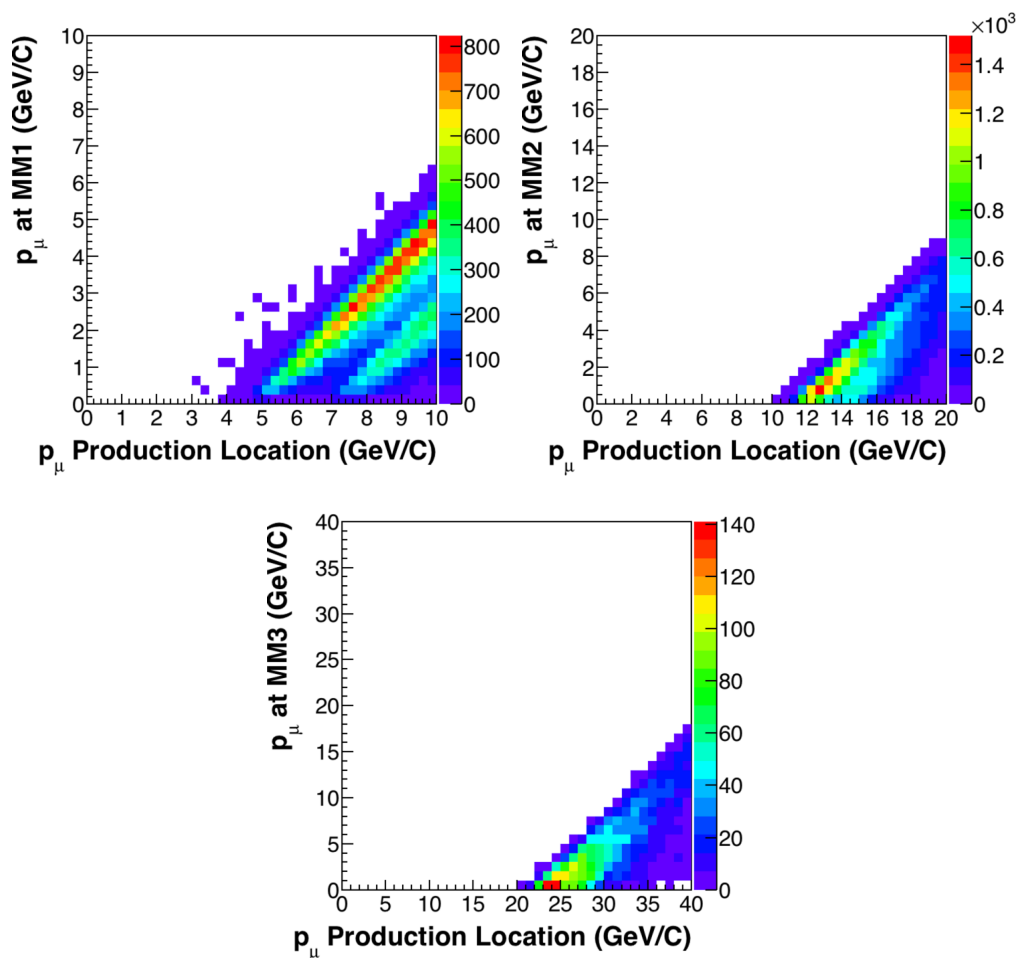
Figure 2.17: Momentum of the muons when they are produced in the decay pipe (x axis) and when they reach the muon monitors (y axis). The X axis shifts as we go from muon monitor 1 and muon monitor 3 because of the increase in materials from first to third monitor. The double band structure seen is due to the hadron absorber as besides earth, muons also have to pass through steel aluminum and concrete resulting in slightly different dEdx profile in various materials.

does not need to be fine. Helium is used as ionization source for all 4 monitors with the hadron monitor operating at the pressure of 1 psi and the muon monitor operating at 3 psi. A detailed description of the construction and operation of the beam monitor is given in [161], Chapter 6.

One part of my neutrino flux work was the simulation of performance of the muon monitors. This chapter will discuss the muon monitors from the perspective of simulations. The simulation of muon monitor events are done in two steps. The first part is the simulation of the neutrino event all the way from protons hitting the target to production of neutrinos. Then the kinematics of the muons are calculated by looking at the decay kinematics of the pion. Then the second part of the simulation takes these muons and propagates them through hadron absorber, earth materials and muon monitors. The simulation is done using g4numi-v2 which is based on geant4.9.p6 .

Figure 2.18 shows the data and simulation for the horizontal beam scan and the response of the muon monitor 1. This shows that the muon monitor is sensitive to both horn current and displacement of the proton beam. The simulation cannot replicate the data but it shows similar attributes. Works are underway to improve simulation and understand data as of writing this thesis.

Figure 2.19 through 2.21 show the number of events seen by muon monitors when the horn is on or off. The 81 pixels represent each pixel of the muon monitor. The collimation
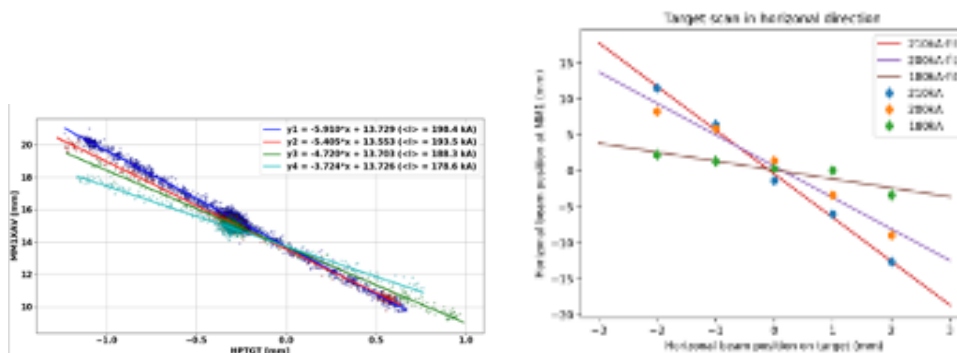
Figure 2.18: Horizontal beam scan and the response of muon monitor 1 with the data (left) and in the simulation (right). Although the simulation tries to follow the trend from the data, works are ongoing to understand data and simulation. Muon monitor data are calibrated and needs to be corrected for various beamline effects. A more detailed understanding of the corrections that go into the data and the simulation of muon energy loss at low energy has to be understood to get a clearer picture. Figure taken from [158].
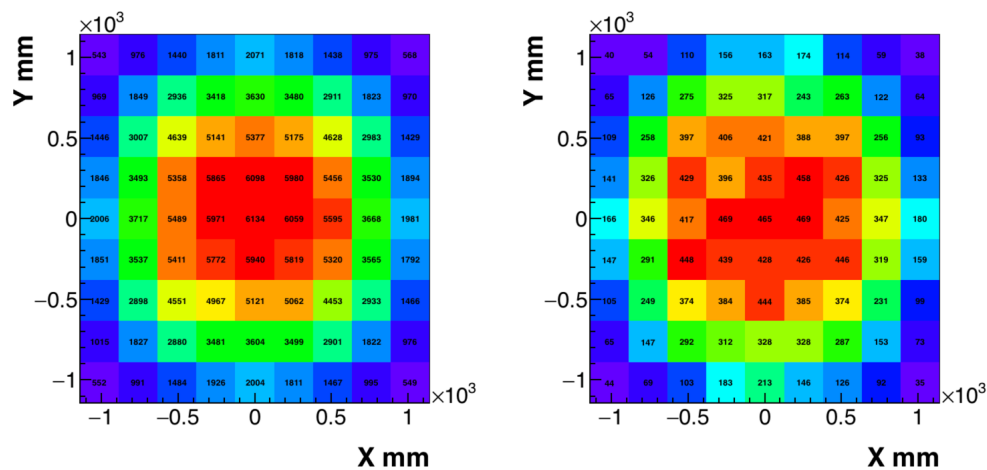
Figure 2.19: Number of muons seen by Muon Monitor 1 when the current is on (left) and when the current is off (right) from the simulation. Both plots are made with same number of protons on target.
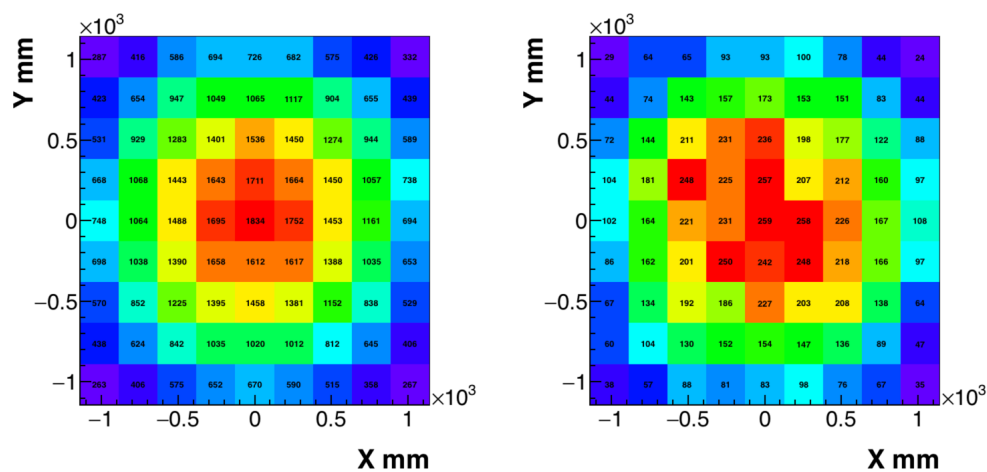
Figure 2.20: Number of muons seen by Muon Monitor 2 when the current is on (left) and when the current is off (right) from the simulation. Both plots are made with the same number of protons on target
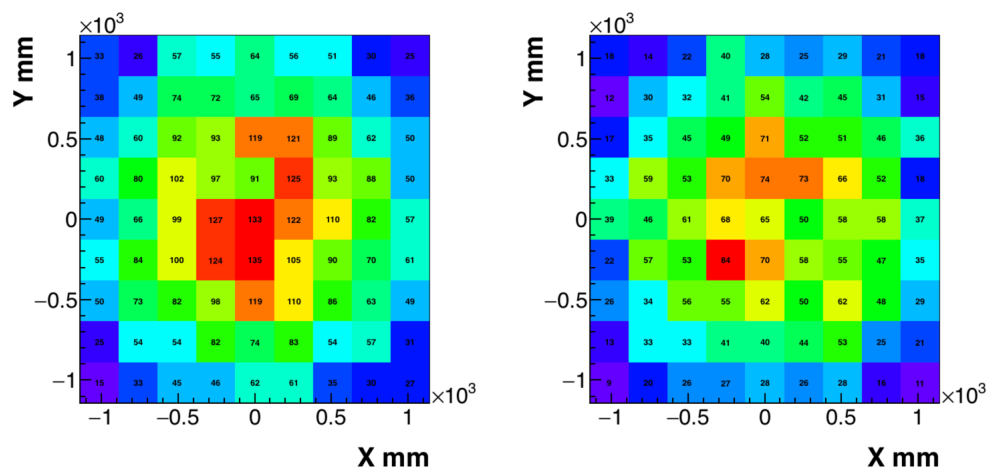
Figure 2.21: Number of muons seen by Muon Monitor 3 when the current is on (left) and when the current is off (right) from the simulation. Both plots are made with same number of protons on target.

effect due to 2 meters diameter decay pipe and in the case of horn-on data, focusing shows more events in the central part of the MM compared to the periphery. In the case of horn-off data also, since the beam is divergent, we can see similar features. Both simulations were done with 500 million protons on target. In both cases the muon beam is azimuthally symmetric i.e. left to right or top to bottom on a given row or column, the numbers of muons seen by a pixel is similar to the pixel on the other side of the center.

2.10   Muon Monitors and Neutrino, Muon Correlations

The muons that are seen by the muon monitors are correlated to the neutrinos because both the neutrinos and the muons come from the same pion or kaon decay. Since the muon monitors are placed in different locations of the NuMI beamline, it is in a unique situation of sampling the muons of different energies (see figure 2.15) and correlate them to the neutrino flux. Because of the poor energy resolution of the muon monitors, reconstructing the energy profile of the incoming muon beam is difficult. However, based on the ranging out of muons, we can estimate the minimum energy of the incoming muon flux seen by each of the muon monitors and correlate it to the neutrinos that were produced by the same decay reaction. Since the muon monitors are sensitive to change in beam parameters like horn current and

target displacement, they could, in principle, be used to constrain the focusing uncertainties of the neutrino flux [106].

Figures 2.22 and 2.23 shows the correlation between neutrino flux and muon flux for off-axis (NOvA) and on axis (MINERvA) decay kinematics. Appendix A.1 discusses the kinematics of off axis neutrinos in more detail. Appendix A.4 has a brief information on the NOvA experiment. To understand properly, the neutrino fluxes and the muon fluxes are created in the decay pipe (most of the time). The off-axis and on-axis neutrino detectors see different neutrino energy spectra coming from the same decay due to decay kinematics. Since the minimum energy required to the muons to reach MM1 (MM2) is 5 GeV (10 GeV), figure 2.23 and 2.22 shows the coverage of muon monitors 1 and 2 for the neutrino flux seen by NOvA and MINERvA . MM1 covers most of the focusing peak of the neutrinos in both case and MM2 covers the tail of the focusing peak.
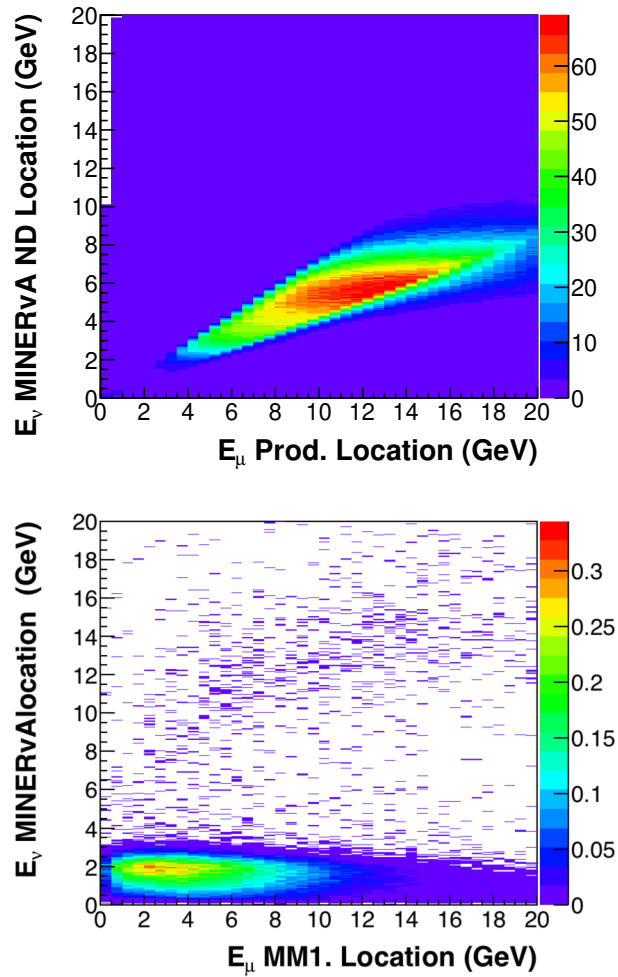
Figure 2.22: Energy of the ν_μ and ν_e produced from the pion decay (left). The left plot shows the correlation between the neutrino energy as seen by the MINERvA detector and muon energy. The right plot shows the energy of the muon when they reach the MM1 versus energy of the neutrino as seen by the MINERvA detector.
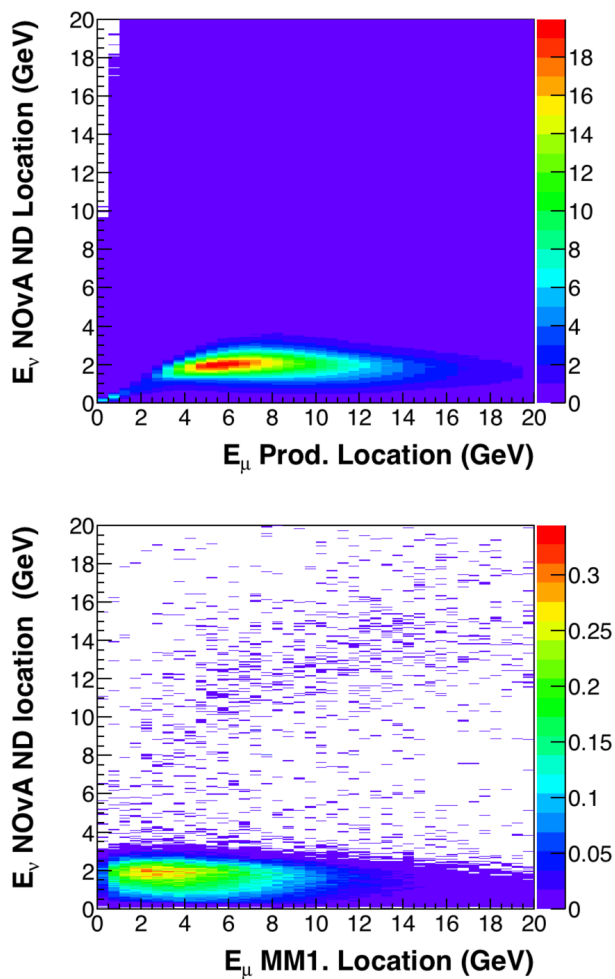
Figure 2.23: Energy of the ν_μ and ν_e produced from the pion decay (left). The left plot shows the correlation between neutrino energy as seen by the NOvA detector and muon energy. Since the NOvA near detector is 14 mrad off-axis from the neutrino beam, the kinematics of pion decay produce a very narrow neutrino energy profile. On the right is the energy of the muon when they reach the MM1 versus the neutrino energy as seen by the NOvA near detector.

3   Long Baseline Neutrino Facility Beam line

3.1   The LBNF Beamline

The LBNF facility will be designed to support and facilitate the neutrino beam that fulfills the physics requirement of the DUNE experiment. DUNE is a long baseline neutrino experiment that will sit on-axis of the LBNF beamline. With a near detector at 574 meters from the target and the far detector 1200 km away at South Dakota, DUNE will be a multi-decade neutrino physics experiment to measure the unknown parameters of Standard Model and search for physics beyond standard model [3].

The LBNF beamline is optimized to measure the CP violation with high precision in the lepton sector. The optimization process was done by implementing a genetic algorithm that took beamline parameters as the fit parameters and floated them to find the parameter configuration that maximized the estimated CP sensitivity [68]. The fit parameters floated the focusing horn, target and beam properties simultaneously. The horn parameters included more than 20 fit parameters to adjust the shape and size of the horn along with the thickness of the conductor, horn current. The 3 target parameters included the length of the target, width of the target fin and the radius of the target can. The beam parameters included the
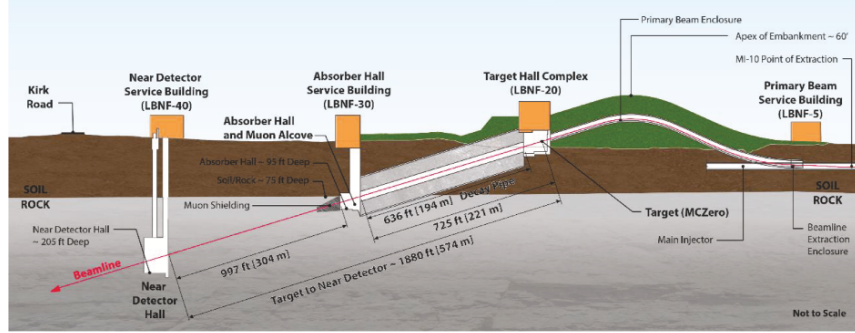
Figure 3.1: Schematic diagram of the DUNE Beamline showing the Target Hall, Decay pipe, Absorber hall and Near Detector Hall. Figure taken from [4].

beam spot size and proton energy. Figure 3.2 shows the various parameters of the horns that were optimized to determine their shape. The CP violation is generally written as [4]:

$$A_{CP} = \frac{P(\nu_\mu \rightarrow \nu_e) - P(\bar{\nu}_\mu \rightarrow \bar{\nu}_e)}{P(\nu_\mu \rightarrow \nu_e) + P(\bar{\nu}_\mu \rightarrow \bar{\nu}_e)} \qquad (3.1)$$

The oscillation probability term which is given by $P(\nu_\mu \rightarrow \nu_e)$ for muon to electron neutrino oscillation and $P(\bar{\nu}_\mu \rightarrow \bar{\nu}_e)$ for muon to electron anti-neutrino oscillation are functions of differences in neutrino mass eigenstates (Δm_{ij}^2), CP violation term (δ_{CP}, distance between neutrino source and detector, and energy of the neutrino. Chapter 1.2.2 goes through the detailed discussion of the neutrino oscillation physics. The oscillation probability can be written as a function of neutrino energy. The focusing of the neutrinos in the desired energy phase space depends upon the properties of various beamline parameters. The genetic algorithm uses the beamline parameters as fit parameters to get the best fit values optimized for
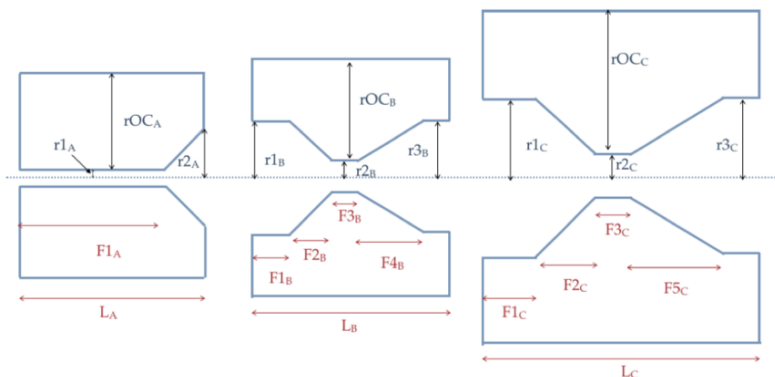
Figure 3.2: Figure showing various shape parameters of the 3 focusing horns that were floated in the optimization process. Figure taken from [68].

maximum sensitivity to the CP violation. Like any other accelerator neutrino beamline, the overall configuration of the LBNF beamline is similar with a beam source, target, focusing horns, decay pipe and an absorber. The functions of each of these components are explained in the NuMI beamline section. As some of the beamline components are still under review as of this writing, there might be discrepancies in the final version of the beamline and the information provided below.

3.1.1 Proton Beam

The proton beam that will be delivered to the LBNF beamline is going to be at 1.2 MW intensity to 2.4 MW intensity with ability to operate from 60 to 120 GeV [4] .
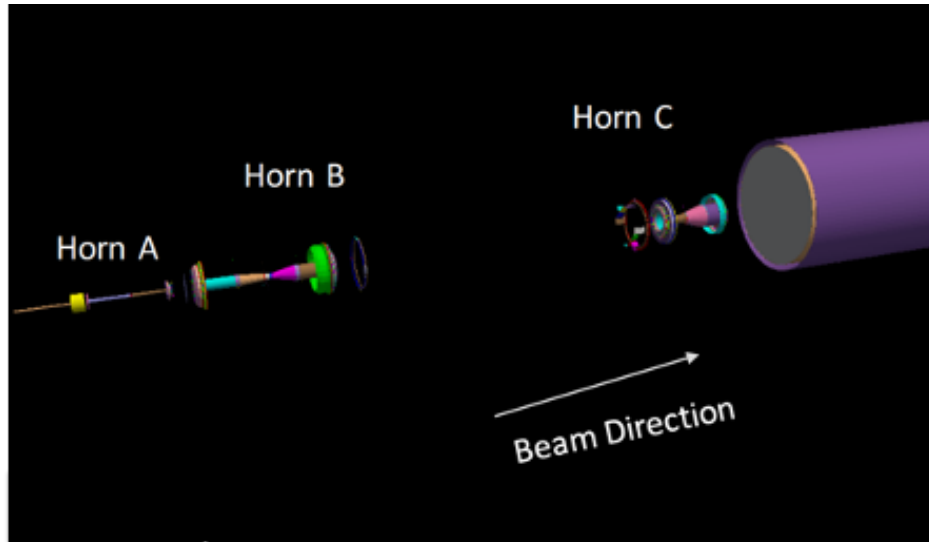
Figure 3.3: Schematic diagram of the Optimized beamline showing the Horn Inner Conductors and the Start of the Decay Pipe.

3.1.2   Target

Optimization of the beamline shows that the improvement in CP sensitivity prefers a longer target. The optimization seems to prefer a 4 interaction length target (i.e. ≈ 2 meters long target). Engineering constrains the design of the target up-to 1.5 meters (see figure 3.4) and studies done in Warwick University have shown that the target performance improved if the beam spot size is 1/3 of the target radius. The target will be fully inserted inside the first horn (Horn A). The preference towards longer target comes from neutrino flux from more secondary interactions that would otherwise escape the target.
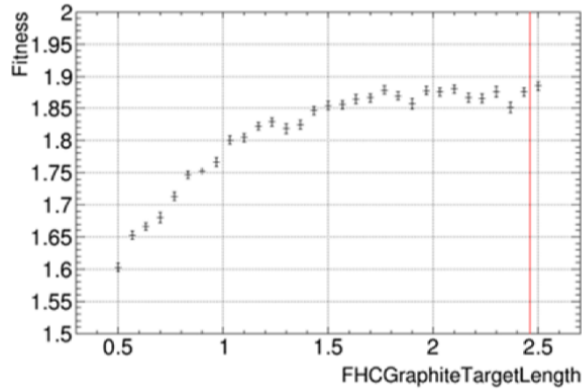
Figure 3.4: CP Sensitivity versus Length of the Target. Note that the optimization prefers a longer target but after 1.5 meters the sensitivity still increases but with a smaller slope. Figure taken from [68].

3.1.3 Focusing System

Unlike the NuMI focusing system, the DUNE focusing system will have 3 focusing horns namely Horn A, Horn B and Horn C respectively. Horn A is cylindrical with the target completely inserted inside it. Horns B and C are biconical. The lengths of the 3 horns are 2.2 meters, 3.9 meters and 2.2 meters respectively operating above 290 kA [126]. Because of their arrangement, Horn A and B will enhance the peak and rising part of the neutrino spectrum whereas Horn C will enhance the falling part of the neutrino spectrum. Compared to the 2 horn NuMI -style design, the 3 horn design will produce a neutrino flux with a broad focusing peak and a suppressed tail. It should be noted that second oscillation maximum is at 0.8 GeV and the first oscillation maximum is at 2.4 GeV for the DUNE far detector location. In both energy regions, the flux is enhanced with a 3 horn design.
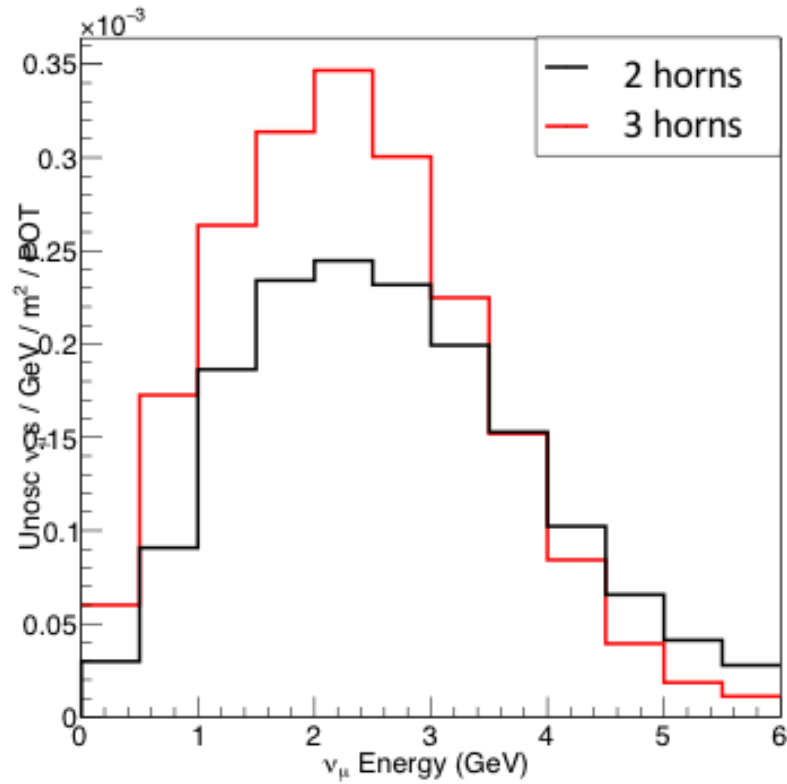
Figure 3.5: Neutrino Flux at DUNE Near Detector with the 2 horns (NuMI style) and 3 horns design. The 2 horn flux was obtained by simulating with a 1 m long NuMI style target with 2 NuMI style horns. The 3 horns was simulated with 2 meters long target with 3 focusing horns that were slightly larger than the final optimized version.

3.1.4 Decay Pipe

The decay pipe is going to be 194 meters long with 4 meters diameter. The decay pipe is long enough to allow the parent pions giving neutrinos at oscillation maxima to decay. The larger decay pipe radius allows the low energy pions with high transverse momentum to decay before getting absorbed in the decay pipe. Studies with a 50 meter longer decay pipe showed little to no improvement in the CP sensitivity (See figure 3.31 of [4] for more detail).

3.2 Neutrino Flux in the NuMI and the DUNE

This section goes through the neutrino flux produced by a NuMI style beamline (LBNF AND NuMI). In the real experiments, the beamline parameters can be tuned fairly precisely so that the properties of the neutrino flux like the focusing peak, width of the focusing peak, enhancement or suppression of certain energy phase space can be manipulated. The physics goals of the experiment drive the tuning of the beamline parameters which in turn produce a broad beam of neutrino flux with a focusing peak at the desired energy region. Figure 3.6 shows the neutrino fluxes for low energy and medium energy runs seen by the MINERvA detector (on-axis to the beamline) and NOvA near detector (14 mrad off-axis to the beamline. See appendix A.4 for more info regarding NOvA.) in the NuMI beamline. A detailed explanation of the MINERvA experiment is given in chapter 4. As seen in 2.12, the
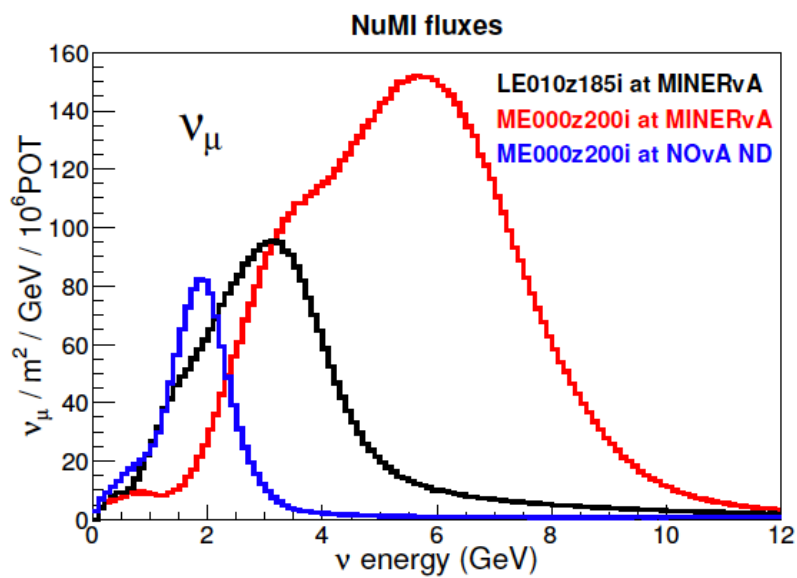
Figure 3.6: Neutrino Flux produced by NuMI beamline for low energy (LE) and medium energy (ME) runs. Low energy neutrino flux seen by NOvA is also shown for offaxis/onaxis comparisons.

[19].
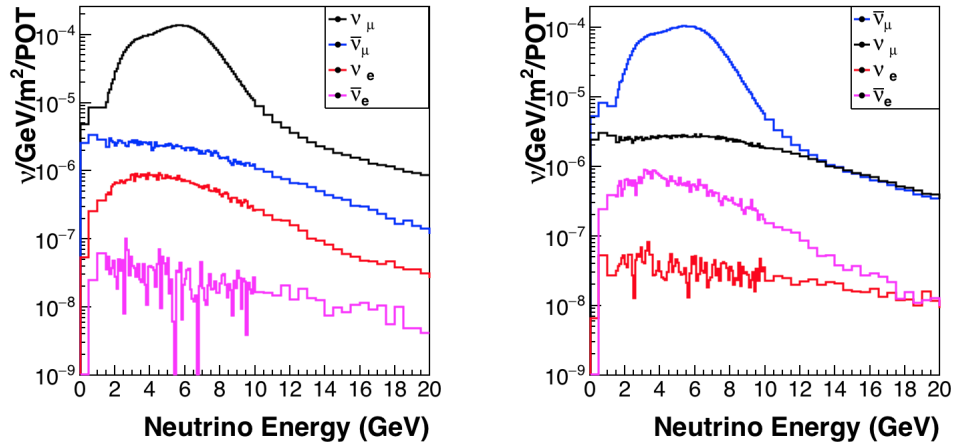
Figure 3.7: Neutrino flux for various species for forward horn current (FHC) in the left and reverse horn current (RHC) in the right for MINERvA medium energy run.

rising part of the neutrino spectrum comes from the pions that are over-focused by horn 1 but corrected by horn2. Similarly, the falling part of the focusing peak comes from the under-focused pions which are coming from high energy pions that were not focused completely by horn 1 and get an additional magnetic kick in the second focusing horn. In the case of the DUNE, the third horn can correct the over-focused or under-focused pions that are not fully corrected by the second focusing horn. Figure 3.7 shows the contribution of various neutrino species in forward and reverse horn current configurations. Compared to the FHC (Forward Horn Current, where positive charge particles are focused and negative charge particles are defocused) , the RHC (Reverse Horn Current, where the negative charged particles are focused and positive charged particles are defocused) has more background contamination in the high energy tail due to more π^+ production and the focusing of the kaons. The DUNE

flux also shows similar distribution in terms of the neutrino species but with a broader focusing peak and a suppressed high energy tail.

Figures 3.8 and 3.9 shows the muon and the electron neutrino flux coming from the neutrino parents with different intermediate interactions at the DUNE near (neutrinos delivered by the LBNF beamline) and the MINERvA detector (neutrinos delivered by the NuMI beamline) locations. Since the NuMI target is 1 meter long compared to the 2 meters long target used to simulate the DUNE flux in figure 3.8, the contribution from neutrinos with more than 2 ancestors is smaller compared to that of the DUNE beamline. In both cases, the electron neutrinos are mostly coming from neutrino parents with multiple interactions. Most of the electron neutrinos come from μ^+ decay $p + p \rightarrow \pi \rightarrow \mu \rightarrow \nu_e$ which have at least 3 ancestors. Muons decaying to produce neutrinos are called the Michel decay. For a positively charged muon, for example, the Michel decay looks like:

$$\mu^+ \rightarrow e^+ + \nu_e + \bar{\nu}_\mu$$

The high energy electron neutrinos mostly coming from the decay of kaons in the decay pipe.

Figures 3.10 and 3.11 shows the various decay channels that contribute in the ν_μ seen at MINERvA detector and DUNE near detector location respectively. In both cases, the focused region comes from the pion decay since the beamline is tuned to focus the pions of
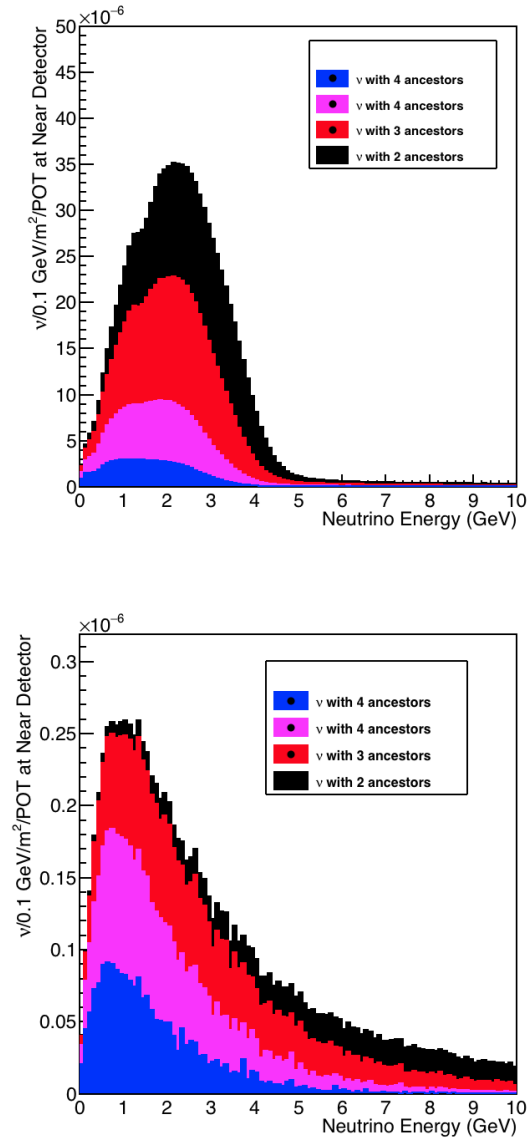
Figure 3.8: Flux ancestry for muon neutrino (top) and electron neutrino (bottom) at DUNE near detector (neutrinos delivered by the LBNF beamline). Plots shown are stacked. Here 2 ancestor means $p + p \rightarrow \pi \rightarrow \nu$ and 3 ancestors means $p + p \rightarrow \pi \rightarrow X \rightarrow \nu$ and so on. Here $p + p$ means proton hitting the target which produces a π^{+}. If the pion doesn't go through further intermediate interactions and produces a neutrino, the neutrino is said to have 2 ancestors (proton and pion). If the pion goes through an intermediate interaction to produce intermediate particle X which then decays to give neutrino, then that neutrino is said to have 3 ancestors.
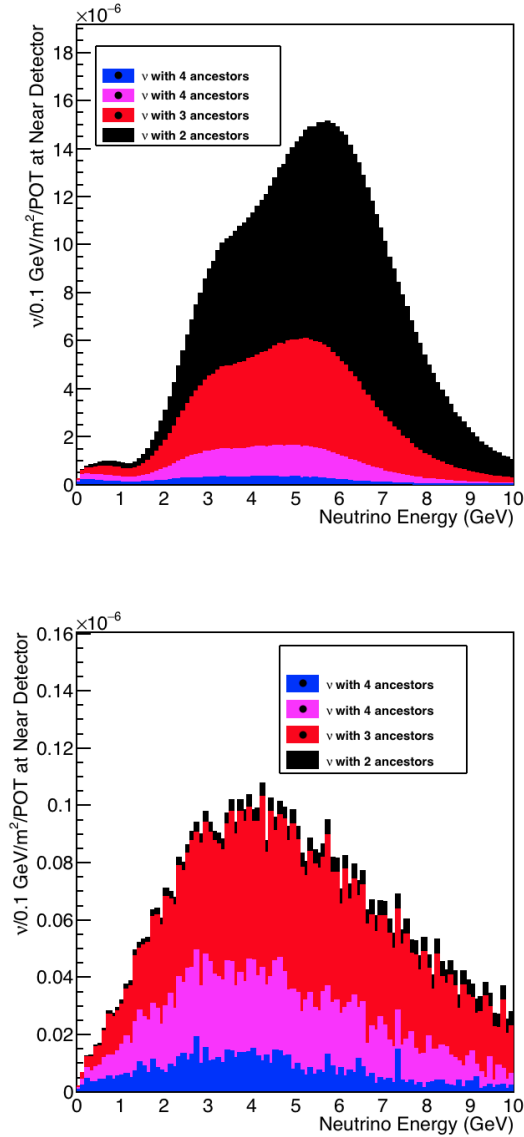
Figure 3.9: Medium energy neutrino flux ancestry for muon neutrino (top) and electron neutrino (bottom) in the MINERvA detector (on axis in the NuMI beam). Here 2 ancestors means $p + p \to \pi \to \nu$ and 3 ancestors means $p + p \to \pi \to X \to \nu$ and so on. Here $p + p$ means proton hitting the target which produces a π^+. If the pion doesn't go through further intermediate interactions and produces a neutrino, the neutrino is said to have 2 ancestors (proton and pion). If the pion goes through an intermediate interaction to produce intermediate particle X which then decays to give a neutrino, then that neutrino is said to have 3 ancestors.
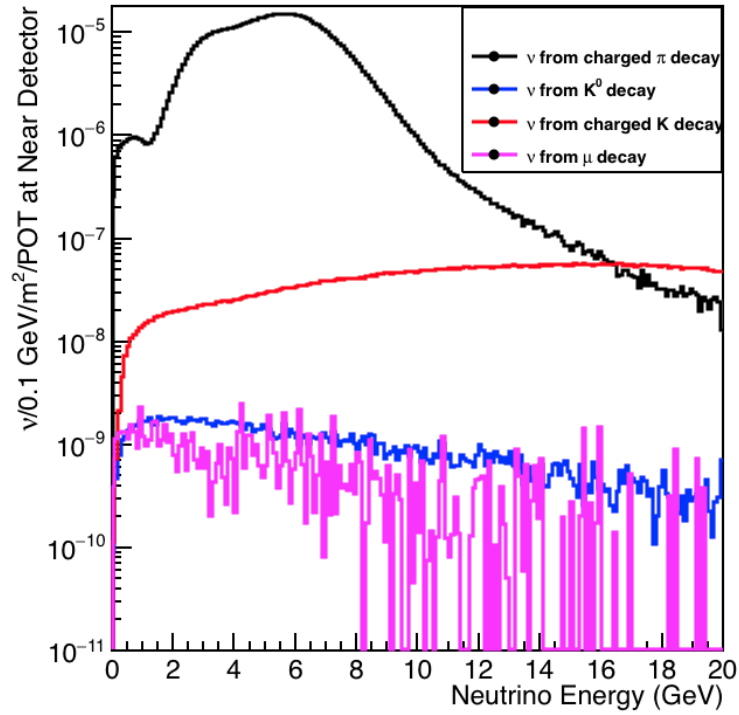
Figure 3.10: ν_μ produced from various decays seen at the MINERvA detector in the NuMI beam.

ν_e Flux Fraction from Decay	DUNE	MINERvA
π^+ decay	0.0	0.0
K^0 decay	0.146	0.035
K^+ decay	0.273	0.128
μ^+ decay	0.58	0.836

Table 3.1: Electron neutrinos (0 to 20 GeV) coming from different decay modes of their parent hadrons.
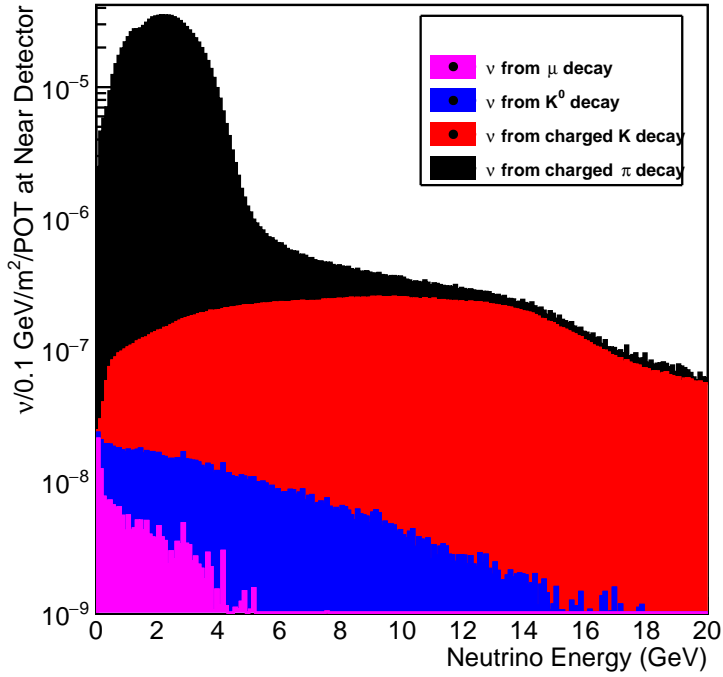
Figure 3.11: ν_μ produced from various decays seen at the DUNE near detector in the LBNF beam.

ν_μ Flux Fraction from Decay	DUNE	MINERvA
π^+ decay	0.965	0.988
K^0 decay	0.001	0.0002
K^+ decay	0.033	0.011
μ^+ decay	0.0002	0.0001

Table 3.2: Muon neutrinos (0 to 20 GeV) coming from different decay modes of their parent hadrons.

those energy regions. In the high energy region, the contribution from charged kaon decay increases. Fractions of the ν_e and ν_μ flux in MINERvA and DUNE coming from various decay modes are given in tables 3.1 and 3.2 respectively.

3.3   Neutrino Flux Uncertainties

Since we rely on the simulation to estimate the neutrino flux, the flux comes with uncertainties based on:

- The underlying models of neutrino ancestor (like pions, kaons etc.) production and interactions in various materials

- Knowledge/understanding regarding the accuracy of beamline parameters (for example 230 kA horn current might be 230.5 or 229 kA but the beam instrumentation might not be sensitive enough to know such small changes).

Uncertainties that fall in first category are also called hadron production uncertainties whereas the second category are called focusing uncertainties. The following 2 sections will describe these two categories of uncertainties in the context of MINERvA and DUNE neutrino flux.

3.3.1   Focusing Uncertainties

For both the NuMI and LBNF beamlines, the neutrino flux is simulated using a GEANT4 simulation [9]. For the neutrino flux simulation, a detailed beamline geometry is written based on the nominal values of the beamline parameters. For example, according to the engineering design report [56], the NuMI medium energy target is 120 cm long with 48 fins and 2 Budal Monitors. They are made up of graphite and are placed adjacent to one another with gap in between. In the medium energy configuration, the target is 143 cm upstream of the start of the first focusing horn. The properties of target, like its density, shape, surrounding structures are written in the simulation to match with the actual target. This procedure is followed for all beamline instruments including the focusing horns, decay pipe, target chase and horn chase, decay pipe snout and so on. However, although this information can be implemented accurately in the simulation, in the real experiments, we do not know these exact values of the beamline parameters. For example, we cannot know the position of the target or horns with 100% accuracy. The horn current is not exactly 230 kA and the magnetic field is not completely toroidal. Some of the uncertainties come from the limitation of the secondary instruments which we use to get these measurements while others could be due to the limitations in our modeling. For example, it is hard to model the magnetic field at the equalizer sections of the horns. The NuMI and LBNF experts have provided the estimates of the 1 σ deviations of these parameters from their nominal values

Parameter	Nominal Value	1 σ shift from Nominal Value
Beam Position (X)	0 mm	1 mm
Beam Position (Y)	0 mm	1 mm
Beam Spot Size 1.5	mm	0.3 mm
Horn Water Layer 1	mm	0.5 mm
Horn Current	200 kA	1 kA
Horn 1 Position (X)	0 mm	1 mm
Horn 1 Position (Y)	0 mm	1 mm
Horn 1 Position (Z)	30 mm	2 mm
Horn 2 Position (X)	0 mm	1 mm
Horn 2 Position (Y)	0 mm	1 mm
Target Position (X)	0 mm	1 mm
Target Position (Y)	0 mm	1 mm
Target Position (Z)	-1433 mm	1 mm
POT Counting	0	0.02% of Total POT
Baffle Scraping	0	0.25% of POT

Table 3.3: Beam Parameters that are used in the NuMI / MINERvA Medium Energy run configuration. The nominal uncertainties are based on advice from the NuMI experts.

[1].

The neutrino flux is very sensitive to the horn parameters (mostly horn 1) and target parameters. DUNE flux uncertainties are also estimated using similar procedures but will have additional uncertainties to account for due to the additional horn. Figure 3.12 shows that the flux is more sensitive to change in position of the horn and water layer than the rest of the parameters. The water layer is the estimated depth of the water accumulated from the spraying of water to cool down the horns. Here a 1 σ fractional shift means, for

---

[1]The equalizer sections are the portions of the horns where the current enters the horn and is spreading out (or equalizing).
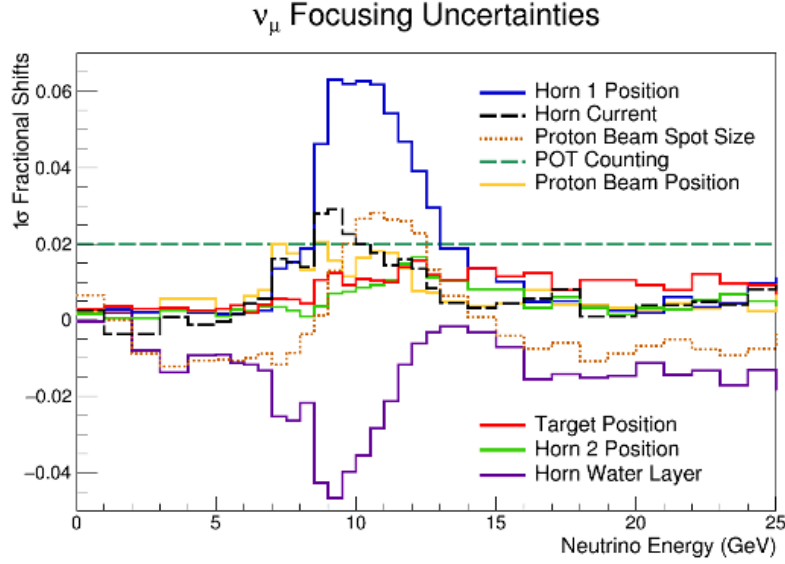
Figure 3.12: Fractional shift in the MINERvA flux when the beam parameters are shifted by 1 σ. The plot shows the $+1$ σ fractional shift uncertainties due to various focusing parameters.

example, horn current at some given neutrino energy E_ν is :

$$F(+1\sigma, E_\nu)_{HC} = \frac{\phi(HC = 200kA; E_\nu) - \phi(HC = 201kA), E_\nu)}{\phi(HC = 200kA, E_\nu)}. \qquad (3.2)$$

Here ϕ is the flux seen by the MINERvA detector.

And the average fractional uncertainty is calculated as:

$$\frac{abs(F_{fit}(+1\sigma, E_\nu)_{HC} + abs(F_{fit}(-1\sigma, E_\nu)_{HC}}{2} \qquad (3.3)$$

where F_{fit} is the fractional shift from the fit done by fitting shift in neutrino flux when

the horn current is at nominal position and shift by $\pm 1\sigma$. A more detailed MINERvA flux uncertainty break down is given in [117] done by Ben Messerly. Similarly for DUNE, a more detailed study has been done by Peter Madigan and is available in [109]. Detailed discussion of the origin and calculation of each of these category in the case of MINERvA is in [20]. Since 2016, parameters like longitudinal target position (Z) is revised from 1 cm to 1 mm [20] and additional uncertainties like the uncertainty due to the shape of the horn has been added. The horn shape uncertainty was based on study done by Paul Le Brun [101].

3.3.2   Hadron Production Uncertainties

The beam simulation tool (in the case of DUNE and MINERvA , it is GEANT4 [66]) relies on hadron production models to estimate the production of the hadrons and their interactions in various beamline materials. A typical neutrino beam simulation starts from the proton entering the baffle, hitting the target leading to a cascade of hadron production. The resulting hadrons either go through intermediate interactions, or get absorbed, or decay in decay pipe to produce neutrinos and other particles.
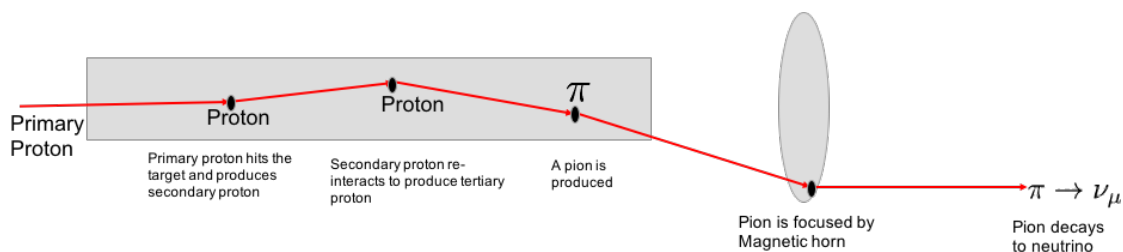
Figure 3.13: Schematic diagram showing the process of neutrino production in a typical accelerator beamline with hadronic interactions inside the target
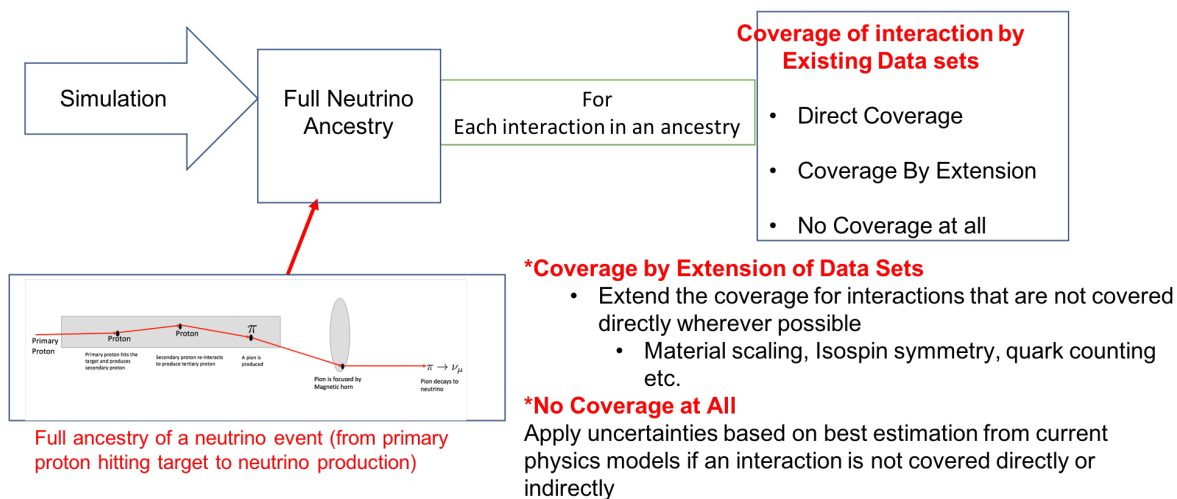
Figure 3.14: Schematic diagram showing how PPFX constrains the hadron production uncertainties using the available data sets

3.3.3 Constraining Hadron Production Uncertainties-MINERvA

The interactions inside the target and beamline materials are simulated using the phenomenological hadronic models like QGSP-BERT and FTFP-BERT [74] in GEANT4. As these models are not accurate enough to get a precise flux, they are tuned using available hadron production measurements. MINERvA devised a method to use the hadron production measurement data to constrain the hadronic models used in the simulation [19]. Also known as PPFX (Package to Predict Flux), it constrains the hadron production from proton on carbon interactions using the NA49 [110] and MIPP [147] data-sets and extends the data-sets to other materials using the procedure from Barton et. al.[65]. Further extension to neutron-carbon interaction is done by utilizing the iso-spin symmetry of proton and neutron and K^0 production is constrained using $K^{\pm}$ production data sets utilizing symmetry in quark patron model [18]. Scaling the data from NA49 at 158 GeV to NuMI 120 GeV was done by Feynman scaling (x_F) which gives the fraction of momentum carried by the outgoing hadron from an inelastic collision. Recent results from NA61 [95] will extend the data coverage once included in the framework. Existing data sets are binned in x_F, p_T and a 100% bin to bin correlation is assumed.

To constrain the hadronic interactions, the simulation needs to have information on or
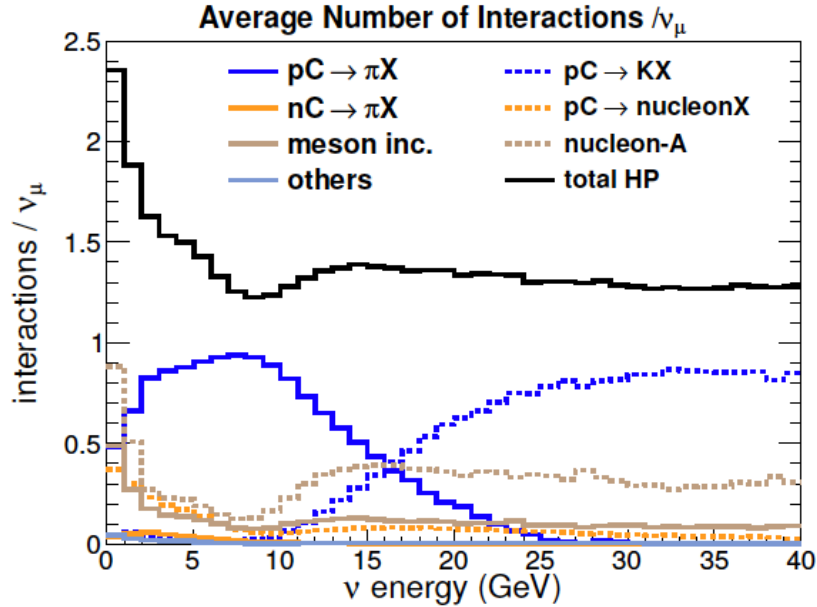
Figure 3.15: Average interactions per neutrinos from the NuMI beamline (neutrinos at MINERvA detector). Figure is taken from [19].

regarding production, interaction and absorption of neutrino ancestors. PPFX as devised by MINERvA uses dk2nu ntuples [90] (designed to store information relevant to neutrinos and neutrino flux calculation). The ntuples contain information of the neutrino ancestors like production location, materials they traversed through, kinematics and decay products. A more detailed explanation on the structure of dk2nu ntuples is given in the appendix A.2 of this thesis. The PPFX uses these information and for each neutrino event, it checks all the information regarding the neutrino ancestors and assigns weights and uncertainties. This process is shown schematically in figure 3.14.

Figure 3.15 shows the average number of hadronic interactions that happen in the NuMI

beamline before a neutrino (that passes through the MINERvA detector) is produced. To produce a neutrino, at least 1 hadronic interaction needs to happen $(p + p \rightarrow \pi + X)$. Since the pions have to travel through the target material, some of them go through additional quasi-elastic or inelastic interactions. Neutrinos between 3 to 9 GeV region mostly come from focused pion beam with only one interaction in the target. The high energy tail comes from the kaon decays. Neutrino parents produced in multiple interactions (meson incident (meson inc. in the plot) for example, $\pi^+ + C \rightarrow \pi^+$) and nucleon incident (for example, $p + p \rightarrow n + p \rightarrow \pi$) contribute the very low energy bins. The category nucleon-A consists of nucleon incident interactions that are not covered by the data sets. A more detailed explanation of this figure is given in section 5.3 of [20].

3.3.4   Constraining Hadron Production Uncertainties-DUNE

Figure 3.16 shows that the focused pions contribute less than 5% to the total flux uncertainty. The nucleon absorption (nucleon-A) dominates the uncertainty in both rising and falling part of the focusing peak. Uncertainty from this category is large because these interactions are not constrained by thin target data-sets. Target attenuation is the uncertainty due to the amount of carbon traversed by the neutrino ancestors in the target. Absorption
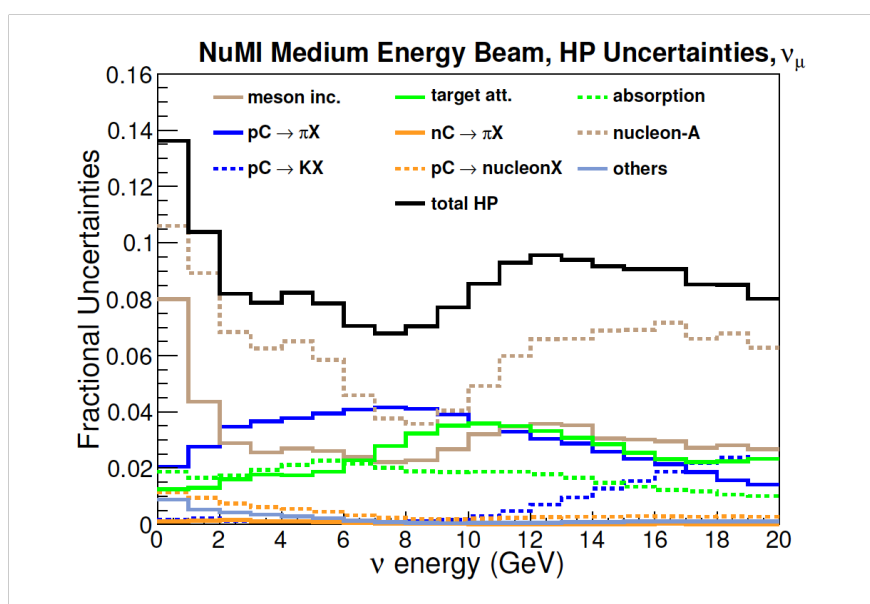
Figure 3.16: Hadron Production Uncertainty on MINERvA neutrino flux in medium energy configuration. Although the neutrinos in focusing region comes from $p + p \to \pi$. some of these pions go through further interactions increasing the uncertainties in the low energy bin[20].

includes the uncertainty due to absorption of the particles outside the target (mainly focusing horns). The meson incident contribute large uncertainty to the low energy neutrino flux. Incident pion data from the NA61 [147] will help to lower the uncertainty coming from meson incidents. The thin target data corrected flux was tested against an alternate flux extracted by low-nu method [58] and seemed to be in good agreement in the low energy run.

With a target 1.5 meters long, the DUNE neutrino flux will produce more hadrons per neutrino compared to the NuMI beamline. This section goes through the implementation of the MINERvA 's method of hadron production uncertainties in DUNE to get the first estimates of hadron production uncertainties in DUNE near and far detectors and estimate its contribution in the near/far flux ratio. Furthermore, this study was also done to compare the two competing beamline designs at that time. The now abandoned NuMI style two horn design beamline is referred to as the Reference design and the currently nominal 3 horn design is referred to as the optimized design throughout this section. The first optimized design here has a target length of 2 meters which is half meter longer that the one finalized in 2018. However, the overall theme and the conclusion of this section doesn't change because of this difference.
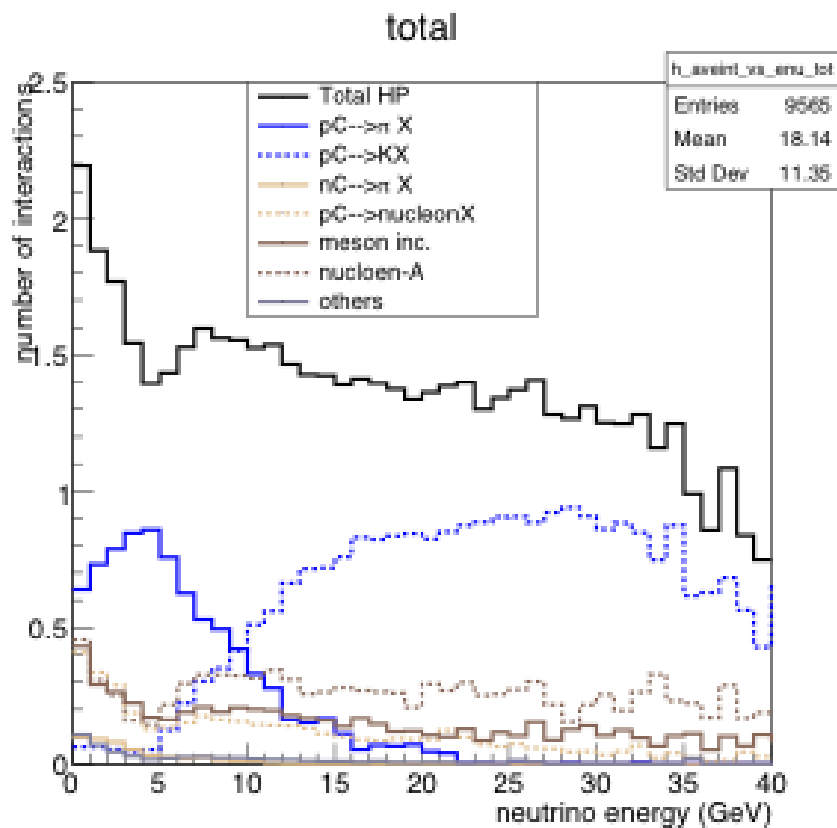
Figure 3.17: Hadron interactions per neutrino in the DUNE beamline. This was simulated with 3 horns and a 2 meter long target. The focusing peak is dominated by focused pion beam that were produced in the target (solid blue line). The tail is dominated by kaons produced in the target.

Index	Legend	Description
1	Total HP	Total Hadron Production Interactions
2	Others	Interactions(excluding 8) not covered by
-	-	any of the below categories
3	$pC \to \pi X$	Pion production in proton Carbon Interaction
4	$pC \to KX$	Kaon Production in proton Carbon Interaction
5	$nC \to \pi X$	Pion Production in neutron Carbon Interaction
6	$pC \to$ nucleonX	Nucleon Production in proton Carbon Interaction
7	meson inc.	Meson incident Interaction
8	nucleon-A	Nucleon Incident Interaction not covered by any data
9	other abs.	Absorption outside the target
10	Target Absorption	Absorption inside the target

Table 3.4: Categorization of PPFX Uncertainties

3.3.4.1 Interaction Maps

Figure 3.3.4.1 and 3.19 shows the interactions per near detector neutrino on different materials in the beamline. The Y axis labels are the incident particles and the X axis labels are the materials. The number of protons incident per neutrino on target (carbon) is higher than 1 because protons can interact with the target more than once before exiting the target or producing hadrons. Because the optimized target is longer, the number of proton incident on carbon is higher by 8%. Similarly, the pions incident on carbon is 27% higher in the case of the optimized beam. In the case of K^+, it is 46% higher. Overall, all kind of incident interactions in the target are significantly higher for the optimized beam. In general, the optimized beam neutrino flux has larger ancestry length than that of the reference beam.

Next, we look at the pions produced from various particles incident on the various materials. In figures 3.20 and 3.21, the X axis labels are the materials where the interaction occurs and the Y axis labels are the various incident particles that give pions. The numbers are interactions per near detector neutrino.

Due to the higher proton re-interactions, the average number of protons giving pions is smaller in the case of the optimized beam. However, the average number of $\pi \to \pi$ (quasi elastic and elastic scatters) is higher by around 30% in the case of the optimized beam. In general, the contribution from protons giving pions is smaller but mesons giving pions interactions are larger in the optimized beam. Figures 3.17 gives a more quantitative picture of this case as a function of neutrino energy for the DUNE optimized beam.

3.3.4.2   Fractional Uncertainty Due to Hadron Production

One of the deliverables of my research project was to produce the first estimate of uncertainties due to hadron production in the DUNE flux using PPFX. Uncertainties on DUNE flux shown in this thesis are produced using 100 systematic universes and 50 million protons on target(POT). The systematic universes are the alternate fluxes produced by varying under-
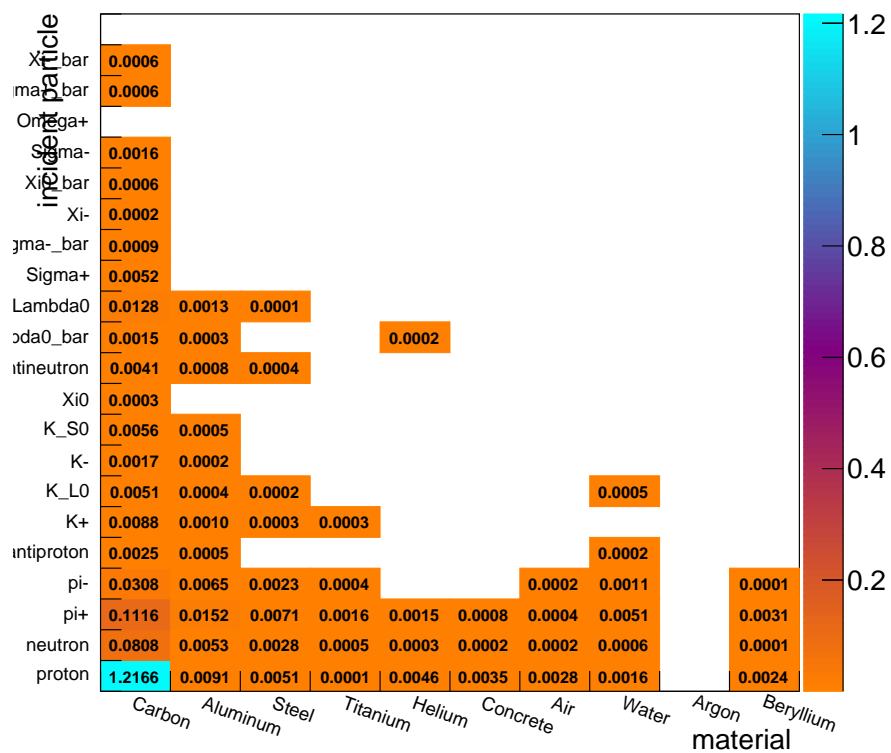
Figure 3.18: All interactions in different materials for the near detector neutrinos are shown for the nominal configuration (120 GeV). Most of the interactions are proton on carbon and then pions on carbon as expected.
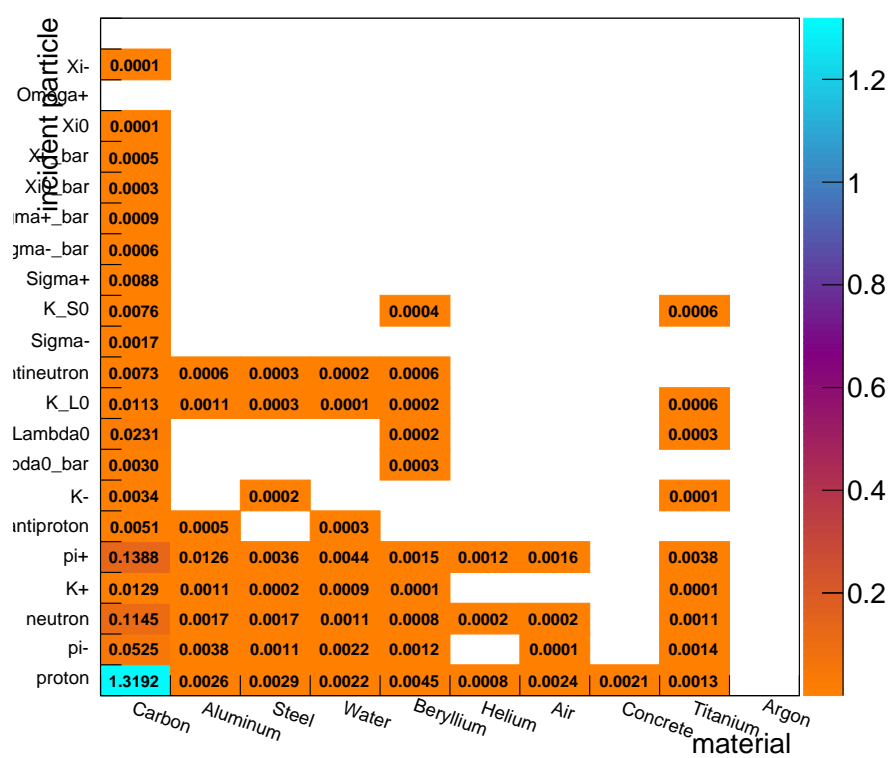
Figure 3.19: Number of interactions by different particles in different materials for the far detector neutrinos are shown for the optimized configuration.
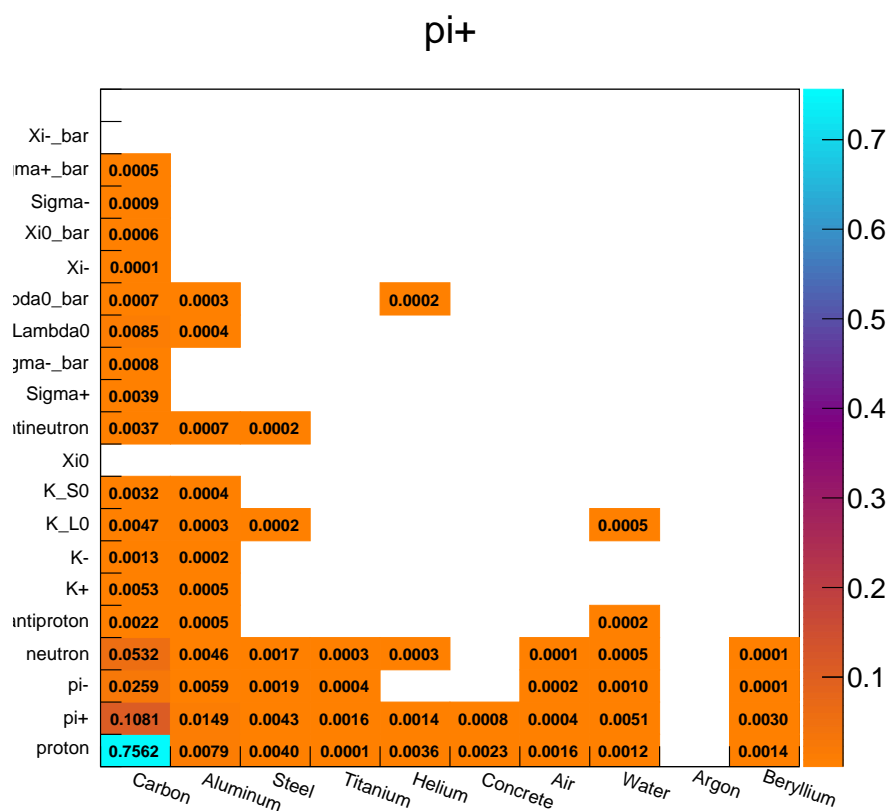
Figure 3.20: Pion produced by various particles in various materials in reference beam design. It includes all types of interactions.
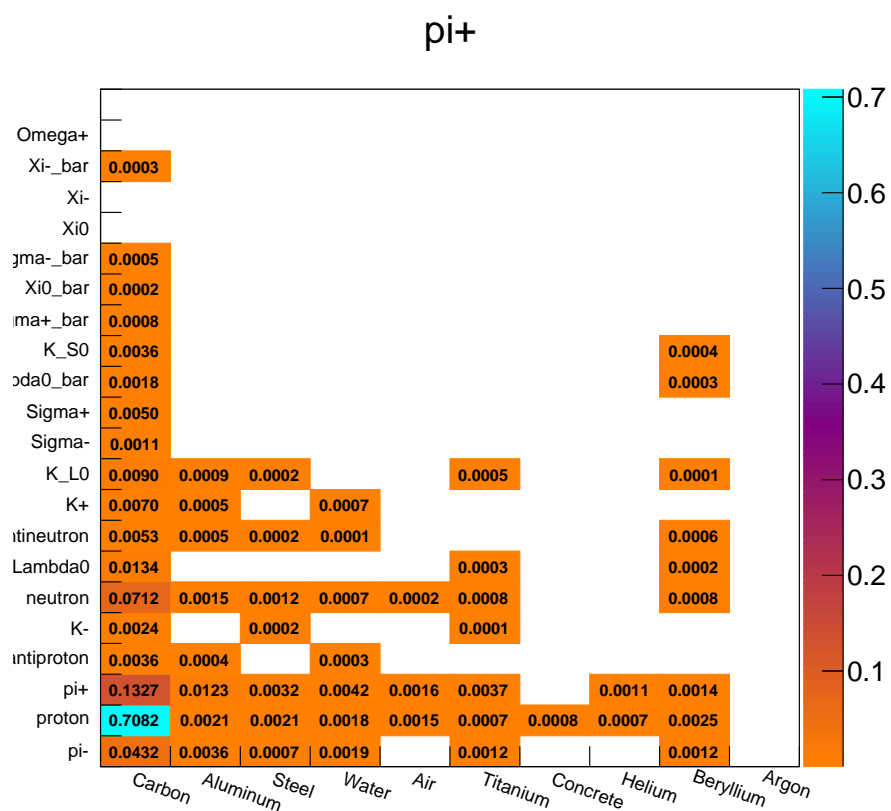
Figure 3.21: Pions produced by various particles in various materials in optimized beam design. Includes all interactions

lying model parameters within 1 σ of their nominal values. Correlation between the model parameters are taken into account when shifting the model parameters. A more detailed explanation of flux systematic universes is given in section 6.17.4.2 of the thesis. The optimized beam design has a relatively higher uncertainty but it is compensated by larger neutrinos per proton yield as seen in figure 3.22. While the uncertainties in the reference beam are pretty flat after 7 GeV, the optimized beam has a dip at around 4 GeV and a peak in 8 to 10 GeV region. That peculiar shape in the optimized beam comes mainly from the uncertainties from nucleon-A type uncertainties (see table 3.4 nucleon-A) that are not covered by thin target data. These interactions cover the proton and neutron re-interactions, and with a longer target, it is plausible to get large contributions in uncertainties from re-interactions.

In the case of both beam designs, going from 0 to 5 GeV, the uncertainty from nucleon re-interactions goes down and is dominated by the uncertainties from $pC \rightarrow \pi X$ interactions mainly due to the increase in neutrinos coming from these interactions. As we go to higher energies, the nucleon incident interactions dominate the overall uncertainties. Having 1 m long target, for the reference beam, the uncertainties from nucleon incident interactions remains low and flat.

In the case of the optimized beam, the uncertainty from target absorption and the un-

certainty from nucleon A. (see 3.4) interactions both peak at 8-10 GeV region. This means that the rise in the uncertainty in this region is from the interactions in the target. The peak in the particular region is a function of interaction length. Peaking of target attenuation implies that the high energy nucleons see more target in the case of optimized beam. With more material, the interaction probability also goes up hence the multiple interactions and rise in uncertainties due to nucleon A. However, it should be noted that the nucleon-A uncertainties are almost the same (around 0.08) for high energy neutrinos in DUNE optimized beam and NuMI beam. It is around 0.05 in the case of DUNE Reference beam.

In short, the total fractional uncertainty in the optimized beam from hadron production is higher by at most 4% (beyond 6 GeV). In the focusing region of 2-4 GeV neutrino energy, the uncertainty is almost similar at around 6%. Major contributions in uncertainty comes from interactions handled by nucleon-A, meson incident and target absorption (see 3.4) reweighters. In the case of the optimized beam, uncertainties handled by other absorption reweighters (absorptions outside target) are significantly lower compared to those of the reference beam design. We assume that there will be some increase in uncertainties of this category once we implement a more detailed optimized horn.
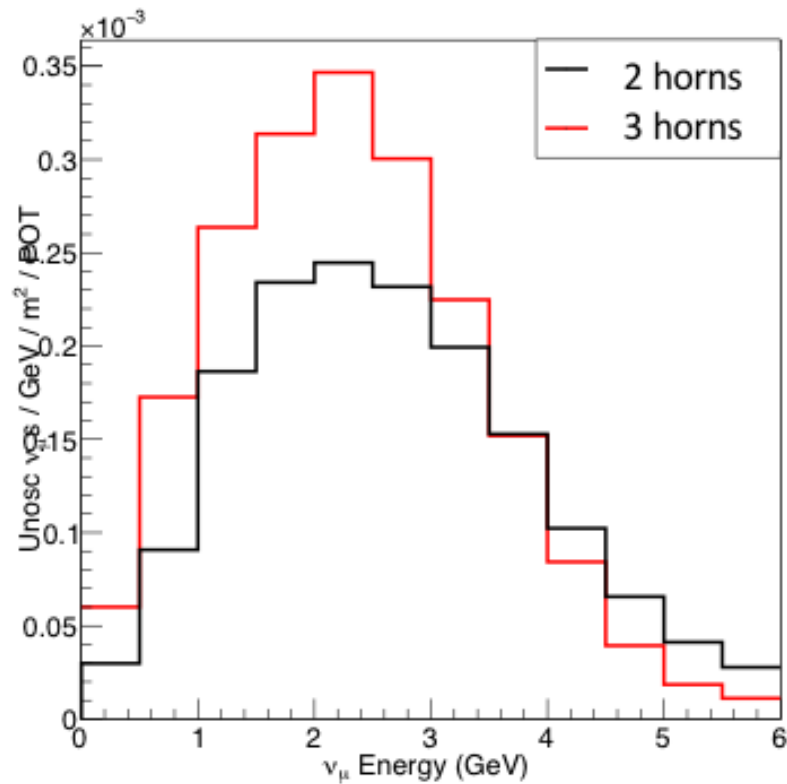
Figure 3.22: Neutrino Flux at DUNE Near Detector with the 2 horns (NuMI style) and 3 horns design. The 2 horn flux was obtained by simulating with a 1 m long NuMI style target with 2 NuMI style horns. The 3 horns was simulated with 2 meters long target with 3 focusing horns that were slightly larger than the final optimized version.
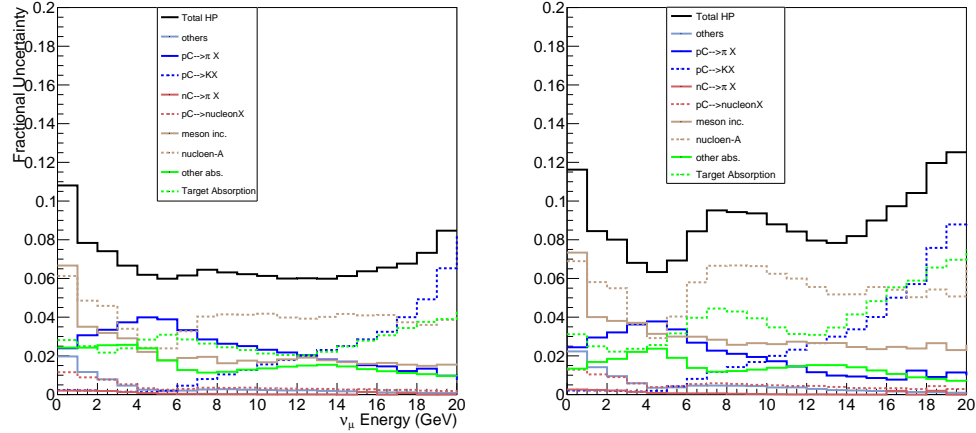
Figure 3.23: Fractional Uncertainty on flux for Reference Design Beam (left) and the optimized design beam (right) for 120 GeV POT.

3.3.4.3 Uncertainty on the Far/Near Flux Ratio

For oscillation studies, the ratio of far to near fluxes is the most important quantity. Uncertainties on this ratio affect the overall sensitivity to CP. Figures 3.24 shows the fractional uncertainty on far to near flux ratio for the reference and optimized beam designs respectively. The binning scheme used by the near detector group is used to produce these uncertainty histograms. The overall fractional uncertainty for the near and far ratio is very small although the shapes are different. However, it should be acknowledged that these fluxes do not include detector effects. These studies are done with the fluxes that are projected at the center of the detectors instead on the fiducial volume and might have significant effect in the near detector flux. The far detector being far from the beamline, sees the beamline
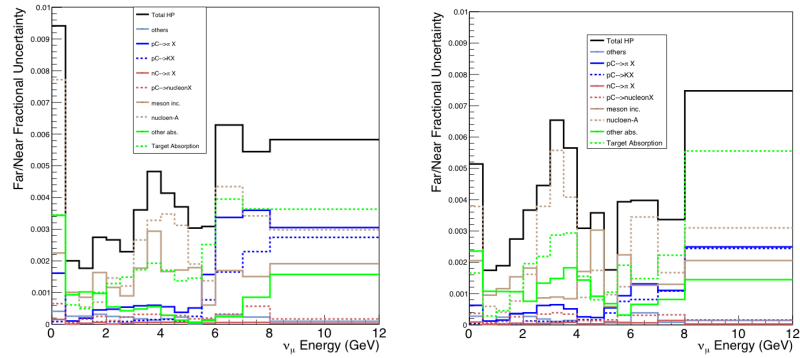
Figure 3.24: Far near fractional uncertainty for Reference Beam design (left) and optimized beam design (right)

as a point source. However, the near detector sees the beamline as a line source and covers

a wider momentum range.

3.3.4.4 Covariance and correlation matrix

One of the deliverables of the project was to provide the near detector group with an estimation of the correlations across neutrino energy bins, neutrino flavors, and the detectors. By utilizing the method used in the MINERvA experiment, this project delivered estimates of these quantities for the DUNE experiment.
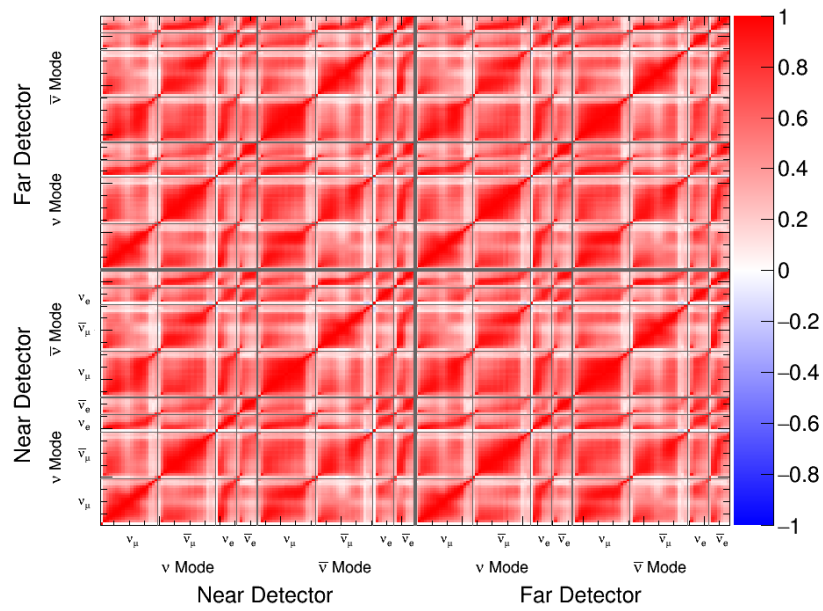
Figure 3.25: Correlation Matrix for the optimized beam
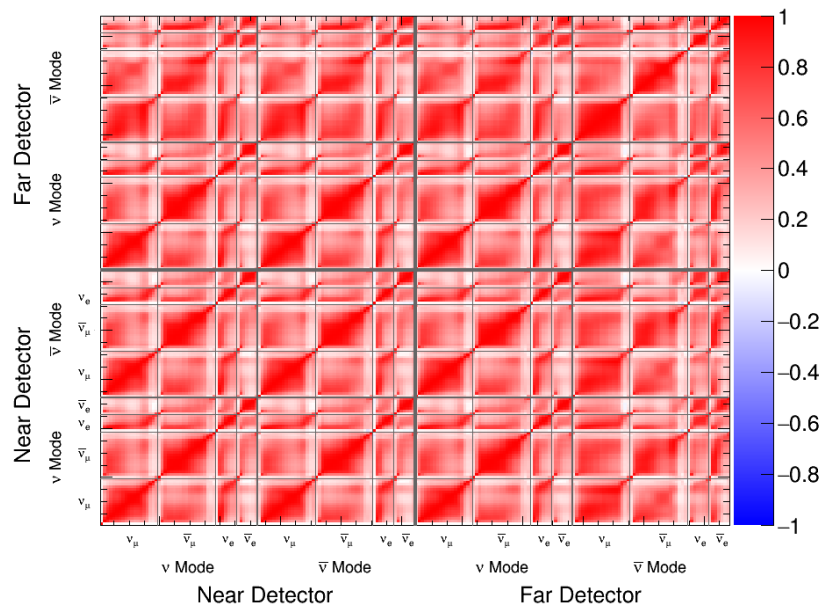
Figure 3.26: Correlation Matrix for the Reference beam
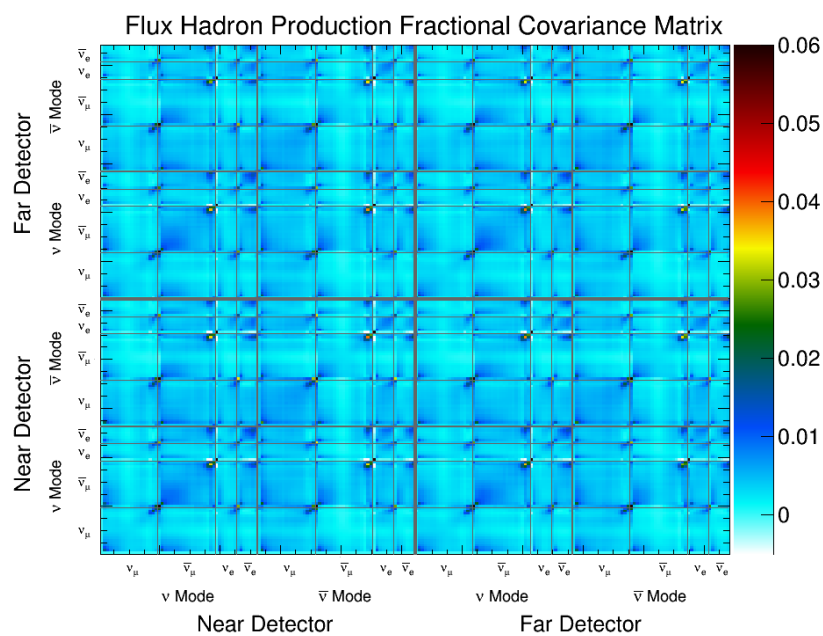
Figure 3.27: Covariance Matrix for the optimized beam
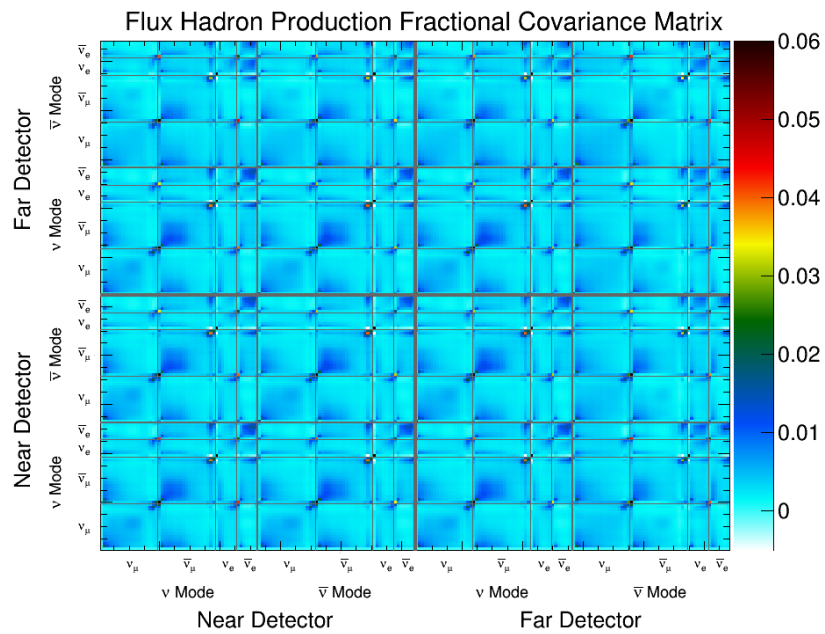
Figure 3.28: Covariance Matrix for the Reference beam

3.4   Neutrino Flux at DUNE Near and Far Detector

As an oscillation experiment, DUNE will rely on the near detector to characterize the neutrino flux and far detector to measure the oscillated the flux. The energy of the neutrino formed by the focused pion beam is given by:

$$E_\nu = \frac{0.43E_\pi}{1 + \gamma^2\theta^2} \tag{3.4}$$

And the corresponding flux at a detector location z (from neutrino production location) is given by:

$$\phi = \left(\frac{2\gamma}{1 + \gamma^2\theta^2}\right)^2 \frac{A}{4\pi z^2} \tag{3.5}$$

where $\gamma = \frac{E_\pi}{m_\pi}$, θ is the decay angle (angle between pion and direction of the neutrino) and A is the area of the detector. The energy spectra of the neutrino flux seen by the detector depends upon two variables: θ and z. Figure 3.29 shows the change in neutrino flux when projected to different locations from the beamline. The decay angle depends upon how well focused the hadron is and the location of the near detector. Since the near detector is near to the decay volume, it will see the beamline as a line source i.e. decay location of the neutrino parent will affect the spectra of the near detector flux. Furthermore, while the low energy pions are well focused, the high energy pions are little to no focused
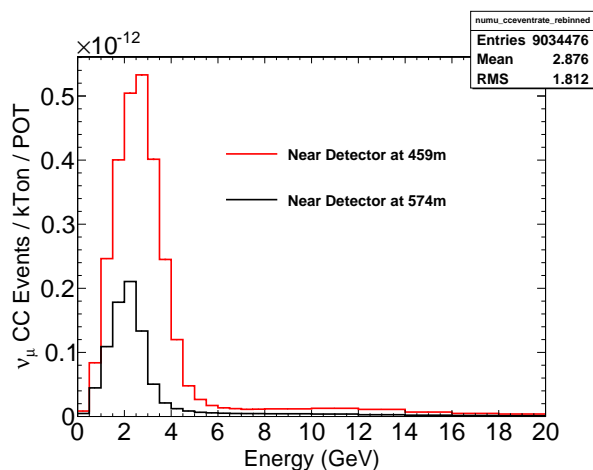
Figure 3.29: The R^2 effect as seen in 2 near detector locations. The Y axis is arbitrary for this plot.

at all (because of their small transverse momentum). Figure 3.30 shows how the pions with different transverse momenta can subtend different decay angles at the near detector. Pions that decay in upstream part of the decay volume subtends smaller angle compared to the pions decaying in the downstream of the decay volume giving different neutrino energy
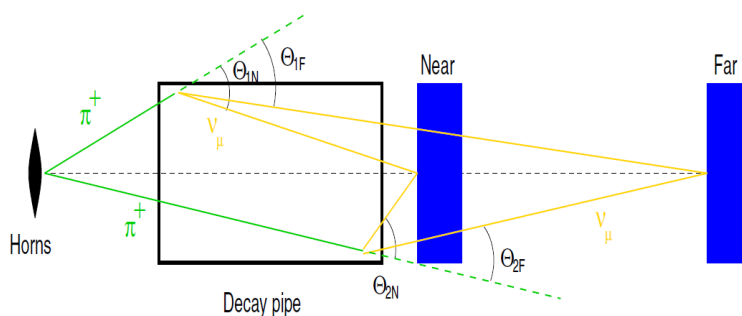
Figure 3.30: Decay angles subtended by the parent pion at near and far detectors [151].

spectra. The far detector being far from the beamline, sees the beamline as a point source such that $E_\nu \approx 0.43E_\pi$. Hence, finite size of the decay volume and the angular divergence of the pion beam means the near and far detector will see a systematic difference in the spectra of the neutrino coming from same hadrons.

Since the DUNE will use the near detector to extrapolate the flux at the far detector, it is important to understand the correlation between near and far detector flux. Because of their location, the far detector will see a systematically higher energy spectra for neutrinos at a given energy range in the near detector.
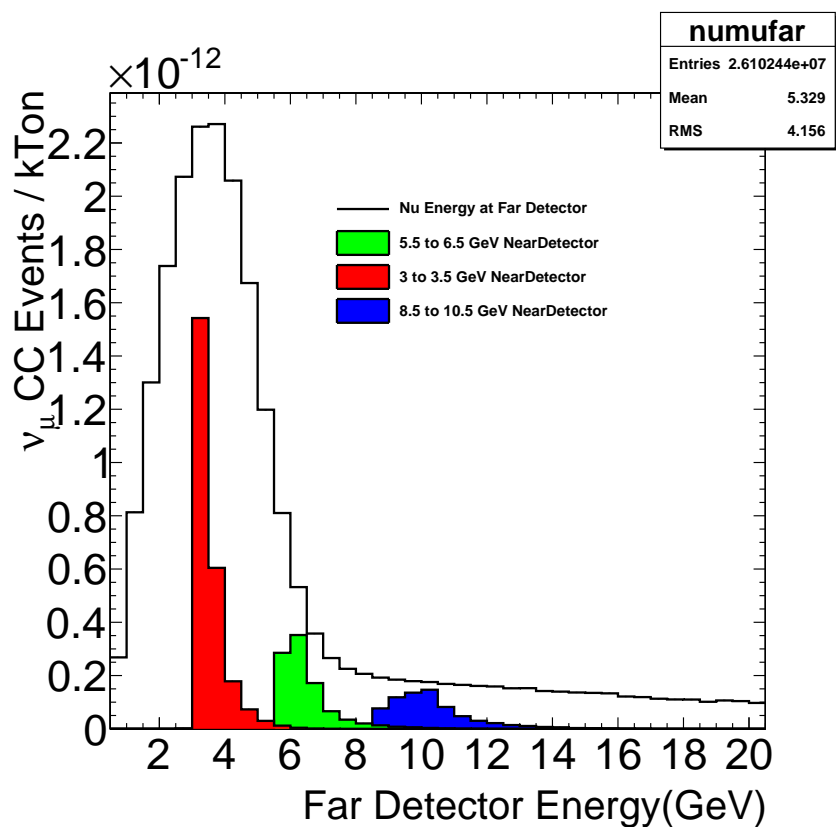
Figure 3.31: Neutrino energy spectra at the far detector. Filled color plots show the spectra of neutrinos from different energy ranges in near detector extrapolated at the far detector. The far detector systematically sees higher energy neutrinos than the near detector for neutrinos coming from same hadrons. The smearing into higher energy becomes more prominent in the high energy tail which is composed of the neutrinos coming from the high energy hadrons that see little to no magnetic field in the beamline.
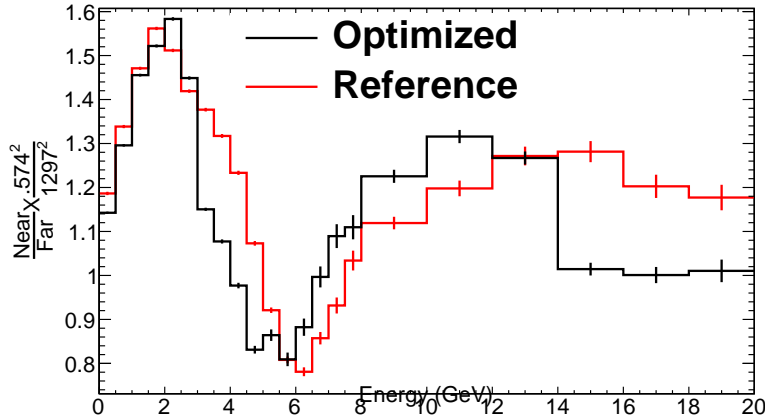
Figure 3.32: Near to Far Flux ratio scaled by the squared of the detector distance for a 3 horn design (black) and the old 2 horn design (red).

Figure 3.31 shows the smearing effect seen by the far detector. Hence, the near and far neutrino spectra are not one to one correlated. Besides the difference in the flux seen by divergence of the neutrino beam, the smearing effects give different shapes in the near to far flux ratio.

Figure 3.32 shows the ratio of near detector flux to the far detector one. After cancelling the distance effect, the shape in the ratio comes from the systematic difference in flux seen by the near and far detector. The first peak in the focusing region mainly comes from the different acceptance of the near and far detector (acceptance is the function of distance between decay point of a neutrino parent and the detector location). The second peak in the flux ratio in the high energy comes from the unfocused pions which decay at downstream

of the decay pipe. These pions have larger transverse momentum at the decay point than the focused pion. Hence, they decay at various off-axis location of the downstream end producing relatively low energy neutrino spectra at near detector.

3.4.1 Near to Far Flux Extrapolation Method

For most neutrino oscillation experiments, there are 2 detectors. One detector is near the source of the neutrino to characterize the neutrino flux (called near detector) and the other one is far from the source to measure the oscillated flux. The far detector being far from the neutrino source, we need to rely on the near detector to predict the flux at the far detector (after all that is what a near detector is there for). Given the knowledge of the decay kinematics of the neutrino parents (momentum and decay location), the neutrino flux at the near detector can be used to approximate the flux at far detector. However, the detector acceptance and other beamline properties result to a systematically different neutrino spectra for near and far detector. This subsection will go through two different methods used to extrapolate the far detector flux

- Near to Far Ratio method

- Transfer Matrix Method

This study tests these two methods and studies the robustness of each method to predict the flux at the far detector.

To characterize both methods, two hadronic models are used: QGSP BERT and FTFP BERT. As seen in figure 3.32, the ratio of near to far flux will reflect the various focusing effects of the beamline and the resulting spectra at the two detectors due to their difference in acceptance. The ratio will cancel the hadronic model effects. Hence to extrapolate the far detector flux, we can use a double ratio method such that:

$$(\frac{dN_{far}}{dE})_{Data} = (\frac{\frac{dN_{far}}{dE}}{\frac{dN_{near}}{dE}})_{MC} \times (\frac{dN_{Near}}{dE})_{Data} \tag{3.6}$$

[151]. While this method is only viable for on-axis experiment, this method doesn't take into account the smearing effect as seen in figure 3.32.To test robustness of the extrapolation method using double ratio, a study was done to extrapolate the far detector flux of one hadronic model using its near detector flux of same hadronic model and double ratio of different hadronic model. In the context of above equation, the study was done assuming:

- QGSP BERT $\rightarrow$ MC

- FTFP BERT $\rightarrow$ Data

Figure 3.33 shows the simulated neutrino flux at the near detector coming from the two different hadronic models.
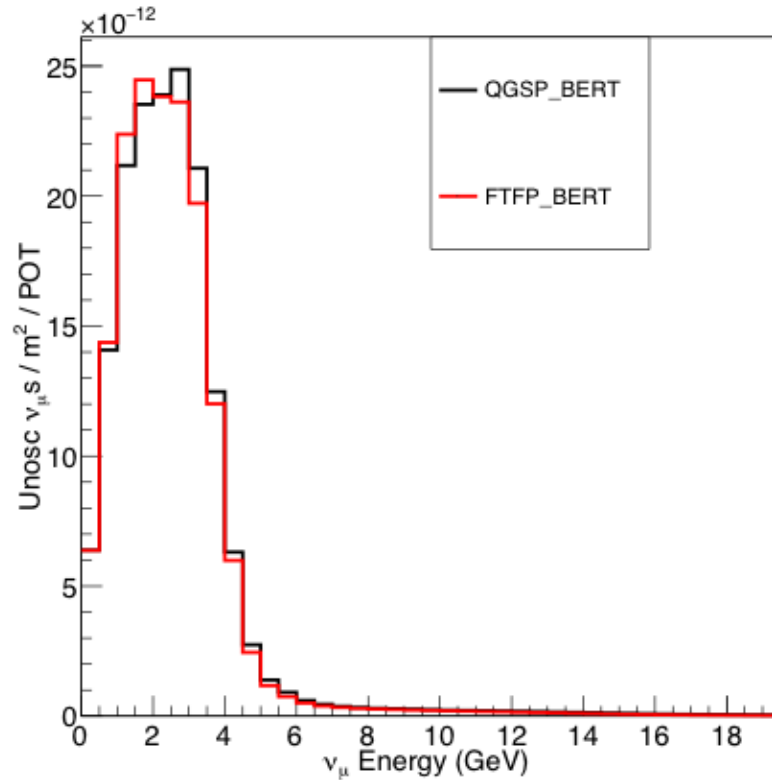
Figure 3.33: Simulated near detector flux using two different hadronic models

The limitation of the ratio method is that it doesn't account for the smearing of the neutrino spectra at the far detector for a given near detector energy. This smearing of spectra into higher energy in the far detector can be represented by a near to far correlation matrix. Figure 3.35 shows the correlation between near to far detector flux from 0 to 5 GeV. The bin by bin 1 D projection of this matrix is equivalent to 3.31. Although the matrix is mostly diagonal, as we go to the higher energies, the smearing effect increases. The percentage of
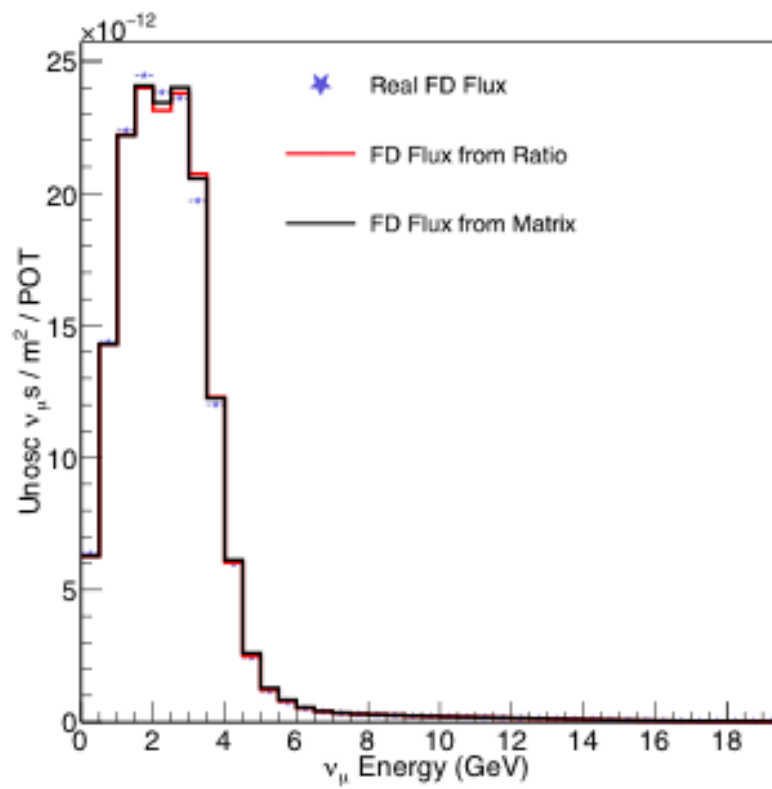
Figure 3.34: Extrapolated far detector flux using the double ratio extrapolation method and matrix method. Here, Real means the Far Detector Flux from the assumed Data i.e. FTFP
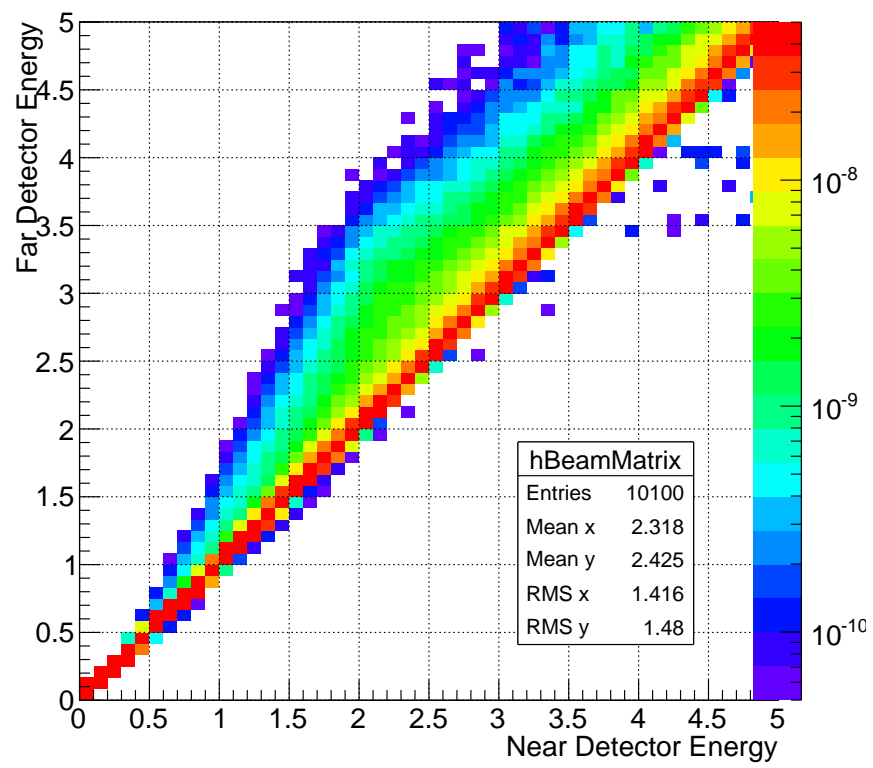
Figure 3.35: Beam Matrix showing the Near to Far Detector flux correlation for 3 horn design beamline.

Near/Far	0-0.5	0.5-1	1-1.5	1.5-2	2-2.5	2.5-3	3-3.5	3.5-4	4-4.5	4.5-5
0-0.5	**99.33**	0.79	0	0	0	0	0	0	0	0
0.5-1	0.33	**97.5**	2.51	0.0	0	0	0	0	0	0
1-1.5	0	0.053	**94.63**	5.27	0.06	0		0	0	0
1.5-2	0	0	0.053	**89.21**	10.27	0.45	0.002	0	0	0
2-2.5	0	0	0	0.05	**82.66**	15.89	1.36	0.03	0	0
2.5-3	0	0	0	0	0.05	**78.54**	18.98	2.31	0.11	0.0
3-3.5	0	0	0	0	0.0	0.06	**76.63**	20.29	2.74	0.28
3.5-4	0	0	0	0	0	0.0	0.04	**74.30**	21.95	3.21
4-4.5	0	0	0	0	0	0	0.01	0.05	**71.52**	23.95
4.5-5	0	0	0	0	0	0	0	0.01	0.05	**68.18**

Table 3.5: Smearing of neutrinos from near to far detector shown in percentage of neutrinos observed in near detector bin. Smearing of less than 0.01% is rounded off to 0.

events that get smeared into different bins of far detector is given in the table 3.5. For example from 0.0 to 0.5 GeV neutrino energy, 99% are observed in the same bin in far detector whereas the 0.33% are observed in 0.5 to 1 GeV.

Since the matrix method takes into account the smearing effect as well, it is less sensitive to focusing effect compared to the matrix method. To test the matrix method with the DUNE flux:

$$(\frac{dN_{far}}{dE_i})_{Data} = \sum_j (M_{ji})_{MC}(\frac{dN_{near}}{dE_j})_{Data} \tag{3.7}$$

$$M_{ji} = \frac{\frac{dN_{far}}{dE_{ji}}}{\frac{dN_{near}}{dE_j}} \tag{3.8}$$

where $\frac{dN_{far}}{dE_{ji}}$ is the neutrino flux seen in the far detector of bin E_i produced by the hadrons that would yield neutrino flux in bin E_j at the near detector.

Figure 3.36 shows that the both method perform somewhat similar but in overall the
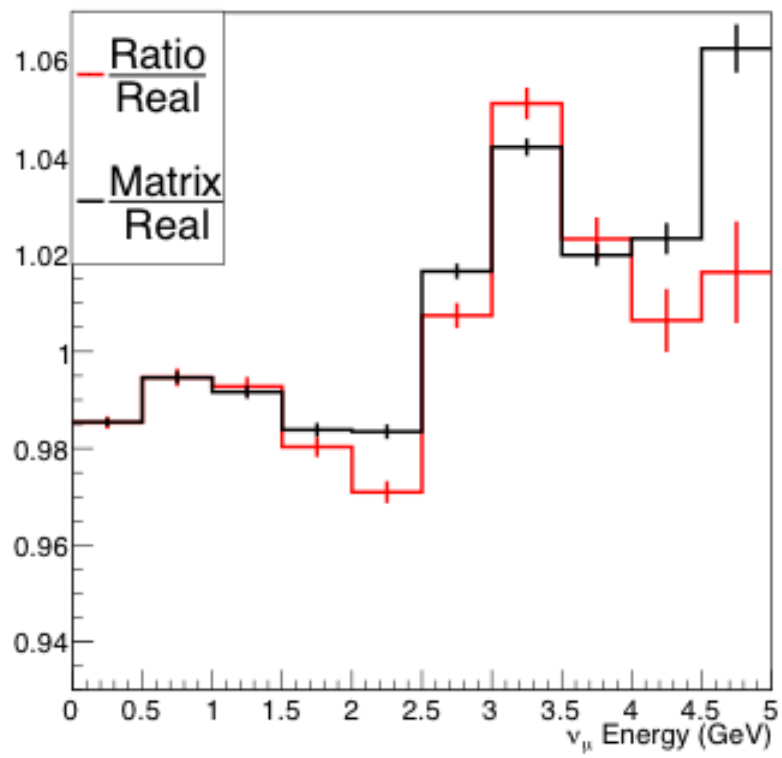
Figure 3.36: Ratio between the extrapolated "data" and Model "MC" flux using the matrix method.

matrix method is a little better than the ratio method to extrapolate the far flux. The errors shown are only the statistical errors. Focusing uncertainties are likely to have a big effect to extrapolate the far flux.

4   The MINERvA Experiment

4.1   Introduction

The MINERvA (Main Injector ExpeRiment ν-A) is a neutrino-nucleus scattering cross-section measurement experiment situated in the NuMI underground hall at Fermilab, Batavia, IL. The experiment uses various materials from plastic (carbon and hydrogen) to lead, iron, oxygen, helium and water as target materials to measure the neutrino scattering cross section. The active tracker region consists of doped polystyrene scintillator arranged in 3 different orientations to allow a 3D track reconstruction. Upstream of the tracker region lies the passive nuclear target region consisting of lead, iron, water, carbon and helium. Downstream of the MINERvA detector lies the MINOS near detector (Main Injector Neutrino Oscillation Search) which is magnetized and hence is used as a muon spectrometer to measure the charge and momentum of the muons exiting the MINERvA detector.

This section will briefly go through the MINERvA experiment and the detector design. A more detailed description is given in [17].

4.2   Motivation

The MINERvA experiment was proposed in 2005 with the goal of measuring the neutrino nucleus scattering cross-sections in the nuclear environment. At that time, the K2K experiment had just published the first oscillation results where 44 neutrino events were observed compared to the expected 63.9 events assuming no oscillation [12]. This depletion confirmed the maximum mixing ($\sin^2 2\theta = 1$) and the mass splitting (Δm^2) assumption from atmospheric neutrino experiments and came with large systematic uncertainty of around 9-10% (current oscillation experiments have around 5% systematic uncertainties, and DUNE aims to have no more than 1% systematic uncertainties in its signal events). Experiments like T2K and NOvA were being designed which aimed to measure Δm^2, neutrino mixing angle and measurement of CP violation with increased sensitivity. These physics goals required a significant reduction in neutrino interaction uncertainties. A more robust method to identify signal and background processes and the ability to reconstruct the incoming neutrino energy based on final state particles were required for the upcoming oscillation experiments. Since the oscillation experiments rely on nuclear models to understand and simulate the initial and final state interactions in the target nucleus, improvement of the models was required. MINERvA experiment was proposed to provide neutrino cross-section measurements that could improve these models and reduce the systematic uncertainties in the upcoming neutrino experiments.
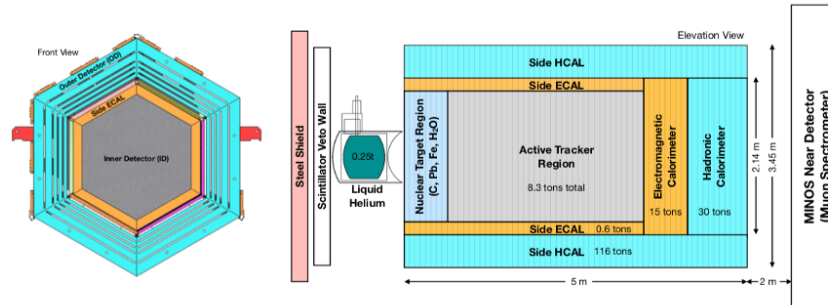
Figure 4.1: Schematic diagram of the MINERvA detector. The left plot shows the front face of the detector. The right plot shows the side view of the detector with the position of MINOS near detector downstream. Figure is taken from [17].

4.3   The MINERvA Detector

The design of the MINERvA detector is driven by the physics goal of the experiment. The MINERvA detector is required to resolve multiple final state particles, be able to track charged particles in the range of MeVs, be able to fully contain the electro magnetic and hadronic showers and measure cross-section in a wide range of nuclear targets for nuclear dependence of neutrino interactions. MINERvA also aimed to develop new and better reconstruction tools to reconstruct the final state particles by taking advantage of large statistics and existing technology. The core part of the detector (also called Inner Detector or ID) consists of the solid scintillator strips mixed with nuclear targets in the upstream region and the active tracker region downstream (see figure 4.1). Upstream of the MINERvA detector is a veto wall which tags the muons which are produced from the neutrino interactions from

the rock (surrounding the detector and between the NuMI absorber and the MINERvA detector). The veto wall has 5 cm thick plane of steel, 1.9 cm thick plane of scintillator followed by another 2.5 cm thick plane of steel and 1.9 cm thick plane of scintillator. A cryogenic vessel is placed between the veto wall and the main detector to accommodate a He target. The ID is surrounded by electro magnetic calorimeters (Side ECAL and downstream ECAL) followed by the hadron calorimeters. The region outside the inner detector (ID) is called outer detector (OD). The OD is made of a frame of steel with embedded scintillator. Both ID and OD are in the shape of a regular hexagon. A single unit of MINERvA detector consists of the scintillator and the outer frame. For the sake of 3D tracking, the scintillator strips are arranged in 3 different orientation with an angular offset of 60% corresponding to the plane along the X axis.

The direction of the beam is denoted by a z axis with the x-y origin at the center of the ID. The front of the downstream MINOS detector is set at $z = 1200cm$. The center of the neutrino beam is in the $y - z$ plane and points downward at an angle of 3.34 degrees.
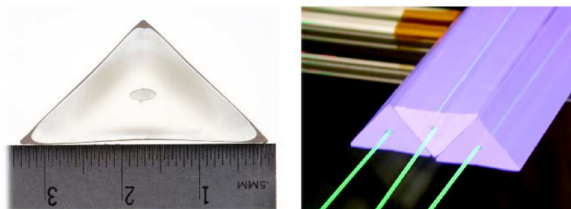
Figure 4.2: Cross-section view of a scintillator strip (left) and the arrangement of strips. The green line represents the wavelength shifting (WLS) fiber in the center of each triangular strips.

4.4   Inner Detector

The tracking modules in the inner detector are the parts of the active tracking region. The analysis mentioned in this thesis is done with the interactions in this region. The active tracker region is made up of scintillator planes. Each scintillator plane consists of 127 strips of doped polystyrene scintillator coated with titanium dioxide. Each strip has a triangular cross-section of height 17 ±0.5 mm and width 33.5 ±0.5 mm. Each scintillator strip has a hole of diameter 2.6 ± 0.2 mm centered at 8.5 ± 0.25 mm above the widest part of the triangle in which the wavelength shifting fibers are placed. The green wavelength shifting fibers read out the interactions in the scintillator strips. The diameter of each fiber is 1.2 mm. The strips are arranged in zig-zag configuration to allow the position measurement of the particle by charge sharing between at least two strips. Although the scintillator strip is primarily a hydro carbon (86.6% carbon and 7.42% hydrogen), it also contains small amount of oxygen
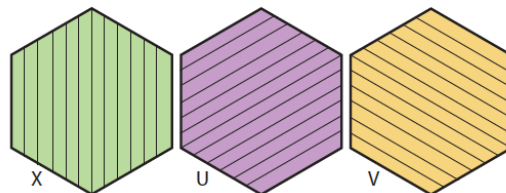
Figure 4.3: Orientation of the scintillator planes in the X,U and V planes.

(3.18%5), aluminum (0.26%), silicon (0.27%), chlorine (0.55%) and titanium (0.69%) coming from the gluing material (to glue the strips together) and TiO_2 coating, doping materials and epoxy.

Scintillator planes are installed in 3 different orientations in the planes of X,U and V alternately. The X orientation is vertical or parallel to the Y-axis. The U and V planes are oriented at an offset of 60% clockwise and counter clockwise direction with respect to the X plane as shown in figure 4.3. The arrangement of the planes follows the UXVX configuration. The active scintillator region is placed on the top and bottom of the scintillator region to contain the electromagnetic showers.

The downstream of the active scintillator region consists of electromagnetic and hadronic calorimeters. A 2 mm sheet of lead is placed between the active scintillator region and the downstream ECAL region as a transition region. The lead sheet increases the overall photon and electron interactions, which can be tracked in the ECAL region. A set of 20 hadronic

calorimeters (HCAL) modules are placed downstream of the ECAL. Each HCAL module has one scintillator plane followed by a 2.54 cm thick plane of steel.

Upstream of the active tracker region lies the nuclear target region with passive tracking. The nuclear target region consists of 5 modules made of steel, lead, graphite and water planes. A 1 m^3 volume cryostat is placed in the upstream of the target region which consists of liquid helium.

4.5   Outer Detector

The OD is located on each of the 6 sides of the inner modules. The OD is made of steel structure which acts as both the supporting structure and the HCAL region.

4.6   Simulation of Interactions in the MINERvA Detector

The MINERvA collaboration uses simulation to model the detector performance. The neutrino interactions are modeled by the GENIE v2.12.6 [25] and the final state particle interactions in the detector are modeled by GEANT4 9.4.p02 [21]. The detector materials are modeled with GEANT4 and the response of the scintillator and the electronics is modeled by custom MINERvA code.
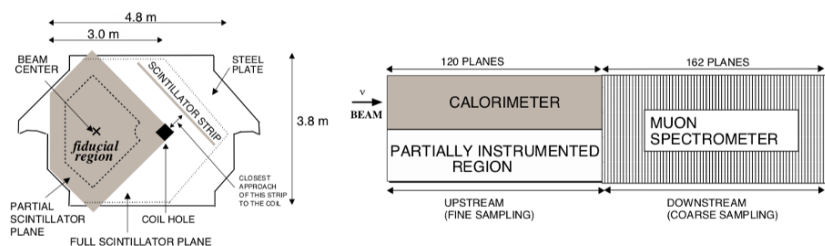
Figure 4.4: Schematic diagram of the MINOS near detector. The left plot shows the cross section of the detector and the right plot shows the side view of the detector.

4.7   MINOS near Detector

The MINOS near detector is situated 2.1 meters downstream of the MINERvA detector. The detector is primarily a tracking calorimeter composed of magnetized iron and plastic scintillator. The magnetic field is toroidal with a strength of between 1 to 2 Tesla [89] produced by a current carrying coil passing the detector through a coil hole as shown in figure 4.4. The detector consists of 282 steel plates each with 2.54 cm thickness. 154 of these steel plates are instrumented with 1 cm thick scintillator planes.

Muons exiting the MINERvA detector pass through the MINOS detector where the curvature of the muon track is measured to determine the momentum and the direction of curvature determines the charge of the muon. Muons fully contained in the MINOS detectors are used for this analysis where the energy of the muon is reconstructed from both the MINERvA and MINOS detectors. See appendix 5.11 for more information on muon momentum reconstruction in the MINERvA experiment.

4.8   Muon Energy Reconstruction in MINERvA Experiment

The CCQELike (see chapter 6 for the definition of CCQELike) cross-section measurement part of the thesis relies on muon kinematics. This section will briefly go through the muon reconstruction process in MINERvA experiment.

Since MINERvA relies on the MINOS near detector (which is downstream of the MINERvA detector), the reconstruction process happens in both detectors. All the muon tracks start at the MINERvA detector and then continue to the MINOS near detector. Figure 4.5 shows this process in the schematic diagram.

Hence, the reconstructed energy of the muon is given by:

$$E_\mu = E_{MINERvA} + E_{MINOS}$$

where, $E_{MINERvA}$ and E_{MINOS} are the energies of the tracks reconstructed in the MINERvA and MINOS detectors respectively. This also means the overall reconstructed muon will have the systematic uncertainties due to both detector properties which are bundled together as muon reconstruction systematic uncertainties.

In the MINERvA detector, anchored tracks (or the most energetic tracks that emerge from the neutrino interaction vertex) are usually the muon tracks and they deposit energy as
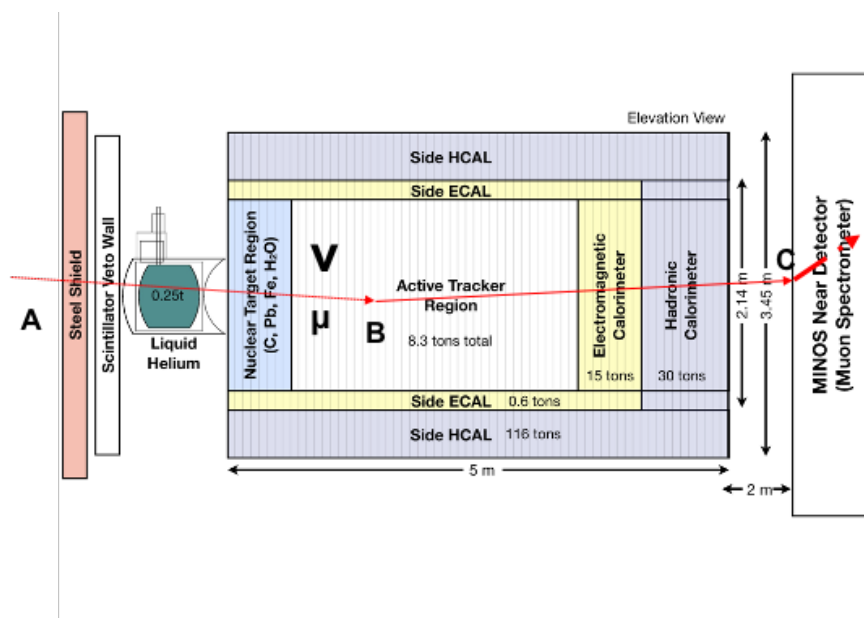
Figure 4.5: Schematic diagram of a muon track formed in the MINERvA detector and continuing to the MINOS Near Detector. (A) A ν_μ enters the MINERvA detector and interacts. (B) ν_μ interacts with the detector material and a muon track is formed that exits the MINERvA detector downstream. (C) The muon track enters the MINOS near detector where it is bent by the magnetic field.

minimum ionizing particle (MIP).To reconstruct the muon tracks, invidual clusters of energy (deposited by particles) are grouped together according to their time stamp (that corresponds to a given neutrino interaction). The grouped clusters are used to generate the *track* candidates. *Track* candidates are combinations of ionizing energy clusters and can be fitted into a straight lines. Multiple *track* candidates that show similar characteristics in terms of energy profile, time stamp and orientation are combined to form a muon track. Note that for the quasi-elastic interactions, muon tracks are required to be long enough to exit the MINERvA detector and matched in the MINOS detector. A more detailed explanation of muon reconstruction in MINERvA is given in section 3.8 of [128]. Based on the MIP of muon in different materials of the detector and taking into account the material assay of the detector [157], uncertainties on muon reconstruction due to each target materials are calculated in terms of absolute energies. Adding these uncertainties in quadrature, we get a total of 53.99 MeV uncertainty on MINERvA detector. This is the possible maximum overestimation or underestimation of muon energy that is reconstructed in MINERvA .

The muon momentum in the MINOS is determined by either by range or by curvature method. The range method looks into the amount of material traversed by the muon tracks that are completely contained inside the MINOS detector. The systematic uncertainties on the muon energy reconstruction by range are derived from the simulation of the MINOS

detector, detector mass, dEdX parameterization and track vertex reconstruction [17]. The range based muon reconstruction is assigned a 0.984% uncertainty on the reconstructed muon momentum.

The curvature method uses the algorithm developed by the MINOS collaboration [53] that relates the track curvature, magnetic field and the momentum component of the muon (perpendicular to the B field) as:

$$K = \frac{1}{R(cm)} = \frac{0.3B(kGaus)}{P(MeV)}$$

This method is used for muons that are produced in the MINERvA detector but are energetic enough to escape the calorimetric region of the MINOS detector. The systematic uncertainties on curvature methods were determined by studying the momentum reconstruction of the rock muons whose vertex are formed at the front part of the MINOS detector. The momentum of the rock muons were reconstructed by both range and curvature method and $\frac{1}{P_{curve}} - \frac{1}{P_{range}}$ distributions were made in 6 different P_{rang} bins. The mean for this distribution is given by $\bar{\mu}_{mc}$ for the simulated events and $\bar{\mu}_{data}$ for the reconstructed data. Then the curvature uncertainty is given by $\Delta K = |\bar{\mu}_{mc} - \bar{\mu}_{data}|$ which in the case of small curvatures can be written as $\Delta P_{curv} = -P_{curv}^2 \Delta K$. Since this method uses the range based method as well, besides the .984% uncertainty from the range based systematic uncertainties, an additional 0.6% uncertainty is assigned for muons with momentum greater than 1 GeV/c

and 2.5% uncertainty for those less than 1 GeV/c.

Note that, compared to the LE era analyses, the muon energy scale in the ME era analyses is shifted to 1.036 (from 1.00) with an uncertainty of 0.984% on the shift (Before the fit, the uncertainty was 2.0%). This comes from the low-ν fit works explained in chapter 5 of the thesis.

5 Data MC Discrepancy in the MINERvA Medium Energy Flux

From the start of its medium energy program (9/12/2013 to 07/07/2017), MINERvA reported a discrepancy between reconstructed data and simulated events. This discrepancy is seen in final states of all channels and is energy dependent [138] [133]. In any detector, reconstruction of event distribution depends upon the incoming flux of neutrinos and the cross-section between neutrinos and detector materials. The starting point of investigating this discrepancy involved looking at the flux, cross-section modeling and detector calibrations. All of these effects the energy reconstruction of the neutrino events. However, since this discrepancy is also seen in the low-nu events, whose cross-section is known to be independent of neutrino energy, cross-section modeling didn't seem to cause this discrepancy. So, the cross-section mismodeling was removed as a possible source of discrepancy. Initially, a fit between low-nu data and MC with the flux related parameters (beam parameters) as fit parameters was constructed. The fit predicted a correction to the low-nu MC distribution that made the MC agree well with the data. The shift in parameters from their *prior* positions informed about the possible source of the discrepancy. Although shape of the low-nu event depends upon the shape of flux, reconstructing the low-nu events means relying on our detector calibration to get the reconstructed energy. Later on, the muon energy reconstruc-
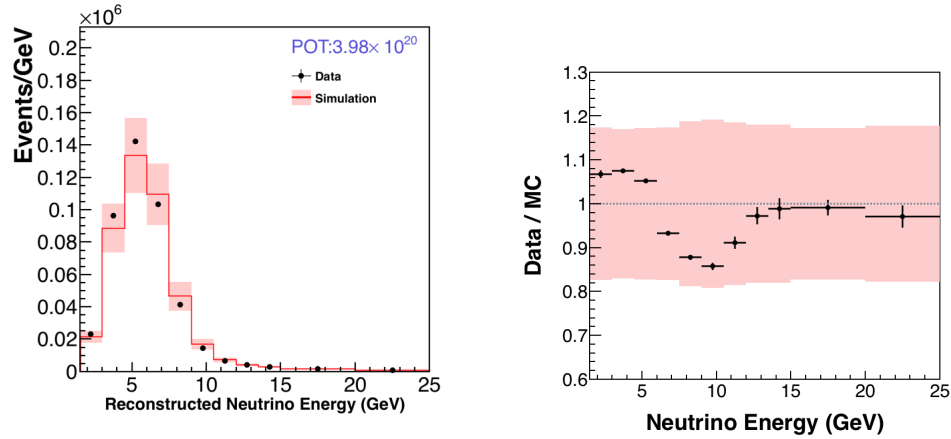
Figure 5.1: low-nu event distributions for data and simulation (left) and the ratio between data and MC (right).

tion parameters were also considered as a possible source of the discrepancy. This new fit preferred a pull towards the muon energy reconstruction parameters, specially reconstruction by range. This section will go through the fitting procedure developed to investigate this discrepancy.

5.1   Low-nu Events

The word nu (ν) means q_o from figure 5.2 where q_o is the energy transferred by the leptonic system to the hadronic system. For a neutrino-nucleus interaction like figure 5.2, the energy of the incoming neutrino can be reconstructed as:
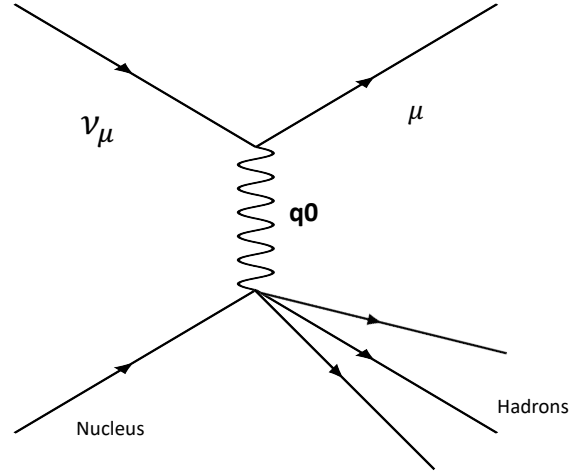
Figure 5.2: Feynman diagram showing a charged current inclusive event

$$E_\nu = E_\mu + q_o \qquad (5.1)$$

Here E_μ is the energy of the final state lepton (here the muon) and q_o is the recoil energy

transferred to final state hadronic system. The neutrino-nucleus interaction cross-section as

a function of ν can be written as:

$$[58]\frac{d\sigma}{d\nu} = \frac{G_F^2 M}{\pi} \int_0^1 (F_2 - \frac{\nu}{E_\nu}[F_2 \pm xF_3] + \frac{\nu}{2E_\nu^2}[\frac{Mx(1 - R_L)}{1 + R_L}F_2] + \frac{\nu^2}{2E_\nu^2}[\frac{F_2}{1 + R_L} \pm xF_3])dx \quad (5.2)$$

Here x is the Bjorken x (see appendix A.3 for more info on Bjorken x), F_1 and F_2 are the

structure functions of the struck nucleon and $R_L = \frac{F_2}{2xF_1}$. Positive sign is for the neutrinos and negative sign is for the anti-neutrinos. In the limit where $\nu << E_\nu$,

$$\frac{d\sigma}{d\nu} \approx \frac{G_F^2 M}{\pi} \int_0^1 (F_2) dx \tag{5.3}$$

The above equation shows that when the energy transferred to the hadronic system is small, the neutrino-nucleus cross section becomes almost constant as a function of neutrino energy. This means that the low-nu cross-section shape is independent of any cross-section modeling and $\frac{d\sigma}{d\nu}$ approaches a constant. Hence the interaction rate is just proportional to the flux and is given by:

$$N(E_\nu)|_{\nu<\nu_o} = \phi(E_\nu)\sigma(E_\nu)|_{\nu<\nu_o} \propto \phi(E_\nu) \tag{5.4}$$

Here ν_o separates the low-nu events from the overall inclusive sample. Once the number of low-nu event is known and since the cross-section of low-nu events are well understood, the flux shape can be extracted.
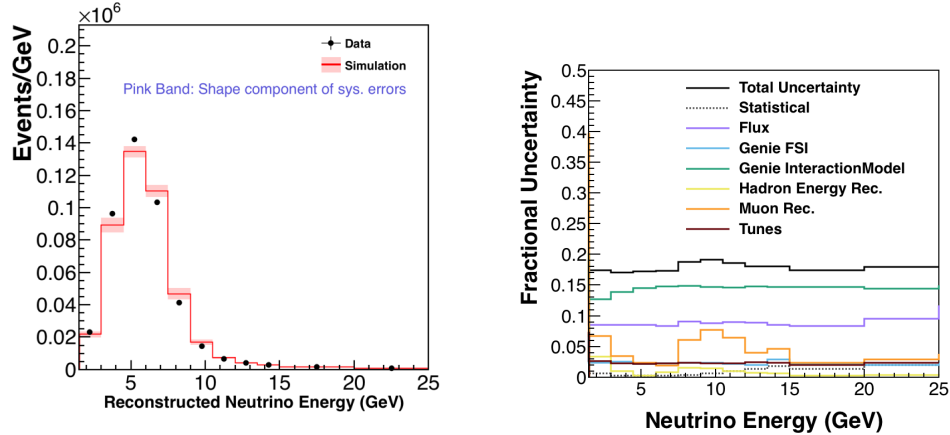
Figure 5.3: Left:Shape distribution of the low-nu data and simulated event distributions used in fit. The pink band represents the systematic error on the simulated event distribution. Right: The fractional error on the simulated low-nu distribution.

5.1.1 Input low-nu sample

The input low-nu sample is generated using the NukeCCQE package. NX version of mc sample was used with playlists minervame1A through E. This recoil energy transfer cut off after which the events becomes sensitive to cross section mis-modeling depends upon the energy of the neutrino. For the purpose of this study, events passing a recoil energy cut (q_o) of 800 MeV are defined as the low-nu sample. This cut is optimum for neutrino energies greater than 5 GeV [57]. For events with reconstructed neutrino energy less than 5 GeV, the inclusive sample overlaps with the low-nu sample increasing the correlations between low-nu flux (and hence flux parameters) and the inclusive cross-section parameters.
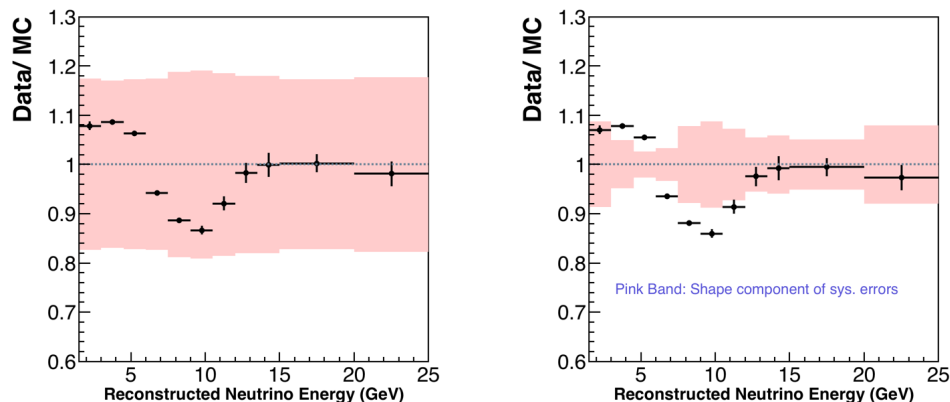
Figure 5.4: The ratio between area-normalized low-nu data and MC. On the left is the ratio with the uncertainty on the ratio shown with a pink band. On the right is the ratio with the uncertainty on the shape of the ratio in the pink band.

Figure 5.3 shows shape distribution of the data and MC low-nu events and the related systematic and statistical errors on the MC sample. The MC sample is pot scaled to show the discrepancy. The pink error band is the systematic uncertainties in the sample and the error bars (too small to be seen here) are statistical errors. The sample contains a set of standard GENIE systematics, Flux and Reconstruction systematics. All the GENIE systematics are related to the cross-section modeling. Figure 5.4 shows the ratio between area normalized data and MC sample. The investigation and possible solution to the wiggle shape seen in this figure is the topic of this chapter.

PPFX is the uncertainty on the low-nu sample due to hadron production in the beam-line. Uncertainty due to Hadronic Energy Reconstruction comes from the uncertainty on

Genie FSI	Genie InteractionModel	Tunes	Hadron Energy Rec.	Muon Rec.	Flux
FrAbs N	AGKYxF1pi	RPA-Model	Hadronic Energy Rec.	Muon Energy Rec.	PPFX
FrAbs pi	AhtBY	Non Resonant Pion		Muon Angle Rec	
FrCEx N	BhtBy	2p2h Model			
FrCEx pi	CCQEPauliSupViaKF				
FrElas N	CV1uBY				
FrElas pi	CV2uBY				
FrInel N	EtaNCEL				
FrInel pi	MaCCQE				
FrPiprd N	MaCCQEShape				
FrPiProd pi	MaNCEL				
MFP N	MaRES				
MFP pi	McRES				
	NormCCQE				
	NormCCRES				
	NormDISCC				
	NormNCRES				
	RDecBR1gamma				
	Rvn1pi				
	Rvn2pi				
	Rvn3pi				
	Rvp1pi				
	Rvp2pi				
	Theta_Delta2Npi				
	VecFFCCQEshape				

Table 5.1: List Of Systematics in Each categories show in figure 5.3
.

Particle	Error
Proton (KE>100 MeV)	3.0%
Proton (KE between 50 MeV and 100 MeV)	3.5%
Proton (KE<50 MEV)	4.0%
Pion (KE between 400 and 1900 MeV)	4.0%
Pion (KE less than 400 MeV and more than 1900 MeV + other Mesons	5.0%
EM	3.0%
Neutron(KE>150 MeV)	20%
Neutron (KE between 50 MeV and 150 MeV)	10%
Neutron (KE<50 MeV)	25.0%
Others	20.0 %

Table 5.2: Breakdown of hadronic energy uncertainty for each type of particles depositing energy on the MINERvA detector

the calorimetric reconstruction of the energy deposited by different hadronic particles on the MINERvA detector. A complete breakdown of this uncertainty is given in table 5.2.

Figure 5.5 shows the true composition of the low-nu MC sample used in the fit. The sample has 35% true charged current quasi elastic (CCQE), 38% true resonance (CCRES), 17% 2p2h (MEC) and 5 % deep inelastic events. The 2p2h is simulated using Valencia Nieves model.

5.2 Flux Fitting Procedure

Because of the wide energy distribution of the neutrinos, the data collected in the medium energy era allows to explore kinematics regions previously unavailable in the LE era. Since
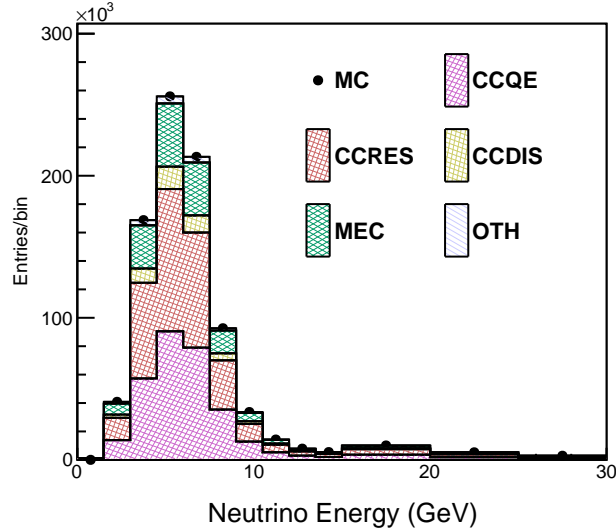
Figure 5.5: Break down of the reconstructed low-nu MC sample into true components (as predicted by GENIE (2.12.6) generator).

MINERvA is a cross section measurement experiment, flux is an important ingredient to get the final cross-section results. The following general formula for cross section calculation shows the relation between flux and cross section.

$$\left(\frac{d\sigma}{dx}\right)_\alpha = \frac{\sum_j U_{j\alpha}(N_{data,j} - N_{bkgd,j})}{A_\alpha \Phi T \Delta x_\alpha} \tag{5.5}$$

where Φ is the flux.

$U_{j\alpha}$ is the migration matrix element mapping j^{th} true bin to α^{th} reconstructed bin.

A_α is the product of reconstruction efficiency and detector acceptance for the reconstructed bin α.
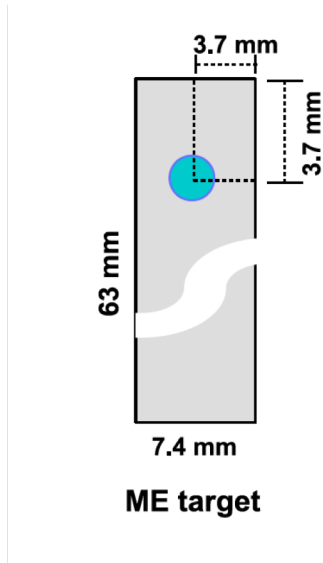
Figure 5.6: XY view of the NuMI ME target. Target is longer along vertical direction and the beam is not at the center along Y.

T is the number of targets in the MINERvA detector.

Δx_α is the bin width of the reconstructed bin α.

5.3   Daisy Regions

The default NuMI neutrino flux assumes beam-line parameters at their nominal position. The beam-line parameters are optimized to get small uncertainties around the focusing peak of the neutrino flux. The uncertainties on the nominal values of beam parameters and correlation between beam parameters means even a small shift in one of the parameters' nominal value would result in a very different neutrino flux. The NuMI medium energy flux
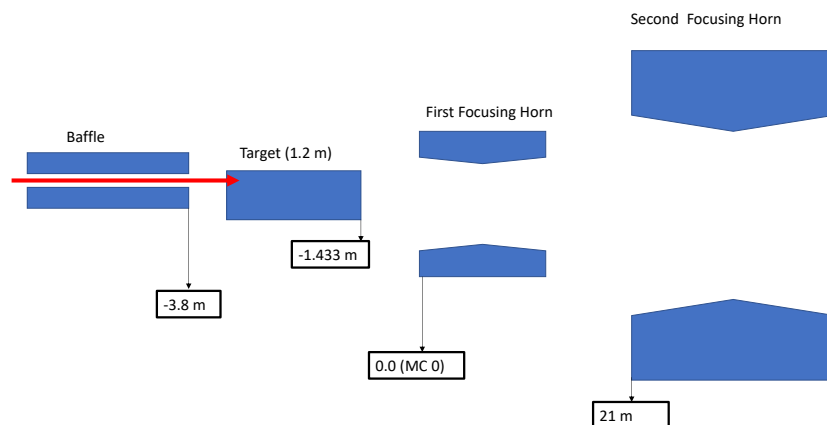
Figure 5.7: YZ view of the NuMI Medium Energy beamline configuration. The red arrow shows the direction of the proton beam which is along Z. The Sizes and relative positions of the beam-line parameters are exaggerated and not on scale. The **MC 0** is the start of the first focusing horn. Positions of other parameters are shown relative to the MC 0 which is the usual convention. As shown in figure 5.6, the vertical position (along Y axis) of the proton beam on target is above the center.

uncertainties evaluated for MINERvA is less than 10%. This level of precision requires the parameters to have very small uncertainties. Table 5.3 shows that position of beam-line parameters are required to be known within 1 mm. Similar level of accuracy are required for other parameters.

The daisy binning of the MINERvA detector allows us to divide the detector into various regions symmetrically. A central circular region of radius 350 mm and the petals made by connecting the hexagonal edges of the MINERvA detector to edge of the central region by a straight lines that would meet at the center of the circle if interpolated.
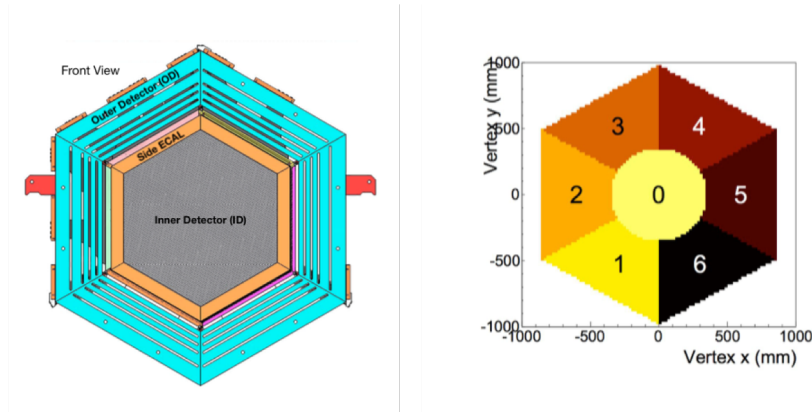
Figure 5.8: Front face of the MINERvA detector (left) and the daisy binning of the MIN-ERvA detector.

Mathematically, for a neutrino event seen at some position (x, y) of the MINERvA detector,

the daisy region j in which the event lies is given by:

For a neutrino event to be seen at daisy region 0,

$$\sqrt{x^2 + y^2} < 35 \; cm \rightarrow j = 0$$

. For a neutrino event to be seen at some daisy region $j \neq 0$

$$j = (\frac{tan^{-1}(\frac{y}{x})}{\pi/3} + 4)$$

where the numbers after following the decimal in j is ignored. Taking the start of the focus-

ing horn as the origin, the location of the front of the MINERvA detector is (x,y,z) cm =

(-24.86,-24.0067,103168). Being close to the neutrino beam source makes the different part of the MINERvA detector sensitive to focusing parameters in different regions especially if the change in some focusing parameter is not symmetric along X and Y. Figure 5.9 shows the ratio of ν_μ fluxes at different daisy bins of the MINERvA detector to the bin 0. Fluxes at the lower face of the MINERvA detector (daisy bins 1,2 and 6) are very different from fluxes at the upper face of the detector (daisy bins 3,4,5). In fact, relative to the central daisy bin (bin 0), bin 1 (blue) sees the maximum deficit of fluxes between 5 to 10 GeV whereas, bin 6 (black) which is at the other end sees a maximum excess of fluxes in the same energy region. The sensitivities of different parts of the MINERvA detector for different energy regions of the neutrino flux cancels out in average.

Figure B.2 shows the change in flux when the position of the proton beam on target is shifted by 1 mm from the center. Different daisy bins show different kind of sensitivities to the change in this parameter. For example, when the beam is shifted by 1 mm along right (solid lines), the right part of the MINERvA detector (daisy bin 5) sees a reduction in flux from 5 to 10 GeV but sees excess in the high energy tail of 10 to 15 GeV. But moving the beam by 1mm along left (dotted lines) causes opposite changes in flux. The lower part of the MINERvA detector (bin 1) shows similar changes in fluxes for both positive and negative shift of the beam until 10 GeV. Daisy bin 2 which is the left part of the MINERvA detector shows different sensitivities to different shifts in proton beam. However, unlike the

left part of the MINERvA detector which sees a negative correlation in fluxes for positive and negative beam shifts in regions of 5 to 15 GeV, the right part of the detector doesn't show similar behavior. This difference is due to the MINERvA detector being slightly offset from the center (more towards left from the center where center is the (x,y) position of the MCZERO).

The MINERvA detector has different sensitivities to the neutrino flux at different energy regions which get washed out when the flux is averaged over the entire detector. Hence, to take into account that the sensitivity of different beam-line parameters is different across the MINERvA detector, the fit is done individually over different parts of the detector as shown in figure 5.8 and a cumulative χ^2 is calculated to evaluate the goodness of fit. The next section explains the fitting procedure in detail.

5.4   The Minimization Function

The beam flux fitting procedure relies on the ROOT Math Package called TMinuit [139] which is a multi-parameter fit function. The fit takes the low-nu data and mc histograms for each daisy bin as input parameters and utilizes the $\pm 1\sigma$ shift templates of the fitting parameters to vary the MC or Data and does the minimization of the χ^2 for the difference

between simulation and data over several iterations. The fit parameters are normalized to their nominal uncertainties and hence they are dimension-less. In each iteration, a χ^2 is calculated in each of the daisy bins of the MINERvA detector individually. The χ^2 from each daisy bin is added to get a cumulative χ^2 which is then minimized to get the lowest possible value.

Data events are the events reconstructed in the MINERvA detector. Each observed event can be simulated as a function of the flux (and hence focusing parameters), reconstruction effects and the underlying theoretical models that account for neutrino-nucleus interactions and nuclear effects. Mis-modeling of any of these parameters would cause the simulated energy spectrum to be different than that of the data. Mis-modeling of the focusing parameters would cause the simulated energy spectrum to be different than that of the data. Similarly, wrongly estimated reconstruction effects makes our data to be reconstructed with wrong neutrino energy estimation. All of these mismodeling cause a shift in energy for the reconstructed events and the ratio of data/mc would give a wiggle like structure. Since this is also seen in the low-nu sample whose shape depends upon the flux and the detector parameters only, cross-section mismodeling was removed as a possible suspect leaving the flux and the detector parameters.

Parameter Name	Nominal Values $\pm$ 1 σ Uncertainty
Beam Position (X)	0 $\pm$1 mm
Beam Position (Y)	0 $\pm$ 1 mm
Beam Spot Size	1.5 $\pm$ 0.3 mm
Horn 1 Position (X)	0 $\pm$ 1 mm
Horn 1 Position (Y)	0 $\pm$ 1 mm
Horn 2 Position (X)	0 $\pm$ 1 mm
Horn 2 Position (Y)	0 $\pm$ 1 mm
Horn Current	200 $\pm$ 1 kA
Horn Water Layer	1 $\pm$ 0.5 mm
Target Position (X)	0 $\pm$ 1 mm
Target Position (Y)	0 $\pm$ 1 mm
Target Position (Z)	-143.3 $\pm$ 3 mm

Table 5.3: Nominal (*prior*) value of the focusing parameters and their 1 σ values. All the 1 σ values correspond to the NuMI Medium Energy (ME) beamline configuration except for the *Target Position Z* which has the nominal 1 σ uncertainty of 1 mm for the NuMI beamline.

5.5 Flux Fit with Focusing Parameters only

The flux or focusing parameters are discussed in detail in chapter 2. The focusing parameters that are used in the fit were chosen over several MINERvA flux meetings and studies. The parameters like the position of the second focusing horn and the position of the MINERvA detector, which had minimal effect on the flux shape were dropped. The final sets of the focusing parameters with their nominal values are given in table 5.3. Along with these fit parameters, a normalization parameter is also added to take into account for the normalization of the low-nu cross-section, which, unlike the shape as a function of neutrino energy, is not well known. Usually the fit preferred a normalization of 1.10 for this study. The

normalization is not considered when the results of the fit are applied to other MINERvA data since we are only interested in the shape distribution. The minimization formula is written as:

$$\chi_i^2 = \sum_j \frac{(Data_{ij} - MC_{rewgt;ij})^2}{\sigma_{ij}^2}$$

$$\sigma^2 = \sqrt{\sigma_{Data}^2 + \sigma_{MC_{rewgt}}^2} \tag{5.6}$$

$$MC_{rewgtij} = MC_{nominalij} \times \prod_k w(\alpha_{ijk})$$

The error σ, is just the statistical error of the input low-nu data histograms and the MC histograms.

Here i denotes the energy bins and j the daisy bins. The MC_{rewgt} is the nominal sample reweighted by the fit parameters weights $\prod_k w(\alpha_k)$ coming from the $\pm 1\sigma$ shift templates.

It is possible that relying on just χ^2 might result in the minimization value which is biased by one particular parameter. The result is a χ^2 dominated by a large pull on one parameter and the rest of the parameters phase space not explored properly. The best fit acquired by such bias will not be physically reliable although a global minimum might have been reached. To avoid this issue, we added a penalty term on the χ^2 while evaluating/exploring the parameter space. The penalty is given by:

$$penalty_{Tot} = \sum_k (\alpha_k)^2 \tag{5.7}$$

The fit function is the χ^2 minimization where the nominal MC sample is re-scaled by the weight function of focusing parameters such that the χ^2 is minimized. The nominal MC sample can be roughly written as:

$$MC_{nominal\ j} = \epsilon_j \times \Phi_{nominal\ j} \tag{5.8}$$

where

ϵ_j accounts for cross-section terms as a function of energy (j).

Φ is the flux as a function of energy+beamline parameters (α_k)

The flux can be considered to be a function of all the focusing parameters given as:

$$\Phi_j = \prod_{k}^{N} f(\alpha_k) \tag{5.9}$$

where $f(\alpha_k)$ is a function of some k^{th} focusing parameter and N is the total number of focusing parameters. The nominal flux $\Phi_{nominal}$ is simulated with the focusing parameters at their prior nominal values given in table 5.3. During the minimization, at each iteration, alternate MC templates are generated by reweighting by the function $f(\alpha_k)$ from a nominal focusing parameter to that of shifted focusing parameter flux ratio. Let $\delta\alpha_k$ represent the shift of focusing parameter α_k from its nominal position in sigmas. Then the nominal flux

can be written as:

$$\Phi_{nominal} = \prod_{k}^{N} f(\alpha_k; \delta\alpha_k = 0)_k \tag{5.10}$$

To generate an alternate flux where some focusing parameter k is shifted by some σ_k value, the nominal flux is reweighted as:

$$\Phi_{reweighted;k} = \prod_{i}^{N} f(\alpha_k; \delta\alpha_k = 0)_i \times R(\alpha_k; \delta\alpha_k = \sigma_k) \tag{5.11}$$

where the $R(F.P; \delta\alpha_k = \sigma_k)$ is the ratio of the flux due to all focusing parameters except α_k in their nominal position and α_k shifted by some σ_k value to the nominal flux:

$$R(\alpha; \delta\alpha_k = \sigma_k) = \frac{\prod_{i;i\neq k}^{N} f(\alpha\delta\alpha = 0)_i \times f(\alpha; \delta\alpha_k = \sigma_k)}{\prod_{i}^{N} f(\alpha_i; \delta\alpha_i = 0)} \tag{5.12}$$

Then the MC template where one of the flux parameter k is shifted by σ_k is given by:

$$MC_{reweighted;k} = MC_{nominal} \times R(\alpha; \delta\alpha_k = \sigma_k) \tag{5.13}$$

The statistical error on the reweighted MC includes the error due to the reweighting. The flux reweighting terms $R(\alpha; \delta\alpha_k) = \sigma_k)$ are generated from the 1 σ shift templates of the focusing parameters. These shift templates are the ratios of the nominal fluxes to the new fluxes where focusing parameters are shifted by $\pm$ 1 σ from their nominal position. For each
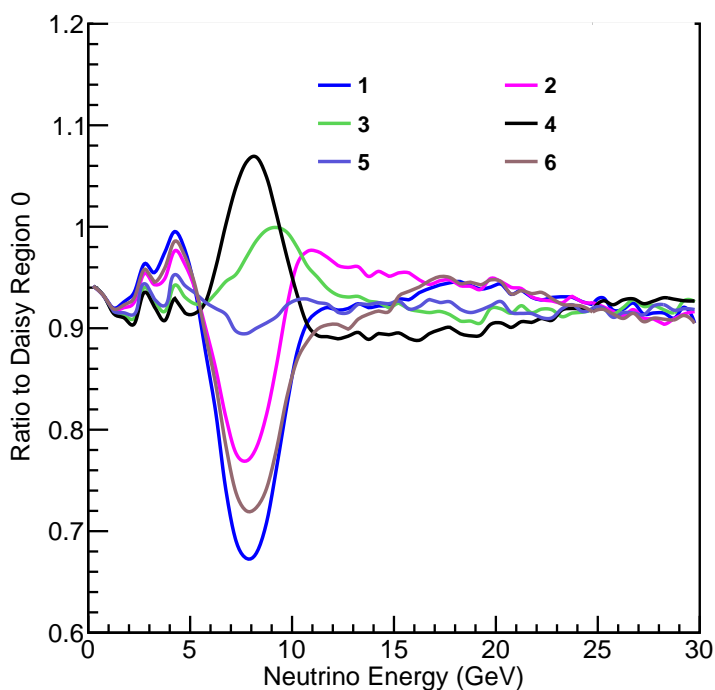
Figure 5.9: Ratios of fluxes in various daisy bins with respect to the central daisy bin 0.

focusing parameter, the ratio is known at 3 points ($\sigma = 0; \pm 1$). The interpolation between ± 1 σ is done by creating a spline function. Beyond $\pm$ 1 sigma, the linear extrapolation is done from the end point as shown in figure 5.10.

Figure 5.9 shows the ratios of the muon neutrino flux seen by the different daisy regions (daisy regions as shown in figure 5.8) to the central daisy region. Flux across the MINERvA detector face is not uniform and the beam parameters have different sensitivities to the flux in the different parts of the detector. Furthermore as seen in figure 5.6, because the nominal

value of some of the beam-line parameters (Y position of the beam in the target in figure 5.6)

are not symmetric along positive and negative shifts from their nominal position, changes in

flux due to these shifts are not symmetric.

Splines created by joining points at σ shifts accounts for such asymmetric effects and also

helps the fit to transition from positive to negative shifts without any discontinuities. The

linear interpolation beyond $\pm$ 1 σ shifts avoids unrealistic predictions from spline functions

at large sigma pulls and instead relies on our knowledge of 1 σ shift templates. Relying on 1

σ shift templates can be unrealistic at large shifts of focusing parameters and assumes that

the change in flux due to shifts is continuous. Since the fit is done in each energy bin in each

daisy bins of the MINERvA detector, σ shift templates for each daisy bins are required and

the reweighting is done bin by bin. The best MC predicted from the fit is given by:

$$MC_{best} = MC_{nominal} \times R_{best} \tag{5.14}$$

where:

$$R_{best} = R(F.P; \delta FP = best\ \sigma)_i \tag{5.15}$$

The best MC is the MC corrected by the prediction from the fit and the **Total** χ^2 between

the data and this MC is minimum. 1 σ shifts of the focusing parameters are also given in

table 5.3 and the new nominal values of the focusing parameters that gives R_{best} is given in

table 5.4.
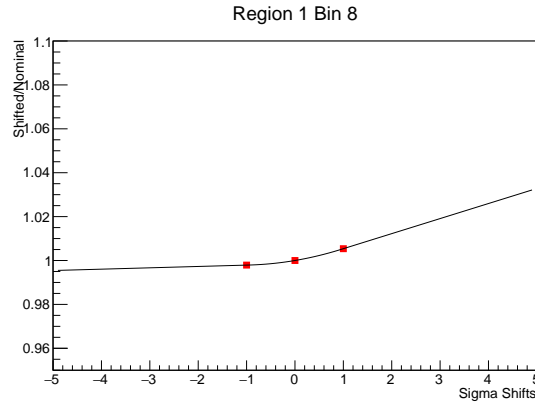
Figure 5.10: Ratio vs. σ shift in nominal flux for parameter Target Position (z) for bin 8 (4-4.5 GeV E_ν) for Region 1 of detector. Shift in nominal flux at $\pm 1\sigma$ shifts (solid black boxes) are joined by a cubic spline function to estimate the shift in the nominal flux inside the region of $\pm 1\sigma$ shift. Beyond ± 1 σ, linear interpolations are done. In case of focusing parameters, only 1 σ templates are used to construct the spline functions. This means larger pull predicted by the fit might be less reliable since we are assuming the change in nominal flux based on $\pm 1\sigma$ pulls.

5.6   Weight Function

By fitting the low-nu MV sample against the data with focusing parameters, we get a weight function (see figure 5.11), with which nominal MC can be reweighted to remove the data/mc discrepancy. This can be thought of as the fractional correction to the low-nu sample predicted by the fit to remove the discrepancy between the data and the MC assuming all of the discrepancy is coming from the mis-modeling of focusing parameters only. The fitting is
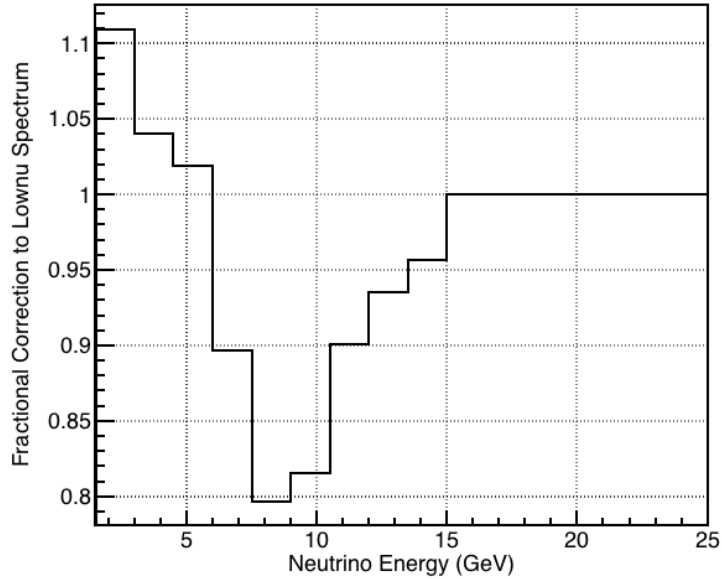
Figure 5.11: The Final CV Weight function (fractional correction to low-nu spectrum)

done from 1.5 GeV to 15 GeV. Hence the weight function is set to 1.0 after 15 GeV.

Since the fit is done in each of the daisy bins of the MINERvA detector simultaneously, we get a set of best shifted fit parameters for which the fit converged to a minimum total χ^2. The weight function due to the new shifted fit parameters for a given energy bin is given by:

$$w = \frac{MC_{best}}{MC_{nominal}} \tag{5.16}$$

where the best MC is:

$$MC_{best} = MC_{nominal} \times R_{best} \tag{5.17}$$
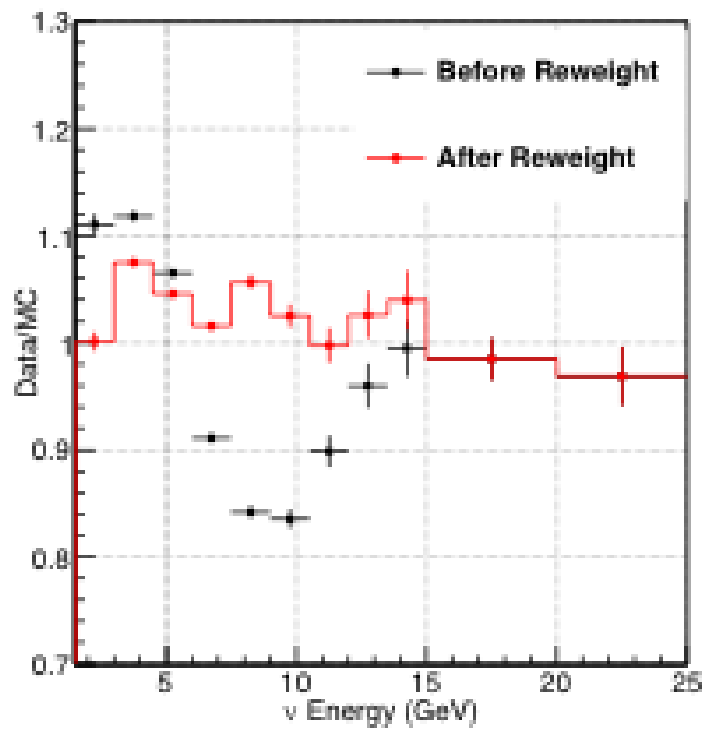
Figure 5.12: The low nu distribution before reweighting 5.11 (black) and after reweighting (red). The weight function removes the wiggle from the ratio. Errors shown are just the stat errors.

where

$$R_{best} = \prod_k R(\delta\alpha_k = best\ \alpha_k)$$

is the overall re-weight function or the correction to the low-nu spectrum. $R(\delta\alpha_k = best\ \alpha_k)$ is the correction predicted by the fit with the focusing parameter α_k is shifted by $best\ \alpha_k$ from its nominal position keeping the other parameters unchanged. However R_{best} is different in different daisy bins of the MINERvA detector. So, the MC_{best} is calculated for each daisy bin i for a given neutrino energy bin as:

$$MC_{best;i} = MC_{nominal;i} \times R_{best;i} \tag{5.18}$$

And overall weight function for a given neutrino energy bin becomes:

$$w = \frac{\sum_{i=1}^{7} MC_{nominal;i} \times R_{best;i}}{\sum_{i=1}^{7} MC_{nominal;i}} \tag{5.19}$$

Table 5.13 shows the systematic uncertainties on the weight function coming from the fit. Since the χ^2 minimization is a function of both data and MC, the systematic uncertainties are propagated from the MC sample to the weight function when the fit is done.

In the MINERvA experiment, systematic effects due to various parameters are simulated by creating an alternate set of MC shifting the parameter by 1 σ from its central value. This
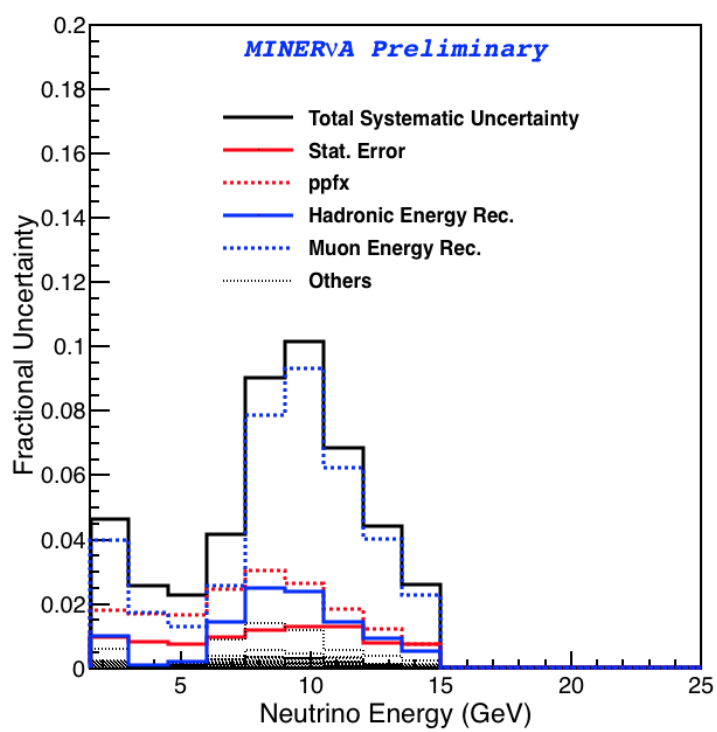
Figure 5.13: Fractional uncertainties introduced by fit on the weight function

alternate MC is called a "universe". For cross-section systematics which usually have 1 parameter, two alternate MC templates are generated by shifting the parameter by $\pm 1\,\sigma$ from the central value (CV). The average shift gives uncertainty on the MC sample due to that parameters. In case of flux and reconstruction systematics which have multiple parameters and their correlations to take into account, MINERvA uses the multi universe approach [19]. A certain number of alternate MCs are created by randomly shifting these parameters based on a probability distribution that accounts for the correlation between these parameters. The spread of these alternate universes gives the systematic uncertainty for a many-parameters systematic source. A more detailed description of 2 universe method and multi universe method to evaluate uncertainty is in Sections 6.17.4.1 and 6.17.4.2 respectively. Doing a fit in each of these systematic universes gives a unique fit result and hence a unique weight function for each universe. By doing the fit in all systematic universes of the MC sample, we end up with a weight function with its own systematics propagated from the input MC sample.

The uncertainty on the weight is calculated as:

$$RMS = \sqrt{\frac{\sum_i (w_i - \bar{w})^2}{N^2}} \tag{5.20}$$

where, the w_i is the weight of some i^{th} universe of a parameter. The summation is done over all given universe.

Similarly, the average weight $\bar{w}$ is given by:

$$\bar{w} = \sum_i w_i/U \tag{5.21}$$

where, again w_i is the weight in some systematic universe i and the U is the total number of universes for that parameter.

The total systematic error is just the sum of individual systematic errors in quadrature.

$$\sigma_{sys} = \sqrt{\sum_s RMS_s^2} \tag{5.22}$$

where s is running index over systematics of the weight function:

$$\sigma_{tot} = \sqrt{\sigma_{sys}^2 + \sigma_{stat}^2} \tag{5.23}$$

The final weight function shows strong bin to bin correlation (in the bins of neutrino energy) as seen in figure 5.14. The correlation is between neighboring bins in two regions (1 through 5) and (6 through 10). It is consistent with the shape of the wiggle. The bins in the rising edge and and the falling edge of the wiggle are highly correlated to one another.
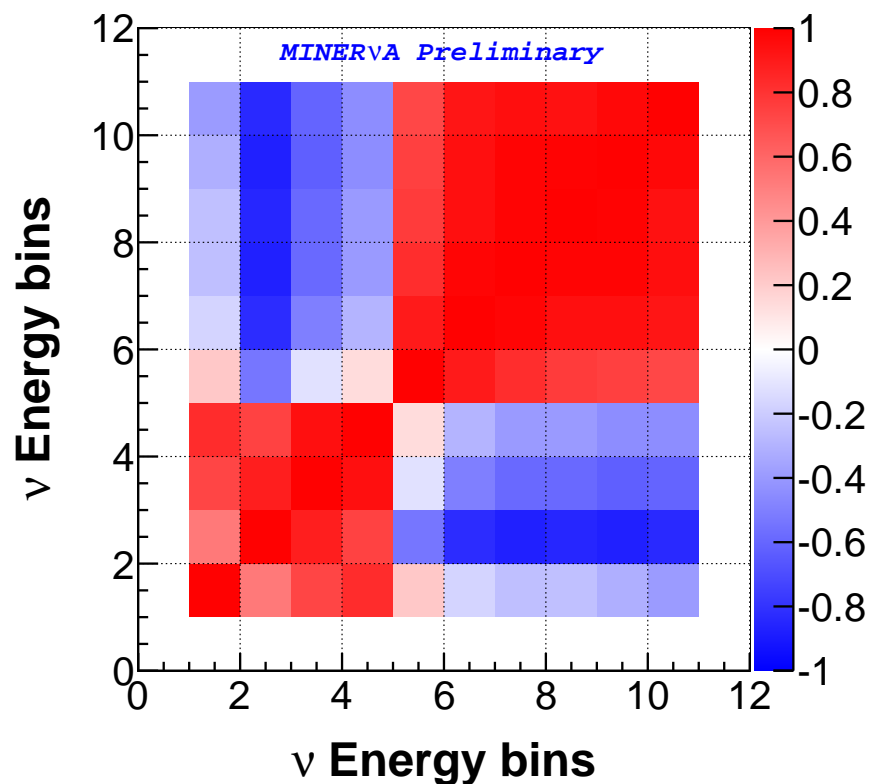
Figure 5.14: Bin to Bin correlation in the Weight Function

5.7 Correlation between Focusing Parameters

The table 5.3 gives the nominal values of the fit parameters and their 1 σ equivalent shift.

When calculating the nominal uncertainties on the flux, 1 σ shift in targetZ position is taken

as 1mm. The *prior* uncertainty on targetZ was taken as 3 mm for the fit to increase its

sensitivity to the change in flux shape.

Table 5.4 shows that the fit is mostly sensitive to the targetZ shift (longitudinal shift of

Parameter	Nominal Value	New Value
Beam Position (X)	0 mm	-0.2 ± 0.12 mm
Beam Position (Y)	0 mm	-0.53 ± 0.14
Beam Spot Size	1.5 mm	1.22 ± 0.14 mm
Horn Water Layer	1 mm	0.895 ± 0.16 mm
Horn Current	200 kA	197.41 ± 0.76 kA
Horn 1 Position (X)	0 mm	0. ± 0.17 mm
Horn 1 Position (Y)	0 mm	-0.39 ± 0.17 mm
Target Position (X)	0 mm	-0.32 ± 0.17 mm
Target Position (Y)	0 mm	1.65 ± 0.5 mm
Target Position (Z)	-1433 mm	-1419.44 ± 1.83 mm

Table 5.4: Shifts of focusing parameters predicted by the fit done with focusing parameters only.

Parameter Name	Best Fit Shifts (in σ)
TargetPosition (z)	6.96 ± 0.38
Beam Position (Y)	-0.23 ± 0.22
Horn 1 Position (Y)	-0.28 ± 0.14
TargetPosition (Y)	1.83 ± 0.5
Horn Water Layer	0.08 ± 0.28
Normalization	1.04 ± 0.01

Table 5.5: Best fit with the horn current and some parameters removed.

the target) and the horn current. Figure 5.15 shows that these two parameters are strongly correlated. The next biggest shift is the shift in vertical position of target (Target Position (Y)). The rest of the parameters do not have large contributions to the fit weight function.

The correlation matrix shows that there are strong correlations between the fitting parameters. Some interesting features of the matrix are as follows:
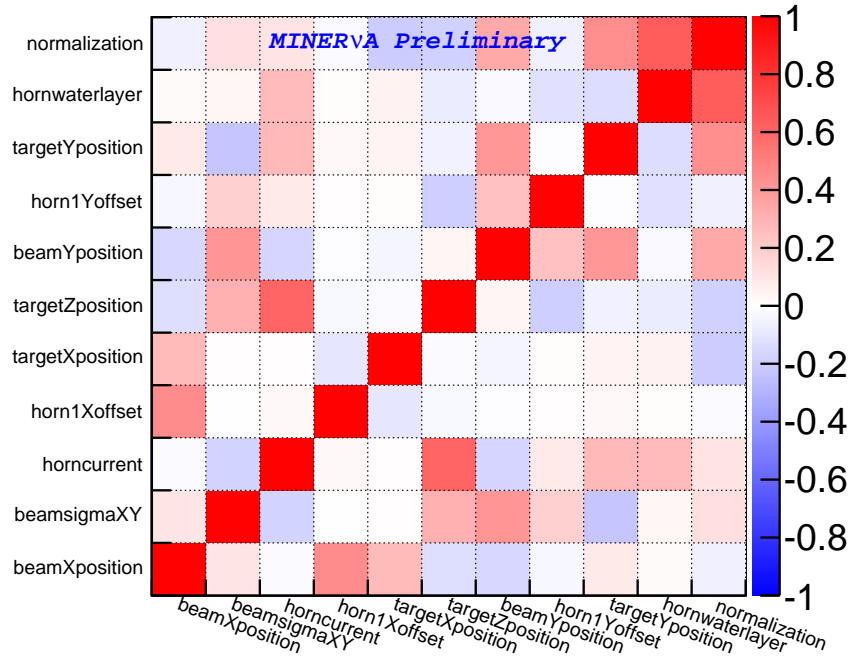
Figure 5.15: Correlation Matrix for the parameters of the fit

Parameter Name	Best Fit Shifts (in σ)
Horn Current	-6.82 ± 0.42
Beam Position (X)	-1.26 ± 0.12
Horn 1 Position (X)	-0.14 ± 0.15
Target Position (X)	0.43 ± 0.18
Normalization	1.04 ± 0.00

Table 5.6: Best fit with the target longitudinal position and some parameters removed.

- There is a strong correlation between horn current and targetZ position. We had done a separate study where fitting parameters were divided into two groups with one group having targetZ position and another group having horn current. In both cases, the fits converged. Tables 5.5 and 5.6 shows the best fit values (in σ shifts). Table 5.5 shift shows that in case of targetZ shift, the σ shift increases from 4.55 to 6.96 σ. Similarly, in case of horn current, the σ shift decreases from around -2 to -6 σ. The rest of the parameters remained the same. This is consistent with the correlation between these two variables seen in the correlation matrix.

- X offsets (horizontal offsets) and Y offsets (vertical offsets) of the focusing parameters are positively correlated. For example, beamXposition and targetXposition are positively correlated. Similarly, beamYposition and targetYposition are also positively correlated.

5.8   Fit with Muon Energy Reconstruction Parameters

Since the downstream MINOS near detector is magnetized, MINERvA relies on MINOS near detector to identify the charge and reconstruct the energy of the muons produced in the MINERvA detector. Once the muons exit the back of the MINERvA detector, we rely on the MINOS near detector to reconstruct the energy of the muon. If the muon track is fully contained in the MINOS detector, we look at the path length of the track in the MINOS and the MINERvA detector and reconstruct the energy of the muon. If the muon track is not contained in the MINOS detector, we look at the curvature (due to MINOS magnetic field) of the muon track to determine the energy of the muon. Depending on the method used to determine the energy of the muon, muon energy reconstruction can have the following sources of uncertainty:

- Uncertainty on muon energy due to the reconstruction of muon path length in MINERvA detector.

- Uncertainty on muon energy due to the reconstruction of muon path length in the MINOS detector.

- Uncertainty on muon energy due to the reconstruction by curvature of the track in MINOS near detector.

A more detailed explanation of the muon energy reconstruction in the MINERvA and the MI-

NOS near detector and their corresponding uncertainties is given in section 4.8 of this thesis.

Figure 5.13 shows that most of the uncertainty on the weight function comes from the muon energy reconstruction. The uncertainty rises at the tail of the focusing peak of the neutrino flux with a maximum uncertainty of around 9%. This systematic uncertainty is due to the uncertainty on measurements of muon energy as it passes through the MINERvA and the MINOS detector. Since the fit is done in $\pm 1\sigma$ shift systematic uncertainty, it meant that changing the distribution by 1 σ would translate into a change in the fit function by as much as 9%. In this energy region, the data/mc discrepancy in low-nu distribution is as much as 20 % as seen in figure 5.12. The possibility of muon energy reconstruction mimicking the wiggle when shifted by 2 σ motivated us to introduce it as one of the fit parameters.

Another motivation to reconsider the MINOS muon energy scale came from the discovery of the wrongly implemented correction scale in MINERvA 's reconstruction tool algorithm [108]. Historically, the MINOS had done simulation with a 0.9% less massive detector due to limitations of GEANT3 to simulate the variable thickness of the detector. In order to account for this, additional studies showed that the muon momentum should be shifted by 0.8% in the data. However, the MINERvA 's reconstruction had a wrong implementation of this correction in the MC (instead of the data) resulting in a 0.8% correction of muon momentum in the MC in wrong direction. Subsequent studies led to the conclusion that
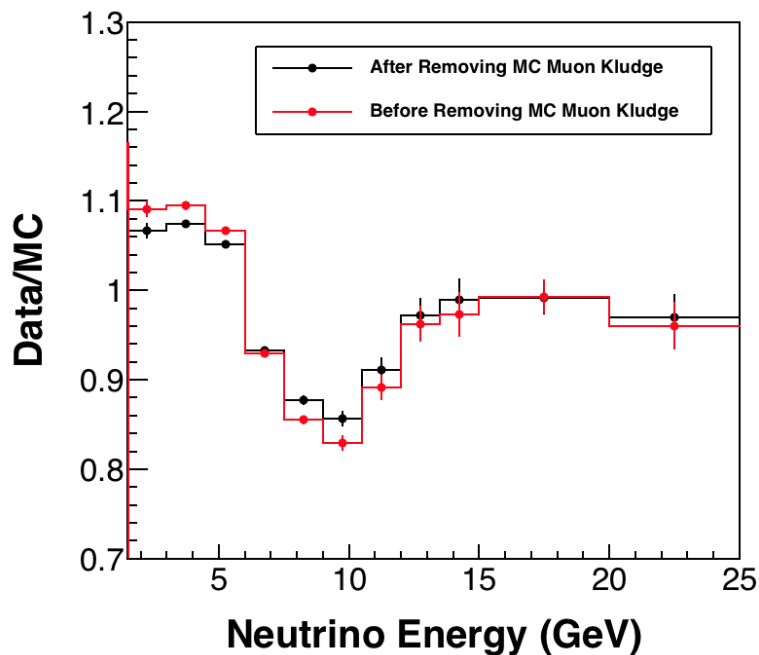
Figure 5.16: The discrepancy between the data and mc before and after removing the muon momentum correction (kludge) that was wrongly implemented in the MINERvA reconstruction algorithm.

this scale was already applied in the MINOS framework and the correct procedure would be

to remove this correction to the MC in the MINERvA framework altogether. [121]. Figure

5.16 shows the effect of this correction on the data/MC discrepancy.

Error Source	Error
MINOS range	2% of P_μ (changed to 0.984 after fit)
MINOS Curvature (pmu<1 GeV)	2.5% of P_μ
MINOs curvature (pmu>1 GeV)	0.6% of P_μ
MINERvA	53.94 MeV

Table 5.7: Table of muon Energy systematic uncertainties used by the MINERvA experiment.

5.9 Muon Energy Scale as a Fitting Parameter

As explained in section 4.8 of the thesis, the MINERvA relies on the MINOS to reconstruct the energy of the muons that are produced by neutrino interactions in the detector. So, the reconstructed muon energy has uncertainties coming from the both detectors. The systematic uncertainties are summarized in table 5.7. MC templates were generated based on these $\pm 1\sigma$ templates. However, unlike the focusing parameters, muon energy scales are detector parameters and hence do not affect the incoming neutrino flux. To implement them as fit parameters, the ratio of shifted low-nu spectrum (when each of these parameters are shifted by $\pm 1\sigma$ from their nominal position) to the nominal low-nu spectrum (when all parameters is in their nominal positions) are used as the fit templates.

The 1 σ shifts for each of these parameters are given in table 5.7. So a new fit with focusing+muon energy scale parameters was created such that the focusing parameters templates would re-weight the MC and the muon energy scales would modify the data as prescribed in [121]. So, the fit function was modified as:
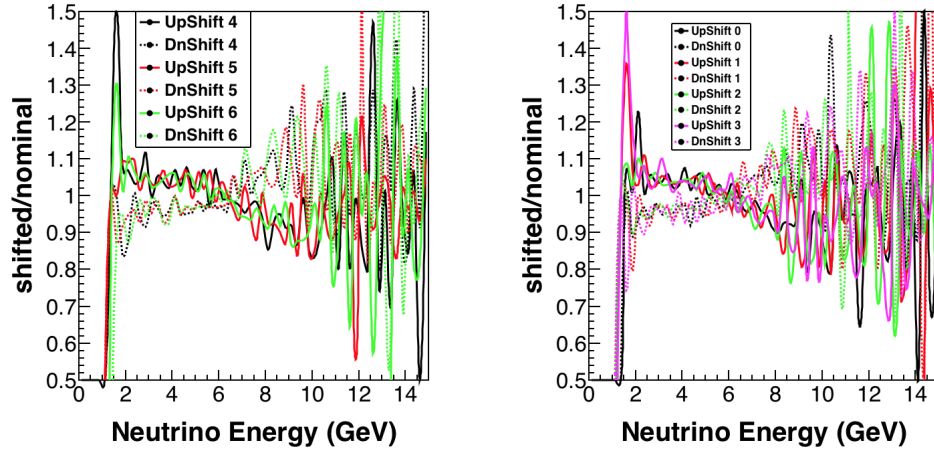
Figure 5.17: 1 σ fit templates for muon energy range for all daisy bins of MINERvA detector

$$\chi_j^2 = \sum_i \frac{(D'_{ij} - M'_{ij})^2}{(\sigma_{D'}^2 + \sigma_{M'}^2)}$$

where:

$$M'_{ij} = M_{ij} \times \prod_{k_{F.P}} R(\alpha_k)$$

$$D'_{ij} = D_{ij} \times \prod_{k_{M.S}} R(\alpha_k)$$

Here M_{ij} and D_{ij} are simulated and data low nu events in daisy bin i and neutrino energy bin j. k_{FP} and $k_{M.S}$ represents the focusing and muon energy scale fit parameters.

Table 5.8 shows that the fit is not very sensitive to the curvature related systematic

Combination	Penalty	χ^2	NDF	χ^2/NDF
All bins and 3 muons parms	12	95	50	1.9
No low bins 3 muon parms	11	84	43	1.95
All bins 4 muon parms	12	95	49	1.93
All bins 1 muon parms	6	136	52	2.61
No low bins 1 muon parms	9.32	90	45	2

Table 5.8: Tables for various combinations of the fit. All bins means 1.5 to 15 GeV and No low bins means excluding the first bin (1.5-3 GeV). 3 muon parameters are Muon energy reconstruction by range, curvature and MINERvA (curvature systematic uncertainty for 2 momentum ranges are merged together to form 1 single parameter). 1 muon parameter means only the muon energy reconstruction by range was included in the fit along with other focusing parameters.

uncertainties. Improvement in the χ^2/NDF after including all muon energy reconstruction related uncertainties is not significant. The penalty term in the first column is the number added by the fit to the χ^2 term during minimization so that the parameters do not go very away from their prior values. The penalty term is the sum of number of shifts in σ of each fit parameters.

The fit function when including the penalty term is given by:

$$\chi^2_j = \sum_i \frac{(D'_{ij} - M'_{ij})^2}{(\sigma^2_{D'} + \sigma^2_{M'})} + \alpha^2_k \tag{5.24}$$

where the α_k is the prior (or penalty) term for the fit parameter k. Hence, we can see that by adding the prior term, the χ^2 cannot be minimized if the fit prefers really large pull on one particular parameter and no pull on other parameters. Although the priors help to constrain

Parameters	Best Fit ± Stat Error ± Sys. Errors (Priors)	Best Fit ± Stat Errors ± Sys Errors (No Priors)	1 σ Shift
Beam Position (X)	-0.26 ± 0.22 ± 0.12	-0.34 ±0.26 ± 0.12	1 mm
Beam Position (Y)	0.70 ± 0.22 ± 0.17	0.77 ± 0.26 ± 0.25	1 mm
Target Position (X)	-0.8 ± 0.28 ±0.14	-0.84 ±0.28 ± 0.14	1 mm
Target Position (Y)	1.71 ± 0.56±0.79	2.27 ±0.72 ±1.17	1 mm
Target Position (Z)	0.36 ± 0.61 ±0.13	0.20 ±0.78 ±0.11	3 mm
Horn 1 Position (X)	-0.14 ± 0.32 ±0.10	-0.29 ± 0.44 ±0.47	1 mm
Horn 1 Position (Y)	0.02 ± 0.33 ± 0.25	-0.13 ±0.48 ± 0.47	1 mm
Beam Spot Size	0.59 ±0.31 ±0.12	-0.34 ± 0.26 ± 0.12	0.3 mm
Horn Water Layer	0.63 ± 0.46 ± 0.24	0.43 ± 0.60 ± 0.14	1 mm
Horn Current	-0.98 ± 0.69 ± 0.49	-2.0 ± 1.39 ± 1.4	1 kA
Muon Energy Scale	1.75 ± 0.17 ± 0.33	1.58 ± 0.24 ± 0.43	2% on P_μ

Table 5.9: Best fit values for the fit parameters from the fit with (second column) and without priors (third column). Note that the shifts on focusing parameters are applied to the MC and shift on muon energy scale is applied to the data.

the fit and give the minimum in a physically acceptable parameter phase space, they are based on the certain assumptions. This fit method assumes that the all priors are Gaussian in nature. The penalty term $(p[j]^2)$ ensures that the χ^2 grows in quadratic as the fit does large pull on a given parameter and is 0 when there is no pull. However, since this term is based on our belief of $\pm 1\sigma$ MC templates, removing this term helps to check if the fit has biased preference over one or few particular MC templates. The final fit configuration is done by using only the muon energy range and the focusing parameters as the fit parameters excluding the first low-nu bin. The fit is performed both with and without adding the extra penalty term on the χ^2.

Table 5.9 shows the best fits for the fitting parameters with and without including the
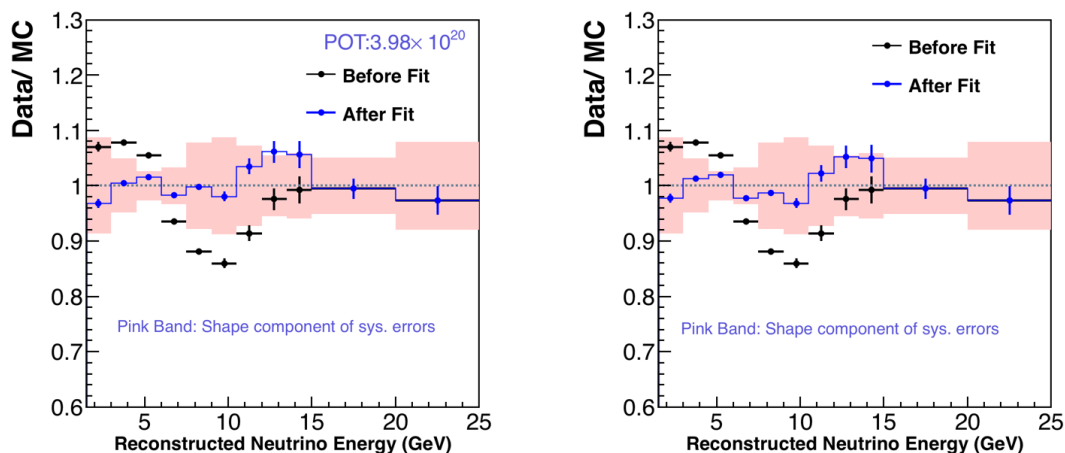
Figure 5.18: Ratio between Data and MC before the fit (black) and after reweighting the data with the muon energy correction predicted by the fit. Left (right) plot is the data reweighted by the correction predicted by the fit with (without) prior. Error band is the shape of the systematic error on the ratio of nominal data to MC.

priors (penalty) in the minimization function. Figure 5.18 shows the ratio between the data (before and after the data is reweighted by the correction on the muon energy scale parameter predicted by the fit) and the MC.

The fit with and without priors, both prefer a large shifts to the muon energy range but small shifts to the focusing parameters, meaning the prior knowledge of fitting parameters doesn't change the final answer. Results without priors prefer a smaller shift in muon energy scale but with large errors on fit parameters. When the priors are removed from the fit, the parameters have larger area of the phase space to explore and hence have large errors on the best fit values.

231
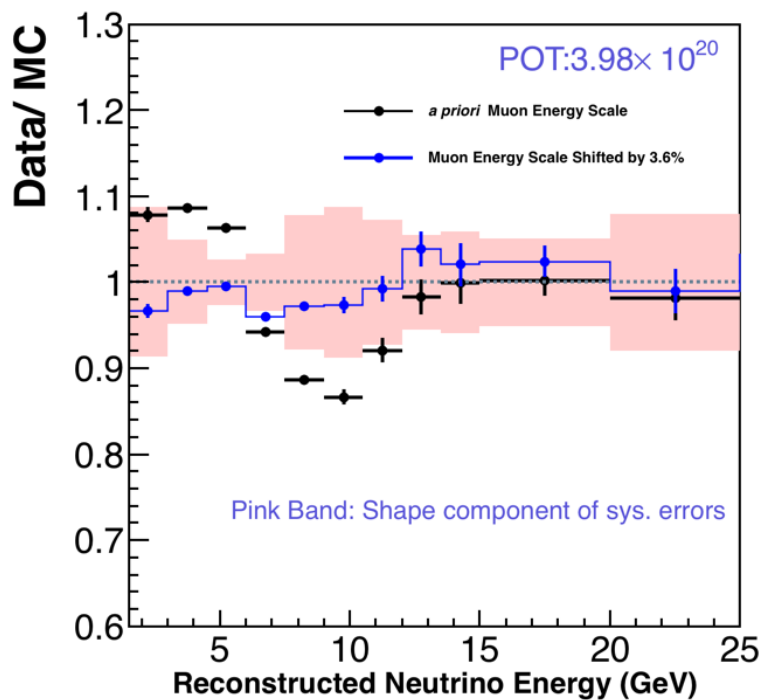
Figure 5.19: Area normalized Data/MC ratio before applying a 1.8 σ correction on the data (black) and after applying 1.8 σ correction on the data (blue).

Based on the results from the fit, a new low-nu sample was generated in which the muon momentum is scaled by +3.6% on the data. As seen in figure 5.19, applying the correction to muon momentum in the data gets rid of the wiggle without having to change the nominal values of the focusing parameters.
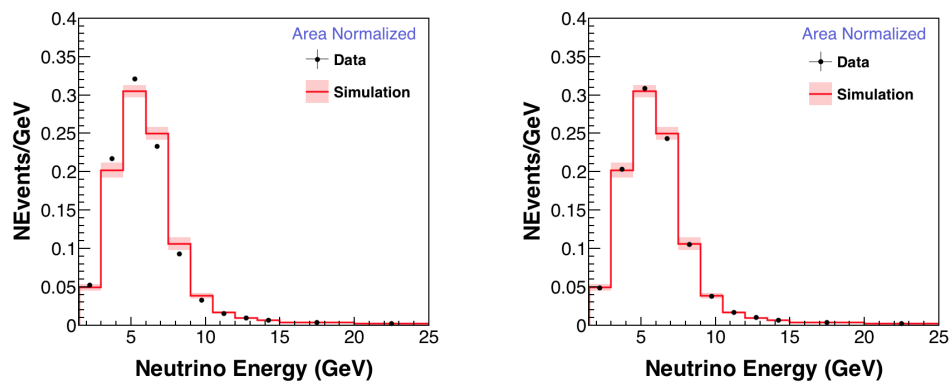
Figure 5.20: low-nu distributions before (left) and after (right) applying the 1.8 σ shift in muon momentum in data.

Systematic Uncertainties	Mean Priors	RMS Priors	Mean No Priors	RMS No Priors
PPFX	1.7	0.23	1.52	0.27
Hadronic Energy Rec.	1.75	0.15	1.59	0.19
GENIE	1.76	0.18	1.58	0.29

Table 5.10: Systematic Uncertainties on muon energy scale parameter

5.10 Systematic Uncertainties on Best Fit Parameters

As seen in figure 5.9, the best fit values for the muon energy scale has both statistical and systematic errors. The systematic errors are due to the fact that the MC sample on which the fitting is being done has systematic uncertainties. In each systematic universes, a fit gives a set of best fit values and hence we get the final best fit values with the systematic uncertainties.

Table 5.10 shows that the flux (PPFX) introduces the largest systematic uncertainty on the muon energy scale fit parameter followed by the hadronic energy reconstruction. The
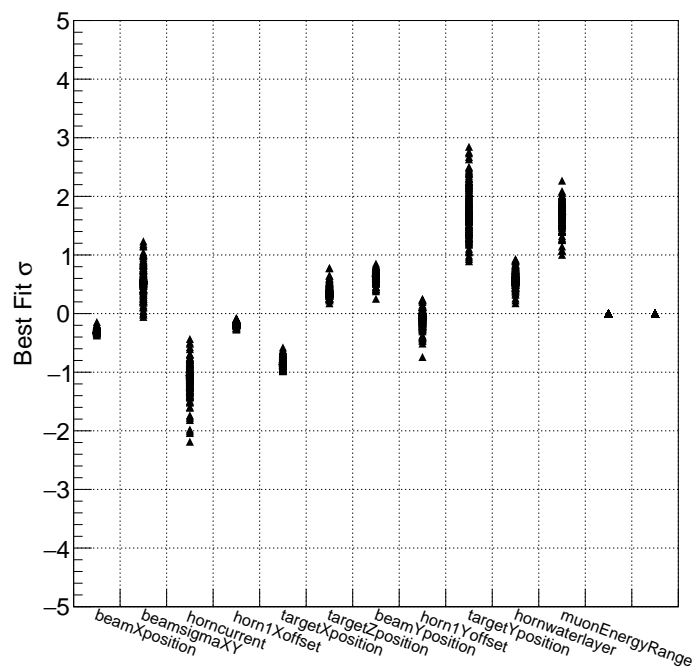
Figure 5.21: Distribution of the best fit shifts in sigmas for the fitting parameters with fit done in the systematic universes of the MC sample with priors.

GENIE Parm	RMS No Priors	RMS Priors
MaCCQE	0.21214	0.136825
NormCCQE	0.11176	0.06953
2p2h-Model	0.070297	0.0440497
MaRES	0.068105	0.044595
NormCCRES	0.062475	0.035785

Table 5.11: Leading GENIE systematic uncertainties on Muon Energy Scale parameter in σ.
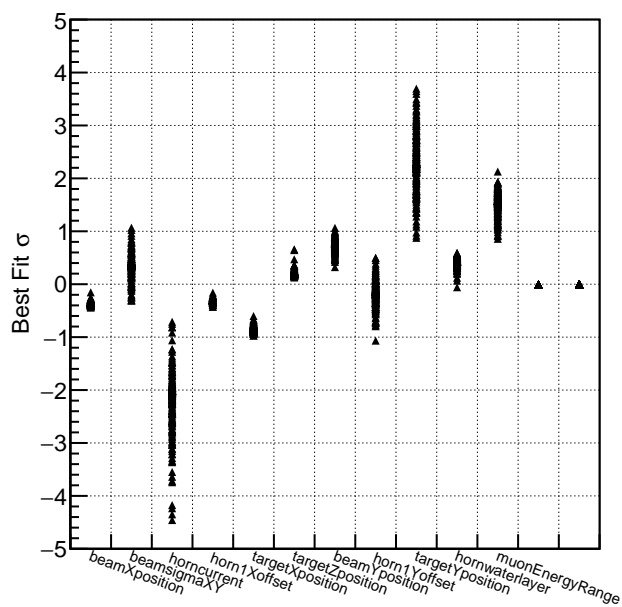
Figure 5.22: Distribution of the best fit shifts in sigmas for the fitting parameters with fit done in systematic universes of the MC sample without priors. The RMS of the best fit shifts for each parameters gives the systematic uncertainty on the best fit values. Compared to the fit with priors, the fit without priors have wider distributions of the best fit values, especially for the TargetY position and the HornCurrent parameters. This wider distribution gives larger errors to best fit values of the fit parameters which is listed in table 5.9.

hadronic energy reconstruction uncertainty is the uncertainty on energy deposited by the hadrons in the MINERvA detector [52]. and the uncertainties are different depending on the type of particles.

Breaking down the contribution from GENIE model systematic uncertainties, largest uncertainty is coming from MACCQE (Table 5.11). MaCCQE is the uncertainty on the axial mass for CCQE. Compared to the parameter uncertainty on the model itself (third column of table 5.11), the uncertainties on fit due to these parameters are not significant. The most significant sources of the uncertainty on the best fit parameters are flux and statistics.

5.11   Correlation Matrices

Figures 5.23 and 5.24 shows that the overall correlation among the fit parameters are similar for fit with and without priors.

Correlations between the muon energy scale and the focusing parameters are small but not negligible. The MINERvA collaboration developed an elaborate method to take into account these correlations when shifting the muon energy scale. MINERvA shifts the flux, as predicted by the fit, in the systematic universes of muon energy scale to account for these
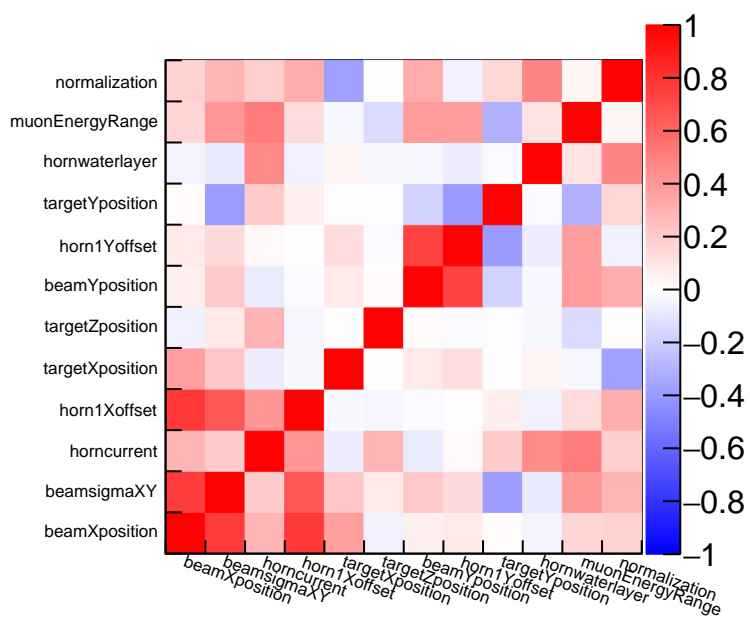
Figure 5.23: Correlation matrix for the fit parameters predicted by the fit without priors
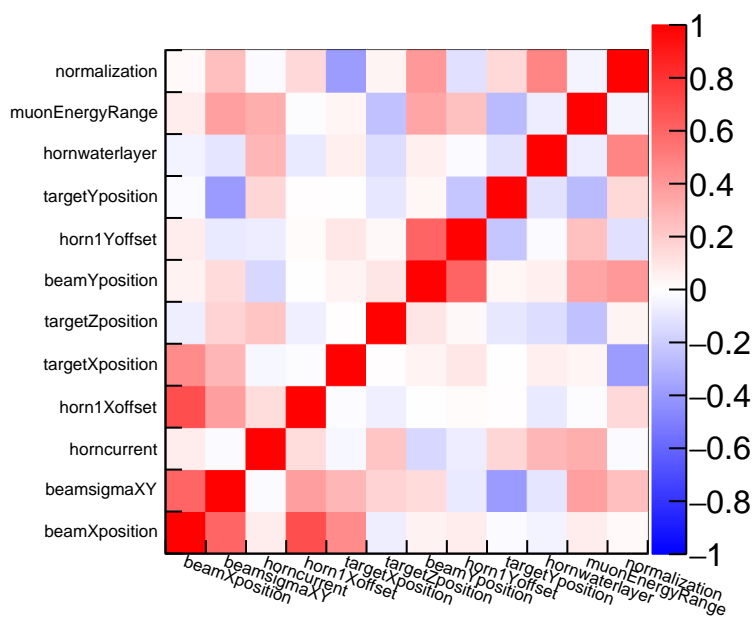
Figure 5.24: Correlation matrix for the fit parameters predicted by the fit with priors

correlations.

5.12   Summary of Low-nu Flux fits

The low-nu fit study can be summarized as follows:

- There is a discrepancy between the medium energy data and simulations.

- Since the discrepancy is also seen in the low-nu samples, cross-section mismodeling as a possible issue is ruled out leaving only flux parameters and reconstruction scales.

- Fitting based on the hypothesis that the discrepancy is coming from the mismodeling of the focusing parameters predicts a nonphysical pull on the longitudinal position of the target or horn current (taking correlation among these parameters into account).

- Fitting based on the hypothesis that the discrepancy is coming from either the mismodeling of the focusing parameters or the muon energy scale in the MINOS predicts almost no large pull on focusing parameters while preferring a large pull on muon energy scale with very small uncertainties.

- Fits with and without assuming the priors of the fit parameters prefers a pull on muon energy scale.

- A shift of 3.6% on muon momentum (or 1.8 σ from the nominal value) seems to resolve the data/mc discrepancy.

- Fit parameters have large errors mainly from PPFX (flux) and hadronic energy scale.

- Total uncertainty contribution from GENIE model is very small. GENIE models that have leading contribution are the models with large uncertainty on their parameters (For example MaCCQE has -15% to 20 % uncertainty on the axial mass [25].)

- MINERvA came up with a strategy to take into account the correlation between focusing parameters and muon energy scale as predicted by the fit when the scale is shifted.

This work explores the two possible sources which would mimic the discrepancy between the data and the MC. Assuming all the discrepancy is coming from the focusing parameters only, the fit suggests a large pull on the target longitudinal position and the horn current. Assuming the discrepancy might be coming from mismodeling of focusing parameters or muon reconstruction energy scale, the fit suggests that the muon energy reconstruction by range as the possible source of discrepancy. After several internal discussions within the MINERvA collaboration, the collaboration decided to adopt the results from the fit done using the priors. Currently, the MINERvA experiment shifts the muon energy scale on (reconstruction by range) by 1.8 σ (energy scale = 1.036) from its nominal value with a total
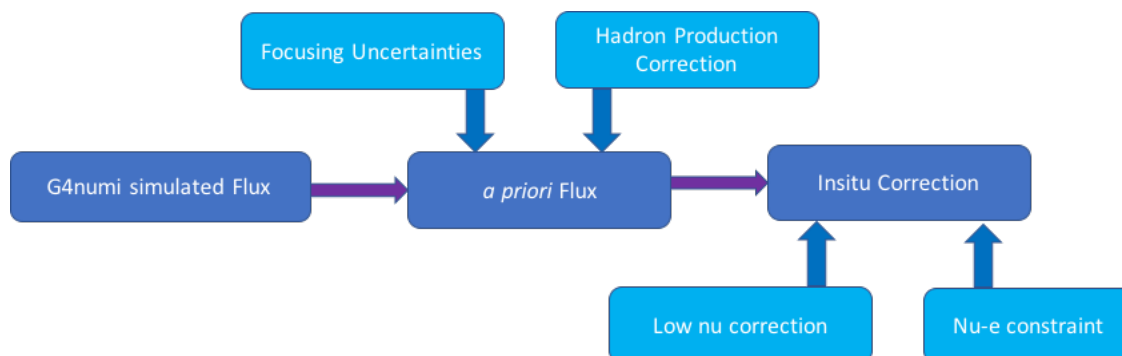
Figure 5.25: Schematic Diagram showing the Flux strategy of MINERvA experiment.

uncertainty of 0.37 σ on the shift itself. Since muon energy scale is correlated to focusing parameters, the energy scale systematic has to corrected for this correlation effect to fully account the prediction by the fit.

5.13   MINERvA Flux Strategy and Lessons for DUNE - A Summary

Over the years MINERvA has developed and adopted various methods to constrain the neutrino flux. To utilize these methods, MINERvA experiment has come up with a strategy to constrain the flux uncertainties as much as possible. This section will briefly go through this strategy and new methods under development.

The MINERvA flux is simulated using a simulated NuMI beamline based on GEANT4 (g4numi).The g4numi simulated flux is then assigned focusing uncertainties. Then the flux is corrected for the hadron production using the PPFX package. This flux which is assigned
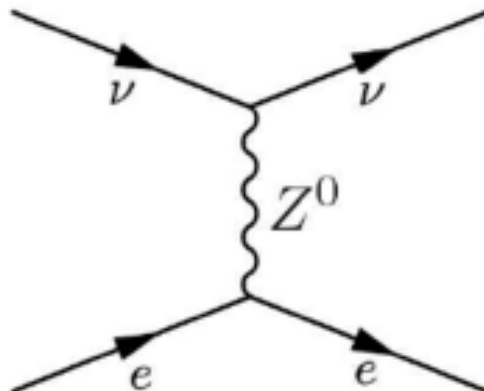
Figure 5.26: Feynman diagram showing the $\nu + e \rightarrow \nu + e$ reaction.

focusing uncertainties and corrected for the hadron production (along with uncertainties) is called *a priori* flux. Then the flux is corrected using the low-nu method and the $\nu - e$ constraint. The $\nu - e$ constraint [154] method corrects for the flux normalization whereas the low-nu method corrects for the flux shape. The second ingredient of the *in situ* correction includes constraining the flux using the $\nu - e$ constraint. Figure 5.26 shows the Feynman diagram of a $\nu - e$ interaction. Since this is a neutrino-electron interaction, it is theoretically well-understood unlike the neutrino-nucleus interactions where nuclear effects complicate the final state particles. MINERvA reconstructed 810 neutrino-electron scattering events [154] in the medium energy neutrino mode run. This is a normalization correction to the neutrino flux. For the medium energy neutrino mode, $\nu - e$ scattering events constrained the flux uncertainties from 8% to less than 5% [154].

Like the MINERvA , the DUNE near detector will also see an intense beam of muon neu-trinos. The larger uncertainty and the challenge to reduce overall systematic uncertainties significantly means that the DUNE will have to constrain the flux uncertainties better than the MINERvA or any existing experiments. While having two detectors will help to cancel out most of the hadron production uncertainties as seen in section 3.3 of this thesis, things like assumptions on bin to bin correlations between existing data-sets that are used to cor-rect for the hadron productions, material scaling methods and assignment of uncertainties on interactions not covered by data needs to be improved to make the uncertainties more reliable. The low-nu flux fit method could provide a way to understand the effect of focusing uncertainties on flux related mismodeling and possible correlations between detector and focusing parameters which can make the flux prediction more reliable.

6 CCQELike Cross-Section Measurement in CH Target

6.1 Introduction

The goal of this analysis is to extend the CCQE cross-section measurement of [128] to the higher energy kinematics region with larger available statistics using the MINERvA ME (Medium energy) data-sets. The details of the signal definition is given in chapter 4 of [128]. The 2D cross-sections are measured as a function of muon longitudinal and transverse momentum and as a function of four-momentum transfer squared (Q^2_{QE}) and neutrino energy ($E_{\nu\,QE}$). The QE here means the variables are based on CCQE hypothesis and they are defined in equation 1.27. Comparison of the data and various models will inform about our understanding of neutrino-nucleus interactions and help the theoretical community to further improve these models. MINERvA has developed various tunes (or corrections) that are applied in the GENIE models to make the agreement between the data and models better. These data driven tunes modify physics processes in the GENIE simulation. These modifications to certain physics processes in certain kinematic regions tell us about the possible avenues where the theoretical framework needs to be improved. These tunes are mostly based on the MINERvA low energy (LE) data and using these tunes in the medium

energy will show the strength and the validity of these tunes in different data sets with much higher statistics and larger kinematic phase space. These high statistics CCQELike cross-section data will help future oscillation experiments like DUNE which will see these type of interactions as one of the dominant interactions.

6.2   Data and MC Ntuple format

MINERvA uses the standard ROOT 5.34 framework resource to store events (both data and simulated). Specifically, it uses a TTree class and its derivatives to store information in a user friendly way [45]. The overall structure of the data format is already discussed in [128]. For all of the MINERvA analyses, usually 4 types of ntuples (A tuple is a finite ordered list of elements. n-tuple means a list of n ordered elements.) are used:

- **Data ntuples** are a list of actual events that are reconstructed in the MINERvA detector. The information contain energy deposited, time of interaction and position of interaction in the detector. Using these information, we can guess the identity of the particles and their kinematics.

- **Reconstructed ntuples** contain simulated information similar to that of data ntuples but it will also contain the generator level information (like interactions inside the nucleus, very low energy particles which are not seen by the MINERvA detector etc.).

Events that are simulated, but can be reconstructed using the reconstruction tools are stored here.

- **Truth ntuples** contain all the generator level information. Not all simulated events can be reconstructed. For example, some of our requirements, like requiring muons to make it to the MINOS detector, are not met by all CCQELike events and hence will not end up in Reconstructed ntuples. This category contains the generator level information of all the signal and background processes that may or may not be in the reconstructed ntuples category. To put it another way, the reconstructed ntuples are a subset of truth ntuples.

- **Meta ntuples** This ntuple contains the meta information like the number of protons on target used to reconstruct these events and the total number of entries.

6.3 Data used in the Analysis

The data used for this analysis are taken using the NuMI medium energy beam in the anti-neutrino mode (Reverse Horn Current). The data was taken from 29 June 2016 to 7 June 2018 [51]. This analysis was done using 8 different playlists.

As seen in table 6.1, different number of POTs (Protons on Target) are used from each playlists to get the neutrino events that are used in the analysis. Here, playlist basically

Playlists	Data POT
minervame5A	5.45E19
minervame6A	1.60E20
minervame6B	1.03E20
minervame6C	1.10E20
minervame6D	1.16E20
minervame6E	8.68E19
minervame6F	1.40E20
minervame6G	7.31E19
Total	8.47E20

Table 6.1: Playlists and the total number of Protons on Target (POT) used in the analysis from each of the playlists

corresponds to a specific period of data collection. A data run period is assigned a new playlist when a focusing parameter (for example, horn or target position), detector condition or read-out firmware is changed. For example, one of the differences between minervame5A and minervame6A is that minervame5A ran without helium target whereas minervame6A ran with helium target (change in detector condition). This analysis was done using the data collected from the tracker part of the MINERvA detector. Overall detector performance and the aspects of the configuration relevant to this analysis remained same for this part of the detector throughout all playlists.

6.4 Simulated Sample

This subsection is mostly based on talks given in MINERvA 101, which is a workshop designed to introduce new collaborators to the MINERvA experiment.

We cannot know the kinematics of the incoming neutrino or the nuclear interactions and processes that happens inside the nucleus. From the data, we can only reconstruct the information of the final state particles (particles that exit the nucleus). Hence we need to rely on the simulation to guess the nuclear processes that happened inside the nucleus. From the simulation, both the variables required to construct the reconstructed variables analogous to the ones reconstructed from data ntuples, and the truth variables, are created and stored. To get the MC prediction of the neutrino events, a simulation chain all the way from neutrino production in the beamline to neutrino interaction in the MINERvA detector is carried out. However the simulation tools that are currently used to model the neutrino-nucleon interactions are not accurate enough to predict processes that happen during and following the neutrino interaction in the detector. Based on past results and analyses, MINERvA has built a strategy to correct the neutrino flux (explained in section 5.13 of this thesis) and the neutrino interactions. In the remaining part of the section, I will go through the details on how neutrino events are simulated and how MINERvA uses her data to make the simulation more accurate.

The simulation of neutrino events in the MINERvA consists of the following steps:

- **g4numi**: This GEANT4 based NuMI beamline simulated (g4numi) is used to simulate the neutrino flux. The kinematics and decay information of the neutrino parents are stored in the dk2nu ntuples (see A.2 in the appendix for more info).

- **GENIE** Using neutrino kinematics and type, we use GENIE to simulate the neutrino-nucleus interaction. The MINERvA detector geometry is used in the simulation based on where GENIE simulates neutrino-nucleus interactions in the detector volume. GENIE simulates both the neutrino-nucleus interactions and the subsequent processes inside the nucleus. After simulating various nuclear effects, the produced particles and kinematics of the produced particles are stored. This includes both intermediate particles that are produced in the nucleus as well as final state particles that will eventually exit the nucleus. GENIE uses several nuclear models and interaction models to simulate nuclear effects and neutrino-nucleus interactions.

- **Detector Simulation** The final state particles and their kinematics information come from the GENIE simulation. Then the GEANT4 package uses its own physics model to propagate them through detector materials. During particle propagation, GEANT4 uses its physics models to simulate events like minimum energy deposition, bremsstrahlung, pair production, break up of nucleons or mesons etc. Outputs from

the GEANT4, like particles produced during propagation and related kinematics (in terms of energy deposits) are saved for future use. Some of these particles, like muons, exit the MINERvA detector and enter the MINOS detector. These exited particles are further simulated in the MINOS software framework. In MINOS as well, the muons are propagated through MINOS detector materials and the output final particles and kinematics(in terms of energy deposits) are saved.

The data events from the detector are stored in the forms of electronic readouts (*digits*). Since we want the simulated events to be as close to the data as possible, energy deposits from various particles in the simulated detector are digitized to match the electronic readout of the MINERvA and the MINOS detector. We call these simulated events MC (Monte Carlo) events. To make the simulated events look similar to the data, the simulation should also show the effects of data-pile up.

The NuMI beam delivers 25 to 50 trillion protons in each spill. Each spill happens every 1.33 seconds and lasts ten micro-seconds. Just before the spill starts, recording of the activities seen by the MINERvA electronics starts. This recording lasts a few micro-seconds after the spill ends. This duration of data-taking is called the readout gate. During this time, when a PMT (Photo Multiplier Tube) registers a charge activity, it takes some time to count the charge and reset the electronics. During this reset time (also called dead time)

if another neutrino event takes place, there will not be a complete readout of the event. In the simulation, this effect is simulated by using a procedure called data overlay where a data read-out is added on the top of MC events. The process is described in detail in [128]. MINERvA uses the GENIE v2.12.6 [25] and the GEANT4 v9r4p02 [9] as the base simulation tool. [98].

6.4.1 MINERvA Tunes

The base simulation tool used to simulate neutrino-nucleus interaction in the MINERvA detector is GENIE 2.12.6. In GENIE, the neutrino-nucleus interaction is based on several interaction models where the nucleus is described by relativistic Fermi gas model with the nucleon momentum given by Fermi momentum distribution (as described in section 1.7 of this thesis) with the high momentum tail enhanced by Bodek-Ritchie spectral function-like addition[41]. GENIE uses the Llewellyn Smith model to simulate the QE processes which is described in section 1.6.7.

Based on earlier studies and physics motivations, MINERvA has developed a set of corrections on the base model GENIE that would best describe the MINERvA data. These corrections are made on the default GENIE parameters and applied on an event by event

basis in the form of event weights. The sets of these corrections based on previous MINERvA analyses, that best describe the MINERvA data are called MnvTunes (or MINERvA Tunes). In this subsection, we will go through the tunes that make up MnvTunes.

6.4.1.1 Correction on Non Resonant Pion events

This re-weight is based on a combined re-analysis of the ANL (Argonne National Lab) bubble chamber experiment [31], [29] and the BNL (Brookhaven National Lab) bubble chamber experiment (description in [82]) [137] data. Single pion production data-sets between these two experiments differ in normalization by 30 to 40%. The GENIE parameters (also called knobs) that give the systematic uncertainties on non-resonant pion production are based on these data-sets. Because of this huge discrepancy, GENIE by default assigns a 50% uncertainty on the nominal values of these non-resonant parameters [25]. A combined analysis of these two data-sets done by Wilkinson, Rodrigues *et al* [137] got rid of this normalization discrepancy and the overall error is reduced to around 4%. Based on this analysis, it was observed that the non-resonant components of $\nu_\mu + n \to \mu^- + p + \pi^0$ and $\nu_\mu + n \to \mu^- + n + \pi^+$ channels are over-predicted by GENIE. Hence, the non-resonant pion produced GENIE events are suppressed to 40% of the GENIE predicted weight and a $\pm$ 4% uncertainty is applied on this suppression.

6.4.1.2   2p2h and RPA Corrections

Details on the multi-nucleon events and 2p2h processes are given in section 1.8. MINERvA uses the IFIC Valencia model to simulate the 2p2h events [123],[84], [144] in GENIE. Studies done with the MINERvA low energy data showed that the 2p2h events modeled by the IFIC Valencia model better predicted the data than the default empirical model used in GENIE [136]. The same study also showed that while implementing the Valencia model made the MC distribution shape change to better agree to that of data, the 2p2h events predicted by the model had to be enhanced to bring the simulation even closer to the data.

The empirical enhancement of the 2p2h events based only on MINERvA 's measured ν_μ nucleus cross-section not only brought the neutrino event distribution in the FHC closer to data but also the anti-neutrino event distribution closer to the data in the RHC run.

Analysis of low energy MINERvA data as a function of available energy showed that in addition to the enhancement of the 2p2h events based on the recoil fits, a suppression of low Q^2 events due to the RPA effect on top of the GENIE Fermi gas model was required [136] based on the calculation given in [123].
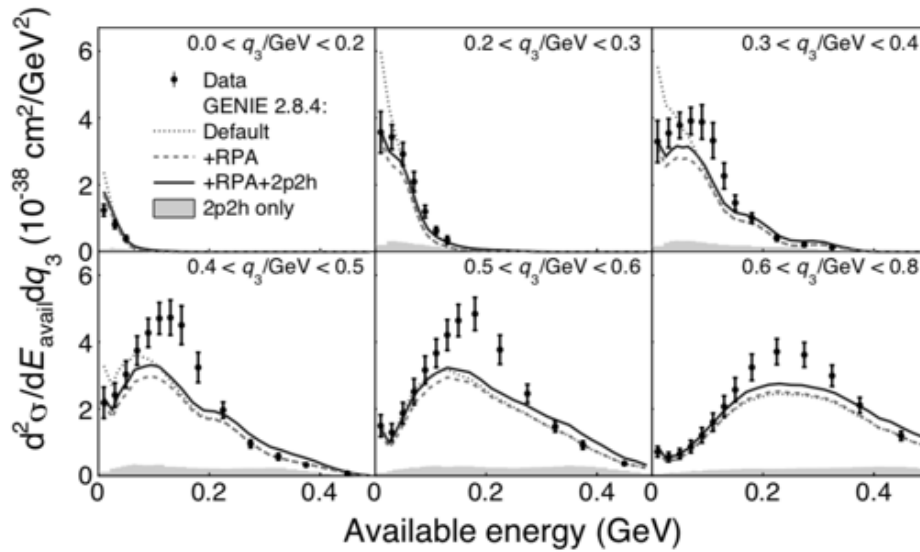
Figure 6.1: Charged current ν_μ nucleus cross-section as a function of available energy. Here, available energy is the sum of proton and charged pion kinetic energy and total energy of the neutral pions, electrons and photons. This doesn't include the contributions from the neutrons which are hard to measure experimentally in the MINERvA detector. q_3 is the 3-momentum-transfer from the leptonic to the hadronic vertex in the charged current interaction. The upper 3 q_3 bins show an excess of GENIE predictions in the low available energy regions. Adding the Random Phase Approximation effect (RPA) brings down this over-prediction in this region and makes the MC prediction closer to the data. The 2p2h contributions modeled by IFIC Valencia is shown by the solid color. Although the RPA+2p2h corrections brings the MC closer to the data, there are still discrepancies in all q_3 bins due to under-prediction of the 2p2h events by the Valencia model. Figure is taken from [136].
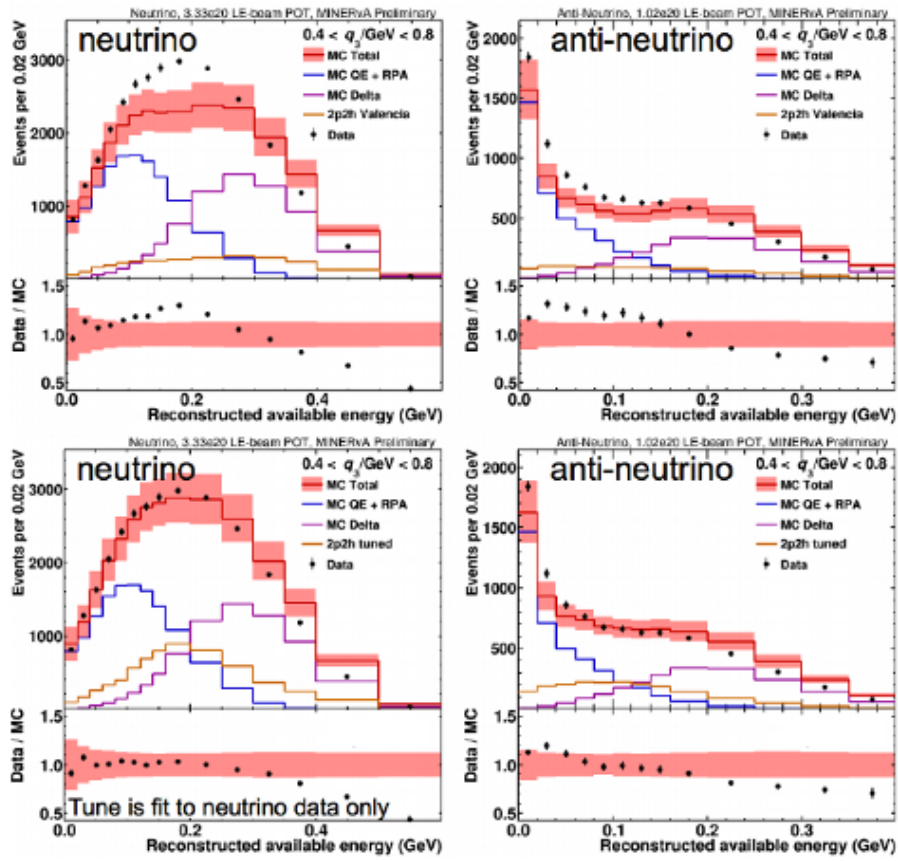
Figure 6.2: The event distribution before the tuning of 2p2h (top) and after the tuning of 2p2h (bottom) events for the neutrinos in forward horn current (left) and the anti-neutrinos in reverse horn current (right). Figure is taken from [71].

6.4.1.3 Suppression of Non Resonant Pion Production at Low Q^2

The existing pion production models that are used in the neutrino physics community are unable to explain their data completely. There are tensions between results published by the T2K, the MiniBoone and the MINERvA experiments which are mostly coming from the charged and the neutral pion production channels [148]. Stowell *et. al.* used NUISANCE [149], a software framework which allows to compare and tune various neutrino interaction generators (like GENIE) against the world data, to tune MINERvA 's LE data on 4 different pion production channels (single charged pion production with neutrino and anti-neutrinos as probes ($\nu_\mu CC1\pi^\pm$ and $\bar{\nu}_\mu CC1\pi^\pm$), single neutral pion production with neutrino and anti-neutrino as probes ($\nu_\mu CC1\pi^0$, $\bar{\nu}_\mu CC1\pi^0$)) by doing the fit between the data and the GENIE models. The fit between the MINERvA pion production data and the GENIE models with priors on fit parameters coming from the ANL/BNL bubble chamber data predicted new fit parameter values that improved the agreement between the models and the data. However, some tension between the data and the new fitted model still exists, especially in the low Q^2 region. Similar discrepancy between data and MC at the low Q^2 was also reported by the MINOS [8] and the MiniBooNE [127] experiments. Motivated by the MINOS strategy [8],an *ad hoc* Q^2 suppression function is created such that at small Q^2, the correction weight is less than 1 and approaches 1 at larger Q^2. A fit was performed for all 4 data sets individually using various GENIE pion production parameters as free parameters. Figure 6.3 shows the
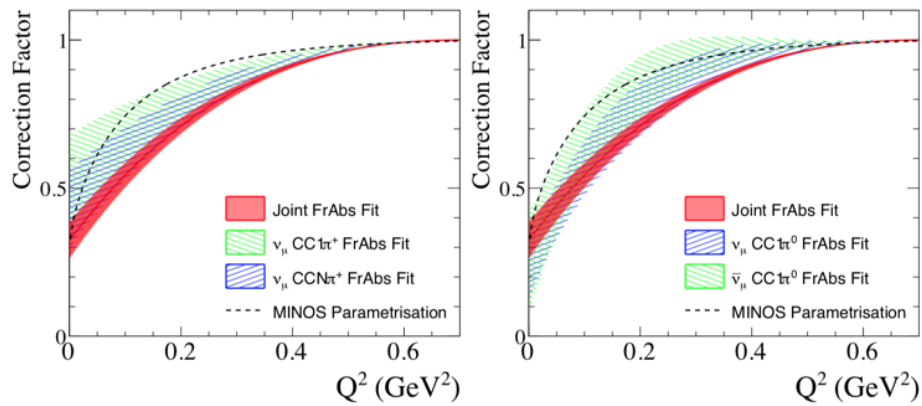
Figure 6.3: The extracted low Q^2 function constructed by tuning GENIE FrAbs (pion absorption) parameter and low Q^2 tuned to charged pion data-sets (left) and neutral pion data-sets(right). MINOS parameterization is shown with a dotted black line for reference. The Q^2 suppression function differs with different channels from which the function is constructed suggesting that the origin of discrepancy between data and MC is yet to be found. On the left and right, the joint fit (red shaded band) is the uncertainty extracted from the joint fit of all 4 available data-sets. Figure taken from [149]

.

suppression weight as a function of Q^2 which is constructed by fitting the GENIE pion absorption parameter (FrAbs) against 4 different MINERvA data-sets. Figure 6.4 shows the model prediction with and without using the Q^2 suppression fit parameter for two different GENIE parameters. Overall, there is a better agreement between data and MC after the fit with resulting Q^2 suppression but there is still tension between data and MC.

6.4.1.4   MINERvA Tune v1 and MINERvA Tune v2

The combination of the non-resonant pion reweight, tuned Valencia 2p2h with an RPA correction in default GENIE 2.12.6 is called the MINERvA Tune v1 or the MnvTune v1. This is the default combination of corrections that the MINERvA collaboration has come up with to address some of the tensions between their data and the GENIE predictions. Combination of the MnvTune v1 ingredients and the low Q^2 suppression is called MnvTune v2. As mentioned earlier, this analysis uses MINERvA Tune v1 as the default MC model.

6.5   True CCQE Events

With muon anti-neutrinos as probe, the charged current quasi-elastic (CCQE) anti-neutrino interaction is given by:

$$\bar{\nu}_\mu + p \rightarrow \mu^+ + n$$
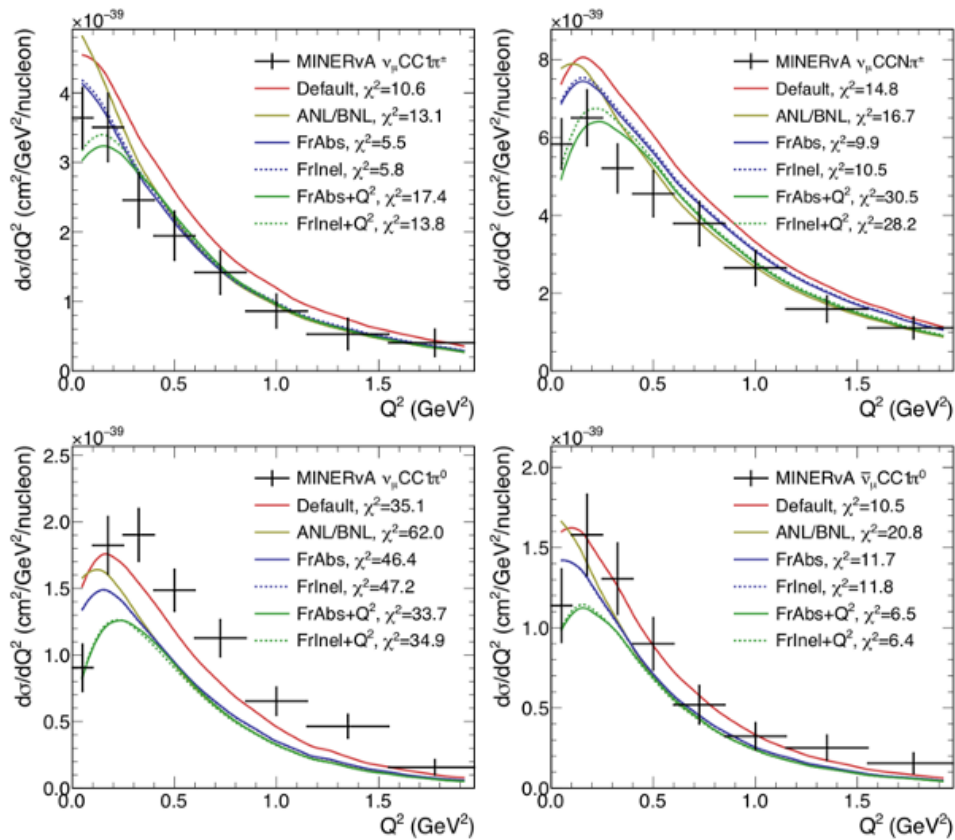
Figure 6.4: Comparison of MINERvA data for 4 different pion production channels with various models. The red is the default GENIE model. The light green model (with legend saying ANL/BNL) is the GENIE model that is tuned with the ANL/BNL bubble chamber data. The FrAbs shows the cross-section prediction using the FrAbs model with the default value and FrAbs+Q^2 when using the value coming from fit with FrAbs as the free parameter. FrInel and FrInel+Q^2 also show similar information. Here, FrAbs is the GENIE parameter for pion absorption in the final state interactions (FSI) whereas FrInel is the GENIE parameter for pion inelastic scattering in the FSI [148].
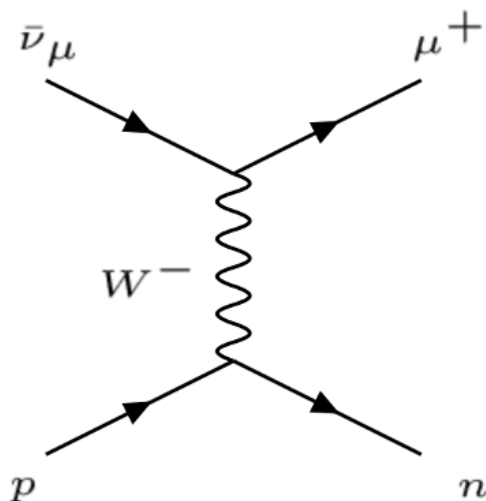
Figure 6.5: A true CCQE process with $\bar{\nu}_\mu$ as a probe.

This analysis measures the CCQE interactions from $\bar{\nu}_\mu$ in the tracker region of the MINERvA

detector. The tracker region of the MINERvA detector is made of scintillator targets (CH).

The theory of CCQE interactions is already explained in detail in section 1.6.7. In a true

CCQE interaction (in the case of $\bar{\nu}_\mu$ as a probe), an incoming neutrino hits the proton to

produce a positively charged muon and a recoil neutron. The overall strategy of the analysis

is to remove the non CCQE events. Events with different final states can be identified easily

and be removed. However, there are processes, which are not CCQE but still give CCQE like

final states. Figure 6.5 shows the Feynman diagram of a true CCQE process. Figure 6.6

shows the two non-CCQE processes that give final states similar to that of CCQE processes.

In the case of the resonant process shown in the left of figure 6.6, an intermediate Δ (Delta)

(a) Resonant pion production   (b) Deep inelastic scattering
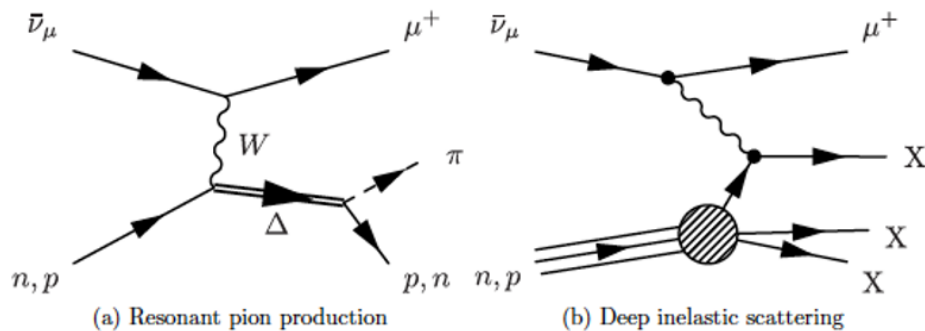
Figure 6.6: A resonant process (left) and a DIS process (right) that give similar final states. Figure taken from [128].

particle is produced inside the nucleus which quickly decays to give a π and nucleons which can mimic the recoil neutron activity. Similarly, a true DIS event (as shown in the right of 6.6) can also mimic a true CCQE event since hadronic activities can look like recoil neutron activity in the MINERvA detector. Figure 6.7 shows a true CCQE event that is seen by the MINERvA detector whereas figure 6.8 shows a true CCRES (Charged Current Resonant) event display. Both events give similar signals in the detector. It is not possible to separate the true CCQE events from non CCQE events just based on the final state particles because:

- Final State Interaction (FSI) results in the non-CCQE events producing the final state particles (FSP) of the true CCQE events.

- FSI results in the CCQE events producing the final state particles of the true non CCQE events.
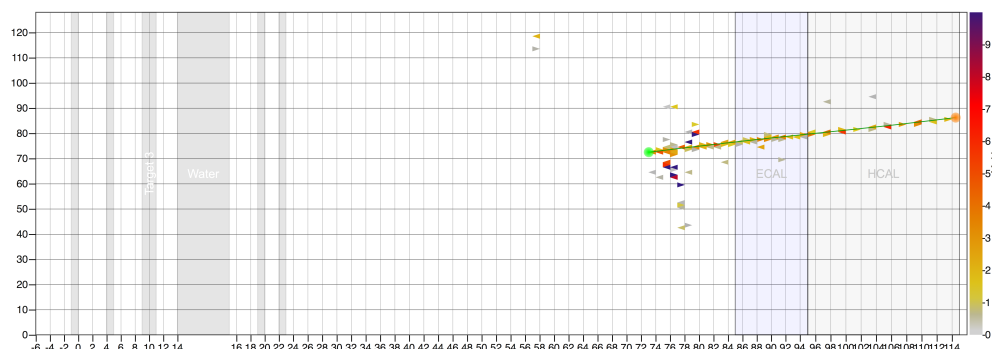
Figure 6.7: Simulated event of a true CCQE event that would be seen by the MINERvA detector. The long track is the μ^+ track and the recoil activity below the interaction vertex is due to the neutrons. The above track is recreated using the MINERvA arachne tool with event of run 123001, subrun 453, gate 333 with software version of v21r1p1. Color scale shows the energy deposited by the particles in the MINERvA detector. True information of this event is known because it is a simulated event.

- Nuclear effects and the FSI result in some of the final state particles, which are not part of true CCQE final state particles, but not seen by the detector, faking a true CCQE event.

Figure 6.9 illustrates how a true CCQE looks like a non-CCQE event and vice versa due to the FSI effect. Due to the nuclear effects and the final state interactions that happen as the outgoing particles exit the nucleus, the final state particles can get modified. These events inside the nucleus cannot be "seen" or inferred by the available reconstruction tools. Therefore, it is not viable to search for true CCQE events. Instead an inclusive signal definition based on final state particles can be constructed which will be dominated by true CCQE events but will also contain the non CCQE events which produce the final state
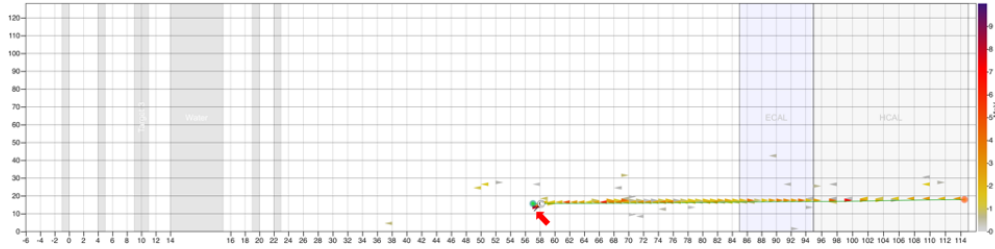
Figure 6.8: Simulated event of a true CCRES event that looks like a CCQE event in the MINERvA detector. The long track is the μ^+ track. This particular event has 2 neutrons, 1 π^- and 1 proton in its final state (although most of the neutrino energy is carried away by the muon). The small black line (pointed by a red arrow) shows the true π^- track which is not energetic enough to make a track that can be reconstructed in the detector. The above track is recreated using the MINERvA arachne tool with event of run 122000, subrun 223 and gate 413 with software version v21r1p1. Color scale shows the energy deposited by the particles in the MINERvA detector. True information of this event is known because it is a simulated event.

particles similar to that of true CCQE events. From here, these events will be referred to as

CCQELike Events. The following section will go through true samples which end up as

CCQELike Events.

6.6   CCQELike Events: Signal Definition

Details on the definition of CCQELike events and the complications arising from this definition are explained in depth in chapter 4 of [128]. This section shall briefly go through the overview of the CCQELike events. CCQELike events (Charged Current Quasi-Elastic Like events) are the events that produce the final state particles similar to that of the true CCQE events. The signal definition of a true CCQELike event is given as:
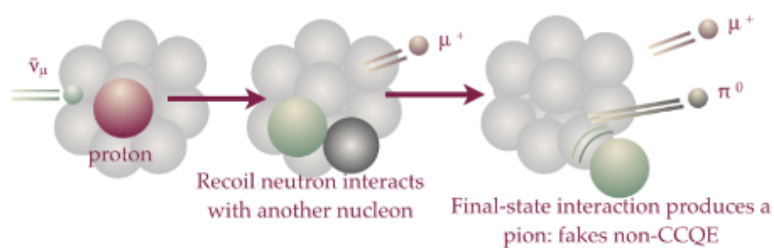
(a) Resonant process with a QE-like final state
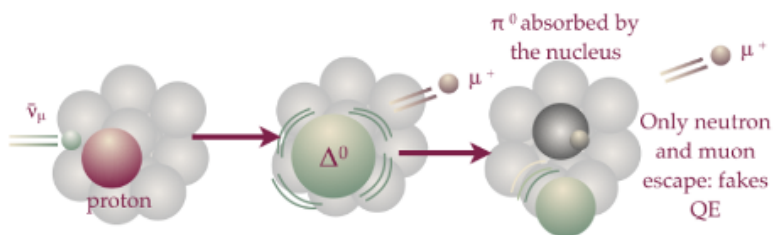
(b) QE process with pion in the final state

Figure 6.9: Illustration of how a non-CCQE process fakes a CCQE process (top) and a CCQE process fakes a non-CCQE process (bottom) due to final state interaction (FSI). Figure is taken from [128].

- Event should have an interaction vertex inside the fiducial volume of the detector (inside the active tracker region).

- There should be a final state μ^+.

- Event can have any number of final state neutrons.

- Event can have any number of final state protons with kinetic energy under 120 MeV.

- Event cannot have any mesons, photons (more than 10 MeV) or heavy weakly decaying baryons.

In the following subsections, the motivation behind each of the requirements will be discussed.

6.6.1   Interaction vertex inside the fiducial volume of the detector

This analysis only selects events inside the active tracker region of the MINERvA detector. In the MINERvA coordinate system, the interaction vertex must be contained within a hexagon of apothem 850 mm, and with a z position between 5980 mm and 8422 mm. This corresponds to modules 27 to 80. These modules are entirely made of scintillator planes with each planes made of 127 strips of doped polystyrene scintillators.

6.6.2   Event should have a final state positively charged muon

Since this analysis is about the CCQELike anti-neutrino events (events which has final states similar to that of CCQE events), the final state lepton should be a positively charged muon.

6.6.3   Event can have any number of final state neutrons

A true CCQE event will have 1 final state neutron. However, multi-nucleon effects can lead neutrinos to interact with a correlated nucleon pair resulting two nucleons in the final state. However, nuclear effects can produce additional nucleons as well. For example, if a pion is produced inside the nucleus and immediately "absorbed", it can produce at least 2 nucleons in addition to the nucleons that are already produced. Hence, any number of neutrons is allowed in the final state particles.

6.6.4   Event can have any number of protons with kinetic energy under 120 MeV

A true CCQE event can only have a muon, a neutron and no protons or hadrons. However, multi-nucleon effect modifies the final state particles and can end up with protons in the final state. As mentioned in section 6.6.3, 1 to 2% of the time multi-nucleon effect produces

a *np* pair. The correlated proton usually is of low energy. A kinetic energy cut of 120 MeV is based on the sensitivity of the detector to reconstruct the proton track. We only want events with only muons as charged particle track in this analysis. Protons with more than 120 MeV kinetic energy can be reconstructed as additional tracks in the MINERvA detector. Studies done with the LE sample showed that we can select CCQELike events with additional proton with as much as 90% efficiency maintaining 80% purity as long as the kinetic energy of the most energetic final state proton is less than 120 MeV [128]. Hence, any number of protons is allowed as long as their KE is less than 120 MeV. The number of protons is unconstrained to address additional nucleons that could be produced from nuclear effects. Figure 6.11 shows that loosening up the 120 MeV cut will not help us to improve the sample in case of 1 track sample. The cumulative efficiency in this plot is calculated as:

$$Cumulative\ Efficiency(x_j) = \frac{\sum_{i=0}^{i=j} x_i}{\sum_{i=0}^{i=N} QELIKE + QELIKENOT} \tag{6.1}$$

Here x are various components like QELike,QELikenot,QELike-QE etc., j is the proton KE at which the efficiency is calculated. N is the total number of KE bins. Here, we only look at samples with proton KE less than 300 MeV.
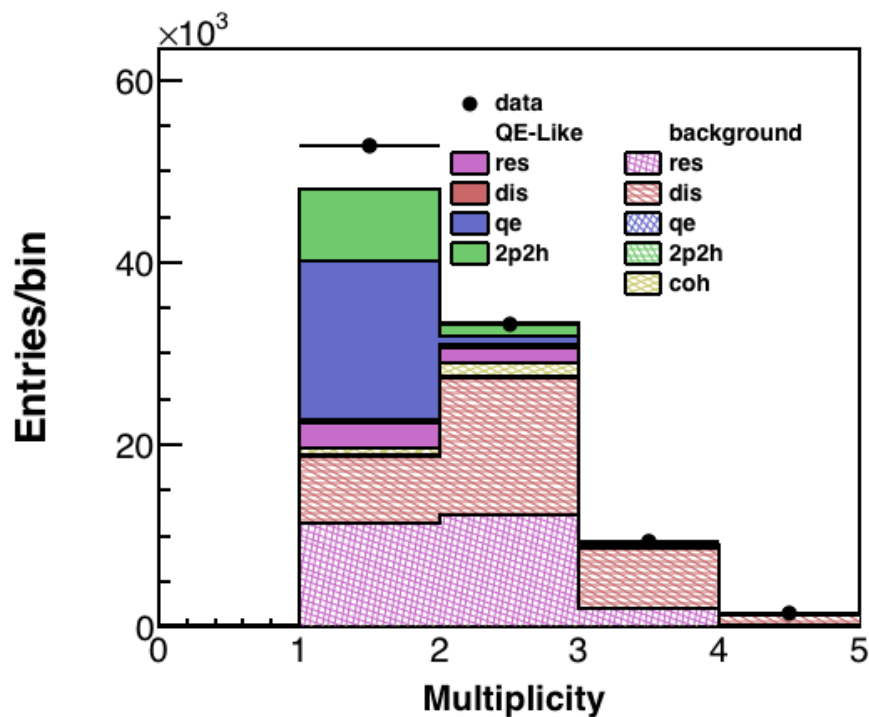
Figure 6.10: Number of outgoing track from the interaction vertex. The second bin has events with 1 outgoing tracks. The third bin has events with 2 outgoing tracks and so on. Events with 1 track only have muon tracks whereas the events with multiple tracks can have proton or pion tracks as additional tracks. Almost 85% of the CCQELike events are 1 track events. 59% of 1 track events are CCQELike. Similarly, only 11% of the multi-track events are CCQELike. The MC is normalized to data in the above plot. Fiducial volume and MINOS match muon cut is applied in the above plot.
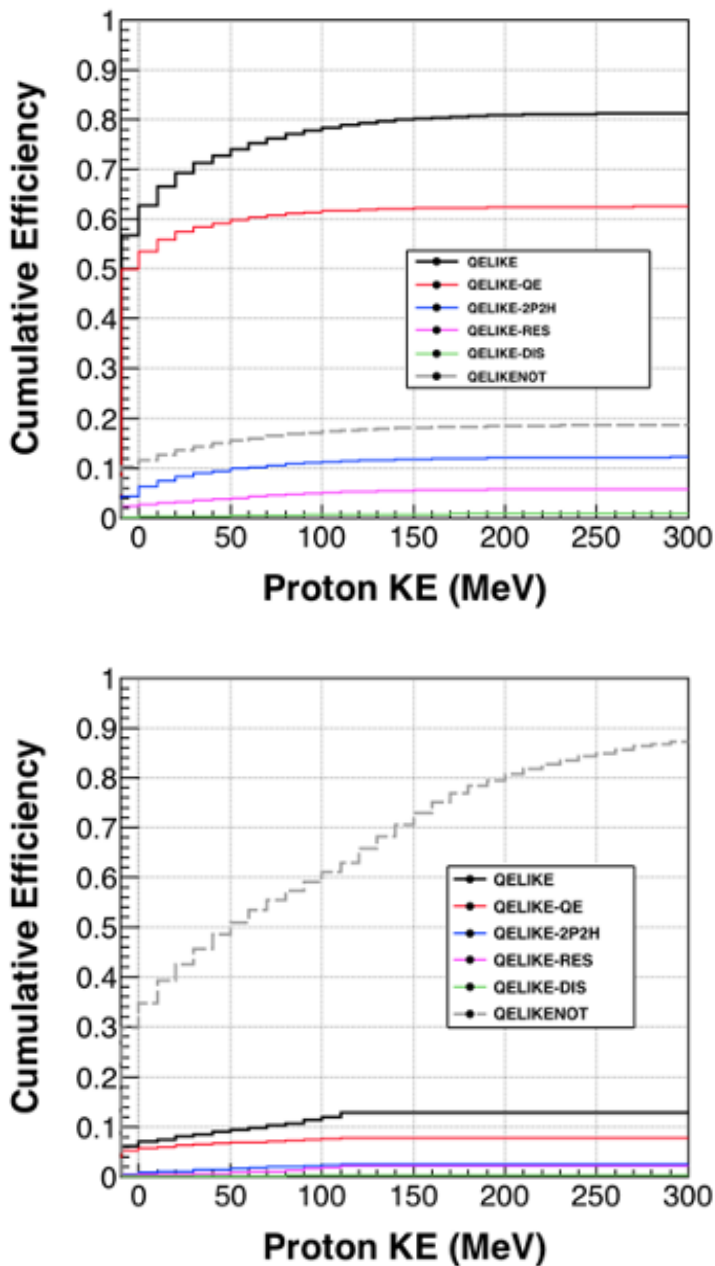
Figure 6.11: Cumulative Efficiency (fraction) at truth level of selecting various sample types as a function of proton KE cut. 1 track samples are shown on the top and multi-track samples are shown on the bottom. To make these plots, the 120 MeV proton KE cut was removed from the true CCQELike definition. According to the plots above, with 120 MeV KE cut, we select more than 80% of the selected sample that is QELike whereas in the multi-track event only around 15% of the selected sample is QELike. It should be noted that the multi-track sample is always dominated by the background (QELikeNot). Loosening up the cut will not change the sample content significantly in the case of 1 track sample.

6.6.5 Events cannot have any mesons, photons (more than 10 MeV) or heavy baryons

A true CCQE event final state doesn't include any mesons or photons (less than 10 MeV photons which are usually de-excitation photons, are allowed) or long lived heavy baryons like strange and charm baryons. Hence, to keep the signal definition consistent with the final states of a true CCQE process, we exclude events with these particles as final states.

6.7 CCQELike Events: Reconstruction

Section 6.6 goes through the requirements of an event to be a CCQELike event. All the requirements mentioned in that section are truth level requirements and to reconstruct and select the CCQELike events, we must rely on reconstructed variables that are available in the data. This section will go through the list of selection cuts that we apply on the reconstructed data and the MC events to select the CCQELike events.

6.7.1 MINOS matched muon

One of the requirements of the CCQELike event is that the final state lepton should be a positively charged muon (μ^+). The muons that come out of the NuMI neutrino interactions

are typically of energy in GeV range. In this range, muons act as minimum ionizing particles (MIP) with a constant energy loss of few $MeV g^{-1} cm^2$ [87] and the behavior is well understood. In the detector, the muon usually makes a clean long track as seen in figure 6.7. However, the track alone is not sufficient to distinguish between a negative and a positive muon. In order to know the polarity of the muon, the detector should be magnetized so that the bending of the track can tell us about the polarity of the muon. The MINOS detector is located just downstream of the MINERvA detector and is magnetized. Hence we use the MINOS detector to know the polarity of the muons. This means we only select the muons which make it to the MINOS detector. An angle cut of $20 \deg$ with respect to the neutrino beam direction is required on the muon track to ensure that the muons will make it to the MINOS detector.

6.7.2   Detector Dead time Cut

After each neutrino interaction is recorded, the detector instruments take some time to reset. If an interaction occurs in the detector region which is connected to the readout instrument that is experiencing dead time, it will not be recorded. If a muon track, for example, is created outside the MINERvA detector due to neutrino interaction in the earth materials that lies between the NuMI beamline and MINERvA detector, enters the detector through

the first module, when some of the upstream instruments are experiencing the dead time, it will look like a CCQELike event (since it will seem as if the track was originated inside the MINERvA detector). To avoid such cases, for each event, two upstream modules from the point of apparent origin of the muon track are checked. If more than two modules are experiencing dead time, such events are rejected.

6.7.3 Fiducial Volume cut

The fiducial volume cut is already discussed in section 6.6. The reason it appears in both physics definition and the signal reconstruction is because this analysis is only concerned about the neutrino events in the tracker region of the MINERvA detector.

6.7.4 Only muon track

The final state particles of the CCQELike interactions are a muon and very low energetic protons and neutrons. Since we limit protons to have kinetic energy less than 120 MeV, they are not usually energetic enough to make reconstructable tracks. Neutrons on other hand deposit energy only in the form of isolated blobs. Besides muons, only pions and protons with enough kinetic energy can make reconstructable tracks in the detector. Hence, we select events with only a muon track and no additional track reconstructed. We look at

the number of tracks coming out of the interaction vertex to select events with muon track. Generally, events with more than one track seem to have protons above 120 MeV or pions in the final state as seen in figure 6.11. As seen in the top plot of figure 6.11, almost all of the CCQELike events with one proton in their final state have protons with less than 120 MeV kinetic energy .

6.7.5   Cuts on Muon Longitudinal Momentum

The reconstruction of the muon becomes more challenging above 15 GeV/c. At high enough energy, the momentum reconstruction of the muons by curvature in the MINOS becomes less accurate. Hence, we limit the longitudinal momentum of the muon to be between 1.5 GeV/c and 15 GeV/c. Low momentum muons have lower momentum resolution and can suffer from high reconstruction systematic uncertainties. Although there is no lower bound selection cut on muon momentum, this analysis only looks at muon between 1.5 GeV/c and 15 GeV/c longitudinal momentum.

6.7.6   Recoil Energy Cut

Recoil energy is the energy deposited by the hadrons (nucleons and mesons) that are produced during the neutrino-nucleus interaction. Besides the muon, we allow any number of

neutrons and low energy protons. These neutrons, low energy protons and the pions which were not identified by our reconstruction algorithms contribute to the recoil energy in the CCQELike events. Since most of the energy of the incoming neutrino is carried away by the muons in the CCQE events, the energy deposited by recoil nucleons is small. Hence, we use the recoil energy as the main variable to distinguish between a signal like and a background like event. In a CCQELike interaction we define the true recoil energy as the sum of energy deposited by the hadronic system that comes out of the neutrino-nucleus interaction. The recoil energy is related to the neutrino energy as:

$$E_\nu = E_\mu + E_{recoil} \tag{6.2}$$

In this analysis, we include all isolated energy clusters that are not part of the muon tracks in our recoil energy definition. Because of nuclear effects like 2p2h processes, there can be recoil activities from additional recoil nucleons. The definition of CCQELike event allows up to 120 MeV KE protons in the final state. These final state protons can produce low energy recoil activity near the vertex region. Hence, a region of 100 mm around the interaction vertex is excluded when summing up the non-muon recoil activity. As seen in figure 6.12, most of the signal components lies in the low recoil energy region. The background is dominated by the resonant component. These are mostly events with low energy pion final states which are
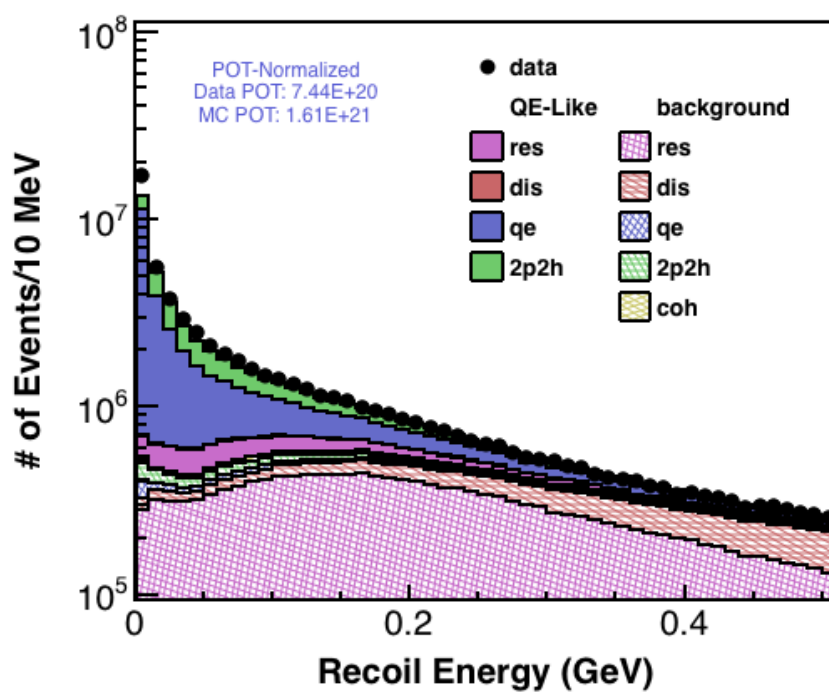
Figure 6.12: Recoil energy distribution. Solid colors are signal components and the checkered colors are background components. Dotted black points are data. Simulation is normalized to the data.

not caught by our reconstruction cuts.

6.8 Construction of the Recoil Energy Cut

Because most signal events live in the low recoil region, the recoil energy is used as the reconstructed variable to distinguish signal and background. However, we want the recoil cut to fulfill at least 3 requirements:

- Does the cut select most of the signal events from the overall sample?

- Is the selected sample pure enough (i.e. small background contamination)?

- Is the cut allowing enough statistics in the region where signal events are less populated?

The first requirement is also called selection efficiency and is given as:

$$Efficiency = \frac{N_{Selected}^{QELike}}{N_{Total}^{QELike}} \tag{6.3}$$

Signal selection efficiency gives us the fraction of signal events that are selected by a given reconstruction cut. The second requirement is also called signal purity or purity of the

selected sample and is given as:

$$Purity = \frac{N_{Selected}^{QELike}}{N_{Selected}^{QELike} + N_{Selected}^{QELikeNot}} \tag{6.4}$$

The purity basically tells us the fraction of signal events in the selected sample. Note that the denominator term

$$N_{Selected}^{QELike} + N_{Selected}^{QELikeNot}$$

amounts to total number of selected events. The third requirement ensures that the recoil cut is not constructed in such a way that it is biased towards the signal rich region i.e. the shape of the recoil cut does not over-constrain the signal poor region in order to maximize the efficiency and purity of the signal rich region. The overall optimization of the recoil cut was done for the LE version of this analysis. Optimization studies done with the medium energy data also preferred similar shape but couldn't identify a more optimal solution. Figure 6.13 shows how the recoil cut separates the signal rich and background rich region in the Q^2 versus recoil energy phase space. The recoil cut (black line in figure 6.13) as a function of Q^2 is given by:

- Recoil Energy = 0.08 GeV if Q^2 <0.175 GeV^2
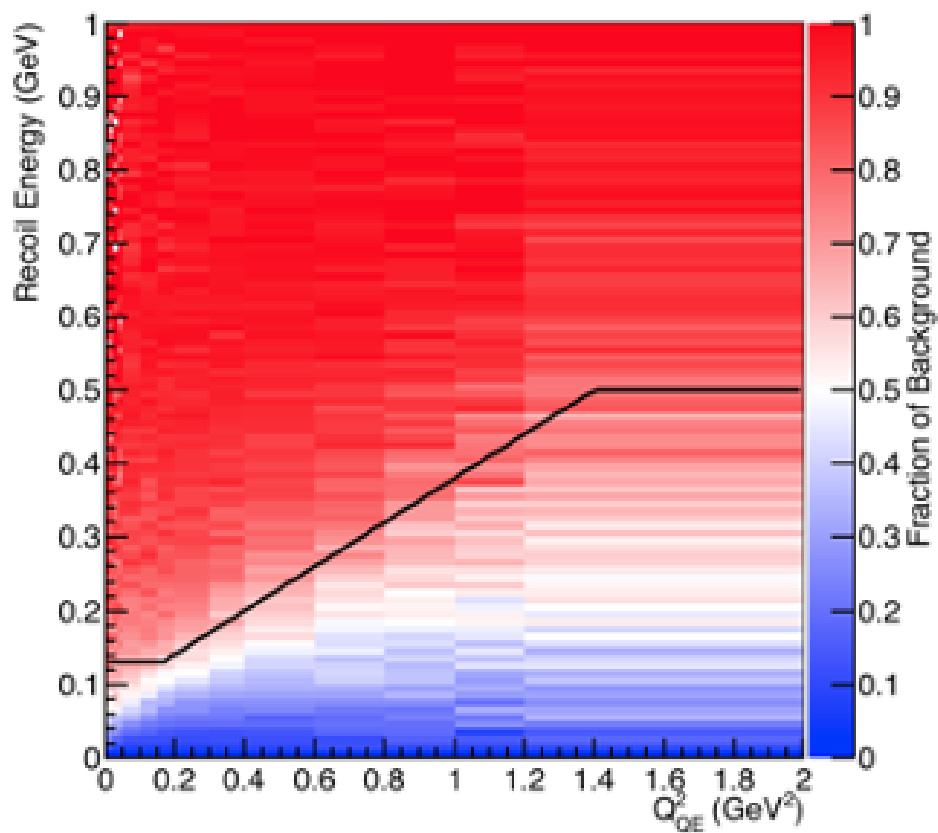
Figure 6.13: Recoil Cut drawn on the top of background fraction. The area under the black line is selected during the analysis.

- Recoil Energy = $0.03 + 0.3\times Q^2$ GeV if $0.175 \geq Q^2 \geq 1.4$ GeV^2

- Recoil Energy = 0.45 if $Q^2 \geq 1.4$ GeV^2.

- The above recoil energy cut is loosened by 50 MeV. The medium energy data has signal events spread out in higher recoil energy regions because the neutrino beam is of higher energy. This additional loosening of recoil energy cut allows to include signal events that are at higher recoil energy.

6.9   Categorization of the simulated sample

We look at the simulated sample to learn about the characteristics of our data. For example, in figures 6.15 and 6.12 we can see that the MC is divided into various categories. These categories are based on GENIE predictions and this section will go through each of these categories. Note that all the categories are charge current processes.

6.9.1   Charge current Quasi-elastic (QE)

In GENIE, the true QE processes are the true quasi-elastic processes. An example of this reaction is:

$$\bar{\nu}_\mu + p \rightarrow \mu^+ + n$$
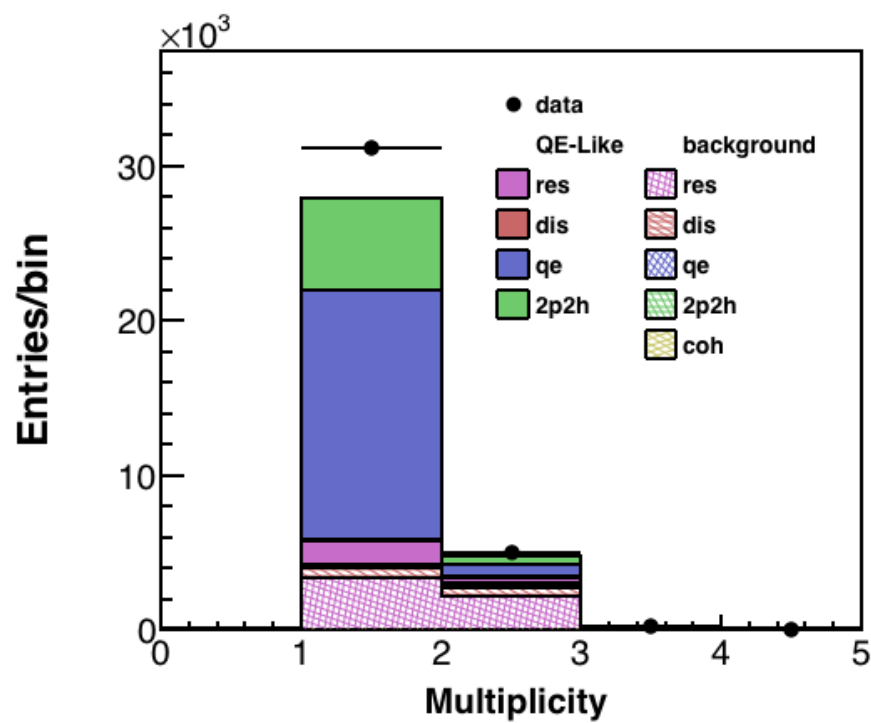
Figure 6.14: Multiplicity or the number of outgoing tracks after applying the Q^2 dependent recoil cut. The first populated bin shows the number of events with 1 muon track only. Similarly the second bin shows the events with 1 muon track and 1 pion or proton track. The third bin shows the events with 1 muon track and 2 pion or proton tracks. Note that this analysis only looks at 1 track events.
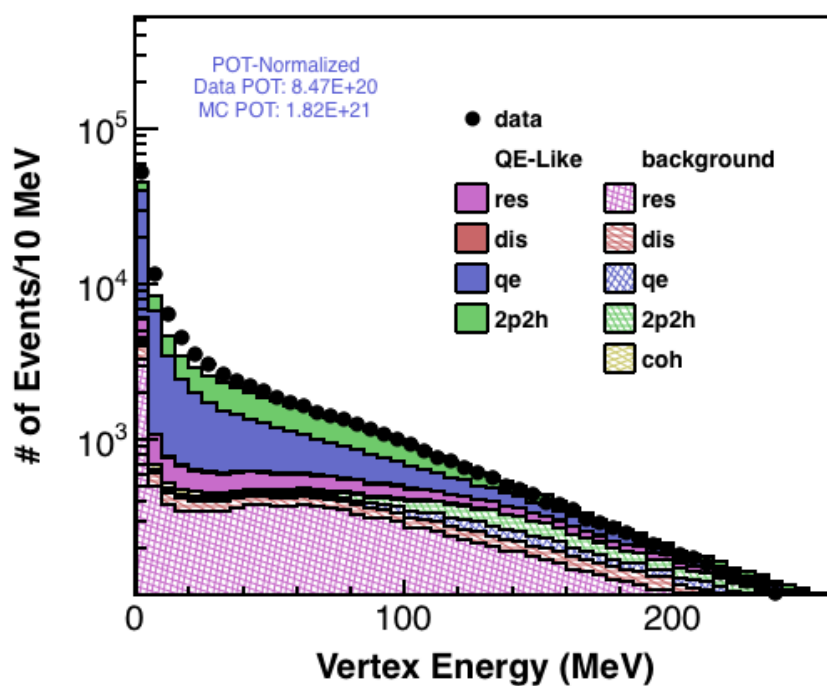
Figure 6.15: Vertex Energy (energy inside the 100 mm vertex after applying all the reconstruction cuts. True QE and 2p2h processes dominate the recoil activity inside the 100 mm radius spherical vertex region.

The CCQE interactions are explained in more detail in 1.3.0.1 of this thesis. The final state of this process could be modified by the nuclear effects. Since the signal definition of this analysis only requires processes to have final state particles that resemble the product of QE processes (i.e. a μ^+ and neutrons), true QE process could be reconstructed as background if its final processes gets modified. For example a true processes with 1 μ^+ and 0 π could end up producing a pion when the recoil nucleon re-interacts.

6.9.2 Charge Current Resonances (RES)

A more detailed explanation of RES processes is given in section 1.3.0.1 of this thesis. Looking at the resonance event example given in that section:

$$\bar{\nu}_\mu + n \rightarrow \mu^+ + \Delta^-$$

. However the Δ particle is short-lived and quickly decays:

$$\Delta^- \rightarrow n + \pi^-$$

If the pion is absorbed in the nucleus, then the final states are a neutron and a muon and hence counts as a CCQELike event. If the pion becomes a final state particle, then it will

count as a background event. Resonance processes are the dominating background processes in this analysis.

6.9.3 Charge Current Deep Inelastic (DIS)

A more detailed explanation of DIS processes is given in 1.3.0.1. DIS processes show large hadronization (ejection of several hadrons from the nucleus). Usually these are the events that leave large recoil activity in the detector. If the DIS produces several neutrons and a muon due to hadronization, they can look like a CCQELike process. The recoil cut gets rid of most of the DIS processes. The selected sample has less than 4% of DIS background processes.

6.9.4 2 particle 2 hole (2p2h)

2p2h processes are multi-nucleon processes which are explained in detail in 1.7.5. In this analysis, based on the selected sample has 21% of 2p2h events out of which almost 19% are signal events. The 2p2h events are tuned and enhanced based on the recoil fits done with the low energy sample as explained in section 6.4.1.2. This analysis uses 2p2h to denote the 2p2h events which are enhanced based on the low recoil fits results.

6.9.5 Charge Current Coherent (Coh)

When a neutrino interacts with a nucleus and produces a pion and a muon without modifying the initial state nucleon, this is categorized as a coherent processes. These processes usually include forward going muon and pion as the final state particles. MINERvA has done cross-section measurements of these processes [100]. These processes can be written as:

$$\bar{\nu}_\mu + A \rightarrow \mu^+ + \pi^- + A$$

Here A denotes the target nucleus which doesn't change after the interactions. Coherent processes are background in this analysis.

6.10 Ingredients for Cross-Section Extraction

The double differential cross-section as a function of variables x and y in a bin (i, j) is given as:

$$\left(\frac{d^2\sigma}{dxdy}\right)_{ij} = \frac{\sum_{\alpha\beta ij} U_{\alpha\beta ij}(N_{data,\alpha\beta} - N_{data,\alpha\beta}^{bkg})}{\epsilon_{ij}\Phi T \Delta x_i \Delta y_j} \tag{6.5}$$

[128].

Here,

- i, j are the true bins

- α, β are the reconstructed bins.

- $(N_{data,\alpha\beta} - N^{bkg}_{data,\alpha\beta})$ is the background subtracted data in the reconstructed bins of α, β.

- Δx_i and Δy_j are the bin-widths of binned variables x, y.

- ϵ_{ij} is the efficiency of the signal selection in the true bins i, j.

- $U_{\alpha\beta ij}$ is the migration matrix element related to true bins i, j and reconstructed bins α, β.

- Φ is the incoming neutrino flux. If the cross-section is as a function of neutrino energy, it is the flux for a given neutrino energy. Otherwise, it is integrated flux.

- T is the total number of scattering targets. In the case of anti-neutrinos, it is the number of nucleons.

The following sections will go through the various process through which each of these ingredients are reconstructed/calculated.
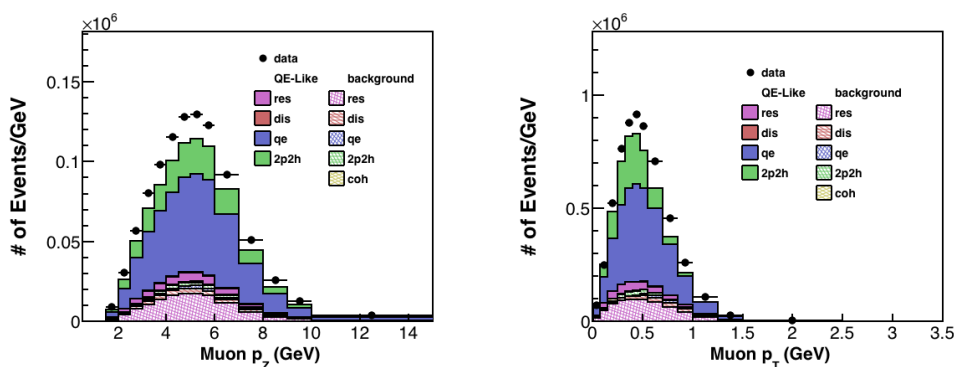
Figure 6.16: CCQELike event distribution as a function of reconstructed muon longitudinal momentum (left) and muon transverse momentum (right) that passed the selection cuts. Solid colors shows the various components of the signal and crossed components shows the background components.

6.11   Reconstructed Event Distribution

Figure 6.16 shows the reconstructed data and simulated events that pass the selection cuts. The selected sample is more than 50% true QE and around 20% true 2p2h events. The background is dominated by the resonant events that constitute 15% of the total selected sample. Figure 6.17 shows the data and simulated events as a function of reconstructed neutrino energy and four momentum transferred (both based on QE hypothesis).

Figures 6.22 and 6.23 shows the raw distribution of data and MC events in different muon kinematic bins. Looking at 6.22, we can see that the true QE component dominates the signal distribution in all bins. In the low transverse momentum bins, the 2p2h has significant contribution and decreases as we go to higher transverse momentum bins. Similarly, the
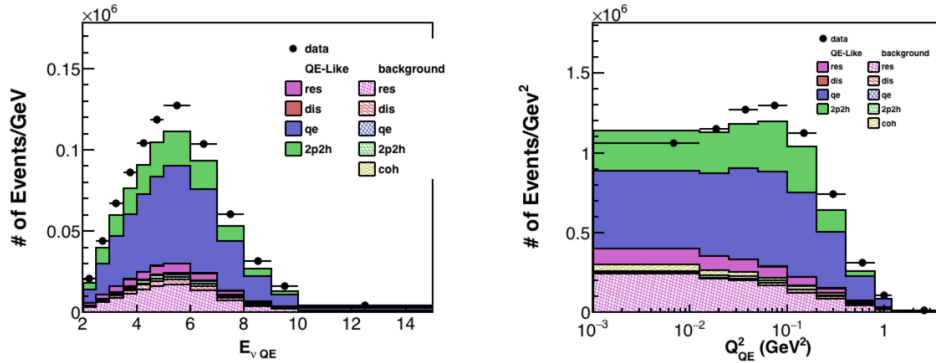
Figure 6.17: CCQELike event distribution as a function of neutrino energy (left) and four momentum transferred squared (right). Both variables are based on CCQE hypothesis.

events with high transverse momentum have significant background processes. The transverse momentum (p_T) distribution is mapped to the four momentum squared distribution Q^2_{QE}. Since the recoil cut is loosened at high Q^2_{QE}, more background processes pass the recoil cuts. Most of the background processes are dominated by the resonance processes.

6.12 Signal Selection Efficiency

The definition of a signal event is based on the truth level information. For an event to be CCQELike, we require the event to be a charged current anti-neutrino event with any number of neutrons and a muon in the final state. However, we rely on reconstruction algorithms to select these events. These algorithms which are based on energy deposition or charge information of the outgoing particles are not perfect. A muon track formed during
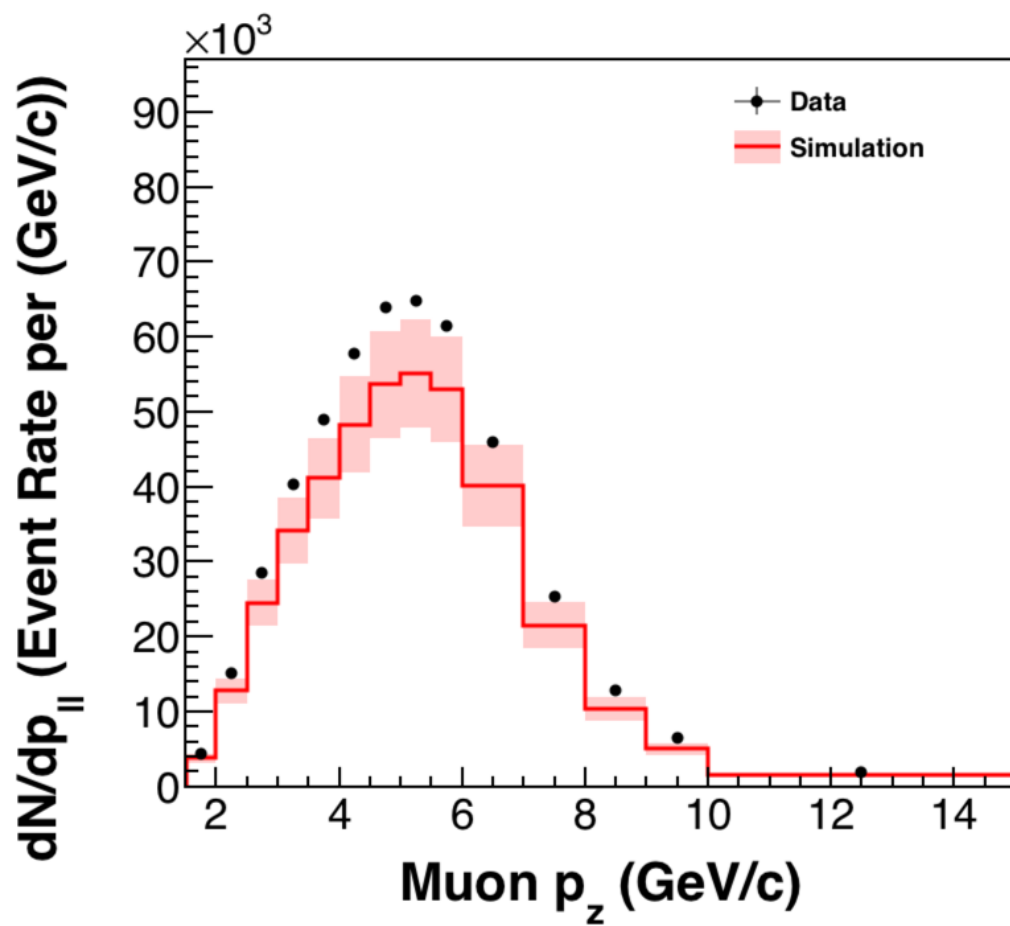
Figure 6.18: Raw data and MC distribution as a function of muon p_Z. Pink band is the systematic error on the raw MC.
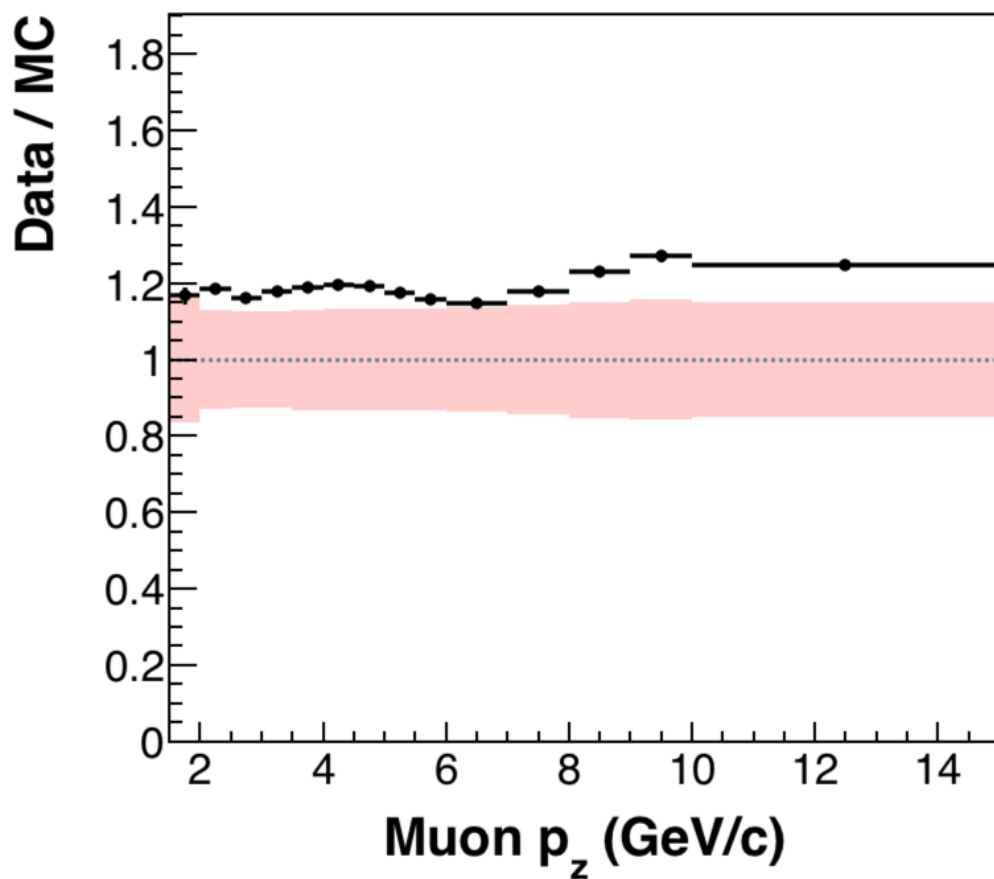
Figure 6.19: Ratio of raw data and MC distribution as a function of muon p_Z. Pink band is the systematic error on the raw MC.
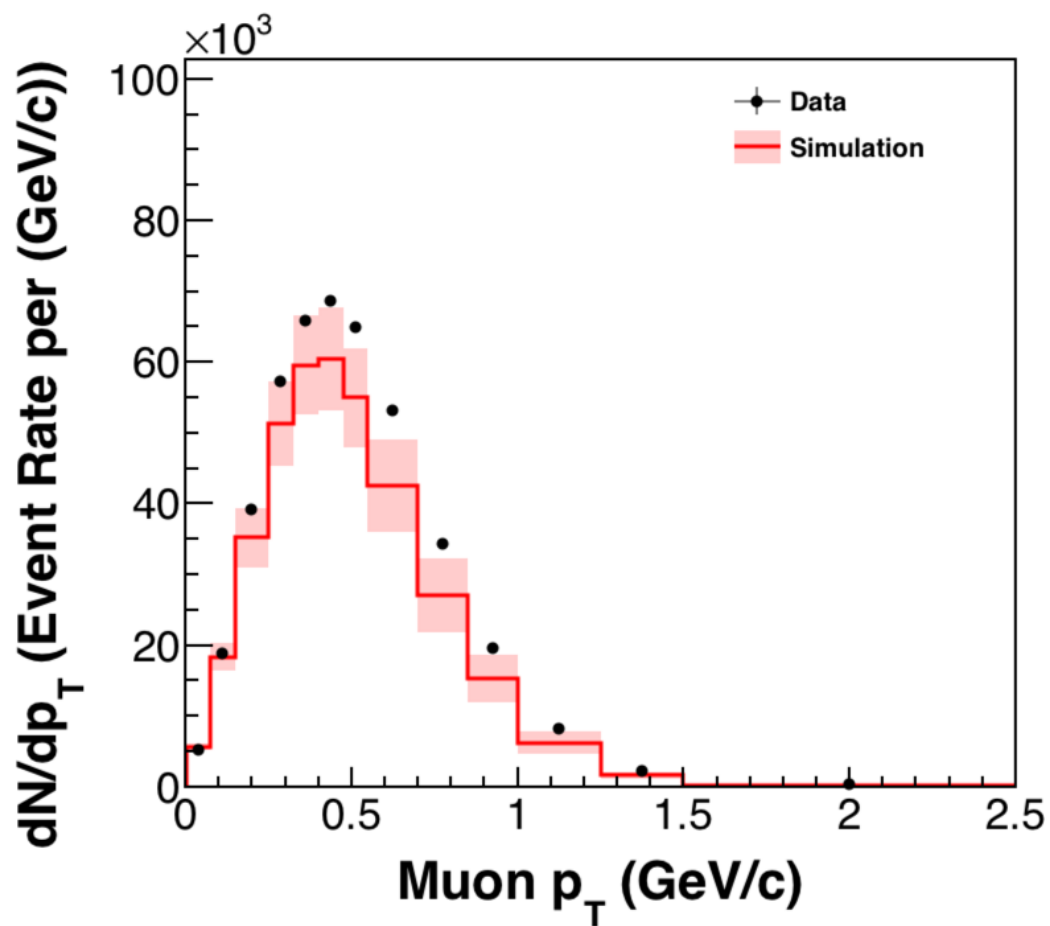
Figure 6.20: Raw data and MC distribution as a function of muon p_T. Pink band is the systematic error on the raw MC.
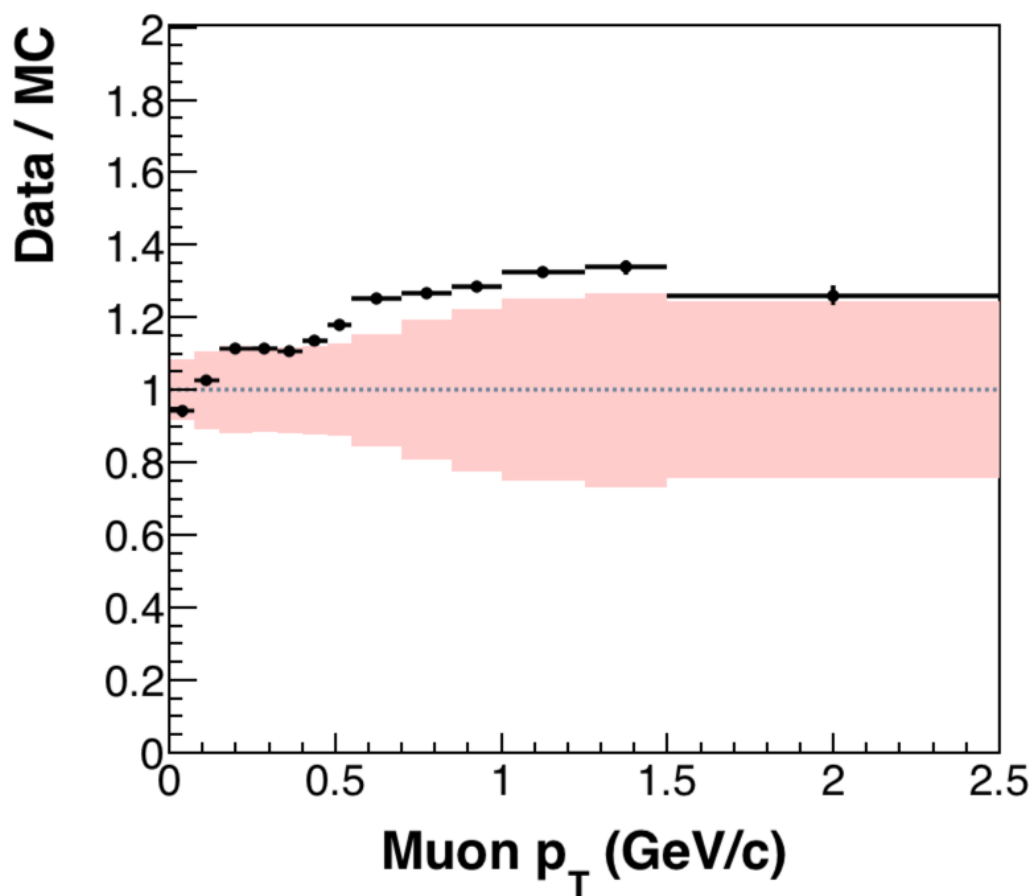
Figure 6.21: Ratio of raw data and MC distribution as a function of muon p_T. Pink band is the systematic error on the raw MC.
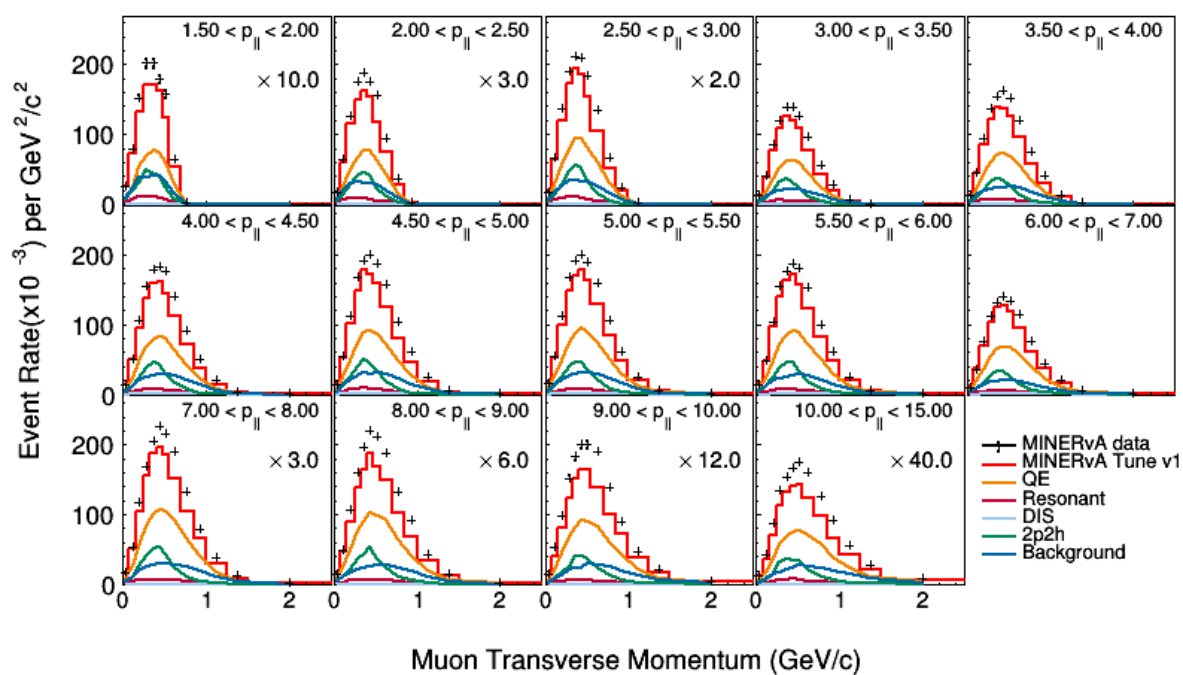
Figure 6.22: Raw event distribution as a function of muon transverse momentum (p_T) in the bins of muon longitudinal momentum
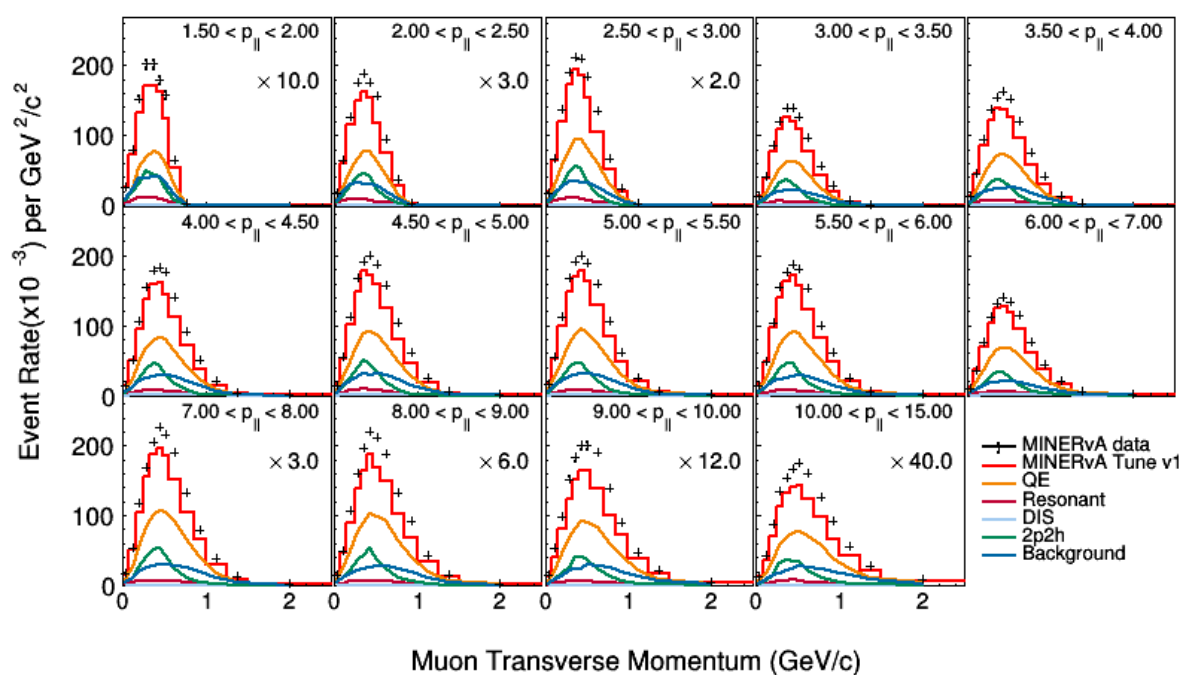
Figure 6.23: Raw event distribution as a function of muon longitudinal momentum $(P_\parallel)$ in the bins of muon transverse momentum

the detector dead time could lead the reconstruction algorithm to tag a true CCQELike event as a background event. CCQELike activities with recoil activity above the recoil cut threshold will fail the recoil cut. The MINOS detector may not reconstruct the charge of the muon correctly if the muon is highly energetic. These reconstruction limitations decrease the efficiency of our signal selection. The signal selection efficiency basically tells us the fraction of true signal events that are selected by our reconstruction cuts. It is given as:

$$Efficiency_{QELIKE} = \frac{N_{QELIKE}^{Pass\ Cut}}{N_{QELIKE}^{Total\ Events}} \qquad (6.6)$$

Here N is the number of truth events. The numerator is the number of true CCQELike events that pass the reconstruction cut and the denominator is the total number of true CCQELike events. Reconstruction efficiency of the signal components can be broken down into individual sub components by replacing the numerator with that particular sub component.

$$Efficiency_{QELIKE-X} = \frac{N_{QELIKE-X}^{Pass\ Cut}}{N_{QELIKE}^{Total\ Events}}$$

$$X = [QE, RES, DIS, 2P2H] \qquad (6.7)$$

Figure 6.24 shows the signal selection efficiency versus p_T and p_Z. Similarly, figures 6.25 and 6.26 show the 2D selection efficiencies for QELike events as a function of muon kinematics and neutrino energy versus four momentum transfer squared respectively. 1D projected
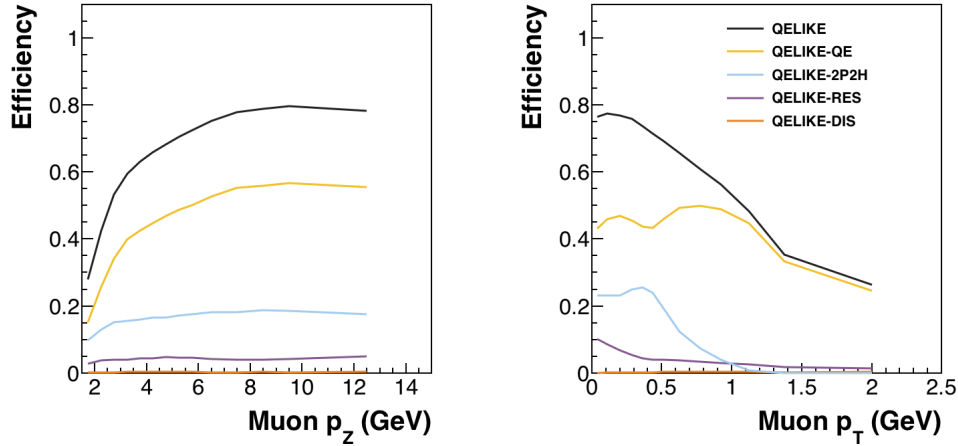
Figure 6.24: 1D projection of the signal selection efficiencies as a function of muon p_Z (left) and muon p_T (right).

efficiency plots show that the selection efficiency is very high for true QE components followed by 2p2h, resonance and DIS events. As a function of p_T, the selection efficiency decreases due to the 20 degrees muon angle requirement followed by the recoil cut itself. In the 2D plot (figure 6.25), there is a lack of events at high p_T between 0 and 4 GeV/c $p_{||}$. This is due to the 20 degrees angle requirement to ensure that the muons track make to the downstream MINOS detector. We can see similar behavior in figure 6.26, since Q^2_{QE} and p_T scale similarly. The selection efficiency is around 70% in the low transverse momentum region. There is a loss of efficiency as the muon angle approaches 20 degrees cut threshold.
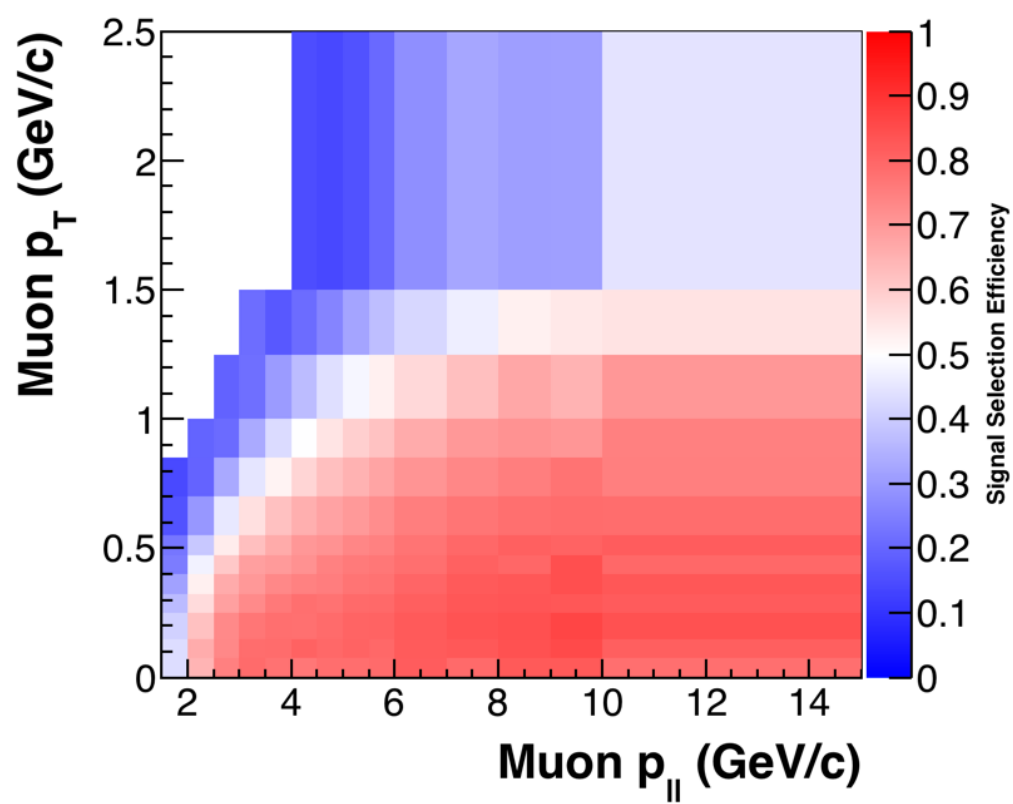
Figure 6.25: Signal selection efficiency for QELike events as a function of muon kinematics
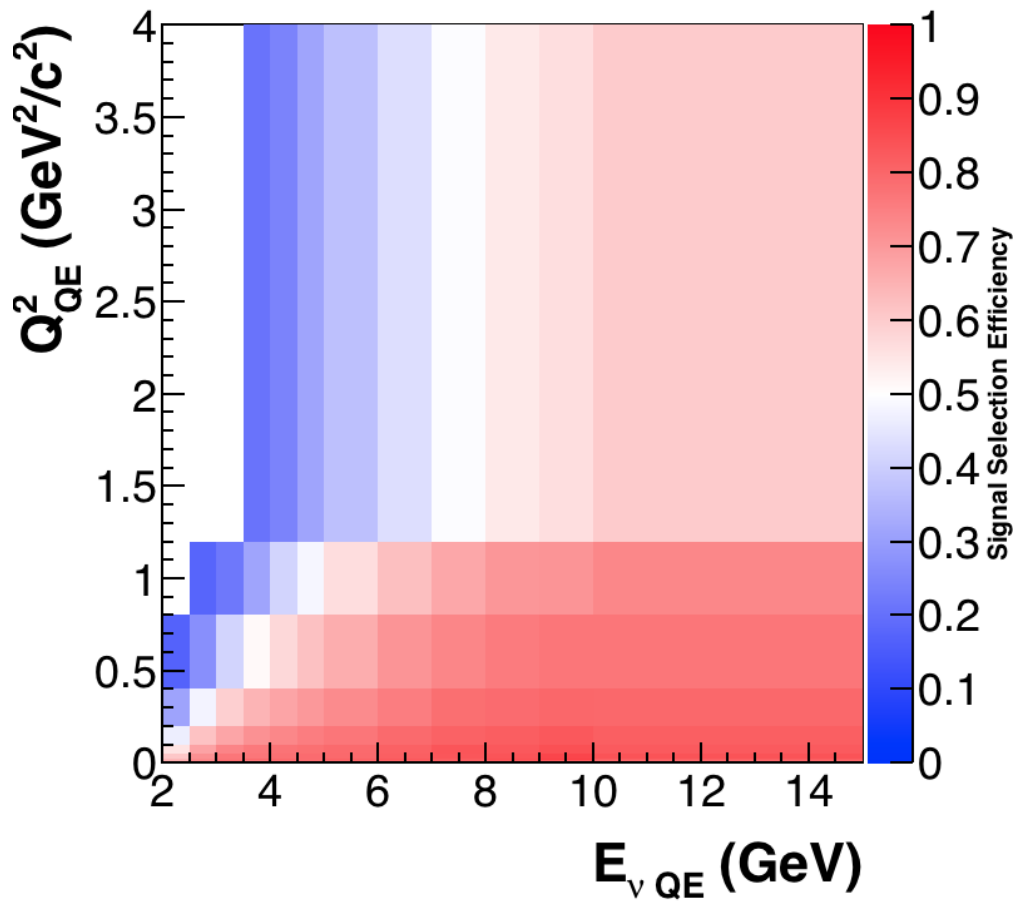
Figure 6.26: Signal selection efficiency for QELike events as a function of $E_{\nu QE}$ and Q^2_{QE}

6.13   Purity of the Selected Sample

The purity of the selected sample is given by:

$$Purity_{QELIKE} = \frac{N_{QELIKE}^{PASS\,CUTS}}{N_{QELIKE}^{PASS\,CUTS} + N_{QELIKENOT}^{FAIL\,CUTS}} \tag{6.8}$$

Purity basically gives us the fraction of true signal events from the total events that passed our selection cuts. In general, it is desirable to keep the selected signal sample as pure as possible. With the existing selection cuts, the purity can be maximized by tightening these cuts. However, tightening the cuts could not only reject the background events but also the signal events. A highly pure signal sample with low statistics can introduce large statistical uncertainties in the final result. The importance of balance between signal selection efficiency and purity will show up in various stages of the analyses. With this in mind, the shape of the recoil energy cut was tuned to maximize both selection efficiency and purity simultaneously. Figure 6.27 shows the 2D purity distribution as a function of muon kinematics. The color scale goes from 0.5 to 1 (50% to 100%) purity and the average purity is around 70%. The purity decreases as the transverse momentum increases where the resonant events dominate.
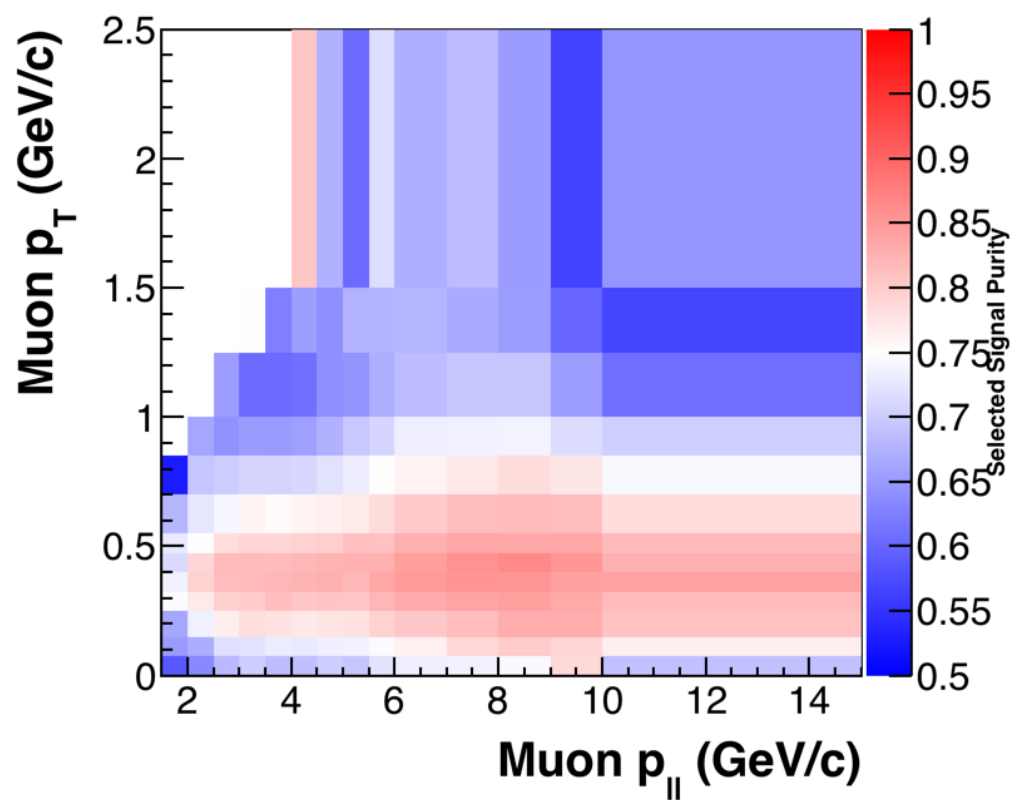
Figure 6.27: Purity of the selected sample as a function of muon momentum kinematics

6.14   Background in Data

Since the signal selection process is not perfect, the final selected sample is contaminated by the background processes. We can rely on the simulation to get an estimate of the background in our data. However, we cannot completely believe the MC prediction. After all, we do these measurements to correct for the simulation models as well. In fact, previous analyses done with MINERvA data [115], [63] showed that the simulation over-predicts the resonance pion production. Most of the background processes that pass our signal selection processes are resonance events. They could be events with a muon track and a pion that didn't make an additional track with recoil energy low enough to pass the recoil cut. Figure 6.28 shows that most of the background processes in the selected sample is dominated by non QE events.

Instead of relying on the simulation completely, a data driven fit is done to estimate the fraction of signal and background in the data. We use the TFractionFitter package developed by the ROOT [70] to do the fit. This package uses a likelihood fit between the data and the MC by taking statistical uncertainties into account. The fit takes data and MC templates (signal and background templates) as fit parameter and does a log likelihood fit. A χ^2 minimization is done where the χ^2 is calculated using the prescription of Baker and Cousins [30].
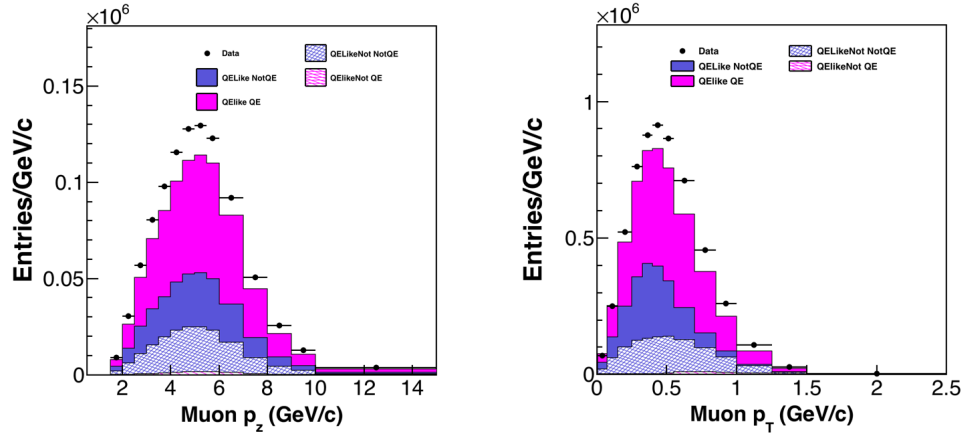
Figure 6.28: Signal and background processes as a function of muon kinematics are broken down into true QE and non QE categories. Most of the signal events are *true QE* components whereas most of the background events are *not true QE*. The non QE component is mostly dominated by resonance processes. The QELikenot QE are the events which are initially true QE events that pass the recoil cut but the recoil hadron is absorbed or a pion or proton above 120 MeV kinetic energy is produced in the final state.

6.14.1 Fitting Procedure

In this analysis, the MC templates are divided into the signal and the background templates such that the fit will only give the estimation of overall signal and background fraction in the data. Since we look at the recoil energy distribution to differentiate signals from background, the fit is done as a function of recoil energy. The overall contribution of the signal and the background processes in the recoil energy changes going from low to high p_T. Hence we divide the data into 14 different regions in the muon p_T vs. p_z phase space. There are 6 fit regions in the rising part of the p_z distribution and 6 fit regions in the falling part of the

p_z distribution. The remaining 2 are in the tail of the p_z distributions. The boundaries of p_z and p_T are matched against the bin edges of the p_T and p_z. The binning for the fit is given in table 6.2. The fit returns the best MC prediction such that the total number of events in the best MC and the input data inside the fit region are equal. The fit is done between 100 and 500 MeV recoil energy. Note that the recoil energy cut used in this analysis is a Q^2 dependent function with a tight recoil cut in the low Q^2 region which gradually loosens and finally saturates at high Q^2 region. In the low Q^2 region, the signal (recoil energy less than the recoil cut) partially overlaps with the fit region and in the high Q^2 region, completely contains the fit region. However, a fit between 100 to 500 MeV region excludes the signal rich low recoil region making the fit prediction less dependent on the shape of the signal distribution. Figure 6.29 shows the ratio of the data to the nominal MC (black) and ratio of the data to the best MC (red) for fit bin 0. The fit returns the MC whose integral (within the fit region) is equal to that of the data along with the fraction of background and signal in the sample. Since, the fit is done between 100 MeV and 500 MeV recoil energy, these estimations of the fractions are for that region only. However, we need to estimate the fractions in the overall signal region (that passes recoil cut) that includes the signal rich region of less than 100 MeV recoil energy. Figure 6.30 shows the signal and background distributions inside and outside the fit region. The purple lines represents the start and end of recoil energy on which the fit is performed. In this figure:
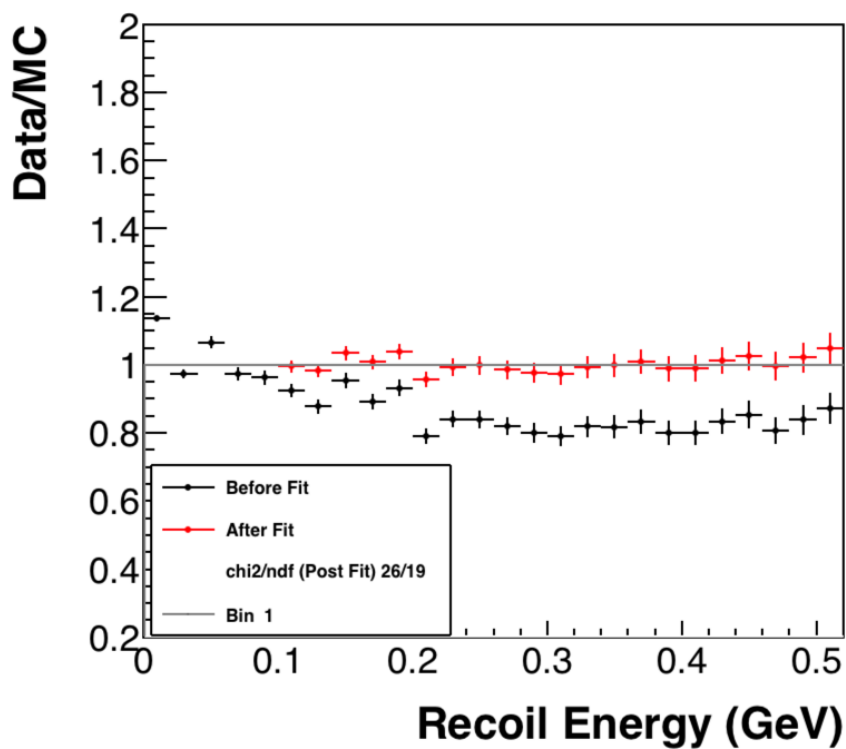
Figure 6.29: Ratio of the data to nominal mc (black) and data to best mc returned by the fit (red) as a function of recoil energy for muon p_z between 1.5 and 5 GeV/c and p_T between 0 and 0.25 GeV/c. The best MC is just the prediction of the total MC based on the input parameters that best describes the data and doesn't correspond to the input MC. The best MC prediction is only within the fit region (recoil energy between 100 and 500 MeV).
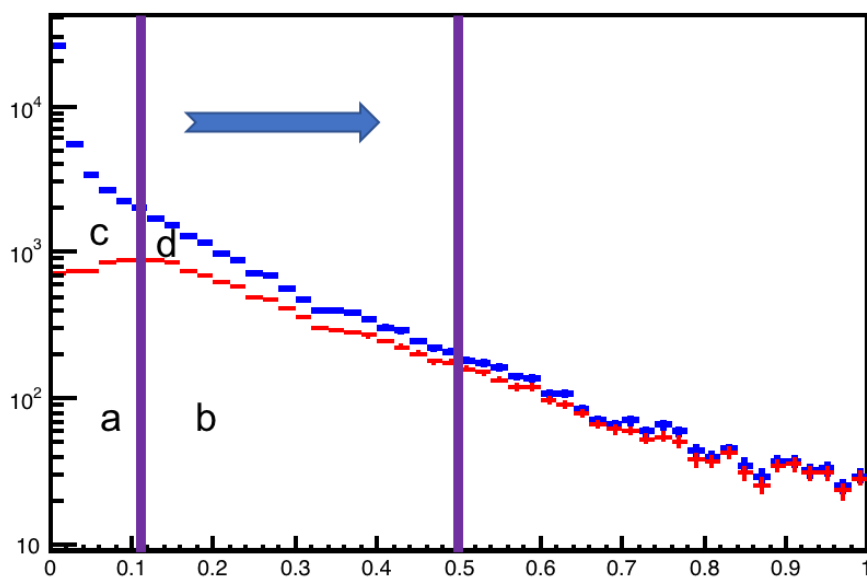
Figure 6.30: Diagram showing the fit region and the signal rich region. Red histogram is the background and the blue histogram is the total MC. Letters **a,b,c,d** represent the background and the signal events inside and outside the fit region. The purple line represents the area in which the fit is done. All the 4 regions are the estimated events in the data. Hence, the fractions $\frac{b}{b+d}$ and $\frac{d}{b+d}$ are the background and signal fractions that come from the fit. The fractions $\frac{a}{a+b}$ and $\frac{b}{a+b}$ are unknown.

- **a** represents the area under the red histogram i.e. the background events between 0 and 100 MeV which are outside the fit region but inside the signal rich region.

- **b** represents the area under the red histogram i.e. the background events between 100 and 500 MeV which are inside the fit region.

- **c** represents the area between the blue histogram and red histogram i.e. signal events between 0 and 100 MeV which is outside the fit region but inside the signal rich region.

- **d** represents the area between the blue and red histogram i.e. signal events between 100 and 500 MeV which are inside the fit region.

From the fit, we need to estimate the total signal and background fractions between 0 and 500 MeV recoil energy. Let:

- $fBkg_{Tot}$ be the fraction of background in the data between 0 and 500 MeV.

- $fSig_{Tot}$ be the fraction of signal in the data between 0 and 500 MeV.

Also these two fractions are constrained as:

$$fBkg_{Tot} + fSig_{Tot} = 1.0 \tag{6.9}$$

The overall procedure to find either of the two fractions is the same. Hence we can only go through the process of finding total background fraction $fBkg_{Tot}$ as an example. The total background fraction is given by:

$$fBkg_{Tot} = \frac{c+d}{a+b+c+d} \tag{6.10}$$

We want to write a,b,c and d in terms of the known quantities. From the fit we can get the fraction of signal and background in the fit region (i.e. in d and b). Lets say the fractions from the fit are f_{Bkg} and f_{Signal} respectively. Let n_{above} be the number of events in the best MC inside the fit region. Note that this number is also equal to the number of data events inside that region. Also let us define the fraction of signal and background inside the fit region as xS and xB such that:

$$xS = \frac{d}{d+c} \tag{6.11}$$

and

$$xB = \frac{b}{a+b} \tag{6.12}$$

Note that xS and xB are constant before and after the fit since the fit doesn't change the relative fraction of signal and background above and below the 100 MeV cut. Then the

variables, a,b,c and d can be written as:

$$a = \frac{f_{Bkg} \times n_{above} \times xB - f_{Bkg} \times n_{above}}{xB} \tag{6.13}$$

$$b = f_{Bkg} \times n_{above} \tag{6.14}$$

$$c = \frac{(f_{Bkg} \times n_{above} - n_{above})(xS - 1)}{xS} \tag{6.15}$$

and

$$d = n_{above} - f_{Bkg} \times n_{above} \tag{6.16}$$

Substituting these values of a,b,c and d in $fBkg_{Tot}$ and after simplification, we get:

$$fBkg_{Tot} = \frac{f_{Bkg} \times xS}{f_{Signal} \times xB + f_{Bkg} \times xS} \tag{6.17}$$

Using similar procedure for $fSig_{Tot}$, we get:

$$fSig_{Tot} = \frac{f_{Sig} \times xB}{f_{Bkg} \times xS + f_{Sig} \times xB} \tag{6.18}$$

Hence we have the total fractions of background and signal. To determine if the fractions

predicted by the fit actually agrees with the data, we can scale the nominal signal and the background histograms by scale factors such that:

$$Scale_i^{qelike} = \frac{\int_{100MeV}^{500MeV} best_i^{qelike}}{\int_{100MeV}^{500MeV} nominal_i^{qelike}} \qquad (6.19)$$

$$Scale_i^{qelikenot} = \frac{\int_{100MeV}^{500MeV} best_i^{qelikenot}}{\int_{100MeV}^{500MeV} nominal_i^{qelikenot}} \qquad (6.20)$$

Note that our signal and background fraction predictions are coming from best signal and backgrounds predicted by the fit. Then the total best MC can be roughly constructed as:

$$best_{mc}^{tot} = Scale_i^{qelike} \times qelike_i + Scale_i^{qelikenot} \times qelikenot_i \qquad (6.21)$$

We can take the ratio of the data to nominal MC and compare against the ratio of the data to the total best MC (MC after reweighting with scales from the fit) to evaluate the performance of the fit in each fit bins.

Figures 6.31 through 6.44 shows the performance of the fit. In all the bins, the fit brings the data/MC discrepancy down. The first fit bin (6.31) performs relatively worse than the rest of the fit bins. At this point, we have estimated the background and signal fraction in the data for recoil energy between 0 and 500 MeV. However, since the recoil cut is Q^2
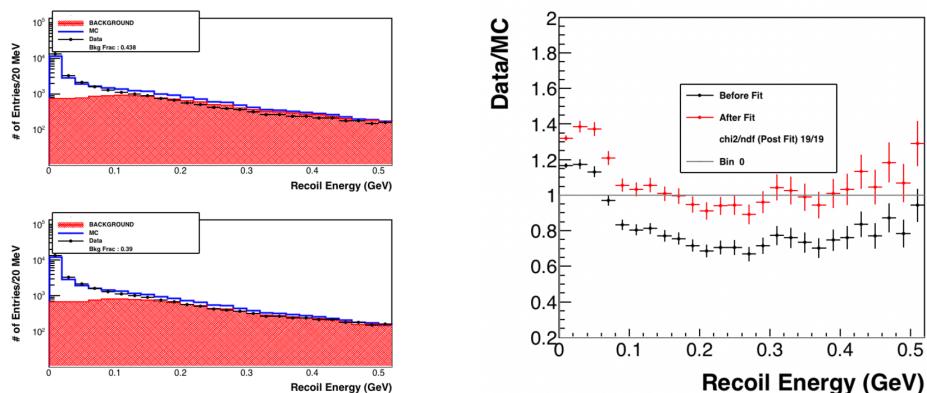
Figure 6.31: Recoil distribution before fit (top left) and after fit (bottom left). On the right is the ratio before (black) and after fit (red) between data and MC for p_z between 1.5 to 5 GeV/c and p_T between 0 to 0.25 GeV/c.
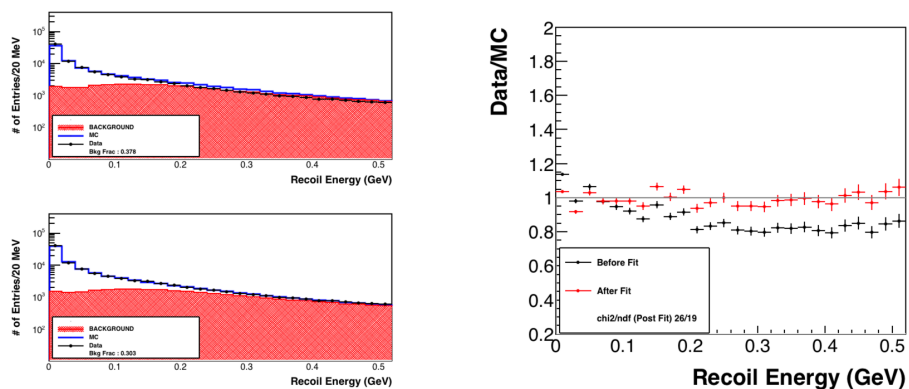
Figure 6.32: Recoil distribution before fit (top left) and after fit (bottom left). On the right is the ratio before (black) and after fit (red) between data and MC for p_z between 1.5 to 5 GeV/c and p_T between 0.25 to 0.4 GeV/c.
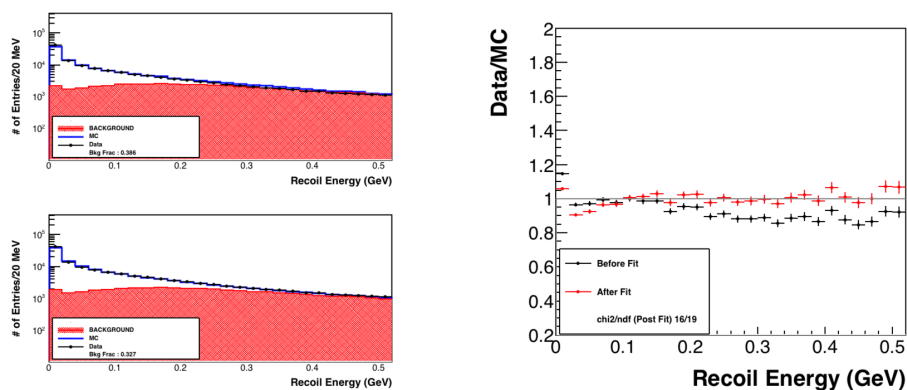
Figure 6.33: Recoil distribution before fit (top left) and after fit (bottom left). On the right is the ratio before (black) and after fit (red) between data and MC for p_z between 1.5 to 5 GeV/c and p_T between 0.4 to 0.7 GeV/c.
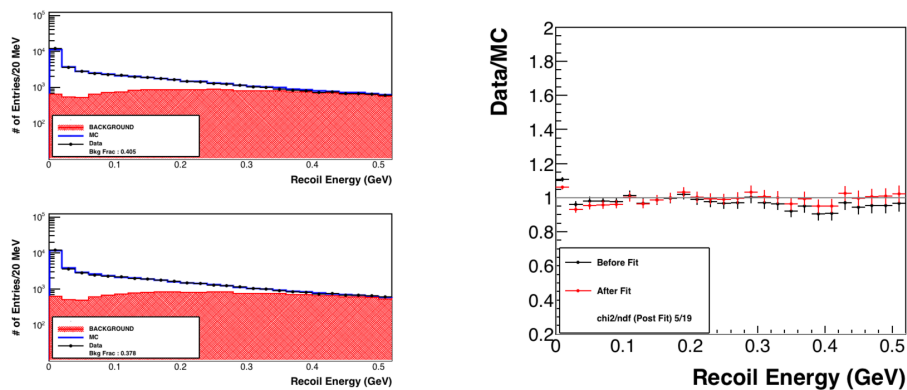
Figure 6.34: Recoil distribution before fit (top left) and after fit (bottom left). On the right is the ratio before (black) and after fit (red) between data and MC for p_z between 1.5 to 5 GeV/c and p_T between 0.7 to 0.85 GeV/c.
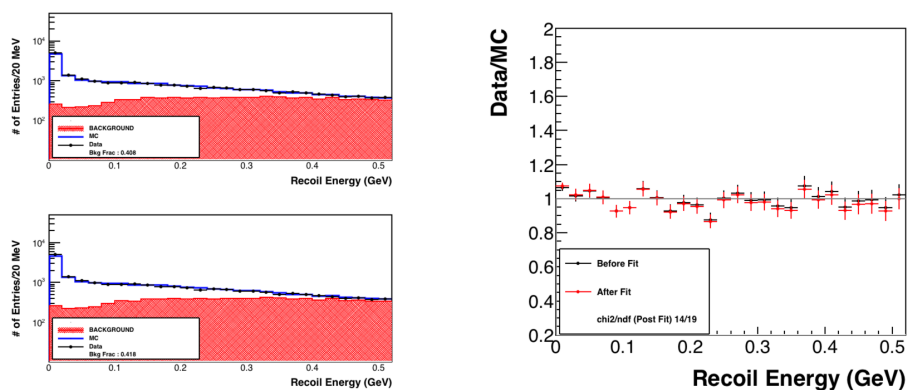
Figure 6.35: Recoil distribution before fit (top left) and after fit (bottom left). On the right is the ratio before (black) and after fit (red) between data and MC for p_z between 1.5 to 5 GeV/c and p_T between 0.85 to 1.0 GeV/c.
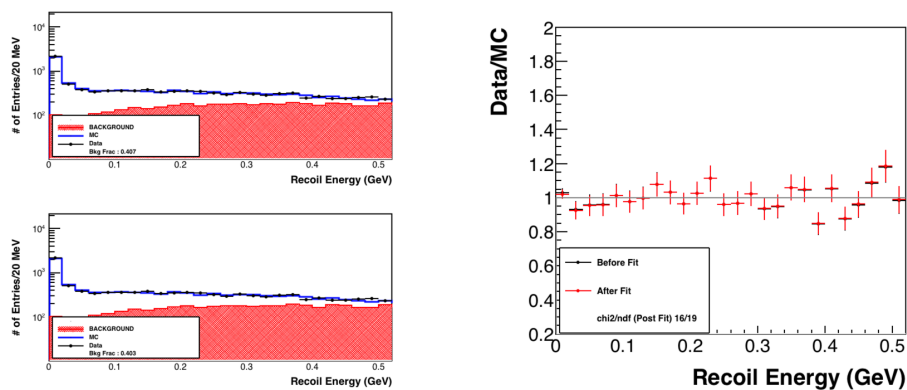
Figure 6.36: Recoil distribution before fit (top left) and after fit (bottom left). On the right is the ratio before (black) and after fit (red) between data and MC for p_z between 1.5 to 5 GeV/c and p_T between 1.0 to 2.5 GeV/c.
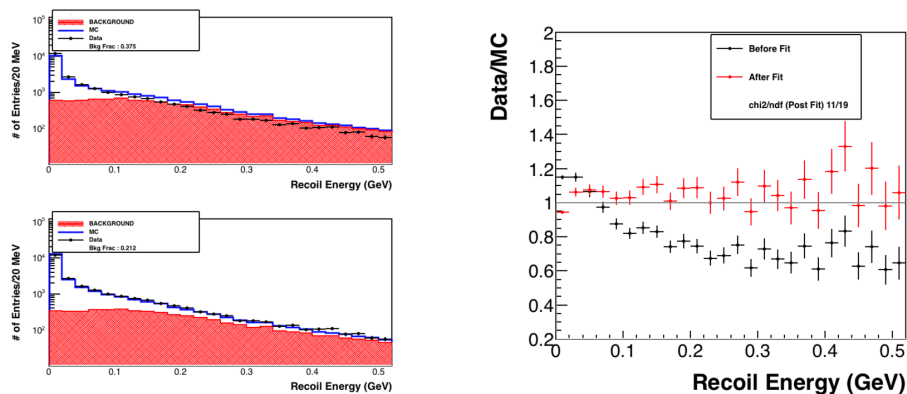
Figure 6.37: Recoil distribution before fit (top left) and after fit (bottom left). On the right is the ratio before (black) and after fit (red) between data and MC for p_z between 5 to 8 GeV/c and p_T between 0.0 to .25 GeV/c.
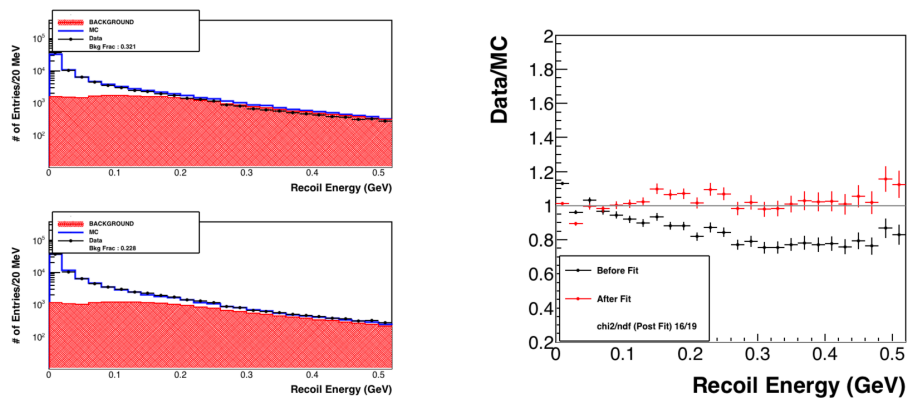
Figure 6.38: Recoil distribution before fit (top left) and after fit (bottom left). On the right is the ratio before (black) and after fit (red) between data and MC for p_z between 5 to 8 GeV/c and p_T between 0.25 to 0.4 GeV/c.
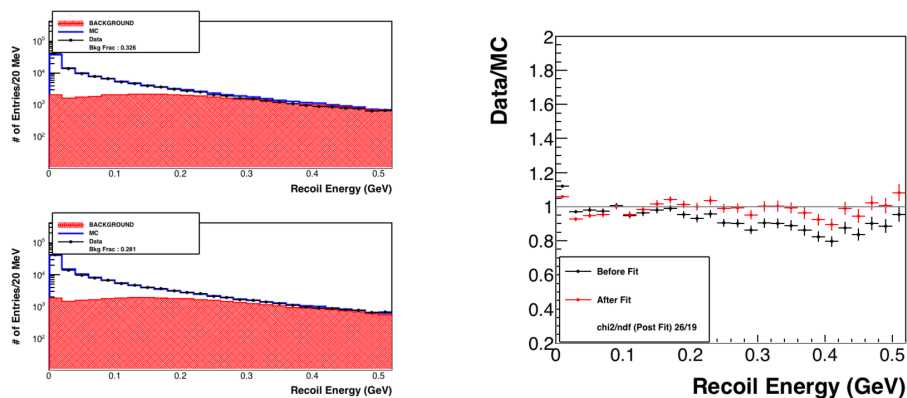
Figure 6.39: Recoil distribution before fit (top left) and after fit (bottom left). On the right is the ratio before (black) and after fit (red) between data and MC for p_z between 5 to 8 GeV/c and p_T between 0.4 to 0.7 GeV/c.
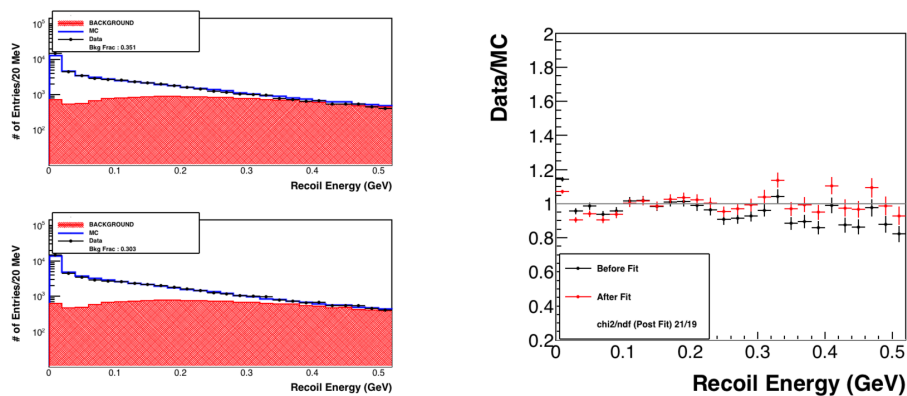
Figure 6.40: Recoil distribution before fit (top left) and after fit (bottom left). On the right is the ratio before (black) and after fit (red) between data and MC for p_z between 5 to 8 GeV/c and p_T between 0.7 to 0.85 GeV/c.
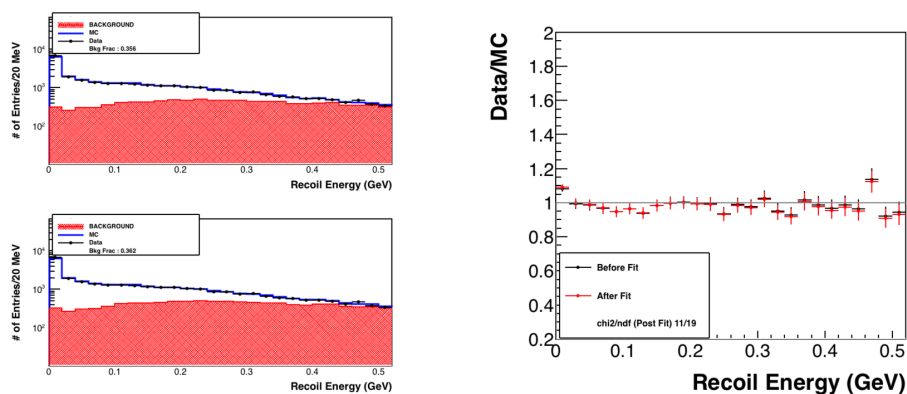
Figure 6.41: Recoil distribution before fit (top left) and after fit (bottom left). On the right is the ratio before (black) and after fit (red) between data and MC for p_z between 5 to 8 GeV/c and p_T between 0.85 to 1.0 GeV/c.
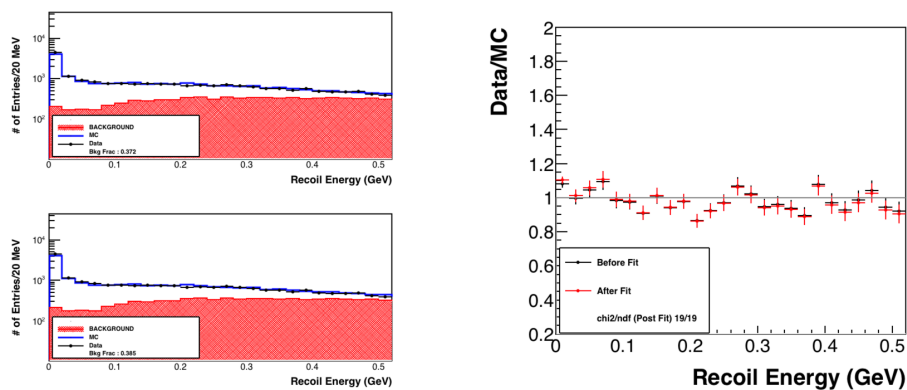
Figure 6.42: Recoil distribution before fit (top left) and after fit (bottom left). On the right is the ratio before (black) and after fit (red) between data and MC for p_z between 5 to 8 GeV/c and p_T between 1.0 to 2.5 GeV/c.
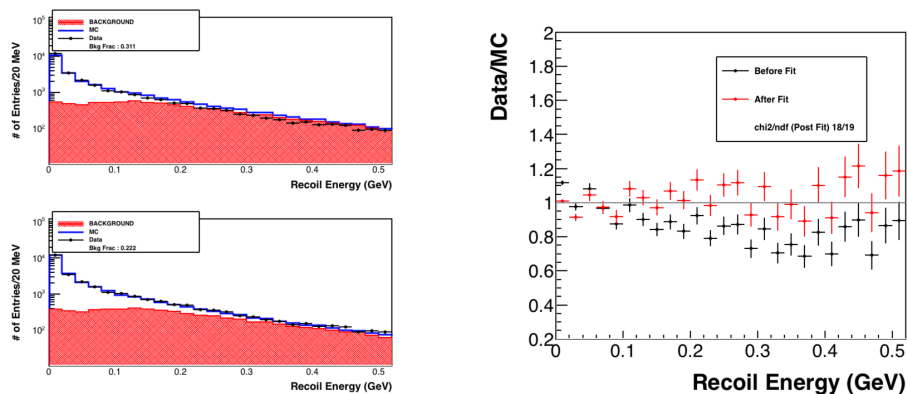
Figure 6.43: Recoil distribution before fit (top left) and after fit (bottom left). On the right is the ratio before (black) and after fit (red) between data and MC for p_z between 8 to 15 GeV/c and p_T between 0.0 to 0.5 GeV/c.
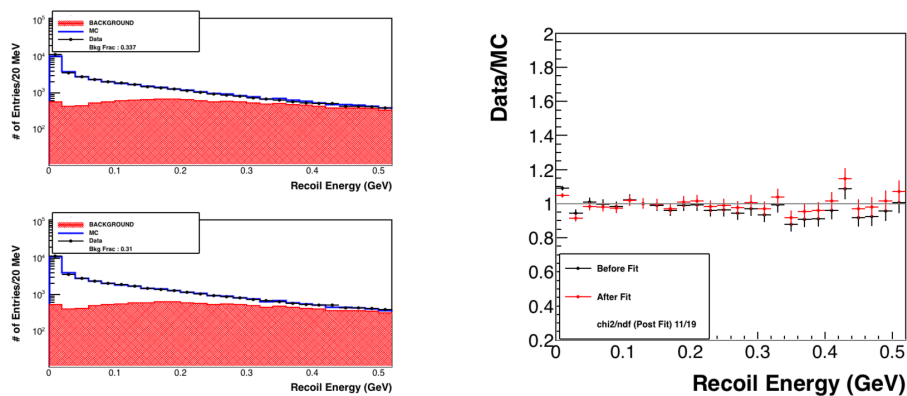
Figure 6.44: Recoil distribution before fit (top left) and after fit (bottom left). On the right is the ratio before (black) and after fit (red) between data and MC for p_z between 8 to 15 GeV/c and p_T between 0.5 to 2.5 GeV/c.
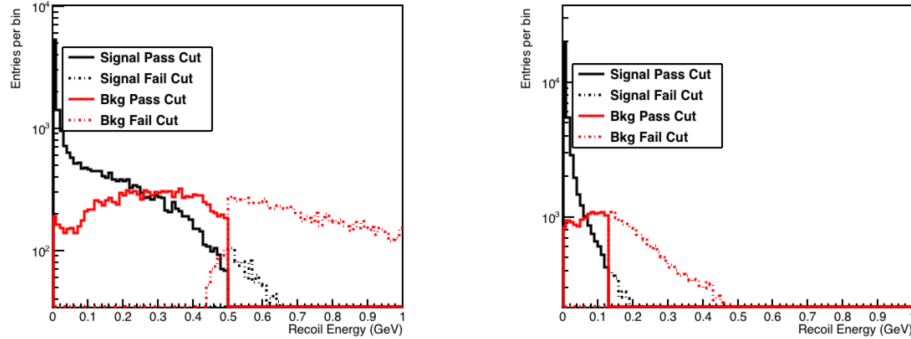
Figure 6.45: Signal and backgrounds prediction that pass and fail the recoil cuts in p_z between 5 to 8 GeV/c and p_T between 1.0 to 2.5 GeV/c phase space (left) and p_z between 1.5 to 5 GeV/c and p_T between 0.0 to 0.25 GeV/c.

dependent cut, the signal and background fraction estimation needs to be corrected for each fit bins.

Figure 6.45 shows the signal and the background events that pass and fail recoil cut as a function of recoil energy for high p_T (left) and low p_T right. In the low p_T fit bins, the recoil cut is tighter and there are no events passing recoil cut at or near 500 MeV. Hence, the signal and background efficiencies are different. The efficiency corrected signal fraction is given as:

$$f_{SigFrac}^{EffCorr} = \frac{Eff_{Sig} \times N_{Sig}^{Best}}{Eff_{Sig} \times N_{Sig}^{Best} + Eff_{Bkg} \times N_{Bkg}^{Best}} \tag{6.22}$$

where:

$$Eff_{Sig} = \frac{N_{Sig}^{Pass\ Recoil\ Cut}}{N_{Sig}^{Tot}} \quad (6.23)$$

$$Eff_{Bkg} = \frac{N_{Bkg}^{Pass\ Recoil\ Cut}}{N_{Bkg}^{Tot}} \quad (6.24)$$

The N_{Bkg}^{Best} and N_{Sig}^{Best} are the total number of signal and background events from the fit prediction between recoil energy 0 to 500 MeV. These numbers can be calculated since we know the overall fraction of signal and background in the data.

Finally, in a given fit bin i, the background subtracted data is given by: $Data_{Bkg\ Subtracted}^{i} = Data_{Signal\ Region}^{i} \times f_{SigFrac}^{EffCorr}$

The errors on the fractions come from the fit themselves. This background subtraction procedure is different from the LE era background subtraction procedure, where instead a scale factor is calculated for each fit bin by doing a fit from 0 to 500 MeV.

The table 6.2 shows the summary of fit with signal fractions before and after fit, signal efficiency and efficiency corrected signal along with the χ^2 prediction from the fit.

Figures 6.48 and 6.46 shows the data and MC (signal component) after the background subtraction in the projected muon p_T and p_Z phase space respectively.

p_T GeV/c	p_z Gev/c	Signal Before	Signal After	Signal Efficiency	Final Signal Fraction	χ^2/NDF
0.0 - 0.2	1.5 - 5.0	0.56	0.610 ± 0.027	0.901	0.78	18.12/19
0.2 - 0.4	1.5 - 5.0	0.62	0.700 ± 0.011	0.905	0.86	26.82/19
0.4 - 0.65	1.5 - 5.0	0.61	0.673 ± 0.008	0.901	0.84	16.08/19
0.65 - 0.82	1.5 - 5.0	0.59	0.622 ± 0.012	0.922	0.75	5.96/19
0.82 - 1.0	1.5 - 5.0	0.59	0.582 ± 0.0188	0.951	0.66	14.74/19
1.0 - 2.5	1.5 - 5.0	0.0.59	0.597 ± 0.0373	0.988	0.61	16.44/19
0.0 - 0.2	5.0 - 8.0	0.62	0.788 ± 0.0367	0.923	0.89	11.43/19
0.2 - 0.4	5.0 - 8.0	0.67	0.772 ± 0.015	0.922	0.89	16.64/19
0.4 - 0.65	5.0 - 8.0	0.67	0.719 ± 0.010	0.918	0.85	26.45/19
0.65 - 0.82	5.0 - 8.0	0.65	0.700 ± 0.0119	0.930	0.80	21.69/19
0.82 - 1.0	5.0 - 8.0	0.64	0.638 ± 0.0166	0.952	0.71	11.33/19
1.0 - 2.5	5.0 - 8.0	0.62	0.615 ± 0.026	0.983	0.63	19.48/19
0.0 - 0.5	8.0 - 15.0	0.69	0.778 ± 0.026	0.926	0.89	18.86/19
0.0 - 0.5	8.0 - 15.0	0.66	0.69 ± 0.0156	0.950	0.77	11.87/19

90

Table 6.2: Table with the signal fraction (before and after), efficiencies and efficiency corrected fractions in each of the fit bins.
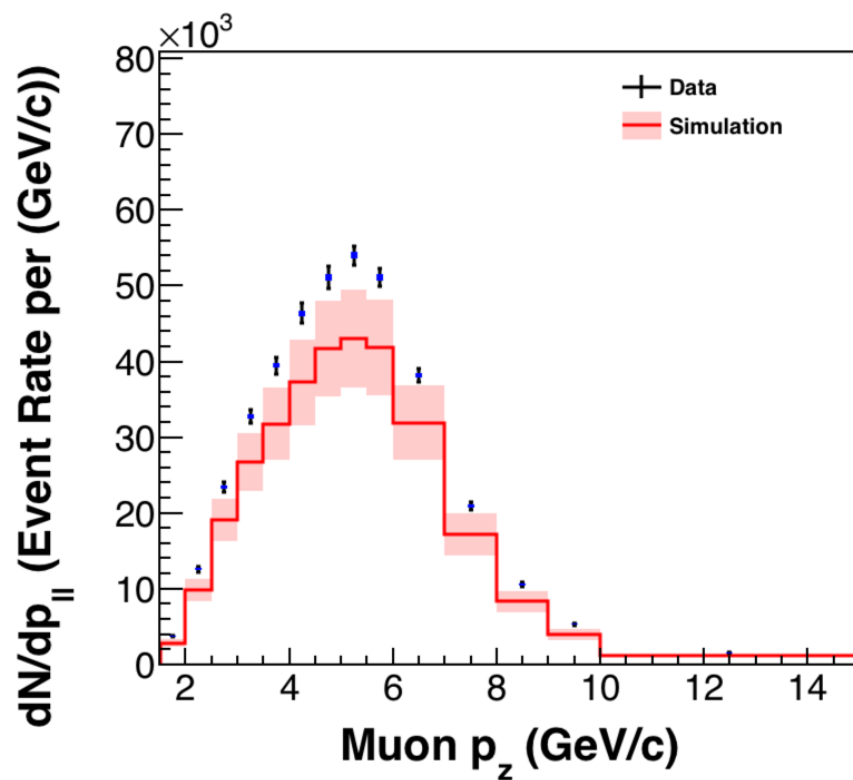
Figure 6.46: Background Subtracted data and MC signal component as a function of muon p_z. The pink band is the systematic error on the MC. The error bars on the data is total error (stat errors and systematic errors coming from the fit). Blue rectangles show the statistical errors on the data.
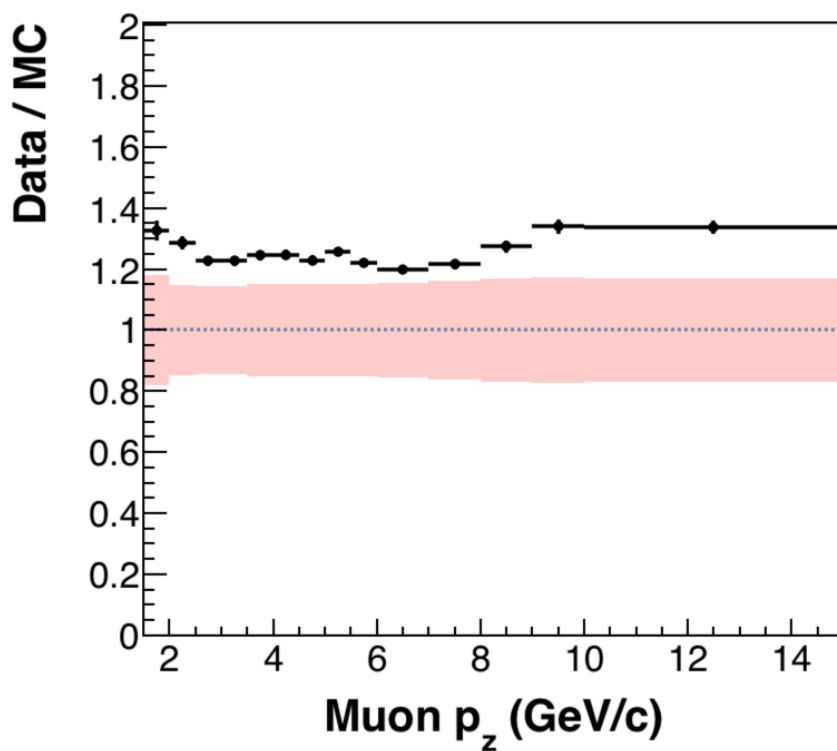
Figure 6.47: Ratio between Background Subtracted data MC signal component as a function of muon p_z. The pink band is the systematic error on the MC. The error bars on the data is total error (stat errors and systematic errors coming from the fit).Blue rectangles show the statistical errors on the data.
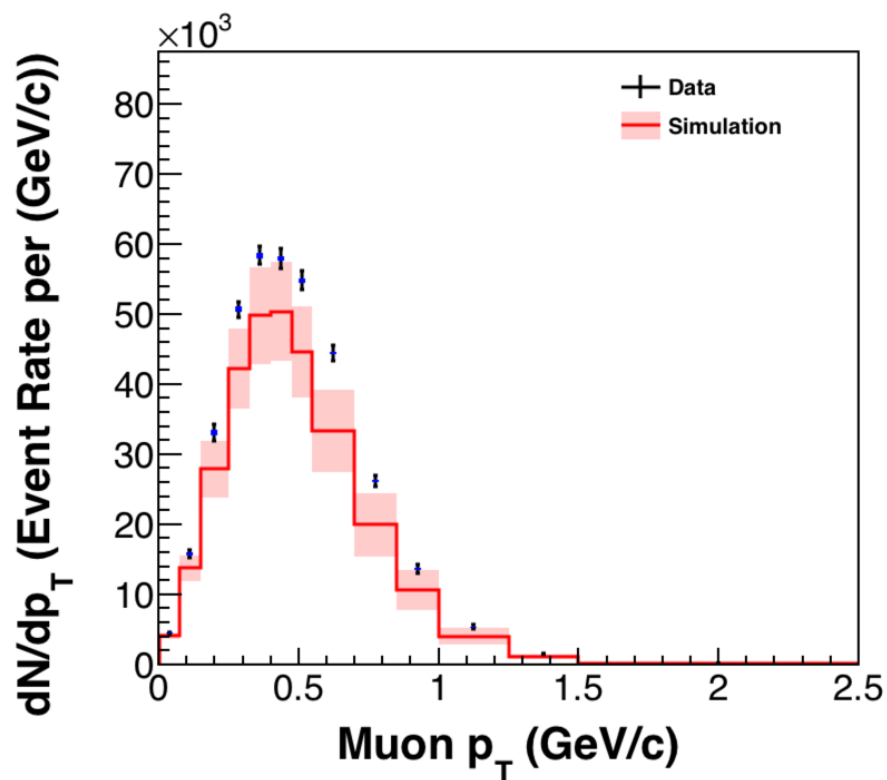
Figure 6.48: Background Subtracted data and MC signal component as a function of muon p_T. The pink band is the systematic error on the MC. The error bars on the data is total error (stat errors and systematic errors coming from the fit). Blue rectangles show the statistical errors on the data.
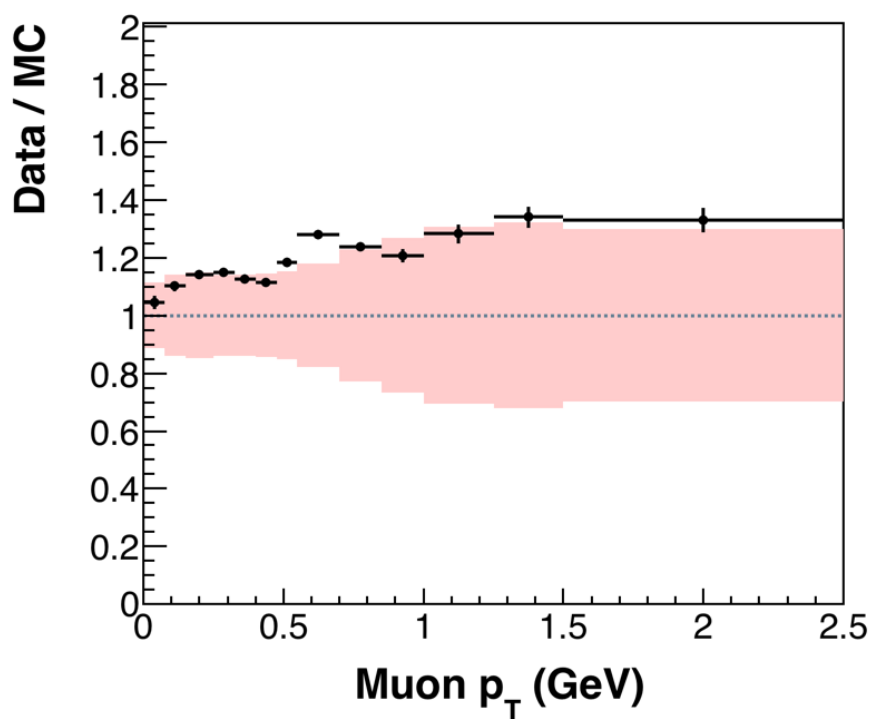
Figure 6.49: Ratio between Background Subtracted data MC signal component as a function of muon p_T. The pink band is the systematic error on the MC. The error bars on the data is total error (stat errors and systematic errors coming from the fit)
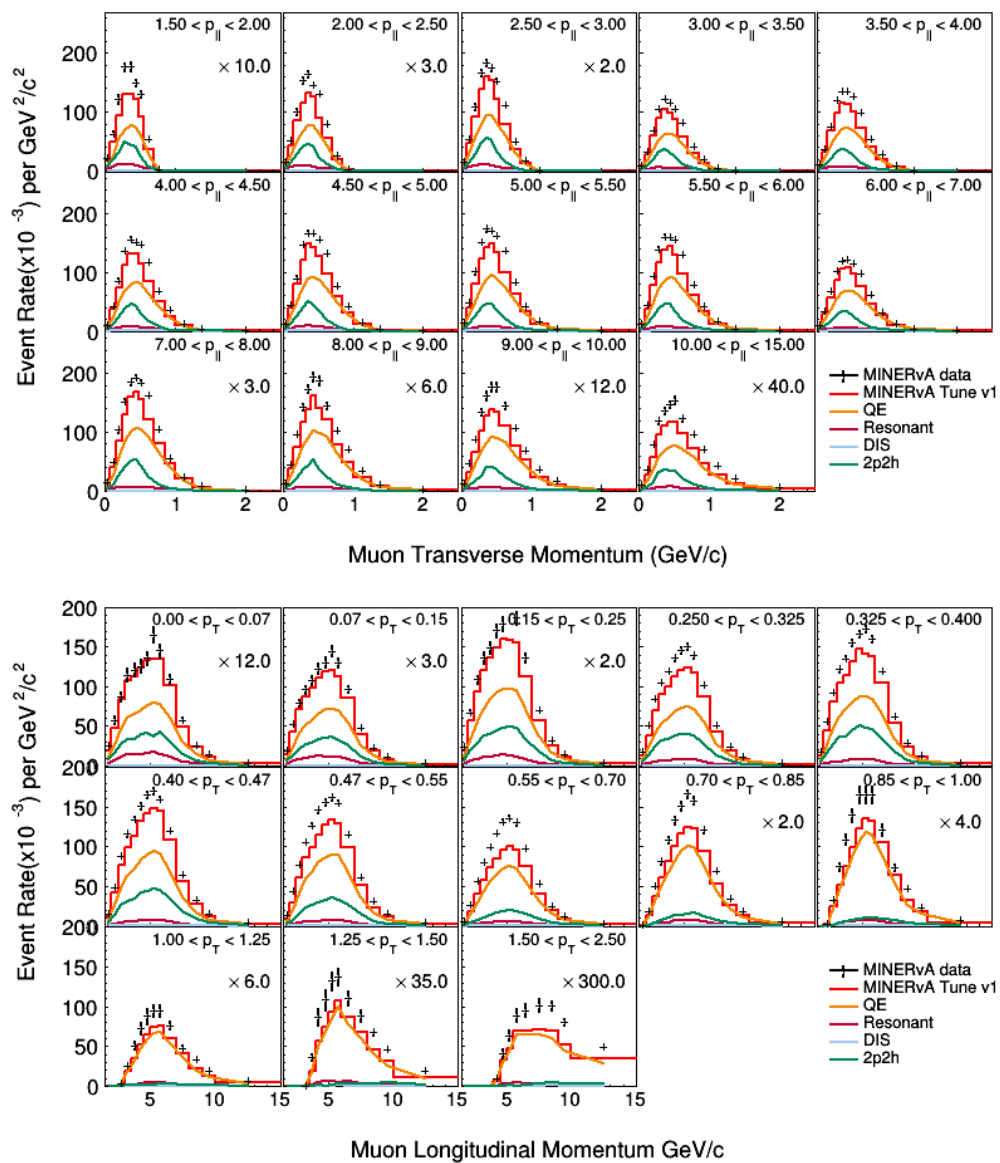
Figure 6.50: (Background subtracted event-rate as a function of p_T in the bins of p_Z (Top) and as a function of p_Z in the bins of p_T (bottom). Black crosses are data points with vertical bars representing errors. Solid line shows the Signal MC and its breakdown.
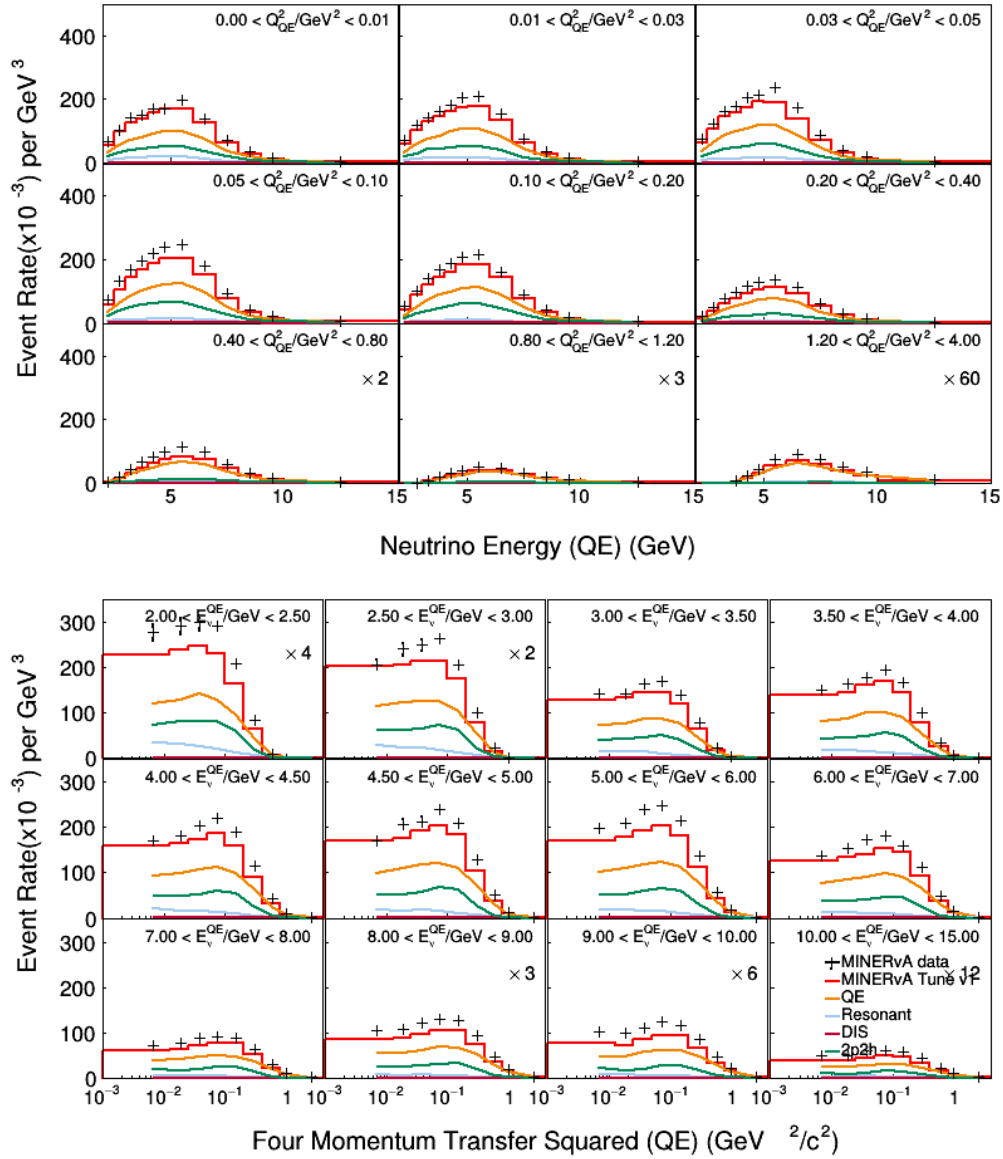
Figure 6.51: Background subtracted event-rate as a function of E_ν in the bins of Q^2 (top) and as a function of Q^2 in the bins of E_ν. The black cross shows the data and the colored lines are simulation with various signal components.

6.15 Migration Matrix or Smearing Matrix

The neutrino events are measured as a function of reconstructed variables. In this analysis, the measurements are done as a function of reconstructed muon momenta and neutrino energy and four momentum transfer squared. However, the final cross-section measurements are more informative when measured as a function of true variables because they can be compared against various models allowing theoretical predictions of cross-section parameters (for example M_A,M_V, modeling of nuclear effects etc) to be tested. However the reconstructed variables and true variables do not have one-to-one mapping.   Figures 6.52 through 6.54 show the smearing of the reconstructed variables into various true bins. The smearing happens because variables that are being measured cannot be reconstructed perfectly. The position of the blobs, for example, can only be known within the width of the scintillator strips in the detector. Similarly, the accuracy of energy reconstruction depends upon the detector response to various charge particles, calibration etc. These limitations cause the variables to be reconstructed in higher or lower true bins. Using the information from the Monte Carlo, we can estimate the amount of smearing as seen in figures 6.52 through 6.54.

Since this is a 2 dimensional analysis, we need to account for the smearing/migration of events in a 2 dimensional phase space. For example, for each given p_T bins, there can be migration of an event from one p_Z bin to another.
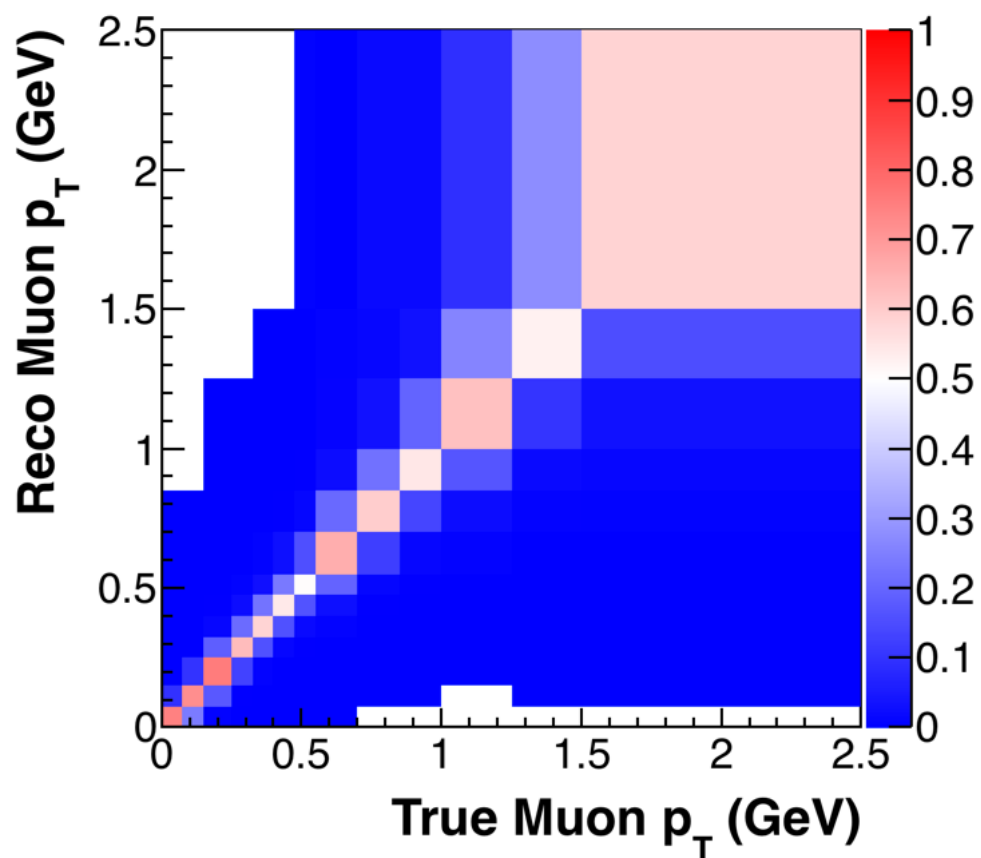
Figure 6.52: Smearing of the reconstructed p_T into different bins of true p_T. The plot is row normalized which means the plot shows the smearing of a given reconstructed p_T bins in different true p_T bins. More diagonality means less smearing.
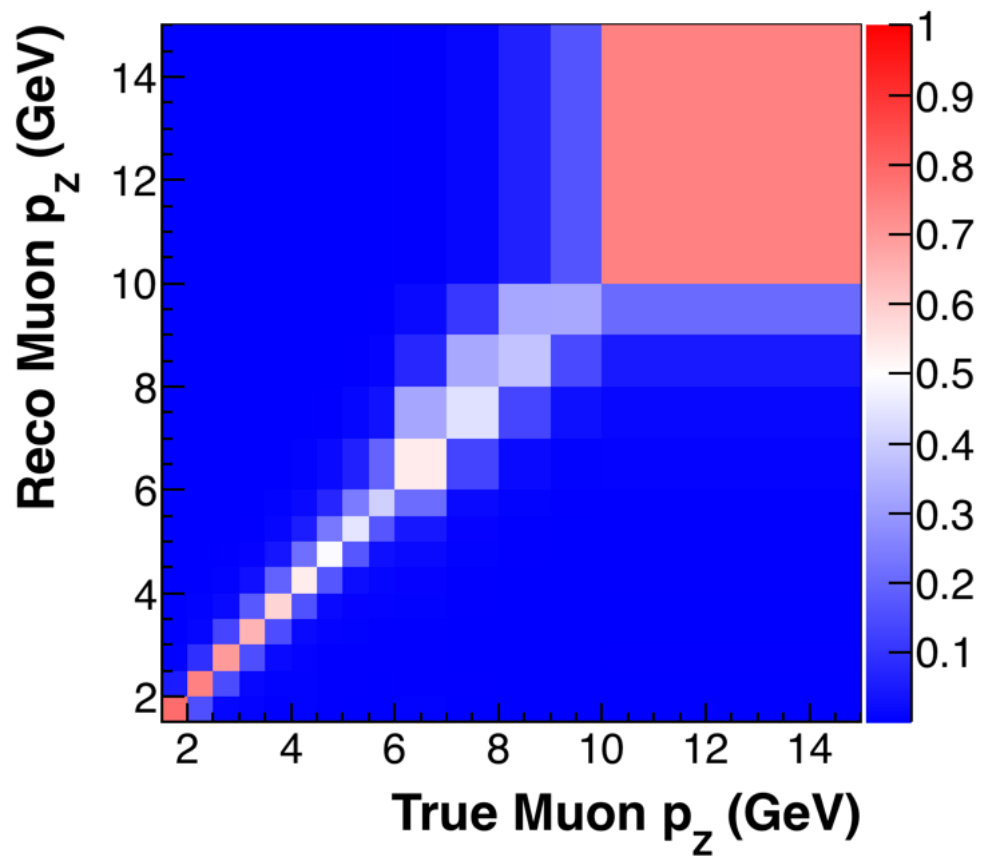
Figure 6.53: Smearing of the reconstructed p_z bins. The plot is row normalized.
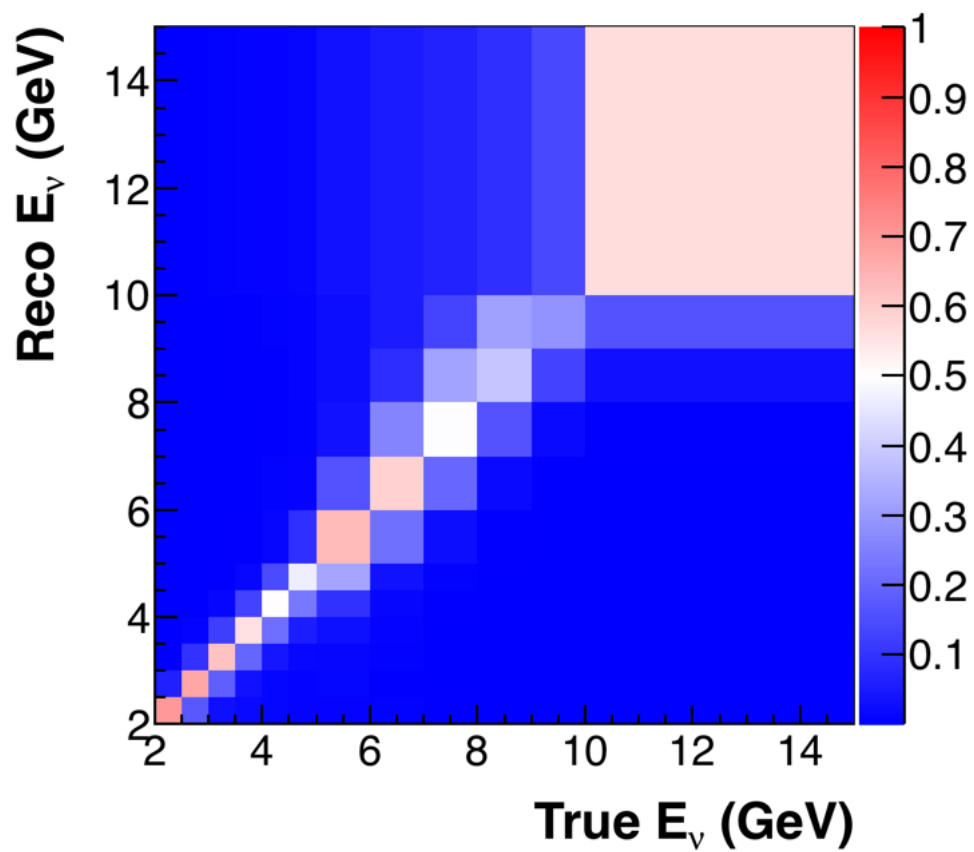
Figure 6.54: Smearing of the reconstruction E_ν bins. The plot is row normalized.
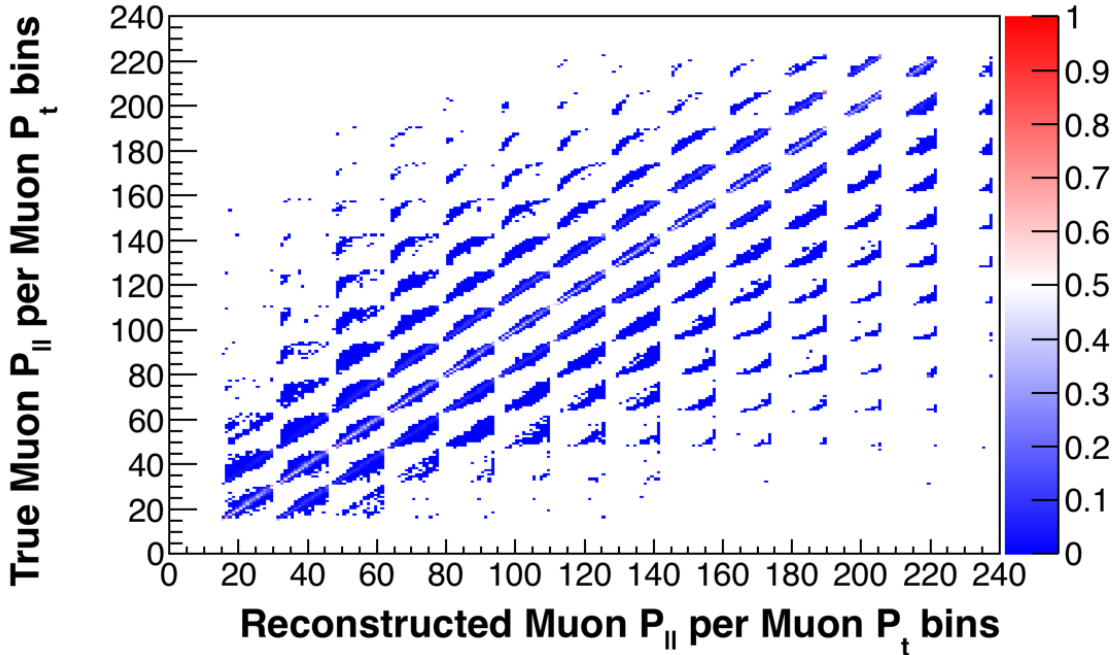
Figure 6.55: Migration matrix for muon $p_{||}$ vs. p_T distribution. The X axis corresponds to the reconstructed bins and the Y axis to the truth bins. The matrix is row normalized to show the diagonality. Each small block contains the migration of $p_{||}$ in each p_T bins.

Figures 6.55 and 6.56 show the migration of the events in the encoded space for muon $p_{||}$ vs. p_T and $E_{\nu\,QE}$ vs. Q^2_{QE} distribution. One of the axis will correspond to the reconstructed bins and another one to truth bins. In the MINERvA , the X axis usually corresponds to reconstructed distribution and the Y axis to truth bins. Each small block is a migration matrix of X component ($E_{\nu\,QE}$ or $p_{||}$) in each bin of Y component (Q^2_{QE} or p_T). The size of the migration matrix is $(x_{bins}+2)\times(y_{bins}+2)$ where the extra 2 factor accounts for underflow and overflow bins. Since we have 14 $p_{||}$ bins and 13 p_T bins, the size of the migration matrix
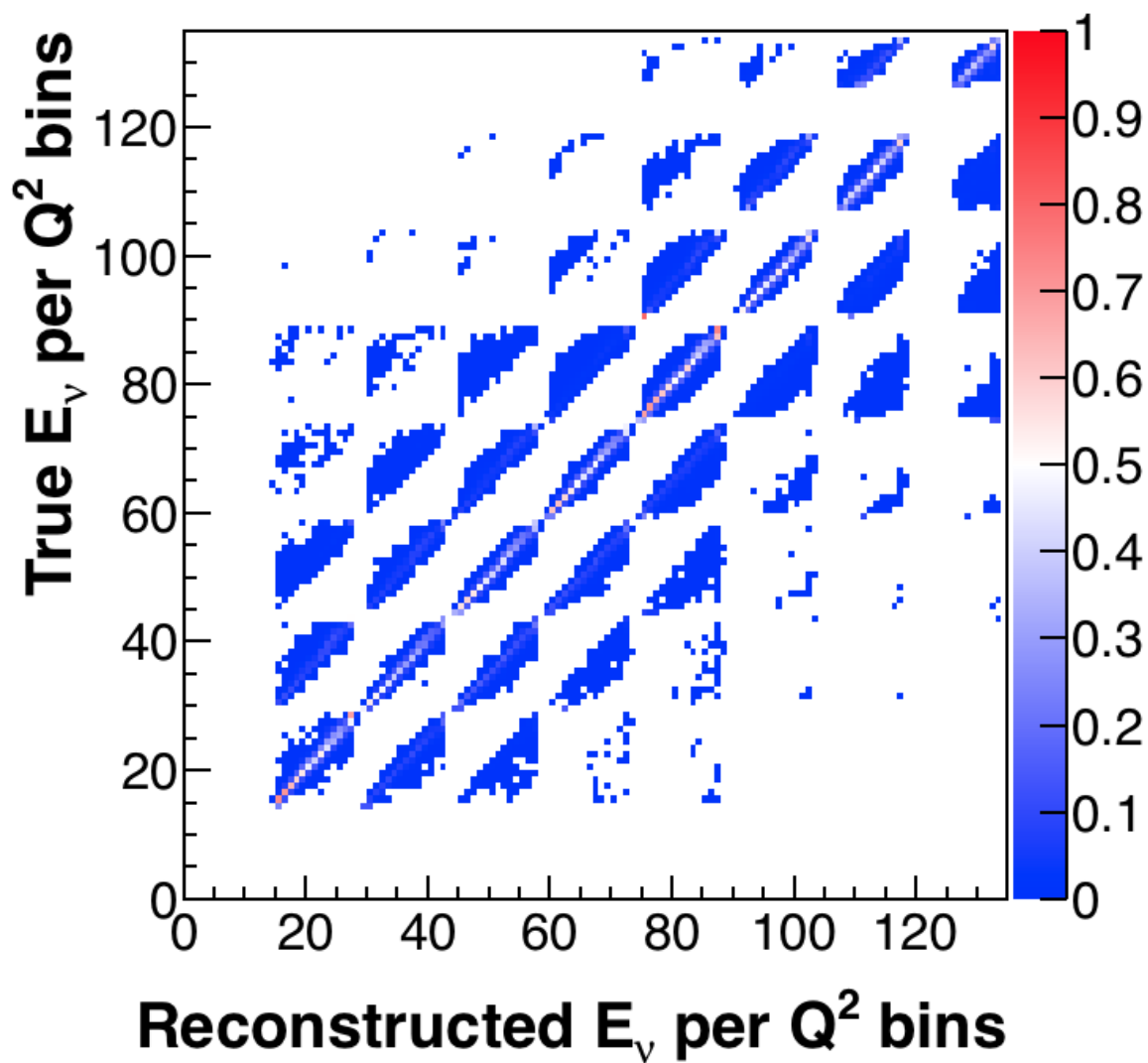
Figure 6.56: Row normalized Migration matrix for $E_{\nu\,QE}$ vs. Q^2_{QE}.

for this distributions is 240×240. Similarly, we have 12 $E_{\nu\,QE}$ bins and 9 Q^2_{QE} bins and the size of the migration matrix is 154×154.

In the figures 6.55 and 6.56, the migration matrices are row normalized. Hence each bin content of the migration matrix represents the probability of an event that is generated in a given true bins, for example, of p_T and p_z to be reconstructed in each of the reconstructed bins of p_Z and p_T. Hence each element of the smearing matrix can be represented as:

$$U_{ij\alpha\beta} = \frac{N^{reconstructed\,\alpha\beta}_{generated\,ij}}{N^{reconstructed}_{generated\,\alpha\beta}} \tag{6.25}$$

[128].

The relation between smearing matrix, true quantities and reconstructed quantities can be thought of as:

$$N^{reconstructed}_{data} = U N^{true}_{data} \tag{6.26}$$

where N^{true}_{data} and $N^{reconstructed}_{data}$ are the column matrices whose element arrangement corresponds to the encoded spacing of smearing matrix U. In principle, the N^{true}_{data} can be calculated if the smearing matrix is invertible i.e.:

$$N^{true}_{data} = U^{-1} N^{reconstructed}_{data} \tag{6.27}$$

A straight forward matrix inversion for a huge matrix like this (for example p_z vs. p_T migration matrix has 57600 elements) is a daunting task. Furthermore, the unfolded true data also depends upon the models from which the matrix is generated. The MINERvA analyses instead use an alternative method to unfold the data.

The MINERvA employs the iterative Bayes' method prescribed by D'Agostini [78] for unfolding it's data from the reconstructed phase space to the true phase space. Since the MINERvA has its way of managing and handling systematic uncertainties, it uses its unfolding tool called the MINERvA Unfold which is based upon the ROOUnfold. In the iterative Bayes' method, in each iteration, the reconstructed distribution is unfolded and a covariance matrix is calculated. The unfolded distribution of a given iteration is an input for the next iteration. The errors from unfolding are added to the unfolded distribution with the correlations taken into account. We rely on the simulation models to figure out the number of iterations after which the unfolded distribution is close to the true distribution. Furthermore, we also need to test the stability of the migration matrix. For example, a poorly constructed migration matrix could lead to large inflation of errors or even further divergence of the unfolded distribution from the true distribution. There are various ways unfolding procedure can be tested against those errors. The following subsection will go through the testing of unfolding procedure.

6.15.1   Testing the Unfolding Procedure

Signal event rate in the experiments cannot be reconstructed perfectly as a function of true physical quantities. There are 3 ways we can miscount the number of events in a given bin: statistical fluctuations, detector effects and background processes.

Our measurements are basically the events drawn from a Poisson distribution which come with some statistical uncertainty. Some of the background events can mimic the signal events and pass our reconstruction events which causes an overestimation of the signal processes. Finally, our detector has a finite energy resolution and angular acceptance of the events. This causes the events to be reconstructed in different bins (bins of physical quantity in which measurements are being done) or get completely lost.

In the context of the MINERvA experiment, the migration matrix (smearing matrix) encodes the information of the true events of certain bins migrating to various reconstructed bins. In principle, we want the migration matrix to be as diagonal as possible i.e. events of a given true bins to be reconstructed in the same bins. Since we are interested in the cross-sections as functions of muon longitudinal and transverse momentum variables as well as four momentum transfer and neutrino energy, we want to make sure that the reconstructed variables are not very far away from the true bins of these variables. The row normalized migration matrices in figures 6.55 and 6.56 show the diagonality of the matrix itself. The migration matrices for muon p_z vs. p_T measurements (shown in figure 6.55) and neutrino energy vs

Q^2_{QE} (shown in figure 6.56) show the overall migration of events in these two different phase spaces. Since these matrices are used to unfold the data to its true spectrum (unsmearing of the reconstructed events), we have to test these matrices. Unfolding studies need to verify that:

- The matrix correctly represents the smearing of the true variables due to detector effects.

- The unfolding is numerically stable. The matrix should be able to unfold events into their true phase space without blowing out the errors. Background events that pass the reconstruction cuts introduce randomness in the reconstructed to the true mapping in the migration matrix. If the background events are significant in the sample, then the unfolded distributions will not be near the true phase space.

To verify that the migration matrix fulfills the above two requirements, unfolding procedure is tested by using fake data. Since the migration matrix is constructed out of MINERvA Tune-v1, the *fake data* are constructed out of the alternate MC samples. Because they are MC samples, the unfolding distribution can be compared against the true distribution to see if the unfolding procedure reproduces the true distribution. This analysis uses the multi

universe method to test the statistical stability of the matrix. Here, the *fake data* is varied within its statistical errors by doing random Poisson throws around the central value. The unfolding is done in each of the statistical universe and a χ^2 is calculated for each iterations. The unfolded distribution of $(i-1)^{th}$ iteration becomes the input *fake data* for the unfolding of ith iteration. In each iteration, a covariance matrix is calculated and the errors are propagated from the previous iteration to the new *fake data*.

One of the initial test of the unfolding procedure is the closure test. Here the migration matrix that is constructed using the MINERvA Tune-v1 is used to unfold the reconstructed *fake data* to the true *fake data* where the *fake data* is also constructed using the MINERvA Tune-v1. Since both the matrix and the fake data are constructed using the same models, reconstructed *fake data* should be able to unfold immediately to the true *fake data* in all statistical universes as seen in figure 6.57. Figure 6.58 shows the χ^2 between the data and the unfolded MC as a function of iteration number for one fake data sample. A detailed study was done by using various alternate models as fake data. Based on those studies, the number of suitable iterations to unfold the reconstructed data in p_z vs. p_T phase space is 4 and in $E_{\nu\,QE}$ vs. Q^2_{QE} phase space is 8. As we can see beyond those number of iterations in figure 6.58, there isn't much improvement in χ^2 and the χ^2 approaches to a minimum around those values in all corresponding statistical universes.
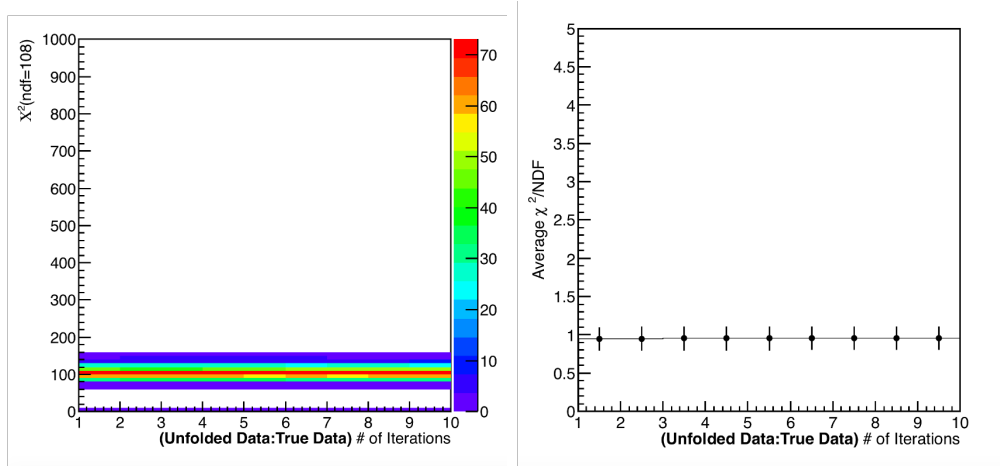
Figure 6.57: χ^2 as a function of number of iteration with fake data and migration matrix constructed out of MINERvA Tune-v1 . Left plot shows the χ^2 distribution in all 200 statistical universes whereas the right plot shows the average χ^2 of those universes as a function of number of iterations. There is one universe whose χ^2 is 0 in the left plot. This is the central value universe based on which the remaining statistical universes are constructed by varying the central values of each bin within their statistical errors.
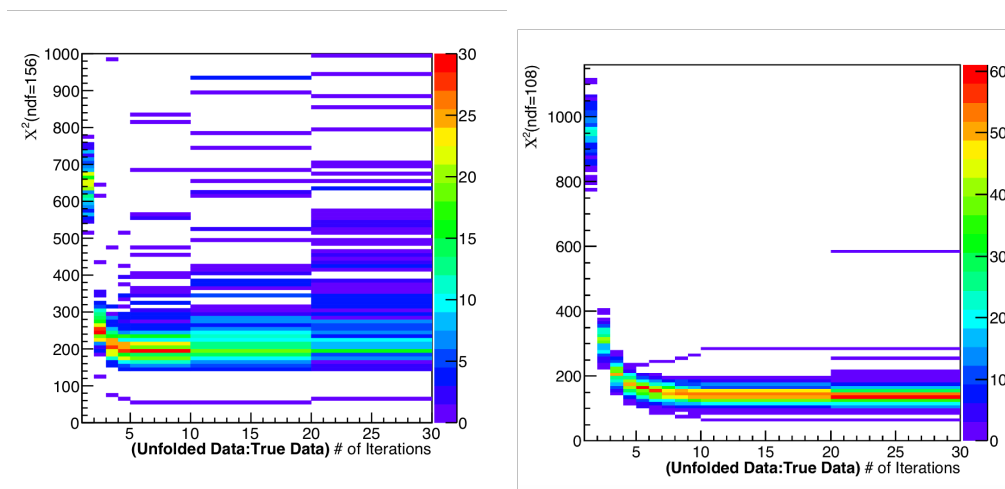
Figure 6.58: χ^2 as a function of number of iteration where fake data is constructed out of GENIE+pion tune and migration matrix is constructed out of MINERvA tune. The left plot shows the χ^2 distribution for 200 stat universes for p_z vs. p_T distribution and the right plot for $E_{\nu\,QE}$ vs. Q^2_{QE} distribution.

The χ^2 calculated in each iteration is given by:

$$\chi_k^2 = [n_k - n_{true}]_i V_{i\alpha}^{-1} [n_k - n_{true}]_\alpha \tag{6.28}$$

Here n_k is number of events in the distribution that is unfolded k^{th} times. n_{true} is the number of true events. i is the true bin and α is the reconstructed bin. $V_{i\alpha}$ is the covariance matrix calculated in that particular iteration.

The migration matrix is constructed for the signal events only since the final cross-section measurements are done for QELike events. Reconstructed data will have background contamination due to our imperfect signal selection cuts. Hence, we need to estimate the background in our data and subtract it from the sample.

6.16   Cross-Section Extraction

Revisiting the cross-section formula in equation 6.5:

$$\left(\frac{d^2\sigma}{dxdy}\right)_{ij} = \frac{\sum_{\alpha\beta ij} U_{\alpha\beta ij}(N_{data,\alpha\beta} - N_{data,\alpha\beta}^{bkg})}{\epsilon_{ij}(\Phi T)(\Delta x_i)\Delta(y_j)}. \tag{6.29}$$

In this section, we will go through the distribution after each operation in the cross-section formula give above. Figures 6.50 and 6.51 shows the background subtracted distribution for

muon p_z vs. p_T and E_ν vs. Q^2. This background subtracted distribution needs to be unfolded to the true distribution. The migration matrix U maps the reconstructed distribution to the true distribution.

6.16.1   Unfolded Data Distribution

Based on the unfolding studies with various alternate MC samples, the number of iteration to unfold the $p_z vs. p_T$ distribution is 4. Similarly, to unfold the $E_\nu vs. Q^2$ distribution is 8.

The unfolded distribution of the background subtracted data corresponds to the CCQE-like events as a function of true variables. This distribution is corrected for detector smearing. During the unfolding, the events move from one bin to another. Since the migration matrix accounts for the migration in the underflow and overflow bins, the events could move in and out of the sample as well. One of the effects of unfolding is that uncertainties like muon energy scale gets inflated. The bin to bin migration of data during unfolding moves some of the data events to the higher or lower true bins. In figures 6.59 through 6.62, the error bars on the unfolded data is the total error. The blue rectangles show the statistical errors on the data. The pink band is the error on the unfolded MC.
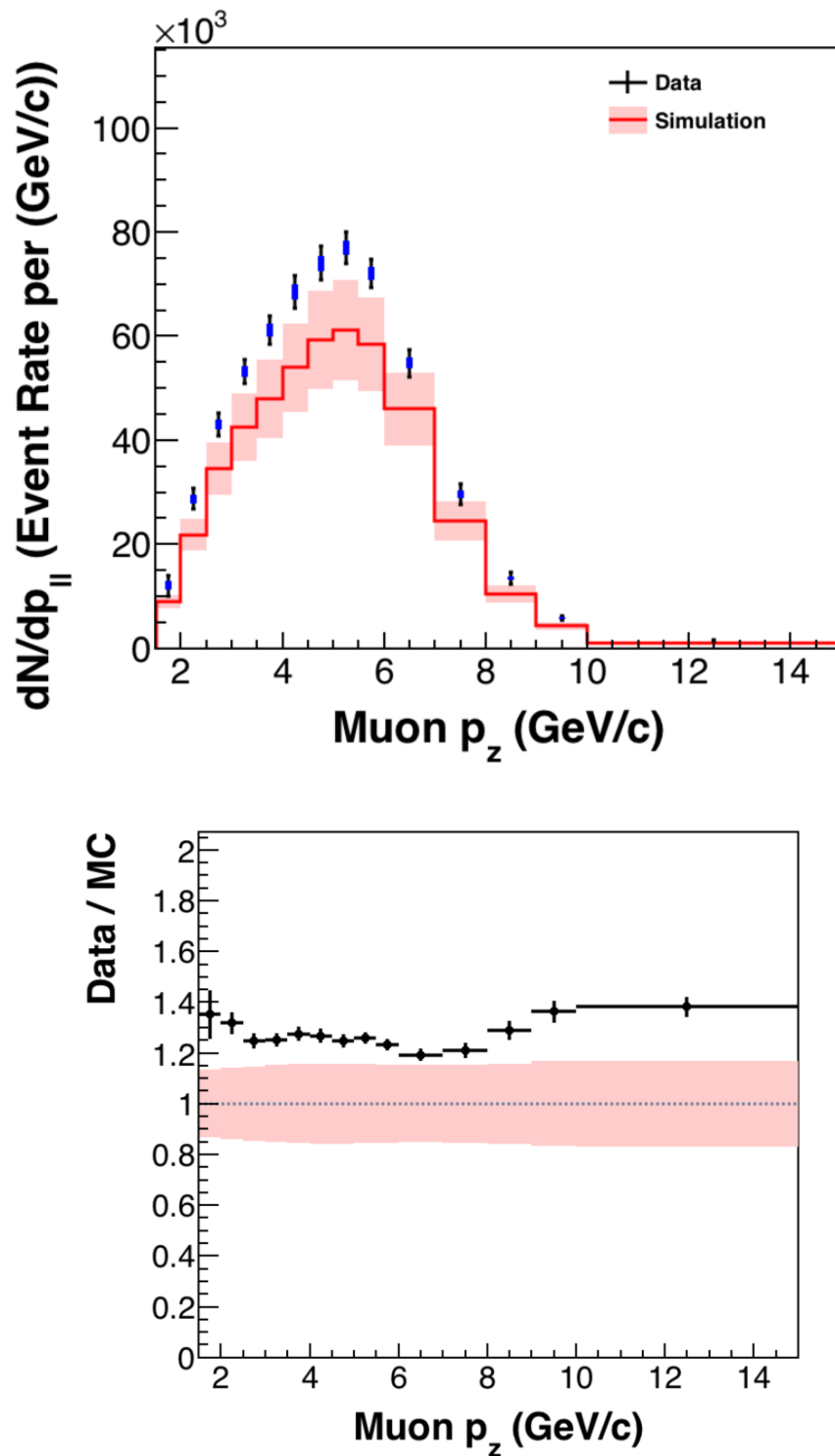
Figure 6.59: The unfolded distribution projected on muon p_Z phase space. The top plot shows the unfolded data and MC with the pink error band showing the systematic errors on the MC. Blue rectangles show the statistical error on the data. The bottom plot shows the ratio of data to MC of the top plot.
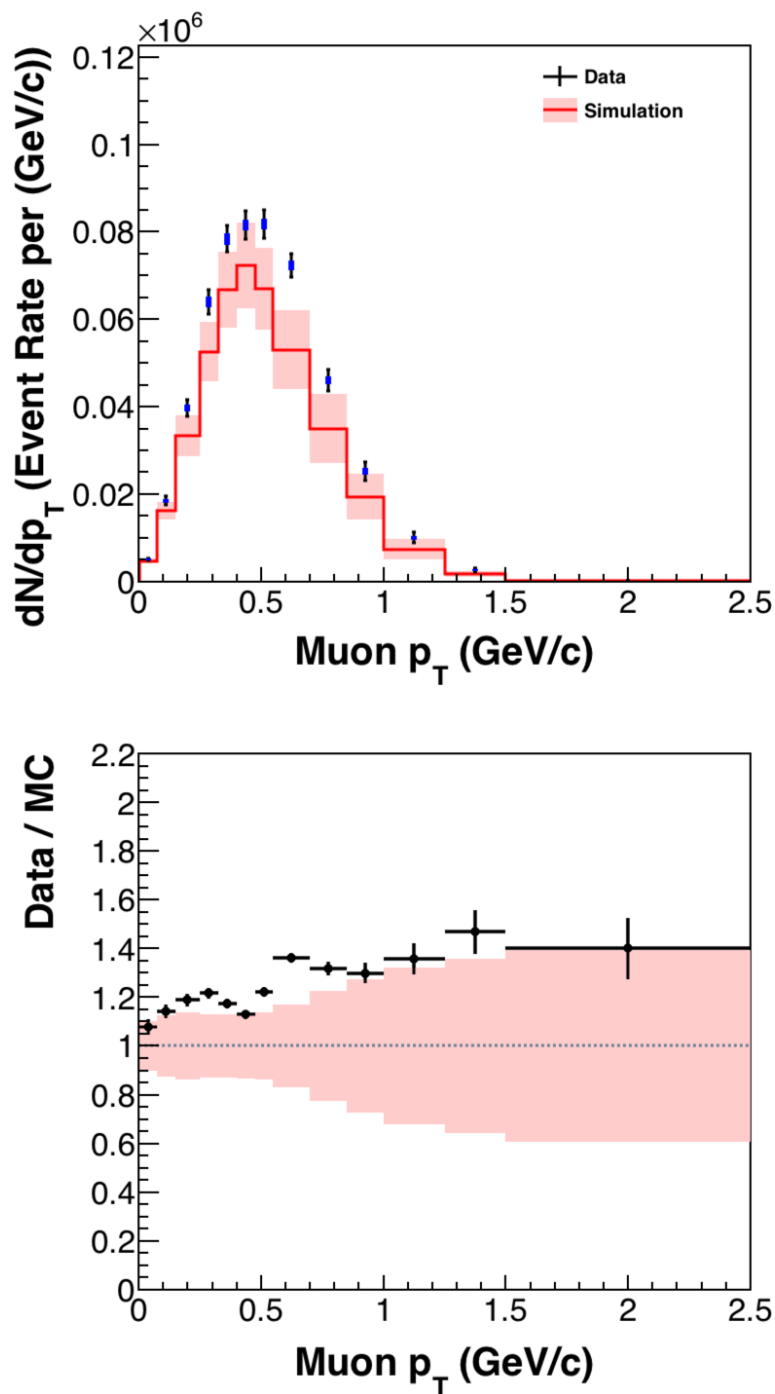
Figure 6.60: The unfolded distribution projected on muon p_T phase space. The top plot shows the unfolded data and MC with the pink error band showing the systematic errors on the MC. Blue rectangles show the statistical errors on the data. The bottom plot shows the ratio of data to MC of the top plot
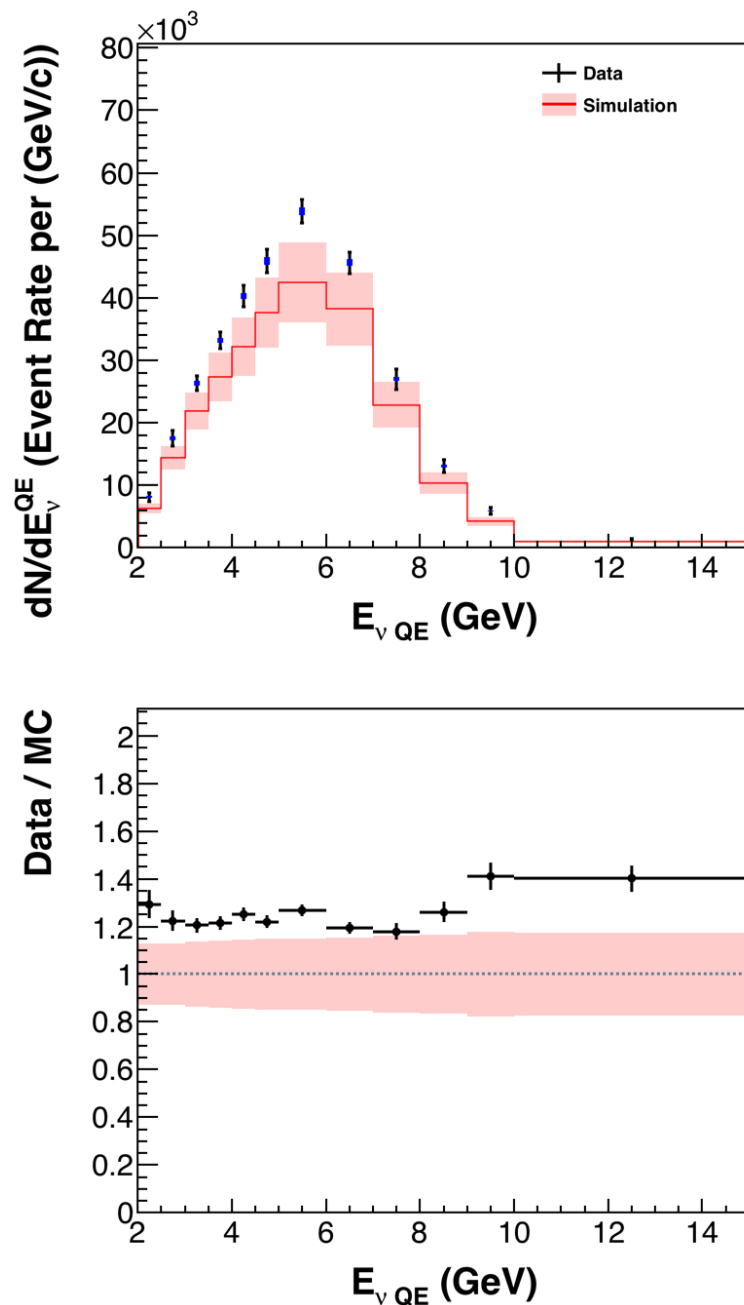
Figure 6.61: The unfolded distribution projected on $E_{\nu\,QE}$ phase space. The top plot shows the unfolded data and MC with the pink error band showing the systematic errors on the MC. Blue rectangles show the statistical errors on the data. The bottom plot shows the ratio of data to MC of the top plot.
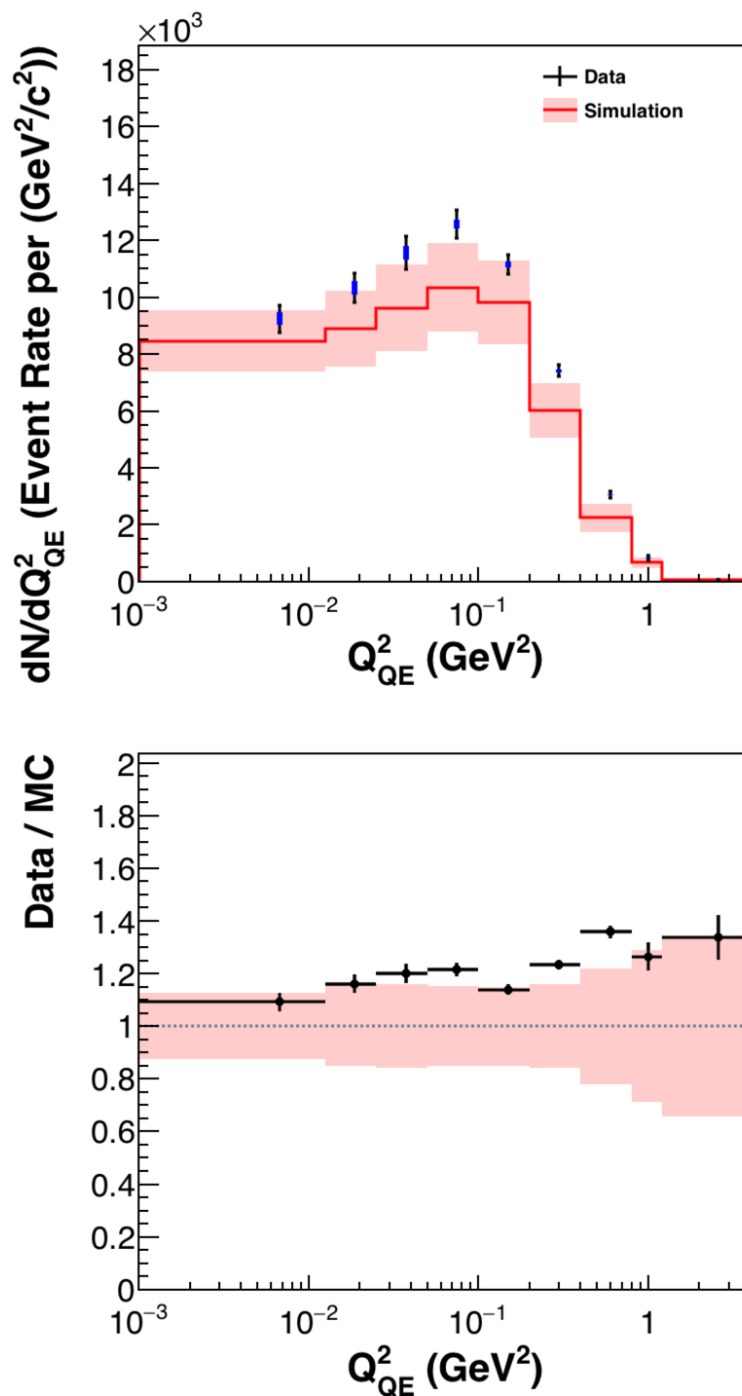
Figure 6.62: The unfolded distribution projected on Q^2_{QE} phase space. The top plot shows the unfolded data and MC with the pink error band showing the systematic errors on the MC. Blue rectangles show the statistical errors on the data. The bottom plot shows the ratio of data to MC of the top plot.

6.16.2   Efficiency Correction

As discussed in 6.12, our signal selection procedure is not perfect. Hence the selected sample doesn't account for all the true signal events in the sample. Overall, we select 70 to 80% of the total true signal events as shown in figures 6.25 and 6.26 respectively. The loss in efficiency comes from the limitation of our detector's acceptance and the reconstruction algorithms. Because of the limitations due to detector technology, acceptance etc., a fraction of signal events cannot be seen. For example, we require the final state muons tracks in the MINERvA detector to match with a track in the MINOS detector. Because the MINOS detector is 2 meters downstream of the MINERvA detector, not all muon tracks reconstructed in the MINERvA detector can make it to the MINOS detector which is required to get the charge and momentum info of the final state muon. We require the muon tracks to be less than 20 degrees with respect to the beamline to assert that they are matched with a muon track in the MINOS. This 20 degrees requirement leads to the loss in signal events with high transverse and low longitudinal muon momentum. Similarly, muons with low longitudinal momentum can never make it to the MINOS detector.

The Q^2 dependent recoil energy cut is constructed to optimize the signal selection efficiency and the purity of the selected sample. Hence, we lose a fraction of our signal events that are outside the recoil cut.

High energy muon tracks are forward and escape the downstream MINOS detector as well. Momentum of the muons that escape the MINOS detector are reconstructed by looking at the bending of their tracks due to the magnetic field of the MINOS detector. However, if the muon is very high energy, the curvature of the track might be too small to determine the charge and momentum of the muons. Hence we exclude muons above 15 GeV/c longitudinal momentum from our signal sample. This results in the loss of signal events with forward tracks and high momentum final state muons.

This loss in efficiency due to the limitations of reconstruction algorithms and detector acceptance has to be accounted for in the unfolded data sample. Since both limitations cause the reduction of signal events, they are corrected by constructing a 2-D efficiency histograms (p_t vs. p_z and $E_{\nu\,QE}$ vs. Q^2_{QE}) such that each bin content (i,j) is populated by ϵ_{ij} as $\epsilon_{ij} = \frac{N_{ij}^{Generated\,and\,Reconstructed}}{N_{ij}^{Generated}}$.[128] Here, the numerator is the true signal sample that passes our reconstruction cuts and the denominator is the true signal sample. We rely on the generator level (or truth level) information to select the true signal events. The true signal events populate the denominator histogram and true signal events that pass our reconstruction cuts populate the numerator histogram as shown in equation 6.16.2. Since the unfolded data sample now is a function of true variables, the efficiency correction can be done bin by bin for the given set of true variables. Any systematic uncertainties on the efficiency also gets

propagated to the data during efficiency correction.

6.16.2.1 Muon Tracking Efficiency Correction

We rely on the muon tracks to identify our signal events and reconstruct the muon kinematics. There are three different efficiency corrections related to muon tracks that needs to be accounted for: the MINERvA tracking efficiency, the MINOS tracking efficiency and the MINOS matching efficiency. The next few paragraphs will briefly go through these tracking efficiencies.For both the MINERvA and the MINOS, the loss in efficiency comes from the failure of the track reconstructing software to identify a muon track. Events happening during the detector dead time and broken tracks result in failure to reconstruct the muon tracks. Since the muon tracks are simulated one at a time, dead time effects are simulated by overlaying the actual data events [73].

The tracking efficiency for the MINERvA detector is estimated by looking at the MINOS matched muon tracks and extrapolating back to the MINERvA detector and calculating the fraction of the extrapolated tracks that match those reconstructed in the MINERvA detector [128]. The MINERvA tracking efficiency is around 99.5%. Detailed study on MINERvA tracking efficiency is given in [142].
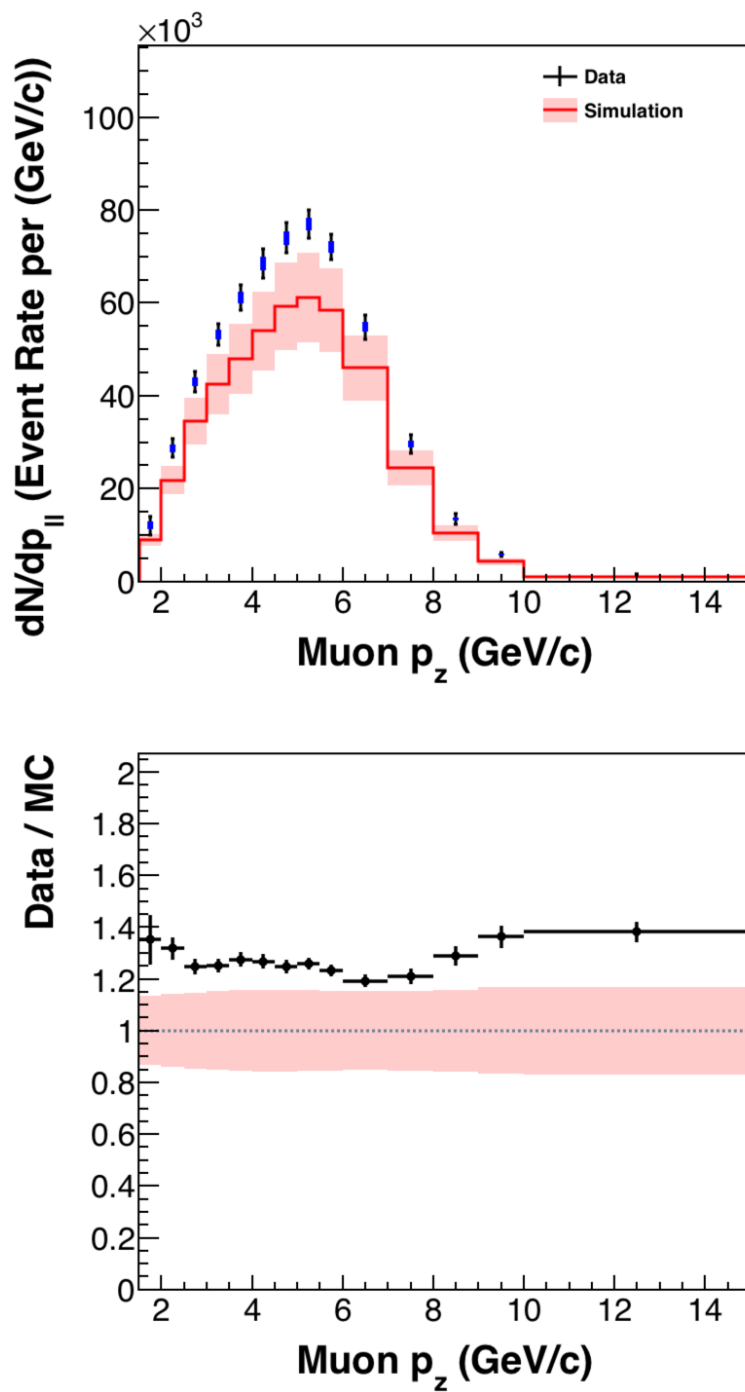
Figure 6.63: Data and MC distribution after unfolding and efficiency correction as a function of p_z. Blue rectangles show the statistical errors on the data.
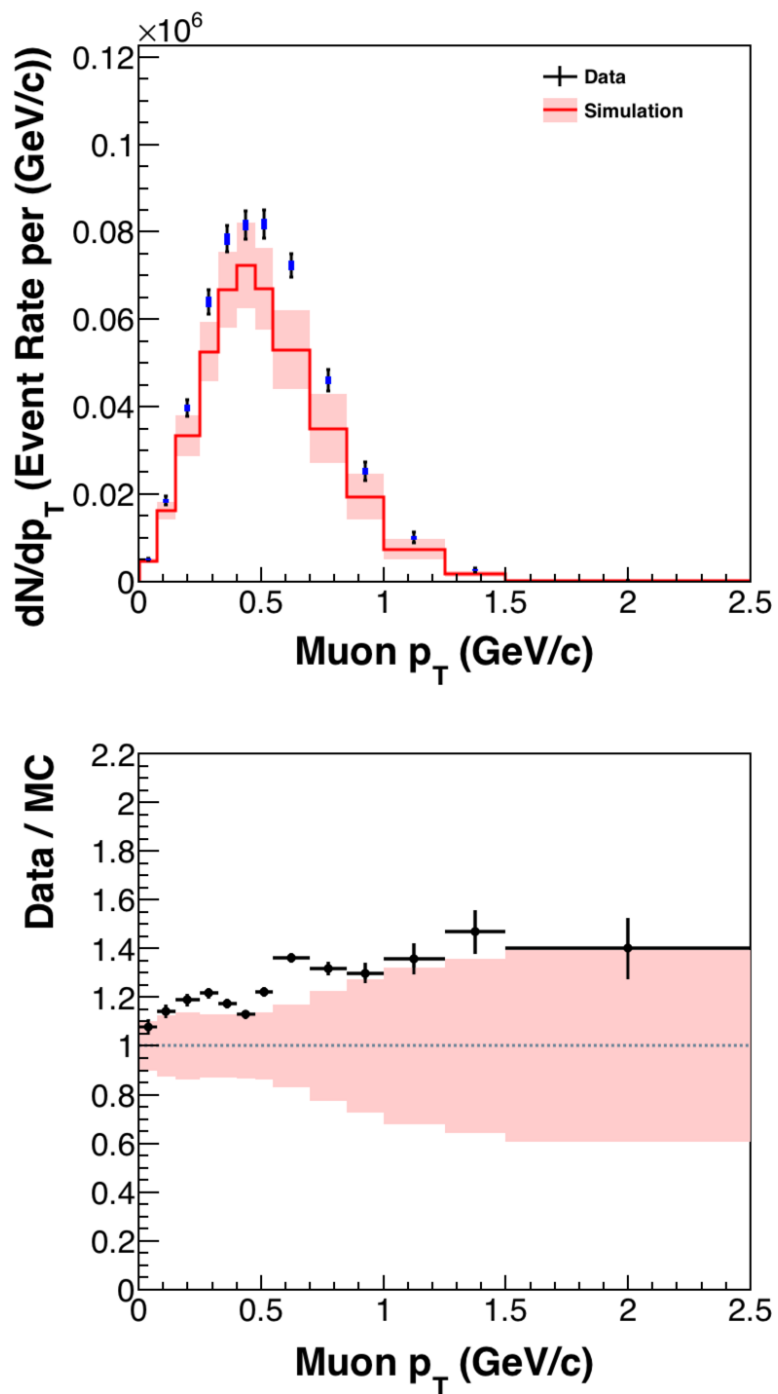
Figure 6.64: Data and MC distribution after unfolding and efficiency correction as a function of p_T. Blue rectangles show the statistical errors on the data.
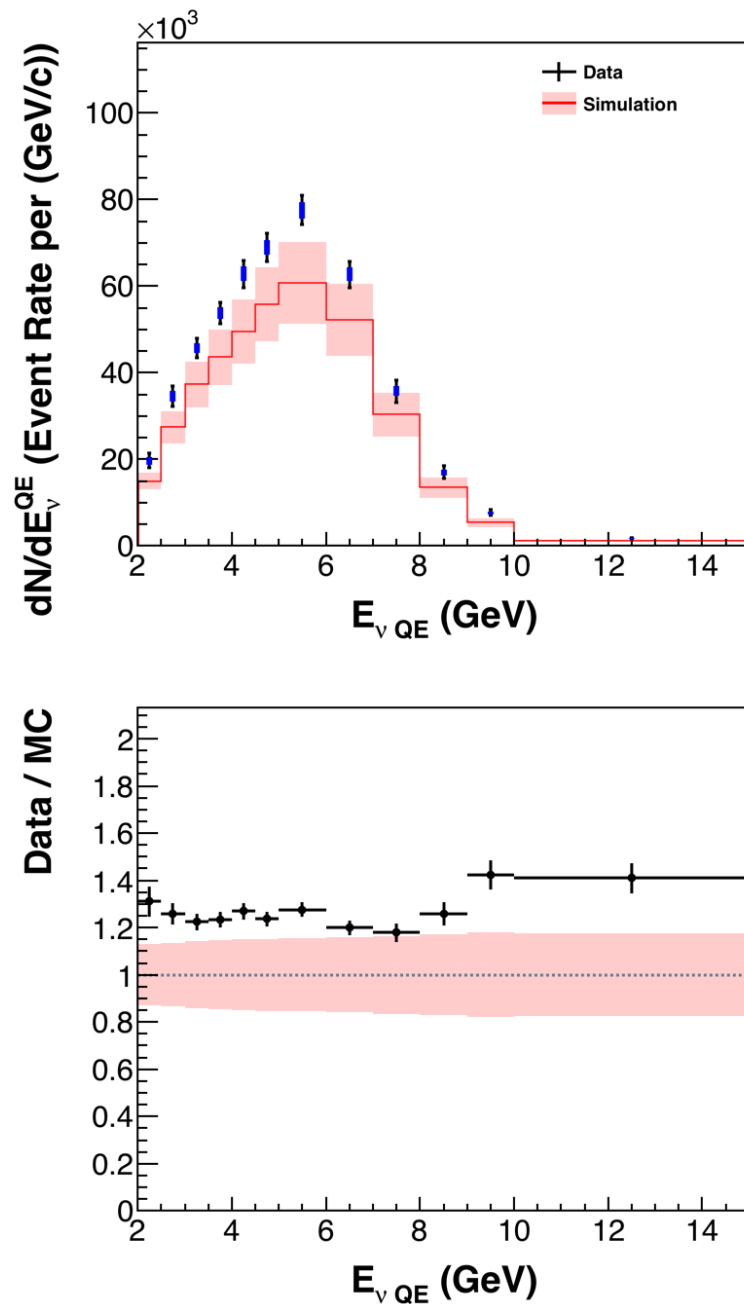
Figure 6.65: Data and MC distribution after unfolding and efficiency correction as a function of $E_{\nu\,QE}$. Blue rectangles show the statistical errors on the data.
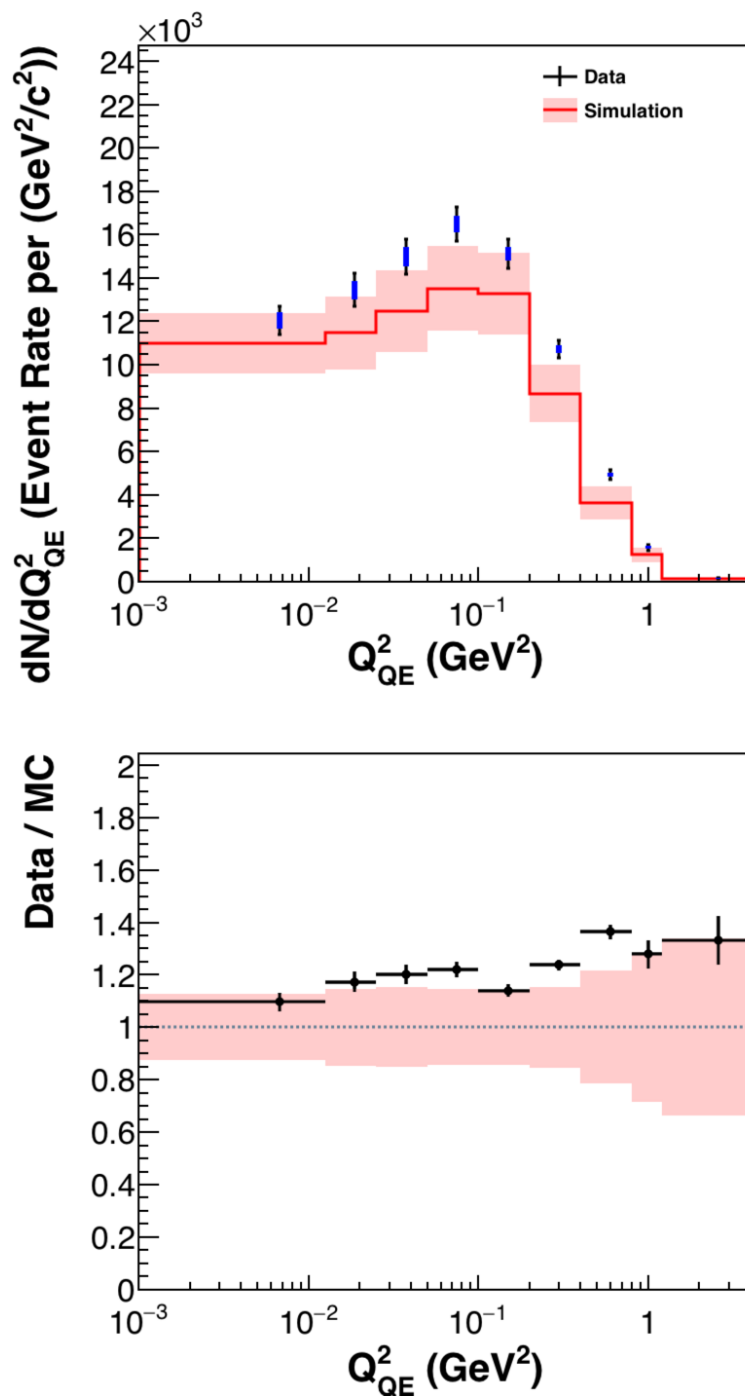
Figure 6.66: Data and MC distribution after unfolding and efficiency correction as a function of Q^2_{QE}. Blue rectangles show the statistical errors on the data.
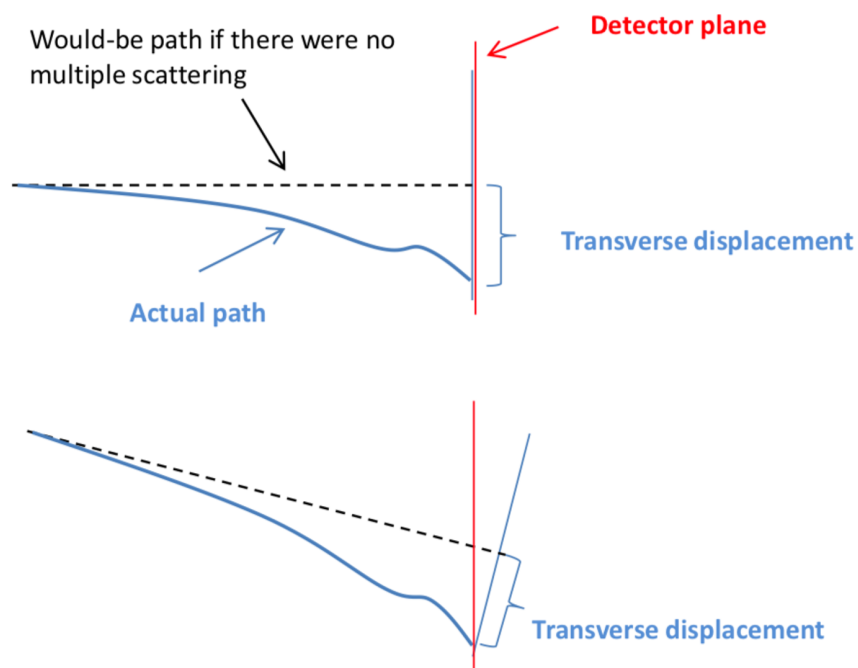
Figure 6.67: Example of the transverse displacement of muon tracks due to multiple scattering. The upper figure is the muon track parallel to the beam axis and the lower figure is the muon track at some angle with the beam axis. Figure taken from [99].

To calculate the MINOS tracking efficiency, we look at the momentum distribution of muons as a function of transverse displacement (due to multiple scattering) of the muons from their ideal track (had there been no multiple scattering) in the downstream ECAL and HCAL regions of the MINERvA detector. In the low energy (LE) analyses, the efficiency was calculated for the muon momentum below (above) 3 GeV/c by looking at the transverse displacement less than 10 mm (greater than 40 mm). This method gave an overall efficiency correction of 5% and 1% for the low (less than 3 GeV/c) and the high (more than 3 GeV/c)

momentum muons.

The new method, as explained in [13], divides the transverse displacement into small ranges and looks at the muon momentum distribution in those ranges. For each displacement range, the momentum distribution for data and MC can be reconstructed and the most probable value of the momentum is calculated doing a Landau fit as shown in figure 6.68. The tracking efficiency for data and MC is calculated by dividing the number of MINOS matched MINERvA tracks with the MINERvA tracks that point towards the MINOS fiducial area. An efficiency correction is calculated by taking the ratios of the efficiency for the data to the MC as shown in figure 6.69 and doing a 5th order polynomial fit to the correction factor. This efficiency correction as a function of muon momentum also depends upon the intensity of the proton beam. The NuMI beam in the anti-neutrino mode ran on two different beam intensities. The error on this efficiency correction is calculated as a function of muon track angle. Hence, the efficiency correction is done as a function of muon momentum and the error on this efficiency correction is calculated as a function of muon track angle. The efficiency correction and related error is handled by MinosMuonEfficiencyCorrection in PlotUtils.
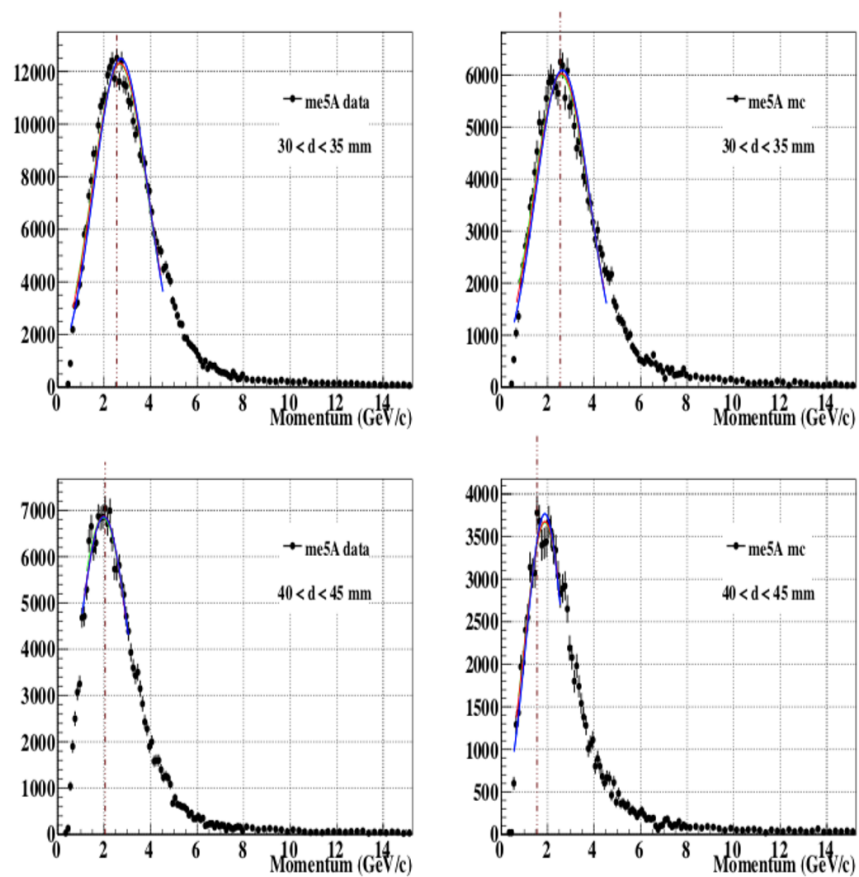
Figure 6.68: Momentum distribution of the muons for the data (left) and the MC right) for two different transverse displacement ranges. The most probable value (MPV) of the momentum is shown with dotted vertical line. Figure taken from [13].
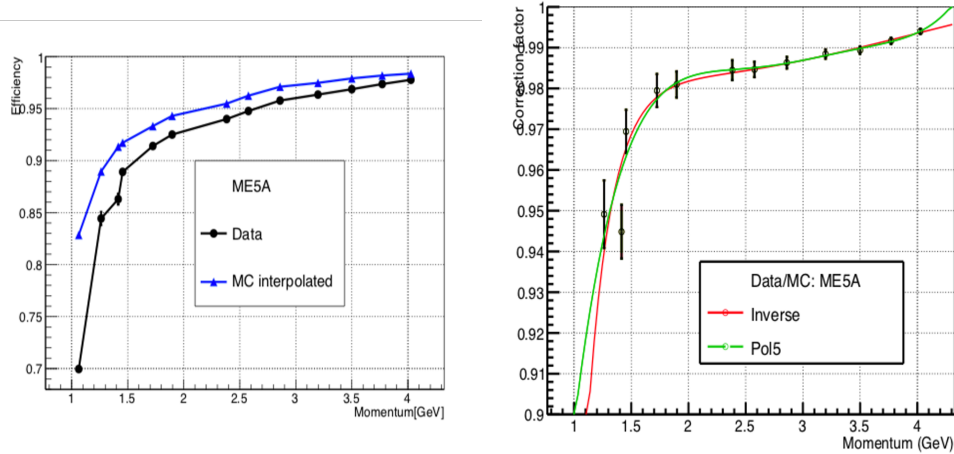
Figure 6.69: MINOS tracking efficiency for data and MC for MINERvAME5A playlist (left) and efficiency correction for the same playlist. Figure taken from [13].

6.16.3 Flux and Target Normalization

The neutrinos that interact in the MINERvA detector are produced in the NuMI beamline whose average neutrino energy is around 6 GeV. The neutrino-nucleus interactions are measured over a fiducial volume (the tracker region for this analysis) of the MINERvA detector. The average neutrino-nucleus cross-section is extracted by dividing the unfolded and efficiency corrected signal data events by incoming neutrino flux and the number of targets in the fiducial volume. The fiducial volume has 3.23×10^{30} scintillator nucleons which is calculated using the MINERvA 's TargetUtils code. In the case of muon momentum variables, the unfolded and efficiency corrected signal data distribution is normalized by integrated flux. However, in the case of $E_\nu vs. Q^2$ distribution, the flux normalization is done bin by

bin so that the data events of a given neutrino energy bin is normalized by the flux of the corresponding neutrino energy bin. The latter distribution produces a cross-section measurement that is independent of the shape of the energy spectrum of the incoming neutrino flux. The Q^2_{QE} projected cross-section is extracted by dividing by the integrated flux. Since the overall aim of this analysis is to get the cross-section measurements as a function of these 4 variables, 6.20 will go through the detailed discussion on the cross-section results.

6.17   Systematic Uncertainties and propagation through the analysis

6.17.1   Uncertainties

Like any real experiments, the measurements or the observations are subject to uncertainties. Since MINERvA experiment is essentially a counting experiment, it is subjected to statistical errors. Similarly, MINERvA uses various instruments to count the neutrino interactions. These measurement devices and procedures are not perfect and can systematically bias the observed number of interactions. Similarly, we rely on various simulation models to measure variables like energy deposited by the various particles in the MINERvA detector. Parameters that are used in these models might have uncertainty which gets propagated into the simulation models as well. These uncertainties which arise from counting neutrino event rates should be propagated all the way to cross-section to get a reliable estimate of our final

measurements.

6.17.2 Statistical Uncertainties

Like any counting experiment, this analysis is also subject to the statistical errors. Since the neutrino interaction is a random process, each neutrino entering the MINERvA detector has the probability of interacting or not interacting with the detector material. With large number of interactions, this inherently binomial distribution can be approximated as a Poisson distribution in which the errors on the interaction rate can be estimated as the square root of the interaction rate [91]. While the interaction counts in our data are truly random processes, we simulate these random processes in the simulation by using random number generators. For this analysis, the neutrino events are simulated by twice the number of protons on target (POT) used to generate data. The statistical uncertainties in data and MC are not correlated and hence added in quadrature to get the total statistical uncertainties.

6.17.3 Systematic Uncertainties

We want to count the neutrino interactions as a function of certain physical quantities. We rely on various instruments to measure those quantities. Similarly, we rely on theoretical

models and simulations that describe the experimental observations of the quantities. The measurement devices are not infinitely precise and their measurements will have systematic uncertainty due to the nature of the devices. For example, a PMT could have a limited energy resolution. The width of the scintillator strip introduces a position uncertainty equivalent to its width for a track or a blob that forms in that strip. We rely on various models to estimate the background and signal processes. These models rely on parameters that have uncertainties which get propagated to the final prediction from the simulation. Systematic uncertainties need to be propagated through various stages of the analysis to the final cross-section results. We can divide the MINERvA systematic uncertainties into the following categories:

- **Reconstruction systematic uncertainties:** The reconstruction systematic uncertainties arise from the limited ability of our detector to reconstruct physical quantities like the energy or the position of a blob. It also arises from our reconstruction algorithms that we use to reconstruct those blobs or tracks in our detector. Some particles like pions and protons have similar dEdx profile. Hence the PID, (particle identification) which depends upon the energy deposition profile, assigned to a particle could have uncertainty.

- **GENIE Model Uncertainties** We rely on the GENIE models to estimate our cross-section. Specifically, we rely on the models to get the estimates of our backgrounds,

migration of the signal events from reconstructed to generated bins and the efficiency of the signal selection process. These uncertainties get propagated to our data during the background subtraction, the unfolding and the efficiency correction.

- **Flux Uncertainties** Flux uncertainties can be taken as a part of the model uncertainties. We rely on the GEANT4 to simulate the neutrino flux produced in the NuMI beamline, the source of the neutrinos for the MINERvA detector. Neutrino production relies on our knowledge of the beamline. The uncertainties on the beamline parameters like the horn current, the energy of primary proton etc need to be propagated to the simulated neutrino flux. Similarly, the hadron production models that are used to simulate the neutrino parents have uncertainties that needs to be accounted for. The MINERvA experiment has implemented various methods (like low-ν and $\nu + e$ constraints) to constrain the uncertainty on the flux. This analysis uses 200 flux universes that are $\nu+e$ constrained. Chapter 3.3 of this thesis goes through the flux uncertainties in detail.

A table of parameters in the above the systematic uncertainty categories and their corresponding 1σ uncertainties is given in appendix D.

6.17.4   Calculating Systematic Uncertainties

In the MINERvA experiment, we use a multivariate method called the universe method to calculate the systematic uncertainties. Here, a set of alternate samples are generated by varying the models by shifting within their normalized $\pm 1\sigma$ shifted values. The RMS of the alternate samples gives the uncertainty on our measurement. The distribution where the parameter values are fixed at their central value is called the central value distribution (or CV distribution). Similarly, the distribution where one or more parameters are shifted from their central values is called a systematic universe (or simply the universe). Depending on the number of parameters with uncertainties, we use two different approaches to estimate the systematic uncertainties.

6.17.4.1   Two Universe Method

Systematic uncertainties arising from the models where there is only one uncertain parameter, can be estimated by using the 2 universe method. Here, the parameter is shifted by $+1\ \sigma$ (from central value of the parameter) to generate one universe and again shifted by $-1\ \sigma$ to generate another universe. The RMS of the two distributions gives the uncertainty on the measurement due to that model. Most of the model related uncertainties and the reconstruction related uncertainties arise from one free parameter and hence employ two
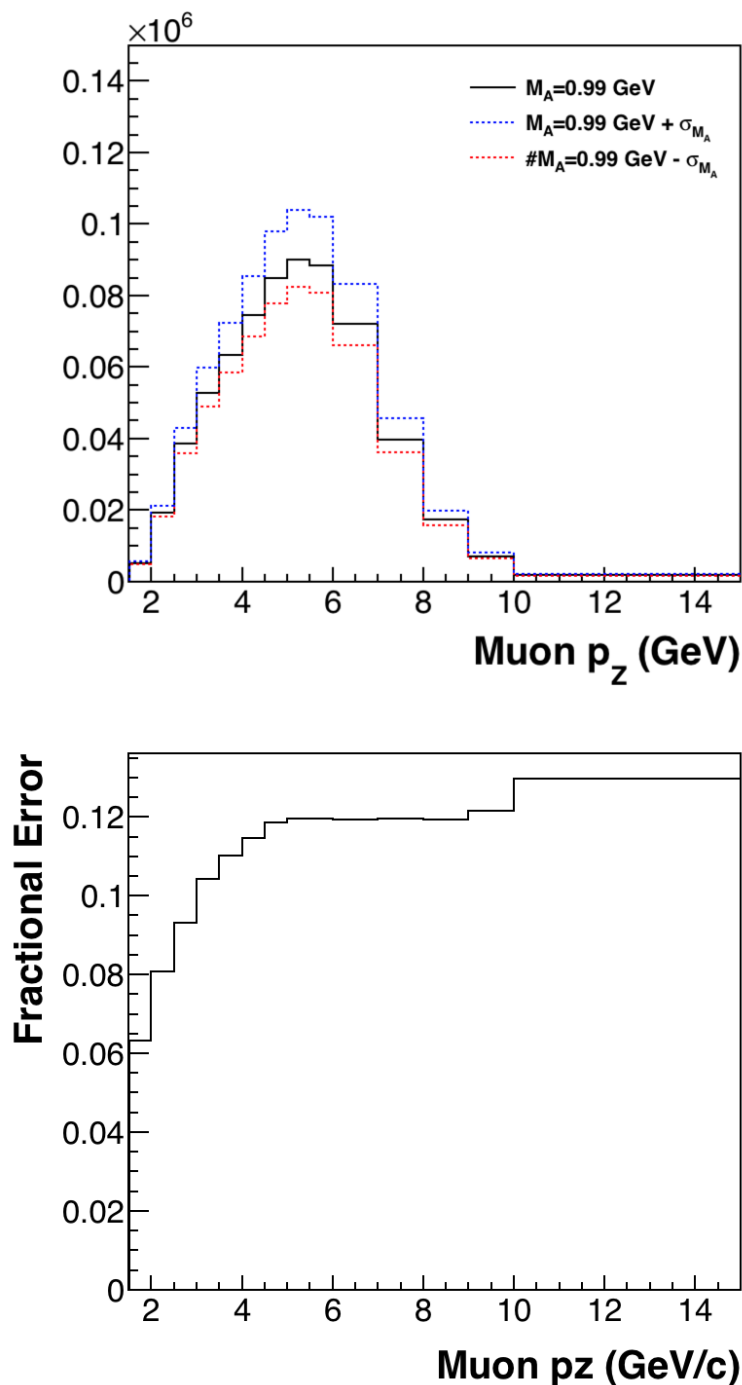
Figure 6.70: Two universes where the axial mass is shifted by $\pm 1\sigma$ from its central value of 0.99 GeV (left). The uncertainty on the axial mass in the GENIE's framework is -15% +25% [25]. The black histogram shows the central distribution where the axial mass is not shifted (i.e. $M_A = 0.99 GeV$). On the right is the fractional uncertainty on the p_z distribution due to uncertainty arising from M_A.

universe method.

6.17.4.2 Multi Universe Method

Flux models, for example, have multiple unknown parameters. Furthermore, these parameters could be correlated to one another which makes a 2 universe like method unfeasible. Hence, we use a multi-universe method [20] to estimate the uncertainty by taking the correlation between parameters into account. We assume that the covariance matrix of the parameters is known. Then for this model with n number of parameters, a varied set of parameters is generated as:

$$\vec{v} = \vec{v}_o + \mathbf{L}.\vec{r} \tag{6.30}$$

Here $\vec{v}_o$ is a column vector of central values of parameters whose size is $1 \times n$. Similarly, $\mathbf{L}$ is the Cholesky decomposition of the covariance matrix. $\vec{r}$ is a vector of random number generated from a normal distribution. Finally $\vec{v}$ is the vector of varied parameters. Using these varied parameters, an alternate universe is generated. The number of alternate universes depends upon the covariance matrix and the size of the vector v_o. This analysis uses 200 random universes to model the uncertainties on flux due to the hadron production and the focusing in the beamline.
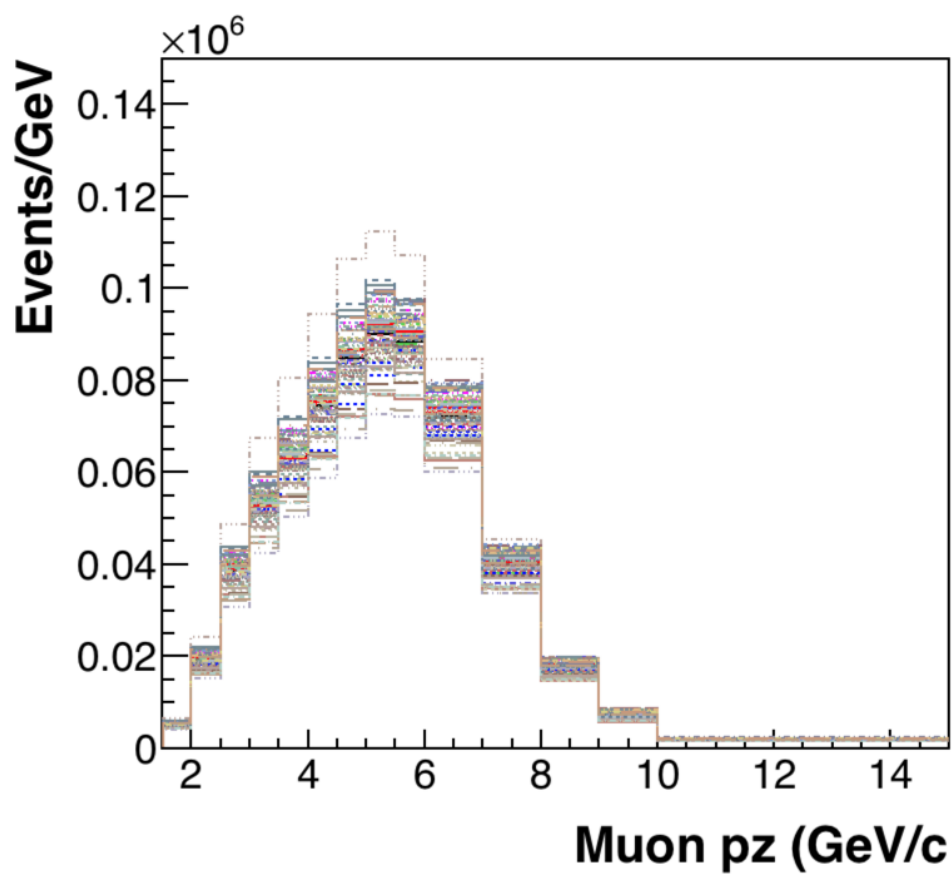
Figure 6.71: Distribution of 100 flux universes coming from the Flux systematic uncertainties in the muon p_z distribution

6.18 Classification of Uncertainties

In this analysis, we evaluate more than 50 uncertainties. Plotting all of these systematic uncertainties in an informative way is not possible. Hence we further categorize these uncertainties into various categories. Figure 6.72 shows the error summary on the raw event distribution of the simulation. The error is dominated by the cross-section model. We can further breakdown each of these groups to see the overall contribution from each of these systematic uncertainties.

6.18.1 Cross-Section Models

The Cross-section model systematic uncertainties include the various cross-section models that the GENIE uses to simulate various neutrino-nucleus interaction events producing initial state particles.

- **MaCCQE** This cross-section model systematic uncertainty is dominated by systematic uncertainties due to axial mass since the default uncertainty on the M_A is large in the GENIE ($-15\% + 25\%$). Since our signal sample is mostly true QE, this uncertainty affects our signal sample.

- **MaRES** This is the GENIE model that is used to produce a charged current resonance
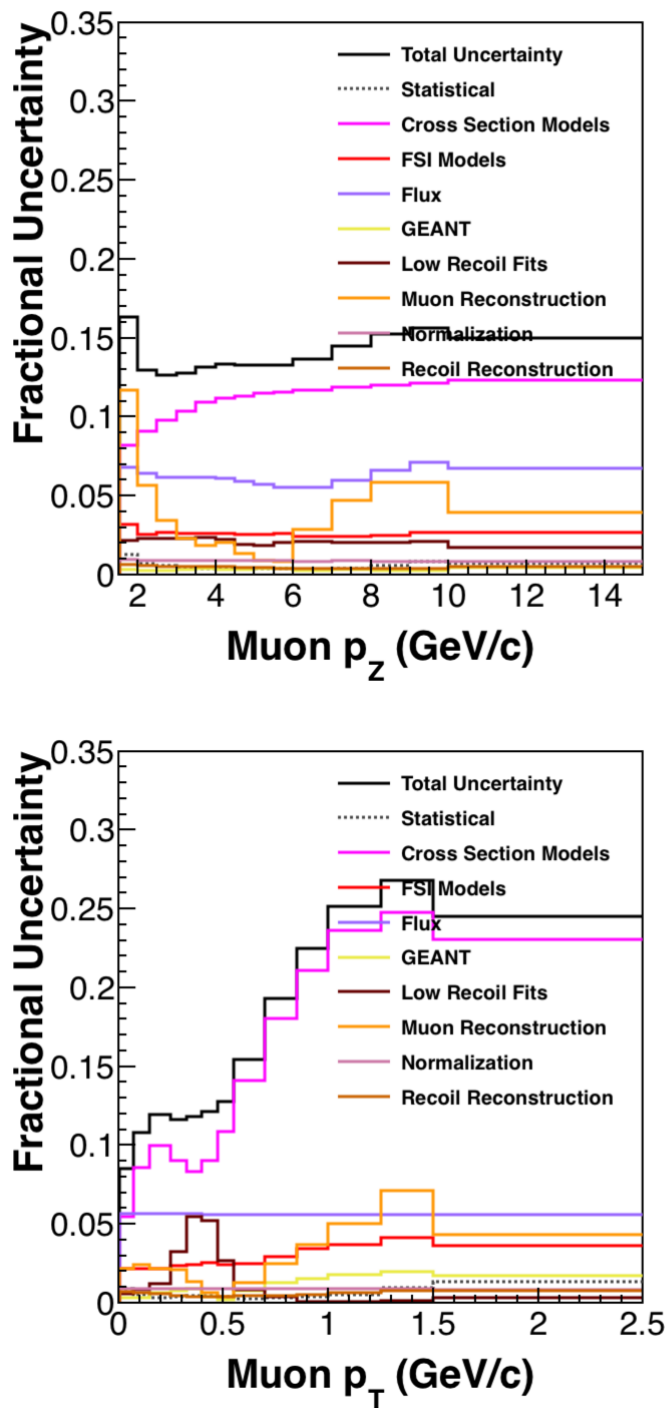
Figure 6.72: Error Summary on the raw event distribution of the simulation. All the possible systematics are divided into these 8 systematic uncertainties + 1 statistical uncertainty categories.
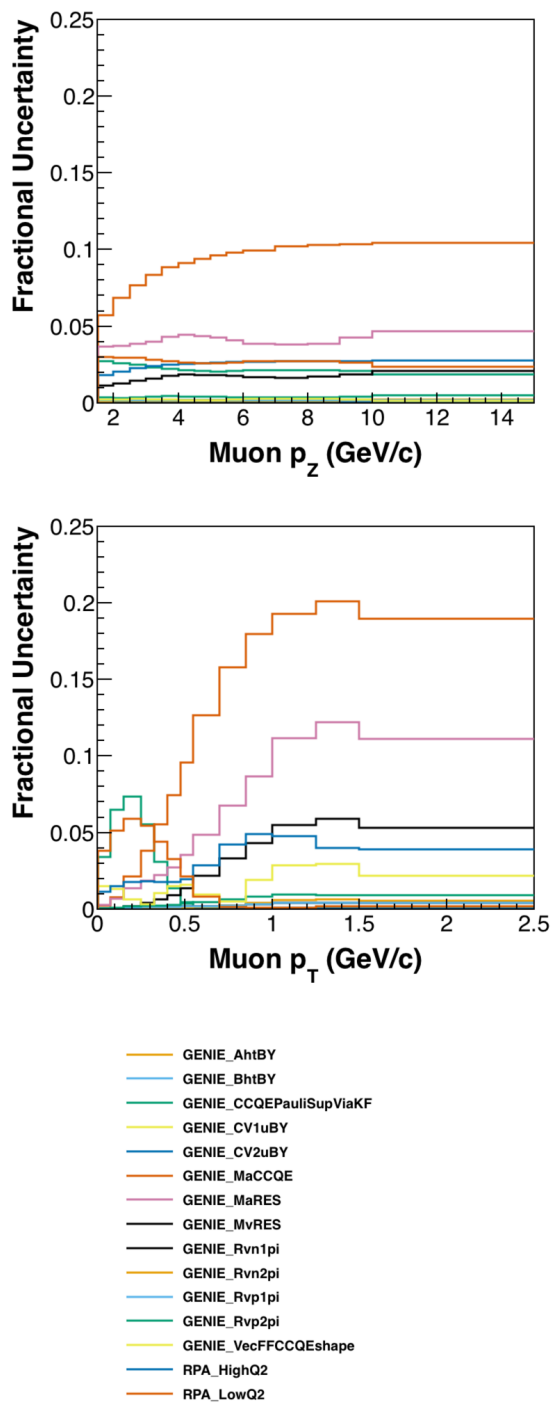
Figure 6.73: The cross-section models are the systematic uncertainties from the GENIE models that are used in various signal and background processes. The cross-section model uncertainty is dominated by MaCCQE which is the uncertainty on the axial mass (M_A).
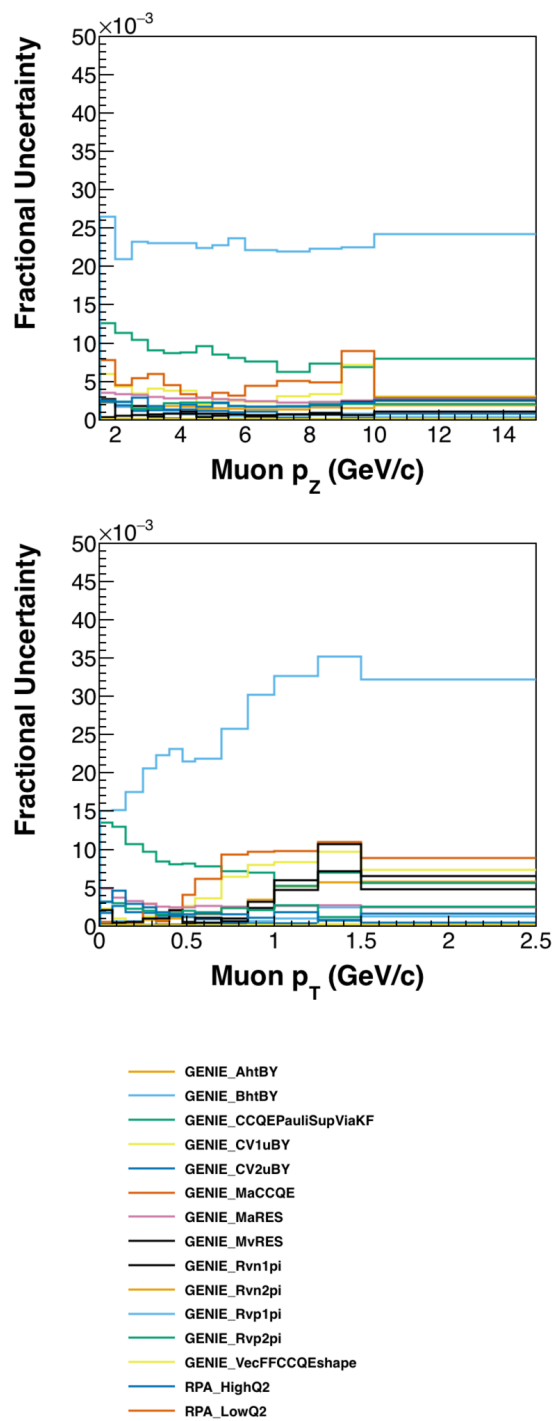
Figure 6.74: The final state interaction models are the systematic uncertainties due to the final state particles. This uncertainty is dominated by mean free path of neutron (MFP N) followed by mean free path of pion (MFP N).
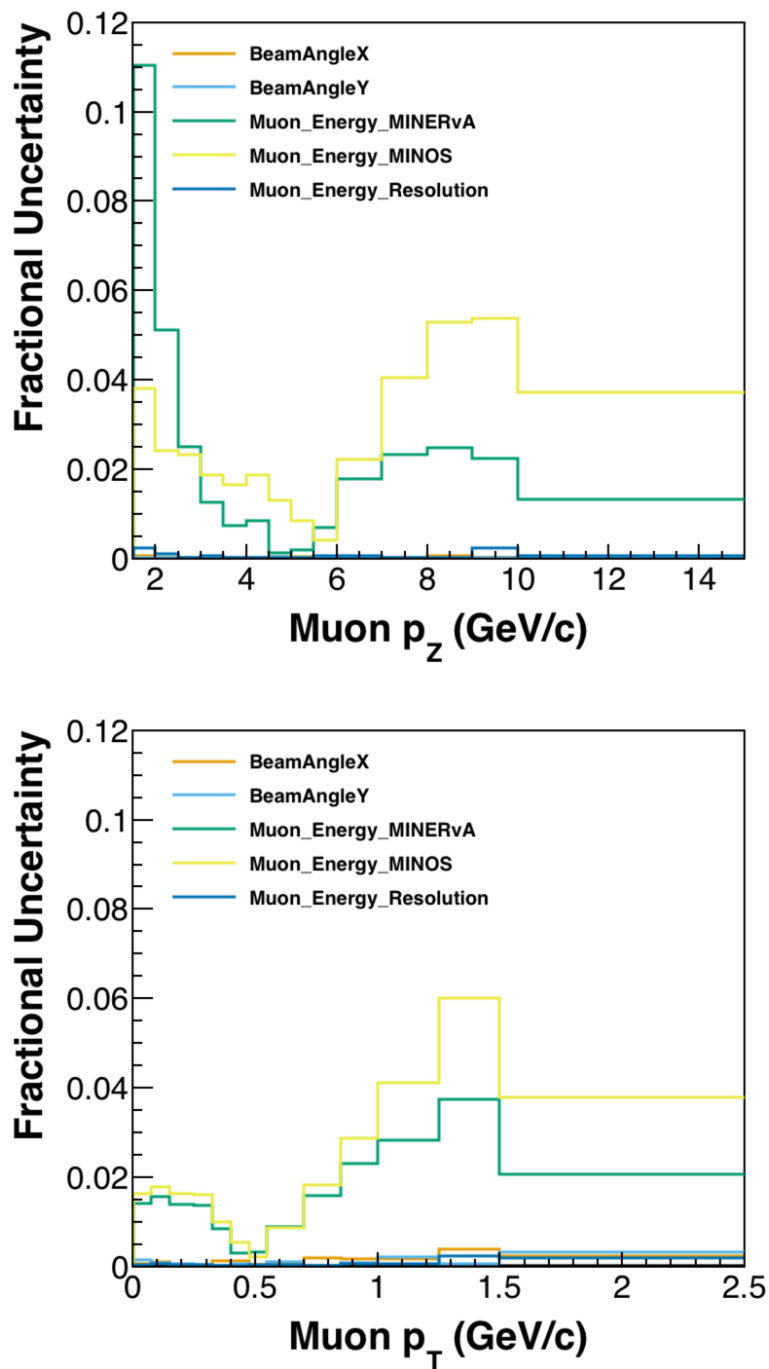
Figure 6.75: Systematic uncertainties related to the muon angle and the muon energy reconstruction. The muon energy related systematic uncertainties in the first two bins is dominated by reconstruction systematic uncertainties in the MINERvA detector followed by the reconstruction in the MINOS near detector systematic uncertainties. The angle and energy resolution systematic uncertainties are negligible.
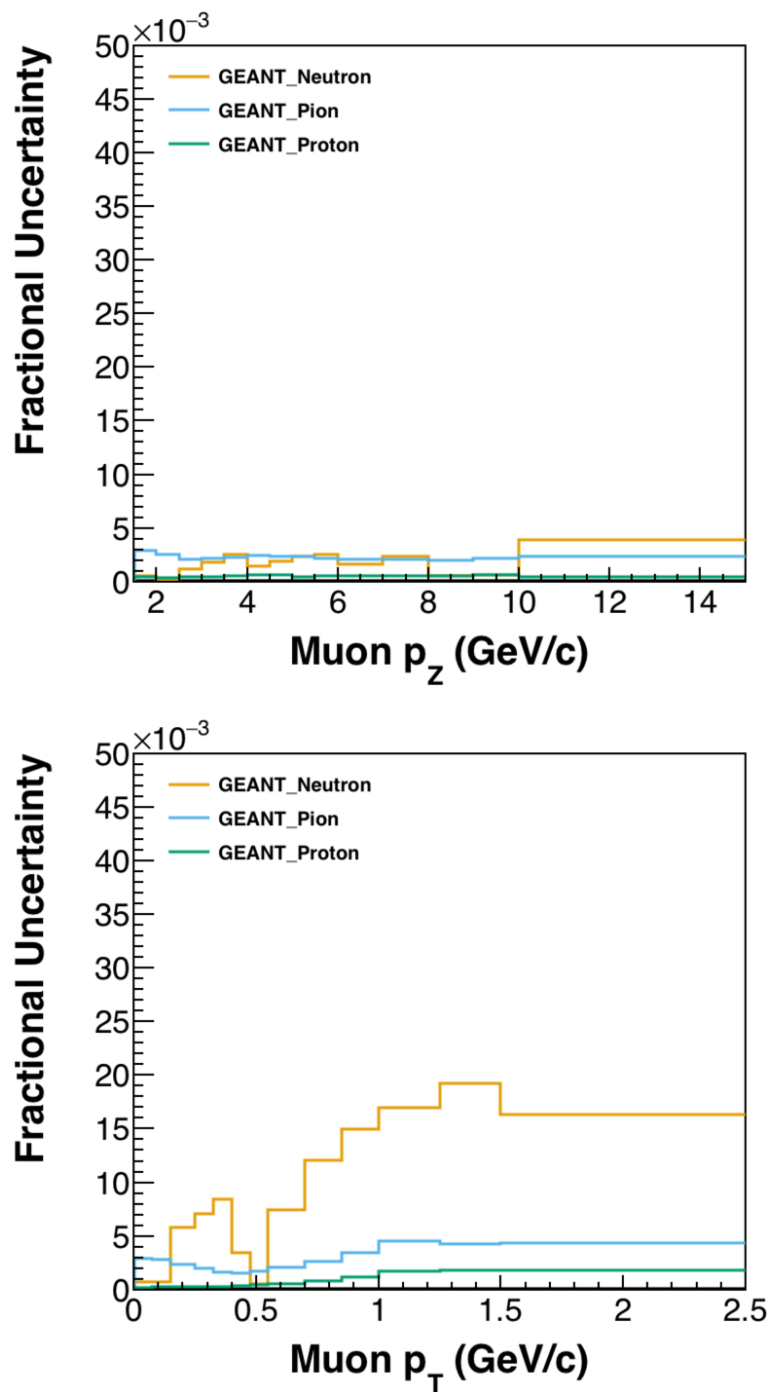
Figure 6.76: Systematic uncertainties related to the hadronic interactions of the final state particles in the MINERvA detector (categorized as GEANT). This uncertainty is dominated by the uncertainty due to the neutrons since we rely on the models to estimate neutron cross-section for neutron-detector interactions.
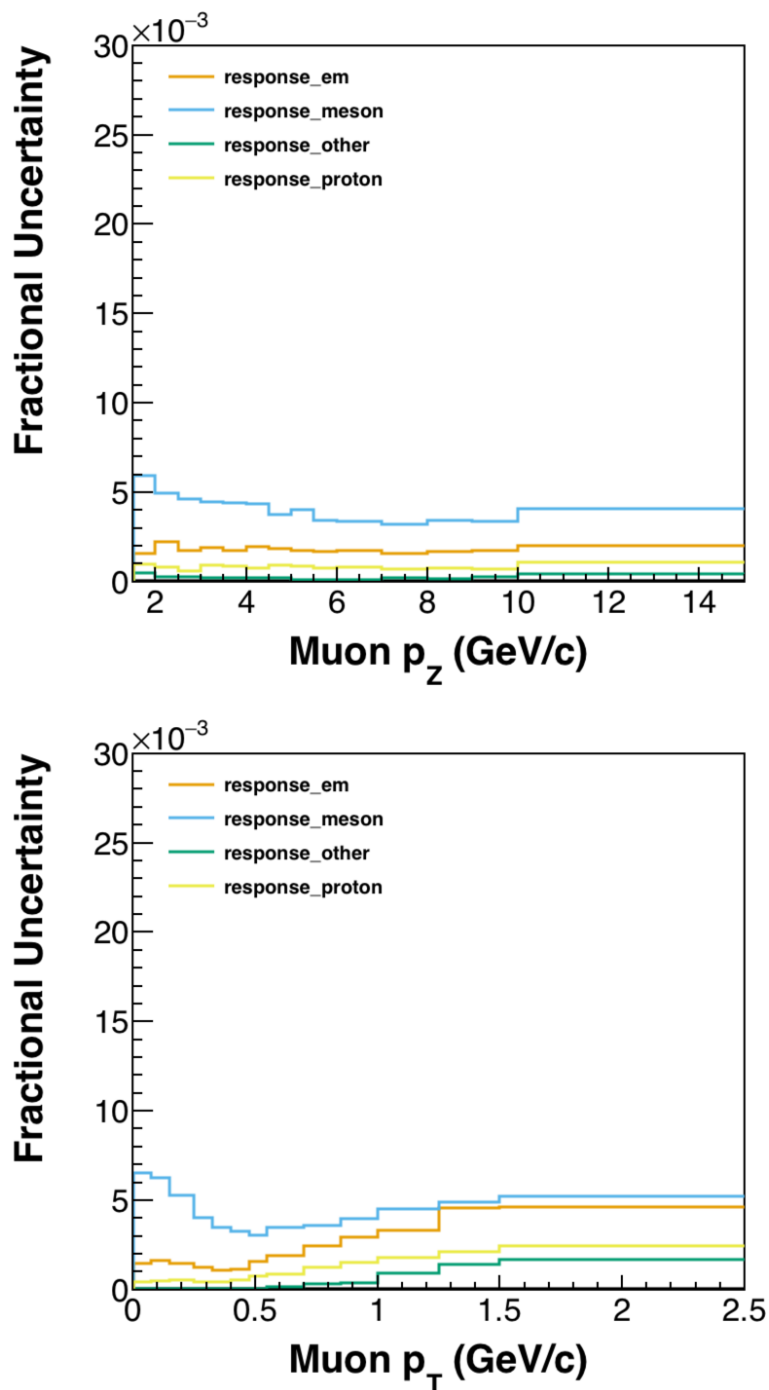
Figure 6.77: Systematic uncertainties due to the recoil energy reconstruction. The recoil energy is contributed by various non-muon particles. The detector's response to various particles is different and energy reconstruction of each contributing particle is different. Neutron related systematic uncertainties are not present here. They are handled by the GEANT systematics.
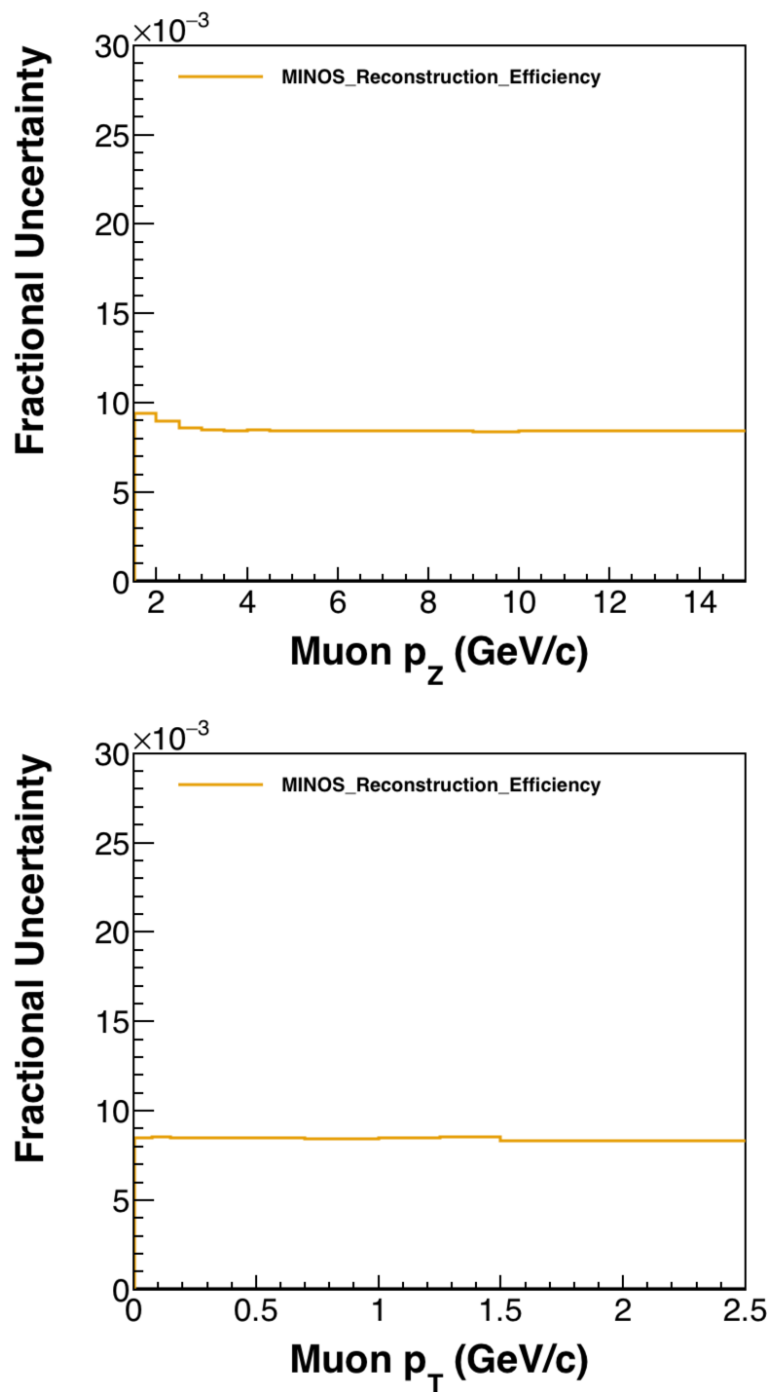
Figure 6.78: Systematic uncertainties due to the normalization. This category includes the uncertainty coming from the efficiency correction to the muon tracks. This efficiency correction is already explained in section 6.16.2.1 of the thesis.

(CCRES) event from an incoming neutrino. After the neutrino-nucleon interaction, target nucleon gets excited to a resonance state which immediately decays to a nucleon and a pion. The final state products from such type of interaction could include a muon, a pion and a recoil nucleon. If the pion is absorbed, then the event will look like a CCQELike event. If the pion doesn't get absorbed, then it could exit the nucleus. If the pion is energetic enough to produce a track, the event is rejected. Otherwise, it could end up as a background in the signal sample. In fact, most of the background events in our sample come from the resonance process. In the GENIE, the central value of the resonance axial form factor is 1.12 GeV with an uncertainty of 20%.

- **MvRES** The vector form factor of the CCRES has a central value of 0.84 with an uncertainty of $\pm 10\%$. GENIE uses the Rein-Sehgal model [132] where the form factors appear as:

$$G^{V,A} = (1 - \frac{q^2}{4M_N^2})^{1/2-n}(\frac{1}{q^2 - M_{V,A}^2})$$ (6.31)

- **Bodek-Yang Parameters (AhtBy,BhtBy,CV1uBy,CV2uBy)** The Bodek-Yang model is used in the GENIE for the inelastic neutrino-nucleus scattering using the effective leading order parton distribution functions [42]. Using the PDF's (Parton Distribution Function), the inelastic interactions can be well described at the high Q^2 and can be scaled down up to $Q^2 = 0.8 GeV2$. The structure functions for the neutrinos

and the anti-neutrinos at the high Q^2 can be written as a function of PDF's:

$$F_2^\nu = 2 \sum_i [\zeta_w q_i(\zeta_w, Q^2) + \zeta_w \bar{q}_i(\zeta_w, Q^2)] \tag{6.32}$$

$$x F_3^\nu = 2 \sum_i [\zeta_w q_i(\zeta_w, Q^2) - \zeta_w \bar{q}_i(\zeta_w, Q^2)] \tag{6.33}$$

where

$$x = \frac{Q^2}{2M\nu}$$

and

$$\nu = E_o - E'$$

is the energy transferred to the recoil system and M is the mass of the struck nucleon.

where ζ_w is the scaling variable given by:

$$\zeta_w = \frac{2x(Q^2 + M_f^2 + B)}{Q^2[1 + \sqrt{1 + 4M^2 x^2/Q^2}] + 2Ax} \tag{6.34}$$

M_f is the mass of the final state quark after the neutrino inelastic scattering. Here A and B are the parameters with central values 1.735 and 0.624 respectively. These two parameters allow the inelastic scattering to scale down to the very low Q^2 region. The

GENIE has $\pm 25\%$ uncertainty on each of these parameters.

- **CCQEPauliSupViaKF** For a final state nucleon to exit the nucleus, it must have the energy above the Fermi energy E_F that is enough to break the nuclear binding energy E_B. When an energy transfer w is transferred from the neutrino to the nucleon system, the energy of the final state nucleon is given by:

$$E_N = \mathcal{K}(E_F - w + E_B) \tag{6.35}$$

[128] Here $\mathcal{K}$ is the Pauli blocking factor and ideally would be 1. However, based on the fit on the MiniBooNE data, the value of $\mathcal{K}$ is implemented as 1.007 with an uncertainty of 35% on $\mathcal{K}$ in GENIE. [11]. This systematic uncertainty is relevant for the CCQE processes only.

- **CV1uBY and CV2uBY** These are also the Bodek Yang parameters related to the vector form factors of the valence quarks.

$$K_{valence}^{vector}(Q^2 = [1 - G_D^2(Q^2)] \times \frac{Q^2 + C_{v2}}{Q^2 + C_{v1}} \tag{6.36}$$

Here $G_D = \frac{1}{(1+Q^2/0.71)^2}$ is the proton elastic form factor [42]. In the GENIE, the

CV1uBY and the CV2uBY have an uncertainty of $\pm 30\%$ and $\pm 40\%$ respectively.

- **Non-Resonant Pion Production Rvn1pi,Rvn2pi,Rvp1pi and Rvp2pi** While most of the pions are produced by the resonant processes, some of them are produced by the non-resonant processes [42]. The Rvn1pi and the Rvn2pi deal with the 1 and 2 pion production from νn or $\bar{\nu} p$ interactions. The Rvp1pi and the Rvp2pi deal with the νp and $\bar{\nu} n$ pion production interactions. By default, the GENIE has 50% uncertainty on these models. However based on the fit done on pion production data of the bubble chamber experiments at the ANL and the BNL, the central value for the Rvn1pi is reweighted and the uncertainties are reduced to 5% shift effect [132].

- **CCQE vector Form Factor Model** The CCQE model based on the Llewyllyn Smith formulation includes the vector form factor for the protons and the neutrons. GENIE by default uses the BBA05 model [46]. This systematic uncertainty takes into account the effect of changing the vector form factor from the BBA model to the dipole form factor on the shape distribution.

- **RPA** The RPA or the random phase approximation takes into account the effect of the long range correlation between the nucleons. This effect is similar to the screening effect produced by the charged particle in a dielectric medium. In this case, the charge of the W boson is screened by the polarization effect due to this nucleon-nucleon long
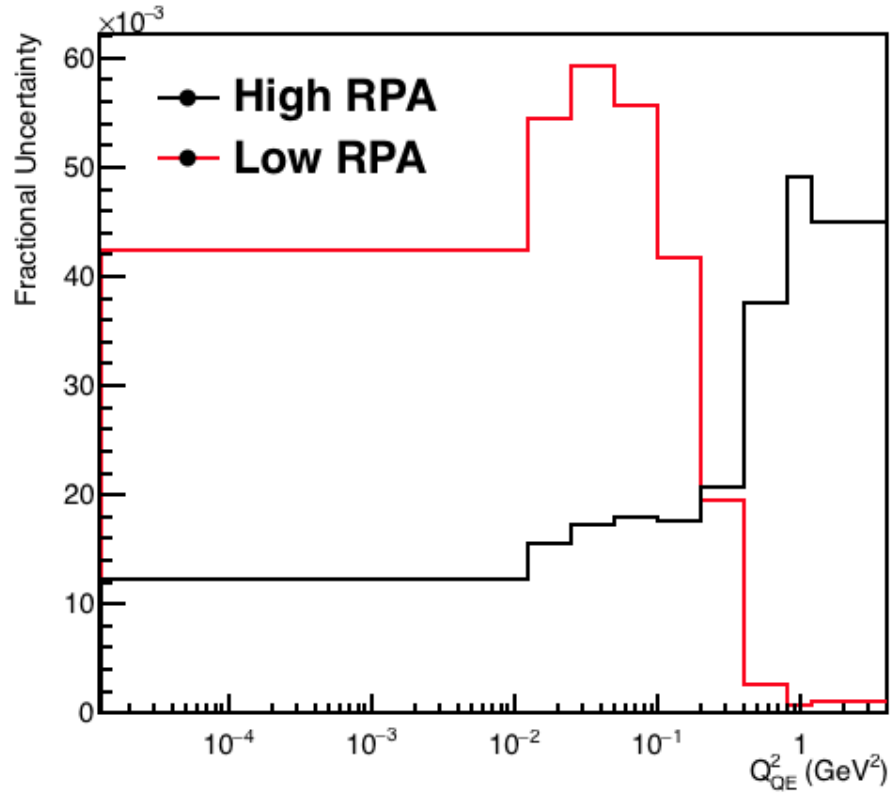
Figure 6.79: Uncertainty due to the RPA weights at the low and the high Q^2_{QE}.

range correlations. In MINERvA, the RPA weight is applied differently for low and high Q^2 to account for the different RPA effects at different Q^2 regions [83].

6.18.2   Final State Interactions

Once the incoming neutrino interacts with the nucleus or the nucleon, it is followed by the final state interactions. The particles produced by the initial interactions re-interact inside the nucleus as they pass through the nuclear medium. This re-interaction will determine what comes out of the target (and basically what we see in the detector). For example, an anti-neutrino interacting with the nucleus could produce a muon, a neutron and a pion. The pion could re-interact and get absorbed inside the nucleus making the event CCQELike. If the pion exits the nucleus, then it will end up as a non CCQELike event. Final state interactions usually deal with the nucleons and the mesons that are produced from the interaction and the re-interactions after the neutrino-nucleus interaction.

- **AKYxF1pi** The AGKYxF1pi deals with the hadronization process generating one nucleon and any number of pions. Here the Feynman scaling variable (x_F) has an uncertainty of $\pm 20\%$[25].

- **Absorption Cross-sections (FrAbs N,pi)** The fate of the hadrons produced inside the nucleus determines whether an event is going to be a signal or a background. Even though a large number of pions are produced by hadronization, absorption of these pions inside the nucleus makes these event CCQELike. Our selected signal sample has a significant fraction of the true resonance events, most of which have absorbed pions.

The GENIE has a default uncertainty of $\pm 30\%$ on this absorption cross-section for a given total scattering cross-section [25].

- **FrCEx N,pi** The charge exchange systematic uncertainties deal with the events with final state interactions where the charge of the initial hadron is different from that of the final state hadron. For example, a $\bar{\nu}_\mu$ interacting with the proton produces a nucleon which could go through the FSI and end up with a proton being ejected. Charge exchange between the nucleons and the pions are dealt with the FrCEx-N and the FrCEx-pi respectively. The uncertainty on these processes are $\pm 50\%$ of total re-scattering probability [25].

- **FrElas N,pi** The elastic scattering is the scattering where the particles before and after the interaction do not change. Nucleons and mesons produced inside the nucleus from the neutrino-nucleon interactions can undergo elastic scattering before they are absorbed or go through other modes of scattering or exit the nucleus. GENIE has $\pm 10\%$ uncertainty on the elastic scattering of pions and $\pm 30\%$ on the nucleons [25].

- **FrInel N,pi** The inelastic scattering processes generally breaks the target nucleus. The uncertainty on these processes for nucleon (N) and pions (pi) is $\pm 40\%$ of the total scattering cross-section [25].

- **FrPiProd N,pi** If the final state pion produced from the neutrino-nucleus interaction

has enough energy, it can produce additional pion or nucleon. These are mostly background processes due to the presence of pions in the final state (2 pions or 1 pion and 1 nucleon). The uncertainty for both productions is $\pm 20\%$ respectively [25].

- **MFP N,pi** Mean free path is the average distance that a particle travels between two scatterings. The mean free paths (λ) of the pions and the nucleons are used to calculate the probability of scattering after travelling some distance x inside the nucleus.

$$P(x, \lambda) = \frac{e^{-x/\lambda}}{\lambda} \tag{6.37}$$

  In the GENIE, the uncertainty on mean free paths for the pions and the nucleons are taken to be $\pm 20\%$ [25].

- **RDecBR1gamma** This is the systematic uncertainties due to the variation in the branching ratio of a resonance state decaying to give a photon. The 1σ variation of this branching ratio corresponds to $\pm 50\%$ [25].

- **Theta Delta2Npi** This systematic uncertainties is related to the angular decay of the Delta (Δ) particle to a nucleon and a pion. This systematic uncertainty is obtained by turning on or off this systematic knob in the GENIE.

6.18.3 Muon Reconstruction

Muon related systematic uncertainties are the important systematic uncertainties for this analysis since we completely rely on the muon angle and the kinematics to reconstruct the physical variables, reject the wrong sign neutrino events and select 1 track events. As seen in figure 6.75, there are 2 angle related and 3 energy related muon systematic uncertainties.

- **Beam Angle** It is the systematic uncertainty related to the angle of the neutrino beam. Since the angle of the neutrino beam determines the angle at which the outgoing lepton (in our case the muon) exits the nucleus, it affects the muon reconstruction in the analysis. We have two beam related systematic uncertainties namely along X (left/right direction with respect to the neutrino beam direction) and along Y (top/bottom direction with respect to the neutrino beam direction). The uncertainty on beam angle along X and Y are given as:

$$\delta\theta_x = 0.001$$

$$\delta\theta_y = 0.0009$$

The central value of θ_X and θ_Y are 0. These uncertainties are calculated by looking comparing the low-nu muons in the data and the MC [153]. So, the shifted universe

will have the beam angle as:

$$Universe(\pm 1\sigma_{x,y}) = \theta_{x,y} \pm \delta\theta_{x,y} \qquad (6.38)$$

The beam angle uncertainties get propagated to muon angles as the uncertainties on the muon angle reconstruction.

- **Muon Energy Resolution** Muon energy resolution is the ability to measure the minimum muon energy in the detector. In general, the fractional resolution for any variable x is estimated by looking at the distribution of the following quantity:

$$\%Resolution = \frac{x_{generated} - x_{reconstructed}}{x_{generated}} \qquad (6.39)$$

The muon energy resolution error is calculated as:

$$P_{mod\,\mu} = (P_{reco\,\mu} - P_{generated\,\mu}) \times (1 \pm 0.004) + P_{generated\,\mu}$$
$$\Delta P_{Resolution} = P_\mu - P_{mod\,\mu} \qquad (6.40)$$

Here P is the muon momentum and $\Delta P_{Resolution}$ is the error on the muon energy due to resolution. This systematic error gets propagated to the muon transverse and longitudinal momenta.

Uncertainty Source	Uncertainty
MINERvA dE/dx (scintillator)	30 MeV
MINERvA dE/dx (C,Fe,Pb)	40 MeV
MINERvA mass (scintillator	11 MeV
MINERvA mass (C,Fe,Pb)	17 MeV

Table 6.3: Uncertainty due to MINERvA Material assay in muon energy reconstruction

- **Muon Energy** Since we rely on both MINERvA and MINOS detectors to reconstruct the energy of the muon, there are two muon energy reconstruction related systematic uncertainties: **Muon Energy MINERvA** and **Muon Energy MINOS** . This is because we rely on muons to make it to the MINOS detector in order to find out the charge of the muon. Hence, the muon kinematics are reconstructed both at the MINERvA and the MINOS detector. Each detector has their own systematic uncertainties because of the way the muon energy is reconstructed. The uncertainty on muon energy reconstruction on the MINERvA detector mainly comes from the material assay. These are the uncertainties related to the energy loss by muon track due to energy deposition (dEdx) on various detector materials. The uncertainties are in terms of absolute number and are based on test beam data and past dEdx studies [52]. These uncertainties are added in quadrature to the overall reconstructed energy. Muon energy is reconstructed in the MINOS detector by range (dEdX) or by curvature. A more detailed explanation on muon energy reconstruction is given in the section 4.8 of the thesis. Uncertainty related to the range and the curvature is summarized in table

Uncertainty Source	Uncertainty
MINOS Range	0.984%
MINOS curvature ($p_\mu < 1 GeV$)	2.5%
MINOS curvature ($p_\mu > 1 GeV$)	0.6 %

Table 6.4: MINOS Range and Curvature Uncertainties on muon momentum

below.

As discussed in chapter 5 of the thesis, the central value of the MINOS energy scale was shifted by 1.8 σ (3.6% of p_μ) based on studies done to address the discrepancy between data and MC and the uncertainty on this shifted energy scale is taken as 0.984% (based on the fit results) instead of the prior 2% shift. The shift was based on a fit where the fit parameters were focusing components and muon energy scale. Besides predicting a shift in muon energy scale, the fit also predicts small shifts (within their nominal uncertainties except for longitudinal position of the target, which still has a small impact on flux) in focusing components as a result of correlations between fit parameters. The MINERvA collaboration doesn't shift the central value flux. However, to take the correlation between focusing parameters and the muon energy scale into account, in the systematic universes related to muon energy scale, we use the different flux predicted by this fit. For this analysis, we do not use the shifted flux in the muon energy scale systematic universes.

6.18.4   Response systematic uncertainties

The MINERvA detector's response to various non-leptonic particles that deposit energy in the MINERvA detector is categorized in the response systematic uncertainties. The final state particles are simulated by GENIE and those final state particles are propagated through the detector materials using the GEANT4 simulation. The final state hadrons interact with the detector material and lose energy in the process. The energy clusters that contribute to the recoil energy are grouped together by particle type (proton,pion,neutron) and the cluster energy is varied by 1σ variation of the respective particle type. These 1 σ variations comes from test beam data in case of proton and pion [94]. Contribution of the various recoil particles are added in quadrature based on the contribution they have on the recoil activity for a given neutrino event. For a given particle i if the fraction it contributes to the overall hadronic system is given as:

$$f_i = \frac{E_i}{\sum_i E_i} \tag{6.41}$$

where the sum is over all contributing hadronic particles, the overall uncertainty is calculated as:

$$\sigma_{Etot} = \sqrt{\sum_i [f_i \times \sigma_i]^2} \tag{6.42}$$

This category doesn't include the response due to the neutrons. Systematic uncertainties arising from the neutron activities are handled by the GEANT category.

6.18.5 GEANT

MINERvA relies on the GEANT4 simulation to simulate the final state particles in the detector. MINERvA varies the hadronic inelastic cross-section of the final state hadrons and detector materials (C,Fe,Pb) based on the test beam data (in case of protons and pions) and GEANT cross-sections (in case of neutrons). These variations in inelastic hadronic cross-sections are categorized as GEANT cross-section. Figure 6.76 shows the overall contribution of this category in the raw simulated event. The GEANT systematic error is dominated by the neutrons. The GEANT systematics implementation is based on [37].

6.18.6 Flux

In MINERvA , the flux uncertainties are related to the uncertainties in the neutrino flux. A detailed description of the neutrino flux uncertainties is given in chapter 3.3. The neutrino flux systematics accounts for the uncertainties due to the focusing parameters and the hadron productions in the beamline. The flux uncertainty systematics consists of 200 universes to address the correlation between various parameters in hadron production models and focusing system. The overall uncertainty of neutrino flux on reconstructed neutrino energy is around 6% on the raw MC events as seen in figures 6.80 and 6.81. This accounts for uncertainties from both focusing and hadron productions categories. MINERvA uses

the data from nu-e scattering (electron neutrino scattering off electron) to constrain the flux uncertainties. This analysis uses the nu-e weights computed for the flux universes using the anti-neutrino playlists minervame5A through minervame6G.

6.18.7 Normalization

The normalization category includes the error due to the efficiency correction on the reconstructed muon momentum. The overall procedure of the efficiency correction is discussed in section 6.16.2.1 of the thesis. The muon efficiency correction has a systematic uncertainty which introduces a normalization uncertainty on the reconstructed muon kinematics. Figure 6.78 shows the effect of this uncertainty as functions of muon p_T and p_Z respectively.

6.18.8 Other

The other category includes the error due to 120 MeV cut on true proton kinetic energy in the CCQELike signal definition. Our CCQELike signal definition includes protons below 120 MeV kinetic energy only. This error takes into account due to the possible mis-modeling of the multiplicity cut (which selects events with 1 reconstructed track only).

6.19 Propagation of Uncertainties in the analysis

Originally, the reconstructed data only has the statistical uncertainties since it is just the number of counts of events that passes the recoil cut. The simulation will have both statistical and systematic uncertainties. At various stages, they get propagated to the data with the final cross-section result having both statistical and systematic uncertainties. This section will go through various stages of the analysis and how they are propagated all the way to the cross-section extraction stage.

6.19.1 Event Selection

At this stage, the data has only the statistical error which is equal to $\sqrt{N}$ where N is the number of events. With 584207 events that passed the reconstruction cuts, the uncertainty is 764. The raw MC on the other hand has both systematic and statistical uncertainties.

6.19.2 Background Subtraction

To determine the fraction of the signal or the background in the selected data, we do the data driven fit with the MC signal and the background templates. To account for the systematic effects on these fractions, the fit is done in each of the systematic universes. These fractions
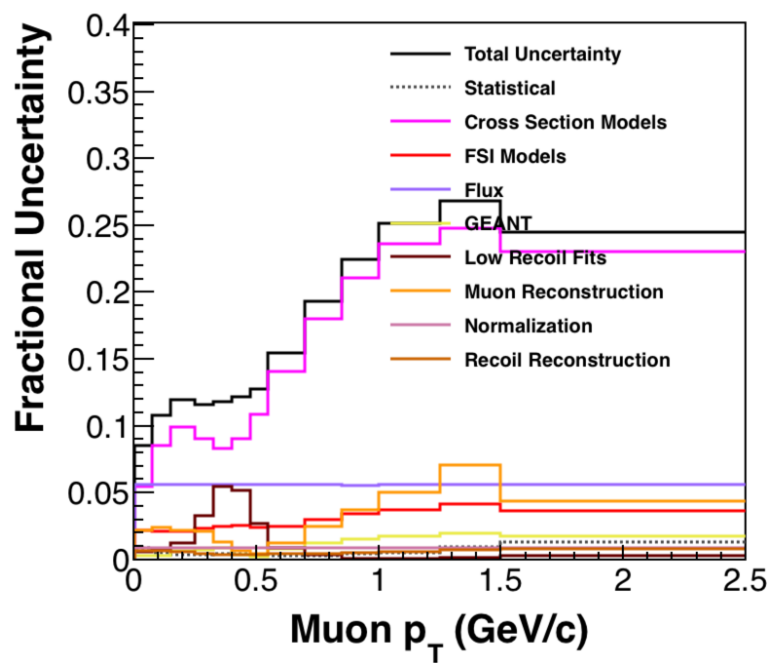
Figure 6.80: Error Summary on the Raw MC as a function of muon p_T.
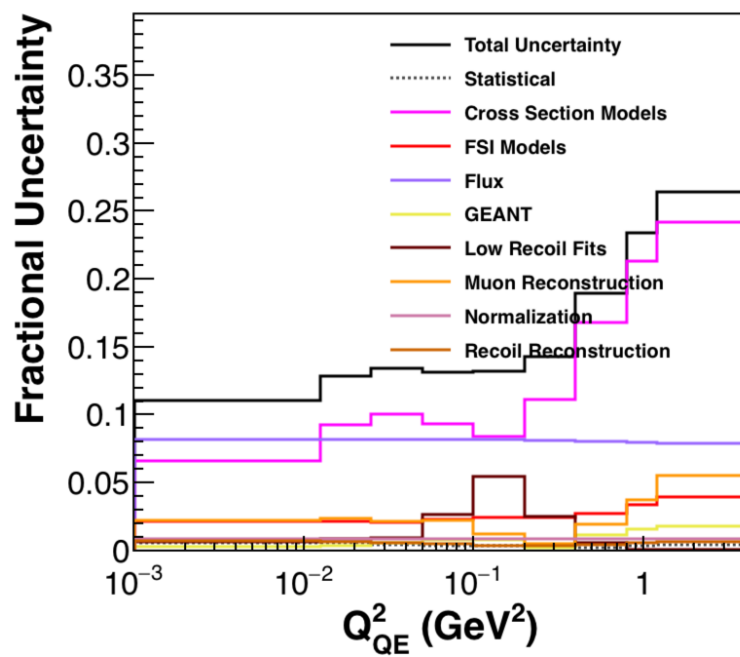
Figure 6.81: Error Summary on the Raw MC as a function of Q^2_{QE}.
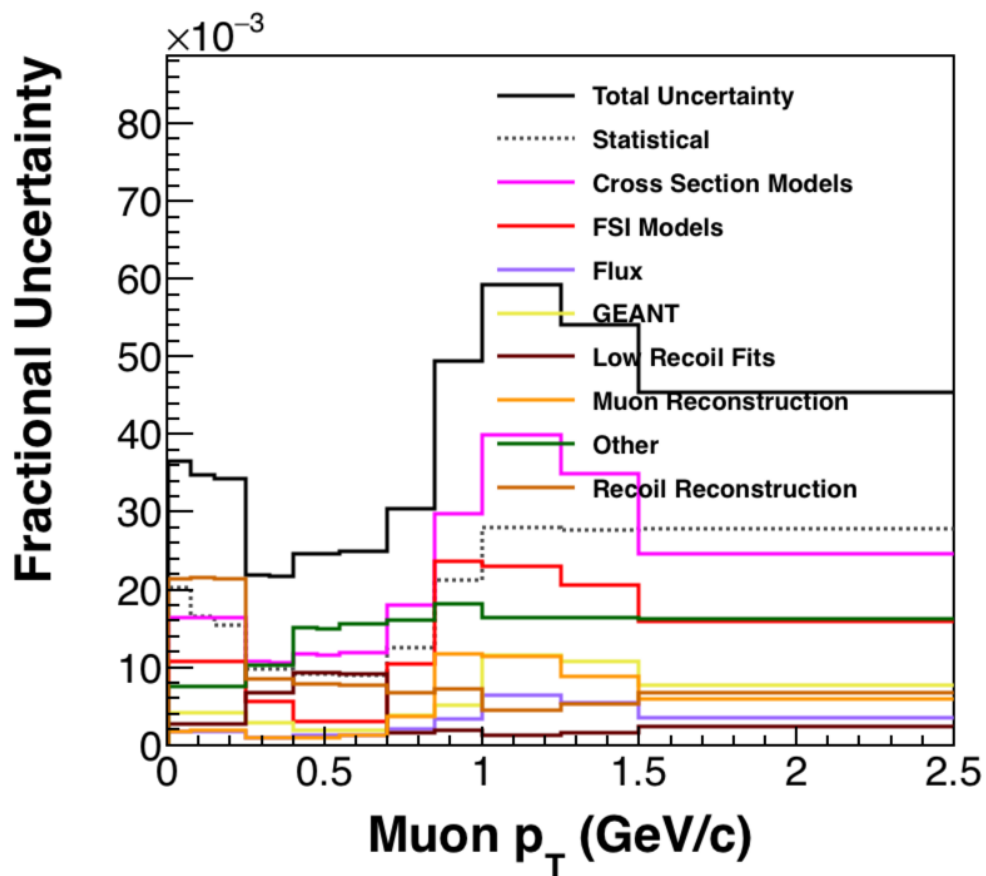
Figure 6.82: Error Summary on the background subtracted data as a function of p_T

on the data are estimated by doing the fit between the data and the central values and the systematic universes of the MC templates which propagates the systematic errors from the MC to the data during the background subtraction. However, the contribution of models on the background subtracted data is not large. This suggests that the background subtracted distribution is not subject to model dependency. This prevents our background subtracted sample from getting biased due to the models used in the simulation.
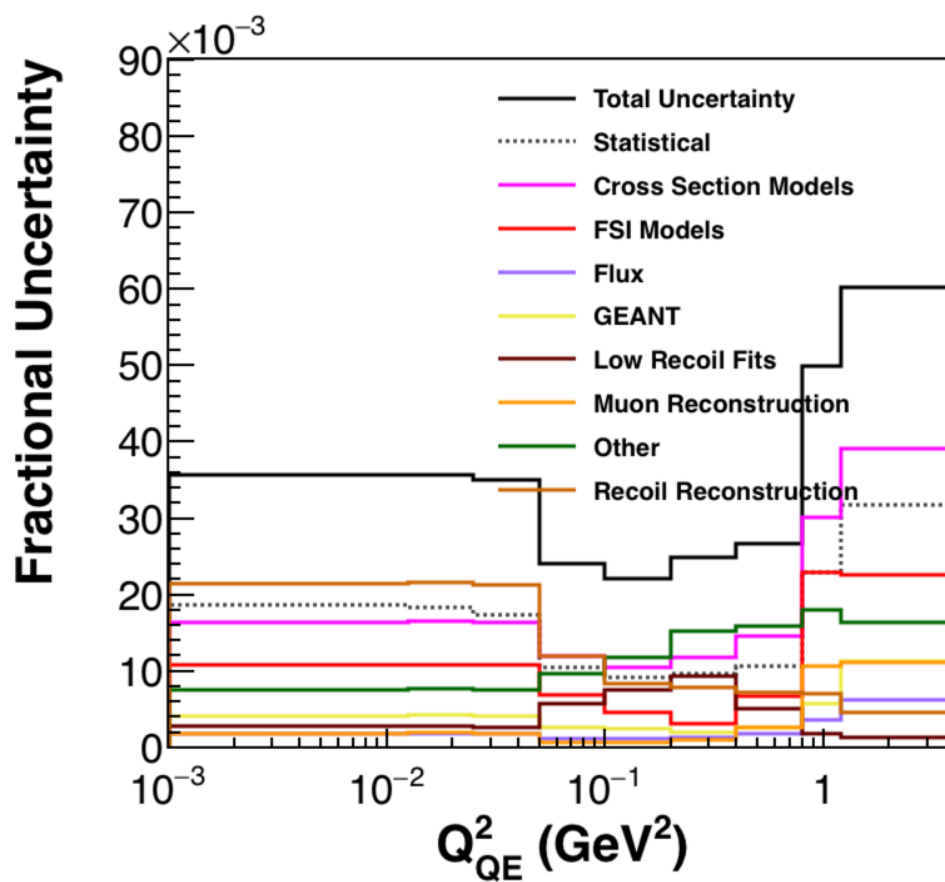
Figure 6.83: Error Summary on the background subtracted data as a function of Q^2_{QE}

6.19.3 Unfolding

During the unfolding of the background subtracted distribution, the events migrate to and from the neighboring bins. In case of bins neighboring the underflow or overflow bins, the migration changes the overall number of events in the sample. Systematic uncertainties that are sensitive to bin to bin migration blow up during the unfolding procedure. An additional uncertainty due to the unfolding procedure is introduced by the unfolding procedure. Figure 6.84 shows the muon energy scale systematic uncertainties before and after unfolding. The unfolding blows up the muon energy scale in MINOS and MINERvA making it the dominant systematic uncertainty in the unfolded distribution as seen in figure 6.85.

6.19.4 Efficiency and Purity

During the cross-section calculation, the unfolded sample has to be efficiency corrected to account for the loss due to our event selection, the reconstruction procedures and the limitations due to the detector itself. Figures 6.86 and 6.83 shows that the overall uncertainty on efficiency is less than 3% with the largest contribution from cross-section models and muon efficiency correction related uncertainties. The contribution of statistical uncertainty is less than 1%.

Although the purity doesn't come up in the overall cross-section calculation, we can look at
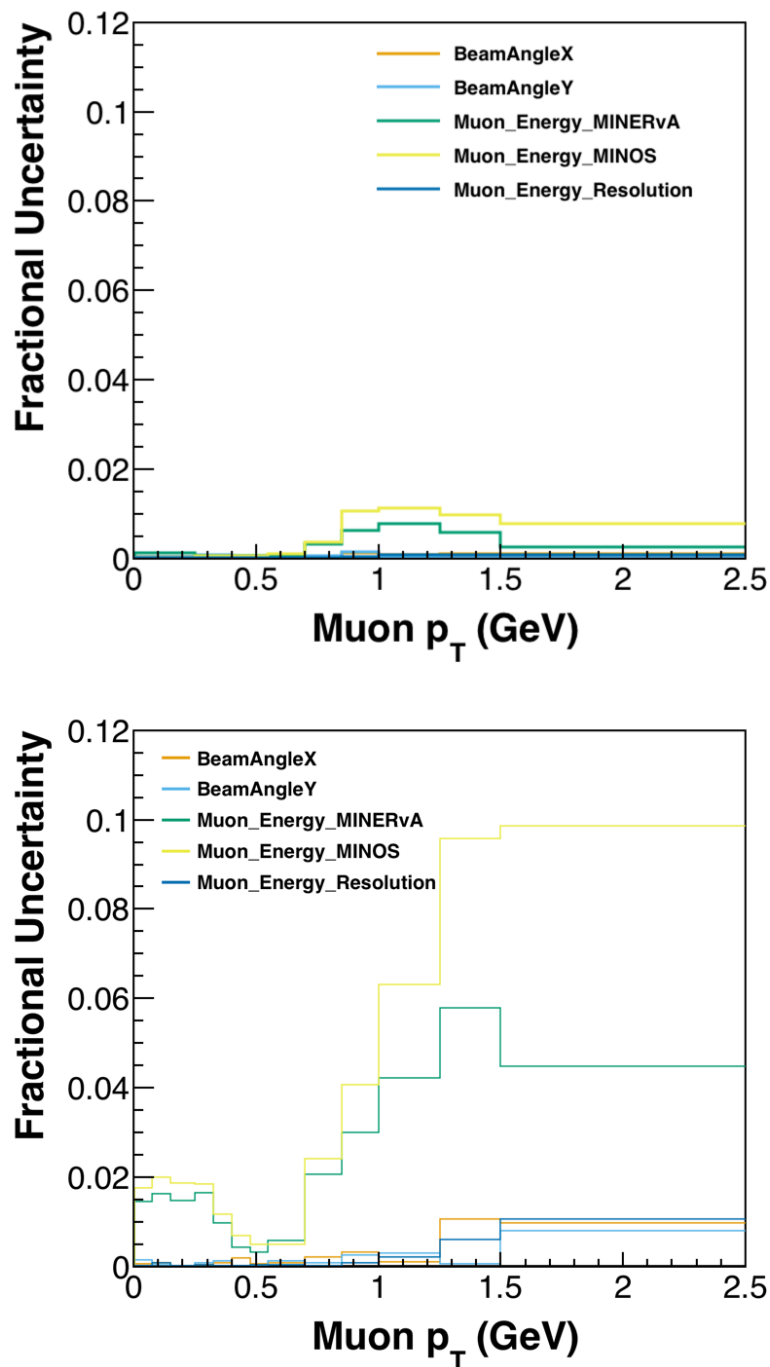
Figure 6.84: Muon systematic uncertainties on the background subtracted data before (left) and after (right) unfolding. Unfolding blows up the systematic uncertainties due to bin to bin migration of events. This analysis is mostly dominated by the muon energy scale in the MINOS systematic uncertainty after the unfolding.
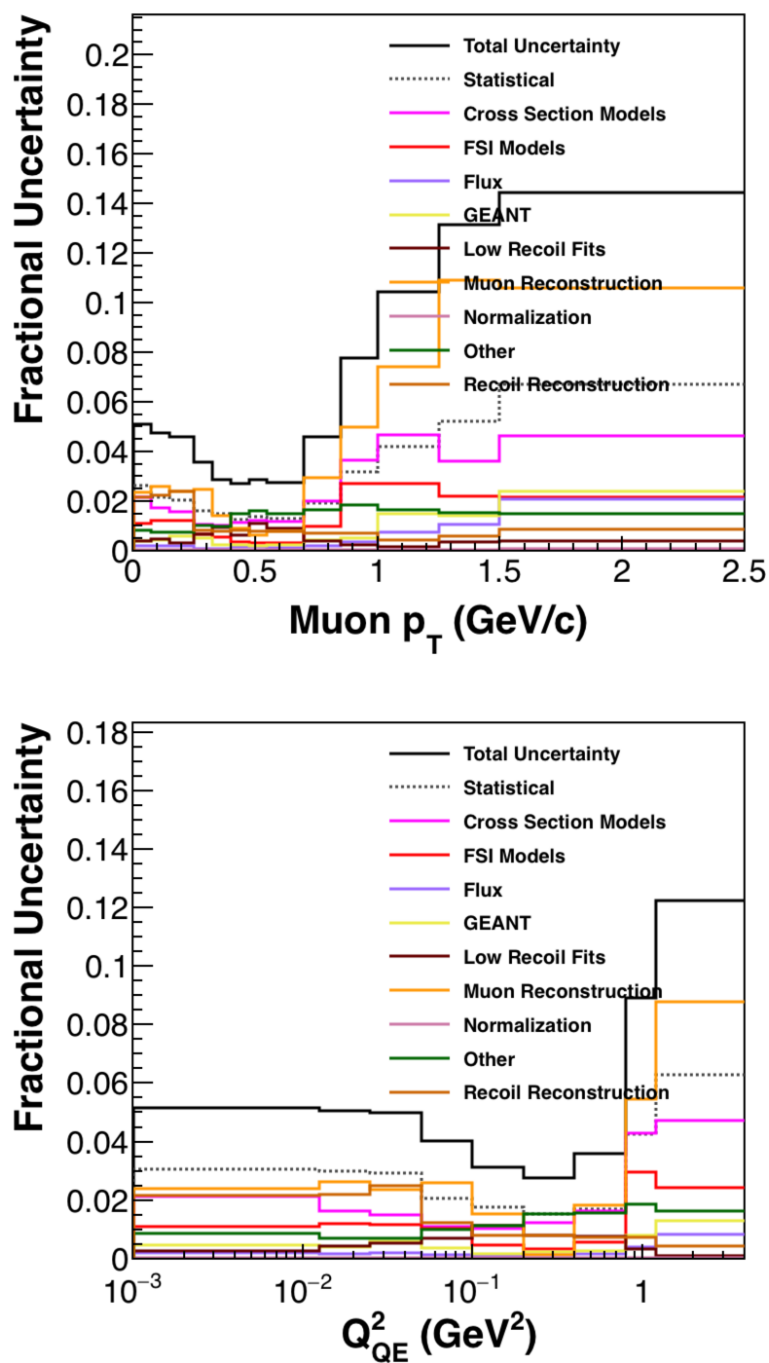
Figure 6.85: Systematic uncertainties on the unfolded data as a function of p_T and Q^2_{QE}. The overall systematic uncertainty is dominated by Muon Reconstruction category.
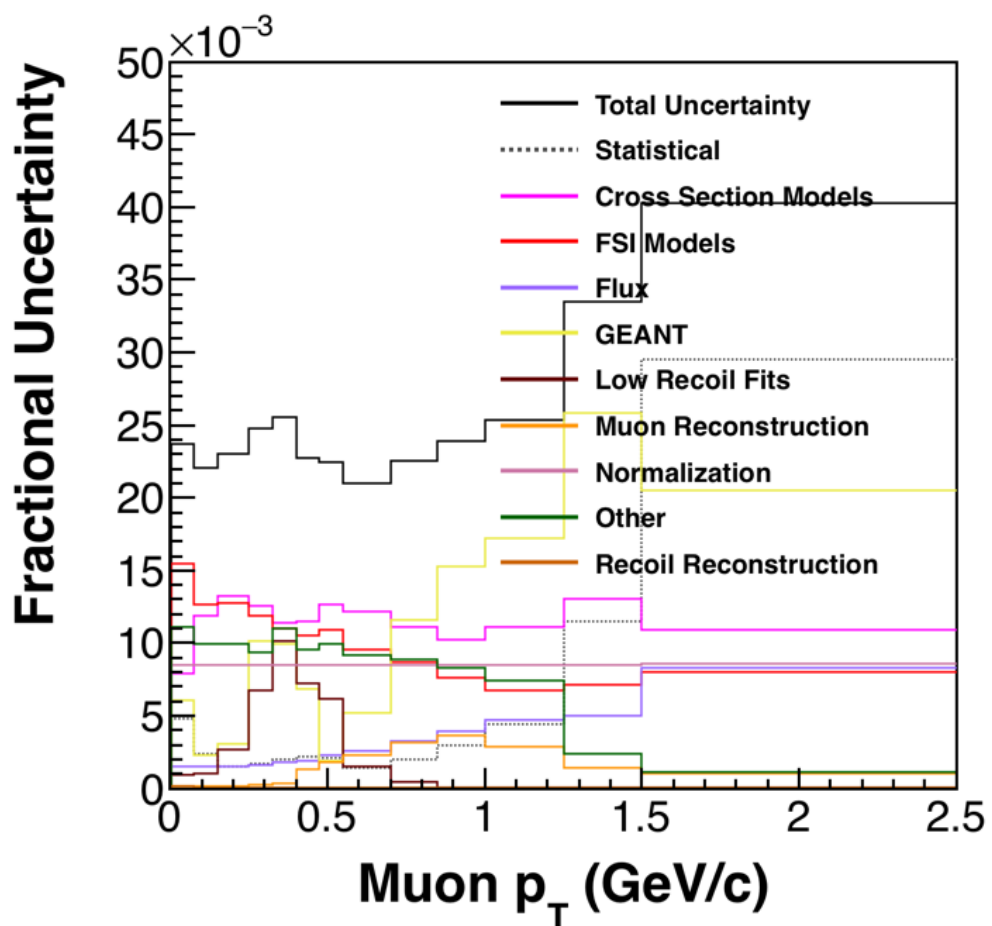
Figure 6.86: Error Summary on the signal selection efficiency as a function of p_T.
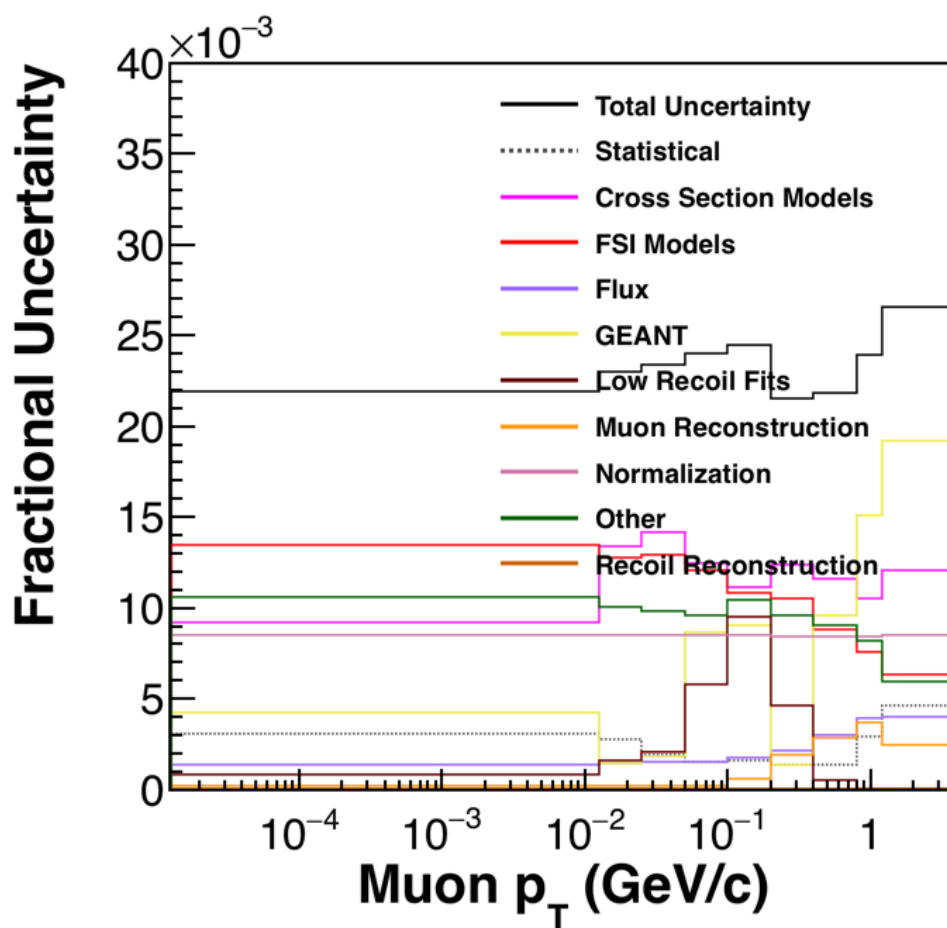
Figure 6.87: Error Summary on the signal selection efficiency as a function of Q^2_{QE}.

the systematic uncertainty on the purity of the sample to know if our estimation is biased by models or suffers from huge uncertainties.

Figures and 6.88 and 6.89 show that in the low Q^2 region, the overall uncertainty is around 4%. At the high Q^2 region the uncertainty on purity is more 10%. The overall uncertainty is dominated by Cross-section models, mostly coming from $MACCQE$ at low and mid Q^2 and $MaRES$ at high Q^2 We should also note that the high Q^2 region is the region with less purity.

6.19.5   Efficiency Correction

As seen in figure 6.19.4, the signal selection itself has the systematic uncertainties. They get propagated to the data when doing the efficiency correction. The efficiency correction is done on the background subtracted and unfolded data.

6.19.6   Target and Flux Normalization and Cross-section

Once the sample goes through the background subtraction, the unfolding, and the efficiency correction, it is a sample in true kinematic phase space and accounts for loss due to our inefficiencies to account for all signal sample. This sample is the collection of the signal processes measured by using neutrino events from 8.47×10^{20} protons on target (POT)
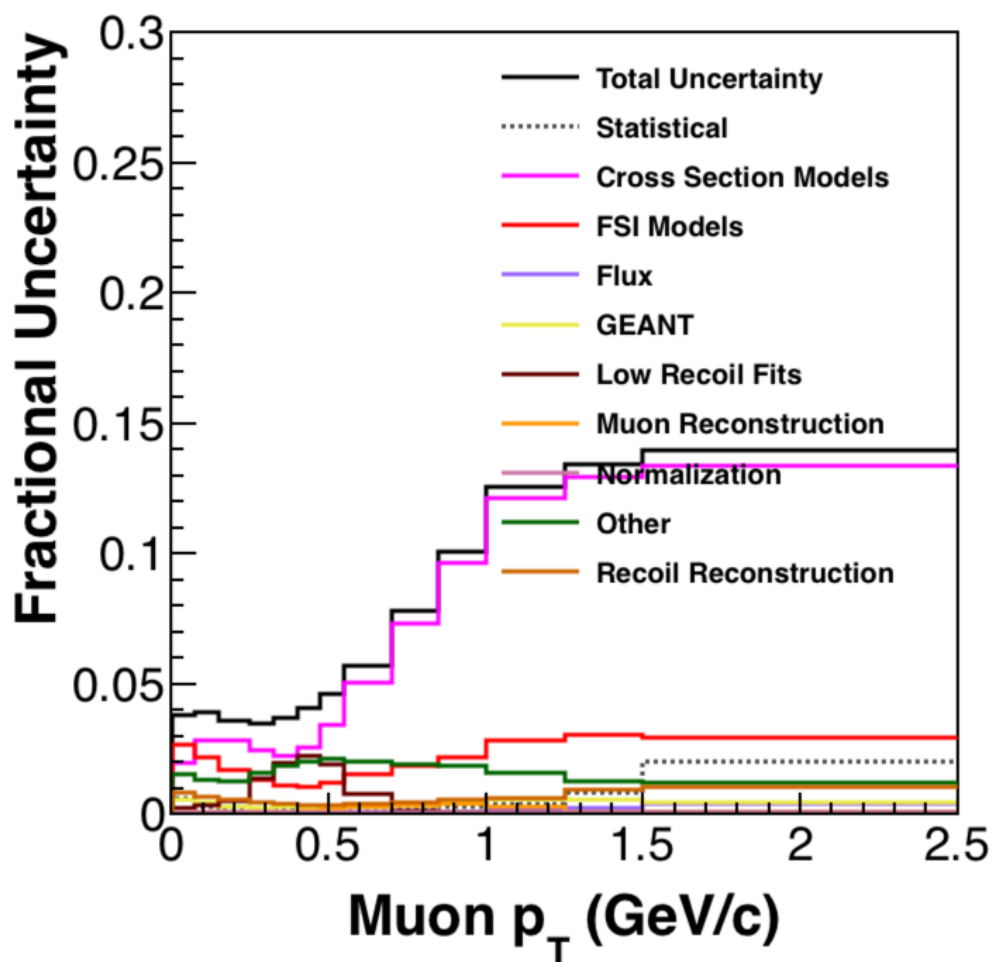
Figure 6.88: Error Summary on the purity of the sample as a function of p_T.
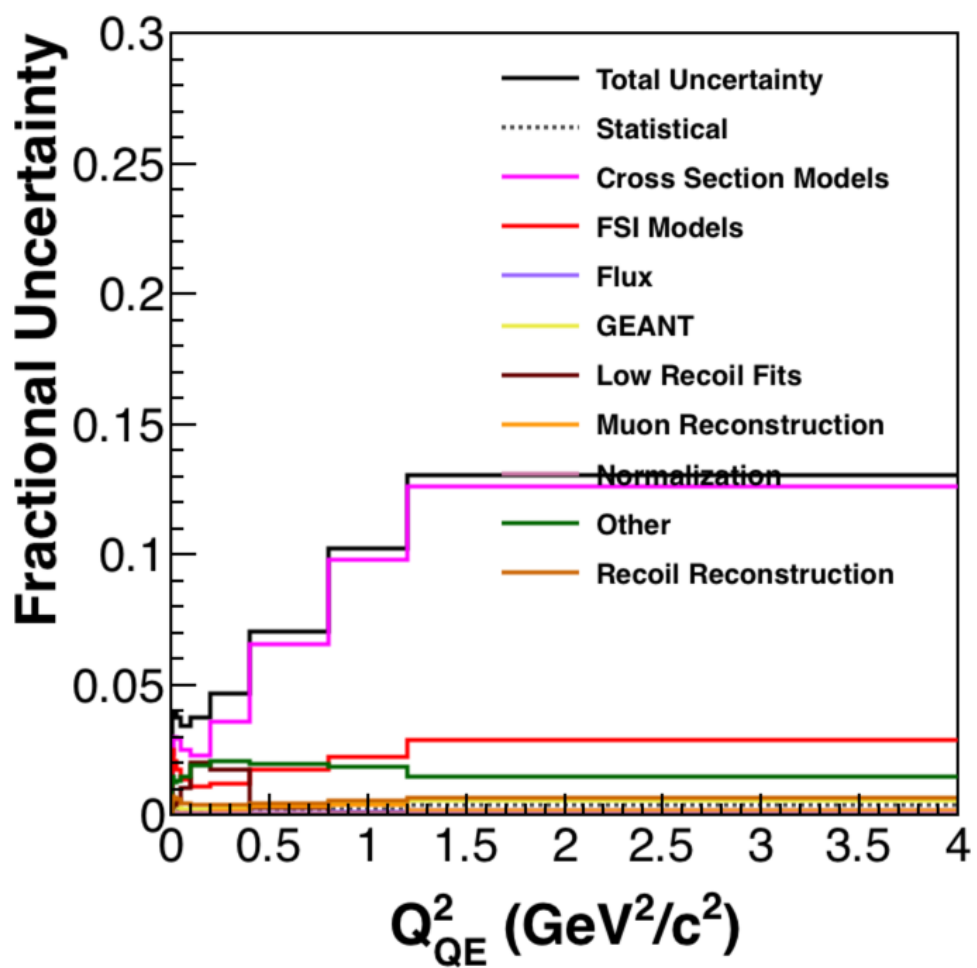
Figure 6.89: Error Summary on the purity of the sample as a function of Q^2_{QE}.
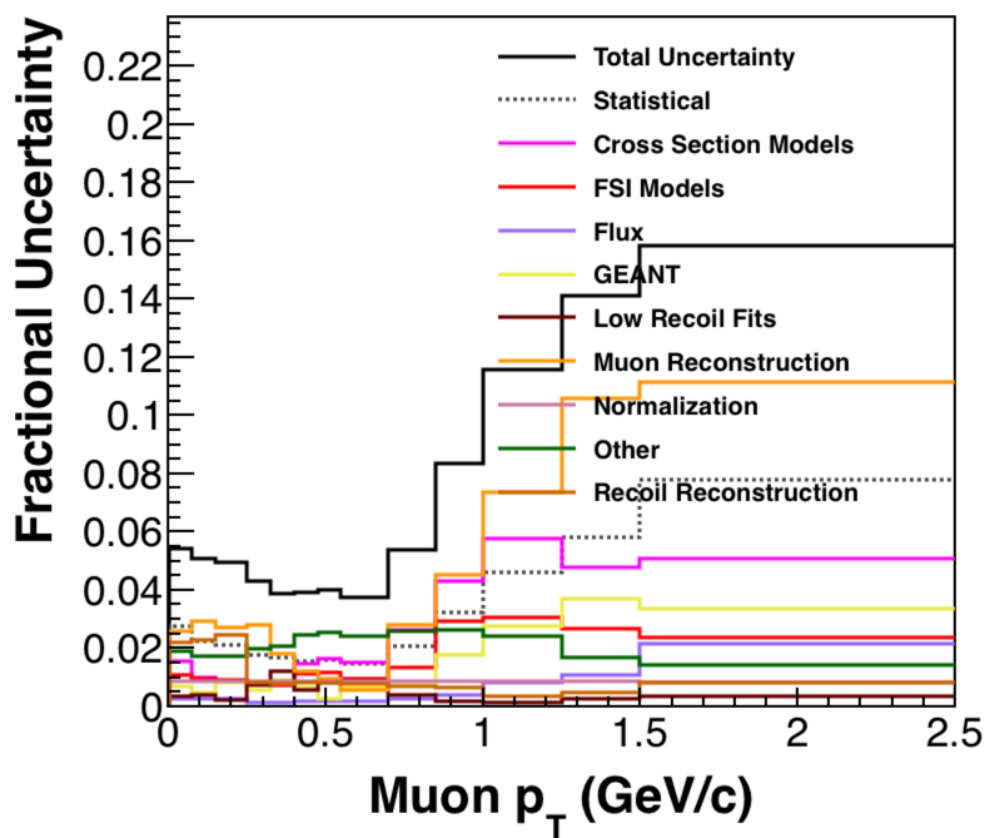
Figure 6.90: Error Summary on the background subtracted, unfolded and efficiency corrected distribution as a function p_T
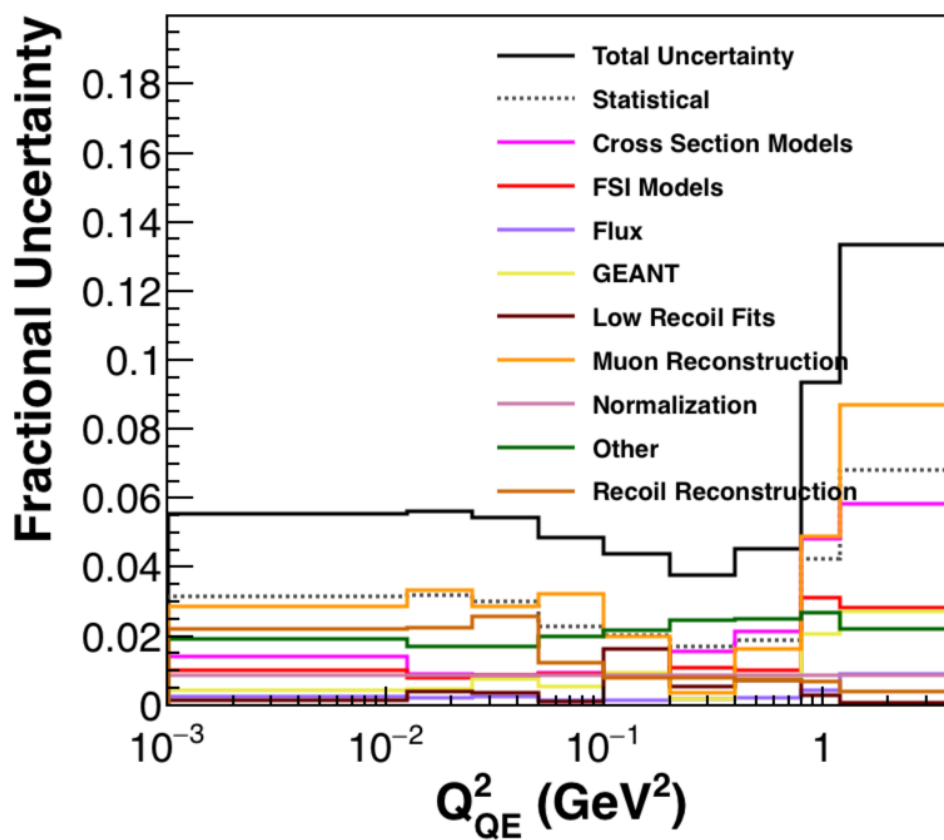
Figure 6.91: Error Summary on the background subtracted,unfolded and efficiency corrected distribution as a function of Q^2_{QE}
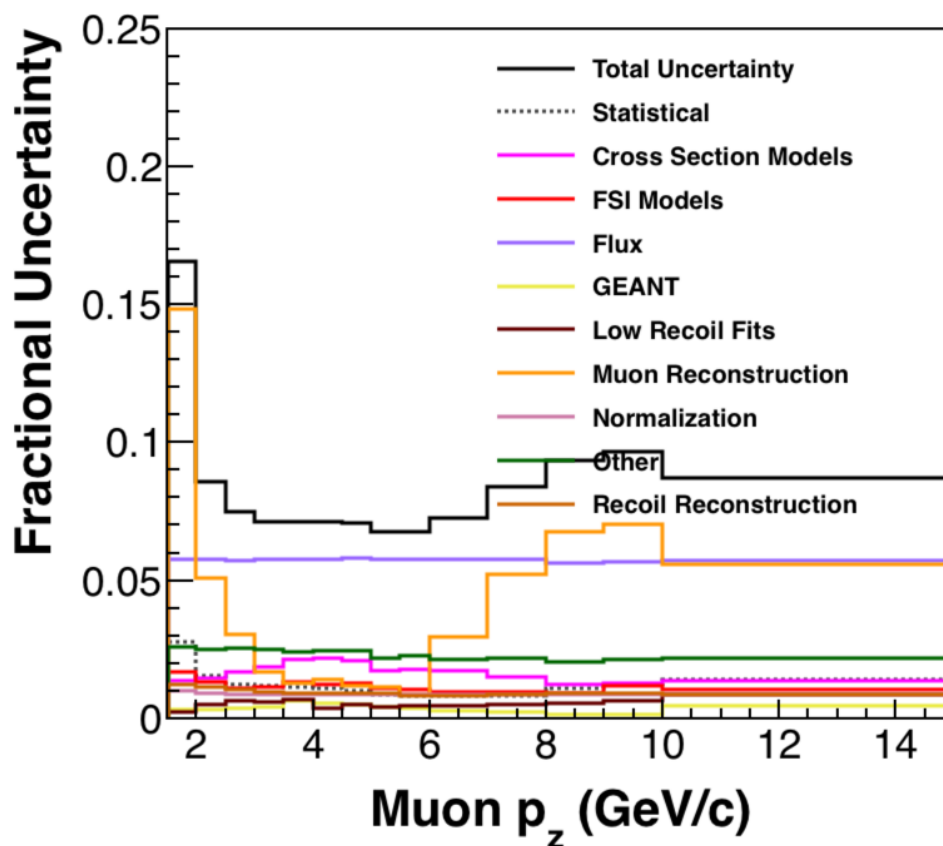
Figure 6.92: Error Summary as a function of p_Z on the final cross-section.

interacting on the fiducial volume of the MINERvA detector that has over 3.23×10^{30} nucleons. To extract the cross-section this sample has to be normalized by the integrated flux (in the case of cross-section as functions of p_z, p_T, Q^2 or by bin by bin flux (in the case of cross-section as a function of E_ν. The uncertainty due to flux goes up after the normalization in the data.
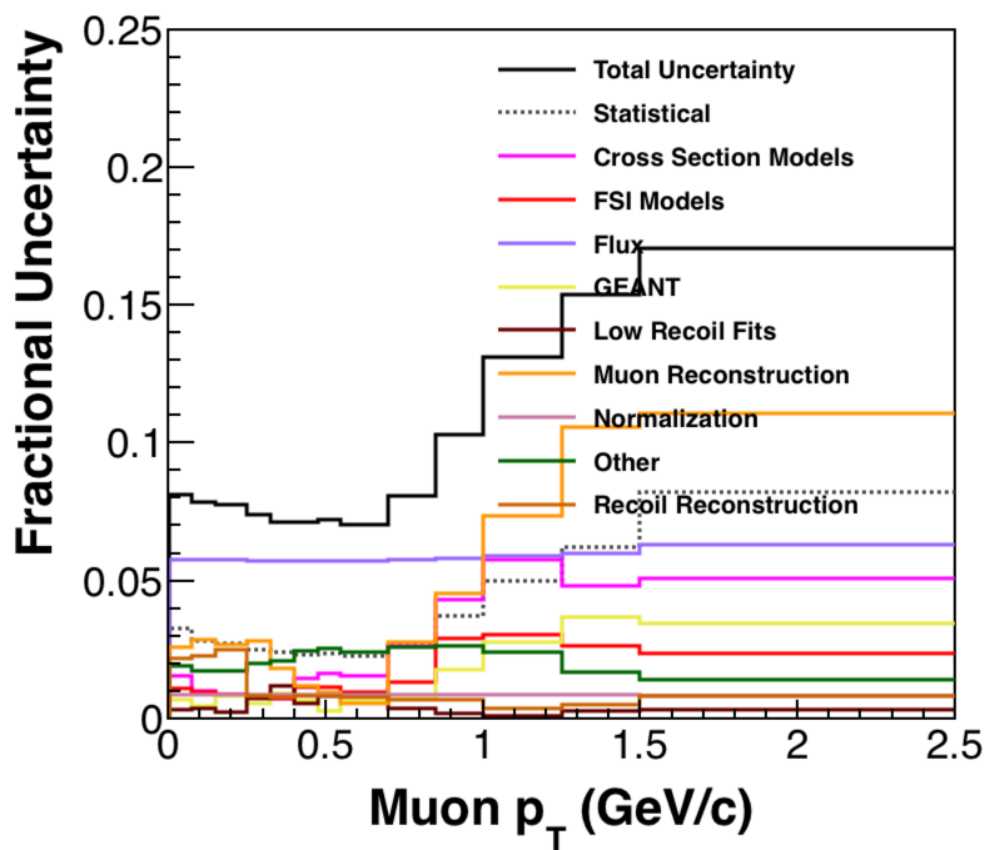
Figure 6.93: Error Summary as a function of p_T on the final cross-section.
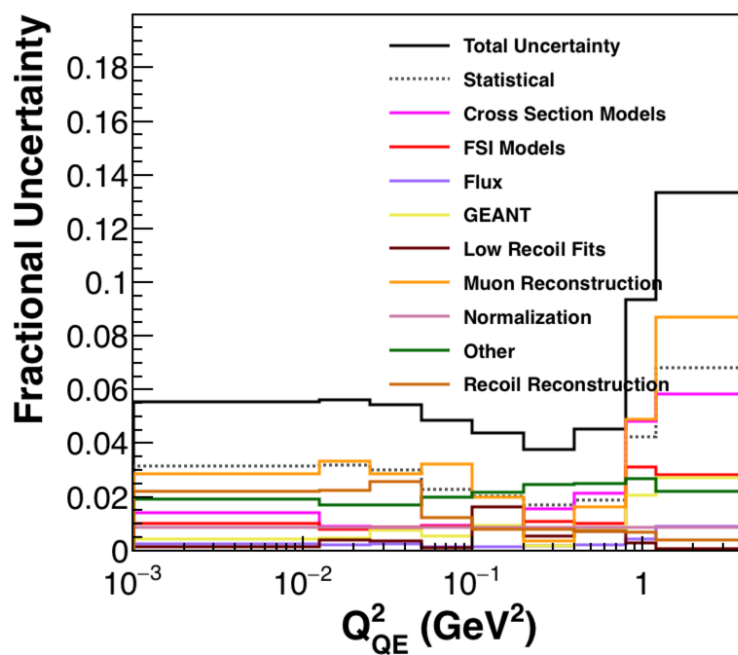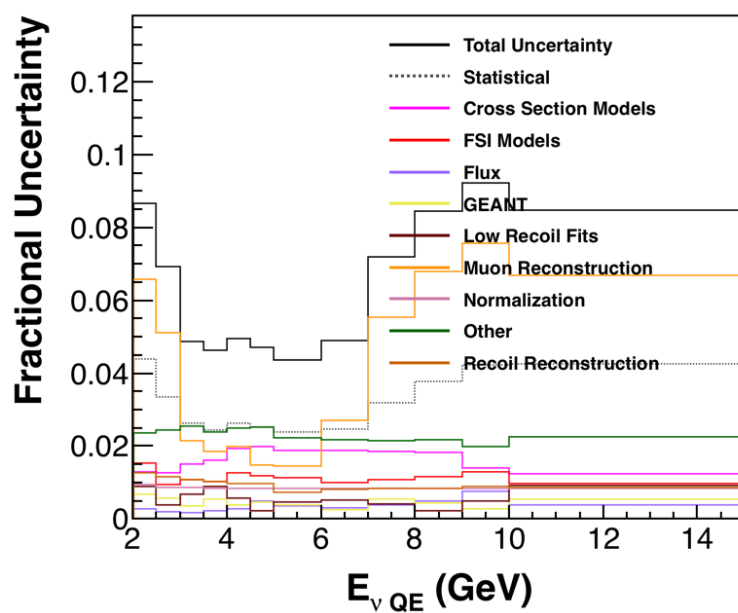
Figure 6.94: Error Summary as a function of Q^2_{QE} and E_ν on the final cross-section
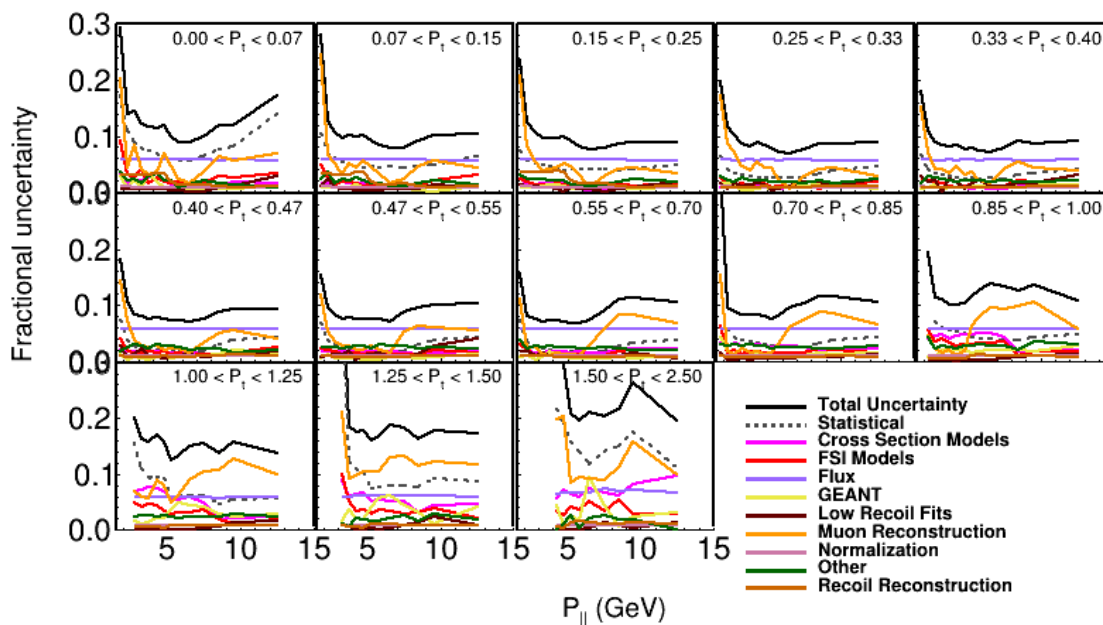
Figure 6.95: Error summary as a function of p_T in the bins of p_Z on the final cross-section
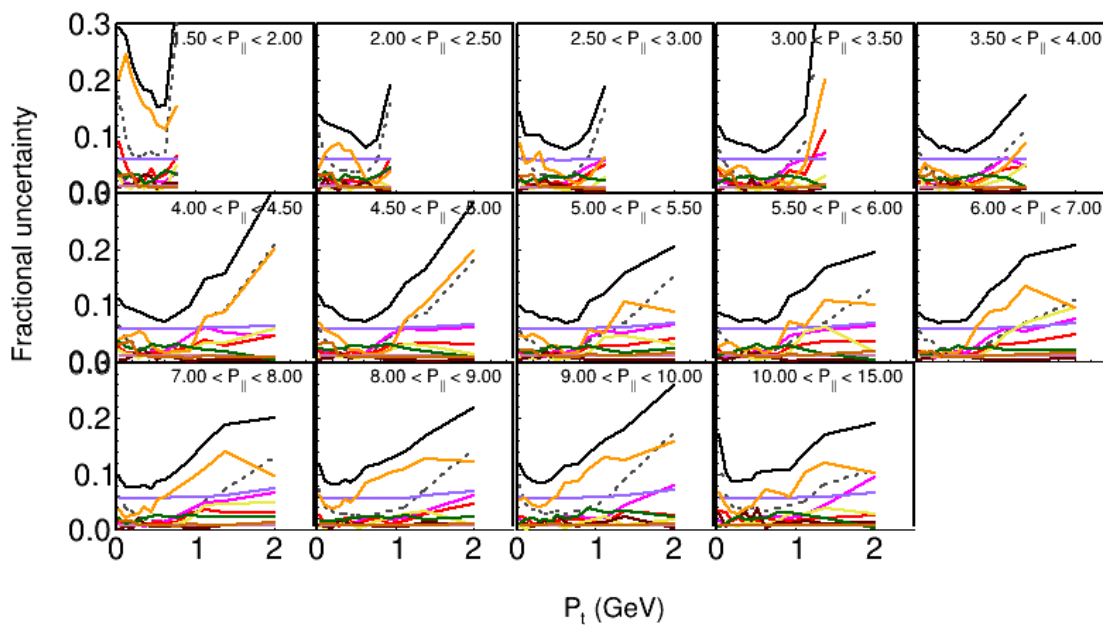
Figure 6.96: Error summary as a function of p_z in the bins of p_T on the final cross-section
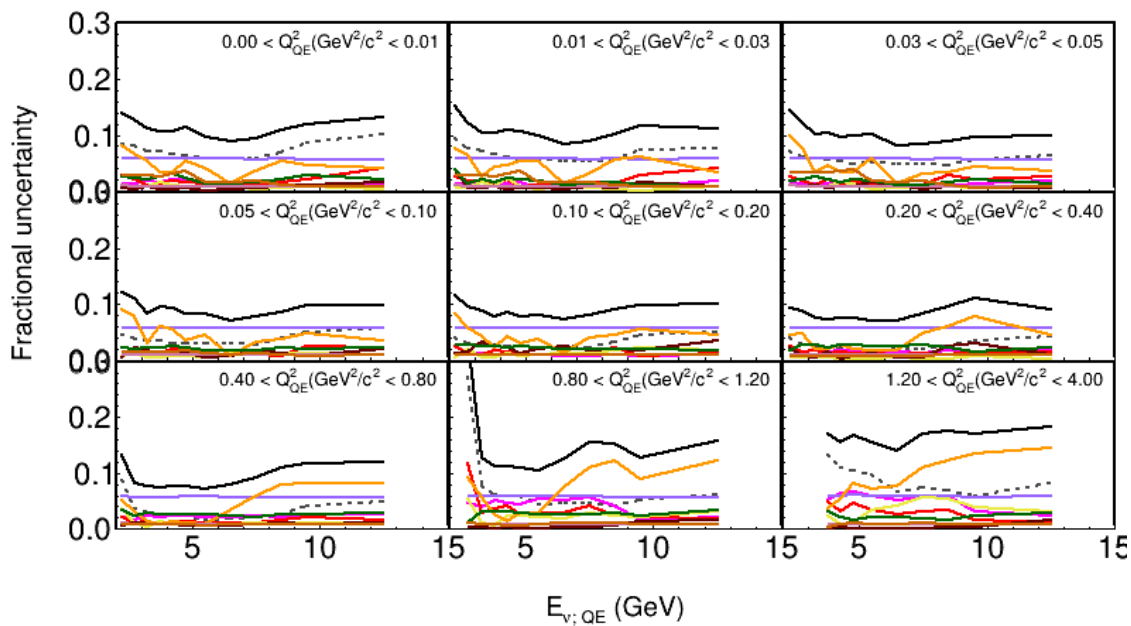
Figure 6.97: Error Summary as a function of $E_{\nu\,QE}$ in the bins of Q^2_{QE} on the final cross-section.
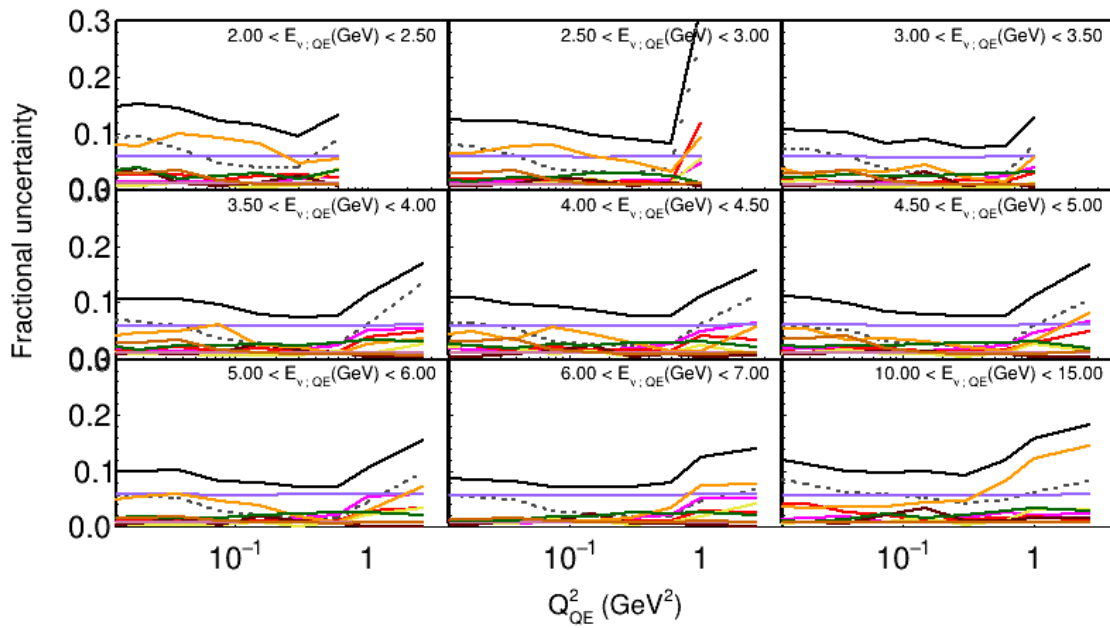
Figure 6.98: Error Summary as a function of Q^2_{QE} in the bins of $E_{\nu\,QE}$ on the final cross-section.

Systematic Uncertainties	Integrated RAW MC(%)	Integrated Bkg. Sub-tracted Data(%)	Integrated Cross-section (%)
Muon Energy MINOS	0.2157	0.1518	0.2669
Muon Energy MINERvA	0.1884	0.1223	0.1452
BeamAngleX	0.0174	0.0198	0.0521
BeamAngleY	0.0109	0.0303	0.0522
Muon Energy Resolution	0.0028	0.007	0.007

Table 6.5: Systematic uncertainties on integrated raw MC, background subtracted data and final cross-section in terms of percentage for Muon Reconstruction group.

Systematic Uncertainties	Integrated RAW MC(%)	Integrated Bkg. Subtracted Data(%)	Integrated Cross-section (%)
AGKYxF1pi	0.1503	0.1493	0.2032
FrAbs N	0.0358	0.1254	0.0405
FrAbs pi	0.841	0.0881	0.8517
FrCEx N	0.3085	0.0446	0.128
FrCEx pi	0.1093	0.1776	0.0739
FrElas N	0.4218	0.1489	0.2264
FrElas pi	0.269	0.1924	0.0567
FrInel N	0.0099	0.0967	0.0639
FrPiProd N	0.0723	0.0611	0.1019
FrPiProd pi	0.0008	0.0024	0.0075
MFP N	2.2735	0.273	0.4907
MFP pi	0.1972	0.1056	0.0784
RDecBR1gamma	0.004	0.0014	0.0
Theta Delta2Npi	0.1904	0.0222	0.0094

Table 6.6: Systematic uncertainties on integrated raw MC, background subtracted data and final cross-section in terms of percentage for Final State Interaction group.

Systematic Uncertainties	Integrated RAW MC(%)	Integrated Bkg. Subtracted Data(%)	Integrated Cross-section (%)
CCQEPauliSupViaKF	2.1499	0.2501	0.0013
EtaNCEL	0.0	0.0	0.0
MaCCQE	9.3788	0.3089	1.1376
MaNCEL	0.0	0.0	0.0
MaRES	4.0954	0.1771	0.3657
MvRES	1.7079	0.0616	0.2472
NormDISCC	0.0	0.0	0.0
NormNCRES	0.0	0.0	0.0
Rvn1pi	0.1642	0.0362	0.0632
Rvn2pi	0.1291	0.7967	0.8861
Rvp1pi	0.1642	0.0362	0.0632
Rvp2pi	0.3793	0.7214	0.7918
VecFFCCQEshape	0.218	0.0088	0.0195
AhtBY	0.0035	0.0073	0.0117
BhtBY	0.005	0.0106	0.0166
CV1uBY	0.0059	0.0182	0.0277
CV2uBY	0.0054	0.0168	0.0254
RPA HighQ2	2.5784	0.0794	0.2936
RPA LowQ2	2.6746	0.355	0.033

Table 6.7: Systematic uncertainties on integrated raw MC, background subtracted data and final cross-section in terms of percentage on GENIE Models group.

Systematic Uncertainties	Integrated RAW MC(%)	Integrated Bkg. Subtracted Data(%)	Integrated Cross-section (%)
response em	0.1773	0.3656	0.3459
response meson	0.3868	0.8491	0.8032
response proton	0.08	0.1522	0.1535
response other	0.0175	0.0706	0.0796

Table 6.8: Systematic uncertainties on integrated raw MC, background subtracted data and final cross-section in terms of percentage for Response group.

Systematic Uncertainties	Integrated RAW MC(%)	Integrated Bkg. Sub-tracted Data(%)	Integrated Cross-section (%)
GEANT Neutron	0.1745	0.0849	0.2367
GEANT Proton	0.0526	0.0364	0.0453
GEANT Pion	0.2228	0.2362	0.2514

Table 6.9: Systematic uncertainties on integrated raw MC, background subtracted data and final cross-section in terms of percentage for GEANT group.

Systematic Uncertainties	Integrated RAW MC(%)	Integrated Bkg. Sub-tracted Data(%)	Integrated Cross-section (%)
Flux	5.5871	0.17	5.7388
Low Recoil 2p2h Tune	2.0665	0.6057	0.4566

Table 6.10: Systematic uncertainties on integrated raw MC, background subtracted data and final cross-section in terms of percentage for Flux,2p2h and normalization.

Systematic Uncertainties	Integrated RAW Data(%)	Integrated Bkg. Sub-tracted Data(%)	Integrated Cross-section (%)
Stat Error	0.13	0.26	0.30
Total Systematic	**0**	**2.21**	**6.65**
Total Stat+Sys	**0.13**	**2.22**	**6.66**

Table 6.11: Systematic uncertainties on integrated raw data, background subtracted data and final cross-section in terms of percentage for Stat and all systematics.

6.20   Cross-section Results

The final cross-section results after going through the analysis stages from **event recon-struction** to **flux and target normalization** stage is discussed in this section.

Figures 6.99 through 6.102 show the cross-sections in the 2D to 1D projected phase spaces. Similarly figures 6.103 through 6.106 shows the 2D cross-section in different variables along with different MC components. As a function of p_z or E_ν, the cross-section distribution
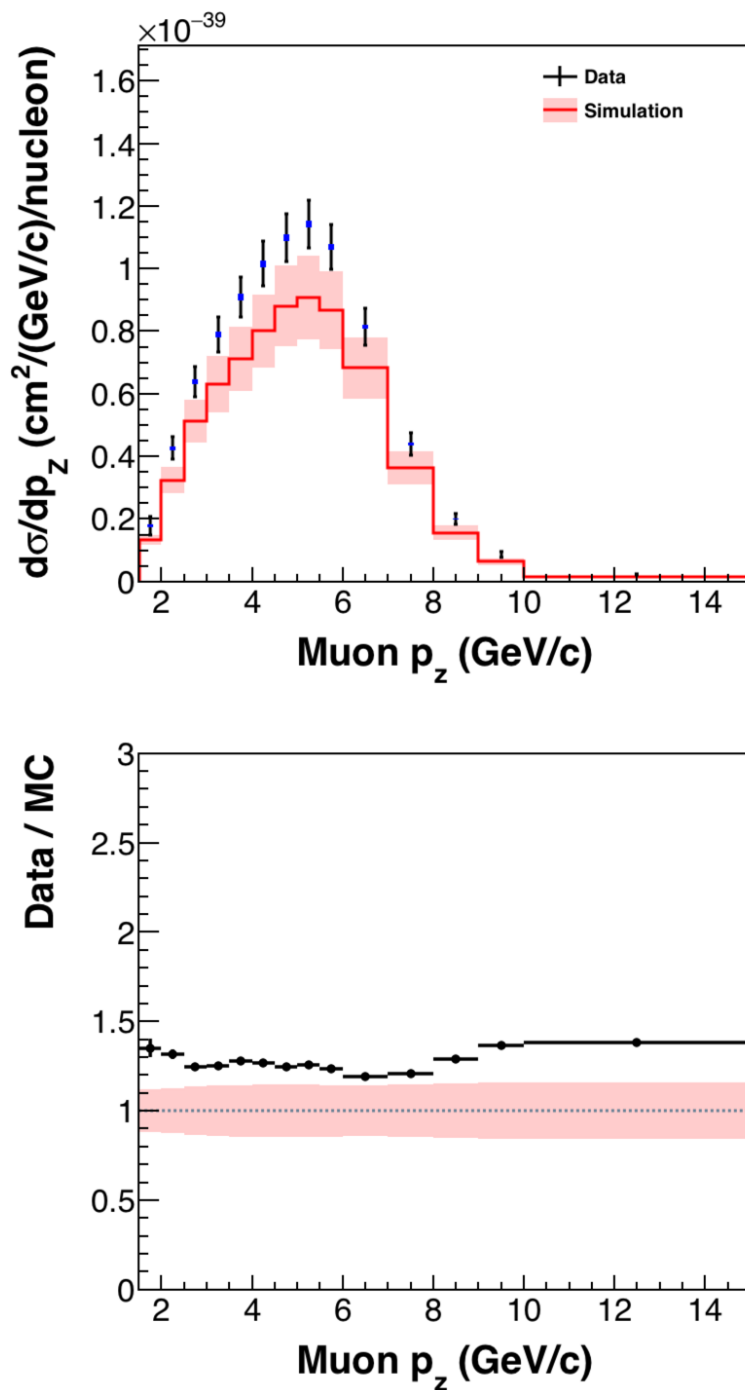
Figure 6.99: Cross-section as a function of muon p_z showing the data and the MINERvA tune v1. The pink error band shows the systematic error band on the model and the error bars on the data is total error. Blue rectangles show the statistical errors on the data.
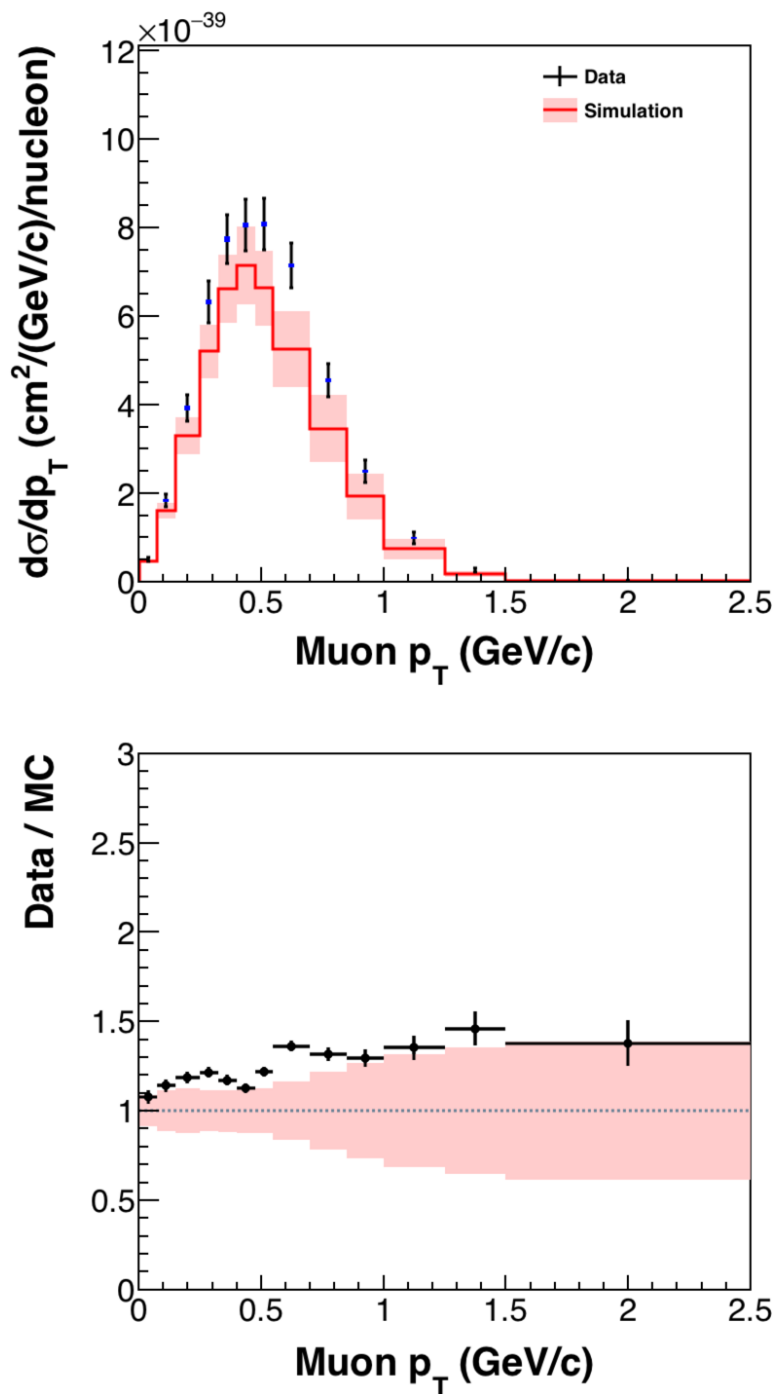
Figure 6.100: Cross-section as a function of muon p_T showing the data and the MINERvA tune v1. The pink error band shows the systematic error band and the error bars on the data is total error. Blue rectangles show the statistical errors on the data.
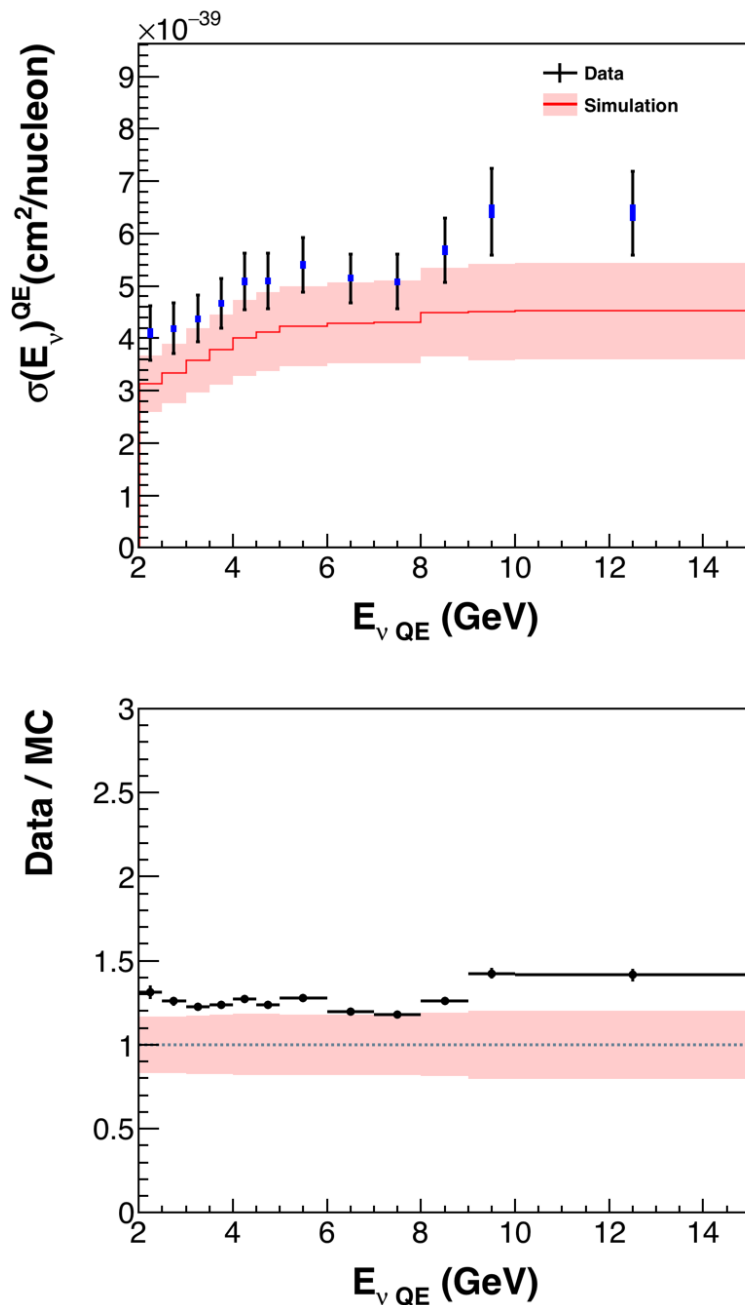
Figure 6.101: Cross-section as a function of muon $E_{\nu\ QE}$ showing the data and the MINERvA tune v1. The pink error band shows the systematic error band and the error bars on the data is total error. Blue rectangles show the statistical errors on the data. Note that this distribution is bin by bin flux normalized.
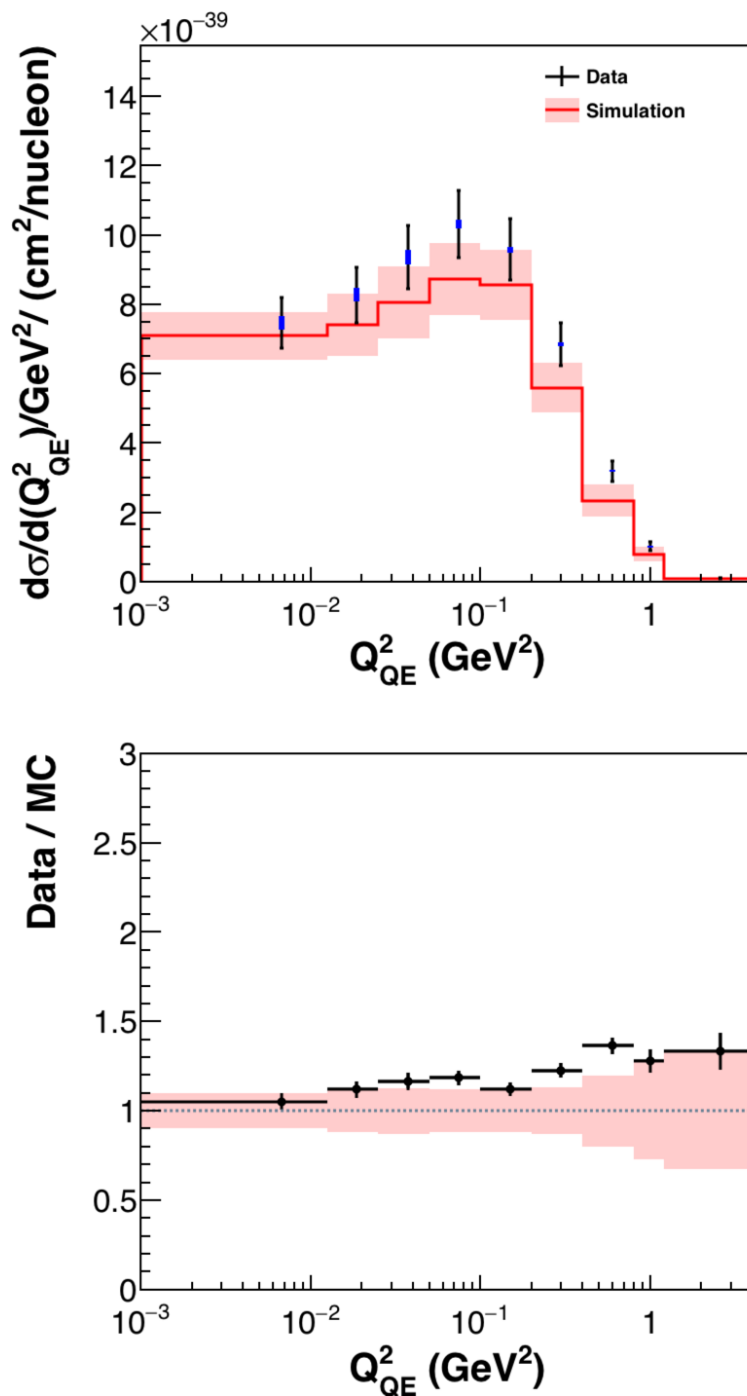
Figure 6.102: Cross-section as a function of muon Q^2_{QE} showing data and MINERvA tune v1. The pink error band shows the systematic error band and the error bars on the data is total error. Blue rectangles show the statistical errors on the data. Note that this distribution is bin by bin flux normalized.
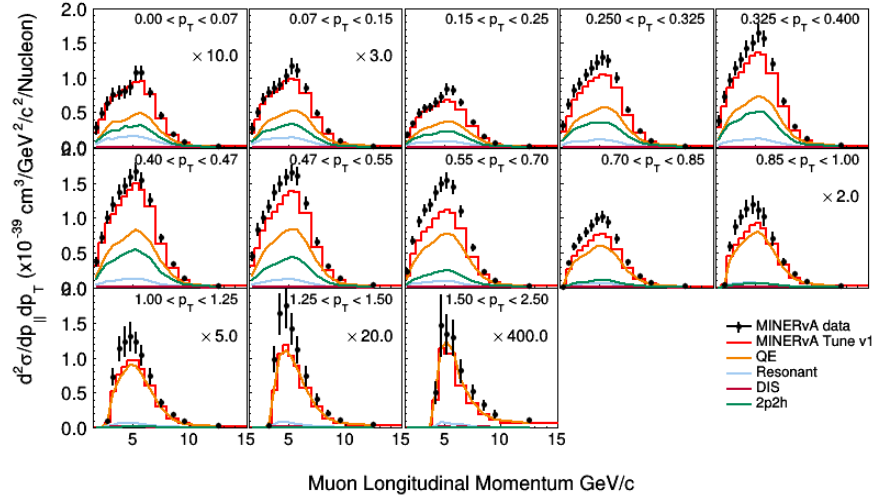
Figure 6.103: Cross-section as a function of p_z in the bins of p_T for the data, the MC and the various components of the MC.
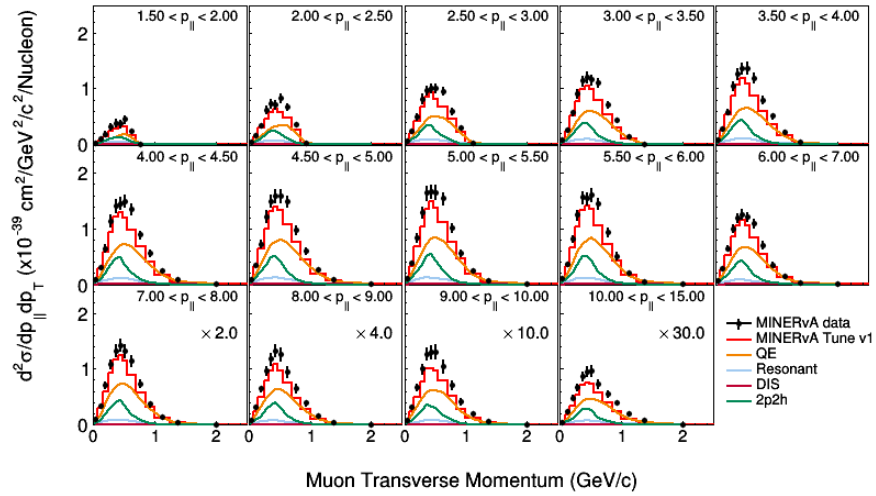
Figure 6.104: Cross-section as a function of p_T in the bins of p_z for the data, the MC and the various components of the MC.
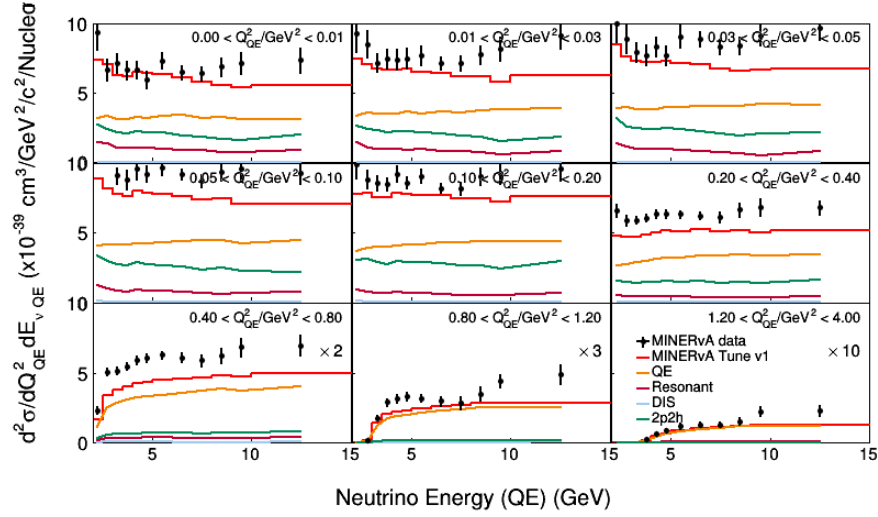
Figure 6.105: Cross-section as a function of $E_{\nu\,QE}$ in the bins of Q^2_{QE} for the data, the MC and the various components of the MC.
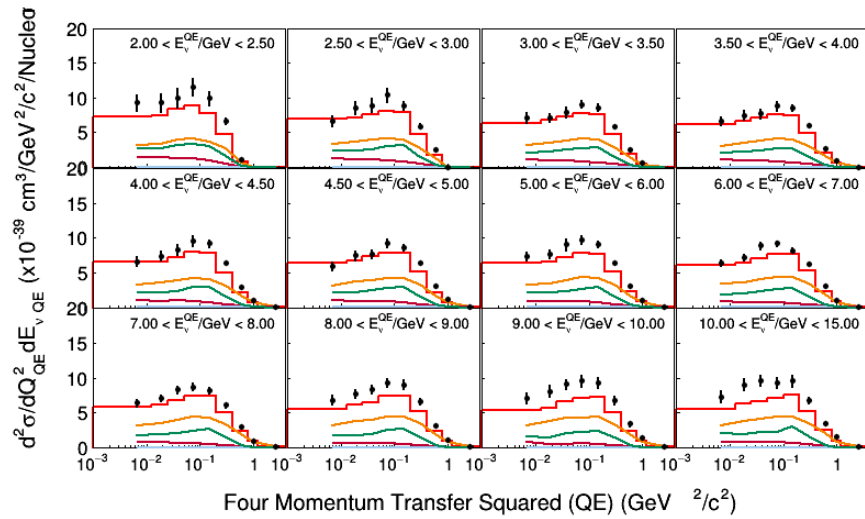
Figure 6.106: Cross-section as a function of Q^2_{QE} bins of E_ν for the data, the MC and the various components of MC.

shows that the MC under predicts the QELike cross-section by 20 to 30% across all bins.

Figure 6.103 shows the cross-section as a function of muon longitudinal momentum in the bins of muon transverse momentum. The low p_T bins are dominated by the true QE and the 2p2h processes. In the high p_T bins, the contribution from the 2p2h processes slowly decreases. Beyond $p_T \geq 0.85 Gev/c$, the QELike processes are mostly compromised of the true QE processes. The resonance processes show larger contributions in very low p_T bins compared to the rest of the p_T bins. The DIS contribution is almost non existent in all bins.

Figure 6.105 shows the neutrino energy (QE) in different Q^2 bins. The neutrino cross-section is almost constant across all Q^2 bins. The drop in cross-section in high Q^2 is mainly due to the angle cut which excludes the high p_T,low p_Z events. The discrepancy between data and MC is is particularly large in the last Q^2 bin (between 1.2 and 4 GeV^2). Poor cross-section modeling (dipole model generally breaks at high Q^2) and possible background contamination in the data could contribute to the discrepancy.

Figures 6.107 show the cross-section comparisons between neutrino and anti-neutrino as a function of Q^2_{QE} for the MINERvA ME run. The neutrino analysis takes into account the events with muon track only as well as the events with muon+proton tracks unlike the anti-neutrino analysis, where we look at the events with a muon track only. However, we can see that the overall distribution is similar between neutrino and anti-neutrino cross-section in terms of the shape. The ratio shows that in the first Q^2 bin, the model over-predicts
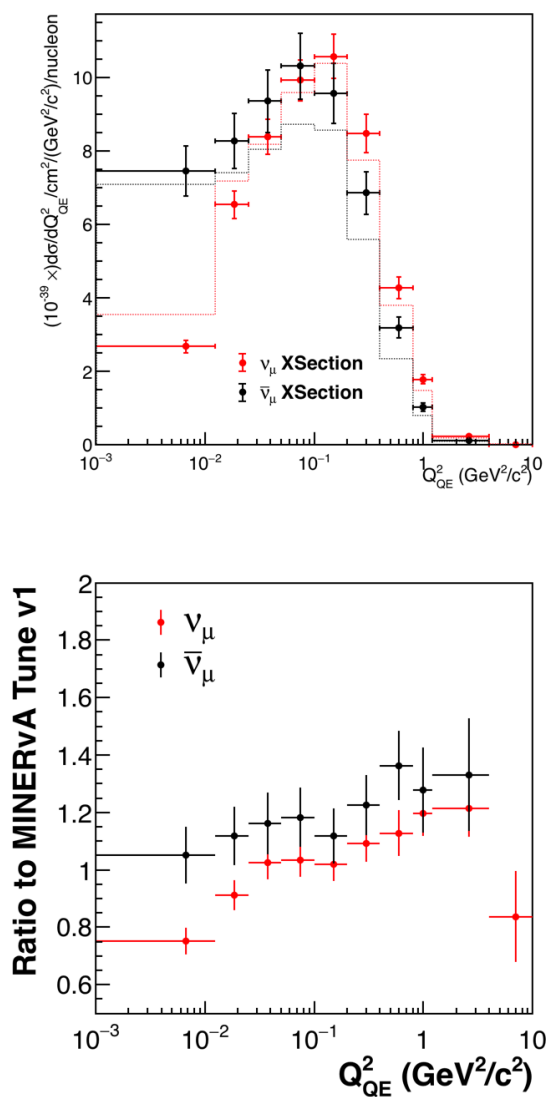
Figure 6.107: Cross-section as a function of Q^2_{QE} for ν_μ and $\bar{\nu}_\mu$ (CCQELike) (top) and the ratio of data to MINERvA tune cross-section (bottom). In the top figure, dotted lines represent the prediction from the MINERvA Tune v1. Both cross-section are extracted using MINERvA 's ME data sets. Errors on data are total errors (systematic+statistical error).

the cross-section compared to the data for the neutrino cross-section. Whereas the model is describing the data well in that bin for the anti-neutrinos. Some of that discrepancy could be coming from the pions that fake as the protons and contribute in the multi-track events for the neutrinos. The low Q^2 suppression (coming from the RPA) that is a part of MINERvA tune model, suppresses the default GENIE's pion production in low Q^2. The last Q^2 bin only has neutrino cross-section ($Q^2 = (4, 10)GeV^2$) since the anti-neutrino analysis doesn't extend to that bin. Figures 6.108 show the cross-section as a function of Q^2_{QE} extracted from the MINERvA LE data and MINERvA ME data. The LE data measured the cross-section upto 2 GeV^2/c^2 whereas this analysis does the measurement up to 4 GeV^2/c^2. In the high Q^2 region, the data and model behave differently for LE and ME extracted cross-section. In the case of the cross-section extracted from the LE data, the model over-predicts the cross-section compared to the data. In the case of cross-section extracted from the ME data, the model under-predicts the cross-section. It should be noted that the muon energy scale is shifted in the ME data. It is possible that we are also seeing the effect of shift on the high Q^2 events in the ME data. The effect of shifting of the muon energy scale in the cross-section are shown in figures C.2 and C.1 respectively in the appendix of the thesis.
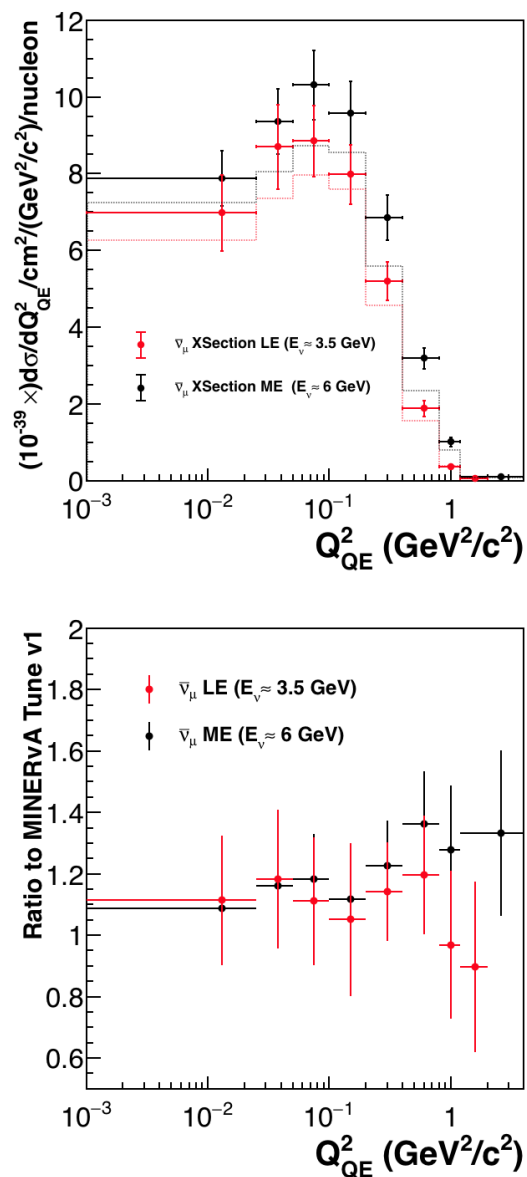
Figure 6.108: Cross-section as a function of Q^2_{QE} for $\bar{\nu}_\mu$ extracted with the LE data (red) and the ME data (black). Top figure shows the measured cross-section (points) and the prediction from the MINERvA Tune v1 (dotted lines). Bottom figure shows the ratio of data to model. Errors on the data are total errors (systematic+statistical errors).
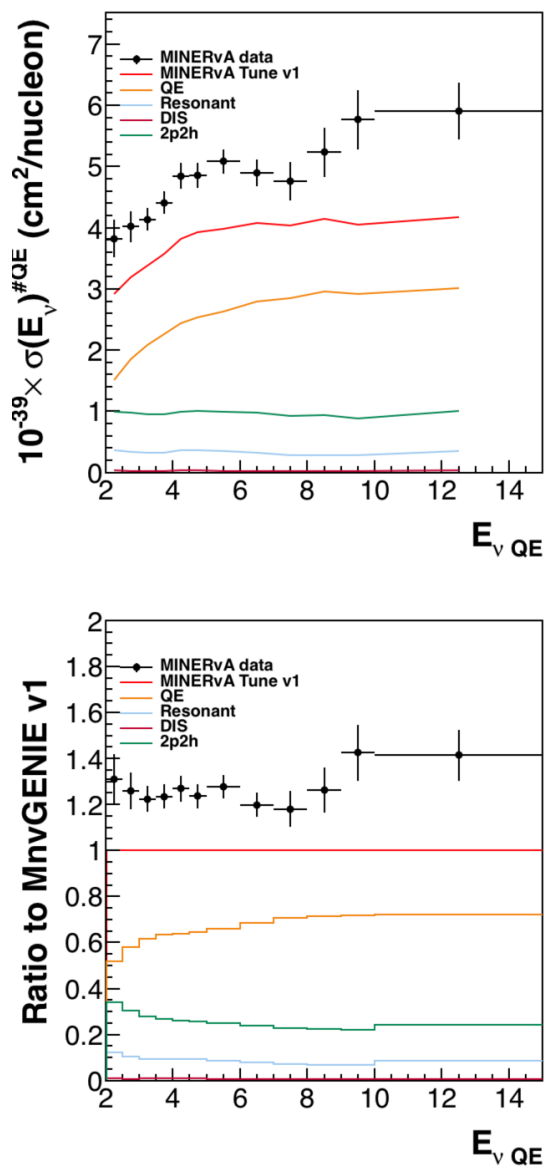
Figure 6.109: The breakdown of cross-section into various model components as a function of neutrino energy (QE). Since this cross-section is obtained by E_ν bin by bin flux normalization, any discrepancy in flux shape would be seen in this distribution. The error bars on the data represents total error (statistical+systematic errors).
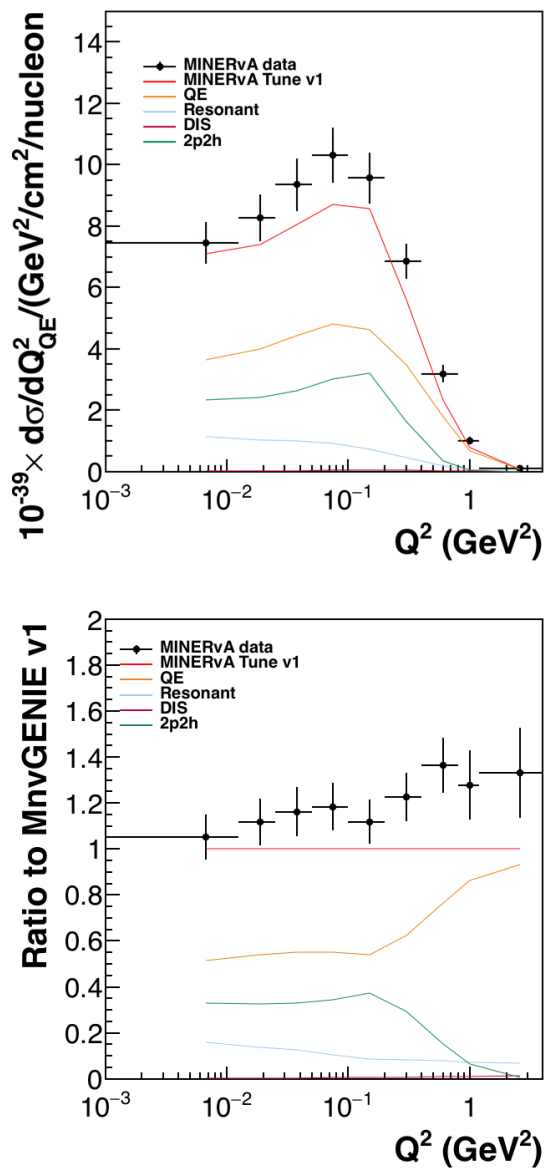
Figure 6.110: Breakdown of cross-section into various model components as a function of Q^2_{QE}. Going from low to high Q^2, the contribution from 2p2h goes down and is dominated by true QE component. The resonance contribution from absorbed pions has larger contribution in low Q^2 region.

Analysis Stage	Measurement
Before Background Subtraction	584207± 764 ±0.0
After Background Subtraction	479158 ± 1251 ± 10604.45
After Background Subtraction+Unfolding	478104.24 ± 1305.43 ± 10585.74
After Background Subtraction+ Efficiency Correction	711749.44 ± 2136.96 ± 24027.16
Integrated Cross-section	5.28E-39 ± 1.59E-41 ± 3.51E-40

Table 6.12: Measurements in various stages of the analysis. Errors are statistical ± systematic errors on the integrated values.

6.20.1   Comparison with Other Models

MINERvA uses MINERvA Tune v1 (GENIE+2p2h+RPA+Pion Tune) as its default model. This section will compare the neutrino cross-section with various models. Since we apply various corrections on the default GENIE (2.12.6), data cross-section and predictions from various models are compared to the default GENIE to see how these corrections affect our models. Figures 6.111 and 6.112 show the cross-section ratio of data and various models to GENIE. For the sake of comparison, the figure 6.113 shows the cross-section as a function of Q^2_{QE} for ν_μ CCQELike events. Note that the ν_μ cross-section ratio goes to higher Q^2_{QE} compared to the $\bar{\nu}_\mu$ cross-section. The solid red line and the dotted red line represent the MINERvA Tune v1 and v2 respectively. The cross-section ratios as a function of neutrino energy (QE) show that the models are always under predicting the cross-section compared to the data. The data follows the MINERvA tune v1 and v2 (v1+Low Q^2 suppression of non-resonant pion production) models and GENIE models with RPA cross-sections. The effect
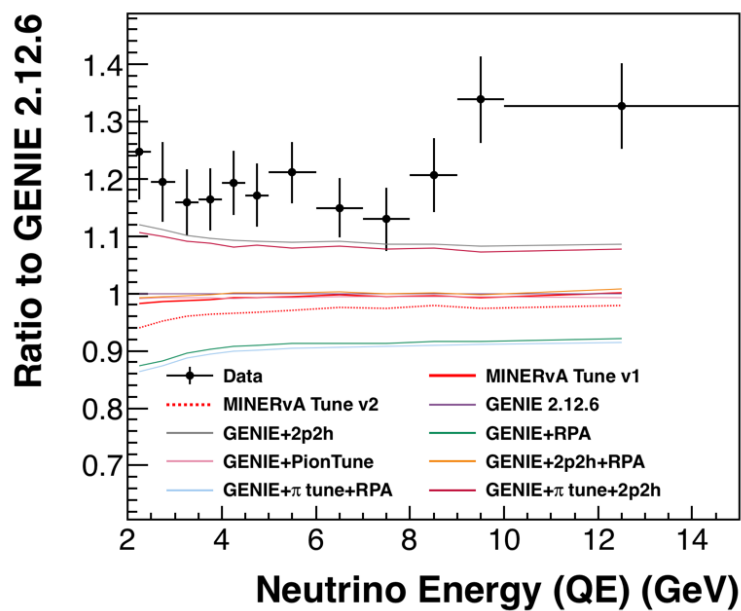
Figure 6.111: Ratio of cross-sections (as a function of neutrino energy (QE based hypothesis) from GENIE to data and various models. $\nu + e$ constrain is not applied to the flux.
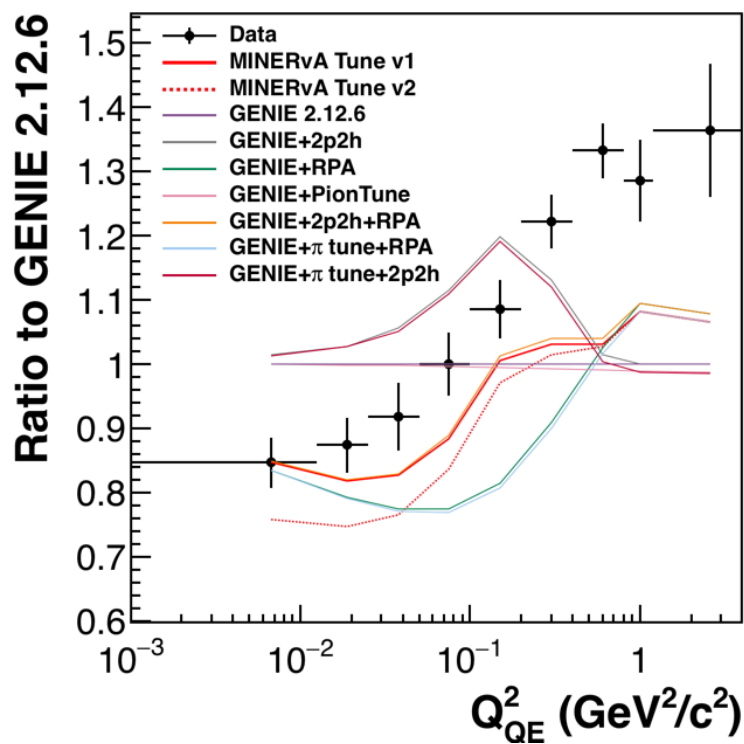
Figure 6.112: Ratio of cross-sections (as a function of Q^2_{QE} with GENIE to data and various models for $\bar{\nu}_\mu$ CCQELike cross-section. The MINERvA Tune v1 and MINERvA Tune v2 are shown in solid red and dotted red line respectively. $\nu + e$ constrain is not applied to the flux.
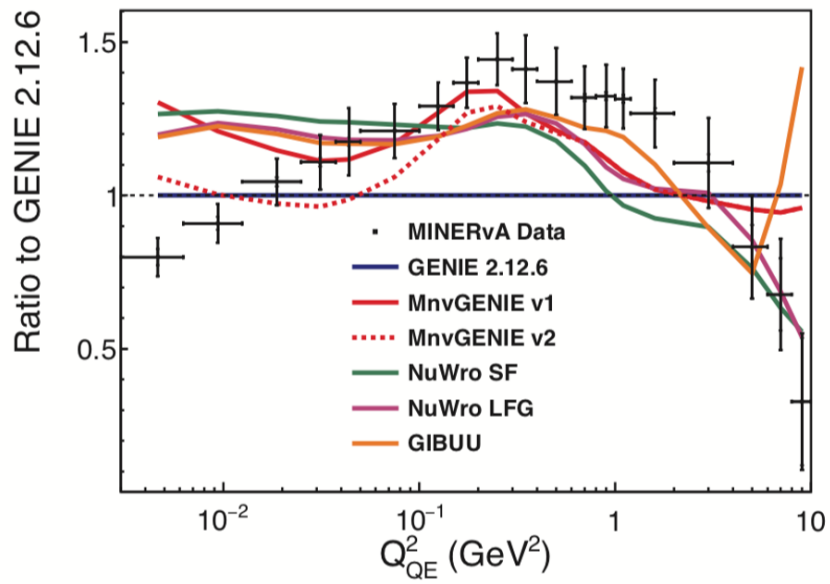
Figure 6.113: Ratio of cross-sections as a function of Q_{QE}^2 with GENIE to data and various models for ν_μ CCQELike cross-section. The MINERvA Tune v1 and MINERvA Tune v2 are shown in solid red and dotted red line respectively. Figure taken from [48].

of applying low Q^2 suppression for the resonant pion production in addition to the standard tunes is seen in MINERvA Tune v2 (dotted red line). The suppression decreases the overall cross-section. Figure 6.112 shows that the tune has greatest effect in the low Q^2 region. The data is best described by both MINERvA Tune v1 and MINERvA Tune v2 in the low Q^2 region. Removing the 2p2h tune from MINERvA v1 (GENIE+ π tune+2p2h) shows an overall decrease in cross-section prediction, especially in the low Q2 region. However, the effect of applying the 2p2h only in the GENIE model (GENIE+2p2h), is an over-prediction of the cross-section. Since the tune is only applied between the phase space of (energy transfer) $q_o = (0.0, 1.2)$ GeV and (momentum transfer) $q_3 = (0.0, 1.2)$ GeV/c, we can see the dip in the 2p2h tuned models after $Q_{QE}^2 = 0.1 GeV^2$ beyond which there are no 2p2h events. Similarly, GENIE+π tune+2p2h shows the effect of RPA correction on the MINERvA tune v1. In fact, GENIE+RPA (orange line) shows the suppression of the events at low Q^2. This is consistent with the overall RPA correction described in [83].

However, it should be noted that none of the model variations describe the data at high Q_{QE}^2. Except for the RPA tune, there are no tunes applied in the high Q^2 events which makes the ratios converge towards 1.

Table 6.13 shows the linear χ^2 between data and model cross-section (as a function of muon p_T vs. muon p_z) for CCQELike analyses. The χ^2 is calculated by taking the total error matrix (statistical+systematic) from the data cross-section and adding the statistical

Models	χ^2/NDF (ME-$\bar{\nu}_\mu$)	χ^2/NDF (LE-$\bar{\nu}_\mu$)	χ^2/NDF (ME-ν_μ)
MINERvA Tune v1	320/171	81/58	1194/184
MINERvA Tune v2	281/171	-	799/184
GENIE (2.12.16)+2p2h	402/171	-	2299/184
GENIE+Low Recoil Fits	511/171	150/58	-
GENIE+PionTune+2p2h	410/171	-	2377/184
GENIE+RPA+2p2h	255/171	70/58	-
GENIE+Low Recoil Fits+RPA	316/171	-	-
GENIE+RPA+PionTune+2p2h	260/171	-	1068/184
GENIE+Low Recoil Fits+PionTune	489/171	-	2714/184

Table 6.13: Linear χ^2 comparison between various models and data for 2D cross-section as a function of muon kinematics. The full covariance matrix (statistical+systematics) is taken into account to compute the χ^2. χ^2 results for low energy(LE) $\bar{\nu}_\mu$ is taken from [129] and medium energy(ME) ν_μ is taken from [48]. The χ^2 calculated in ME ν_μ does not take model statistical errors into account. Muon momenta range for the above 3 analyses are given in table 6.14

Analysis	p_T(GeV/c) range	$p_{||}$ (GeV/c) range
ME $\bar{\nu}_\mu$	0.0-2.5	1.5-15
ME ν_μ	0.0-2.5	1.5-20
LE $\bar{\nu}_\mu$	0.0-1.5	1.5-15

Table 6.14: Range of Muon Momenta for the 3 CCQELike analyses for which the χ^2 result is shown in table 6.13.

Models	χ^2/NDF (ME-$\bar{\nu}_\mu$)
MINERvA Tune v1	58/8
MINERvA Tune v2	34/8
GENIE (2.12.16)+2p2h	164/8
GENIE+Low Recoil Fits	130/8
GENIE+Pion Tune+2p2h	168/8
GENIE+RPA+2p2h	90/8
GENIE+Low Recoil Fits+RPA	57/8
GENIE+RPA+2p2h+PionTune	93/8
GENIE+Low Recoil Fits+PionTune	168/8

Table 6.15: Linear χ^2 comparison between various models and data for 1D cross-section as a function of Q^2_{QE}

error matrix from the models (except for ν_μ ME version where statistical error from the model is not added). Both low and medium energy version of the $\bar{\nu}_\mu$ CCQELike data prefers the RPA corrected model with untuned 2p2h. Tuning the 2p2h seems to increase the χ^2 from 255 to 316 in case of medium energy $\bar{\nu}_\mu$ CCQELike. The effect of the addition of RPA and the low recoil fits for medium energy ν_μ and $\bar{\nu}_\mu$ CCQELike can be seen in the last two rows of the table 6.13 (first column). Although both RPA and 2p2h corrections are applied simultaneously in MINERvA tune v1 as explained in 6.4.1.2, data prefers a low Q^2 suppression due to the RPA without any 2p2h enhancement from low recoil fits although as a function of Q^2_{QE} (as seen in 6.112), the GENIE with MINERvA tune v1 is closer to the data. Table 6.15 shows the linear χ^2 between data and model cross-section calculated as a function of Q^2_{QE}. χ^2 comparison for Q^2_{QE} also shows that data strongly prefers MINERvA Tune v2 over MINERvA Tune v1. The effect of pion tune is very small in MINERvA Tune v1 (see

χ^2 =57 in GENIE+Low Recoil Fits+RPA vs. versus χ^2 =58 in MINERvA Tune v1). χ^2 comparison for Q_{QE}^2 strongly favors the addition of the Low Recoil Fits and the RPA which is also consistent with 2D comparison shown in table 6.13. Both the 2D and 1D distribution favor an addition of low Q^2 suppression for non-resonant pions. All the cross-sections for the ME $\bar{\nu}_\mu$ are extracted using the flux without $\nu + e$ constrain. The χ^2 between data and MnvGENIE v1 extracted cross-section after applying the $\nu + e$ constrain is 328.13.

6.20.2 Neutrino Energy and Four Momentum Transfer Squared:True and QE Hypothesis and Impact on Cross-section

Note that this analysis reconstructs the neutrino energy and Q^2 based on CCQE hypothesis. Assuming the nucleus is at rest and the scattering process is a two body type, neutrino energy and four momentum transferred are reconstructed. Although it is not possible to accurately reconstruct the cross-section as a function of true variables, we can rely on simulation to estimate them. Figure 6.114 shows the event-rate ratio between true and QE based neutrino energy.

As can see in figure 6.115, we can see that in the low Q^2 region, the QE based reconstruction overestimates the number of events in the low Q^2 region and in the high Q^2, it is underestimated. Figure 6.116 shows the systematic uncertainty in the ratio plot of figure
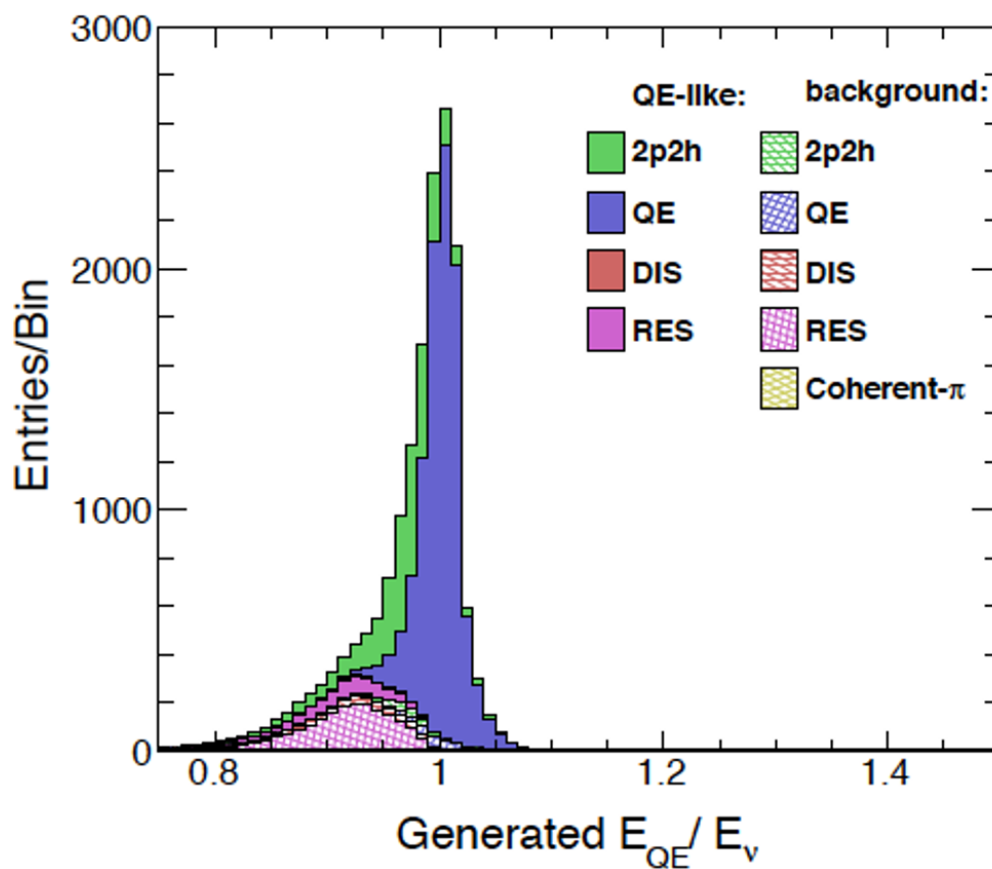
Figure 6.114: Ratio between the neutrino energy reconstructed by QE based hypothesis and the true neutrino energy in the simulation. True QE events (solid blue) shows the distribution around 1 due to Fermi motion. 2p2h and resonance events underestimate the true neutrino energy. Figure taken from [129].
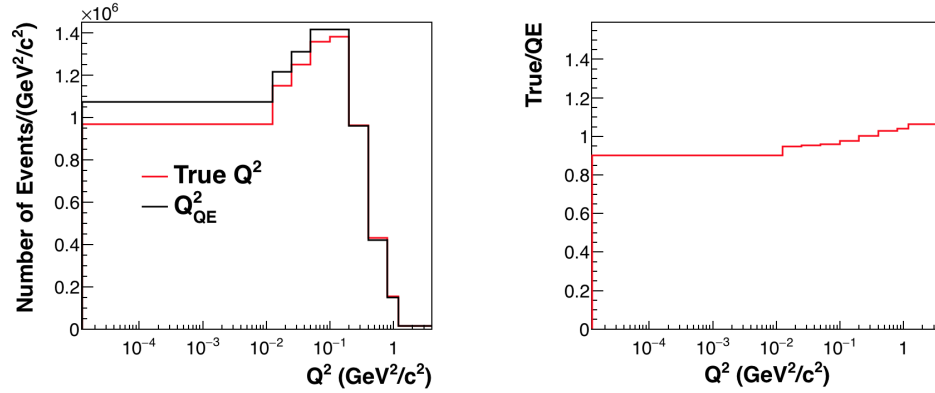
Figure 6.115: Q^2 distribution based on QE hypothesis and true Q^2 (left) and the ratio of true to QE definition of Q^2

6.115. The systematic uncertainty is less than 1% on the ratio dominated by final state and cross section systematic uncertainties. Pion absorption and systematic uncertainty due to the mean free path of pions are the main source of uncertainties in the FSI group. From the cross section group, the systematic uncertainty due to axial mass (MaCCQE) and vector mass for resonance cross section (MvRES) are dominant.

Although not a robust method, we tried to look at the CCQElike cross section as a function of true neutrino energy. An efficiency histogram is constructed that can transform cross section from the QE based variable phase space to true variables phase space. The efficiency histogram is constructed as:

$$\eta_{QE\,to\,True} = \frac{N_{QE}^{Generated}(E_{\nu\,QE}, Q_{QE}^2)}{N_{True}^{Generated}(E_{\nu}, Q^2)} \qquad (6.43)$$
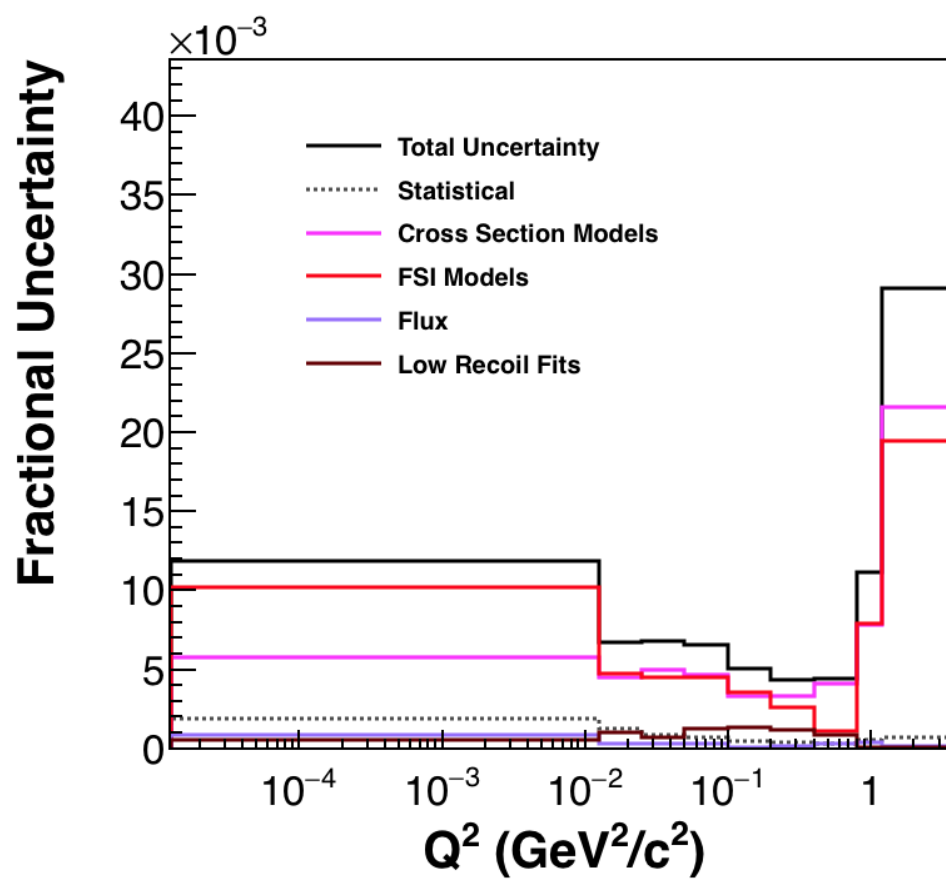
Figure 6.116: Systematics on the Q2 ratio of true to QE distribution in figure 6.115.
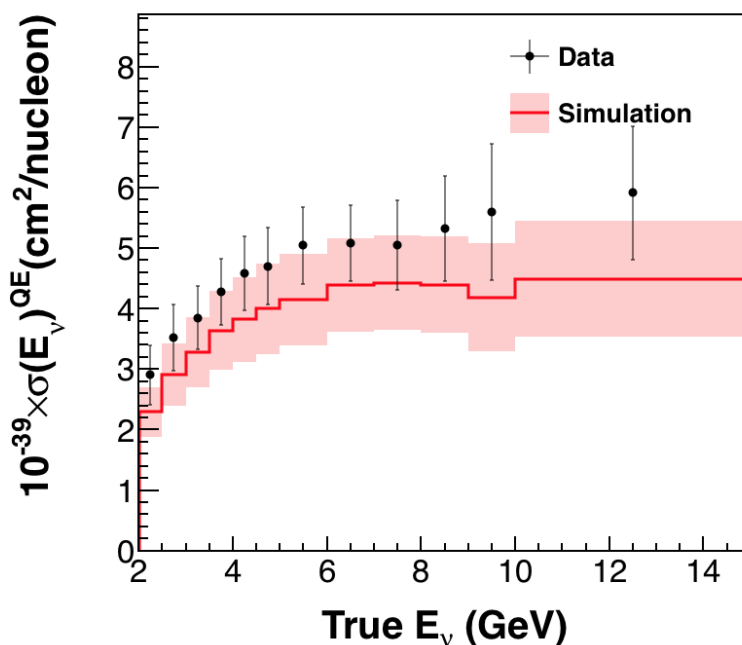
Figure 6.117: Cross section as a function of True Neutrino Energy. For the comparison with neutrino energy based on QE hypothesis, refer to figure 6.101. Cross-section is extracted using the flux without $\nu + e$ constrain.

The final cross section discussed in section 6.20 is divided by this efficiency to get the cross section as a function of true neutrino energy and Q^2. The cross section in figure 6.117 is plotted as a function of true neutrino energy. Compared to the cross section as a function of true neutrino energy (6.118), in the low neutrino energy region, the true neutrino energy is underestimated by about 20%. Beyond 6 GeV, the cross section is over estimated by around 10%. The error bars on the ratio are the total errors (systematic + statistical). Figure 6.120 shows the uncertainty on cross section as a function of neutrino energy. The left plot is the
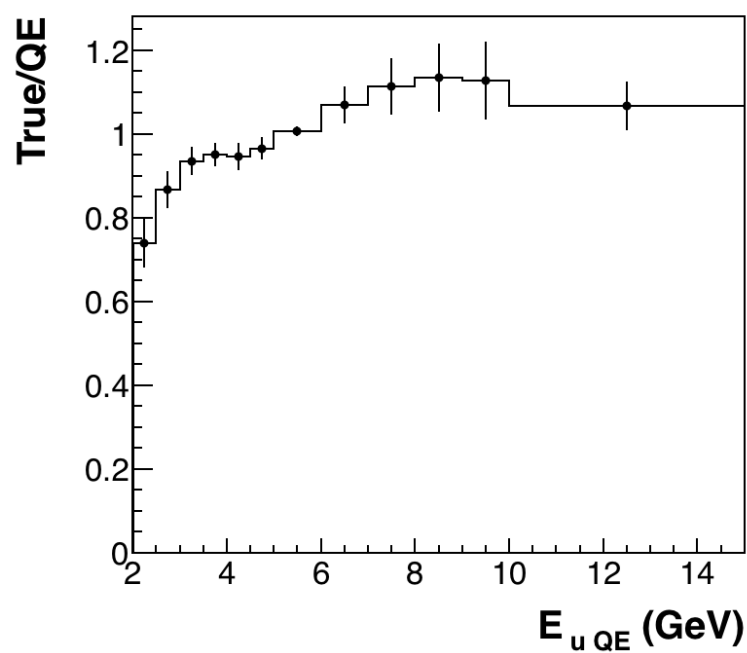
Figure 6.118: Ratio of cross section as a function of True neutrino energy to QE hypothesis based neutrino energy
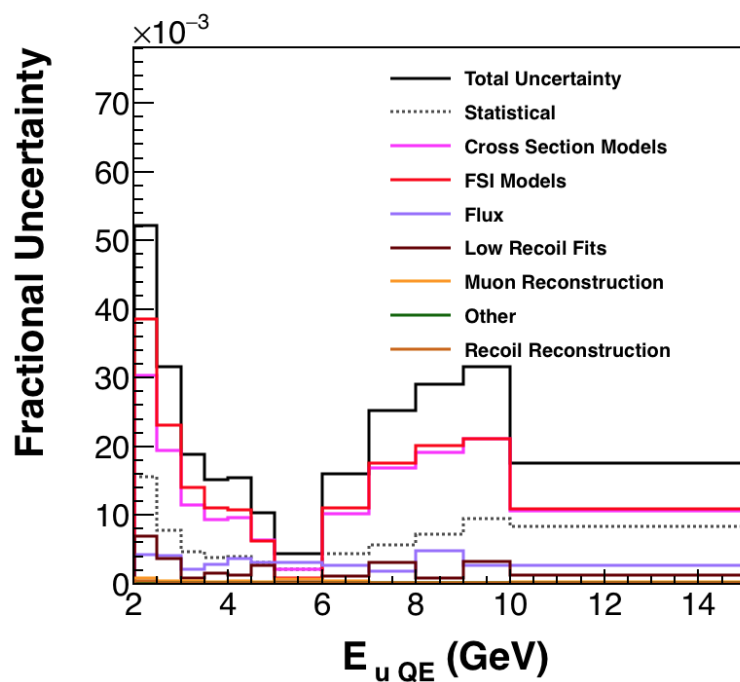
Figure 6.119: Uncertainties on the cross section ratio of figure 6.118.
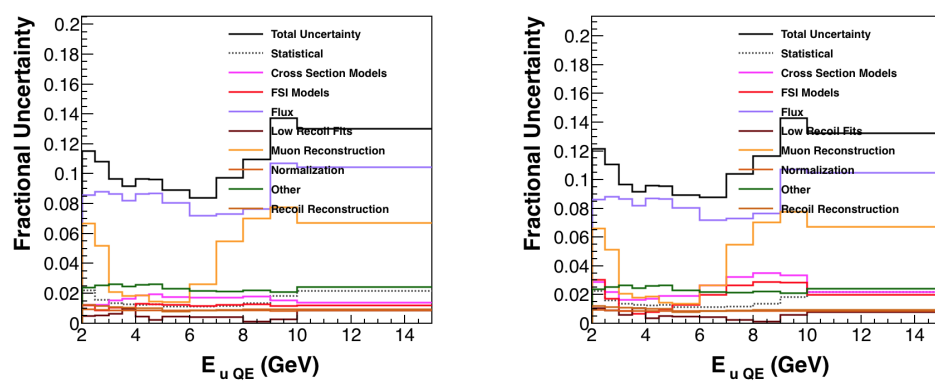
Figure 6.120: Systematic uncertainties on cross section as a function of neutrino energy based on QE hypothesis (left) and true neutrino energy.

neutrino energy based on QE hypothesis and the right one is the true neutrino energy. Both variables are based on generated variables. As seen here, the cross section is not significantly sensitive to FSI and Cross Section Models. However, in the case of cross section ratio as seen in 6.119 shows that the ratio is sensitive to these two categories. The contribution is higher on the either side of neutrino energy peak (which is at around 5 GeV) where the distribution is changing steeply.

In overall, the QE based cross-section will have cross-section over estimated for low energy neutrino and under estimated at high neutrino energies. The change is mostly driven by the cross section models and FSI models (specifically pion production and its mean free path).

7 Conclusion

7.1 Conclusion on Flux Works

This thesis presents the work done to make the flux uncertainties reliable in the DUNE experiment. Overall uncertainties are dominated by meson and nucleon incident interactions. In the low neutrino energy range, where the meson incident interactions occur in 70 to 75% of the interactions, inclusion of new data from NA61 and better approach to address correlation between data bins could further constrain the uncertainties in this category. This thesis also shows that for DUNE, most of the hadron production uncertainties cancel out in the near to far flux ratios.

This thesis also presents a new method to investigate the mismodeling of focusing parameters and its effect on overall reconstructed data. The multi-parameter fit is designed to disentangle the flux mismodeling like effect due to focusing or energy scale parameters and the correlation between these two sets of parameters. This method could be used in the future to understand the correlation between focusing and energy scale parameters in the future experiments which will be much more sensitive to mismodeling of either of these sets of parameters.

7.2   Conclusion on CCQELike Cross-section Analysis

The CCQELike cross-section measurement with the medium energy data sets has extended the previous measurements done with low energy into higher kinematics with much better statistics. The agreement between models and data seem to have improved although the normalization discrepancy between data and MC is not covered by the systematics in the ME data set.

Comparison of data cross-section with various GENIE model shows that the MINERvA GE-NIE doesn't describe the data properly over all the measured kinematic range. In fact, some variations of MINERvA GENIE where one or more tunes are removed seemed to describe the data well in some kinematic range. Similar observations were also made with the ME neutrino mode analysis [108]. The cross-section as a function of Q^2_{QE} shows similar trend to that of ME neutrino mode measurements. The data prefers the suppression of pion production in the low Q^2 region. Similarly, in the high Q^2 region, we might have to rethink our approach of extending the dipole approximation to calculate the CCQE interactions (L. Smith formalism).

The MINERvA tunes that were inspired by the LE analyses and later tuned to describe the

LE data are tested against the ME data which has higher kinematic reach. Comparing the tuned model at these kinematic ranges has allowed to test the physics assumptions behind the tunes in wider energy range.

The ME data sets are helping the MINERvA collaboration to review and correct the tunes to model the LE and ME data in better ways. With higher kinematic reach, models like SuSA has been studied to extend the 2p2h effects beyond $q_o, q_3 = 1.2 GeV$ which is the limit of Nieves model that is currently implemented in GENIE 2.12.6 (used by MINERvA).

Bibliography

[1] K. Abe et al. Constraint on the matter–antimatter symmetry-violating phase in neutrino oscillations. *Nature*, 580(7803):339–344, 2020. [Erratum: Nature 583, E16 (2020)].

[2] E. Ables et al. P-875: A Long baseline neutrino oscillation experiment at Fermilab. 2 1995.

[3] R. Acciarri et al. Long-Baseline Neutrino Facility (LBNF) and Deep Underground Neutrino Experiment (DUNE). 2015.

[4] R. Acciarri et al. Long-Baseline Neutrino Facility (LBNF) and Deep Underground Neutrino Experiment (DUNE): Conceptual Design Report, Volume 1: The LBNF and DUNE Projects. 1 2016.

[5] M. Acero et al. First Measurement of Neutrino Oscillation Parameters using Neutrinos and Antineutrinos by NOvA. *Phys. Rev. Lett.*, 123(15):151803, 2019.

[6] M. Adamovic. Woods-saxon and square-well potentials for nuclear shell model, 2015.

[7] P. Adamson et al. Measurement of neutrino velocity with the MINOS detectors and NuMI neutrino beam. *Phys. Rev. D*, 76:072005, 2007.

[8] P. Adamson et al. Study of quasielastic scattering using charged-current ν μ -iron interactions in the MINOS near detector. *Phys. Rev. D*, 91(1):012005, 2015.

[9] S. Agostinelli and Others. Geant4, a simulation toolkit. *Nuclear Instruments and Methods in Physics Research Section A: Accelerators, Spectrometers, Detectors and Associated Equipment*, 506(3):250 – 303, 2003.

[10] A. Aguilar-Arevalo et al. The MiniBooNE Detector. *Nucl. Instrum. Meth. A*, 599:28–46, 2009.

[11] A. Aguilar-Arevalo et al. First Measurement of the Muon Neutrino Charged Current Quasielastic Double Differential Cross Section. *Phys. Rev. D*, 81:092005, 2010.

[12] S. Ahn et al. Detection of accelerator produced neutrinos at a distance of 250-km. *Phys. Lett. B*, 511:178–184, 2001.

[13] F. Akbar. *MINOS Matched Muon Tracking Efficiency in ME.* `"https://minerva-docdb.fnal.gov/cgi-bin/private/RetrieveFile?docid=22203&filename=MINOS_efficiency.pdf&version=1"`.

[14] A. Akhiezer and M. Rekalo. HADRONIC DECAYS OF THE HEAVY LEPTON AND P ODD EFFECTS IN THE PRODUCTION OF PI AND RHO MESONS IN E+ E-COLLISIONS. *Sov. Phys. Dokl.*, 26:47–49, 1981.

[15] W. Alberico, M. Barbaro, S. M. Bilenky, J. Caballero, C. Giunti, C. Maieron, E. Moya de Guerra, and J. Udias. Strange form-factors of the proton: A New analysis of the neutrino (anti-neutrino) data of the BNL-734 experiment. *Nucl. Phys. A*, 651:277–286, 1999.

[16] W. Alberico, A. Molinari, T. Donnelly, E. Kronenberg, and J. Van Orden. Scaling in electron scattering from a relativistic Fermi gas. *Phys. Rev. C*, 38:1801–1810, 1988.

[17] L. Aliaga et al. Design, Calibration, and Performance of the MINERvA Detector. *Nucl. Instrum. Meth.*, A743:130–159, 2014.

[18] L. Aliaga et al. MINERvA neutrino detector response measured with test beam data. *Nucl. Instrum. Meth. A*, 789:28–42, 2015.

[19] L. Aliaga et al. Neutrino Flux Predictions for the NuMI Beam. *Phys. Rev. D*, 94(9):092005, 2016. [Addendum: Phys. Rev. D 95,no.3,039903(2017)].

[20] L. Aliaga Soplin. *Neutrino Flux Prediction for the NuMI Beamline.* PhD thesis, William-Mary Coll., 2016.

[21] J. Allison et al. Geant4 developments and applications. *IEEE Trans. Nucl. Sci.*, 53:270, 2006.

[22] L. Alvarez-Ruso et al. NuSTEC White Paper: Status and challenges of neutrino–nucleus scattering. *Prog. Part. Nucl. Phys.*, 100:1–68, 2018.

[23] J. E. Amaro, M. Barbaro, J. Caballero, T. Donnelly, A. Molinari, and I. Sick. Using electron scattering superscaling to predict charge-changing neutrino cross sections in nuclei. *Phys. Rev. C*, 71:015501, 2005.

[24] L. Andivahis et al. Measurements of the electric and magnetic form-factors of the proton from $Q^{**2} = 1.75$-GeV/c^{**2} to 8.83-GeV/c^{**2}. *Phys. Rev. D*, 50:5491–5517, 1994.

[25] C. Andreopoulos, C. Barry, S. Dytman, H. Gallagher, T. Golan, R. Hatcher, G. Perdue, and J. Yarba. The GENIE Neutrino Monte Carlo Generator: Physics and User Manual. 10 2015.

[26] P. Astier et al. Prediction of neutrino fluxes in the NOMAD experiment. *Nucl. Instrum. Meth. A*, 515:800–828, 2003.

[27] D. Ayres. The NOvA Technical Design Report. 2007.

[28] D. Ayres et al. The NOvA Technical Design Report. 10 2007.

[29] N. Baker, P. Connolly, S. Kahn, M. Murtagh, R. Palmer, N. Samios, and M. Tanaka. Total Cross-sections for Muon-neutrino N and Muon-neutrino P Charged Current Interactions in the 7-ft Bubble Chamber. *Phys. Rev. D*, 25:617–623, 1982.

[30] S. Baker and R. D. Cousins. Clarification of the Use of Chi Square and Likelihood Functions in Fits to Histograms. *Nucl. Instrum. Meth.*, 221:437–442, 1984.

[31] S. Barish et al. Study of Neutrino Interactions in Hydrogen and Deuterium. 1. Description of the Experiment and Study of the Reaction Neutrino d –¿ mu- p p(s). *Phys. Rev. D*, 16:3103, 1977.

[32] P. Barreau et al. COULOMB SUM RULE ON C-12. *Nuovo Cim. A*, 76:361–368, 1983.

[33] M. Bass. Effect of neutrino interaction systematics for future long baseline searches for cp-violation and mass hierarchy determination. Talk given at NuInt 2014, Boston,MA,USA, 2014.

[34] O. Benhar. The electroweak nuclear response in the impulse approximatino regime. WorkShop on Intersections of Nuclear Physics with Neutrino and Electrons,JLab, 2006.

[35] O. Benhar, A. Fabrocini, S. Fantoni, and I. Sick. Spectral function of finite nuclei and scattering of GeV electrons. *Nucl. Phys. A*, 579:493–517, 1994.

[36] O. Benhar, N. Farina, H. Nakamura, M. Sakuda, and R. Seki. Electron- and neutrino-nucleus scattering in the impulse approximation regime. *Phys. Rev. D*, 72:053005, 2005.

[37] A. Bercellie. *MnvHadronReweighter and GEANT Uncertainties.* "MINERvA-doc-28462-v1".

[38] B. Bhattacharya, R. J. Hill, and G. Paz. Model-independent determination of the axial mass parameter in quasielastic neutrino-nucleon scattering. *Phys. Rev. D*, 84:073006, Oct 2011.

[39] A. Bodek, S. Avvakumov, R. Bradford, and H. S. Budd. Vector and Axial Nucleon Form Factors:A Duality Constrained Parameterization. *Eur. Phys. J. C*, 53:349–354, 2008.

[40] A. Bodek, H. Budd, and M. Christy. Neutrino Quasielastic Scattering on Nuclear Targets: Parametrizing Transverse Enhancement (Meson Exchange Currents). *Eur. Phys. J. C*, 71:1726, 2011.

[41] A. Bodek and J. Ritchie. Fermi Motion Effects in Deep Inelastic Lepton Scattering from Nuclear Targets. *Phys. Rev. D*, 23:1070, 1981.

[42] A. Bodek and U.-k. Yang. Axial and Vector Structure Functions for Electron- and Neutrino- Nucleon Scattering Cross Sections at all Q^2 using Effective Leading order Parton Distribution Functions. 11 2010.

[43] N. Bostan, K. Yonehara, L. A. Soplin, A. Wickremasinghe, P. Snopok, Y. Yu, and A. Bashyal. Neutrino flux analysis and monitoring for power improvements in numi. 1 2020.

[44] R. Bradford, A. Bodek, H. Budd, and J. Arrington. A new parameterization of the nucleon elastic form factors. *Nuclear Physics B - Proceedings Supplements*, 159:127–132, Sep 2006.

[45] R. Brun, P. Canal, and F. Rademakers. Design, Development and Evolution of the ROOT System. *PoS*, ACAT2010:002, 2010.

[46] H. S. Budd, A. Bodek, and J. Arrington. Modeling quasielastic form-factors for electron and neutrino scattering. In *2nd International Workshop on Neutrino-Nucleus Interactions in the Few GeV Region*, 8 2003.

[47] J. Carlson, J. Jourdan, R. Schiavilla, and I. Sick. Longitudinal and transverse quasielastic response functions of light nuclei. *Phys. Rev. C*, 65:024002, 2002.

[48] M. Carneiro et al. High-Statistics Measurement of Neutrino Quasielasticlike Scattering at 6 GeV on a Hydrocarbon Target. *Phys. Rev. Lett.*, 124(12):121801, 2020.

[49] G. F. Chew. The inelastic scattering of high energy neutrons by deuterons according to the impulse approximation. *Phys. Rev.*, 80:196–202, Oct 1950.

[50] M. Collab. *MINERvA NSF Defaults.* `"https://cdcvs.fnal.gov/cgi-bin/public-cvs/cvsweb-public.cgi/AnalysisFramework/Ana/PlotUtils/PlotUtils/NSFDefaults.h?cvsroot=mnvsoft"`.

[51] M. Collaboration. *Data Run Periods (Playlists).* `"https://cdcvs.fnal.gov/redmine/projects/minerva-sw/wiki/Data_Run_Periods"`.

[52] M. Collaboration. *Muon Energy Scale Systematics*, 2011 (accessed October 20,2020). `https://cdcvs.fnal.gov/redmine/projects/minerva/wiki/NX_systematics`.

[53] T. M. Collaboration. A Long Base-line Neutrino Oscillation Experiment at Fermilab. *Technical Report (1996) 105*, 1996.

[54] P. de Salas, S. Gariazzo, J. Lesgourgues, and S. Pastor. Calculation of the local density of relic neutrinos. *JCAP*, 09:034, 2017.

[55] P. F. de Salas, S. Gariazzo, O. Mena, C. A. Ternes, and M. Tórtola. Neutrino mass ordering from oscillations and beyond: 2018 status and future prospects. *Frontiers in Astronomy and Space Sciences*, 5:36, 2018.

[56] N. T. S. Department. *NuMI Target System.* `"https://web.fnal.gov/project/TargetSystems/NuMI/Target/_layouts/15/start.aspx#/SitePages/Home.aspx"`.

[57] J. Devan et al. Measurements of the Inclusive Neutrino and Antineutrino Charged Current Cross Sections in MINERvA Using the Low-ν Flux Method. *Phys. Rev. D*, 94(11):112007, 2016.

[58] J. D. Devan. *Measurement of Neutrino and Antineutrino Charged-Current Inclusive Cross Sections with the MINERvA Detector.* PhD thesis, Coll. William and Mary, 2015.

[59] W. H. Dickhoff and C. Barbieri. Self-consistent green's function method for nuclei and nuclear matter. 2004.

[60] S. Dolan, G. Megias, and S. Bolognesi. Implementation of the SuSAv2-meson exchange current 1p1h and 2p2h models in GENIE and analysis of nuclear effects in T2K measurements. *Phys. Rev. D*, 101(3):033003, 2020.

[61] T. Donnelly and I. Sick. Superscaling in inclusive electron - nucleus scattering. *Phys. Rev. Lett.*, 82:3212–3215, 1999.

[62] P. Dunne. Latest neutrino oscillation results from t2k. Talk given at Neutrino 2020, Chicago,IL,USA, 2020.

[63] B. Eberly et al. Charged Pion Production in ν_μ Interactions on Hydrocarbon at $\langle E_\nu \rangle$= 4.0 GeV. *Phys. Rev. D*, 92(9):092008, 2015.

[64] K. Egiyan et al. Measurement of 2- and 3-nucleon short range correlation probabilities in nuclei. *Phys. Rev. Lett.*, 96:082501, 2006.

[65] D. B. et. al. *Phys. Rev. D*, 27, 1983.

[66] S. A. et al. *Nucl. Instrumental Method.*, A506:250, 2003.

[67] R. Feynman and M. Gell-Mann. Theory of Fermi interaction. *Phys. Rev.*, 109:193–198, 1958.

[68] L. Fields. *Genetic Optimization of the LBNF/DUNE Beamline II*, 2016. DUNE-doc-1151-v3.

[69] L. Fields et al. Measurement of Muon Antineutrino Quasielastic Scattering on a Hydrocarbon Target at Eν∼3.5 GeV. *Phys. Rev. Lett.*, 111(2):022501, 2013.

[70] F. Filthaut. *TFractionFitter*, 2011 (accessed September 30, 2020). `https://root.cern.ch/root/html532/TFractionFitter.html`.

[71] R. Fine. Measurement of the medium energy numi flux using the low-ν and high-ν methods at minerva. 8 2020.

[72] G. Fiorentini et al. Measurement of Muon Neutrino Quasielastic Scattering on a Hydrocarbon Target at $E_\nu \sim 3.5$ GeV. *Phys. Rev. Lett.*, 111:022502, 2013.

[73] G. A. Fiorentini. *Tracking Matching Efficiency and Data Overlay MC.* `"https://minerva-docdb.fnal.gov/cgi-bin/private/RetrieveFile?docid=7644&filename=20120518_AnaMeeting.pdf&version=4"`.

[74] G. Folger. Recent developments in Geant4 hadronic physics. In *2013 IEEE Nuclear Science Symposium and Medical Imaging Conference and Workshop on Room-Temperature Semiconductor Detectors*, 2013.

[75] N. Fomin et al. New measurements of high-momentum nucleons and short-range structures in nuclei. *Phys. Rev. Lett.*, 108:092502, 2012.

[76] J. Formaggio and G. Zeller. From eV to EeV: Neutrino Cross Sections Across Energy Scales. *Rev. Mod. Phys.*, 84:1307–1341, 2012.

[77] Y. e. a. Fukuda. Evidence for oscillation of atmospheric neutrinos. *Phys. Rev. Lett,*, 1998.

[78] G.D'Agostini. A multidimensional unfolding method based on bayes theorem. *Nuclear Instrumental Method (19895)*, A 362, 1995.

[79] S. Gershtein and Y. Zeldovich. Meson corrections in the theory of beta decay. *Zh. Eksp. Teor. Fiz.*, 29:698–699, 1955.

[80] S. Golan and Azmuda. NuWro: the WrocACaw Monte Carlo Generator of Neutrino Interactions. *Nucl. Phys. Proc. Suppl.,229-232*, 2012.

[81] R. GonzalÃ©z-JimÃ©nez, G. Megias, M. Barbaro, J. Caballero, and T. Donnelly. Extensions of Superscaling from Relativistic Mean Field Theory: the SuSAv2 Model. *Phys. Rev. C*, 90(3):035501, 2014.

[82] K. M. Graczyk, J. Żmuda, and J. T. Sobczyk. Electroweak form factors of the $\Delta(1232)$ resonance. *Phys. Rev. D*, 90(9):093001, 2014.

[83] R. Gran. Model Uncertainties for Valencia RPA Effect for MINERvA. 2017.

[84] R. Gran, J. Nieves, F. Sanchez, and M. Vicente Vacas. Neutrino-nucleus quasi-elastic and 2p2h interactions up to 10 GeV. *Phys. Rev. D*, 88(11):113007, 2013.

[85] D. Griffiths. *Introduction to elementary particles.* 2008.

[86] Groom. Passage of particles through matter. *Eur. Phys. K. C 15*, 2000.

[87] D. Groom and Others. *Muon Stopping Power and Range Tables, 10 MeV -100 TeV.*

[88] R. Gupta, Y.-C. Jang, H.-W. Lin, B. Yoon, and T. Bhattacharya. Axial-vector form factors of the nucleon from lattice qcd. *Physical Review D*, 96(11), Dec 2017.

[89] A. Habig and E. W. Grashorn. The MINOS detectors. In *29th International Cosmic Ray Conference*, volume 9, pages 319–322, 7 2005.

[90] R. Hatcher. Proposal for a unified flux n-tuple format. *MINOS-doc-9070-v4*, 2012.

[91] R. Hogg and E. A. Tannis. *Probability and Statistical Inference, Eigth Edition.* Pearson, Upper Saddle River, NJ., 2010.

[92] J. Hylen, W. M. Smart, A. Wehmann, S. R. Menary, A. Malensek, D. Johnson, J. Morfin, G. Koizumi, and P. Lucas. Conceptual design for the technical components of the neutrino beam for the main injector (NuMI). 9 1997.

[93] B. Kayser. Neutrino physics. *eConf*, C040802:L004, 2004.

[94] J. Kleykamp. *Hadron Reweight.* "https://minerva-docdb.fnal.gov/cgi-bin/private/RetrieveFile?docid=12323&filename=Kleykamp_2016-7-19_HadronReweight.pdf&version=2".

[95] S. Kowalski and S. Pulawski. Recent results from NA61/SHINE. *Acta Phys. Polon. B*, 50:1765–1770, 2019.

[96] K. S. Kuzmin, V. V. Lyubushkin, and V. A. Naumov. Quasielastic axial-vector mass from experiments on neutrino-nucleus scattering. *Eur. Phys. J. C*, 54:517–538, 2008.

[97] L. Lapikas. Quasi-elastic electron scattering off nuclei. *Nucl. Phys. A*, 553:297c–308c, 1993.

[98] T. Le. *MINERvA101: Detector Simulation.* "https://minerva-docdb.fnal.gov/cgi-bin/private/RetrieveFile?docid=12242&filename=detsim-minerva-101.pdf&version=5".

[99] T. Le. *MINOS Tracking efficiency study using MINERvA Tracks.* "https://minerva-docdb.fnal.gov/cgi-bin/private/RetrieveFile?docid=8549&filename=MINOS-efficiency-study-v5.pdf&version=6".

[100] T. Le et al. Measurement of $\bar{\nu}_\mu$ Charged-Current Single π^- Production on Hydrocarbon in the Few-GeV Region using MINERvA. *Phys. Rev. D*, 100(5):052008, 2019.

[101] P. Le Brun. *On Focusing Uncertainties of NuMI Beam.* "https://minerva-docdb.fnal.gov/cgi-bin/private/ShowDocument?docid=23542".

[102] T. Leitner, O. Buss, L. Alvarez-Ruso, and U. Mosel. Electron- and neutrino-nucleus scattering from the quasielastic to the resonance region. *Phys. Rev. C*, 79:034601, 2009.

[103] J. M. Levy. Kinematics of an off axis neutrino beam. 2010.

[104] L.-c. Liu. Pauli blocking and final-state interaction in electron-nucleus quasielastic scattering. *Phys. Rev. C*, 79:014605, 2009.

[105] C. Llewellyn Smith. Neutrino reactions at accelerator energies. *Physics Reports*, 3(5):261 – 379, 1972.

[106] L. J. Loiacono. *Measurement of the Muon Neutrino Inclusive Charged Current Cross Section on Iron using the MINOS Detector*. PhD thesis, Texas U., ARL, 2010.

[107] T. J. Loredo and D. Q. Lamb. Bayesian analysis of neutrinos observed from supernova sn 1987a. *Phys. Rev. D*, 65:063002, Feb 2002.

[108] C. M. Ballad of the muon momentum fix and other stories. *MINERvA-doc-21349-v1*, 2018.

[109] P. Madigan. *LBNF Beam Alignment Parameters and DUNE Neutrino Flux Uncertainties.* `"https://docs.dunescience.org/cgi-bin/private/ShowDocument"`.

[110] S. Mahajan, V. Bhatnagar, B. C. Choudhary, and R. Raja. Particle Production Measurements Using the MIPP Detector at Fermilab. *Springer Proc. Phys.*, 174:389–393, 2016.

[111] C. Maieron, J. Amaro, M. Barbaro, J. Caballero, T. Donnelly, and C. Williamson. Superscaling of non-quasielastic electron-nucleus scattering. *Phys. Rev. C*, 80:035504, 2009.

[112] A. Mann. Calculate like a Llewellyn. 2018.

[113] M. Martini, M. Ericson, G. Chanfray, and J. Marteau. Unified approach for nucleon knock-out and coherent and incoherent pion production in neutrino interactions with nuclei. *Phys. Rev. C*, 80:065501, Dec 2009.

[114] K. T. McDonald. An Off-axis neutrino beam. 11 2001.

[115] C. McGivern et al. Cross sections for ν_μ and $\bar{\nu}_\mu$ induced pion production on hydrocarbon in the few-GeV region using MINERvA. *Phys. Rev. D*, 94(5):052005, 2016.

[116] S. v. d. M. Meer. A Directive Device For Charged Particle And Its Use In An Enhanced Neutrino Beam). 02 1961.

[117] B. Messerly. *ME Focusing Uncertainties plots-Final.* `"https://minerva-docdb.fnal.gov/cgi-bin/private/ShowDocument"`.

[118] T. Miceli, V. Papavassiliou, S. Pate, and K. Woodruff. Improving Dark Matter Searches by Measuring the Nucleon Axial Form Factor: Perspectives from MicroBooNE. *Phys. Procedia*, 61:495–501, 2015.

[119] S. Mondal. Physics of neutrino oscillation, 2015.

[120] J. G. Morfin, J. Nieves, and J. T. Sobczyk. Recent Developments in Neutrino/Antineutrino - Nucleus Interactions. *Adv. High Energy Phys.*, 2012:934597, 2012.

[121] J. Nelson. Summary of muon energy scale systematics. *MINERvA-doc-21421-v3*, 2018.

[122] J. Nieves, J. E. Amaro, and M. Valverde. Inclusive quasielastic charged-current neutrino-nucleus reactions. *Phys. Rev. C*, 70:055503, Nov 2004.

[123] J. Nieves, I. Ruiz Simo, and M. Vicente Vacas. Inclusive Charged–Current Neutrino–Nucleus Reactions. *Phys. Rev. C*, 83:045501, 2011.

[124] J. Nieves, I. R. Simo, and M. J. V. Vacas. Inclusive charged-current neutrino-nucleus reactions. *Phys. Rev. C*, 83:045501, Apr 2011.

[125] A. Osipowicz et al. KATRIN: A Next generation tritium beta decay experiment with sub-eV sensitivity for the electron neutrino mass. Letter of intent. 9 2001.

[126] V. Papadimitriou. Design of the LBNF Beamline. In *38th International Conference on High Energy Physics*, 6 2017.

[127] E. Paschos, M. Sakuda, I. Schienbein, and J. Yu. Comparison of a new Delta resonance production model with electron and neutrino data. *Nucl. Phys. B Proc. Suppl.*, 139:125–133, 2005.

[128] C. Patrick. *Measurement of the Antineutrino Double-Differential Charged-Current Quasi-Elastic Scattering Cross Section at MINERvA*. PhD thesis, Northwestern U., 2016.

[129] C. Patrick et al. Measurement of the Muon Antineutrino Double-Differential Cross Section for Quasielastic-like Scattering on Hydrocarbon at $E_\nu \sim 3.5$GeV. *Phys. Rev. D*, 97(5):052002, 2018.

[130] A. Puckett et al. Polarization Transfer Observables in Elastic Electron Proton Scattering at $Q^2 =$2.5, 5.2, 6.8, and 8.5 GeV^2. *Phys. Rev. C*, 96(5):055203, 2017. [Erratum: Phys.Rev.C 98, 019907 (2018)].

[131] I. Qattan et al. Precision Rosenbluth measurement of the proton elastic form-factors. *Phys. Rev. Lett.*, 94:142301, 2005.

[132] D. Rein and L. M. Sehgal. Neutrino Excitation of Baryon Resonances and Single Pion Production. *Annals Phys.*, 133:79–153, 1981.

[133] D. Rimal. *Medium Energy Inclusive Events in the tracker.* `"https://minerva-docdb.fnal.gov/cgi-bin/private/RetrieveFile?docid=12545&filename=MEIncFlux.pdf&version=1"`.

[134] N. Rocco. Neutrino cross-section. International Neutrino Summer School, 2019.

[135] N. Rocco, L. Alvarez-Ruso, A. Lovato, and J. Nieves. Electromagnetic scaling functions within the Green's Function Monte Carlo approach. *Phys. Rev. C*, 96(1):015504, 2017.

[136] P. Rodrigues et al. Identification of nuclear effects in neutrino-carbon interactions at low three-momentum transfer. *Phys. Rev. Lett.*, 116:071802, 2016. [Addendum: Phys.Rev.Lett. 121, 209902 (2018)].

[137] P. Rodrigues, C. Wilkinson, and K. McFarland. Constraining the GENIE model of neutrino-induced single pion production using reanalyzed bubble chamber data. *Eur. Phys. J. C*, 76(8):474, 2016.

[138] P. Rodriguez. *ME beam position.* `"https://minerva-docdb.fnal.gov/cgi-bin/private/RetrieveFile?docid=12279&filename=me-beam-position-2016-06-16.pdf&version=2"`.

[139] C. ROOT. *TMinuit Class Reference.* `"https://root.cern.ch/doc/master/classTMinuit.html"`.

[140] M. Rosenbluth. High Energy Elastic Scattering of Electrons on Protons. *Phys. Rev.*, 79:615–619, 1950.

[141] M. Sajjad Athar and J. G. Morfin. Neutrino(Antineutrino)-Nucleus Interactions in the Shallow- and Deep-Inelastic Scattering Regions. 4 2020.

[142] D. W. Schmitz. *Normalization Corrections for Titan Production.* `"https://minerva-docdb.fnal.gov/cgi-bin/private/ShowDocument?docid=8646"`.

[143] M. Schwartz. Feasibility of using high-energy neutrinos to study the weak interactions. *Phys. Rev. Lett.*, 4:306–307, 1960.

[144] J. Schwehr, D. Cherdack, and R. Gran. GENIE implementation of IFIC Valencia model for QE-like 2p2h neutrino-nucleus cross section. 1 2016.

[145] A. Smirnov. Solar neutrinos oscillations or no-oscillations. 2018.

[146] J. Sobczyk, N. Rocco, A. Lovato, and J. Nieves. Scaling within the Spectral Function approach. *Phys. Rev. C*, 97(3):035506, 2018.

[147] G. Stefanek. Recent results from the search for the critical point of strongly interacting matter at the CERN SPS. *Nucl. Part. Phys. Proc.*, 273-275:2596–2598, 2016.

[148] P. Stowell et al. Tuning the GENIE Pion Production Model with MINERνA Data. *Phys. Rev. D*, 100(7):072005, 2019.

[149] P. Stowell and Others. NUISANCE: a neutrino cross-section generator tuning and comparison framework. *Journal of Instrumentation*, 12(01):P01016–P01016, jan 2017.

[150] R. e. a. Subedi. Probing cold dense nuclear matter. *Science*, 320(5882):1476–1478, 2008.

[151] M. Szleper and A. Para. Neutrino spectrum at the far detector systematic errors. 10 2001.

[152] P. Vahle. *Long Baseline Neutrino Oscillation Experiments.* `"https://indico.fnal.gov/event/19346/contributions/51596/attachments/32067/39336/vahle-inss-2019-asdelivered.pdf"`.

[153] E. Valencia. *Neutrino Electron Scattering in ME.* `"MINERvA-doc-11550-v1"`.

[154] E. Valencia et al. Constraint of the MINERνA medium energy neutrino flux using neutrino-electron elastic scattering. *Phys. Rev. D*, 100(9):092001, 2019.

[155] B. Van Der Ventel and J. Piekarewicz. Quasielastic neutrino nucleus scattering. *Phys. Rev. C*, 69:035501, 2004.

[156] J. Van Orden and T. Donnelly. MESONIC PROCESSES IN DEEP INELASTIC ELECTRON SCATTERING FROM NUCLEI. *Annals Phys.*, 131:451–493, 1981.

[157] T. Walton. MINERvA Muon Energy Scale. 2015.

[158] A. Wickremasinghe. Response of mm. Private Conversation.

[159] K. Woodruff. Studying Neutral Current Elastic Scattering and the Strange Axial Form Factor in MicroBooNE. *PoS*, SPIN2018:029, 2019.

[160] e. a. Yao, W-M. Pdg. Particle Data Group, 2006.

[161] R. M. Zwaska. Accelerator Systems and Instrumentation for the NuMI Neutrino Beam. 2005.

APPENDIX

A   Supporting Materials

A.1   Off Axis Neutrino Kinematics

Difference in neutrino spectra coming from the same pion for MINERvA and NOvA detectors as seen in figure 2.22 and 2.23 is due to the on-axis and the off-axis decay kinematics. For $\pi^+ \to \mu^+ + \nu_\mu$, the energy-momentum vector of the neutrino (2 D problem) is given by:

$$(E^*, p^* cos\theta^*, sin\theta^*) \tag{A.1}$$

Here $*$ is used to represent that the vector is in the center of mass frame. The neutrinos mass can be neglected $E^* = p^*$ with the natural units of $c = 1$. Doing the Lorentz transformation to the lab frame we get:

$$E = \gamma(E^* + \gamma\beta E^* cos\theta^*),$$

$$E \cos\theta = \gamma(E^* cos\theta^* + \gamma\beta E), \tag{A.2}$$

$$E \sin\theta = E^* sin\theta^*$$

Here, θ is the decay angle with respect to the beam axis in the lab frame. The above
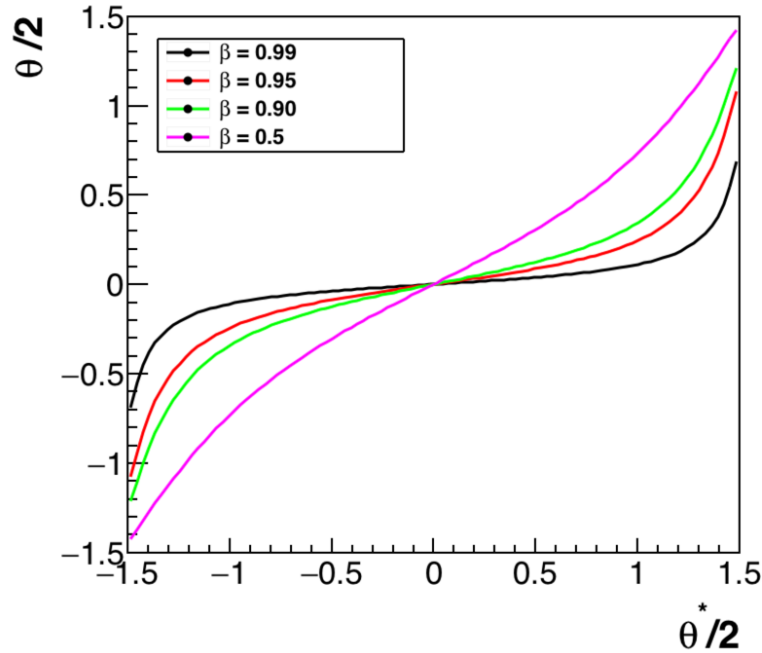
Figure A.1: Relation between the decay angle at CM frame (θ^*) and lab frame (θ).

equation gives us the decay angle in terms of $\int\rangle\backslash\rceil$ and $\rfloor\wr\int\rangle\backslash\rceil$. Using these information,

$$tan\frac{\theta}{2} = \sqrt{\frac{1-\beta}{1+\beta}}tan\frac{\theta^*}{2} \tag{A.3}$$

This equation shows that the decay angle in the lab frame is directly proportional to the decay angle in the center of mass frame. Figure A.1 shows the relation between the decay angle in the lab frame and the center of mass frame for different pion energies. For high energy pions where $\beta \approx 1$, the decay angle in the lab frame remains same for a wide range of center of mass decay angles. Similarly, in the case of on-axis decay, the decay angle in both

the lab frame and the center of mass frame is 0 for all pion energy range.

Again starting with the relation $E sin\theta = E^* sin\theta^*$, we can write the lab angle as:

$$sin\theta = \frac{E^* sin\theta^*}{E} \tag{A.4}$$

Since $sin\theta_{max} = 1$, we can see that:

where E^* is the energy of the neutrino in the center of mass frame and is given by:

$$E^* = \frac{m_\pi^2 - m_\mu^2}{2m_\pi} \approx 30 MeV \tag{A.5}$$

Rewriting this relation,

$$E_{max} = \frac{30 MeV}{sin\theta} \tag{A.6}$$

Hence, there is a bound on maximum neutrino energy that an off-axis detector can see for a given off-axis angle location. This relation is derived for a divergence-less beam and forward pion and a more detailed discussion for the general case is given in [114] and [103].

Figure A.2 shows the threshold of the pion to neutrino decay at various off-axis angles. Since there is a bound on the maximum neutrino energy, for a pion produced at a non zero decay angle, a narrow energy spectra of the neutrino beam is seen by an off-axis detector.
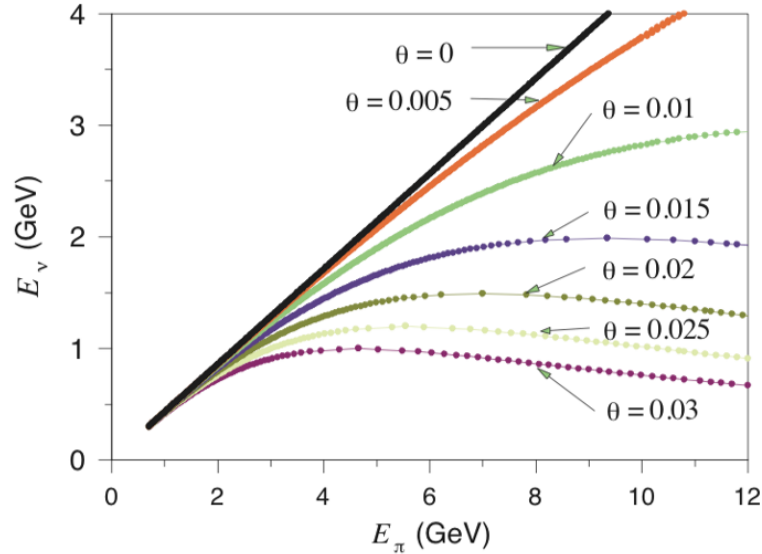
Figure A.2: Relation between pion energy and neutrino energy for various angles. For perspective, NOvA is situated at 0.014 radian angle.

A.2   Dk2nu Branch Information

The PPFX relies on the dk2nu branches which store the particle ancestry information. To get the required information, some changes were made in LBNEAnalysis.cc file to fill in the branches. I will list the names of the branches and the information they fill in:

- tgtexit: Tgtexit basically gives the information of the hadron exiting the target that results in the neutrino. Information like the (x,y,z) target exit location of the particles, the momentum info at the exit location and the PID and the particle generation is recorded in this branch. The information is filled for each neutrino event by looking back at its ancestors' trajectories and identifying the ancestor that makes the transit

and recording the trajectory point and later saving the position and momentum info of that point.

- traj: This branch records the x,y,z and px,py, pz position of the neutrino parent as they exit various boundaries. This branch is not useful for PPFX but can be used for debugging purposes and other analyses.

- vint: This branch stores the ancestry index of the neutrino. For all neutrino, 0 index is the primary proton which is the starting point of the ancestry of the neutrinos. Vint larger than 1 means the neutrinos are coming the parents which were produced from multiple interactions inside the target. This branch also stores the "playlist ID" which gives information about the additional change in target position besides the changes made for different energy configuration.First element of vint always stores the playlist ID. For example, in the MINERvA a playlist ID of 13 means the target is shifted 0.83 cm upstream in addition to the low energy configuration position. In the DUNE, since we do not have this convention, the default playlist ID is set to 0 which means there is no additional movement of the target. The playlist ID is later used in the PPFX script "TargetAttenuationReweighter.cpp" where this information is used to shift the target fins position to its true position relative to the default positions hard coded in the script.

- vdbl: This branch stores the distance travelled by the particle through different volumes of the beamline. This branch only stores the parent, grandparent and great grandparent information of the neutrinos and the distance traversed by them through Horn1 Inner Conductor, Horn2 Inner Conductor, Decay Pipe and rest of the volume. Since it is a vector container, it can be expanded and modified to store distance in additional volumes as per required.

- pprodpx,py,pz: These branches Store the momentum info of the neutrino parent at the time of neutrino production. This branch is filled along with other ancestor class branches. To fill this branch, additional functions are written in LBNESteppingAction and LBNETrajectory in the g4lbnf code. In the LBNESteppingAction, steps at which the momentum production occurs are extracted and a class of containers are created in LBNETrajectory to store these steps.

- horncfg: This is the branch in the dkmetaTree. Previously it contained information like the horn type (NuMI style, Optimized or so on), current and position. Since this information is not used by the DUNE simulation group for any purposes, this branch is modified to carry information with the syntax similar to that of the MINERvA experiment. Currently, it stores the horn current with polarity. For example, if horncfg

reads "230i", it means the horn current is 230 kA with positive polarity.

- tgtcfg: This dkmetaTree branch is modified to store the target configuration information. It will include the energy configuration and additional shift of the target in z co-ordinate. For example, **le010zmi** means the target is in low energy configuration with 10 cm upstream of the default LE position.

A function called **GetDistanceThroughVolume** is written (similar to that done in g4numi). It takes the volume name as the argument and calculates the distance through the volume. We use this function to get the distance through the two inner conductors, decay pipe and decay volume. The decay pipe material is steel in our case and the decay volume is the Helium (or any gas inside the decay pipe). The sum total of distance travelled should are recorded in the vdbl branches. As of May 27,2016, in the DUNE simulation, the inner conductor of the first focusing horn is made up of 28 different volumes and for second focusing horn, it is 36. Similarly, there are alternate focusing system designs which have different inner conductor designs and names. 2 supporting functions are written to parse in the inner conductor volume names as they are initialized in LBNEVolumePlacements. c++ vectors push in the volume names and the function GetHorn1ICList and GetHorn2ICList pass those volume names to LBNEAnalysis where they are used by GetDistanceThroughVolume to compute the distance travelled by neutrino ancestors in those areas.
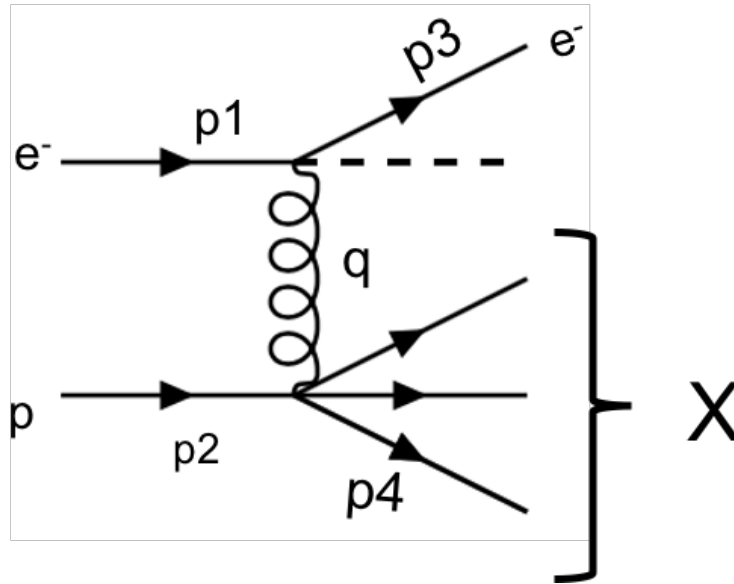
Figure A.3: Feynman diagram of the inelastic scattering between electron and a proton with four momenta shown for 2 initial and 2 final states. q is the 4 momentum transferred to the proton and is given as $q = p_1 - p_3$.

A.3   Bjorken X and Elastic and Inelastic Scatterings

Bjorken x or simply x is the variable to measure the inelasticity of an scattering process.

Based on figure A.3, Bjorken x is defined as:

$$x = \frac{Q^2}{2p_2.q} \tag{A.7}$$

where $Q^2 = -q^2$. q is the 4 momentum transferred by the electron to the proton (in figure A.3), and is given as $q = p_1 - p_3$. By conservation of momentum and energy, we know:

$$p_1 + p_2 = p_3 + p_4 \tag{A.8}$$

Rewriting p_4 in terms of q,

$$p_4 = p_1 + (p_2 - p_3)$$
$$\tag{A.9}$$
$$p_4 = p_2 + q$$

Now, let M_X be the mass of the hadronic system defined in terms of invariant mass as:

$$M_X^2 = p_4^2 = (E_4^2 - |\vec{p_4}|^2) \tag{A.10}$$

Now writing M_X in terms of q:

$$M_X^2 = p_4^2$$
$$= (p_2 + q)^2 \tag{A.11}$$
$$= p_2^2 + 2p_2.q + q^2$$

Now p_2^2 is the invariant mass of the proton. Let M be the mass of the proton. Similarly, $-q^2 = Q^2$. So now writing equation A.11 in terms of M and Q^2,

$$M_X^2 = M^2 + 2p_2.q - Q^2 \tag{A.12}$$

So Q^2 can be written as:

$$Q^2 = 2p_2.q + M^2 - M_X^2 \tag{A.13}$$

For an elastic scattering, $M_X = M$, the proton would remain intact. Hence,

$$Q^2_{Elastic} = 2p_2.q \tag{A.14}$$

This would give $x = 1$ in equation A.7.

Similarly for an inelastic scattering, $M_X > M$ because the invariant mass of the final state hadronic system will be larger than that of the proton rest mass. This would give us:

$$Q^2_{Inelastic} < 2p_2.q \tag{A.15}$$

This means equation A.7 would be less than 1 for an inelastic scattering.

A special case is when the nucleus doesnt break but instead of 1, 2 nucleons are ejected. To understand what happens to the bjorken x in this case, lets assume a reaction where an electron sees a nucleus of an atomic number A such that experimentally one observes the following:

$$e + A \rightarrow e' + (A - 1) + N \tag{A.16}$$

Here, N is the ejected nucleon that is observed in the experiment. If only one nucleon was ejected, the four momentum would still be $Q^2 = 2p_2.q$ since the momentum transferred to the rest of the nucleus (A-1) is negligible. However if the electron struck a nucleon that is correlated to another nucleon, both nucleons are ejected. Experimentally, when only one nucleon is observed, the 4 momentum of that observed nucleon wont give the invariant mass of that nucleon because of the missing momentum taken by the correlated nucleon that is not taken into account. If N is the observed nucleon, let p_m be the missing momentum take is taken by another nucleon. Then $\vec{p_m} = \vec{p_N} - \vec{q}$. So, experimentally the four momentum transferred squared Q^2 would appear to be larger than the product $2p_f.q$ where $\vec{q}$ is constructed from the kinematics of the observed nucleon. This would give $x > 1$ for SRC events (like the 2p2h).

A.4 The NOvA Experiment

The NOvA (NuMI Off-axis Neutrino) experiment lies at 14 mrad offset from the neutrino beam at around 1 km from the target and the far detector at 810 km at Ash River, Minnesota. By mass, the NOvA detectors are 95% liquid scintillator (mineral oil) [27]. The near detector
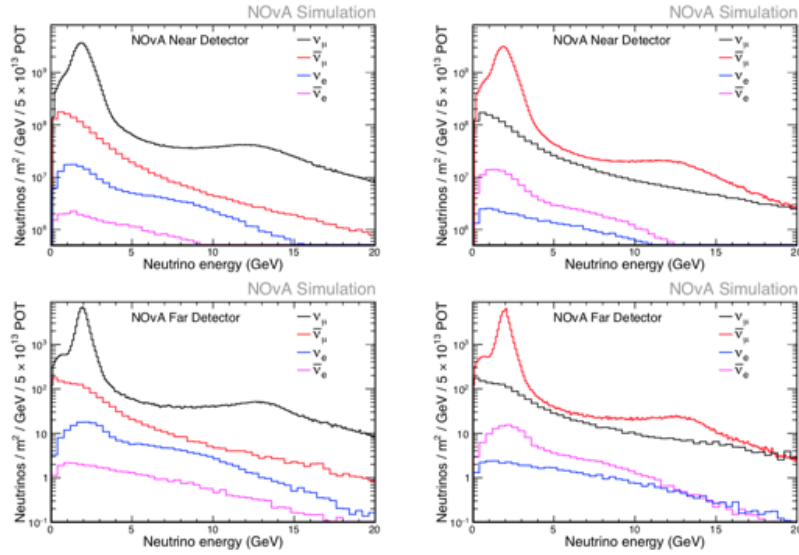
Figure A.4: FHC (left) and RHC (bottom) fluxes for NOvA near detector (top) and far detector (bottom) for the medium energy configuration.

has a fiducial mass of 300 metric tons and has a cross-section of $4.2 \times 4.2m^2$ with a length of 15.8 meters along the beam direction. The far detector has a mass of 14 kilo tons and cross-section area of $15.5 \times 15.5m^2$ with a length of 60 meters. The far detector is also the largest plastic structure in the world. Because of the off-axis detector location, NOvA sees a narrow neutrino flux peaking at the oscillation probability maxima.

B Shifted to Nominal Focusing Parameter Flux Ratio in Different Daisy Bins of MINERvA Detector

Ratio of neutrino fluxes in the 7 daisy regions of MINERvA detector when one of the focusing parameters is shifted by $\pm 1\,\sigma$ from its nominal position are shown from figures B.1 through B.10.
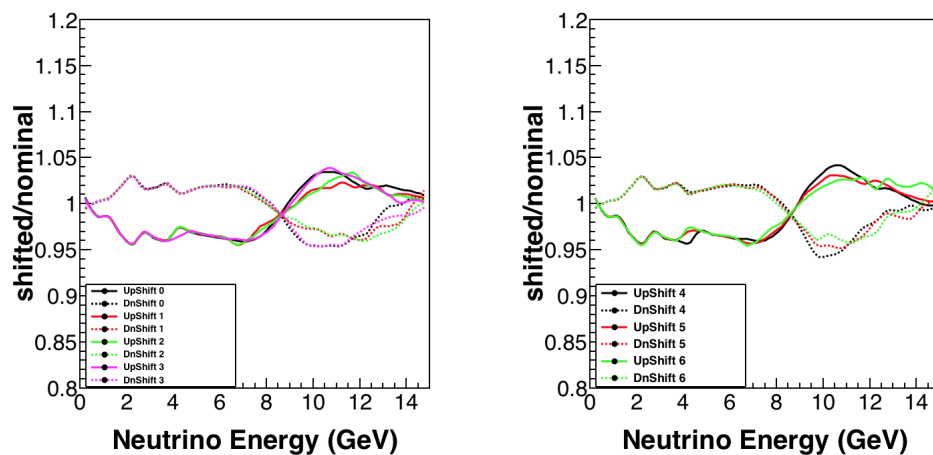
Figure B.1: Shifted to nominal neutrino flux ratio when the proton beam spot size is changed by $\pm 1\sigma$. The left plot has the ratio for the central and left daisy bins of the MINERvA detector and the right plot has the ratio for right daisy bins of the detector.
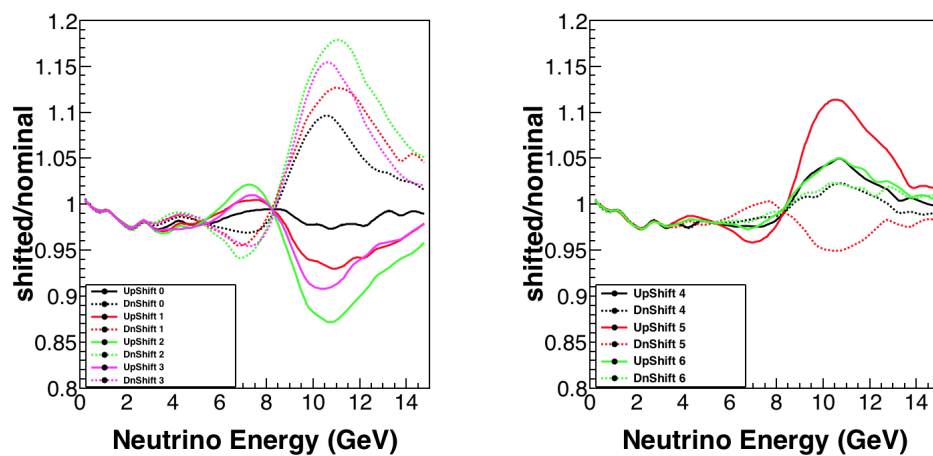
Figure B.2: Shifted to nominal neutrino flux ratio when the horizontal position of proton beam is changed by $\pm 1\sigma$. The left plot has the ratio for the central and left daisy bins of the MINERvA detector and the right plot has the ratio for right daisy bins of the detector.
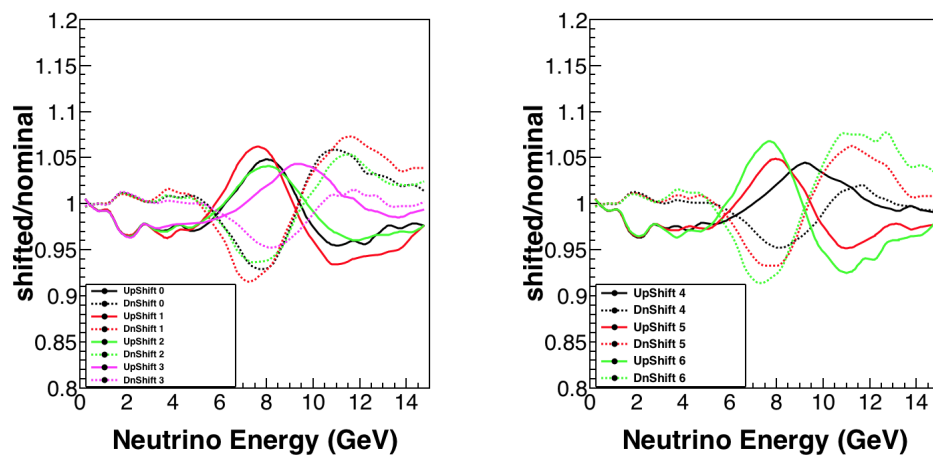
Figure B.3: Shifted to nominal neutrino flux ratio when the vertical position of proton beam is changed by $\pm 1\sigma$. The left plot has the ratio for the central and left daisy bins of the MINERvA detector and the right plot has the ratio for right daisy bins of the detector.
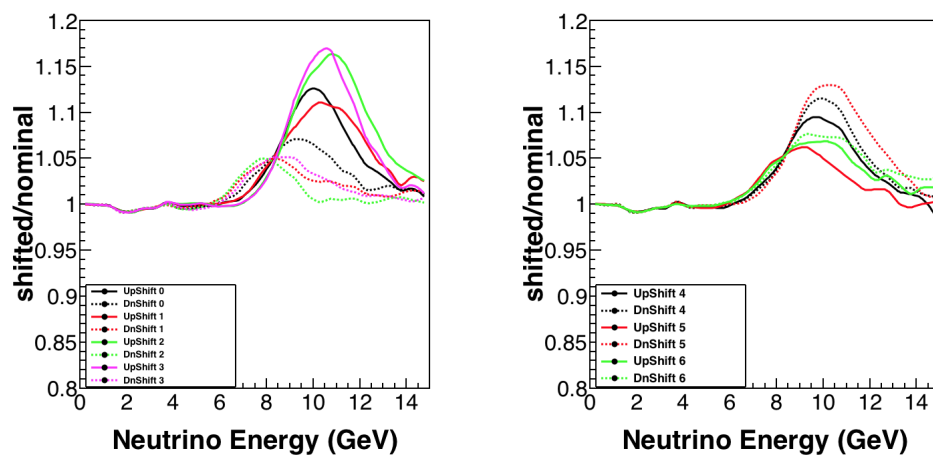
Figure B.4: Shifted to nominal neutrino flux ratio when the horn is moved horizontally by $\pm 1\sigma$. The left plot has the ratio for the central and left daisy bins of the MINERvA detector and the right plot has the ratio for right daisy bins of the detector.
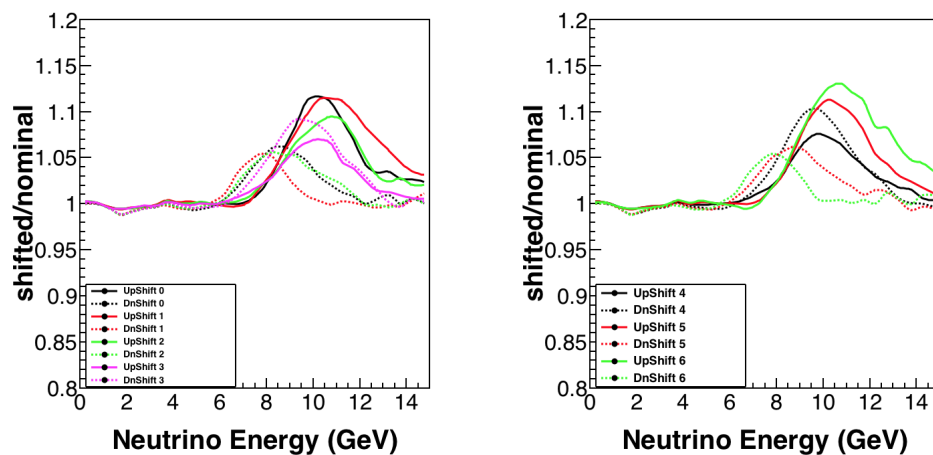
Figure B.5: Shifted to nominal neutrino flux ratio when the horn is moved vertically by $\pm 1\sigma$. The left plot has the ratio for the central and left daisy bins of the MINERvA detector and the right plot has the ratio for right daisy bins of the detector.
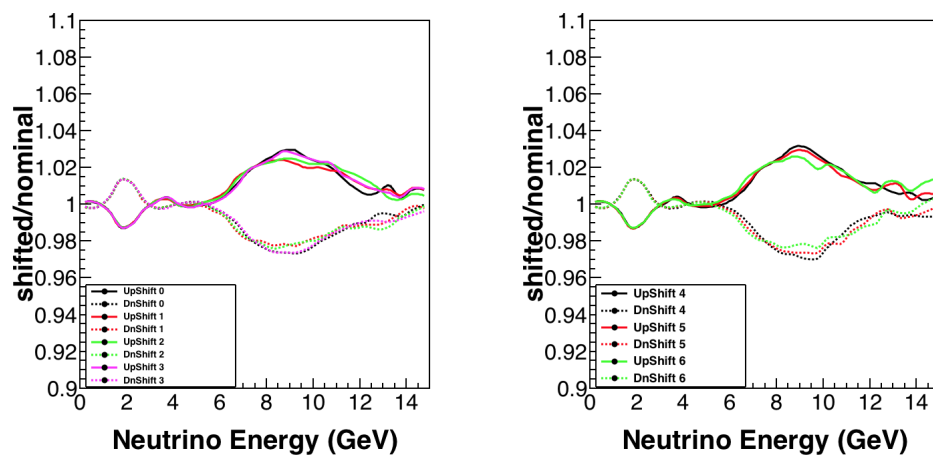
Figure B.6: Shifted to nominal neutrino flux ratio when the horn current is changed by $\pm 1\sigma$. The left plot has the ratio for the central and left daisy bins of the MINERvA detector and the right plot has the ratio for right daisy bins of the detector.
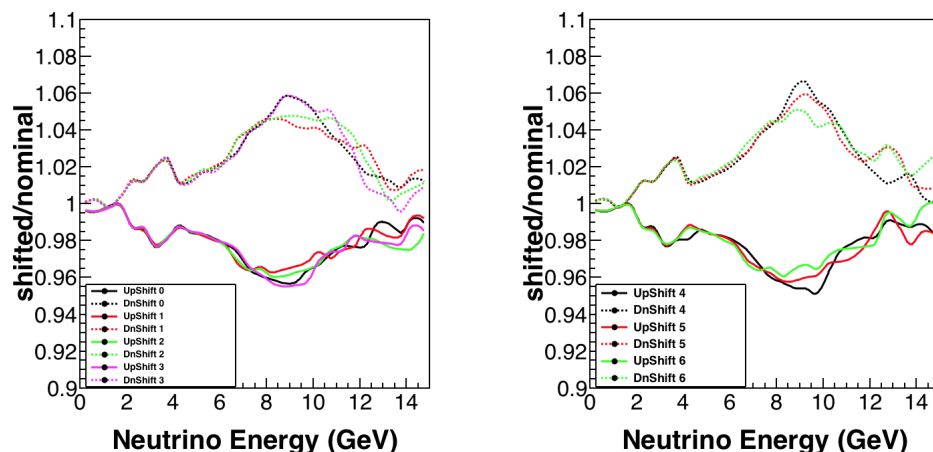
Figure B.7: Shifted to nominal neutrino flux ratio when the horn water layer is changed by $\pm 1\sigma$. The left plot has the ratio for the central and left daisy bins of the MINERvA detector and the right plot has the ratio for right daisy bins of the detector.
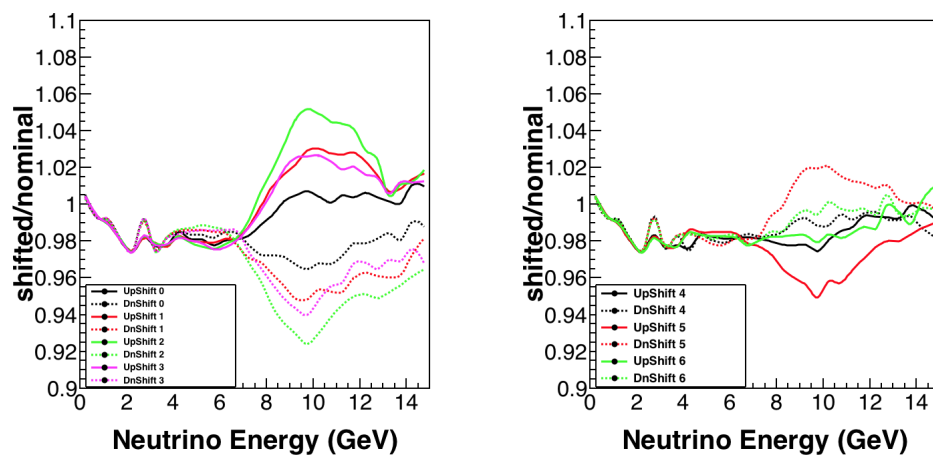
Figure B.8: Shifted to nominal neutrino flux ratio when the target is moved horizontally by $\pm 1\sigma$. The left plot has the ratio for the central and left daisy bins of the MINERvA detector and the right plot has the ratio for right daisy bins of the detector.
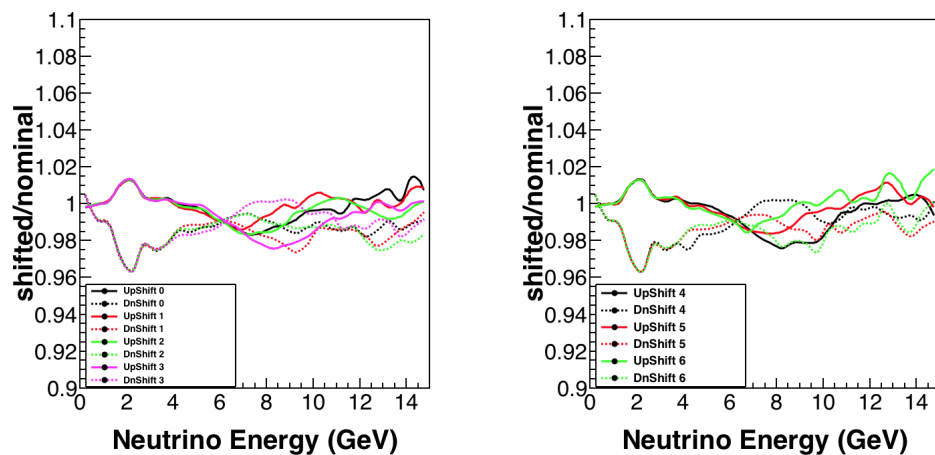
Figure B.9: Shifted to nominal neutrino flux ratio when the target is moved vertically by $\pm 1\sigma$. The left plot has the ratio for the central and left daisy bins of the MINERvA detector and the right plot has the ratio for right daisy bins of the detector.
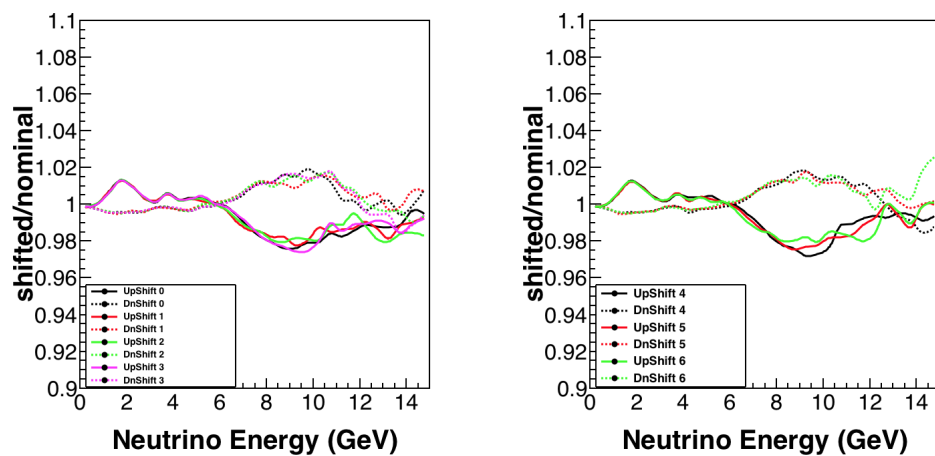
Figure B.10: Shifted to nominal neutrino flux ratio when the target is moved along beam direction by $\pm 1\sigma$. The left plot has the ratio for the central and left daisy bins of the MINERvA detector and the right plot has the ratio for right daisy bins of the detector.

C   Comparison of data with cross-section models (Data unfolded with respective models

Table 6.13 in chapter 6.20 shows the χ^2 comparison between data and various models where data is unfolded with MINERvA Tune v1 generated matrix. In table C.1, data is unfolded with the respective models.

C.1   Effect of Shift in Muon Energy Scale in anti-neutrino CCQELike Cross-section

One of the deliverables of the thesis is the prescription from the low-nu fits (discussed in chapter 5) which suggests that the muon energy scale has to be shifted by 1.8 σ from its original value in the data to remove the discrepancy between the data and the simulation in the MINERvA ME run. In this section, we look at the effect of the energy scale shift in the $\bar{\nu}_\mu$ CCQELike cross-section.

Figures C.1 and C.2 shows the effect of shifting the muon energy scale on the 1D cross-sections as a function of neutrino energy (QE based) and four momentum transfer squared

Models	χ^2/NDF (ME-$\bar{\nu}_\mu$)
MINERvA Tune v1	320/171
MINERvA Tune v2	300/171
GENIE (2.12.16)	391/171
GENIE+2p2h	516/171
GENIE+Pion Tune	405/171
GENIE+RPA	254/171
GENIE+2p2h+RPA	318/171
GENIE+RPA+PionTune	266/171
GENIE+2p2h+PionTune	485/171

Table C.1: Linear χ^2 comparison between various models and data for 2D cross-section as a function of muon kinematics. The full covariance matrix (statistical+systematics) is taken into account to compute the χ^2.
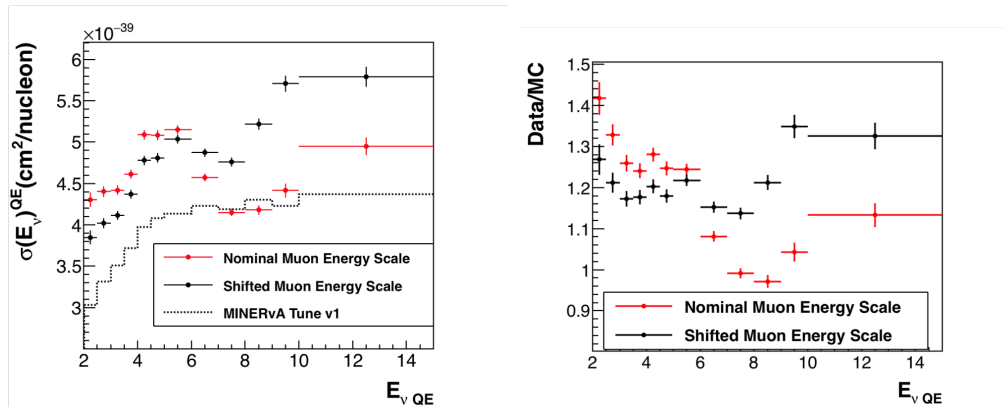
Figure C.1: CCQELike cross-section as a function of $E_{\nu\,QE}$. The errors on the data-cross-section (red and black markers) are stat errors only. Black points are the data cross-section when the muon energy scale is not shifted and red points are the data cross-section when the muon energy scale is shifted. Dotted black line shows the cross-section prediction from MINERvA Tune v1. On the right is the ratio between data and simulation (MINERvA Tune v1). Cross-sections are extracted using the flux without $\nu + e$ constrain.
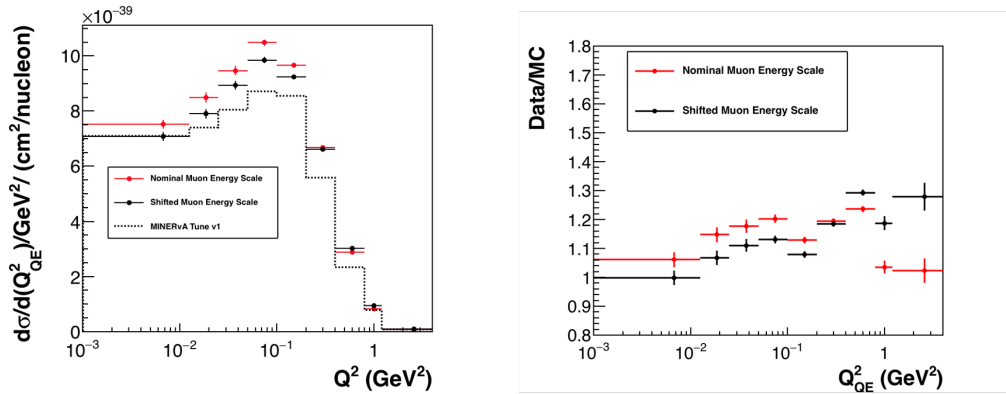
Figure C.2: CCQELike cross-section as a function of Q^2_{QE}. The errors on the data cross-section (red and black markers) are stat errors only. Black points are the data cross-section when the muon energy scale is not shifted and red points are the data cross-section when the muon energy scale is shifted. Dotted black line shows the cross-section prediction from MINERvA Tune v1. On the right is the ratio between data and simulation (MINERvA Tune v1). Cross-sections are extracted using the flux without $\nu + e$ constrain.

(QE based). Ratio plot in figure C.1 shows that the shift in neutrino energy removes the data MC shape discrepancy. Similarly, figure C.2 shows that the high Q^2 events are more sensitive to the shift in muon energy scale. The χ^2 comparison between data and MINERvA Tune v1 MC gives 487 when muon energy scale is not shifted (for cross-section as a function of muon p_T vs. p_z). Note that the χ^2 is 320 when the muon energy scale is shifted in the data. The number of degrees of freedom is 171 in both cases.

D Table of Parameters of Systematic Uncertainties in the Cross-section

Analysis

Cross-section Models	Central Value	1σ uncertainty	Note	Source
MaCCQE	0.99 GeV/c2	-15%+25%	Axial Mass:CCQE	[128]
MaRES	1.12 GeV/c2	±20%	Axial Mass:Resonance	[128]
MvRES	0.84 GeV/c2	±10%	Vector Mass:Resonance	[128]
AhtBy	0.538	±20%	(Bodek Yang Parameter) Scaling on Q^2	[25]
BhtBy	0.305	±20%	(Bodek Yang Parameter) Scaling on Q^2	[25]
Cv1uBy	0.291	±25%	(Bodek Yang Parameter) Scaling on Q^2	[25]
CV2uBy	0.189	±25%	(Bodek Yang Parameter) Scaling on Q^2	[25]
Rvn1pi	1	±50%	(Scale) Resonant (1) pion production cross-section (neutrino-neutron interaction)	[128]

Table D.1: Parameter values (wherever applicable) and corresponding uncertainties in GENIE .
cross-section model category. Table continued in table D.2

Rvn2pi	1	±50%	(Scale) Resonant (2) pions production cross-section (neutrino-proton interaction)	[128]
Rvp1pi	1	±50%	(Scale) Resonant (1) pion production cross-section(neutrino-proton interaction)	[128]
Rvp2pi	1	±50%	(Scale) Resonant (2) pions production cross-section(neutrino proton interaction)	[128]
CCQEPauli-SupViaKF	k=1.007	±30%	Pauli suppression effect on CCQE cross-section	[128]
VecFFCCQE-Shape	BBA05	Dipole variation	Shape of CCQE cross-section when Vector Form Factor changes from BBA05 to Dipole	[128]

Table D.2: Parameter values (wherever applicable) and corresponding uncertainties in GENIE cross-section model category.

Final State Models	Central Value	1σ uncertainty	Note	Source
AKYxF1pi	1	$\pm$ 20%	Variation in Feynman scaling	[128]
FrAbsN	1	$\pm$ 20%	Nucleon Absorption scale	[25] [128]
FrAbsPi	1	$\pm$ 20%	Pion Absorption scale	[25] [128]
FrPiProd N	1	$\pm$ 20%	(Scale) Pion Nucleon Production Cross-section	[25] [128]
FrPiProd Pi	1	$\pm$ 20%	(Scale)of Pion Production Cross-section	[25] [128]
FrCEx N	1	$\pm$ 50%	(Scale) Nucleon Charge Exchange Cross-section	[25] [128]
FrCEx Pi	1	$\pm$ 50%	(Scale) Pion Charge Exchange Cross-section	[25] [128]

Table D.3: Parameter values (wherever applicable) and corresponding uncertainties in final state interaction model. Table continued in table D.4.

Final State Models	Central Value	1σ uncertainty	Note	Source
FrElas Pi	1	$\pm$ 10%	(Scale) Pion Elastic Scattering Cross-section	[25] [128]
FrElas N	1	$\pm$ 30%	(Scale) Nucleon Elastic Scattering Cross-section	[25] [128]
FrInel N	1	$\pm$ 40%	(Scale) Nucleon Inelastic Scattering Cross-section	[25] [128]
FrInel Pi	1	$\pm$ 40%	(Scale) Pion Inelastic Scattering Cross-section	[25] [128]
MFP N	1	$\pm$ 20%	(Scale) Nucleon Mean Free Path	[25] [128]
MFP Pi	1	$\pm$ 20%	(Scale) Pion Mean Free Path	[25] [128]
RDecBR1gamma	-	$\pm$ 50%	Resonant decay photon branching ratio	[128]
Theta Delta 2 N pi	-	On/Off	Delta decay to N pions	[128]

Table D.4: Parameter values (wherever applicable) and corresponding uncertainties in final state interaction model.

Muon Reconstruction	Central Value	1σ uncertainty	Note	Source
Muon Energy MINOS (Range)	1.036	$\pm 0.984\%$	Scale on Muon Momentum reconstructed in MINOS	[52]
Muon Energy MINOS (Curvature (<2 GeV))	1	$\pm 2.5\%$	Scale on Muon Momentum reconstructed in MINOS by curvature	[52]
Muon Energy MINOS (Curvature>2 GeV)	1	$\pm$ 0.6%	Scale on Muon Momentum reconstructed in MINOS by curvature	[52]
Muon Energy MINERvA	P_μ in MINERvA	± 17 MeV	Absolute uncertainty on Muon Momentun reconstructed in MINERvA (Tracker)	[52]

Table D.5: Parameter values (wherever applicable) and corresponding uncertainties related to muon energy reconstruction. Table continue in table D.6.

Muon Reconstruction	Central Value	1σ uncertainty	Note	Source
Beam Angle X	0	± 0.1 mrad	Uncertainty on neutrino beam angle (horizontal)	[153]
Beam Angle Y	0	0.09 mrad	Uncertainty on neutrino beam angle (vertical)	[153]
Muon Energy Resolution	0	$0.004\pm\%$	Uncertainty on the resolution of Muon Energy	[50]
Muon Angle Resolution	0.002	± 0.002 rads	Uncertainty on the resolution of Muon track angle	[50]

Table D.6: Parameter values (wherever applicable) and corresponding uncertainties related to muon energy reconstruction.

Recoil energy Reconstruction	Central Value	1σ uncertainty	Note	Source
EM	1	$\pm 3\%$	Uncertainty on the fraction of the energy due to the EM particles in the total recoil energy	[52]
Meson (Pion between 0.4 to 1.9 GeV KE)	1	$\pm 4\%$	Uncertainty on the fraction of the energy due to Mesons in the total recoil energy	[52]
Meson (Other Pions and mesons)	1	$\pm 5\%$	Uncertainty on the fraction of the energy due to meson in the total recoil energy	[52]
Proton (KE>0.1 GeV)	1	$\pm 3\%$	Uncertainty on the fraction of the energy due to protons in the total recoil energy	[52]
Proton (0.05<KE<0.1 GeV)	1	$\pm 3.5\%$	Uncertainty on the fraction of the energy due to protons in the total recoil energy	[52]
Other	1	$\pm 20\%$	Uncertainty on the fraction of the energy due to particles not included above (except neutrons)	[52]

Table D.7: Parameter values (wherever applicable) and corresponding uncertainties related to recoil energy reconstruction category.

GEANT	Central Value	1σ uncertainty	Note	Source
Pion	GEANT cross-section	±10%	Uncertainty on first pion inelastic interaction cross-section from GEANT4	[94]
Proton	GEANT cross-section	±10%	Uncertainty on first proton inelastic interaction cross-section from GEANT4	[94]
Neutron	GEANT cross-section	±10%	Uncertainty on first neutron inelastic interaction cross-section from GEANT4	[94]

Table D.8: Parameter values (wherever applicable) and corresponding uncertainties related to GEANT Particles category.

Normalization	Central Value	1σ uncertainty	Note	Source
Muon Reconstruction Efficiency	upto 0.995	Muon angle dependent	Uncertainty on the reconstruction on muon tracks in MINOS	[142]

Table D.9: Parameter values (wherever applicable) and corresponding uncertainties related to Normalization category.

Other	Central Value	1σ uncertainty	Note	Source
True Proton KE Cut	120 MeV	$\pm$20 MeV	Uncertainty on the true proton KE cut in the CCQE like Signal Definition	-

Table D.10: Parameter values (wherever applicable) and corresponding uncertainties related to Normalization category.

Low Recoil Fits	Central Value	1σ uncertainty	Note	Source
Low Recoil Fits	-	On/Off	See Figure 6.2 and [83].	-
RPA	-	On/Off	See Figure 6.79 and [83].	

Table D.11: Parameter values (wherever applicable) and corresponding uncertainties related to Low Recoil Fits category.

E   Tables of Cross-sections and Errors

	0.0-0.075	0.075-0.15	0.15-0.25	0.25-0.325	0.325-0.4	0.4-0.475
1.5-2.0	25.21	88.42	208.23	225.69	242.53	229.38
2.0-2.5	16.54	68.09	189.05	253.09	276.12	271.55
2.5-3.0	27.51	76.05	229.73	297.4	296.79	298.42
3.0-3.5	25.98	80.72	239.33	275.17	330.16	346.47
3.5-4.0	26.39	94.92	248.09	293.78	358.62	369.24
4.0-4.5	27.55	100.13	285.27	364.81	425.67	412.33
4.5-5.0	33.63	119.24	331.38	363.5	401.73	426.42
5.0-5.5	32.57	113.61	335.76	365.91	461.22	441.44
5.5-6.0	27.2	98.11	284.81	312.79	408.67	410.41
6.0-7.0	39.47	138.24	407.62	482.72	589.15	635.88
7.0-8.0	26.02	82.27	243.49	292.45	376.69	392.92
8.0-9.0	13.74	45.24	121.92	142.25	191.88	205.35
9.0-10.0	5.55	20.92	53.06	58.15	76.73	83.89
10.0-15.0	6.05	24.82	59.19	63.9	89.54	97.74

	0.475-0.55	0.55-0.7	0.7-0.85	0.85-1.0	1.0-1.25	1.25-1.5	1.5-2.5
1.5-2.0	234.58	242.1	13.28	0.0	0.0	0.0	0.0
2.0-2.5	274.93	371.78	200.91	16.99	0.0	0.0	0.0
2.5-3.0	293.12	513.77	338.97	192.17	29.67	0.0	0.0
3.0-3.5	313.44	569.34	394.82	302.33	222.7	5.21	0.0
3.5-4.0	383.72	629.11	453.18	327.16	353.42	85.91	0.0
4.0-4.5	403.4	711.52	512.12	362.12	434.79	141.07	14.26
4.5-5.0	427.42	772.78	540.69	396.31	423.18	158.32	41.89
5.0-5.5	450.17	770.97	537.8	451.12	333.27	125.55	23.1
5.5-6.0	438.38	724.33	538.85	459.22	308.43	106.03	22.32
6.0-7.0	630.62	1171.42	977.64	688.4	505.15	158.35	35.5
7.0-8.0	425.44	753.26	558.52	352.91	256.96	85.39	19.0
8.0-9.0	213.21	377.16	272.78	174.99	123.61	38.05	12.77
9.0-10.0	92.93	168.35	117.81	79.4	75.05	21.12	9.55
10.0-15.0	114.08	178.86	133.63	94.87	100.86	44.86	22.78

Table E.1: Final cross-section as a function of muon kinematics. The horizontal rows are muon transverse momentum (p_T GeV/c) and vertical columns are muon longitudinal momentum ($p_{||}$ GeV/c). The cross-section is in the units of $10^{-44}/\nu/cm^2/nucleon$.

	0.0-0.075	0.075-0.15	0.15-0.25	0.25-0.325	0.325-0.4	0.4-0.475
1.5-2.0	16.91	32.67	60.13	72.86	90.46	95.98
2.0-2.5	18.42	38.0	78.36	83.84	98.57	94.12
2.5-3.0	19.29	44.12	98.99	91.23	104.34	94.31
3.0-3.5	20.12	45.2	106.82	91.83	112.07	95.41
3.5-4.0	19.9	45.36	105.58	93.04	108.93	99.4
4.0-4.5	18.11	43.75	108.52	91.97	110.76	96.54
4.5-5.0	17.36	44.84	107.54	92.99	107.9	92.71
5.0-5.5	20.22	54.15	133.47	105.27	129.41	95.57
5.5-6.0	19.37	47.15	124.12	96.35	114.06	85.14
6.0-7.0	28.35	75.94	204.73	153.28	176.44	128.9
7.0-8.0	19.14	44.46	110.33	82.23	98.85	83.33
8.0-9.0	10.15	23.61	51.31	51.1	58.57	66.26
9.0-10.0	4.9	10.71	24.97	24.98	29.53	31.29
10.0-15.0	7.56	17.61	34.52	32.88	38.95	43.81

	0.475-0.55	0.55-0.7	0.7-0.85	0.85-1.0	1.0-1.25	1.25-1.5	1.5-2.5
1.5-2.0	107.47	121.48	21.0	0.0	0.0	0.0	0.0
2.0-2.5	110.38	158.26	132.06	21.21	0.0	0.0	0.0
2.5-3.0	98.18	156.25	150.51	122.15	31.51	0.0	0.0
3.0-3.5	95.53	155.51	153.56	149.66	153.81	7.58	0.0
3.5-4.0	99.92	152.07	160.16	158.71	201.26	65.94	0.0
4.0-4.5	98.53	155.35	163.19	167.63	219.5	89.87	11.92
4.5-5.0	92.7	155.58	168.23	168.54	221.59	89.35	32.72
5.0-5.5	97.28	159.73	161.16	134.59	145.97	57.22	24.44
5.5-6.0	88.84	142.44	142.7	121.57	124.72	45.52	21.0
6.0-7.0	121.75	207.62	212.6	167.05	182.69	59.72	21.4
7.0-8.0	76.34	120.55	112.89	84.47	87.51	34.8	16.43
8.0-9.0	60.16	79.11	61.59	45.32	37.17	17.41	10.96
9.0-10.0	31.67	42.92	33.7	21.84	23.02	11.36	7.67
10.0-15.0	43.33	58.08	48.35	39.36	37.99	22.38	13.05

Table E.2: Statistical Error on the final data cross-section as a function of muon-kinematics. The horizontal rows are muon transverse momentum (p_T GeV/c) and vertical columns are muon longitudinal momentum ($p_{||}$ GeV/c). The cross-section is in the units of $10^{-44}/\nu/cm^2/nucleon$.

	0.0-0.075	0.075-0.15	0.15-0.25	0.25-0.325	0.325-0.4	0.4-0.475
1.5-2.0	25.21	88.42	208.23	225.69	242.53	229.38
2.0-2.5	16.54	68.09	189.05	253.09	276.12	271.55
2.5-3.0	27.51	76.05	229.73	297.4	296.79	298.42
3.0-3.5	25.98	80.72	239.33	275.17	330.16	346.47
3.5-4.0	26.39	94.92	248.09	293.78	358.62	369.24
4.0-4.5	27.55	100.13	285.27	364.81	425.67	412.33
4.5-5.0	33.63	119.24	331.38	363.5	401.73	426.42
5.0-5.5	32.57	113.61	335.76	365.91	461.22	441.44
5.5-6.0	27.2	98.11	284.81	312.79	408.67	410.41
6.0-7.0	39.47	138.24	407.62	482.72	589.15	635.88
7.0-8.0	26.02	82.27	243.49	292.45	376.69	392.92
8.0-9.0	13.74	45.24	121.92	142.25	191.88	205.35
9.0-10.0	5.55	20.92	53.06	58.15	76.73	83.89
10.0-15.0	6.05	24.82	59.19	63.9	89.54	97.74

	0.475-0.55	0.55-0.7	0.7-0.85	0.85-1.0	1.0-1.25	1.25-1.5	1.5-2.5
1.5-2.0	234.58	242.1	13.28	0.0	0.0	0.0	0.0
2.0-2.5	274.93	371.78	200.91	16.99	0.0	0.0	0.0
2.5-3.0	293.12	513.77	338.97	192.17	29.67	0.0	0.0
3.0-3.5	313.44	569.34	394.82	302.33	222.7	5.21	0.0
3.5-4.0	383.72	629.11	453.18	327.16	353.42	85.91	0.0
4.0-4.5	403.4	711.52	512.12	362.12	434.79	141.07	14.26
4.5-5.0	427.42	772.78	540.69	396.31	423.18	158.32	41.89
5.0-5.5	450.17	770.97	537.8	451.12	333.27	125.55	23.1
5.5-6.0	438.38	724.33	538.85	459.22	308.43	106.03	22.32
6.0-7.0	630.62	1171.42	977.64	688.4	505.15	158.35	35.5
7.0-8.0	425.44	753.26	558.52	352.91	256.96	85.39	19.0
8.0-9.0	213.21	377.16	272.78	174.99	123.61	38.05	12.77
9.0-10.0	92.93	168.35	117.81	79.4	75.05	21.12	9.55
10.0-15.0	114.08	178.86	133.63	94.87	100.86	44.86	22.78

Table E.3: Total Systematic Error on the final data cross-section as a function of muon-kinematics. The horizontal rows are muon transverse momentum (p_T GeV/c) and vertical columns are muon longitudinal momentum ($p_\parallel$ GeV/c). The cross-section is in the units of $10^{-44}/\nu/cm^2/nucleon$.

	0.0-0.075	0.075-0.15	0.15-0.25	0.25-0.325	0.325-0.4	0.4-0.475
1.5-2.0	7.31	24.49	65.8	85.28	101.25	100.69
2.0-2.5	13.07	44.74	119.17	161.48	191.36	193.68
2.5-3.0	16.74	60.92	174.68	213.88	253.62	269.72
3.0-3.5	19.89	69.35	199.63	236.57	302.06	315.86
3.5-4.0	20.9	75.75	207.58	269.6	330.54	366.5
4.0-4.5	21.08	80.22	230.34	294.49	366.89	386.09
4.5-5.0	23.0	91.1	257.98	322.69	393.83	422.0
5.0-5.5	27.9	101.6	290.83	341.29	431.42	440.24
5.5-6.0	27.42	95.19	281.92	325.59	409.93	405.0
6.0-7.0	40.42	146.36	444.69	519.49	625.12	663.13
7.0-8.0	23.6	85.11	246.86	284.28	348.52	376.28
8.0-9.0	10.16	40.67	112.79	127.16	155.12	176.83
9.0-10.0	4.29	16.63	47.16	51.4	66.12	66.99
10.0-15.0	3.91	20.7	55.4	57.95	76.4	83.25

	0.475-0.55	0.55-0.7	0.7-0.85	0.85-1.0	1.0-1.25	1.25-1.5	1.5-2.5
1.5-2.0	119.81	123.96	5.02	0.0	0.0	0.0	0.0
2.0-2.5	224.23	356.75	178.61	10.47	0.0	0.0	0.0
2.5-3.0	266.23	498.06	298.74	145.74	16.9	0.0	0.0
3.0-3.5	309.68	587.05	354.03	219.19	130.73	1.46	0.0
3.5-4.0	363.69	630.79	405.66	254.72	203.59	45.18	0.0
4.0-4.5	394.88	714.45	451.9	285.95	227.35	76.27	4.77
4.5-5.0	423.06	790.26	502.41	299.54	238.76	81.72	15.13
5.0-5.5	436.07	805.23	530.29	294.57	223.05	66.39	13.79
5.5-6.0	421.84	756.4	491.41	273.67	190.54	52.6	13.25
6.0-7.0	637.57	1149.35	734.99	376.86	273.86	68.91	16.61
7.0-8.0	347.87	600.21	385.58	198.25	131.1	38.01	11.13
8.0-9.0	163.06	237.84	161.43	95.73	62.14	17.43	5.98
9.0-10.0	67.5	101.42	69.35	38.99	31.51	8.8	3.19
10.0-15.0	83.3	121.92	89.38	64.77	51.11	18.77	8.79

Table E.4: Flux Error on the final data cross-section as a function of muon-kinematics. The horizontal rows are muon transverse momentum (p_T GeV/c) and vertical columns are muon longitudinal momentum ($p_{||}$ GeV/c). The cross-section is in the units of $10^{-44}/\nu/cm^2/nucleon$.

	0.0-0.075	0.075-0.15	0.15-0.25	0.25-0.325	0.325-0.4	0.4-0.475
1.5-2.0	6.15	19.68	54.1	68.89	82.78	79.46
2.0-2.5	10.81	36.42	98.27	133.62	155.65	153.87
2.5-3.0	13.63	50.19	142.15	175.18	207.19	216.05
3.0-3.5	16.23	57.33	162.12	195.5	244.01	257.87
3.5-4.0	17.14	61.61	167.69	224.24	271.44	294.35
4.0-4.5	17.31	65.07	186.9	244.74	303.55	313.32
4.5-5.0	18.97	74.45	211.39	265.49	324.54	343.61
5.0-5.5	23.13	84.36	241.3	277.25	352.9	357.81
5.5-6.0	23.06	79.66	234.98	266.82	334.87	331.56
6.0-7.0	34.1	123.13	371.43	431.24	514.04	541.82
7.0-8.0	19.92	71.31	205.13	233.42	284.54	306.18
8.0-9.0	8.39	33.28	92.17	103.62	125.79	141.68
9.0-10.0	3.63	13.65	38.38	42.25	54.13	55.3
10.0-15.0	3.37	17.33	45.74	47.73	62.63	67.92

	0.475-0.55	0.55-0.7	0.7-0.85	0.85-1.0	1.0-1.25	1.25-1.5	1.5-2.5
1.5-2.0	96.97	101.24	4.14	0.0	0.0	0.0	0.0
2.0-2.5	179.77	290.1	153.71	9.04	0.0	0.0	0.0
2.5-3.0	215.92	408.23	256.56	128.26	13.92	0.0	0.0
3.0-3.5	250.0	479.23	305.31	189.87	108.61	1.21	0.0
3.5-4.0	294.7	510.99	345.47	220.19	169.04	36.36	0.0
4.0-4.5	321.97	584.57	387.85	249.65	185.45	61.72	4.11
4.5-5.0	344.39	644.33	425.81	258.63	195.17	66.66	12.13
5.0-5.5	355.18	659.32	437.33	242.01	182.49	53.99	11.21
5.5-6.0	345.14	623.18	405.06	223.14	155.01	42.68	10.75
6.0-7.0	522.51	945.01	605.88	305.05	221.72	56.48	13.75
7.0-8.0	284.81	493.92	319.85	161.96	106.6	32.23	9.44
8.0-9.0	133.51	199.25	136.69	82.03	54.38	16.13	5.64
9.0-10.0	55.78	88.84	61.08	35.24	29.57	8.51	3.42
10.0-15.0	68.42	104.8	78.2	56.49	45.96	17.92	9.33

Table E.5: Error due to Muon Reconstruction on the final data cross-section as a function of muon-kinematics. The horizontal rows are muon transverse momentum (p_T GeV/c) and vertical columns are muon longitudinal momentum ($p_{||}$ GeV/c). The cross-section is in the units of $10^{-44}/\nu/cm^2/nucleon$.

	0.0-0.075	0.075-0.15	0.15-0.25	0.25-0.325	0.325-0.4	0.4-0.475
1.5-2.0	37.64	114.24	254.23	232.11	328.49	411.18
2.0-2.5	51.89	184.56	494.84	425.54	598.26	597.36
2.5-3.0	55.59	197.88	700.75	584.58	822.62	690.51
3.0-3.5	70.23	279.08	837.91	674.8	729.79	853.8
3.5-4.0	69.83	269.31	831.39	717.54	894.59	981.8
4.0-4.5	78.17	290.75	1012.13	832.79	959.81	1057.21
4.5-5.0	81.17	317.35	1093.7	924.9	1001.69	1173.54
5.0-5.5	77.82	270.77	923.07	822.31	1062.15	1120.62
5.5-6.0	68.14	224.22	777.54	799.95	993.62	1055.44
6.0-7.0	102.73	342.28	1255.11	1331.27	1416.65	1670.69
7.0-8.0	58.69	180.91	705.89	820.8	814.13	850.03
8.0-9.0	26.84	93.82	315.27	358.04	432.63	430.59
9.0-10.0	11.86	44.16	135.12	149.81	182.5	159.78
10.0-15.0	10.88	61.44	163.87	185.34	204.52	239.36

	0.475-0.55	0.55-0.7	0.7-0.85	0.85-1.0	1.0-1.25	1.25-1.5	1.5-2.5
1.5-2.0	324.51	391.94	23.86	0.0	0.0	0.0	0.0
2.0-2.5	593.31	829.36	452.72	44.29	0.0	0.0	0.0
2.5-3.0	708.21	961.27	715.83	482.82	80.44	0.0	0.0
3.0-3.5	692.83	1105.21	772.51	830.84	538.06	9.81	0.0
3.5-4.0	936.67	1115.92	934.13	852.72	975.58	208.07	0.0
4.0-4.5	905.84	1401.97	1151.6	1000.5	1054.19	350.04	24.35
4.5-5.0	1053.26	1468.77	1203.57	1085.97	1082.95	352.16	65.88
5.0-5.5	1064.68	1403.66	1086.13	995.24	1005.52	286.06	67.05
5.5-6.0	952.91	1381.56	1085.02	924.4	877.15	256.31	60.82
6.0-7.0	1426.73	1896.35	1569.84	1317.81	1303.17	351.62	99.63
7.0-8.0	770.95	983.19	846.41	655.26	593.44	185.2	49.8
8.0-9.0	335.19	606.28	396.57	258.81	198.49	79.73	30.54
9.0-10.0	171.47	274.88	169.74	117.62	113.74	41.0	15.28
10.0-15.0	237.36	334.55	237.51	212.54	181.76	85.57	45.51

Table E.6: Error due to various models on the final data cross-section as a function of muon-kinematics. The horizontal rows are muon transverse momentum (p_T GeV/c) and vertical columns are muon longitudinal momentum ($p_{||}$ GeV/c). The cross-section is in the units of $10^{-44}/\nu/GeV^2/cm^2/nucleon$.

	0.0-0.0125	0.0125-0.025	0.025-0.05	0.05-0.1	0.1-0.2	0.2-0.4
2.0-2.5	5.11	5.94	14.11	28.01	44.94	41.86
2.5-3.0	3.04	4.02	10.07	22.88	30.73	35.5
3.0-3.5	2.78	2.39	5.97	10.87	25.5	25.26
3.5-4.0	2.17	2.75	6.62	14.88	19.67	23.99
4.0-4.5	2.43	3.2	6.28	15.95	25.97	29.71
4.5-5.0	2.66	3.52	6.45	11.97	19.29	26.56
5.0-6.0	4.05	5.82	14.9	25.37	46.56	48.12
6.0-7.0	2.38	2.35	6.28	13.51	30.34	47.05
7.0-8.0	3.28	3.8	8.19	19.46	41.22	70.55
8.0-9.0	5.08	6.26	10.82	23.68	55.58	95.44
9.0-10.0	5.08	7.3	12.58	29.69	64.64	121.34
10.0-15.0	27.24	32.83	63.15	125.76	310.73	388.71

	0.4-0.8	0.8-1.2	1.2-4.0
0.4-0.8	0.8-1.2	1.2-4.0	
2.0-2.5	18.6	0.0	0.0
2.5-3.0	23.34	1.61	0.0
3.0-3.5	22.42	8.88	0.0
3.5-4.0	22.34	13.59	2.87
4.0-4.5	25.35	15.34	11.04
4.5-5.0	25.48	14.75	17.63
5.0-6.0	47.28	32.79	39.88
6.0-7.0	60.15	45.84	37.98
7.0-8.0	81.4	56.86	48.34
8.0-9.0	108.22	64.29	60.66
9.0-10.0	123.58	57.29	85.65
10.0-15.0	631.09	424.64	475.0

Table E.7: Final cross-section as a function of $E_{\nu\,QE}$ and Q^2_{QE}. The horizontal rows are Q^2_{QE} (GeV^2) and vertical columns are neutrino energy (GeV). The cross-section is in the units of $10^{-42}/\nu/cm^2/nucleon$.

	0.0-0.0125	0.0125-0.025	0.025-0.05	0.05-0.1	0.1-0.2	0.2-0.4
2.0-2.5	0.48	0.59	1.0	1.39	2.05	2.64
2.5-3.0	0.34	0.45	0.79	1.03	1.47	1.78
3.0-3.5	0.32	0.35	0.69	0.88	1.33	1.56
3.5-4.0	0.31	0.35	0.65	0.83	1.25	1.52
4.0-4.5	0.28	0.32	0.65	0.83	1.26	1.5
4.5-5.0	0.25	0.3	0.57	0.79	1.16	1.46
5.0-6.0	0.58	0.63	1.42	1.61	2.3	2.36
6.0-7.0	0.51	0.56	1.31	1.53	2.24	2.67
7.0-8.0	0.49	0.54	1.17	1.41	2.11	2.55
8.0-9.0	0.59	0.58	1.11	2.07	3.54	3.71
9.0-10.0	0.74	0.78	1.42	2.72	4.78	5.37
10.0-15.0	4.46	4.51	8.18	15.39	28.25	32.21

	0.4-0.8	0.8-1.2	1.2-4.0
0.4-0.8	0.8-1.2	1.2-4.0	
2.0-2.5	2.05	0.0	0.0
2.5-3.0	1.91	0.26	0.0
3.0-3.5	1.57	0.96	0.0
3.5-4.0	1.54	1.32	0.44
4.0-4.5	1.6	1.46	1.25
4.5-5.0	1.61	1.54	1.62
5.0-6.0	2.24	2.18	4.22
6.0-7.0	2.74	2.31	3.02
7.0-8.0	2.68	2.1	3.31
8.0-9.0	3.56	2.14	3.61
9.0-10.0	6.43	3.42	4.21
10.0-15.0	39.24	22.41	28.91

Table E.8: Statistical Error on Final cross-section as a function of $E_{\nu\,QE}$ and Q^2_{QE}. The horizontal rows are Q^2_{QE} (GeV^2) and vertical columns are neutrino energy (GeV). The cross-section is in the units of $10^{-41}/\nu/cm^2/nucleon$.

	0.0-0.0125	0.0125-0.025	0.025-0.05	0.05-0.1	0.1-0.2	0.2-0.4
2.0-2.5	0.8	0.9	2.03	4.34	7.23	8.47
2.5-3.0	0.5	0.67	1.53	3.52	5.45	6.92
3.0-3.5	0.5	0.51	1.17	2.53	5.04	6.45
3.5-4.0	0.44	0.54	1.18	2.68	4.67	6.49
4.0-4.5	0.46	0.58	1.24	2.94	5.41	7.18
4.5-5.0	0.44	0.59	1.16	2.6	4.69	6.84
5.0-6.0	0.9	1.09	2.65	5.31	9.89	13.0
6.0-7.0	0.66	0.78	1.95	4.07	7.5	11.42
7.0-8.0	0.7	0.84	1.93	4.19	8.08	12.63
8.0-9.0	0.87	1.07	2.13	4.73	9.76	15.32
9.0-10.0	1.06	1.37	2.85	6.18	12.41	20.14
10.0-15.0	5.39	7.03	14.57	28.31	61.42	84.18

	0.4-0.8	0.8-1.2	1.2-4.0
2.0-2.5	3.21	0.0	0.0
2.5-3.0	5.62	0.19	0.0
3.0-3.5	5.63	1.5	0.0
3.5-4.0	5.87	2.37	0.43
4.0-4.5	6.58	2.67	1.48
4.5-5.0	6.55	2.68	2.21
5.0-6.0	12.87	5.31	5.26
6.0-7.0	11.92	5.83	4.99
7.0-8.0	13.08	6.84	5.96
8.0-9.0	15.78	8.01	7.51
9.0-10.0	20.33	9.06	11.74
10.0-15.0	101.24	57.69	62.03

Table E.9: Systematic Error on final cross-section as a function of $E_{\nu\,QE}$ and Q^2_{QE}. The horizontal rows are Q^2_{QE} (GeV^2) and vertical columns are neutrino energy (GeV). The cross-section is in the units of $10^{-41}/\nu/cm^2/nucleon$.

	0.0-0.0125	0.0125-0.025	0.025-0.05	0.05-0.1	0.1-0.2	0.2-0.4
2.0-2.5	0.58	0.63	1.36	3.13	5.38	7.18
2.5-3.0	0.38	0.53	1.11	2.59	4.41	5.85
3.0-3.5	0.4	0.44	0.98	2.25	4.25	5.87
3.5-4.0	0.37	0.46	0.95	2.16	4.19	5.98
4.0-4.5	0.39	0.47	1.05	2.42	4.67	6.46
4.5-5.0	0.34	0.46	0.95	2.27	4.23	6.25
5.0-6.0	0.79	0.9	2.13	4.58	8.57	11.95
6.0-7.0	0.61	0.74	1.83	3.81	6.78	10.29
7.0-8.0	0.61	0.74	1.72	3.63	6.78	10.13
8.0-9.0	0.67	0.82	1.77	3.97	7.67	11.28
9.0-10.0	0.9	1.11	2.48	5.22	10.11	14.93
10.0-15.0	4.51	6.07	12.87	24.82	51.37	72.88

	0.4-0.8	0.8-1.2	1.2-4.0
2.0-2.5	2.52	0.0	0.0
2.5-3.0	5.07	0.1	0.0
3.0-3.5	5.11	1.17	0.0
3.5-4.0	5.37	1.89	0.3
4.0-4.5	6.02	2.14	0.92
4.5-5.0	5.98	2.19	1.2
5.0-6.0	11.85	4.0	3.12
6.0-7.0	10.1	3.27	2.99
7.0-8.0	9.77	3.14	2.98
8.0-9.0	10.54	3.92	3.61
9.0-10.0	14.96	6.43	6.84
10.0-15.0	74.66	34.8	34.64

Table E.10: Flux error on final cross-section as a function of $E_{\nu\,QE}$ and Q^2_{QE}. The horizontal rows are Q^2_{QE} (GeV^2) and vertical columns are neutrino energy (GeV). The cross-section is in the units of $10^{-41}/\nu/cm^2/nucleon$.

	0.0-0.0125	0.0125-0.025	0.025-0.05	0.05-0.1	0.1-0.2	0.2-0.4
2.0-2.5	0.7	0.73	1.84	4.09	5.94	4.29
2.5-3.0	0.36	0.53	1.37	2.87	3.61	4.58
3.0-3.5	0.37	0.26	0.56	1.07	2.82	1.66
3.5-4.0	0.2	0.32	0.74	1.89	1.64	1.89
4.0-4.5	0.25	0.37	0.49	1.98	2.54	2.47
4.5-5.0	0.27	0.41	0.55	1.32	2.2	1.59
5.0-6.0	0.51	0.7	1.85	3.24	4.98	2.73
6.0-7.0	0.18	0.21	0.36	0.55	1.36	3.1
7.0-8.0	0.42	0.44	1.11	2.44	4.46	7.77
8.0-9.0	0.54	0.88	1.0	3.22	6.04	11.13
9.0-10.0	0.47	1.03	1.54	4.0	8.39	12.89
10.0-15.0	2.41	2.63	7.84	12.37	37.45	46.81

	0.4-0.8	0.8-1.2	1.2-4.0
2.0-2.5	2.22	0.0	0.0
2.5-3.0	2.53	0.18	0.0
3.0-3.5	0.86	0.93	0.0
3.5-4.0	0.73	0.65	0.27
4.0-4.5	0.93	0.49	0.86
4.5-5.0	0.97	0.96	1.69
5.0-6.0	1.7	2.08	3.84
6.0-7.0	6.28	4.55	4.13
7.0-8.0	10.57	6.0	5.69
8.0-9.0	13.58	7.96	7.41
9.0-10.0	15.85	7.06	11.53
10.0-15.0	76.0	54.62	56.44

Table E.11: Error due to muon energy reconstruction on final cross-section as a function of $E_{\nu\,QE}$ and Q^2_{QE}. The horizontal rows are Q^2_{QE} (GeV^2) and vertical columns are neutrino energy (GeV). The cross-section is in the units of $10^{-41}/\nu/cm^2/nucleon$.

	0.0-0.0125	0.0125-0.025	0.025-0.05	0.05-0.1	0.1-0.2	0.2-0.4
2.0-2.5	1.17	1.55	2.78	4.39	7.68	12.54
2.5-3.0	0.72	0.87	2.13	3.9	5.84	7.78
3.0-3.5	0.72	0.86	1.84	3.26	5.93	8.33
3.5-4.0	0.69	0.76	1.86	2.92	6.06	8.13
4.0-4.5	0.84	0.99	1.93	3.67	6.59	8.36
4.5-5.0	0.74	0.91	2.13	3.69	5.34	8.13
5.0-6.0	0.86	1.07	2.66	4.48	11.13	15.5
6.0-7.0	0.89	0.84	2.03	5.05	10.26	15.05
7.0-8.0	0.79	1.1	2.0	5.08	10.16	14.55
8.0-9.0	1.08	1.12	3.17	5.92	14.11	19.55
9.0-10.0	1.32	1.47	3.32	8.38	13.22	23.85
10.0-15.0	8.18	10.17	19.46	36.84	75.88	103.95

	0.4-0.8	0.8-1.2	1.2-4.0
2.0-2.5	5.06	0.0	0.0
2.5-3.0	6.6	0.44	0.0
3.0-3.5	8.09	2.7	0.0
3.5-4.0	8.16	5.26	1.06
4.0-4.5	8.77	6.14	3.85
4.5-5.0	9.39	5.8	5.58
5.0-6.0	17.09	12.62	12.47
6.0-7.0	16.94	12.59	10.79
7.0-8.0	17.75	14.45	12.32
8.0-9.0	21.34	13.02	14.75
9.0-10.0	27.7	11.06	13.05
10.0-15.0	129.42	68.53	62.35

Table E.12: Model error on final cross-section as a function of $E_{\nu\ QE}$ and Q^2_{QE}. The horizontal rows are Q^2_{QE} (GeV^2) and vertical columns are neutrino energy (GeV). The cross-section is in the units of $10^{-41}/\nu/cm^2/nucleon$.